University of Crete Physics Department

Development and characterization of an intense attosecond pulse source for XUV-pump-XUV-probe experiments

Ph.D Thesis

Orfanos Ioannis

Heraklion 2020

Supervisors: Prof. D. Charalambidis

Dr. P. Tzallas

Prof. T.P. Rakitzis

Development and characterization of an intense attosecond pulse source for XUV-pump-XUV- probe experiments

Submitted as doctoral thesis to the Department of Physics of University of Crete, Heraklion Crete, Greece

Presented

by

Orfanos Ioannis

Heraklion Crete, 2020

COMMITTEE

Prof. D. Charalambidis	University of Crete
Dr. P. Tzallas	Forth–Iesl
Prof. T.P. Rakitzis	University of Crete
Prof. S.Couris	University of Patras
Dr. P. Samartzis	Forth–Iesl
Prof. D. Anglos	University of Crete
Assos. Prof. E. Iliopoulos	University of Crete

"Judge your success by what you had to give up in order to achieve it"

The Dalai Lama

Στον αδερφό μου, Χρόνη

Ευχαριστίες

Η παρούσα διδακτορική διατριβή πραγματοποιήθηκε υπό την αιγίδα του τμήματος Φυσικής του Πανεπιστημίου Κρήτης σε συνεργασία με το Ινστιτούτο Ηλεκτρονικής Δομής και λέιζερ του ιδρύματος τεχνολογίας και έρευνας στο χώρο του οποίου στεγάζεται το εργαστήριο Attosecond science and technology Laboratory (AST) , με υπεύθυνους τον Καθηγητή Χαραλαμπίδη Δημήτρη (Καθηγητής Τμήματος Φυσικής της Σχολής Θετικών Επιστημών του Πανεπιστημίου Κρήτης) και Δρ. Τζάλλα Παρασκευά (Ερευνητή Α' του Ινστιτούτου Ηλεκτρονικής Δομής και Λέιζερ του Ιδρύματος Τεχνολογίας και Έρευνας). Οι ευχαριστίες οι οποίες ακολουθούν ανήκουν στα άτομα που ενεργά συνήσφεραν καθόλη την διάρκειά της παρούσας εργασίας και στους οποιους αισθάνομαι την ανάγκη να εκφράσω την ευγνωμοσύνη μου.

Αρχικά θα ήθελα να ευχαριστήσω τον Καθηγητή Χαραλαμπίδη Δημήτρη, καθηγητής Τμήματος Φυσικής της Σχολής Θετικών Επιστημών του Πανεπιστημίου Κρήτης, για την εμπιστοσύνη που μου έχει δείξει όλο αυτό το διάστημα καθώς και την υπομονή του. Η καθοδήγηση του και το συνεχές ενδιαφέρον υπήρξαν καθοριστικοί παράγοντες για την ολοκλήρωση της παρούσας διατριβής ενώ οι επιστημονικές μας συζητήσεις,οι καλοπροαίρετες διορθώσεις και υποδείξεις του έχουν συνεισφέρει πλεον ενεργά στην διαμόρφωση μου αναφορικά με την προσέγγιση μου στα θέματα της έρευνας και των διεκπεραιωσεων της.Το πάθος και η όρεξή του είναι αξιοθαύμαστα και εύχομαι εγκάρδια οι επιστημονικές (και όχι μόνο) ανησυχίες του να αποτελούν πηγή νεότητας, συνεχούς ανανέωσης και κινητηριες δυνάμεις για εκείνον όπως ακριβώς τον γνώρισα.

Ένα τεράστιο ευχαριστώ σε εναν ακούραστο δάσκαλο με αστείρευτη διάθεση και ενέργεια οφείλω επιπλέον στον Δρ. Τζάλλα Παρασκευά (Ερευνητή Α' του Ινστιτούτου Ηλεκτρονικής Δομής και Λέιζερ του Ιδρύματος Τεχνολογίας και Έρευνας. Η επιστημονική του συμβολή αποτέλεσε και συνεχίζει να αποτελεί καταλυτικό παράγοντα για την διεξαγωγή των ερευνητικών δραστηριοτήτων του εργαστηρίου ενώ δεν ήταν λίγες οι φορές που οι συμβουλές και η καθοδήγησή του επεκτείνονται και σε θέματα της καθημερινής ζωής εκτός των εργαστηριακών χώρων. Η νοητική αλλά και έμπρακτη φυσική του παρουσία έκανε πολλά πράγματα εφικτά ,ενθαρρύνοντας με για την συνέχεια. Τον ευχαριστώ για όλες του τις συμβουλές ,διορθώσεις και υποδείξεις ενώ παράλληλα εύχομαι ολόψυχα κάθε χαρά και επιτυχία σε επαγγελματικό και προσωπικό επίπεδο.

καλύτερα σε προσωπικό και επαγγελματικό επίπεδο. Ένα τεράστιο ευχαριστώ στον Στέλιο Κουρή καθηγητή του τμήματος Φυσικής της Σχολής Θετικών Επιστημών του Πανεπιστημίου Κρήτης ο οποίος ακόμα και σήμερα αποτελεί έναν από τους λίγους ανθρώπους των οποίων η γνώμη και καθοδήγηση αποτελεί γνώμονα για τις επιλογές και την πορεία μου. Ευγνώμων είμαι στην Ελένη Κοκκώνη για την απίθμενη υπομονή και στοργή της και ακούραστη στήριξή της στιγμές που πραγματικά χρειάστηκα βοήθεια. Η προσπάθεια της μαζί μου υπήρξε πραγματικά συγκινητική.

Ορφανός Γιάννης

Abstract

Many scientific areas in technology and basic research (atomic-molecular and solid state physics, chemistry, biology) will derive tremendous benefit from the investigation of the light-matter interaction in temporal scales of the atomic unit of time. Also, real time studies of several fundamental processes in the microscopic scale involve characteristic times of the order of the period of the nuclear and electron motion in molecules or atoms. Few-femtosecond (*fsec*) (1 fsec=10^{-15} *sec*) and attosecond (*asec*) (1 asec=10^{-18} sec) temporal resolution is required in order to obtain snapshots of their evolution. Tools for such studies are light pulses with duration in the *asec* time scale in the extreme ultraviolet regime (XUV). Intense *asec* pulses will be beneficial for such investigations since they can induce non-linear processes in a target system and hence can be used for ultra-fast dynamics studies in an XUV-pump-XUV-probe configuration. The aim of my thesis is the development and characterization of a table-top XUV *asec* source with the highest ever reported XUV intensity and the implementation of this source for XUV-pump-XUV-probe studies in the non-linear XUV regime. The work took place in the Attosecond Science and Technology (AST) laboratory in FORTH-IESL.

The subject of this thesis relies on the generation and characterization of intense *asec* pulses. The exploitation of the unique source of coherent radiation will focus in studies of multiple ionization and ultrafast dynamics of atoms. More precisely, studies on the multiple ionization of atoms in the non-linear-XUV region and time-delay spectroscopic studies of atoms which are coherently excited in energetically non-degenerated manifold of bound and/or autoionizing states, will be the main subjects of the exploitation of the beamline that has been developed. For the realization of the proposed research directions the development and the characterization of a high intensity *asec* XUV source is required. Gas phase high-order-harmonic (HOH) generation sources have been used up to now for the generation of intense XUV pulses with duration $< 1\,fs$, which upon focusing can reach intensities sufficient to induce observable non-linear processes in the XUV spectral range. These processes have been used for quantitative studies in the XUV range by means of an ion-microscope device for XUV pulse metrology by means of 2nd-order volume autocorrelation (2-IVAC) measurements [47-53], for time-resolved XUV spectroscopy studies and XUV-pump-XUV-probe measurements of ~1 *fs* scale dynamics in atoms

/molecules [42,43]. Further enhancement of the XUV intensity is beneficial for the extension of the above studies to higher XUV photon energies and shorter time scales. Towards this goal, a loose laser focusing configuration and quasi-phase matching conditions optimizing the harmonic generation process will be developed and used.

At AST laboratory in FORTH-IESL a 10Hz Ti:S laser system, which delivers pulses of 20 fs duration and energy up to 400 mJ/pulse (Fig. 1a). can be exploited for driving two secondary sources. Generation of attosecond pulses with energy on target up to 100 nJ/pulse is the result of the fully operational 10 m long MWatt beamline.
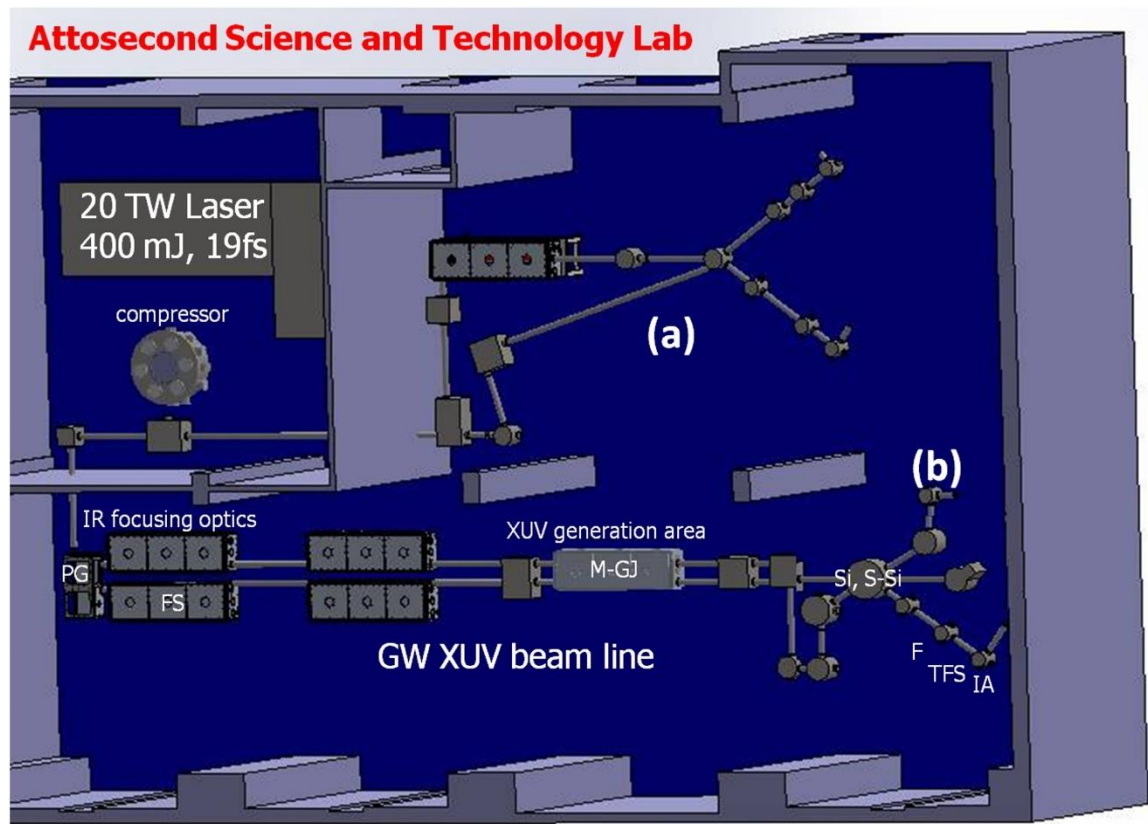
Figure 1. A drawing of the Attosecond Science and Technology(AST) laboratory in FORTH-IESL. The laser room and a drawing of the upgraded 20 TW Ti:S laser system is shown in the up-left corner of the AST lab. (a) The 10 m long MWatt beam line. (b) The 20 m long, GWatt asec beam line. **FS**: IR focusing system; **M-GJ**: Multiple gas jet configuration, **Si**: XUV steering optics; **S-Si**: XUV steering-splitting optics; **F**: Spatial and spectral filters; **TFS**: Toroidal focusing system; **IA**: Interaction area.

This energy value leads to peak intensities on target up to 10^{13}-10^{14} W/cm^2. In order to further increase the intensity of the asec pulses a multiple gas jet configuration in the

~20 m long XUV beam line and were combined with loose focusing geometry (Fig. 1b). According to theoretical calculation and experimental results this can lead to enchantment of the generated XUV flux resulting to μJ level in the interaction region. This is due to the increase of the volume of the interacting medium attributing to the harmonic emission. The beam line shown in Fig. 1b, except the loose IR focusing geometry (FS) and the multiple gas jet configuration (M-GJ), contains high reflectivity XUV optics for steering (Si), splitting (S-Si), filtering (F) and focusing (TFS) the XUV beam in the interaction area (IA).

A detailed description of an ultra-intense attosecond XUV beam line has been presented revealing the up to now highest reported energy of coherent radiation in the XUV spectral region 15–25 eV. The focused intense radiation is resulting a GW class average peak power attosecond source in the XUV spectral with those specifications characterizing the beamline as unique for an XUV source. Attosecond Pulse Trains durations of the order of 650 asec have been measured opening the way to ten-GW class attosecond XUV sources. The pulse duration of both the APT pulses and the envelope have been measured though 2nd IVAC i) in He employing two-XUV-photon ionization as a second order process as well as ii) in Ar exploiting two-XUV-photon ionization of Ar^+ under saturation of neutral Ar ionization. Measurements with both gases resulted in the same pulse durations within the experimental error. High non-linear XUV-optics in terms of multiple multi-XUV-photon ionization of He, Ar and Ne atoms, have been further demonstrated using the above beam line. The combination of high pulse energy and short duration opens up excellent perspectives for sub-fs XUV-pump-XUV-probe experiments in all states of matter. At the same time the XUV intensity levels reached enable the study of strong field effects in the XUV spectral region.

The source under development is complemented with a collinear polarization gating device (PG), that will also be exploited for the generation of intense isolated *asec* pulses. As the XUV and IR beams are spatially expanded towards the interaction area, XUV optical elements will be used in order to separate the XUV beam from the IR radiation (Si, S-Si). The resulting XUV beam will then be tightly focused into the target gas by high XUV reflectivity optical elements. By focusing this radiation in a spot diameter of <10 μm *asec* pulses with intensities up to 10^{15} W/cm^2, can be reached. The interaction products will be detected utilizing a high-resolution and high-collection-efficiency electron/ion spectrometer. An XUV wave-front splitting device (S-Si) will be used for the realization of the dynamical studies in the strong-XUV-field regime and for the characterization of the

asec pulses be means of a 2nd order AC technique. Imaging detectors and ion microscopes with µm resolution will be also implemented for the characterization of the *asec* source.

Concluding, the aim of my PhD thesis is the development and characterization a table-top XUV *asec* source with the highest ever reported XUV intensity and the use of this source for XUV-pump-XUV-probe studies in the non-linear XUV regime and the study of strong field XUV phenomena.

List of Publications

1. "Strong field effects induced in the extreme ultraviolet domain" I. Makos, **I. Orfanos**, E. Skantzakis1, I. Liontos, P. Tzallas, L.A.A. Nikolopoulos and D. Charalambidis. (submitted).

2. "Non-linear processes in the extreme ultraviolet" **I. Orfanos***, I. Makos*, I. Liontos, E. Skantzakis, B. Major, A. Nayak, M. Dumergue, S. Kühn, S. Kahaly, K. Varju, G. Sansone, B. Witzel, C. Kalpouzos, P. Tzallas and D. Charalambidis. Journal of Physics B: Atomic, Molecular and Optical Physics 2020.

3. "A 10-gigawatt attosecond source for non-linear XUV optics and XUV-pump-XUV-probe studies" I. Makos*****, **I. Orfanos***, A. Nayak, J. Peschel, B. Major, I. Liontos, E. Skantzakis, N. Papadakis1, C. Kalpouzos, M. Dumergue, S. Kühn, K. Varju, P. Johnsson, A. L'Huillier, P. Tzallas and D. Charalambidis. Sci Rep,Nature 2020.

4. "Attosecond pulse metrology" **I. Orfanos***, I. Makos*, I. Liontos, E. Skantzakis, B. Förg, D. Charalambidis and P. Tzallas, APL Photonics 2019.

5. "Towards Single-Shot XUV-Pump-XUV-Probe Studies" **I. Orfanos**, I. Makos, N. Tsatrafyllis, S. Chatziathanasiou, E. Skantzakis, D. Charalambidis and P. Tzallas, Book Chapter in Springer Series in Chemical Physics: Progress in Ultrafast Intense Laser Science Volume 118 chapter 11 ISBN: 978-3-030-03786-4, 2019.

6. "Multiple ionization of argon via multi-xuv-photon absorption induced by 20-gigawatt high-harmonic pulses" A. Nayak, **I. Orfanos**, I. Makos, M. Dumergue, S. Kühn, E. Skantzakis, B. Bodi, K. Varju, C. Kalpouzos, H. I. B. Banks, A. Emmanouilidou, D. Charalambidis and P. Tzallas, Phys. Rev. A, 2018.

7. "Towards generation of ultrahigh energy XUV pulses" M. Dumergue, S. Köhn, A. Nayak, E. Skantzakis, I. Makos, **I. Orfanos**, D. Charalambidis, and P. Tzallas, Conference Paper Compact EUV & X-ray Light Sources 2018 Strasbourg France 26–28 March 2018.

Table of Contents

List of Figures

Abbreviations

2-IVAC: Second Order Intensity Volume Autocorrelation

ADK: Ammosov, Delone and Krainov model

AIS: Autoionizing states

ATI: Above threshold Ionization

APT: Attosecond Pulse Train

BBO: Beta Barium Borate

BS: Barrier Suppression / Beam splitter

CCD: Charge Coupled Device

CEP: Carrier Envelope Phase

CPA: Chirped Pulse Amplification

CRAB: Complete Reconstruction of Attosecond Burst

DDI: Direct Double Ionization

DFG: Difference Frequency Generation

DOG: Double Optical Gating

FEL: Free-Electron Laser

FT: Fourier Transform

FTL: Fourier Transform Limited

FROG: Frequency-Resolved Optical Gating

FWHM: Full Width Half Maximum

GD: Group Delay

GDD: Group Delay Dispersion

GV: Group Velocity

GVD: Group Velocity Dispersion

HH: High-order Harmonics

HHG: High-order Harmonic Generation

IR: Infrared

MBES: Magnetic Bottle Electron Spectrometer

MCP: Micro-channel Plate

MPI: Multi-Photon Ionization

NIR: Near-Infrared

OTBI: Over the barrier Ionization

PANTHER: Photoelectron Analysis with Non-Resonant Two-photon-ionization for Harmonic Electric-field Reconstruction

PE: Photoelectron Spectra

PG: Polarization Gating

QPM: Quasi Phase Matching

RABBITT: Reconstruction of Attosecond Beating By Interfering Two-photon Transitions

REMPI: Resonant Multi-Photon Ionization

SDI: Sequential Double Ionization

SFA: Strong Field Approximation

SPI: Single Photon Ionization

SPM: Self-Phase Modulation

TDSE: Time-Dependent Schrödinger Equation

TOF: Time of Flight

X-FROG: Cross-correlation frequency-resolved optical gating

XUV: Extreme Ultraviolet ($10 < \hbar\omega < 124$ eV)

List of Symbols

$a_q{}^L$: Coefficient related to the nature of the long electron trajectories

$a_q{}^S$: Coefficient related to the nature of the short electron trajectories

γ: Keldysh parameter

Γ: Ionization rate

ΔK: Wave-vector mismatch

$\Delta \tau$: Time delay difference

Δn: Difference in linear index of refraction

ε_0: Vacuum permittivity {$8.8541878128(13) \times 10{-}12$ F·m^{-1}}

$\Theta_{S,L}$: divergence of the XUV originating from the short and long electron trajectories

K_ω: Wave-vector of the fundamental field

λ_L: Laser wavelength

$\sigma^{(N)}(\omega)$: frequency dependent generalized multiphoton absorption cross section

ω: frequency

τ_{cycle}: cycle time duration

τ_L: Laser cycle period

τ_{XUV}: extreme ultraviolet pulse duration

φ: phase

$\chi^{(N)}$: generalized non-linear susceptibility

$\chi^{(N)}{}_{eff}$: effective nonlinear susceptibility

$\chi_p(\omega)$: frequency-dependent susceptibility originating from plasma

b: Confocal Parameter of a focusing Gaussian beam

B: Magnetic field

c: speed of light

d: dipole moment operator

D: Beam diameter

d_{eff}: coefficient of the effective nonlinear susceptibility

e: electron charge

E_{kin}: kinetic energy

E_{photon}: Photon energy

f_1: Real part of atomic scattering factor

f_2: Imaginary part of atomic scattering factor

H: Hamiltonian operator function

h: Planck's constant

$\hbar$: Reduced Planck's constant

I: Intensity

I_L: Laser Intensity

I_{Sat}: Saturation Intensity

I_{XUV}: Extreme Ultraviolet Intensity

L_{coh}: Coherence Lenght

L_{drift}: flight distance in the tube of Time Of Flight Spectrometer

L_{medium}: medium legth implemented for frequency upconversion

m_e: mass of electron

$n_{(\omega)}$: Refractive index

n_e: number of produced photoelectrons in the photodiode cupling

n_q: photodiode quantum efficiency

N_α: atomic gas density

q: harmonic order

r_e: classical electron radius

R: Resistance of the oscilloscope (impedance)

R_q: Reflectivity

T_q^{Sn}: Transmission of Sn filter

T_q^{Al}: Transmission of Aluminum filter

U_p: Ponderomotive (quiver) energy

v: frequency of electromagnetic wave

w_x: Beam waist in x axis

w_y: Beam waist in y axis

Y: produced harmonic yield

Z_R: Rayleigh length

Chapter 1: Strong Field Physics & Attosecond Science

Introduction

The processes governing the interaction between light and matter are in the spot of a great interest of the scientific community ever since the quantum mechanics and modern physics approach over the nature were birthed [1-2]. Broadly we can categorize light-matter interaction into different regimes based on the intensity of the interacting light. Thus once a quantum system is exposed into the influence of an external electromagnetic field a numerous of events arise depending on this interaction strength. Linear optics deal with the smallest densities of photons involved in the interaction leading to an excitation in energy levels with energy difference corresponding to the photon energy causing the perturbation. The relaxation of the system to its ground state then results the generation of a photon with equal energy to this energy difference, a mechanism known as spontaneous emission. On the other hand, once the intensity of the exciting field is increased to higher levels $< 10^{12}$ W/cm^2 nonlinear terms are becoming a necessity for an accurate description of the polarization induced in the interacting medium. This regime is widely described as perturbative or weak field regime since it can be successfully treated by time dependent perturbation theory (lowest or low order) of the interaction term in the Hamiltonian of the under investigation quantum system. Scaling upwards to even higher intensities of radiation in the range of 10^{12} -10^{16} W/cm^2 low order perturbation theory can no longer describe the interaction since the electric field strength becomes comparable to the Coulombic binding between the valence electron and the nucleus. The effects resulted from these interactions are called strong field effects and thus the regime itself strong field regime. At even higher field intensities, typically $>10^{16}$ W/cm^2 (dependenting on the wavelength e.g for 800 nm the intensity valid for 10^{18} W/cm^2 for 8 μm 10^{16} W/cm^2), we enter the relativistic regime where the contribution of the magnetic part of the incident light wave can no longer be treated as negligible. In this regime the radiation accelerates the electrons to a significant fraction of the speed of light as a result of the sufficient magnetic dipole interaction. In this chapter these different regimes will be briefly discussed and the Harmonic Generation process will be introduced.
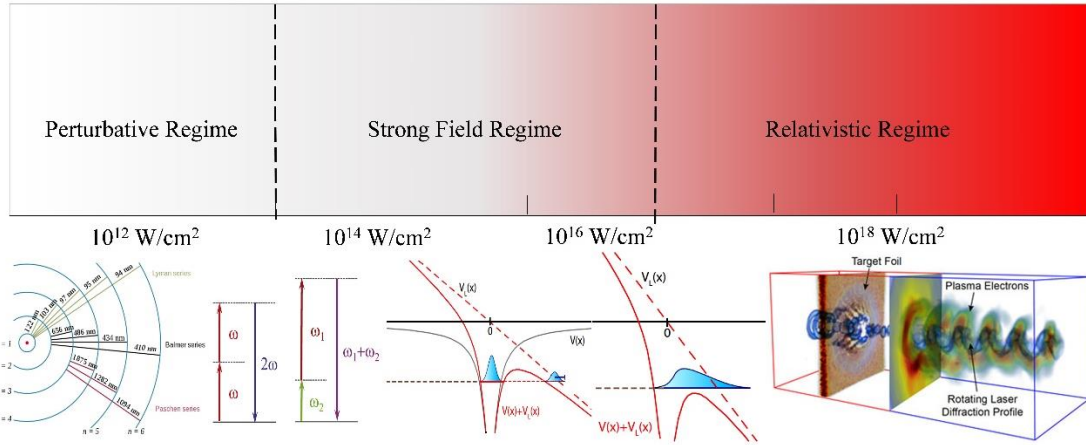
Figure 1.1 The regimes of light-matter interactions. The first region is described by the lowest and low order perturbation theory when the light intensity remains rather low. The strong field regime containing phenomena like the tunneling ionization and barrier suppression is apparent at higher intensity levels 10^{12} -10^{16} W/cm^2. At even higher field intensities, typically $>10^{17}$ W/cm2, the relativistic regime is describing the interaction where the contribution of the magnetic part of the incident EM wave can no longer be treated as negligible.

1.1 Perturbative Regime in the light matter interaction

The electronic motion in the quantum mechanical frame can be derived from the convolution of multiple plane waves accompanied by the boundary conditions set from the potential of an atomic system. The wavefunction, $\Psi(r,t)$, contains the entire information about a quantum system, and the modulus square of the wave function, $|\Psi(r,t)|^2$, denotes the probability density characterizing the physical existence of the quantum particle. The wavefunction depends on both the position vector, r, and the time, t. The general time dependent Schrodinger equation (TDSE) describes the evolution of a quantum system with time, and can be written as:

$$-i\hbar\frac{\partial\Psi(r,t)}{\partial t} = \widehat{H}\Psi(r,t) = -\frac{\hbar^2}{2m}\nabla\,\Psi(r,t) + V\Psi(r,t) \qquad (1.1)$$

Where $\widehat{H}$ symbolizes the Hamiltonian operator containing the kinetic energy as well as the potential V under the influence of which the particle is bounded. In case of linear

interaction between an atomic system and the incident light, first order perturbation theory referring to the dipole moment as the operator exciting the system can be performed and explain the optical allowed transitions acquired when considering the application of an external field. The Hamiltonian consists of two parts. The one of the atom and the one describing the interaction of the atom with the field. In this case the system is treated quantum mechanically while a classical interpretation of the exciting field is usual a way to simplify the problem. In the electric dipole approximation which is valid for optical and IR frequencies and not very high excited Rydberg states, the dipole moment operator is given by:

$$\hat{d} = e\,\boldsymbol{r} \tag{1.2}$$

While the term of Hamiltonian denoting the interaction with the external field E(t) is then given by:

$$\widehat{H}_{\text{int}} = -\hat{d}\,E(t) \tag{1.3}$$

Considering the transition of an electron from the ground state to an excited state can be interpreted by this treatment. Excitation of a bound or continuum (ionization) state can be treated by this Hamiltonian. Excitation of a bound state occurs if the frequency of the field is resonant or near resonant with one of the eigenfrequencies of the system. Ionization will apparently occur if the photon energy is larger than the ionization energy of the system. If the photon energy is smaller than the ionization energy of the atom, but still large enough in order not to enter the strong field regime, ionization can still take place via multiple photon absorption, called multi-photon absorption. Well observable multi-photon ionization requires radiation intensities $\geq 10^{12}$ W/cm^2. In that case multiple photon absorption of the atomic system is required for the ionization. In order to induce such nonlinearity, the intensity must be above the level 10^{12} W/cm^2. Equation 1.4 describes the linear single photon ionization with the kinetic energy corresponding to the equal to the energy difference between the incident photon energy E_{photon} and the ionization potential for the particular transition I_p. This can be equal to zero if the ionizing photon is resonant with the transition [3].

$$E_{kinetic} = E_{photon} - Ip \tag{1.4}$$

The rate of the ionization (single photon linear process) is linearly dependent on the number of photons in the interaction region N as well as the number of the atoms n absorbing the radiation. Furthermore is proportional to the photoionization frequency dependent cross section $\sigma(\omega)$ and thus stands for:

$$\Gamma \propto Nn\sigma(\omega) \qquad (1.5)$$

Considering now lower frequencies of photon interacting with an atomic target in case of high enough intensity characterizing the field multiple photons can be instantaneously absorbed and lead to ionization. The process is widely known as multi-photon ionization with a variety of investigation (theoretically and also experimental) to have been carried out over the years. In this case the electron is promoted into the continuum after absorbing N photons and the excitation is allowed by exciting the electron through a series of virtual states, separated to each other by the single photon energy, and with lifetimes defined by the time-energy uncertainty relation. As long as an additional photon is absorbed within the short-lived virtual state lifetime, the process can continue until a sufficient number of photons has been absorbed to overcome the ionization energy of the atom. Consequently, higher interaction intensities are required to enable this nonlinear process with efficiency compared to that of the single photon ionization. Thus assuming N photons to be required for the ionization of an atomic target, the electron will be freed into the continuum with an energy, K_{inetic}, equal to the energy difference between the sum of the N photons absorbed and the ionization threshold, I_p given by equation 1.6. This can be expressed mathematically as:

$$E_{kinetic} = N\,E_{photon} - I_p \qquad (1.6)$$

The rate of Multi Photon Ionization (MPI) depends both on the frequency dependent generalized absorption cross section, $\sigma^{(N)}$, for the N denoting the order of non-linearity characterizing the process, as well as the intensity, I, of the interacting field as derived in equation 1.7 similarly expressed like in case of single photon ionization rate or alternatively as described by Nikolai B.Delone and Vladimir Krainov [4-8].

$$\Gamma \propto \sigma^{(N)} I^N \qquad (1.7)$$

$$W = \sigma^{(N)}(\omega, \varepsilon) \left(\frac{cE^2}{8\pi\omega} \right)^N \qquad (1.8)$$

where W is the rate of multi photon ionization, E is the electric field amplitude, N is the integer number of photons required for the ionization, I is the field intensity, ε is the ellipticity of the radiation, and ω is the frequency of the dressing field and $\sigma^{(N)}$ is the generalized multiphoton absorption cross section given by:

$$\sigma^{(N)}(\omega, \varepsilon) = \sum_{k,l,m,\dots,p} \frac{d_{ik} d_{kl} d_{lm\dots} d_{pE}}{(\omega_{ki} - \omega)(\omega_{li} - 2\omega)(\omega_{mi} - 3\omega)\dots(\omega_{pi} - (k-1)\omega)} \qquad (1.9)$$

Where $d_{ik}, d_{kl}, d_{lm}, d_{Pe}$ are denoting the diploe moment transition elements in the multiple step excitation while $\omega_{ki}, \omega_{li}, \omega_{mi}, \omega_{pi}$ the corresponding transitions frequencies.

In a special case a number of absorbed photons may be resonant with an eigenstate of the system. In that case the ionization is called Resonantly Enhanced Multi-Photon Ionization (REMPI) and in such an excitation the rather long lifetime of the real electronic state enhances the ionization.
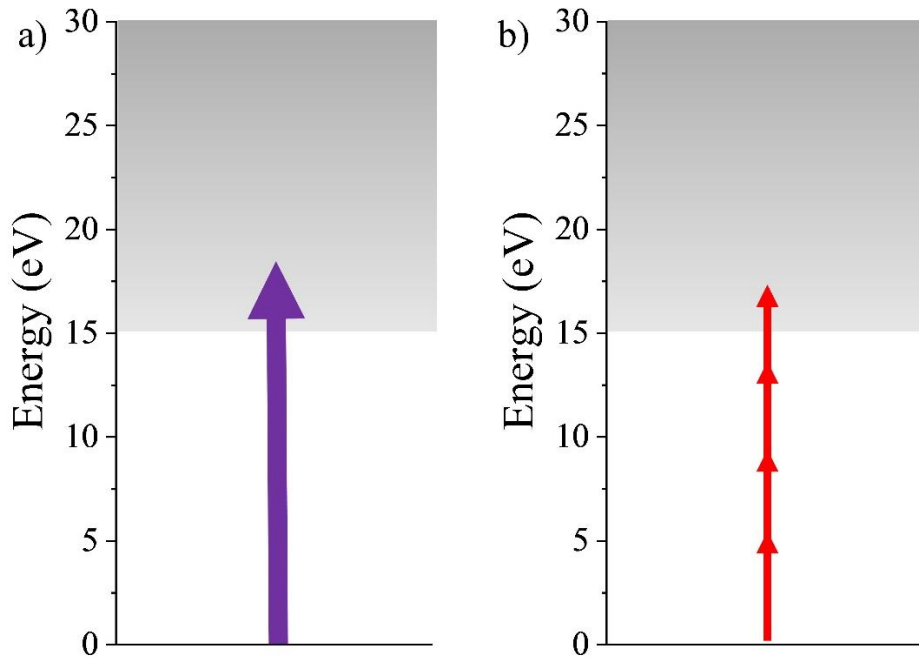
Figure 1.2 Single Photon and Multi-Photon Ionization. (a) The excitation of Argon atom with photon energy in the XUV region sufficient to induce single photon ionization. (b) Multi photon induced ionization, with n=4 photons absorption required for single ionization.

Extending the conceptual consideration of multi photon ionization, upon release, an electron being in the continuum can absorb a greater number of photons than required for the ionization. In this case the electron spectrum consists of peaks spaced by one photon energy. The energy of each peak is given by equation 1.10 with S being the number of photons absorbed in the continuum. The effect is commonly characterized as Above threshold ionization (ATI). ATI was first observed by Agostini et al. in 1979 [9], and devised ATI by Gontier et al [10] in 1980. Assuming an additional S number of photons interacting, the electron freed into the continuum will, for a weak dressing field, have an energy corresponding to:

$$E_{kinetic} = (N + S)E_{\text{photon}} - I_p \qquad (1.10)$$

Similarly, the rate of ionization for the ATI process will be given by:

$$\Gamma \propto \sigma^{(N+s)} I^{N+s} \qquad (1.11)$$

For ever stronger fields, the influence of the electric field on the intra-atomic structure more and more governs the behavior of the atom. The atomic bound states start to be shifted in an oscillatory mode, driven by the oscillation of the external electric laser field. The magnitude of this shift known as (dynamic) AC-Stark shift depends on the coupling between the atomic states and the light field and becomes larger for weakly bounded states [11-13]. The shift in energy of the bound states can sweep them near to a resonance or even into resonance with the light electric field. In that case process is governed be even higher dressing fields intensities enabling the additional continuum-continuum transitions. It should be noted that often these processes can still be treated perturbatively, however at the higher dressing radiation intensities, distinct strong field effects can play a role. In 1983, Kruit et al [14] observed a reduction in amplitude of the lowest ATI peak for a 19-photon absorption in a Xenon target. The increased dressing intensity required to access such high order nonlinear interaction caused the amplitude change through the AC Stark shifting of the effective ionization threshold, increasing the threshold with increasing intensity until the lowest ATI peak energy became smaller than the threshold energy (channel closing) and the relevant peak practically disappears from the spectrum. These experiments highlight the overlap between the perturbative and strong field response for high order ATI.

The AC Stark induced shift of the Ip leads to an additional term required in the energy equation to account for the change. More details but briefly will be later discussed about this transient regime of intensities but briefly the result is that the Rydberg states of an atom shift to higher energy values with an energy difference given by approximately the ponderomotive energy, *Up*. The ponderomotive energy will also be discussed in more detail later on in this Chapter, but corresponds to the cycle-averaged kinetic energy gained by a free electron accelerating in an electromagnetic field. The equation for the above threshold ionization energy distributions of the produced photoelectrons can be derived from:

$$E_{kinetic} = (N + S)E_{\text{photon}} - I_p + U_p \qquad (1.12)$$
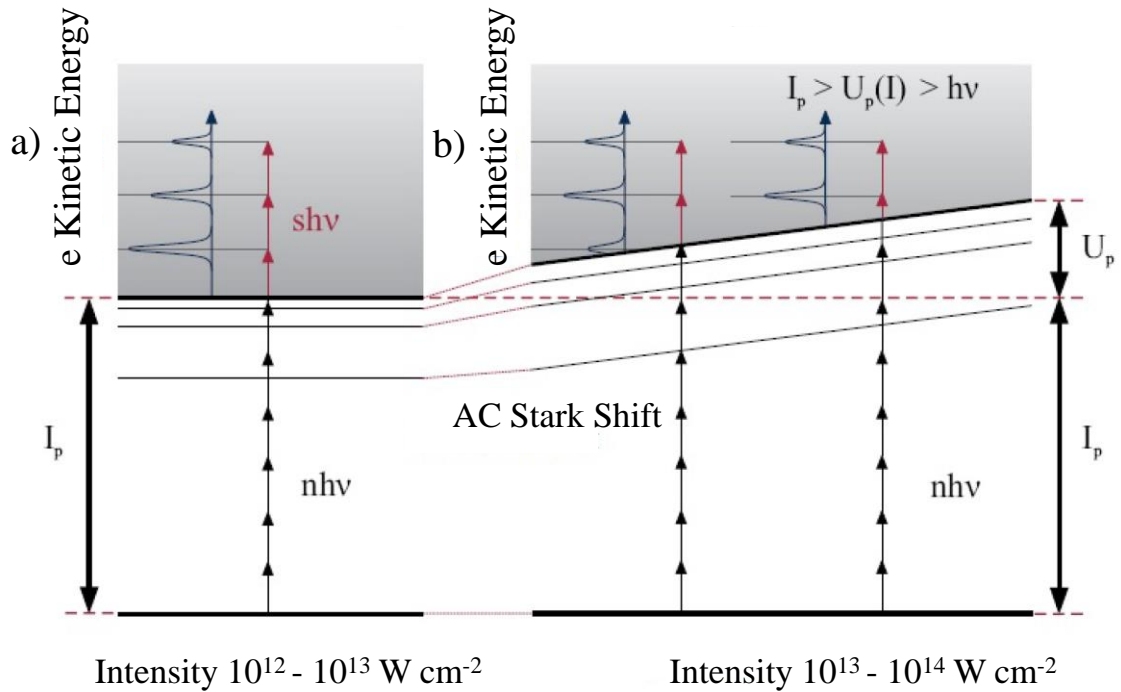
Figure 1.3 Above Threshold Ionization excitation scheme. (a) Illustration of energy levels in an atom. The simultaneous absorption of n photons leads to ionization of the atom. There are s ATI peaks because of the s additional photons absorbed by the electron upon its release in the continuum. (b) With increasing intensity the higher energy levels shift to higher energies and with them the ionization threshold as well by the amount of Up. Above a certain intensity the 1st peak vanishes, an effect known as channel closing potential and eventually to further channel closings Further increase of intensity will lead to even greater energy shift of the ionizaction potential and eventually to further channel closings.

1.2 Strong Field Regime

In the previous section we considered photon energies such that ionization is through multi-photon absorption and not through strong field effects. As previously mentioned in the strong field regime, the intensity of the driving field in conjunction with its photon energy is such that it can strongly distort the bound potential of the valence electrons. The periodicity of the distortion is determined by the periodicity of the dressing light. For a linearly polarized laser field the binding potential distorts in one direction, then the other, presenting the electron with a finite barrier twice per optical cycle as the electric field vector of the dressing laser reverses direction. A schematic of this can be seen in Figure 1.4(b). The largest distortion to the bound potential occurs when the peak of the radiation intensity interacts with the target. As the effective potential barrier is lowered twice per optical cycle, for high dressing intensities it becomes probable that a portion of the electron wavepacket can quantum mechanically tunnel through the classically forbidden barrier, and emerge into the continuum. This process is known as tunnel ionization and will be discussed in the following section. Once again depending on the intensity levels one can distinguish two different subsections of this extreme interference between photon and atoms. In case of intensity ranging from 10^{13} to 10^{15} W/cm^2 tunneling ionization is dominating while for higher than these levels the suppression of the atomic potential is so strong that the entire wavepacket escapes the barrier passing it over. These two phenomena both treated by the strong field approximation are called tunneling ionization and over the barrier ionization.

Tunneling Ionization

Tunnel ionization can occur when the electric field is sufficiently intense to distort the bound electron potential to the extent where appreciable ionization through the classically `forbidden' potential barrier occurs. In tunneling ionization the potential acting as the boundary condition of the electronic wavepacket, V(x,t) , experienced by the bound electron will be the combination of the binding potential of the nucleus, and that of the time-dependent dipole interaction, expressed as:

$$V(x,t) = -\frac{Ze^2}{4\,\pi\,\varepsilon_0\,x} - e\,x\,E_0\cos(\omega t) \qquad (1.13)$$

where Z is the charge state of the target, e is the charge on the electron, ε_0 is the permittivity of free space, x is the distance from the electron to the atomic center, E_0 is the electric field amplitude, ω is the laser central frequency. The rate of tunneling ionisation, Γ_{tunnel}, depends on the exact shape of the bound potential and the properties of the dressing laser field. For an alternating field, the expression giving the tunneling ionization rate was calculated by Ammosov, Delone and Krainov and the theory is known as ADK [15-17]. They determined an exponential dependence for the tunneling rate, given in atomic units. The model is based on the ionization rate of a hydrogenlike atom in a static electric field. The effect of the electronic structure on the tunnel ionization is brought in through the coefficients C_{n*l} and $f(l,m)$ that contain the effective principle number and angular and magnetic quantum numbers l,m:

$$W(E_{(t)}) = \omega_s |C_{n^*l^*}|^2 G_{lm} \left(4\frac{\omega_s}{\omega_t}\right)^{2n^*-m-1} e^{\left(-\frac{4\omega_s}{\omega_t}\right)} \quad (1.14)$$

Where,

$$G_{lm} = \frac{(2l+1)(l+|m|!(2^{-|m|})}{|m|!(l-|m|)!} \quad (1.15)$$

$$\omega_s = \frac{E_s}{\hbar} \quad , \quad \omega_t = \frac{e\,E(t)}{\sqrt{2\,m_e I_p}} \quad (1.16)$$

$$|C_{n^*l^*}|^2 = \frac{2^{2n^*}}{n^*\Gamma(n^*+l^*+1)n^*\Gamma(n^*-l^*)} \quad (1.17)$$

Ip is the ionization potential of hydrogen, l and m are the azimuthal and magnetic quantum numbers and E(t) is the amplitude of the electric field. The probability of ionization, P(t), during a time interval t,(t + dt) is:

$$P(t) = W(E(t))dt \quad (1.18)$$

The exponential dependence on the electric field amplitude for the tunneling rate determines that tunnel ionization can only occur with significant probability for a small window around the peak of the laser field intensity. In addition, it dictates that the least bound electrons will be the most likely to tunnel ionize.

Over the Barrier Ionization

If the interacting field becomes so intense that the potential barrier is suppressed to a level below the ground state of the bound electron, over the barrier ionization (OTBI) occurs and the electron is moving freely into the continuum with no tunneling required. A schematic diagram illustrating the process of OTBI can be seen in Figure1.4. At intensities above the OTBI threshold the ionization rate is no longer time dependent since the potential barrier suppression is greater than the binding potential of the valence electron. The threshold intensity for which OTBI occurs can be calculated by considering the potential experienced by the valence electron. This is comprised from the Coulomb binding and the potential from the peak electric field, where the symbols have the same meanings as for equation:

$$V(x) = -\frac{Ze^2}{4\,\pi\,\varepsilon_0\,x} - e\,x\,E_0 \tag{1.19}$$

The threshold (minimum) intensity required for OTBI is found by setting to zero the differential of the potential with respect to position, obtaining the extremum position, x_{max}, for which the rate of change of potential with distance (the force) is minimum. At, and beyond the x_{max} position the electron is completely removed from the core and no longer feels any force due to the Coulomb binding.

$$\frac{dV(x)}{dx} = \frac{Ze^2}{4\,\pi\,\varepsilon_0\,x_{max}^2} - e\,E_0 = 0 \tag{1.20}$$

$$X_{max} = \sqrt{\frac{Ze}{4\,\pi\,\varepsilon_0\,E_0}} \tag{1.21}$$

Substituting x_{max} into equation 1.20 and evaluating that OTBI will occur if this potential is greater than the ionization potential, Ip, for the bound electron, we derive the threshold equation:

$$\sqrt{\frac{Ze^3 E_{OBTI}}{\pi\,\varepsilon_0}} = I_p \tag{1.22}$$

where E_{OTBI} is the electric field amplitude required to reach the OTBI threshold [16].

$$I_{OTBI} = -\frac{c\,\varepsilon_0{}^3\pi^2 I_p{}^4 n}{2Z^2 e^6} \tag{1.23}$$

Ponderomotive Energy

Following the ionization of an atom resulting an electron into the continuum, interaction between the electromagnetic driving field and the electron persists, and thus electron is accelerated by the coulombic force. The cycle-averaged kinetic energy gained through acceleration of the electron in the laser oscillation is known as the ponderomotive energy, Up. Assuming the only force acting on the continuum electron is that from the strong laser field, an equation for the Up can be derived by applying Newton's second law to the Lorentz force:

$$\vec{F} = m\,\vec{a} = -e\vec{E}(t) + \vec{u} \times \vec{B}(t) \tag{1.24}$$

where m is the mass of the electron, a is the acceleration, e is the charge on the electron, E(t) and B(t) are the electric and magnetic field vectors, and v is the velocity of the electron. Derived from Maxwell's wave equations for electromagnetic radiation, the following equation relates the electric and magnetic fields E=c B where c is the speed of light. Since for the intensities the electron velocities are well below the relativistic limit, the magnetic field component of the Lorentz equation can be considered negligible, simplifying greatly equation. Assuming we are in what is known as the slowly varying envelope approximation (SVEA), where the laser pulse envelope can be considered constant during any given full laser cycle, we can treat the electric field amplitude, E_0, as a constant. For an electric field vector accelerating the electron along the x-axis, the acceleration can therefore be written as:

$$\frac{\partial^2 x}{\partial t^2} = \ddot{x} = -\frac{e\vec{E}(t)}{m} = -\frac{eE_0}{m}\sin(\omega t) \tag{1.25}$$

integrating this equation with respect to x results the velocity of the electron as a function of time:

$$\dot{x} = \frac{eE_0}{m\omega}\cos(\omega t) + C \tag{1.26}$$

where ω is the fundamental angular frequency of the driving laser field. It is assumed that the electron is born into the continuum with zero velocity so the constant, C = 0. Since the ponderomotive energy, Up, is defined as the cycle-averaged kinetic energy of

a free electron exposed to the radiation field where the τ_{cycle} corresponds to the period of the driving laser field, it can be expressed as:

$$U_p = \langle \tfrac{1}{2} m \dot{x}^2 \rangle = \frac{e^2 E_0^2}{4m\omega^2} \langle \cos^2(\omega\tau_{cycle}) \rangle \tag{1.27}$$

Equation 1.27 is very useful since it relates parameters that are measurable in the laboratory to the ponderomotive gain. The linear dependence of the Up on the intensity and the quadratic one on the wavelength play a major role in the generation of high order harmonics.

Keldysh adiabacity Parameter

So far we have discussed ionization processes associated with weak field response, and those associated with strong field response. At the boundary between the perturbative and strong field regimes a mixture of ionization processes occurs. Derived by Keldysh in 1965, the Keldysh parameter, can be used to determine the dominant ionization mechanism for a given set of experimental parameters.

Physically the parameter compares the two timescales involved in tunnel ionization: the time taken for an electron to quantum mechanically tunnel through the forbidden barrier, $T_{tunneling}$, and the period of the driving laser field, T_{laser}, which will determine the rate at which the barrier height is changing. If the tunneling time is large compared with the period of the laser field, little tunneling can occur and the ionization will be dominated by multiphoton effects. For tunneling times much shorter than the changing barrier time, tunneling is more probable and will dominate the ionization process. Considering the parameters that can be measured experimentally in the laboratory, most usefully the Keldysh parameter can be written in the following form relating the ionization potential, Ip, and the ponderomotive energy, Up, of the system to give a value defining the regime of dominance [18-19].

$$\gamma = \sqrt{\frac{I_p}{2\,U_p}} = \frac{T_{tunneling}}{T_{Laser}} \tag{1.28}$$

When $\gamma \gg 1$, the ionization is dominated by multiphoton effects as the Coulomb interaction is much larger than the ponderomotive energy. For $\gamma \ll 1$, the reverse is implied and the magnitude of the ponderomotive energy is much larger than the ionization energy, with the result that tunnel ionization is dominant. In real experiments

the ionization rate is integrated over the laser pulse time evolution and the spatial distribution in the interaction region. The atomic target can be depleted before the laser field fully vanishes, and therefore prognoses a saturation of the ionization process. For long pulses in the ps-range the intensity rise is so slow, that usually saturation sets in before the pulse envelope reaches a value that would permit the initiation of tunnel ionization and the experimental data are dominated by MPI signatures. The strongly nonlinear dependence of the ionization process determines that electrons are preferentially released around the laser electric field oscillation peaks. The emission is temporally confined to a fraction of a half-cycle of the driving laser field; a laser pulse therefore emits electrons only within a certain number of time-intervals corresponding to the number of field cycles that can overcome the ionization potential of the atom.
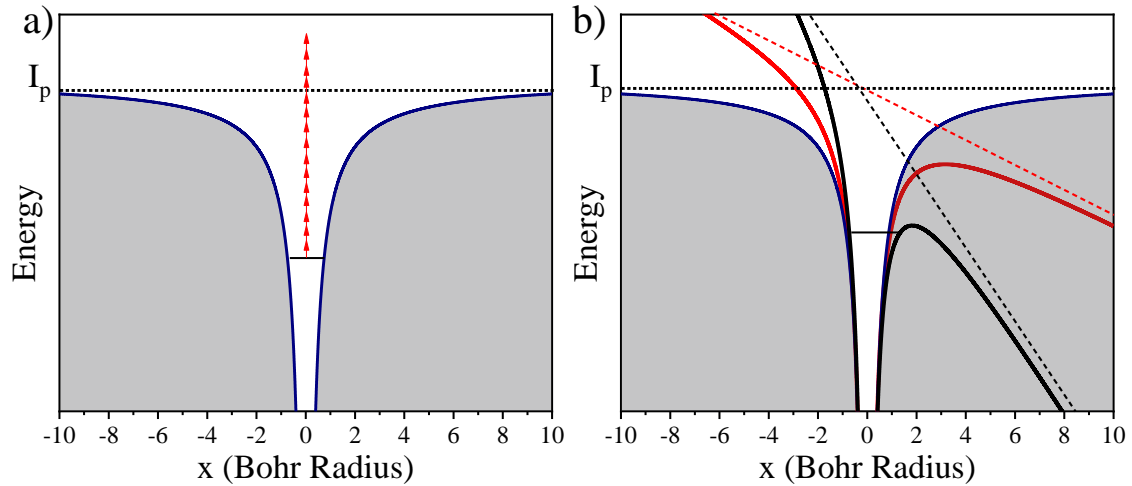
Figure 1.4 Keldysh parameter in ionization process. (a) When $\gamma \gg 1$, the ionization is dominated by multiphoton effects as the Coulomb interaction is much larger than the ponderomotive energy. The red arrows depict the multiple absorbed photons leading to ionization while the blue curve the ionization potential. (b) For $\gamma \ll 1$, magnitude of the ponderomotive energy is much larger than the ionization energy and thus tunneling is dominant. The red curve illustrates the distorted potential through which tunneling occurs. The black curve depicts the coulombic potential bended from the applied field when the later becomes significantly stronger, enabling the over the barrier ionization.

1.3 High Harmonic Generation

In this section theoretical aspects of high-harmonic generation (HHG) will be presented. The result of the highly nonlinear process is the frequency of laser light is converted into its integer multiples. Harmonics of very high orders are generated from atoms and molecules exposed to intense (usually near-infrared) laser fields. Surprisingly, the spectrum resulted from this process, high harmonic generation, consists of a plateau where the harmonic intensity is nearly constant over many orders and a sharp cutoff. Low-order nonlinear frequency conversion processes of the fundamental with the nonlinear dipole response of the interacting medium, leads to the emission of frequency shifted light at comparably low laser intensities. High order harmonics result from the highly nonlinear interaction of ultra-intense laser pulses with typically a gaseous target medium. Coherent radiation is emitted at frequencies that are odd integer multiples of the laser frequency and the shortest wave-length demonstrated so far corresponded to the ~100th harmonic. Since the atom in the gas phase is inversion symmetric, only odd harmonics of the fundamental are emitted, the total harmonic signal is the coherent superposition of the contribution of different individual atoms interacting at different intensities and phases. In the interaction region, only those harmonics propagate that fulfill the phase-matching condition and therefore interfere constructively. Spectrally, the emission is manifested in a strong fall-off after the first few orders followed by an extended plateau-region where adjacent harmonics have almost constant intensities. The highest energetic part of the spectrum is characterized by a "cut-off" region, where the harmonic structure disappears and the spectral intensity drops linearly.

Experimentally by focusing an intense ($> 10^{14}$ W/cm^2) laser pulse into an atomic or molecular target, energy from the laser field can be transferred to the sample, and ultimately to the generation of high energy photons. The specific properties of the high harmonic spectrum will depend on many experimental parameters including the focused laser intensity, pulse duration and wavelength, as well as the target material, backing pressure, position with respect to the focus of the light, and so on. In 1977, Burnett et al. observed the first high harmonic spectra [20] using a 10.6 μm CO2 laser and the plasma plume from laser-ablated aluminum targets. The first observation of HHG from atomic samples was reported a decade later, with McPherson et al. in 1987 [21]. In 1988, Ferray et al. pushed towards an increasingly extended cut-off, observing

a clear plateau region in the harmonic spectrum [22]. This characteristic plateau behavior was investigated further by Li et al. and the exhibited behavior allows scaling of the high order harmonic generation photon energies whilst still maintaining signal levels up to the onset of the cut-off [23].

The process of HHG can be understood by considering separately the microscopic and macroscopic effects that occur, that is, the effects occurring on the single atom level (microscopic), and the combined response of many interacting atoms (macroscopic). The macroscopic effects include interference and re-absorption of generated harmonic light, and will be discussed in more detail in the Phase Matching section later in this Chapter. First, however, we will consider the response of the single atom in the context of the semi-classical three-step model for HHG. The physical processes leading to the extended area of generated frequencies can be either classically or quantum mechanically interpreted for the atomic system. In both ways it is rather reasonable to consider a classical picture regarding the driving field. Thus the two well known and established models describing the high harmonic generation process are referred to classical and semi-classical respectively. In either case the basic conceptual consideration is based on the same approach with an outer cell electron to be responsible for the coherent emission of the atom after following three steps which include tunnel ionization, the motion of the electron inside the laser electric field and the subsequent recombination with the parent ion. Briefly those three steps are individually addressed in the following part while a schematic illustration of the mechanism of HHG is presented in figure 1.5. [23-26]

Optical field ionization

The atomic potential is significantly distorted by the optical driving field of the intense radiation interacting with the atom. This distortion enables the electron to tunnel out of the barrier at time t_0. In this description the tunnel ionization rate is only high around the maxima of the field oscillation. Even though, in principle, possible at every instance, for suitable experimental settings the release of electrons is confined to this time interval. In addition, it is reasonable to accept that the tunneling ionization immediately releases an electron into the continuum.

Acceleration of the electron inside the laser field

After been released in the continuum the electron is subjected to the laser electric field following its variations. The electron set free with zero initial velocity via tunnel ionization is accelerated away from its parent ion and assuming that the electron is released at a phase setting of the electric field that allows for this trajectory to return to the ionic core, the maximum kinetic energy that can be achieved can be calculated using classical or quantum mechanics.

Recombination with the ion

Recombination of the electron with its parent ion can lead to the emission of a broadband extreme-ultraviolet (XUV) radiation with respect to the energy conservation. Thus the quiver kinetic energy accumulated from the electronic motion under the influence of the field is then transformed into radiation. One photon per electron is emitted carrying the sum of the ionization potential and the electron's kinetic energy. The recombination event itself is rather unlikely, the conversion efficiency therefore low
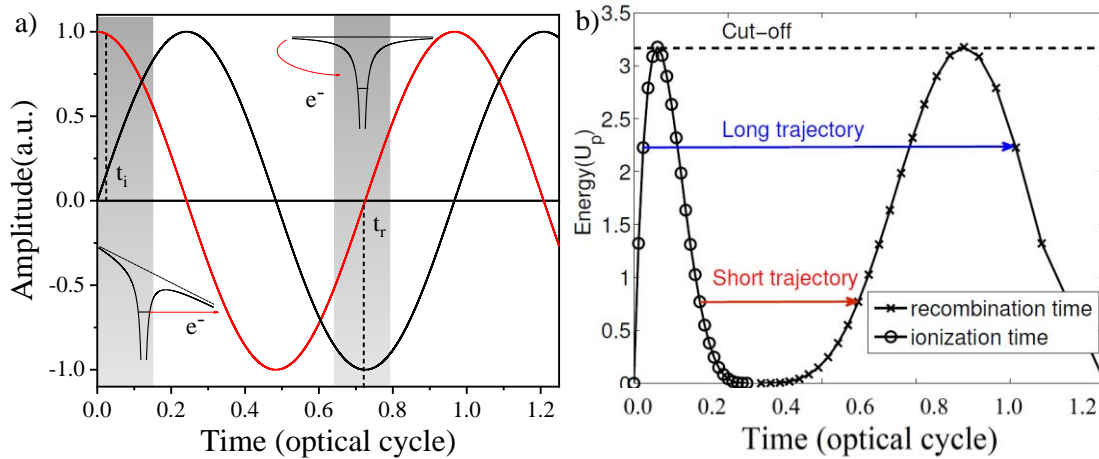
Figure 1.5 Classical description of High Harmonic Generation process. (a) The illustration of high harmonic generation 3 step model. The red curve represents the driving electric field, bending the coulomb barrier twice per cycle at each extrema. When the electric field hits the zero value the coulombic potential is then rearranged and the electron is leaded back to the parent ion. The red curve depicts the momentum accumulated from the electron.(b) is representing the ionization and recombination times in an optical cycle depicting the two different families of trajectories.

1.3.1 Classical description of High Harmonic Generation

The propagation of the unbound electron in a linearly polarized laser field can be described classically using Newton's equations in one dimension [27-35]. This classical theory, named the simpleman model [33], the rescattering model [35], or the three-step recollision model [36], is highly successful in describing certain attributes of HHG and Above-Threshold Ionization (ATI) [9,37-39]. When this model is combined with tunneling and recombination, it is often referred to as the semi-classical three-step model to emphasize the fact that tunneling is not classical. The semi-classical three step model for describing HHG was proposed by Paul Corkum in 1993, based on work by Krause et al. and L'Huillier et al. [31,33] performed the previous year. The model describes the process of HHG through three distinct steps: (1) ionization of an electron, (2) acceleration of the electron by the laser field, and (3) recombination of the electron with the parent ion.

When an intense laser field interacts with an atom, the large electric field component can distort the binding potential of the valence electrons to such a degree that tunnel ionization occurs with a high probability. The distortion to the potential varies periodically with the incident field, presenting a maximum twice per laser cycle corresponding to the times of maximum laser intensity. As the rate of tunnel ionization depends exponentially on the potential barrier, the majority of tunnel ionization occurs around the peaks of the laser intensity. Following the ionization step, the charged electron wavepacket is accelerated by the intense laser field, driven initially away from, and then back towards the parent ion as the direction of the electric field reverses. The acceleration of the electron wavepacket is treated classically within this model and thus the motion is described by Newtonian mechanics.

Let us define the scalar laser field linearly polarized in the z direction as a cosine function:

$$E(t) = E_0 \cos(\omega_0 t) \tag{1.29}$$

Where E_0 and ω_0 denotes the field amplitude and frequency, respectively. All relevant phases will now be dependent on this choice of a cosine field. The acceleration of the electron is given by the Lorentz force, which is integrated twice to derive the position If the electron is ejected at $t = t_i$, by solving the equation of motion for the electron position z(t) with the initial conditions of:

$$Z(t_i) = 0 \quad , \quad \dot{Z}(t_i) = 0 \tag{1.30}$$

One can derive the equations of motion expressed in atomic units:

$$\ddot{Z}(t) = -E_0 \cos(\omega_0 t) \tag{1.31}$$

$$\dot{Z}(t) = \frac{E_0}{\omega_0}[-\sin(\omega_0 t) + \sin(\omega_0 t_i)] \tag{1.32}$$

$$z(t) = \frac{E_0}{\omega_0{}^2}[\cos(\omega_0 t) - \cos(\omega_0 t_i) + (t - t_i)\omega_0 \sin(\omega_0 t_i)] \tag{1.33}$$

It is convenient to introduce the phase θ=ω₀t and thus

$$Z(\theta) = \frac{E_0}{\omega_0{}^2}[(\cos\theta - \cos\theta_i) + (\theta - \theta_i)\sin\theta_i] \tag{1.34}$$

While for the kinetic energy one can derive:

$$E_{kin}(\theta) = 2U_p(\sin\theta - \sin\theta_i)^2 \tag{1.35}$$

One obtains the time (phase) of recombination t_r (θ_r) as the roots of the equation z(t) =0 (Z (θ) = 0). Then the energy of the photon emitted upon recombination is given by:

$$\hbar\omega = E_{kin}(\theta_r) + I_p \tag{1.36}$$

$E_{kin}(\theta r)/Up$ as a function of phase of ionization θi and recombination θr for $0 < \theta i < \pi$ can be interpreted. The electron can be recombined only if $0 < \theta i < \pi/2$, it flies away and never returns to the nuclear position if $\pi/2 < \theta i < \pi$. $E_{kin}(\theta r)$ takes the maximum value 3.17 Up at $\theta i = 17^0$ and $\theta r = 255^0$. This beautifully explains why the highest harmonic energy (cutoff) is given by 3.17Up + Ip. It should be noted that at the time of ionization the laser field is close to its maximum, for which the tunneling ionization probability is high. Thus, harmonic generation is efficient even near the cutoff.

The phase of the driving laser will determine the path, or trajectory, of the subsequent motion. One assumption of SFA is that the only force felt by the electron during the acceleration is that from the laser field; the attraction from the ionic core is considered negligible. This is a reasonable assumption since the majority of continuum electrons born through tunnel ionization arrive into the continuum around the peak of the field intensity, leading to high initial acceleration of the electron, with the result that the electron spends little time in close proximity to the ionic core. Similarly, when the

intensity of the laser field equals zero the assumption is still valid since at this time the electron is now assumed to be far from the charged nucleus, and again its influence negligible. If the electron is born into the continuum after the peak of the laser field, it is possible that it can be steered back to the parent ion where it can recombine with a defined probability. Upon recombination of the accelerated wavepacket with the ground state wavefunction, an oscillating dipole moment is produced, releasing a continuum of high energy light. Trajectories that follow paths enabling recombination are known as returning trajectories. For a continuum electron wavepacket ionized before the peak of the electric field, the field cannot steer them back for recombination with the parent ion and instead they follow non-returning electron trajectories resulting in no harmonic generation, just contribution to the ionization fraction of the target. The trajectory corresponding to the maximum energy gained in the field is known as the cutoff trajectory, The energy corresponding to the cutoff trajectory is equal to:

$$E_{cut-off} = \hbar\omega_{cut-off} = I_P + 3.17U_p \qquad (1.37)$$

High-harmonic generation exhibits two important features that were neglected up to now: The emission is the superposition of the response of several atoms and more importantly those atoms are under the influence of several field cycles in case of multi-cycle fields. In case of multi-cycle laser pulses, the electrons encounter the parent ion every half-cycle of the electric field which results in a series of emissions that manifest themselves in the spectral domain as high harmonic structure. For each half-cycle peak of the laser field, a continuous spectrum of different energy photons are emitted up to the cut-off. If the incident laser pulse consists of just a single or few laser cycles, the produced spectrum is continuous and the broad, chirped bandwidth can be windowed to form isolated attosecond pulses (IAP). More usually, the interacting laser pulse is longer, consisting of several optical cycles, resulting in interference between the spectra produced for each half-cycle peak of the laser intensity. This gives rise to a characteristic discrete harmonic spectrum. If the pulse is many cycles in length, the slowly varying envelope approximation may be applied, where it is assumed that the electric field amplitude within a single optical cycle does not change.

For a centrosymmetric target, such as in case of an atom, the interference of the spectra produced at each half-cycle results in a spectrum consisting of only odd

harmonic orders of the fundamental frequency (the even harmonic orders destructively interfere). This can be understood by considering the effect of reversing the direction of the incident laser field. For a centrosymmetric medium case, the result is identical, so reversing the electric field vector will reverse the sign of the polarization vector too. This implies that for even harmonic orders, the emission from subsequent half-cycles interferes destructively, resulting in zero signal produced for the even components of the nonlinear expansion. The longer the incident laser pulse, the sharper the odd harmonics will be as the destructive interference at the even orders is compounded. A schematic of a typical harmonic spectrum can be seen in Figure 1.6. This illustrates both the characteristic odd harmonic comb structure, as well as the typical shape of the emission with the exponentially decaying amplitude low order harmonics, the extended plateau of approximately equal amplitude harmonics, and the high energy sharp cut-off. The different regions of the high harmonic spectrum can be understood from the harmonic generation process. Low order harmonics can be generated through both tunnel and multi-photon ionization pathways. The probability for multi-photon ionization will be higher for lower energy harmonic orders where fewer photons are needed to interact. The reduction in probability for increasingly high harmonic orders can be understood from the multiphoton ionization rate. The plateau exists since for each half-cycle of the laser, a spectrum covering the whole continuum up to the cut-off is produced. Therefore, nothing differentiates the probability of one frequency in the continuum being produced more readily than another. At the cut-off frequency, a sharp drop in amplitude is observed where higher frequencies cannot be produced. By breaking the symmetry of the system, production of both even and odd harmonic orders is possible. This can be achieved using either a non-symmetric laser field, for example through the addition of a second color field, or a non-centrosymmetric system, for example a heteronuclear diatomic molecule.

In case of an atom the above can be mathematically interpreted considering a given value of E_{kin}, we can view θ_i and θ_r as the solutions of the following coupled equations:

$$(cos\theta_r - cos\theta_i) + (\theta_r - \theta_i)sin\theta_i = 0 \qquad (1.38)$$

$$(sin\theta_r - sin\theta_i)^2 = \frac{E_{kin}}{2\,U_p} \qquad (1.39)$$

If (θ_i, θ_r) is a pair of solutions of Equations 1.38 and 1.39, $(\theta_i + m\pi, \theta_r + m\pi)$ are also solutions, where m is an integer. If we denote $Z(\theta)$ associated with m as $Z_m(\theta)$, we find that $Z_m(\theta) = (-1)^m z_{m=0} (\theta - m\pi)$. This implies that the harmonics are emitted during each half cycle with an alternating phase, i.e., field direction in such a way that the harmonic field E(t) can be expressed in the following form:

$$E(t) = \cdots + Fh\left(t + \frac{2\pi}{\omega_0}\right) - Fh\left(t + \frac{\pi}{\omega_0}\right) + Fh(t) - Fh\left(t - \frac{\pi}{\omega_0}\right) + Fh\left(t - \frac{2\pi}{\omega_0}\right) - $$

$$\cdots \qquad (1.40)$$

One can show that the Fourier transform of Equation 1.40 takes nonzero values only at odd multiples of ω_0. This observation analytically explains why the harmonic spectrum is composed of odd-order components. In Figure 1.6 we show an example of the harmonic field made up of the 11th-35th harmonic components. It indeed takes the form of Equation 1.40. In a similar manner, high harmonics are usually emitted as a train of bursts (pulse train) repeated each half cycle of the fundamental laser field as depicted in figure 1.6 (b)
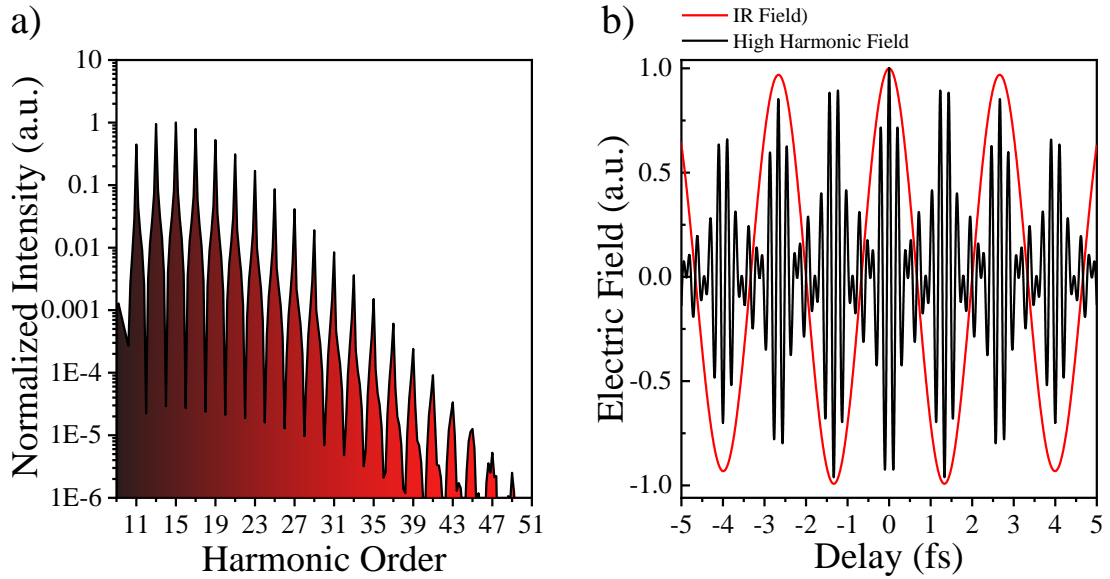
Figure 1.6 High Harmonic Generation in Argon. (a) Spectrum of Argon (b) Resulting Fourier Transform Limited attosecond pulse train.

1.3.2 Semi-classical description of High Harmonic Generation

In 1994 Lewenstein et al.[40], developed an analytical, quantum theory of HHG, called Lewenstein model. The interaction of an atom with a laser field E(t), linearly polarized in the z direction, is described by the time-dependent Schrödinger equation (TDSE) expressed in atomic units in:

$$-i\frac{\partial \Psi(r,t)}{\partial t} = \left[-\frac{1}{2}\nabla^2 + V(r) + zE(t)\right]\Psi(r,t) \tag{1.41}$$

where V(r) denotes the atomic potential.

In order to enable analytical discussion, they introduced the following widely used assumptions (strong-field approximation, SFA) neglecting in the analysis (a)the contribution of all the excited bound states, (b) the effect of the atomic potential on the motion of the continuum electron and (c) the depletion of the ground state of the atomic system. Within this approximation, it can be shown that the time-dependent dipole moment x(t) < Ψ(r, t) | z | Ψ(r, t)> is given by the following expression:

$$x(t) = i\int_{-\infty}^{t}\int d^*\left(\vec{p} - \vec{A}(t)\right)\exp[-iS(\vec{p},t,t')]\, E(t')\, d\left(\vec{p} - \vec{A}(t')\right) d^3\vec{p}\, dt' + c.c \tag{1.42}$$

where p and d(p) are the canonical momentum and the dipole transition matrix element, respectively, $A(t) = -\int E(t)dt$ denotes the vector potential, and S(p, t, t') the semiclassical action defined as:

$$S(\vec{p},t,t') = \int_{t''}^{t}\left(\frac{[\vec{p}-\vec{A}(t)]^2}{2} + I_P\right)dt'' \tag{1.43}$$

Equation 1.4.2 has a physical interpretation pertinent to the three-step model: $E(t')d\left(\vec{p} - \vec{A}(t')\right)$, $\exp[-iS(\vec{p},t,t')]$, and $d^*\left(\vec{p} - \vec{A}(t)\right)$ correspond to ionization at time t' , propagation from t' to t, and recombination at time t, respectively.

If approximation can be made about the ground state by that of the hydrogenlike atom can have the form in which $\Delta \sim I_p^{-1}$

$$\Psi(r) = (\pi\Delta^2)^{-3/4} e^{-r^2/2\Delta^2} \tag{1.44}$$

The dipole moment matrix element for the bund-free transitions is then derived:

$$d(p) = i \left(\frac{\Delta^2}{\pi}\right)^{3/4} \Delta^2\, p\, e^{-\Delta^2/2} \tag{1.45}$$

The integration over the momentum space in Equation (1.14) can be performed using the Saddle Point Approximation. We obtain:

$$x(t) = i \int_{-\infty}^{t} \left[\frac{\pi}{\varepsilon - i\frac{(t-t')}{2}}\right]^{\frac{3}{2}} [d^*(p_s - A(t))] [E(t)d(p_s - A(t))] e^{-iS\,(p_s, t, t')} dt'$$
$$+ c.c$$
$$\tag{1.46}$$

Where ε is a positive regularization constant (associated with the effect of quantum diffusion. The term p_s denotes the stationary value of the momentum determined by setting $\nabla S(\vec{p}, t, t_i) = 0$. In the spectral domain, Equation 1.42 is Fourier-transformed to, d(p) is given by:

$$x(\omega) = i \int_{-\infty}^{\infty} \int_{-\infty}^{t} \int d^*\left(\vec{p} - \vec{A}(t)\right) \exp[i\omega t - iS(\vec{p}, t, t')] E(t')\, d\left(\vec{p} - \vec{A}(t')\right) d^3\vec{p}\, dt\, dt' + c.c$$
$$\tag{1.47}$$

The evaluation of Equation 1.47 involves a five-dimensional integral over p, t, and t', i.e., the sum of the contributions from all the paths of the electron that is ejected and recombined at arbitrary time and position, which reminds us of Feynman's path-integral approach (Salieres et al., 2001). Indeed, application of the saddle-point analysis (SPA) to the integral yields a simpler expression. The stationary conditions that the first derivatives of the exponent ωt- S (p, t, t') with respect to p, t, and t' are equal to zero lead to the saddle-point equations:

$$p(t - t') + \int_{t'}^{t} A(t'') dt'' = 0 \tag{1.48}$$

$$\frac{[p - A(t')]^2}{2} + I_P = 0 \tag{1.49}$$

$$\frac{[pA(t)]^2}{2} + I_P - \omega\hbar = 0 \tag{1.50}$$

The generalized phase term of a specific frequency ω is

$$\Theta(\vec{p}, t, t') = \omega t - S(\vec{p}, t, t') \tag{1.51}$$

The physical meaning of the saddle point equations becomes clearer if we note that $p - A(t)$ stands for the kinetic momentum $mu(t)$. Equation 1.48, rewritten as $\int_{-t'}^{t} mu(t'')dt'' = 0$, indicates that the electron appears in the continuum and is recombined at the same position (nuclear position). Equation 1.50, rewritten together with Equation 1.49 as $mu(t)^2/2 - mu(t')^2/2 = \hbar\omega$, means the energy conservation. The interpretation of Equation 1.4.8 is more complicated, since its right-hand side is negative, which implies that the solutions of the saddle-point equations are complex in general. The imaginary part of t' is usually interpreted as tunneling time. Using the solutions (p_s, t_s, t_s'), $x(\omega)$ can be rewritten as a coherent superposition of quantum trajectories s:

$$x(\omega) = \sum_s |x_s(\omega)| e^{-i\Phi_s(\omega)} \Rightarrow$$

$$x(\omega) = \sum_s \left(\frac{\pi}{\varepsilon + \frac{i}{2}(t_s - t_s')} \right)^2 \frac{i2\pi}{\sqrt{\det S''(t, t')}} d^*\left(p_s - A(t_s)\right) \exp[i\omega t_s$$
$$- i\, S(p_s, t_s, t_s')] E(t_s') d(p_s - A(t_s'))$$

$$\tag{1.52}$$

Where $\Phi_s(\omega)$ is the phase of the complex function $\chi_s(\omega)$ and det(S'') is determined by the matrix of the second derivative of Θ with respect to t and t_i evaluated with the saddle point solutions:

$$\det S''(t, t') = \det\theta' = \left(\frac{\partial^2 S}{\partial t \partial t'} |s \right)^2 - \frac{\partial^2 S}{\partial t^2} |s \frac{\partial^2 S}{\partial t'^2} |s \tag{1.53}$$

$$\frac{\partial^2 S}{\partial t \partial t'} = \frac{(p - A(t)(p - A(t'))}{t - t'} \tag{1.54}$$

$$\frac{\partial^2 S}{\partial t'^2} = \frac{2(\omega_h - I_p)}{t - t'} - E(t)(p - A(t)) \tag{1.55}$$

$$\frac{\partial^2 S}{\partial t'^2} = \frac{2I_p}{t - t'} + E(t')(p + A(t')) \tag{1.56}$$

Considering again that the laser electric field is given by $E(t)=E_0\cos(\omega_0 t)$ and introduce $\Theta = \omega_0 t$ and $k = p\,\omega_0 / E_0$. Then Equations 1.48-1.50 can then be revisited expressed as:

$$k = -\frac{\cos\theta - \cos\theta'}{\theta - \theta'} \tag{1.57}$$

$$(k - \sin\theta')^2 = \frac{I_p}{2U_P} = -\gamma^2 \tag{1.58}$$

$$(k - \sin\theta')^2 = \frac{\omega_h - I_p}{2U_P} \tag{1.59}$$

where γ is called the Keldysh parameter. If we replace I_p and $\omega_h - I_p$ in these equations by zero and E_{kin}, respectively, we recover equations for the three-step model. Figure 1.7 displays the spectrum generated for two different gases as a function of harmonic order. Considering harmonics generated from Argon atom (I_p = 15.7596eV) irradiated by a laser with a wavelength of 800 nm and an intensity of 2×10^{14}W/cm2, the imaginary part of θ corresponds to the tunneling time, as already mentioned. This is much smaller in case of short trajectories that for the long trajectory, in particular, is nearly vanishing below the cutoff (~33rd order), which implies little contribution of tunneling to the recombination process.

It should be noted that the Lewenstein model predicts a cutoff energy $E_{cut\text{-}off}$, slightly higher than the classical three step model. This can be understood qualitatively by the fact that there is a finite distance between the nucleus and the tunnel exit (Fig. 1); the electron which has returned to the position of the tunnel exit is further accelerated till it reaches the nuclear position. Except for the difference in Ec, the trajectories from the TSM and the SPA (real part) are close to each other, though we see some discrepancy in the ionization time of the short trajectory. This suggests that the semi-classical three-step model is useful to predict and interpret the temporal structure of harmonic pulses, primarily determined by the recombination time.
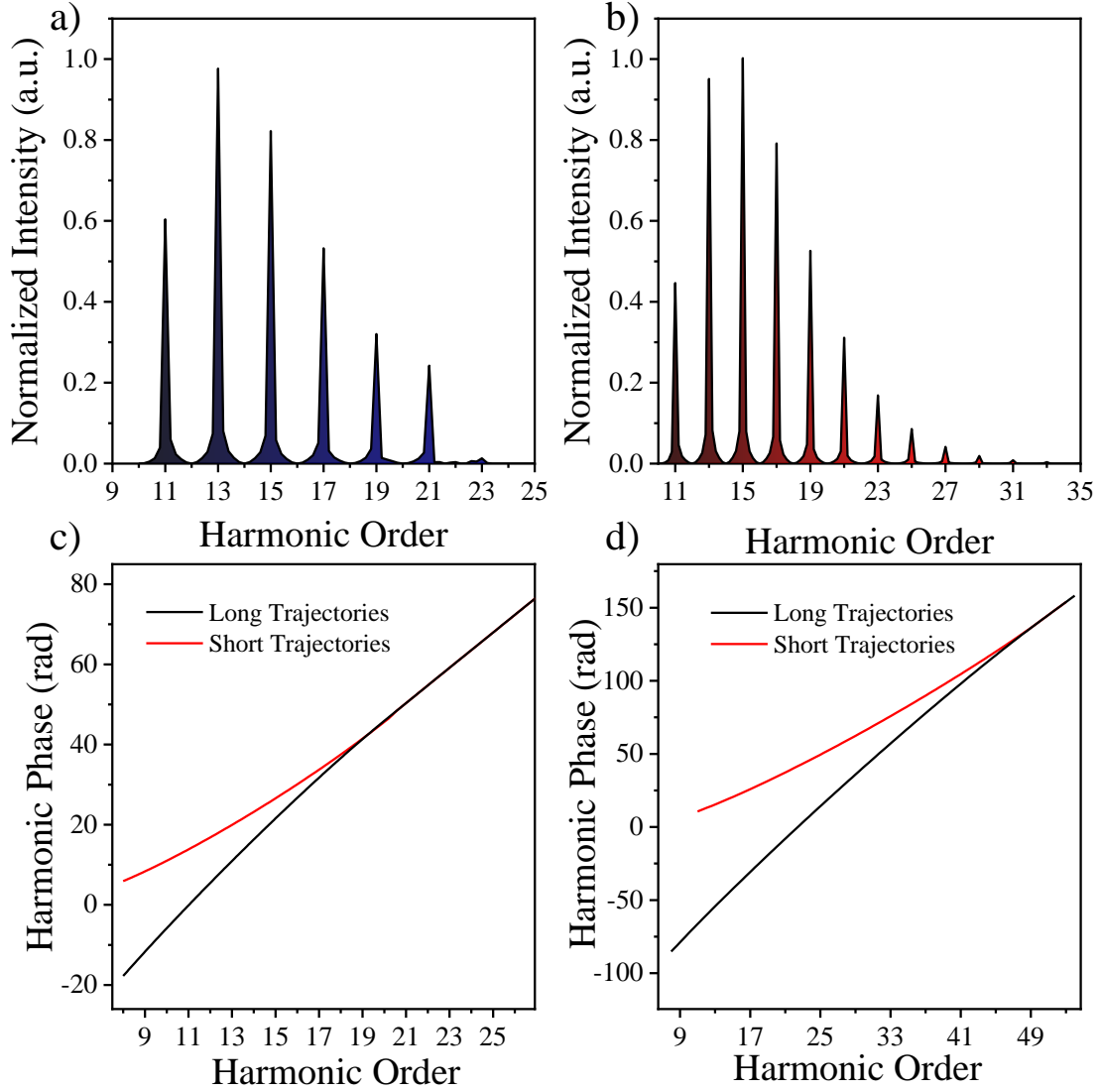
Figure 1.7 High Harmonic Generation spectra and phase. (a), (b) depict the high harmonic generation spectrum in case of Xe and Ar respectively. The intensity of the driving field used for is in both cases below the saturation and corresponds to $0.6 \ 10^{14}$ W/cm^2 in case of Xenon atomic target and $2 \ 10^{14}$ W/cm^2 for Argon. In panels (c) and (d) the phase accumulated from the electron in the continuum regarding the two different trajectories are illustrated for Xe and Ar.

Taking into account the amplitudes and also the phases accumulated by the short electron trajectories one can the derive the attosecond pulse train resulting from the high harmonic generation spectrum. The electric field and the intensity of the attosecond pulse train in the case of Xe is presented in Figure 1.7.
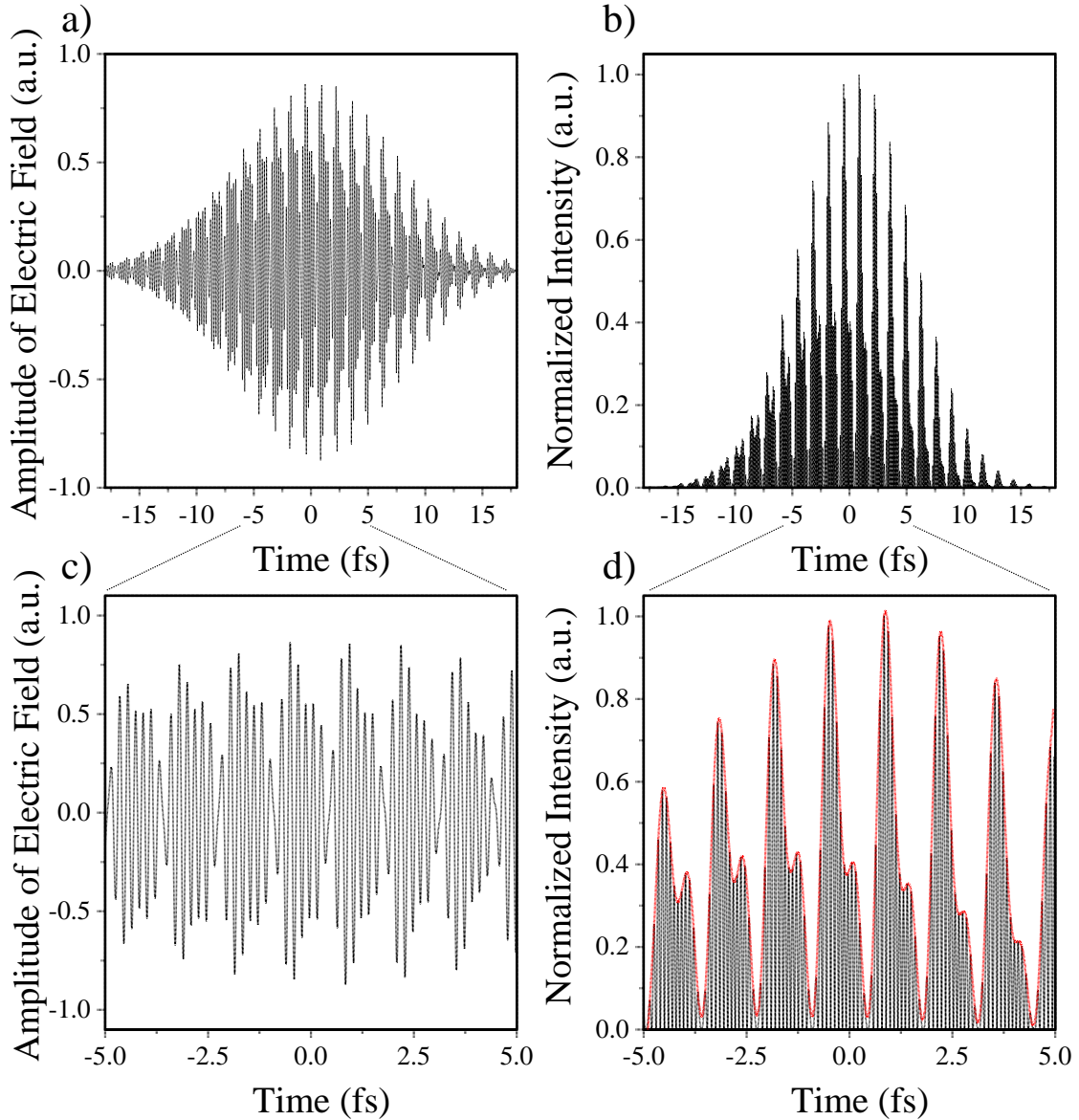
Figure 1.8 Attosecond Pulse Train of Xenon. (a)The attosecond pulse train obtained from the Fourier transformation of the generated spectrum corresponding to ~0.8 eV bandwidth of the harmonic frequencies (b) The intensity of the attosecond pulse train resulted from the sequence of 11th-21st harmonic fields. (c), (d) represents the expanded areas over the center of the electric field and intensity of the upper panels.

The electric field and the intensity in time domain in the case of Xe gas as the generation medium is presented in Figure 1.8. For the synthesis of the superimposed harmonic fields the amplitudes and phases in case of I_L= 0.6 10^{14} W/cm^2 were used. Figure 1.9 is depicting the harmonic radiation in time domain in case of Ar gas.
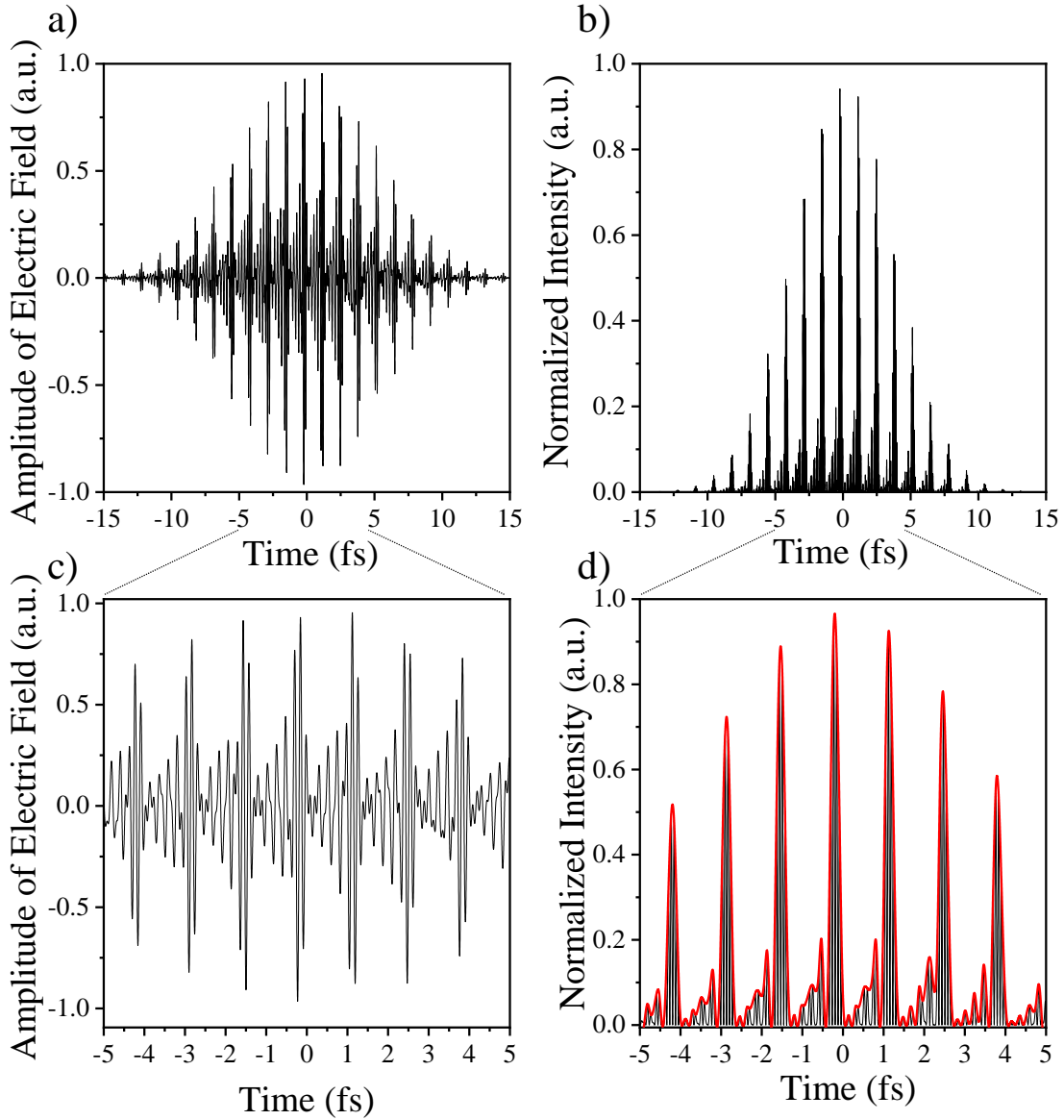
Figure 1.9 Attosecond Pulse Train of Argon. The attosecond pulse train obtained from the Fourier transformation of the generated spectrum corresponding to ~1 eV bandwidth of the harmonic frequencies in case of Argon. The spectrum in spectral domain resulting the train consists of the 11th to the 31th harmonic. (b) The intensity of the attosecond pulse train resulted from the sequence of the harmonic fields. (c), (d) represent the expanded areas over the center of the electric field and intensity of the upper panels.

In both cases (Figure 1.8, Figure 1.9) for the reconstruction of the APTs regarding Xenon and Argon gas respectively amplitudes and phases have been taken into account by solving the Lewenstein's model and considering only the short trajectories.

Chapter 2: Development of the GW attosecond source

Introduction

Several attosecond science laboratories around the world have focused their efforts towards the development of high photon flux attosecond beam lines. The aim of these efforts was to reach sufficiently high attosecond pulse intensities as to induce observable two- (or more) XUV-photon transitions, a central prerequisite for XUV-pump-XUV-probe experiments in the one femtosecond (fs) and sub-fs temporal regime [41-44]. The importance of XUV-pump-XUV-probe schemes relies on the fact that when temporarily overlapping IR and XUV pulses are used for pump-probe studies, the high IR intensities that have to be employed may cause distortions to the system under investigation obscuring its intrinsic dynamics [45]. XUV-pump-XUV-probe experiments benefit substantially from the existence of intense isolated or essentially isolated XUV pulses [46]. At the same time, observable two-(or more) XUV-photon transitions allow temporal characterization of attosecond pulses based on non-linear XUV autocorrelation (AC) measurements [47-53], bypassing complications that may arise from IR-XUV cross-correlation based pulse characterization techniques [54]. It should be noted that these developments were a follow up of pioneering non-linear XUV experiments completed with individual harmonics in the few tens of fs temporal regime, including two-[55], three-[56] and four-XUV-photon [57] ionization, two-XUV-photon double ionization [58,59] as well as the corresponding 2nd and 4th order AC measurements [57], two-XUV-photon above threshold ionization (ATI) [60] and even a FROG based XUV pulse reconstruction [61].

Towards reaching high XUV photon fluxes there are certain hurdles including depletion of the generating medium above a certain threshold of the driving laser intensity, XUV radiation reabsorption by the generating medium, as well as phase mismatch due to high generating gas pressures and high degree of ionization of the generating medium [62]. A way to overcome these obstacles is to use non depleting media as non-linear harmonic generation targets. This is the case in the generation of harmonics from laser induced surface plasma [63-70], often referred to as plasma mirrors. Indeed, for surface plasma harmonics, very high photon fluxes have been predicted in particle in cell (PIC) simulations and sub-fs temporal confinement has been experimentally demonstrated. Laser surface plasma harmonic generation possesses

however, increased technological demands such as high laser peak to background contrast, including elimination of unwanted laser pre-pulses, demanding "cleaning" procedures of the laser pulse through additional plasma mirrors, tedious control of the plasma density gradient, μm positioning of the focus on the target and debris to mention a few. Although laser surface plasma harmonic generation holds promise of high photon flux attosecond pulses, the so far achieved maximum XUV pulse energy is 40 μJ [71].

The alternative to laser surface plasma harmonic generation in avoiding the above mentioned obstacles is to use gas targets combined with loose focusing of the driving laser beam. The scalability of gas phase harmonic generation sources has been recently studied in [72]. The work presented by Heyl *et al.* demonstrates that long focal lengths combined with low pressure gas cells, allowing control of phase matching, can lead to high throughputs and thus to high XUV photon fluxes. At the same time, it has been recently shown that multi-cycle high peak power laser beams, focused in the generation medium using long focal lengths of several meters, in combination with quasi-phase matching arrangements, achieved through a chain of small length gas media i.e. pulsed gas jets, can reach emission of 20-GW XUV harmonic power at the source in the spectral region of 15-30 eV. [73]

In the following sub-chapters an in-detail presentation of the 20m-long 20-GW XUV attobeam line developed at the Institute of Electronic Structure and Laser of the Foundation for Research and Technology-Hellas (FORTH-IESL), operating in the spectral region of 15-30 eV, is provided. More specifically, technical details on the laser system and important information on its working principle will be presented. Vacuum considerations, IR focusing conditions, XUV generation, optimization and temporal and spectral characterization will be presented as well as complete description of the end station where a split-and-delay device implemented for attosecond time delay line, a time-of-flight spectrometer and an XUV spectrometer are located.

While FEL sources have much higher peak brightness at shorter wavelengths and in particular in the x-ray regime [74], in the spectral region of 15-30 eV the measured photon-flux of the present attobeam line is competing with that of FELs and provides a record-high for a table-top source.

2.1 The Attosecond Science & Technology laser system

The attosecond beamline is driven by a powerful TW class laser designed and constructed by Amplitude Technologies; the Pulsar^{TM} laser system. The low-power oscillator infrared output is amplified by Chirp Pulse Amplification (CPA). The final output pulses are the product of a three-stage amplification and are temporally compressed in a grating compressor. In this section a brief description of the Laser system layout will be presented. Figure 2.1 is depicting the chain of the different stages of the Pulsar^{TM} system.
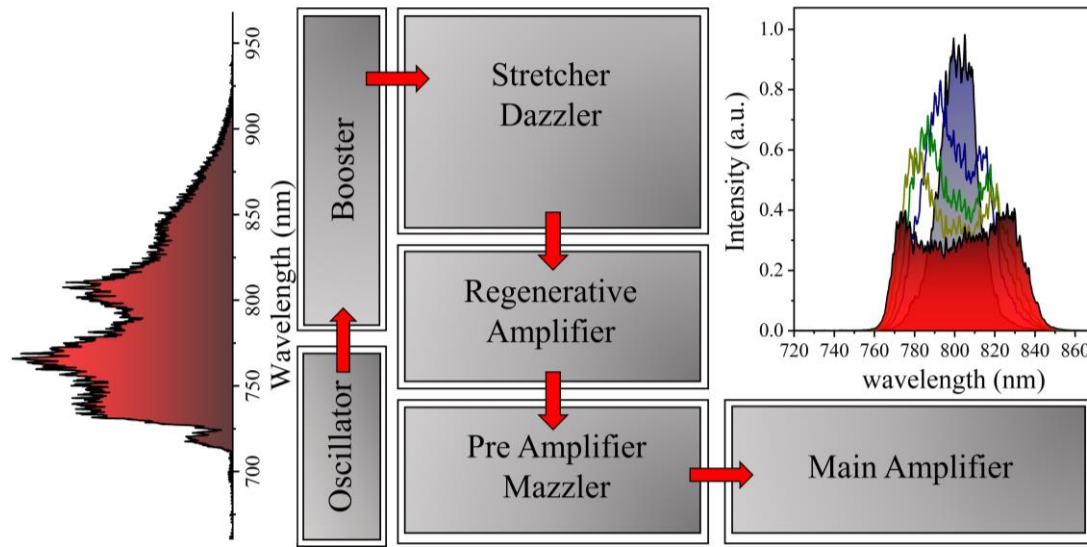
Figure 2.1 A scheme of the ultrafast Laser CPA chain. The different units of the ultrafast Laser system. The left panel is depicting the Oscillator spectrum and the right panel Amplified spectrum with different power applied in the mazzler crystal.

Oscillator

The oscillator (Spectra Physics Rainbow^{TM}) generating the broadband seed beam is the first stage of the Pulsar^{TM} system. It consists of an optical cavity with a 532 nm CW diode-pumped solid state laser (VERDI G7 - Coherent Inc.) pumping a Ti:sa crystal resulting a broad output spectrum exceeding 170 nm centered at 800 nm with repetition rate of ~ 80 MHz and average power of ~ 0.25 W in the mode-lock regime. A typical spectrum of the oscillator is shown in figure 2.1 (left panel) in mode locked operation.

Booster

The oscillator output beam then enters the first stage of the whole amplification. The so-called Booster is a module comprising a compact multi-pass amplifier amplifying the oscillator nJ output up to the μJ level. The Booster cavity also provides the pulse cleaning by means of a saturable absorber eliminating the power fluctuations. Finally, an electro-optical device, the pulse picker, is responsible for the creation of the 10 Hz repetition rate train of pulses, extracted from the 80 MHz radiation, that enters the Booster's unit.

Stretcher

To avoid damaging the amplifier crystal, the 10Hz amplified pulses are stretched to ps duration level in the stretcher unit which also contains an acousto-optic programmable dispersive filter that enables accurate control of the phase and the amplitude of the frequency components of the pulse. This control is able to pre-compensate the group velocity dispersion accumulated in the entire laser chain; a crucial action in achieving for short pulse durations. The Dazzler is used to shape the spectral amplitude distribution in avoiding gain narrowing and maintain a smooth spectral shape. It is also used to flatten the phase over the whole spectrum. More complex pulse shapes can also be achieved such as multiple pulses or optimized pulse shape for a specific experiment. The Dazzler is inserted between the stretcher and the compressor so that its own dispersion can be compensated by the compressor settings. It is placed before the amplifier because of its damage threshold (100MW/cm).

Pre-amplifier

After being stretched and spectrally shaped, the pulsed beam is directly traversed and seeds the regenerative amplifier (RGA) cavity which is pumped by a flashlamp pumped solid state Nd:YAG (CFR ULTRA) laser at 532 nm, 8 ns and with ~32mJ energy/pulse. At the output of the regenerative cavity the second stage of the amplification is located using a multi-pass amplifier. This multi-pass is called preamplifier and is pumped by a ~130mJ, 532 nm, 8 ns flashlamp pumped solid state Nd: YAG (CFR-200 Quantel) providing the gain in the amplifier. In the unit of RGA and pre-amplification also another acousto-optic gain control filter is installed

preventing the limitations originating from gain-narrowing. The so-called Mazzler device tends to flatten the global amplifier gain in order to broaden the spectrum by increasing losses on spectral components located where the gain is the highest such that it can support short pulse generation. The above is achieved by introducing acoustic waves diffracting specific spectral components off the cavity. At this stage of amplification, the pulse energy can be up to 25 mJ.

Amplifier

The main and final amplification is achieved by seeding the beam from the preamplifier into the 4-pass multi-pass amplifier pumped by a powerfull Nd:YAG delivering up to ~0.8J pulse energy (Propulse). The output IR beam with duration in the ps level after final amplification can be up to 650mJ with a spectrum of ~90-100 nm full bandwidth and beam diameter of 35mm.

Grating temporal compressor

A vacuum chamber hosts the temporal compression optics, which are a pair of gratings mounted in translation stages. Varying the distance between the gratings the beam can be re-compressed and the pulse duration is minimized by compensating the accumulated group delay of the stretcher and amplifier units. Both the second and third order dispersion terms can be adjusted or compensated.

Wizzler-time duration measurement

The measurement of the pulse duration and the spectral phase distribution are obtained with the Wizzler device. The operation principles of the device are based on Self-Referenced Spectral Interferometry (SRSI). It is single-beam, single shot, technique that delivers both spectral phase and amplitude measurements, i.e the complete temporal characterization of an ultrashort pulse. For obtaining the shortest pulse duration, the Dazzler pulse shaper is integrated in the laser chain, while the software is able to loop the phase information back to this device to perform pulse optimization, after having determined the compressor's gratings positions. [75-77]
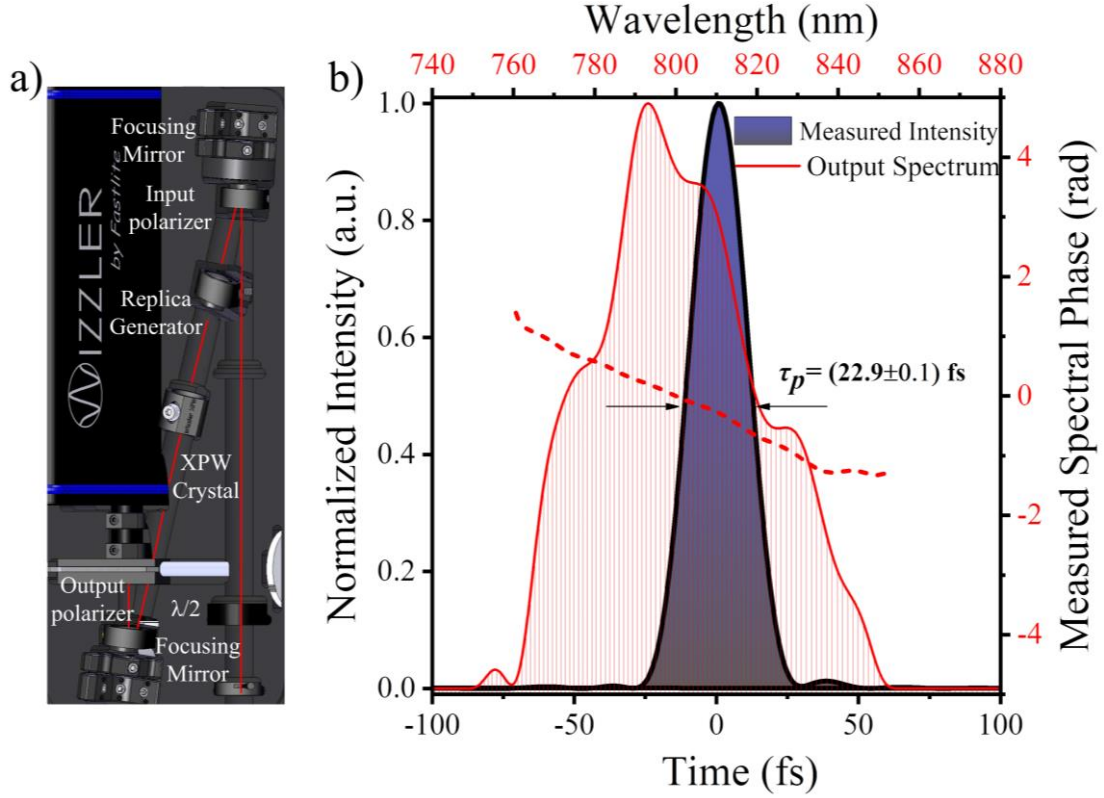
Figure 2.2 Wizzler-time duration measurement (a) Wizzler optical layout and, (b) typical measurement of the output pulse. The blue curve corresponds to the pulse duration measurement, the red solid line to the output spectrum while the dashed line to the measured spectral phase.

The principle is simple: from the pulse to be measured, a replica is created on the perpendicular polarization and delayed, using a birefringent plate cut at $\theta = 90°$ and slightly rotated compared to the input polarization. The main pulse is used to generate a reference pulse with a broader spectrum and a flatter spectral phase, but with the same carrier frequency, via Cross-Polarized Wave Generation (XPW) [78, 79]. XPW generates a linearly polarized wave, orthogonal to the polarization of a high intensity linearly polarized input wave. the XPW effect acts like a temporal filter: a XPW generated pulse is a replica of the initial pulse, filtered by its own temporal intensity. Thus, it is expected to be shorter in time, i.e. to have a broader spectrum and a flatter spectral phase than the input pulse. When the pulse is close enough to the Fourier transform limit, i.e. when the spectral phase is flat enough for the pulse to be filtered by the XPW effect. It is worth noting that XPW generation is more sensitive to the chirp than to higher orders of the spectral phase, and that its efficiency vanished for pulses chirped to above 2 times their FTL pulse duration.

2.2 Vacuum Chambers and conditions

Propagation of an intense IR beam in a medium (e.g. in air) gives rise to numerous of phenomena that above all distort the initial parameters of the initial field. Additionally, the generated XUV radiation is highly absorbed by matter. Therefore, the necessity of maintaining the crucial temporal and spatial characteristics of the driving pulses and also the propagation of the generated beam, can only be fulfilled under vacuum conditions. Figure 2.3 presents the layout of the attosecond beamline. Every chamber in the experimental set up can be isolated by a mechanical valve and the rest vacuum, i.e. the vacuum when all gas jets are off, in all chambers of the beam-line is $\sim 10^{-6}$ mbar except for the "end station" chamber in which it is $\sim 10^{-7}$ mbar. A 1000 l/min turbo-molecular pump in the "end station chamber" and another in the "HHG chamber" secure an adequate vacuum pressure during operation of the gas target jets.
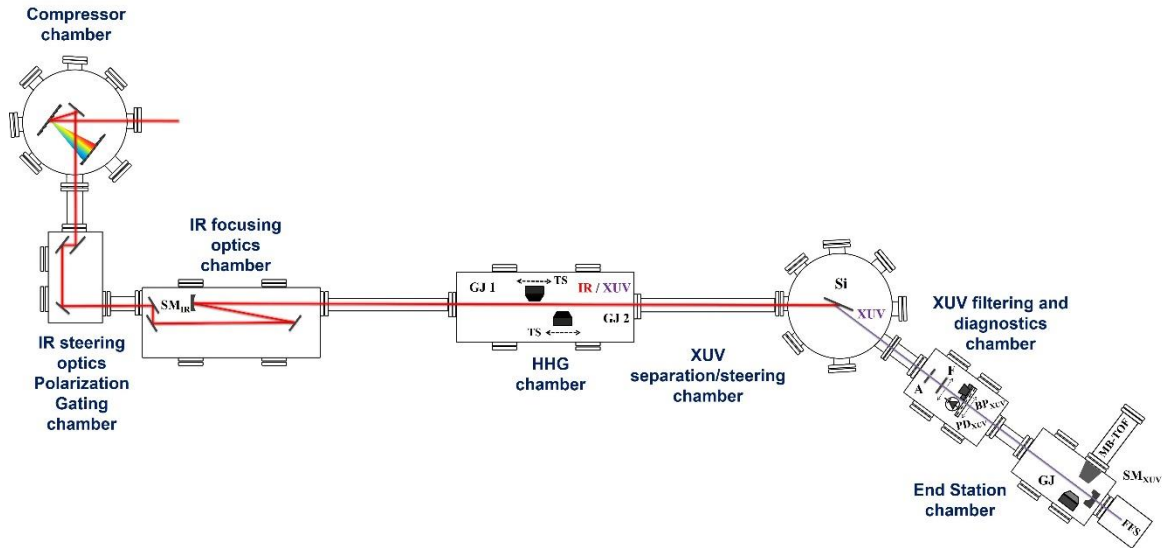
Figure 2.3 Optical layout of the 20-GW XUV beam-line. SM_{IR}: spherical mirror of 9-m focal length. $GJ_{1,2}$: dual-pulsed-jet configuration placed on translation stages (TS). Si: silicon plate. F: Al or Sn filter. A: aperture. BP_{XUV}: XUV beam profiler. SM_{XUV}: gold coated spherical mirror of 5-cm focal length. Ar-GJ: Ar gas jet. MB-TOF: magnetic bottle time-of-flight spectrometer. PD_{XUV}: calibrated XUV photodiode. FFS: flat-field spectrometer.

2.3 IR focusing Unit and Beamline steering optics

The laser steering and shaping takes place in two different vacuum chambers. In the first one a two grating arrangement temporally compresses the amplified laser pulses as described in the previous section and steers it into the focusing unit through three plane silver protected low dispersion mirrors placed in the second chamber. These mirrors are used for the alignment of the laser through the entire beam-line. It's worth to note that in the entrance of the beamline an iris is mounted (not shown in Fig. 2.3) in order to provide the capability of manipulation of the driving beam diameter, a parameter which is crucial for the High Harmonic Generation process. This second chamber hosts also a Polarization Gating (PG) optical arrangement for the generation of isolated attosecond pulses described elsewhere. The polarization of the laser beam entering the focusing unit is *parallel* to the optical table i.e. the beam is p-polarized. The focusing unit uses three silver protected low dispersion plane mirrors and a spherical mirror (SM) of 9 m focal length. This optical layout (shown in Fig. 2.3) aims to reduce astigmatism introduced by the spherical mirror due to the deviation from the normal incidence. The angle of incidence at the spherical mirror is as close as possible to normal (~ 3º) and therefore the astigmatism is kept low but is not negligible.

Figure 2.4 presents the IR beam profile recorded with different beam diameters, at several positions around the focus. This characterization occurs outside the chamber. The IR beam is deflected outside the chamber by a mirror mounted on a motorized linear translation stage that can be placed in and out the beam's path. The beam profile reveals a small degree of elongation along the x-axis as the beam diameter becomes larger. On the contrary when the initial beam diameter is reduced the astigmatism becomes significantly small. Although these imperfections of the IR beam do not affect the XUV beam profile (measured with an XUV beam profiler placed after the metal filter in the "XUV diagnostics" chamber), they may introduce distortions in XUV wavefront and hence influence the duration of the emitted attosecond pulses at the "end station" where the XUV beam is refocused. More details on this are given sub-chapter 2.4.
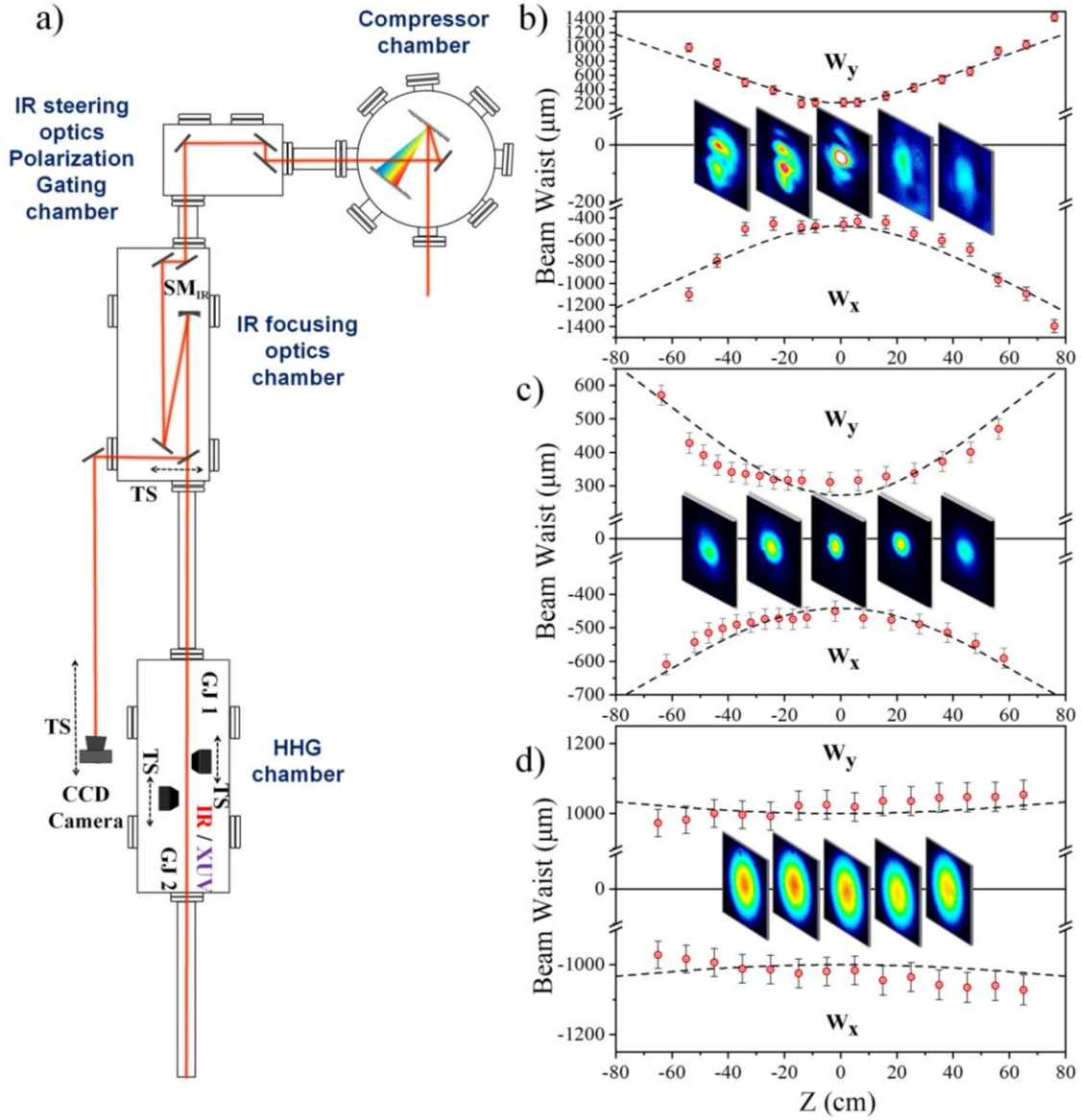
Figure 2.4 IR beam profile. (a) The optical arrangement implemented for the measurements. The CCD images depict the beam spots at several position around the focus for different initial beam diameters (b) 35 mm (c) 23 mm and (d) 8 mm.

The above implemented measurements also determine the focusing position and experimental spatial parameters of the IR beam used for the harmonic generation i.e. the position of the generating medium and the confocal parameter *b*.

While a high reflectivity and low dispersion across the broad spectrum is required for the optical elements reflecting the IR beam, separation of the generated XUV radiation is also a necessity. For the above purpose a successive solution is to introduce an optical element with low reflectivity in the IR region but also characterized at the same time with as high as possible reflectivity at the XUV region of interest. Therefore, after the HHG area at the "XUV separation/steering chamber" a Si plate is mounted at Brewster's angle for the fundamental IR frequency ($\sim 75^0$). This angle of incidence is selected because as it can be seen in figure 2.5 (b) the reflectance of a p-polarized electric field has a minimum at this angle. Thus, reflection on the Si plate significantly attenuates the IR while on the contrary reflects $\sim$ 60 % of the XUV radiation deflecting the beam towards the "XUV filtering and diagnostics" and "end station" chambers.
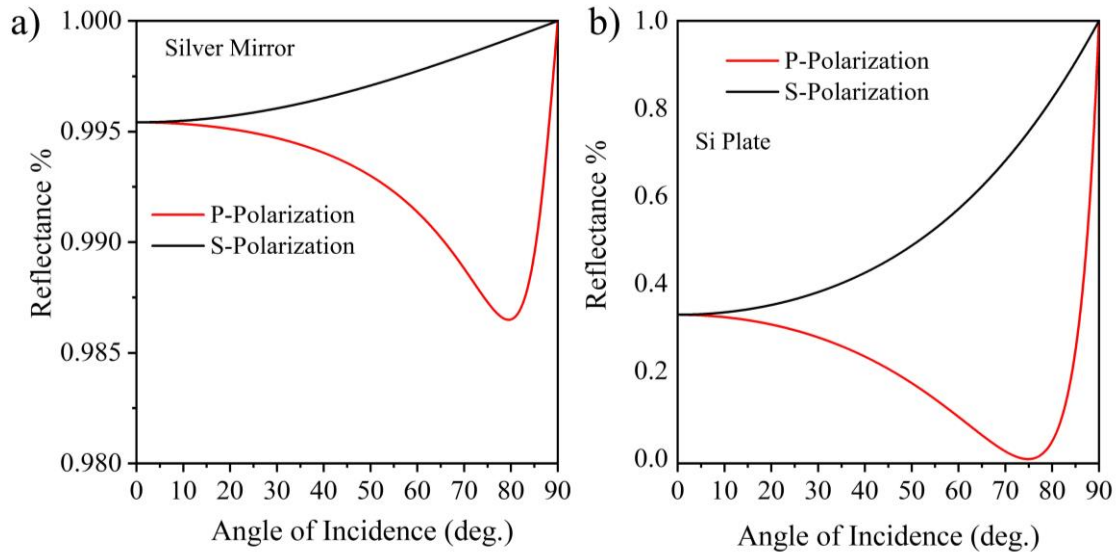
Figure 2.5 Reflectance curve of optical elements. (a) Reflectivity of silver mirrors implemented for steering/focusing the IR driving field for p-polarization (red solid line) an s-polarization (black solid line). For both polarizations the reflectivity is above 98%. (b) Reflectivity of Si plate where for p-polarization is almost negligible (~1%).

Since the development and construction of the beam-line aims also to ultrashort time resolution, stability becomes a very crucial parameter for attosecond resolved experiments such as XUV-pump XUV probe schemes. A big obstacle to this achievement are the vibrations mainly originating from the vacuum pumps. Thus all

chambers have isolators adapted in their bases and moreover the optical bredboards containing the optical elements as well as the connections of the chambers to each other are isolated with bellows. Towards ensuring the elimination of vibrations the pointing stability of the IR was measured with an IR beam profiler placed just in front of the split mirror. The shot to shot position of the maximum of the intensity distribution is plotted in Figure 2.6 for 150 laser shots. The mean FWHM of the contour is about 75 μm.
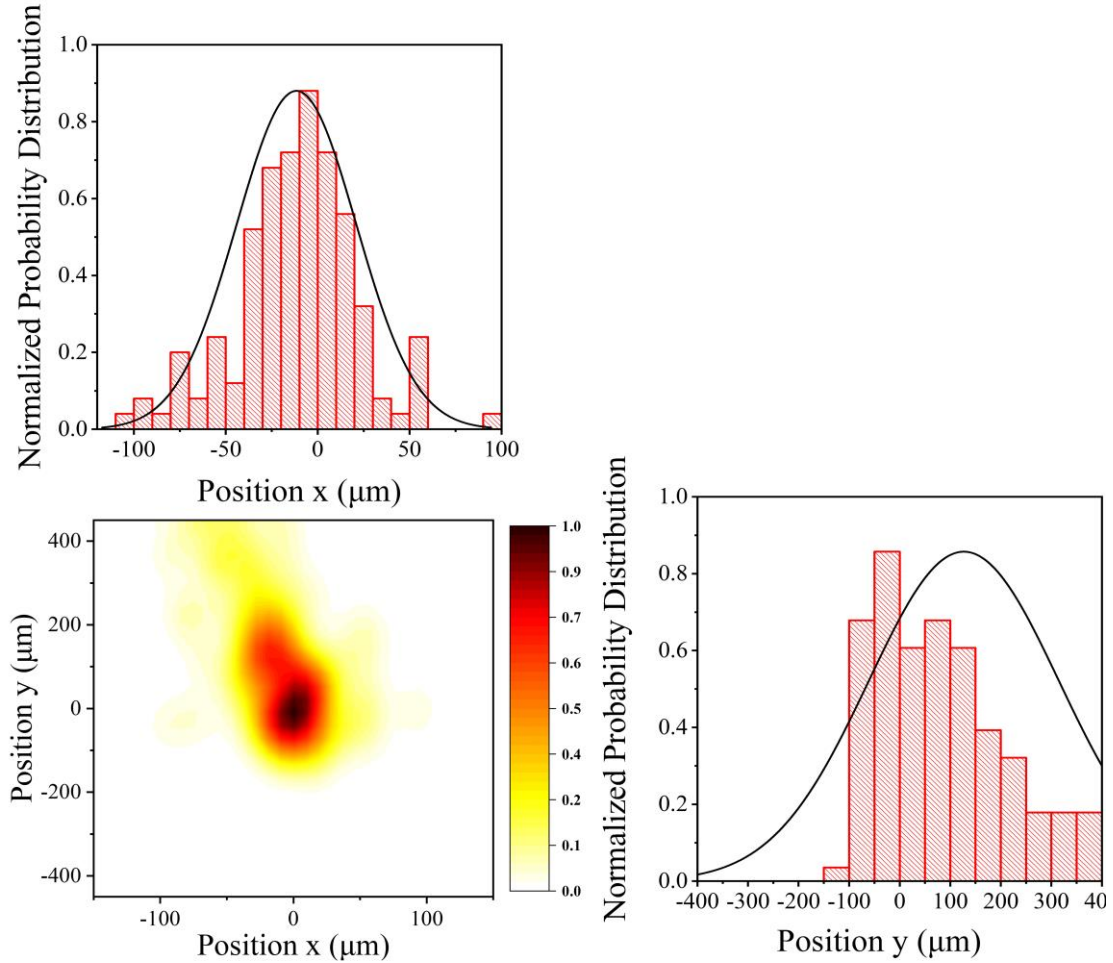
Figure 2.6 Measurement of the IR laser pointing instability. The contour illustrates the shot to shot distribution of the maximum of the IR laser intensity distribution measured just before the split mirror. The color bar shows the normalized probability distribution of laser shots. The upper and the right panel depict the individual variation across the x and y axes respectively.

2.3 Optimization of High Harmonic Generation and measurement of the XUV pulse energy

The development of high-flux attosecond laser pulses for performing nonlinear optics and attosecond pump-attosecond probe experiments has been a topic of interest for many years to the research community. In the effort of overcoming the physical and also technical limitations of the processes leading to this goal, many different approaches led to numerous techniques aiming to increase the photon flux of the produced radiation. Since this topic including the limitations and successive solutions will be extensively discussed in the following chapter only the approaches studied in this work will be presented followed by the comparison between them.

The high photon throughput of the presented XUV beam-line relies on the exploitation of 9 m focal length optics focusing the laser beam into the non-linear medium. Such a configuration is commonly used and aims to increase the number of the emitters that contribute to the process of HHG. In this section a comparative study between two different configurations delivering the gas phase medium into the driving IR pulsed beam path will be presented. In the first case the gas is introduced by means of a homemade piezoelectric crystal based gas-jet, while in the second a 10 cm gas cell is used.

The XUV generation unit host a xyz-translation stage upon which either the Gas Jet or Gas Cell is firmly mounted. The translation is used for optimization of the laser-gas interaction. The translation in the z direction (beam propagation direction) permits the variation of the HHG medium position with respect to the IR focusing position, a parameter that usually dramatically affects the spatial and also the temporal characteristics of the generated harmonics. The minimum step of the motorized translation stage is 5 μm. Regarding the interaction of the pulse with the gas phase medium, since 400 mJ pulse energy, which is the maximum output, would deplete the harmonic generation medium, at the used geometry the energy is reduced to 25-45 mJ after compression, depending on the gas used for the harmonic generation, which in this case is Xe or Ar. For the experimental investigations the iris in the entrance of the setup was set at the position which corresponds to 2.3 cm initial beam diameter of the IR beam. The goal is to increase the interaction volume between the driving pulse and the gas target, increase the confocal parameter which in that case corresponds to $b \approx 70$

cm and also to eliminate as much as possible the distortions (mostly astigmatism) attributed to the geometry of the focusing spherical mirror due to the deviation from the normal incidence. It's worth noting at this point that the experimentally determined confocal parameter is a factor of ≈ 1.22 larger than the value obtained according to the relation $b = 2\pi R^2 / \lambda_L$ (where R and λ_L is the radius and the wavelength of the IR beam) considering by Gaussian optics.

After the HHG area the fundamental as well as the XUV harmonics are collinearly propagating towards the "XUV filter and diagnostics Chamber" after been reflected by the Si plate. In this chamber a motorized x,y translation stage hosts metallic thin foils that act as a band pass XUV spectral selection filter, while effectively eliminate any residual IR radiation. The transmitted XUV beam traverses to the "End Station chamber" containing a pulsed gas jet and an electron/ion Time of Flight Spectrometer operating as a magnetic bottle by applying current to the adapted coils. By operating the spectrometer in electron detector mode the single photon ionization of Argon atoms, delivered be the detection gas jet, can be frequency resolved. At this point it should be stressed that for these measurements the spherical mirror placed in the detection chamber was walked off, in order to ensure that the photoelectrons originate from the interaction of Argon atoms with the incident, unfocused XUV beam, i.e. ensuring a single photon ionization process. Thus the energy of the XUV per pulse is reflected on the electron yield for both configurations implemented for HHG (Gas Jet or Gas Cell) when the diagnostic parameters are fixed (detector's efficiency, pressure of detection gas jet, etc.). In figure 2.7 the comparison of photoelectron yield produced by the harmonic frequency comb generated from Argon supplied by pulsed gas jet (a),(c) and 10 cm long gas cell (b),(d) is presented. For both measurements the IR pulse energy was 45 mJ and the initial beam diameter 23mm so that the intensity of the driving field was kept the same and just below the ionization saturation limit which in case of Ar as the nonlinear medium is $I_L < 3 \times 10^{14} \text{Wcm}^{-2}$.
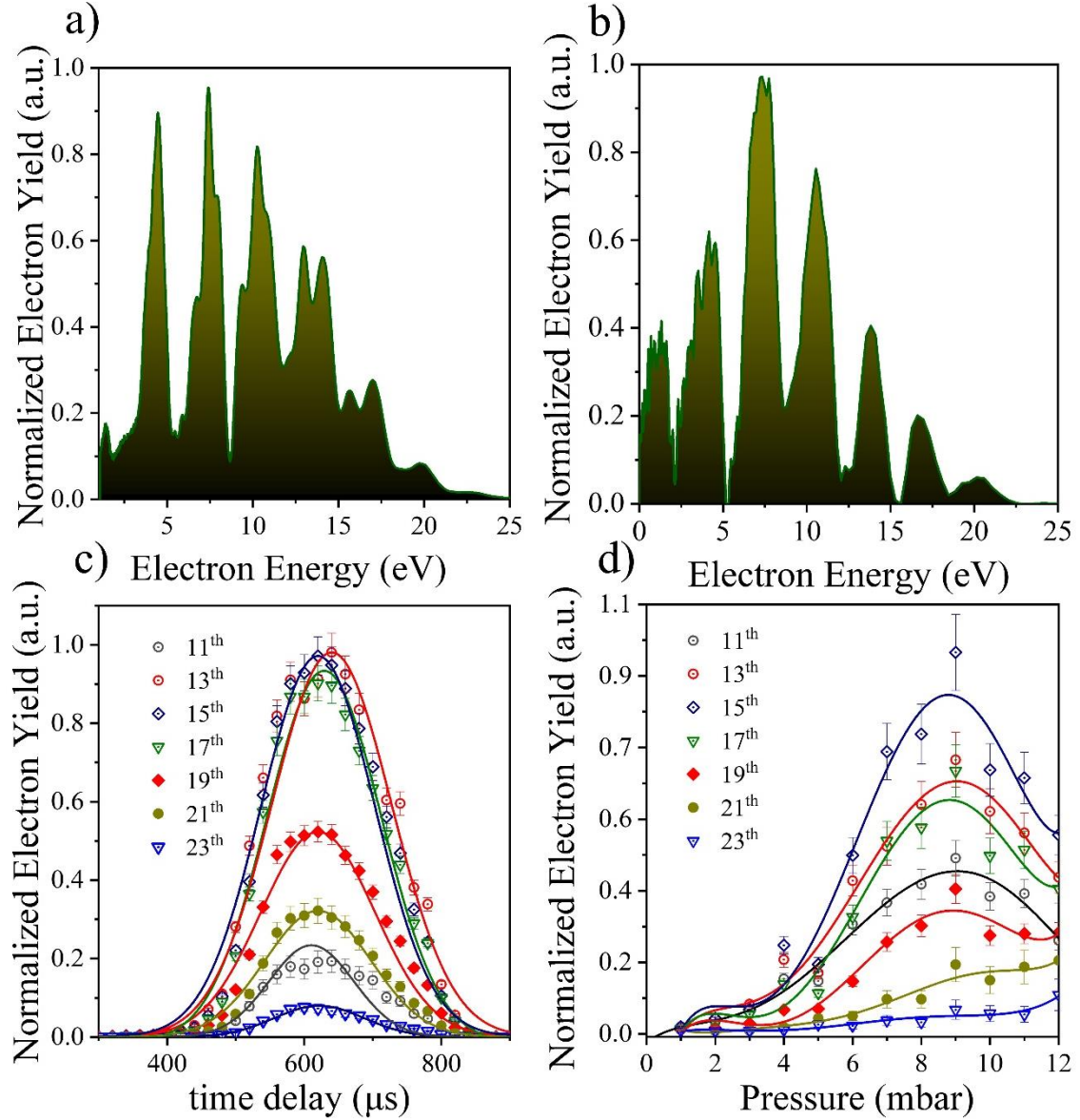
Figure 2.7 HHG produced by Gas Jet and Gas Cell. (a),(b) present the photoelectrons induced by single photon ionization in Ar by the XUV radiation.(c) Electron yield produced by HHG in Argon delivered from Gas Jet as a function of the time delay between the laser pulse arrival at the focus and the opening of the nozzle.(d) Electron yield as a function of the measured pressure of the Gas cell filed with Argon gas.

For both measurements the nonlinear medium (Gas Jet or Gas Cell) was set at the focusing position of the IR beam and the generated radiation was spatially filtered by a 5 mm pinhole located between the silicon and the Al metallic foil. Such a diameter size serves also to cut the outer part of the XUV beam, which mainly consists of

components originating from long electron trajectories contributing to HHG. The slit shaped orifice of the piezo-based pulse nozzle has dimensions 0.3×2 mm. The pressure and the medium length were estimated taking into account the backing pressure of the nozzle, the conductance of the orifice, and the distance between the orifice and the laser focus, which was ∼ 1 mm. The relative variation of the pressure in the generation area is represented from the change of the time delay in x axis of figure 2.7 (c) corresponding to the time spacing between the arrival of the IR pulse and the opening of the pulsed valve nozzle. Regarding the Gas cell measurements, the focused driving radiation is injected in a 10 cm chamber filled with gas, by an entrance pinhole of 2 mm diameter which is also the diameter of the output pinhole from which the beam is exiting. The pipe providing the gas contains also an intersection in which a pressure gauge is adapted for the pressure measurement used for the measurements.

After having optimized the HHG by recording the single photon ionization products of argon with the TOF set in electron mode, the absolute values of the generated photon flux can be measured by an XUV photodiode placed at the filters chamber. The signal in this case is fed to an oscilloscope (50 Ω input impedance) and the measured trace was integrated. The pulse energy E_{PD} measured at the position where the photodiode was placed is calculated by:

$$E_{PD} = \sum_q \frac{n_e \cdot w \cdot h\nu_q}{\eta_q} \cdot e \tag{2.1}$$

where q is the harmonic order, n_e is the number of produced photoelectrons, w is the statistical weight of the qth harmonic, $h\nu_q$ is the harmonic photon energy, η_q is the photodiode quantum efficiency of the photodiode and e is the electron charge. The photoelectron number is given by

$$n_e = \frac{S_T - S_{IR}}{e \cdot R} \tag{2.2}$$

where S_T is the total time integrated photodiode signal, S_{IR} is the time integrated photodiode signal when the harmonic generation is off, e is the electron charge and R is the oscilloscope impedance. The quantum efficiency of the photodiode as a function of the photon energy is provided by the manufacturing company. The pulse energy E at the harmonic generation source is given by:

$$E = \sum_q \frac{n_e \cdot w \cdot h \, v_q}{QE_q \cdot R_q^{Si} \cdot T_q^{Sn}} \cdot e \qquad\qquad (2.3)$$

where T_q^{Sn} is the 4% transmission of the Sn filter in this spectral region measured by recording the harmonic spectrum with and without filter, and R_q^{Si} is the ~50% - 60% reflectivity of the Si plate. The energy measurements regarding the comparison between Gas Jet and Gas Cell arrangements are depicted in figure 2.8.
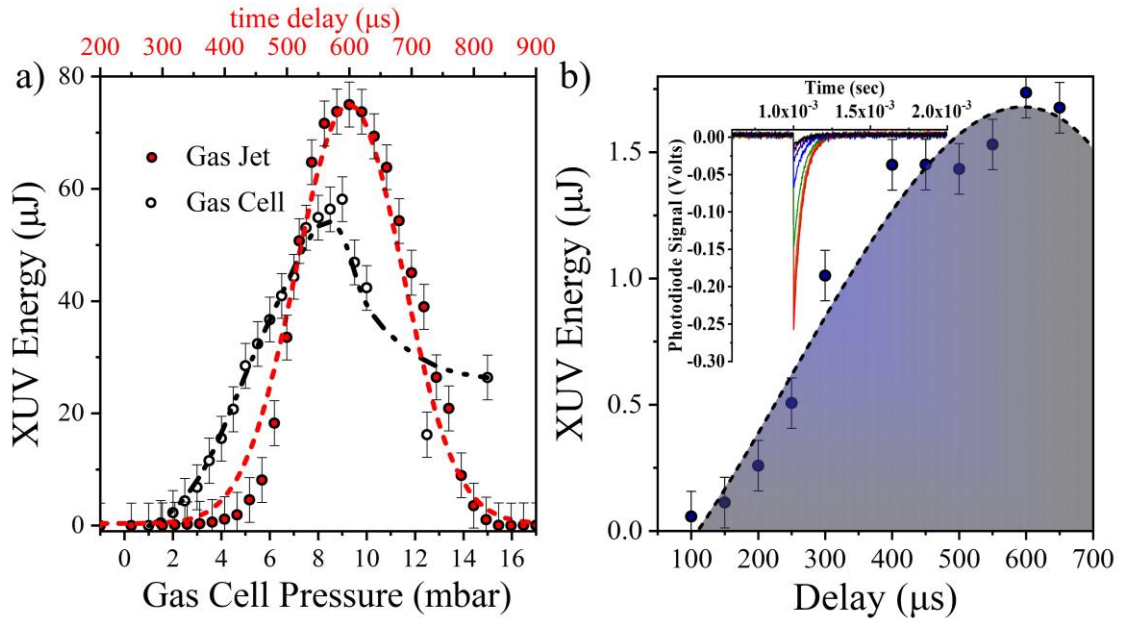
Figure 2.8 XUV energy measurement of Gas Jet and Gas Cell. Comparison of a single gas jet vs 10cm long gas cell yield, for optimized HHG conditions. The upper part axis represents the time delay of the pulsed nozzle while the lower one the measured pressure of the Gas cell. In all panels the generated medium was Ar, while the XUV energy was determined by PD$_{XUV}$ placed after an Sn filter.

The emitted XUV pulse energy as a function of the time delay between the trigger pulse of the GJ_1 nozzle opening and the laser pulse, for an arbitrary IR intensity just below the saturation threshold. The emission maximizes for a time delay of 600 μs. For the given cell length of 10 cm, the emission maximizes for a pressure value between 8 and 9 mbar. The maximum harmonic yield in the cell is found to be slightly lower (~25%) than the one of the gas jet. In these measurements Argon is used as generating medium and thus the pulse energy throughput is not the highest possible. Apart from the gas-jet/cell comparison measurement, the beam-line is operated exclusively with gas-jets, mainly because at 10Hz repetition rate they consume less gas, and because of their demonstrated slightly higher measured XUV energy throughput. After opting for the GJ configuration as the preferable one for the beamline of this work, experimental investigations focused on maximizing the photon flux of the emitted XUV radiation that will be extensively discussed in the following chapter.

It is worth noting that a second slightly different calibration curve is published in the documents of the manufacturing company of the photodiode. Using this second calibration curve the XUV pulse energy values reduce by 35%. The calibration curve for the AXUV100G utilized for the energy calculation of the measurements is presented in figure 2.9 (a) while for comparison reasons the later curve published from the company is also presented.
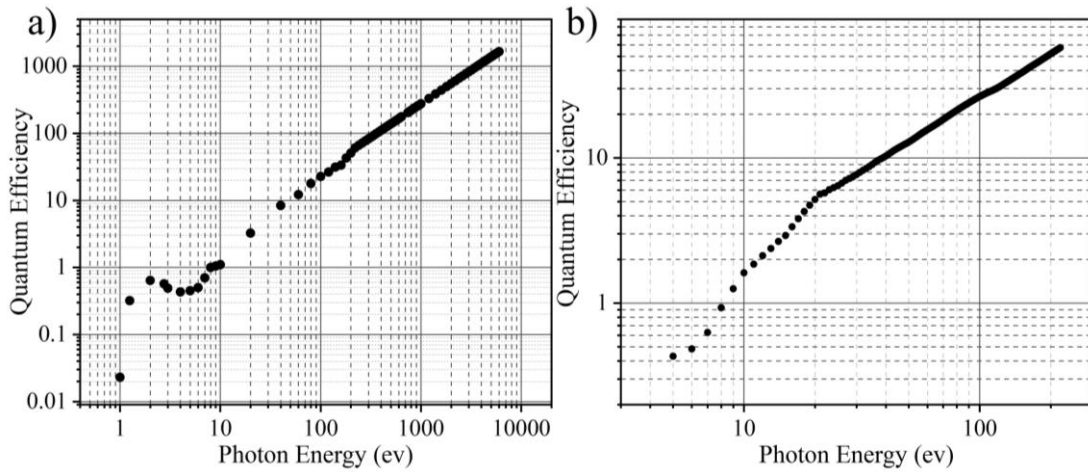
Figure 2.9 AXUV100G Quantum Efficiency curve. (a) Quantum efficiency utilized for energy measurements in this thesis. (b) curve provided by the company in a later manual.

Furthermore, it should be stressed that all of the pulse energy measurements with the XUV photodiode were carried out utilizing a bias circuit. By applying a reverse bias voltage of 9V saturation effects at high intensities, causing a decrease in collected charge per incident photon were prevented. By applying this technique it's worth noting that the total signal of the diode referring to the integration of the voltage recurred curve is negligible compared to the un-biased measurements. This ensures that the measurement it is not an artificial product of the circuit used. On the other hand, significant is the effect on the characteristic drop time of the signal with the un-bias curve, which as easily observed is revealing a rather large decay time.
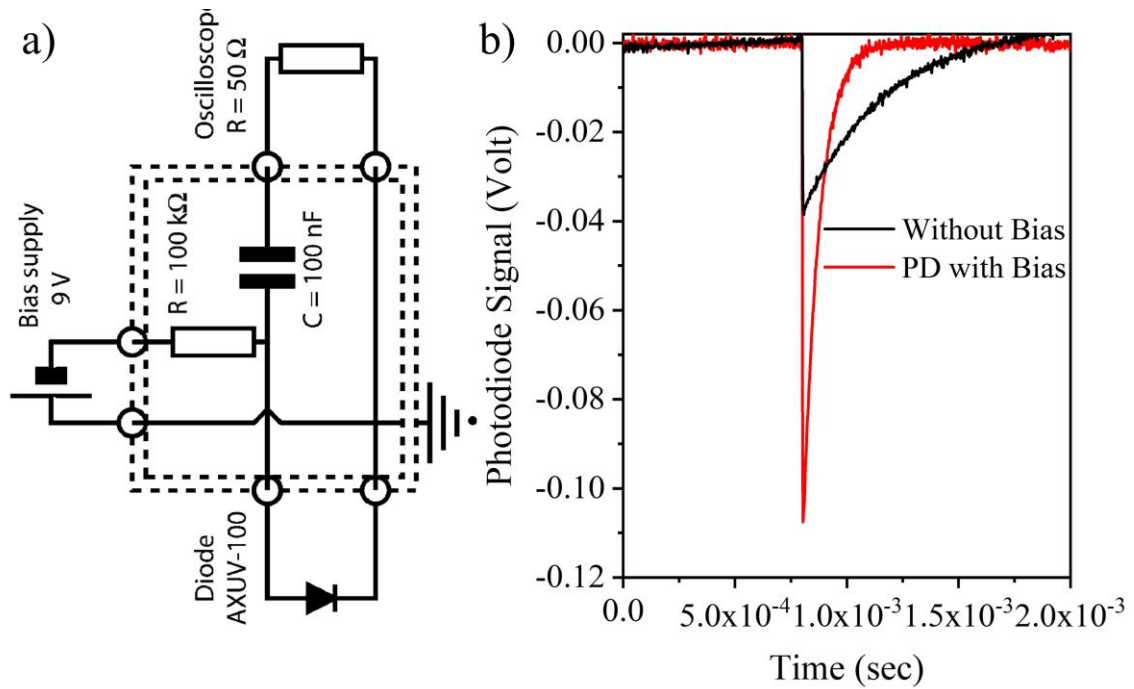
Figure 2.10 AXUV100G Bias circuit. (a) Scheme for biased operation of the XUV Photodiode. The diode is connected to the oscilloscope via a bias electronics circuit. (b) typical measurements of the XUV radiation with the black line to represent the direct signal from the Photodiode and the red curve with the bias circuit connected.

2.4 Spatial characterization of the XUV beam

Optimizing spatial characteristics of the generated harmonic radiation can be of crucial importance, as features originating from HHG or imperfections of the beam spatial distribution can dramatically affect experiments, even more so when attosecond pulse production is involved. In the most experimental investigations, regarding the XUV beam characteristics, as well as in theoretical treatment of the HHG process it has been frequently reported the major impact of the generation medium position relatively to the driving field focusing position. The above is attributed to the two different types of electron trajectories leading to harmonic generation upon recombination with the parent atom, and are favorable at different positions in the laser atom interaction region considering mainly the single atom response as well as the macroscopic phase matching requirements.

In the "XUV filtering and diagnostics" chamber the beam profile can be recorded by introducing an XUV beam profiler (Fig. 2.11), consisting of a pair of multichannel plates (MCPs) and a phosphor screen followed by a CCD camera. Figure 2.11 (b) shows the XUV beam profile recorded with the XUV beam profiler placed after the Al foil filter and with the harmonic generation Gas Jet positioned at the focus of the driving field. For this acquisition the MCP is supplied by a negative voltage of ~2kV while the phosphorus plate with a positive charge of ~3kV. Switching the gas jet off the response of the detector was zero assuring that the electrons emitted in the semiconductor sensor were originated only from the XUV.

To double check the spatial intensity distribution of the XUV beam recorded by the BP_{XUV}, the Knife Edge technique was employed for $z_{GJ}=0$. The XUV radiation consists of photons whose energy singly ionizes argon gas and the photoelectron yield is measured as a function of the knife edge position. The measured curve shown in Figure 2.11 (c) (black dots) is then differentiated resulting in the intensity distribution (red dots). The colored area is defined by a Gaussian fit to the measured data. The results of the Knife Edge measurements were in agreement with the values of the XUV beam radius obtained by the BP_{XUV}. For further investigation, recordings have been carried out for several positions of the GJ1 producing the XUV radiation. No significant change was observed when GJ1 was placed before (zGJ1 =-b, -b/2), on (zGJ1 = 0) or after (zGJ1 = b, b/2) the driving laser focus.
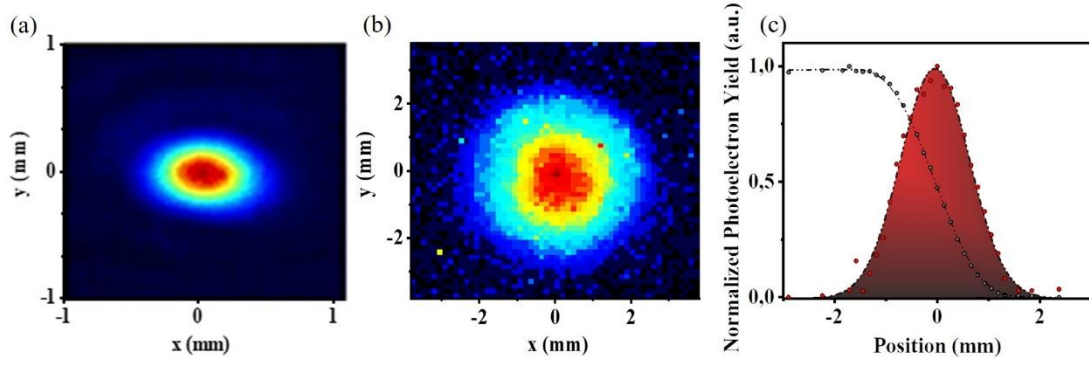
Figure 2.11 IR and XUV beam profiles. (a) IR beam profile at the focal plane measured by a commercial CCD profile camera. (b) XUV beam profile recorded using the BP$_{XUV}$. (**c**) Knife edge measurement of the XUV beam profile presented with black dots while the red dots show the obtained intensity distribution. The colored area is defined by a Gaussian fit to the measured data. In both (b) and (c) measurements, harmonics are generated using xenon with the GJ placed at the IR focus.

For the Knife Edge technique measurement, the total photoelectron yield with Argon gas as target was recorded as a function of the calibrated position of two dimensional obstacle. A metallic plate mounted on a stage with micrometer resolution in the translation movement was introduced into the beam path partially blocking the XUV. For the analysis a Gaussian shape of the harmonic beam was considered with the intensity distribution described by:

$$I(x,y) = I_0 e^{-2x^2/w_x^2} e^{-2y^2/w_y^2} \qquad (2.4)$$

Where I_0 denotes the peak intensity of the distribution, w_x and w_y are the beam's width in the two directions of the transvers plane of the propagation. The integration over the total power of the beam for the two dimensions with the limits of the integration to represent the total translation along the axis, the signal recorded reads:

$$S(x) = \frac{S_{Toatal}}{2}\left[1 - \frac{2}{\sqrt{\pi}}\int_0^x e^{-\frac{2x^2}{w_x^2}} \frac{\sqrt{2}}{w_x} x\, dx\right] \qquad (2.5)$$

2.5 The Magnetic Bottle Time of Flight Spectrometer

A commonly used device to collect ionization products, namely electrons or ions, is the Time of Flight (TOF) spectrometer that detects the species according to their flight times between the interaction region where they are created and the detector. There is a variety of configurations achieving different collection efficiencies and resolutions. Among them, a successful set up appears to be the magnetic-bottle TOF which can achieve high energy resolution and high collection efficiency simultaneously due to its non-uniform magnetic field. In the "End Station chamber" a similar Time of Flight Spectrometer is adapted for collecting the products of the interaction between the XUV beam (or IR beam) and the gas target. With appropriate voltage settings TOF can be operated either in an ion spectrometer (resolving ions according to their m/q ratio) or electron energy analyzer mode.

Referring to the electron energy analyzer mode, in most analyzers, the energy resolution decreases rapidly as the acceptance angle and resulting collection efficiency are increased. In the case of a field free TOF which consists of a drift tube and an electron detector, the products of the light-matter interaction in the case of photoionization are measured as a function of the arrival time at the detector without interacting with any external field. Thus the arrival time corresponds directly to the drifting over the length of the tube time:

$$T_{drift} = \frac{L_{drift}}{u} = \frac{L_{drift}}{\sqrt{2\,E_k/m_e}} \qquad (2.6)$$

where u corresponds to electron's velocity, E_k to the electron kinetic energy ($E_k=E_{photon}$-IP in case of photoionization) and m_e is the mass of the electron. In this case the maximum possible resolution in energy, ΔE, if the minimal time interval that detection electronics can resolve is Δt, is given by the expression:

$$\Delta E = \frac{\sqrt{8}}{\sqrt{m_e}} \frac{\Delta t}{L_{drift}}\, E^{3/2} \qquad (2.7)$$

while the relative resolving power of the spectrometer is determined by the relation:

$$\frac{\Delta E}{E} = \frac{\sqrt{8}}{\sqrt{m_e}} \frac{\Delta t}{L_{drift}}\, E^{1/2} \qquad (2.8)$$

The major drawback of the field free TOF is the low collection efficiency. A magnetic electron spectrometer designed to collect electrons emitted over an angular range of $2\pi\Omega$ while maintaining an excellent energy resolution, is installed in the GW attosecond beamline. The basic operating principle of a magnetic bottle time of flight electron spectrometer is that the non-uniform magnetic field collimates the trajectories of the electrons produced at the interaction region so that the electrons, initially emitted into all directions, form a nearly parallel beam as they fly through the flight tube. Electrons, generated by a photoionization process in the presence of a high magnetic field saddle region in the center of a large cylindrically symmetric electromagnetic circuit, spiral around magnetic field lines towards regions of lower field strength on either side of the saddle. The axially decreasing magnetic field, shaped appropriately for nearly adiabatic electron motion, rotates the electron velocity vectors so that all electrons originally emitted in $2\pi\Omega$ solid angle are eventually directed nearly parallel to the axis of a long solenoid flight tube of low and constant magnetic field strength provided by coils adapted to the flight tube. The Lorentz force of such a field causes each electron to spiral closely around a magnetic field line which goes from the tip of the pole piece to the flight tube. In the spectrometer utilized, a permanent magnet consisting the tip orifice of the detection gas jet pulsed valve, is used to produce the conical-shaped pole of the strong field. The weak field is produced by a solenoid coil wrapped around the flight tube. The electrons are detected at the end of the flight tube by a dual MCP detector.

Considering an electron freed from an atom and emitted in the continuum in an arbitrary angle θ_i with respect to the tube direction, in the presence of the strong static magnetic field B_i leads to a spiral motion with frequency ω_i and radius r_i described by classical electrodynamics. The angular momentum accumulated by the electron is then expressed by:

$$L = \left(m_e \, r_i^2\right) \omega_i \tag{2.9}$$

Where the radius and frequency of the electronic motion are:

$$r_i = \frac{u \, sin\theta_i}{\omega_i} \quad , \quad \omega_i = \frac{e}{m_e} B_i \tag{2.10}$$

Thus, the momentum of the electrons entering the weak magnetic field region is:

$$L = \frac{m_e^2\, u^2\, sin^2\theta_i}{e\, B} \tag{2.11}$$

As the electron enters the region of the weak uniform magnetic field, B_f, in the flight tube, the angular momentum could be conserved if the variation of the field along the spectrometer axis is adiabatic. The adiabaticity here means that the change of the field experienced by an electron is negligible in one revolution of the spiral motion. With the flight distance in the tube to be L_{drift}, the electron flight time is then:

$$T = \frac{L_{drift}}{u_{drift}} \approx \left(1 + \frac{sin^2\theta_i}{2}\frac{B_f}{B_i}\right) \tag{2.12}$$

which is almost independent of the initial emission direction because of the parallelization of the trajectories. It should be noted that for the extraction of the velocity the momentum in the drifting area is set to be the same as the one exiting the strong magnetic field. The maximum difference of the flight time caused by the emission angle and the equivalent resolution product in terms of energy is given respectively by:

$$\frac{\Delta T}{t} = \frac{B_f}{2\,B_i} \quad , \qquad \frac{\Delta E}{E} = 2\frac{\Delta T}{t} = \frac{B_f}{B_i} \tag{2.13}$$

Therefore, the energy resolution can be improved by increasing B_i or decreasing B_f. In the region between the pole piece and the flight tube, the magnetic field and its gradient are both strong, and the flight time is significantly different for electrons with different emission angles. It has been found that the flight time spread in this transition region is larger than that in the flight tube and may be decreased if the length of transition region is decreased.

The above approximation requires that the variation of the magnetic field along the propagation axis is adiabatic, which means that the field experienced by an electron changes negligibly in the course of one revolution of the helical motion. Then the angular momentum is a conserved quantity. The above leads to a ratio between the angle of the helical motion in the two different magnetic field regions to be:

$$L_i = L_i \rightarrow \frac{sin^2\theta_f}{sin^2\theta_i} = \frac{B_f}{B_i} \tag{2.14}$$

However, even electrons that are initially emitted nearly perpendicularly to the field lines in the high-field region are nearly parallel in the low-field region and thus the trajectory exhibits a diverted angle with respect to the field lines. Therefore, the acceptance angle can reach $2\pi\Omega$. If the field strengths in the two regions are sufficiently different, after the electron beam has been parallelized, the electrons travel in a uniform magnetic field down to a flight tube before being detected. The acceptance angle is expressed as:

$$\Theta_{f,max} = sin^{-1}\left(\sqrt{\frac{B_f}{B_i}}\right) \tag{2.15}$$
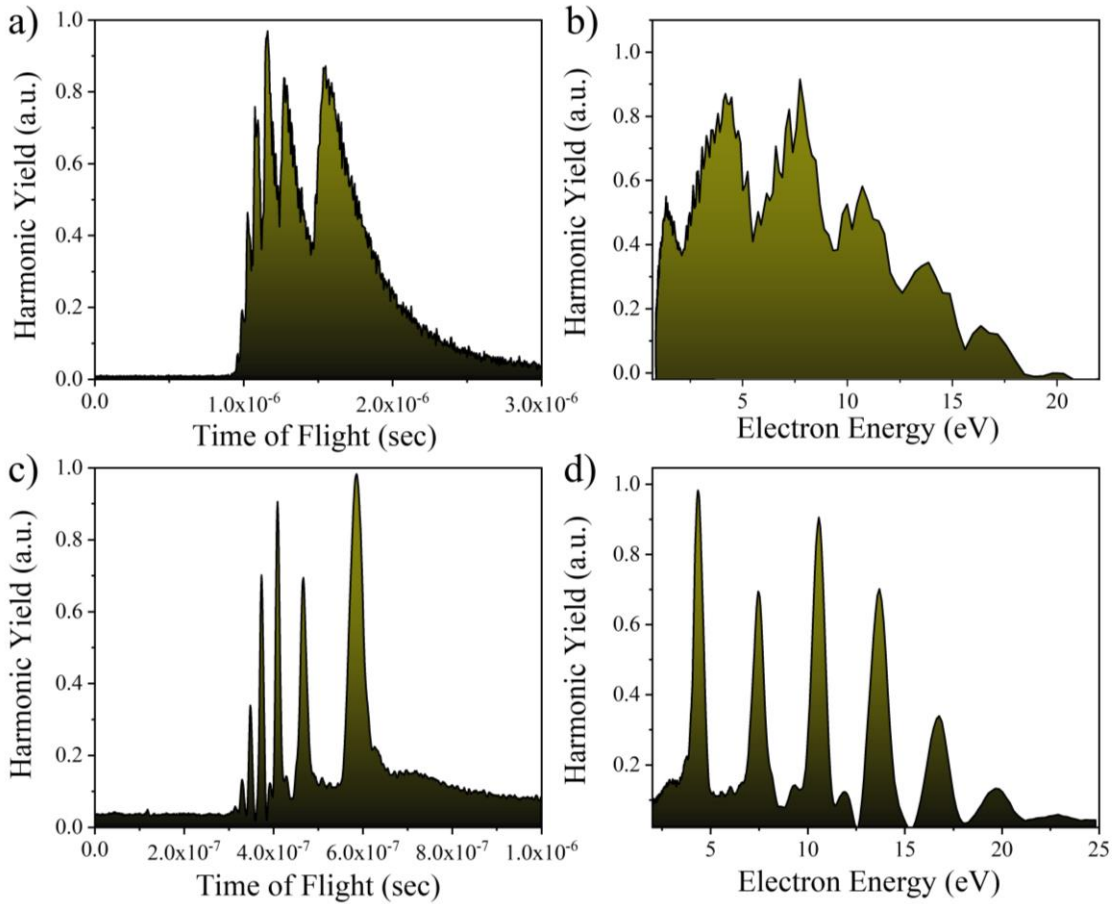
Figure 2.12 Time of Flight Electron spectra. (a), (b) Photoelectron spectra obtained without the permanent magnet. (c), (d) spectra obtained by the magnetic bottle time of flight spectrometer. In both cases the electrons originated from the interaction of Ar and XUV beam generated in Ar and filtered by an Al foil.
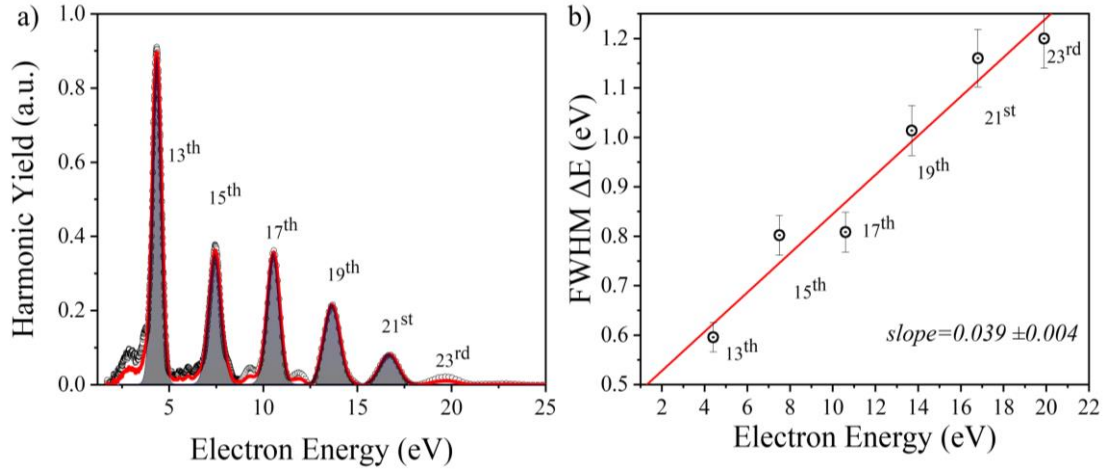
Figure 2.13 Resolution of Time of flight electron spectrometer. (a) Harmonic spectra generated in Argon after spectral selection by Al foil**.** The black circles are representing the measured data, the gray curves the individual Gaussian fits and the red curve the cumulative curve. (b) The determination of spectral resolution of the magnetic bottle electron spectrometer.

A photoelectron spectrum obtained from Argon gas interacting with the harmonic radiation is presented in Figure 2.13 with the highest photon energy to be ~19.9 eV corresponding to 23rd harmonic of the fundamental driving field. A fit of a sequence of Gaussian functions over the photoelectron spectrum reveals the fitting curve of each individual distribution of photon energy. The FWHM of them to is implemented for the determination of the spectral resolution of the Time of flight Magnetic Bottle operating in electron recorder mode. From the data recorded, Gaussian fits are performed over each individual electron distribution and the width is determined. Scaling the width as a function of electron kinetic energy a slope of 0.039 is revealing the energy resolution of the spectrometer $\Delta E/E \approx 4\%$. Measurements requiring although high accuracy also demands ultra-high vacuum in order to ensure the origins of photoelectrons produce. Thus a tedious task appeared to be the absolute calibration of the time scale of the recordings and the correlation to kinetic energy, in cases of gas mixtures contributing simultaneously in the spectra under investigation. In most cases the above situation is emanating from the contamination of the chamber and/or the impurities of the gas supply. For resolving the above obstacle, a cryogenic cold trap can be implemented with liquid nitrogen freezing the contaminations mostly H_2O.

By applying repulsion voltage, TOF can be utilized in ion mass spectrometer mode. In this case a high voltage power supply (up to 5 kV) is floating the piezo based valve at positive charge state. The ions produced in the interaction region are experiencing a Coulomb force driving them towards the detector. The hole configuration except coils supply (which for this case remain off) remains the same for the one implemented for electron detection. Since the permanent magnet described above does not affect the ionic motion the calibration of the observed masses can be calculated from the arrival times of the species.

$$E_k = q\,V = \frac{1}{2}\,m\,u^2 \tag{2.16}$$

$$t = \frac{d}{\sqrt{2\,V}}\sqrt{m/q} = k\sqrt{m/q} \tag{2.17}$$

By focusing the generated XUV radiation after passing through the Sn filter and by applying positive repulsive voltage, ionic distributions of single-photon Xe^+ products, as well as two-photon Xe^{2+}, are observed and are shown in figure 2.14.
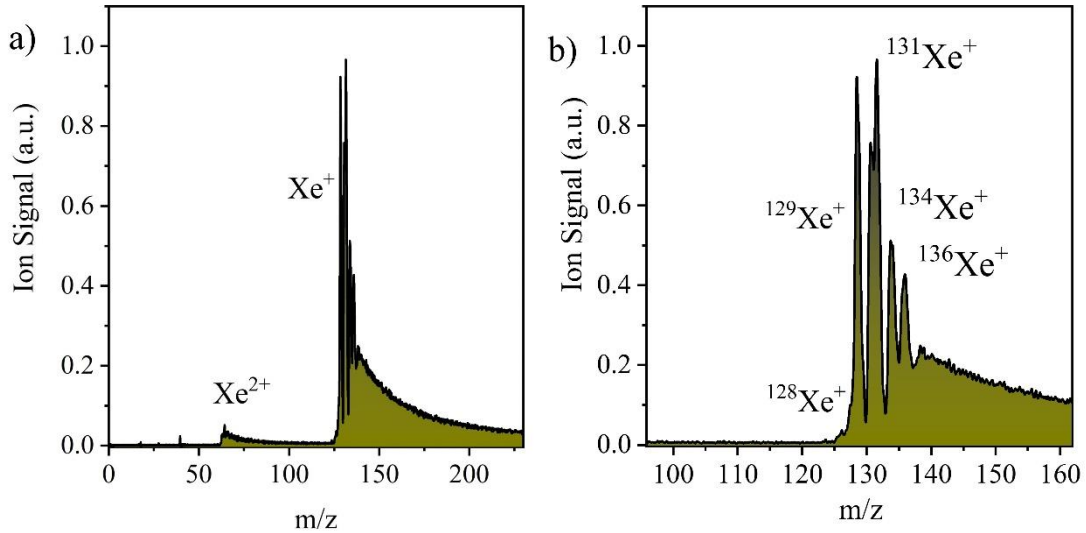
Figure 2.14 Time of Flight spectra of Xenon. (a) TOF mass spectrum produced by the interaction of the focused 11th-15th harmonics with Xe. In the spectrum also Xe^{2+} is observable arising from two photon double ionization. (b) An expanded area of the mass spectrum with the peaks of Xe corresponding to the most abundant isotopes.

The natural abundances of xenon isotopes are, 128: 2%, 129: 26.4%, 130: 4.1%, 131: 21.2%, 134, 10.4%, 136: 8.9% and are clearly resolved in figure 2.14 (b). The dynamic resolution in case of Ion mode operation of the Time of Flight spectrometer can be deduced from mases with that are sharing neighboring regions as in case of the Xenon isotopes presented in the upper figure.

$$Resolution \ = \ M \ / \ \Delta M \ = \ M1/(M1 - M2) \tag{2.18}$$
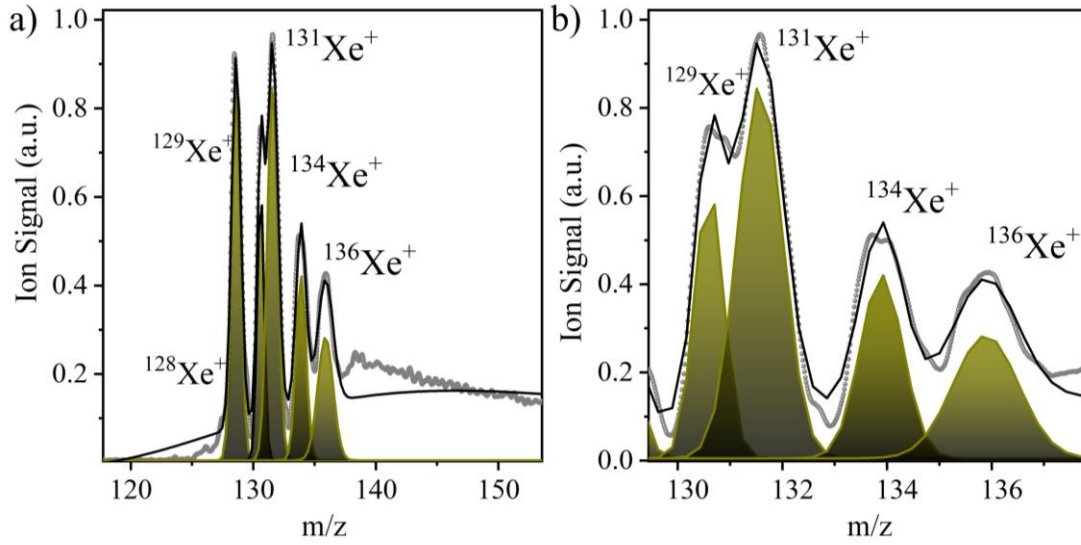
Figure 2.15 Resolution of Time of Flight ion spectrometer. (a) An expanded area of the mass spectrum with the peaks of Xe corresponding to the most abundant isotopes. TOF mass spectrum produced by the interaction of the focused 11th-15th harmonics with Xe. The trace measured is represented by the gray dotted line, the yellow filed curves Gaussian fits over distinguished peaks while the black curve the cumulative curve produced by the sequence of Gaussian fits (b) zoomed area of Xe ion distribution a with sequence of the Gaussian fits and the cumulative curve fitting the measured signal (grey circles)

2.6 The XUV wavefront split and delay unit

For attosecond time resolved measurements such as XUV-pump / XUV-probe a configuration for introducing a time delay between the pump and the probe pulses is required. In most of the cases in ultrafast optics, the delay line is based on the splitting of the initial beam into two parts by means of a beam splitter with the appropriate optical properties regarding the wavelength and spectral characteristics of the radiation. Since no conventional beam splitter is available in the XUV region, the implementation of an XUV wavefront splitting device is a feasible solution.

In the present beam line, the dispersion-free wave-front splitter consists of a gold spherical mirror (SM), which is splitted into two symmetric halves of a 5 cm focal length. The delay unit is firmly mounted on piezo-electric translation-rotational stage. This stage enables control in 3 degrees of freedom for the one D-shaped half of the mirror i.e. the displacement along the z axis (i.e. the beam propagation axis) with a maximum value of 80 μm and rotation in the x-z and y-z plane. The other half of the mirror is translated only along the propagation direction with a maximum translation of 400 μm. All movements of the split-mirror are controlled by piezo crystals operated in closed loop mode. A 1.5 nm minimum step of the translation of the first of the two parts of the bisected mirror introduces a temporal delay between the two parts of the splitted beam. It is worth noting that for such time delays (80 μm total translation), effects of spatial displacements of the two parts of the focused beam are negligibly small. The products of the interaction between the XUV beam and the gas phase target, introduced by the detection gas jet, can be detected by the setting the TOF spectrometer either in ion or electron mode. The above configuration provides a successful solution for XUV-pump / XUV-probe experimental investigations but also for the pulse duration characterization via second order volume autocorrelation, a technique which will be extensively discussed in Chapter 4.

The temporal resolution of the beam line has been tested by measuring the beam pointing stability at the end station, the performance of the split mirror device and its interferometric stability. The characterization was carried out by shining a CW diode Laser (λ=532 nm) onto the split spherical mirror and by focusing the reflected beam with a 1 m lens towards a CCD camera.

In figure 2.16 a schematic of the split mirror assembly is presented. The focal area of the gold coated spherical mirror was magnified by a lens and imaged by a CCD camera. In figure 2.16(b) the calculated (left panels) and measured (right panels) images of the focal spot area for two different delays, i.e. for two different displacements of the one-half of the mirror, are depicted. The upper panels demonstrates the intensity distribution at the focus formed when the phase difference between the two parts of the laser wave-front reflected by the two mirror halves is equal or close to $2n\pi$, $n = 0,1,2,3\ldots$, i.e. when the delay between the two wave-fronts is $\sim n T_L$, with T_L being the period of the laser field. The phase difference is controlled by finely adjusting the position of the piezoelectric translator connected with the one part of the split mirror. The position of the piezo translation stage was measured by a capacitive sensor feedback system of the piezo system. When the phase difference of the two wave-fronts becomes equal or close to $(2n+1)\pi$, $n = 0,1,2,3\ldots$, i.e. when the delay between the two wave-fronts is $(n+1/2)T_L$, the intensity distribution at the focus splits into two bright spots shown at the lower part of the figure 2.16 (b). The two bright spots ideally have the same intensity.

Additionally, a higher-order autocorrelation trace of the fundamental laser field (IR) was recorded. For this acquisition, the harmonic generation was switched off and all filters were removed, thus ionization of Argon occurs only through the fundamental laser frequency by multi-IR-photon absorption. The measured trace is shown in figure 2.16 (c)where the interferometric interference fringes are clearly visible. The red dashed line is the cycle average of the data. The interference fringes are used for the calibration of the delay scale of the measured autocorrelation traces. The period of the observed oscillation, depicted in the expanded AC area trace in figure 2.16 (d) is equal to the laser period that is 2.67 fs, where the red line is a cosine fit in the measured data. Besides the characterization of the special overlap of the two created beams, determined from imaging of the focus, the temporal overlap (i.e. the z translation axis of the piezo) is calibrated by maximizing the ion signal, product of the highly nonlinear ionization of Ar induced by the IR focused pulses. For this case vital parameter consist the accurate spatial overlap, increasing the signal to background ratio, making the frequency resolve highly nonlinear autocorrelation trace a calibrating tool for the displacement between the two mirror's components.
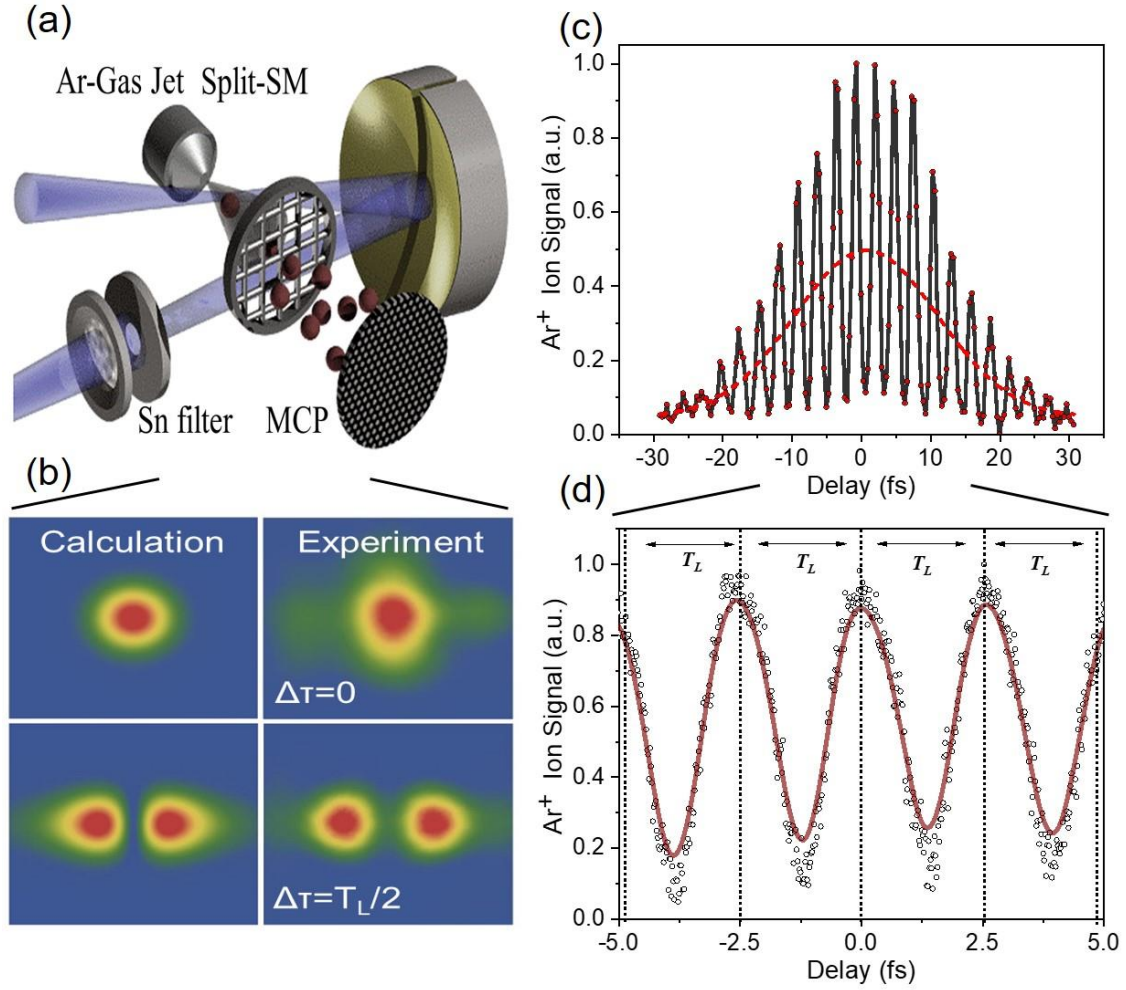
Figure 2.16 Split mirror arrangement. (**a**) A schematic of the experimental set-up of the autocorrelator consisting of a split spherical mirror and a TOF spectrometer. (**b**) Calculated (left panels) and measured (right panels) transverse intensity distribution of a CW 532 nm laser at the focus of the spherical mirror for Δτ=0 and Δτ=T_L/2 (double maximum distribution) delay. (**c**) High-order autocorrelation trace of the fundamental laser field (IR) obtained measuring the Ar+ yield as a function of the time delay between the two pulses produced by the split mirror.(**d**) Expanded area of the AC trace. The signal is oscillating at the laser period of 2.67 fs.

The temporal stability provided by the configuration described has been also determined. The shot-to-shot fluctuations of the XUV intensity distribution may be introduced because of: i) the non-perfect pointing stability of the laser and consequently of the XUV beam, ii) mechanical instabilities of the split mirror arrangement iii) vibrational noise mainly originating from the mechanical vacuum pumps. The above factors affect the interferometric stability of the delay line and

therefore making pump probe studies difficult if not impossible in the extreme short time scale of tens of attoseconds. The interferometric stability of the split mirror was measured using a CW laser of λ=532 nm by the following procedure. The displacement of the two halves of the spherical mirror was fixed such as introducing a delay of $T_L/2$. For the acquisition, 1260 points were measured with the same optical layout described above, referring to the imaging of the focal spot by means of a focusing lens. The signal as described, exhibited a two peak structure over which the two gates were set. Consequently, in the line-out of the focal spot area, the integrated areas of the two gates L and R, introduced in figure 2.17 (b), are essentially equal.

In an ideal case the integration of these two distributions must be the same for the hole acquisition time and moreover equal for both of the cases. Thus the difference between the signal produced by the two gates must be constant at zero. Any deviation from this picture can be correlated to the instability of the split spherical mirror, since it originates from the optical path difference between the two interfering wave fronts. The interferometric stability of the split mirror device is extracted from the standard deviation of the mean value of the probability distribution for 1260 points as a function of time and is found to be $\approx$ 17 asec.

Although the interferometric stability of the device cannot be different when another source of radiation is used, one has to consider that when IR laser is used, the pointing stability is not the same with that of the CW one. The pointing stability of the IR was measured with an IR beam profiler placed just in front of the split mirror as described in section 2.3. The shot-to-shot position of the maximum of the intensity distribution is plotted in figure 2.17(c) for 150 laser shots. The mean FWHM of the contour is about 75 μm and thus substantially smaller than the 3 mm FWHM of the XUV intensity distribution at the split mirror, not affecting the measured interferometric stability and time resolution.
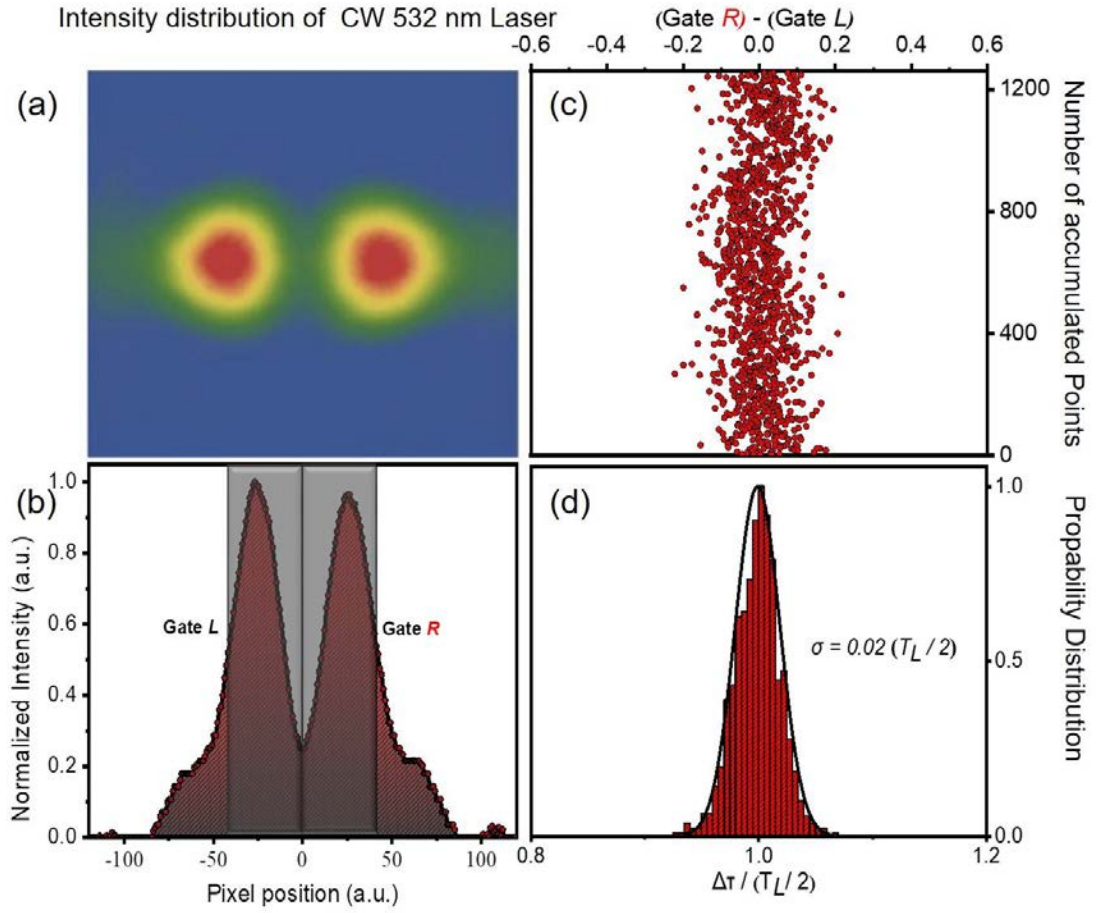
Figure 2.17 Stability measurements of the split-mirror autocorrelator. (a), (b) Measured transverse intensity distribution of a CW 532 nm laser at the focus of the spherical mirror for $\Delta\tau=T_L/2$ (double maximum distribution) delay. It is noted that in this graph T_L corresponds to the period of the 532 nm CW laser. (c) The difference of the integrated signals of the Gate L and R. (d) Probability distribution of the above difference (1260 points were accumulated). The standard deviation of the mean yields a temporal resolution of ~ 17 asec.

2.7 The Spectral characterization of XUV radiation

A variety of information can be extracted from the observed output spectrum, resulted from High Harmonic Generation. Features in the spectral domain of the HHG process may reveal not only the properties of the driving field, such as the pulse duration and shape of the pulse, etc. but also vital information about the interacted target responsible for the frequency upconversion. Although monitoring the produced XUV radiation by implementing time of flight electron spectrometer is a very common experimental approach it may suffer from a variety of limitations, especially in the high photon energy regime (small wavelengths). Extracting the spectrum under investigation, one has to consider several factors such as the spectral response of the gas implemented as target for the single photon ionization (atomic scattering factors and cross sections), space charge effects induced when high densities are required in case of low driving pulse energy flux and relatively small collection efficiency of the detector in case the goal is the enhancement of the resolution and vice versa.

The attosecond beamline besides the time of flight electron spectrometer, incorporates also a commercial flat field spectrometer (FFS) which is adapted in the "End Station Chamber" placed at the end of the beam line. The XUV radiation spectrum is monitored by the XUV radiation passing through the slit (approximately 50-100 microns) formed by the two parts of the bisected mirror, taking advantage of the high photon flux of the generated radiation which makes feasible the spectrum measurement even with this small percentage of it. The XUV beam after being transmitted through a metallic foil for spectral selection mounted with 5 mm pinhole is then passing from the slit (approximately 50-100 μm) created by the two components of the split mirror device. At the rear flange of the end station a mechanical valve can isolate the FFS assembly. The arrangement of the spectrometer is presented in figure 2.18. The beam enters the spectrometer through an entrance slit with adjustable width. The slit can be mounted on a flange connecting the spectrometer with the chamber. Although for the wavelengths implemented the slit is not necessary, it can significantly increase the resolution and also avoid the possible imperfections in the beam's spatial distribution. A mount housing metallic filters provides the additional spectral filtering of the XUV radiation, and in many cases is also useful for attenuation, when the flux is high. The XUV grating (Hitachi corp.) is mounted on a translation stage providing three degrees of freedom. The stage is controlling the alignment of the grating with respect to the

XUV beam and one can adjust the angle of the incident/refracted beam and also the focal position by changing the vertical and horizontal position. A zero-order block is optional for preventing the directly reflected beam and suppress the background signal. The spectrally analyzed diffracted beam is steered towards the detector consisting of a pair of MCPs and a Phosphor screen. The detector arrangement is mounted on a pair of plates with O-ring seal of which the one part can be translated in the vertical direction when the spectrometer chamber is vented. In this way one can select the spectral range impinging the MCP detector. The output of the MCP detector is then spatially resolved by a CCD camera mounted after the phosphor screen. An additional turbo pump differentially pumping the FFS spectrometer ensures that the pressure where the multichannel plate detector is located, is lower than 10^{-6} mbar for, limitation level for safe operation.
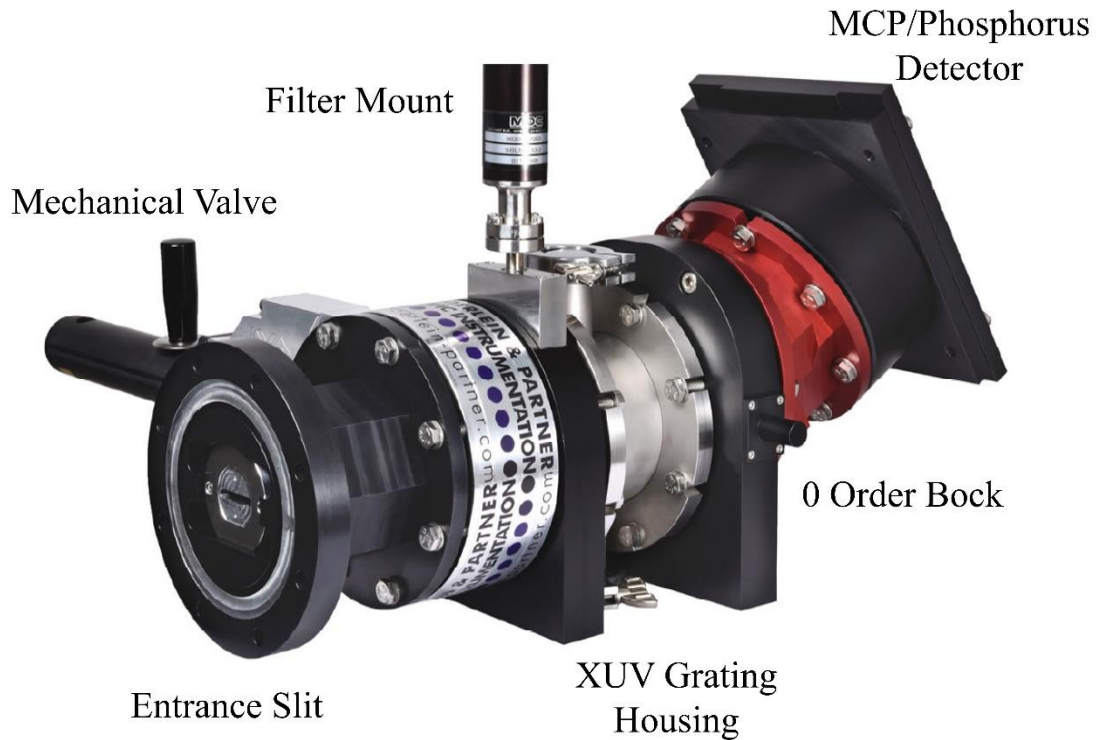
Figure 2.18 Flat Field Spectrometer. A Picture of the spectrometer implemented with the individual components marked. The FFS can be operated with both vertical and horizontal orientations with respect to the XUV diffraction grating.

The XUV spectrometer can provide three possible configurations covering a spectral range spanning from 80nm to 5nm depending on the angle between the grating

and the detector. The XUV grating with grating constant is 1200 grooves/mm hosted in the spectrometer and provides high reflectivity with the requirement of very high grazing incidence (~85^0). The grooves are producing a triangular or a rectangular shape with the triangular grooves case to be usually referred as Blazing grating. These type of gratings are defined by the Blaze angle, which is the angle between the long side of the triangle and the grating normal. The long side of the grating faces into the direction of the incident beam. With the incidence angle α and the exit angle β, the corresponding wavelength for constructive interference can be calculated by the grating equation:

$$d\ (sina + \ sin\beta) = m\ \lambda \qquad (2.18)$$

where d is the grating constant. As a simplification only the first order diffraction is considered with m = 1. Therefore, the resolution per angle is

$$\frac{d\lambda}{d\beta} = d\ cos\beta \qquad (2.19)$$

The angle β, can be written in dependence on the wavelength λ and the incidence angle α

$$\beta = arcsin\left(\frac{\lambda}{d} - sina\right) \qquad (2.20)$$

Thus the minimal wavelength difference dλ, can be calculated through 2.17 and 2.18

$$d\lambda = d\ cos\left[arcsin\left(\frac{\lambda}{d} - sina\right)\right]\ d\beta \qquad (2.21)$$

The spectrometer can support a long range of wavelengths by having three different configurations flanges on which the detector is mounted. These three different configurations, characterized by different angles of the flanges combined by the capability of vertical translation of the screen offer a span from 5 nm to 80 nm (248 eV -15 eV). In the present work due to rather lower photon energies produced in the attosecond beamline the spectrometer is set in the range of 25nm to 80 nm by the implementation of 85^0 flange while the optimum position of the screen can be calculated taking into account: the distance of the screen from the source, the angle of

incidence between the XUV beam and the grating, and finally the diffraction angles of the diffracted spectral components.

Harmonic Order	Wavelength (nm)	Photon Energy (eV)	β_1 1st order (degrees)	β_2 2nd order (degrees)
7	114	10.85	-59.21	-46.21
9	89	13.95	-62.81	-51.52
11	73	17.05	-65.36	-55.26
13	62	20.15	-67.28	-58.06
15	53	23.25	-68.79	-60.26
17	47	26.35	-70.01	-62.04
19	42	29.45	-71.03	-63.53
21	38	32.55	-71.89	-64.79
23	34	35.65	-72.71	-65.99
25	32	38.75	-73.29	-66.84

Table: The calculated diffraction angles of 1 and 2 order of XUV spectral components.

Knowing the distance from the diffraction grating and having determined the above angles one can then place the detector plane in the correct-predicted vertical position for recording the emitted spectrum. A schematic realization is depicted in Figure 2.17 presenting an illustration of the incident –diffracted beam towards the MCP-Phosphorus screen consisting the detector. For the above one has to consider the very small angle of incidence (85^0) with which the beam must reflect on the XUV grating ensuring the high reflectivity provided by the surface of the diffraction optic. After the above considerations, the absolute calibration can be achieved by exploiting different metallic foils with well know spectral cut-off or a spectral line of radiation. While the dispersion of the spectrometer can be calculated for every configuration, small deviations from the calculation of the projection positions of the spectral components requires recalibration with a near absolute interpretation. An efficient way for calibration in case of a bright enough source such as the one presented in this thesis, is the exploitation of the first and second order of diffraction of the same spectral feature for calibrating the grating.
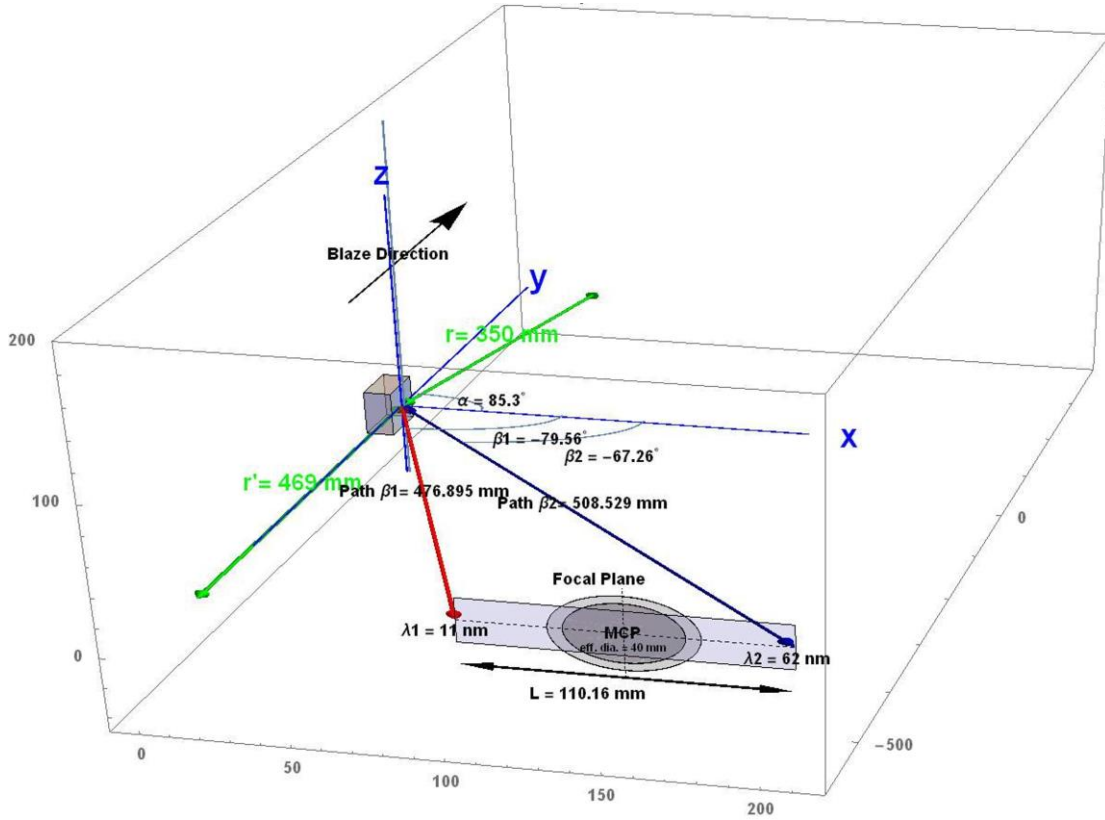
Figure 2.19 Flat Field Spectrometer Configuration. A schematic representation of the beam path of XUV radiation analyzed by the Hitachi XUV grating. The characteristic angles described in the text are represented as well as the extreme values of the diffracted wavelengths supported by the set up and projected at the screen.

Regarding the efficiency of the grating with respect to the incident's beam polarization, as described in the HHG section in chapter 1, harmonics are produced by linear polarized light. P-polarized means that the electric field vector is parallel to the plane defined by the k-vector of the radiation and the grating's normal incidence. The reflectivity dependents on the polarization and because the harmonics will be produced with either s- or p- polarization, this additional factor needs to be consider for the efficiency. P-polarized light will be diffracted deeper into the media, which is in this case the gold coating of the grating. This means that the reflectivity will be smaller than for s-polarized light.

In figure 2.20 a recorded spectrum of HHG in Xenon and Argon are presented in panels (a) and (b) respectively. In both measurements the recordings were made after filtering the radiation with an Al foil (red curves) and a Sn foil (blue curves). The transmission curves are presented as well for 150 nm thickness in both cases.
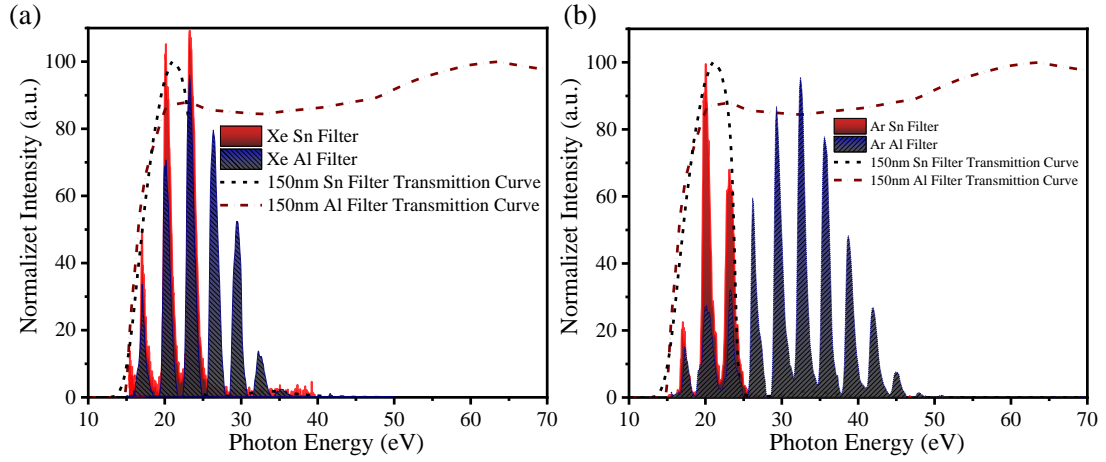
Figure 2.20 Harmonic spectra recorded by FFS after spectral selection by metallic foils. The generation medium was (a) Xe and (b) Ar gas. In both panels, the blue and red peaks correspond to harmonics after transmission through a 150 nm thick Al and Sn respectively, while the red dash-dotted (Al) and black dashed (Sn) are transmission curves for 150 nm thickness.

The spectral resolution of a planar grating is determined by $R=\lambda/\Delta\lambda=m\,N$ where λ is the examined central wavelength, m is the diffraction order, N is the number of grooves illuminated by the beam. The full width half maximum (FWHM) of the examined central wavelength is defined by $\Delta\lambda$. The best resolution R is achieved when the maximum number of grooves is illuminated. The resolution R increases also with the refraction order m. In order to calculate the specific resolution for the gratings, first the grating dispersion has to be determined. The grating dispersion is the distance between two wavelengths in the spectral plane. With equation 2.17 the wavelength dependent angle of reflection can be calculated. The distance between the two wavelengths of interest is then calculated from with respect to the distance r′ between the grating and the spectral plane. The following table contains the specifications of the XUV spectrometer for the case of 1200 lines/mm grating case.

Wavelength Range (nm)	5-20	15-60	25-80
Spacer Flange Angle	0^0	18^0	30^0
Operation Mode	Entrance slit	Slit-less	Slit-less
Dispersion (nm/mm)	0.5-0.7	0.7-1.1	0.9-1.3
Resolution (nm)	~0.06	~0.09	`0.11

Table: The XUV Flat Field Spectrometer 1200 lines/mm Hitachi grating specifications.

A surprising investigation of High Harmonic generation in molecular Hydrogen revealed a significantly high output efficiency accompanied by high photon energy emission extending the cut-off frequencies down to 18 nm. Additionally, to the interest of the above funding itself, it provides a successful way of determining the spectral resolution of the spectrometer over an extended area of photon energies. The recorded spectra are presented in Figure 2.19 with the highest photon energy to be 67 ~eV corresponding to 43th harmonic of the fundamental driving field. A sequence of multiple Gaussian fits reveals the fitting curve of each individual distribution of photon energy with FWHM of them to be implemented for the determination of the spectral resolution.
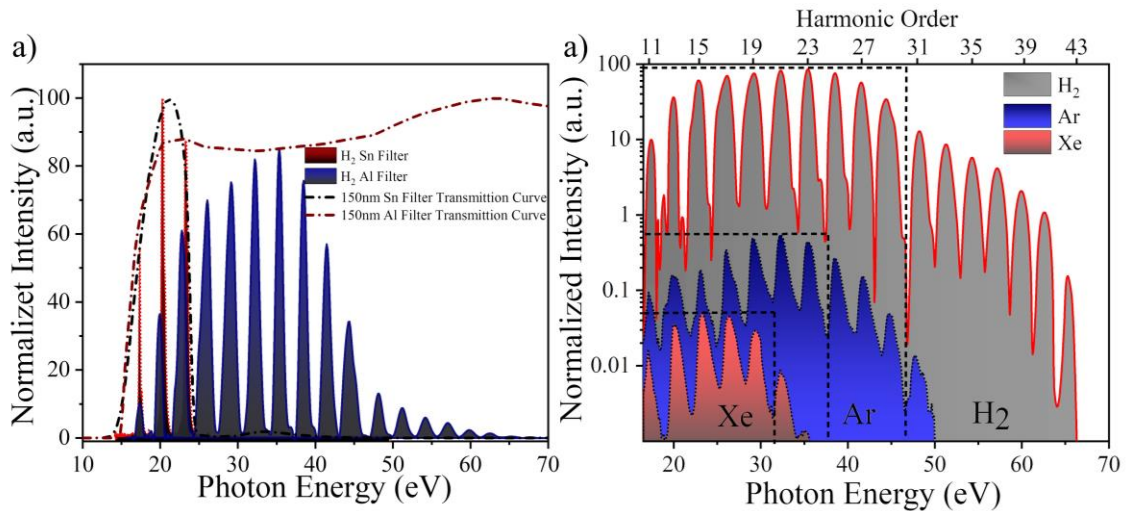
Figure 2.21 Harmonic spectra from molecular Hydrogen (a) Harmonic spectra generated in molecular hydrogen recorded by FFS after spectral selection by metallic foils. The transmission curves of Sn and Al are also presented. (b) HHG spectrum from Xenon, Argon and Hydrogen for comparison reasons in a log scale revealing the plateau and cut-off regions.
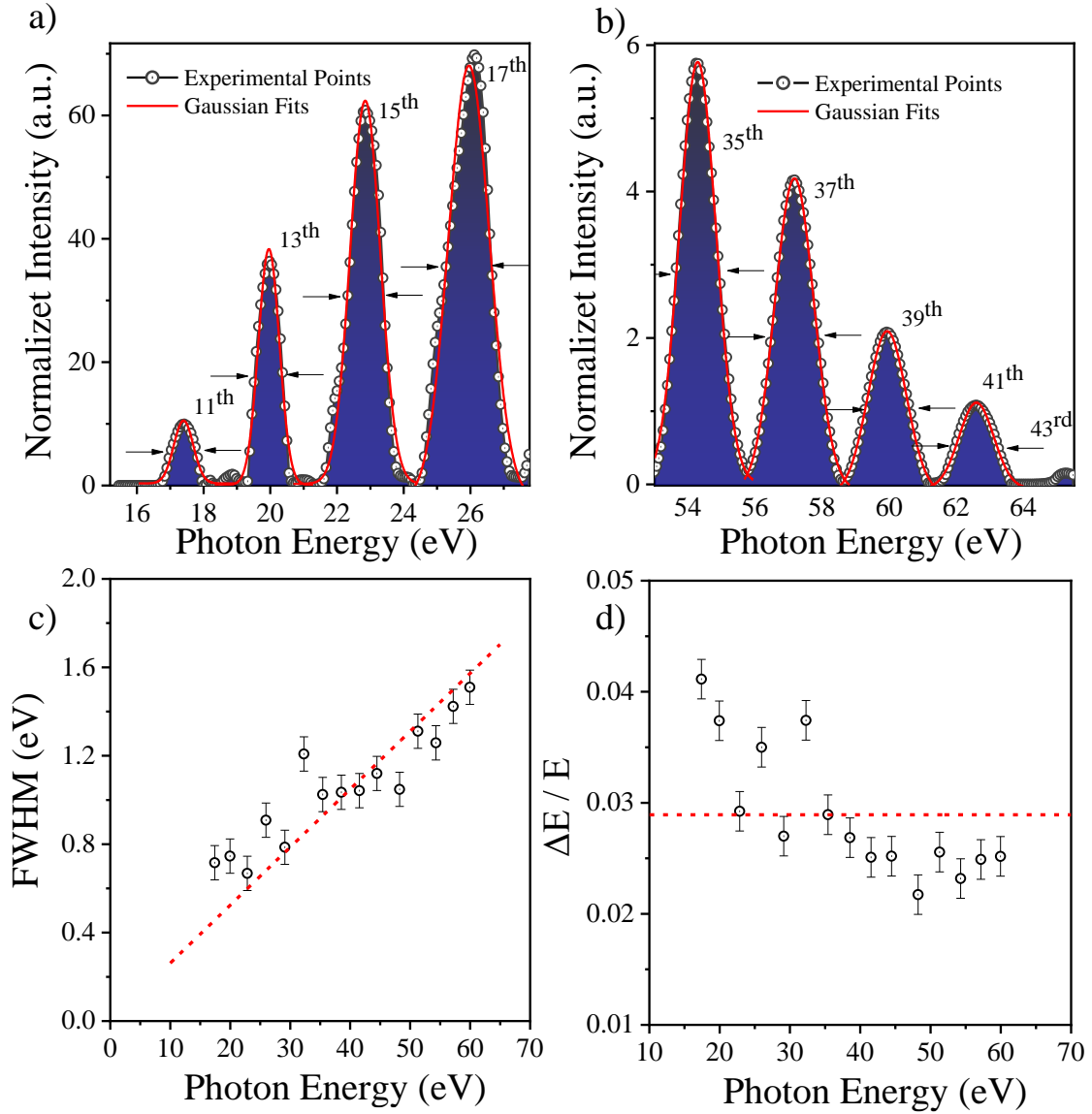
Figure 2.22 Resolution of Time of flight electron spectrometer. (a), (b) Harmonic spectra generated in molecular hydrogen after spectral selection by Al foil. The black circles are representing the measured data, blue filled curves the individual Gaussian fits and the red curve the cumulative curve. (c) The determination of spectral resolution of the flat field spectrometer.(d) the resulted resolution of 2.8% obtained from the linear fit of FWHM as a function of the photon energy.

Chapter 3: Quasi Phase Matched High Harmonic Generation

Introduction

Gas phase High-Order-Harmonic sources have been widely used for the generation of attosecond pulses in the XUV region. Enhancement of the XUV energy is of crucial importance for exploring exciting new paths in non-linear light-matter interaction studies in the non-linear XUV regime [74-84]. However, in most of the cases the low generation efficiency of the HHG process, limits the mean photon flux of gas phase HHG sources [85-100]. The principles of generating high-brilliance energetic radiation in the regime spanning from VUV to X-rays, when gas phase medium is implemented for the frequency upconversion, rely on the detailed knowledge of the macroscopic response of the atoms/molecules considering that the single atom response are considered fulfilled. A variety of experimental and theoretical investigations have been presented, attempting the expansion of the principles of non-linear optics regarding the conditional requirements for generating low order harmonics in the XUV regime. In its simplest manifestation, optimization of the macroscopic response of the non-linear medium achieving the so-called phase matching is realized, when the wavefronts of the fundamental laser and generated harmonics are in phase, so that light signal generated throughout the conversion region adds constructively [100-107]. In the case of High Harmonic Generation, the above requirement becomes a challenging goal due to a variety of physical limitations and also the individual parameters that introduce phase mismatch leading to the reduction of conversion efficiencies. Many proposed configurations have been demonstrated as vital tool for canceling or limiting the effects of phase mismatch and therefore, appear as a promising step towards higher brightness sources [107-120]. Among them stands the idea of increasing the emitters contributing to the produced XUV radiation via a loosely focused driving field in conjunction with an increase of the generating medium length. In the present chapter the conceptual aspects of phase matched harmonic radiation will be discussed. Moreover, the experimental investigations defining the conditions leading to enhanced XUV radiation of the GWatt attosecond beamline, will be presented. The enhancement achieved in the present work combines the loose driving field focusing geometry with a multiple gas jets configuration as generating target of the non-linear interaction process.

3.1 Macroscopic aspects of High Harmonic Generation

The three-step model presented in a previous chapter, describes the single atom response in the extreme light matter interaction leading to frequency upconversion. However, in the macroscopic frame the interaction leading to a sufficient number of produced harmonic photons is arising from the superimposed fields emitted from the atoms ensemble of the gas phase medium. Due to the nature of the HHG process, the macroscopic response resulting in phase matching also requires the coherent superposition of those fields emitted and also propagated at a specific point within the generating medium's volume, to be in phase with those generated in subsequent positions in the medium. Therefore, propagation effects have to be considered for a complete description of the process producing the harmonic beam. As it stands for all of the nonlinear optical processes, the conversion efficiency from the fundamental to the harmonic field is enhanced by eliminating the phase mismatch factors, a topic which will be further discussed in this section.

When a focused IR laser beam interacts with the gas phase atoms the mechanism described for the High Harmonic Generation may lead to the emission of radiation, the flux of which would be proportional to the number of atoms and photons involved in the process. However, the reality quite differs since the driving beam has a spatial intensity distribution that varies throughout its cross-section of the beam, and also different phase velocity components on and off-axis around the focus. Furthermore, propagation effects arise as the laser pulse propagates through the medium, like absorption, dispersion and nonlinear interaction effects that appear at high intensities, like self-focusing and plasma formation. These effects create different conditions for High Harmonic Generation in different parts of medium. Moreover, also the generated radiation propagates in the generating medium, setting more complexity to the quest of matching wavefront conditions between the already generated waves and those created at different areas in the volume of interaction. In the latter quest the phase difference between the atomic sources depends not only on the phase with which harmonics are generated, but also on their phase velocities acquired during propagation in the generation medium with many considerations in need of being taken into account. The above define not only the total emitted harmonic yield, but also the characteristics of the harmonic beam, and finally can significantly alter the intensity distribution and

structure of the generated XUV attosecond pulse trains. Due to the highly nonlinear nature of High Harmonic Generation process, a perfect constructive interference from all radiating point sources within the medium volume would result to a quadratic increase of the harmonic intensity with the number of interacting dipoles. However, destructive interference arising from different parameters can reduce the harmonic yield with the factors leading to mismatch posing as a serious experimental limitation.

Although the origins of phase mismatch are quite different in case of High Harmonic Generation, it will be useful a discussion regarding the simplest low order optical parametric process namely second harmonic generation, originated from the interaction of a fundamental field and an optical non-linear crystal, before addressing the case of the XUV upconversion from a gas target. In order to generate an efficient output of second harmonic fields generated at differently located points of the crystal, those have to be in phase in order to lead to a coherent sum of the superimposed amplitudes. The above condition is the well know term from non-linear optics called phase matching. The phase difference between the fundamental and generated frequency in a general way in that case can be expressed by the wave-vector mismatch with the terms ω and 2ω corresponding to the angular frequencies of the fields respectively.

$$\Delta k = k_{2\omega} - 2k_{\omega} \qquad (3.1)$$

Since the case of perfect phase matching (i.e $\Delta k=0$) is an ideal case, in the presence of a non-vanishing term results in a reduced frequency conversion. The yield of the generated radiation can be derived from:

$$I_{2\omega} \propto I_{\omega} d_{eff}^2 L^2 sinc^2 \left(\frac{\Delta k\,L}{2}\right) \qquad (3.2)$$

Where $d_{eff}=1/2\, x^{(2)}$ is the effective nonlinear susceptibility of the crystal defined from the nonlinear product of the polarization from the Taylor series as a function of the applied external field. As can be obtained from figure 3.1 the output signal of the generated radiation rapidly decreases from its maximum corresponding to perfect phase math ($\Delta k=0$) forming an oscillation $sinc^2$ shaped decay. In case of a known mismatch the harmonic intensity will show a repeated coherent build up per propagation step dL within the so called coherence length $L_{coh}=\pi/|\Delta K|$, followed by back conversion. In

most of the cases regarding a non-linear crystal for Second Harmonic Generation (SHG) the coherence length is typically in the order of few microns due to phase mismatch originating from the refractive index dispersion which causes an unmatched phase velocity between the fundamental and generated radiation. Therefore, the commonest solutions are birefringent nonlinear crystals (BBO, KTP, LBO) having the same refractive index for both frequencies taking advantage of the different optical properties along the different axes of the crystal allowing efficient phase matching [121-123].
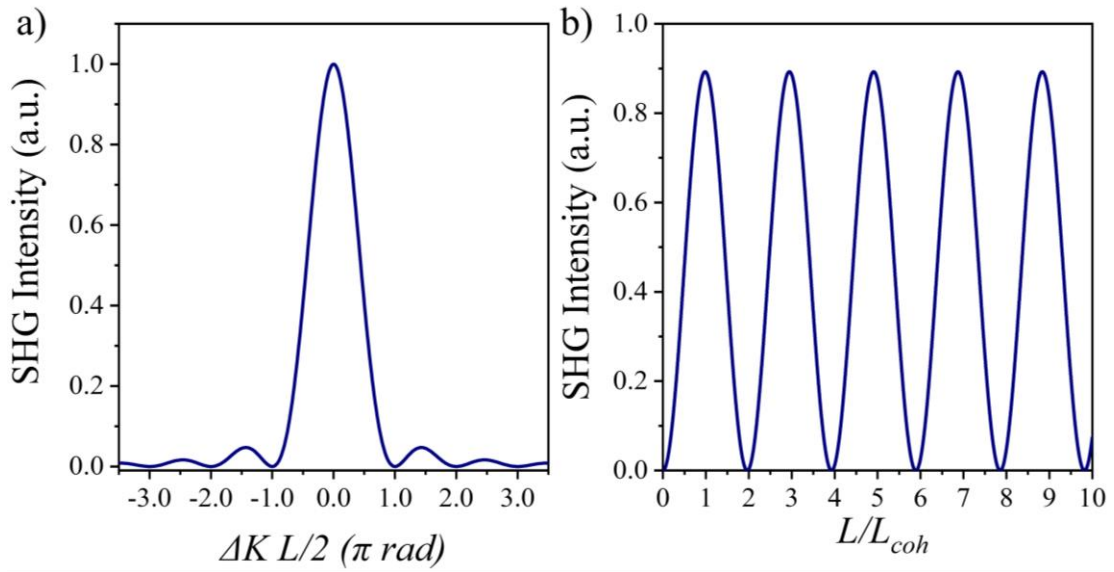
Figure 3.1 Second Harmonic generation. Effect of wave-vector mismatch on the efficiency of sum-frequency generation. (a) Normalized intensity of the second harmonic field as a function of Δk for a fixed length of the nonlinear crystal. (b) intensity of the second harmonic field as a function of the crystal's length for $\Delta k \neq 0$.

The above discussion can be the basis, be extrapolated and address all the nonlinear parametric processes including the highly nonlinear high harmonic generation process. It should be clear though, that a different approach is necessary for studying the phase-matching conditions fulfilment for the HHG case due to the different mechanisms underlying the process and moreover the properties of the driving field and finally the medium exploited as the non-linear generator. For instance, in case of gas phase HHG the medium is considered to be homogeneous and isotropic and does not have birefringent features as opposed to crystals. The lack of birefringence prevents

the possibility of canceling the phase mismatch through introducing different direction between the propagating and generated light. Moreover, the refractive index of a gas medium does not depend on the polarization of the driving field.

As mentioned before, for efficiently generating XUV radiation from a gas phase target the requirement is that generated frequencies at different positions to be added constructively expanding the equation 3.1 of the wave-vector mismatch in:

$$\Delta k = q k_{IR} - k_q \tag{3.3}$$

The most general way of treating the Gaussian IR driving field as well as XUV radiation in both space and time is to solve the Maxwell Wave Equation (MWE) with the single-atom dipole acting as the nonlinear source term. This allows one to combine, for instance, the Time-Dependent Schrödinger Equation with the Maxwell Wave Equation for a complete description of HHG. The basic principle of the generation process is then extracted from the non-linear wave equation with higher order polarization terms induced in the medium.

$$\vec{\nabla}^2 E(\vec{r}, t) - \frac{1}{c^2} \frac{\partial^2 E}{\partial t^2} = \frac{4\pi}{c^2} \frac{\partial^2 P}{\partial t^2} \tag{3.4}$$

It is often convenient though to convert the above equation to the frequency domain, where derivatives are converted to simpler algebraic expressions, such as $\partial/\partial t \rightarrow -i\omega$ when Fourier transformation is applied in which the electric field and the induced polarization are a superposition of the contributing frequencies.

$$\vec{\nabla}^2 \tilde{E}_q + \left(\frac{q\,\omega}{c}\right)^2 \tilde{E}_q = -4\pi \left(\frac{q\,\omega}{c}\right)^2 \tilde{P}_{tot,q} \tag{3.5}$$

The total electric field and the polarization induced, are the products of the superposition of the contributing frequencies derived respectively from:

$$E(\vec{r}, t) = Re\left[\sum_q \tilde{E}_q(\vec{r}, t) \, e^{-iq\omega t}\right] \tag{3.6}$$

$$P(\vec{r}, t) = Re\left[\sum_q P_q(\vec{r}, t) \, e^{-iq\omega t}\right] \tag{3.7}$$

Approximations applied in this treatment can lead to the formula of the generated harmonic field and the induced polarization. Considering the conversion efficiency of HHG low, the polarization induced is attributed only to the fundamental

IR field. Moreover, all indirect processes can be neglected as well as the depletion of the fundamental field. Finally discounting the nonlinear effects of the propagation of the IR field, the total polarization of each harmonic generated can be derived from the sum of linear polarization induced by the harmonic field E_q and the nonlinear polarization originating from the driving field E_l:

$$P_{total} = P_{linear,q}(E_q) + P_q(E_1) \tag{3.8}$$

The inhomogeneous differential wave equation yields the integral representation of the harmonic electric field with the wave vector k_q including the linear polarization term.

$$\vec{\nabla}^2 \tilde{E}_q + k_q^2 \tilde{E}_q = -4\pi \left(\frac{q\,\omega}{c}\right)^2 \tilde{P}_q \Rightarrow \tag{3.9}$$

$$\tilde{E}_q\left(\vec{r'}\right) = \left(\frac{q\,\omega}{c}\right)^2 \int e^{\left(\frac{i\,k_q|\vec{r'}-\vec{r}|}{|\vec{r'}-\vec{r}|}\right)} P_q\left(\vec{r'}\right) dr^3 \tag{3.10}$$

Where $\left|\vec{r'} - \vec{r}\right|$ is the distance between the point in the generation medium and the reference point. For z′>>z far field conditions treatment can be applied as well as a paraxial approximation considering that the harmonic emission takes place close to the propagation axis

$$\left|\vec{r'} - \vec{r}\right| \approx z' - z + \frac{(x'-x)^2 + (y'-y)^2}{2\,(z'-z)} \tag{3.11}$$

Finally introducing slowly varying envelope functions $E_q = \tilde{E}_q e^{-i\,k_q z}$ and $P_q = \tilde{P}_q e^{-i\,qkz}$ and making the assumption of rotational symmetry the emitted electric field as well as the non-linear polarization are then finally expressed in equations (3.12) and (3.13) respectively. J_0 corresponds to zero order Bessel function $\Delta\Phi_q$ the complex phase mismatch N the density of neutral atoms, $d_q(r,z)$ the dipole moment and b the confocal parameter assuming Gaussian intensity distribution of the beam.

$$E(r',z') = 2\,\pi \left(\frac{q\,\omega}{c}\right)^2 \iint e^{\left(\frac{i\,k_q(r^2+r'^2)}{2\,(z'-z)}\right)} J_0\left(\frac{k_q r' r}{z'-z}\right) \frac{P_{q(r,z)} e^{-i\Delta\Phi q(r,z)}}{z'-z}\, drdz \tag{3.12}$$

$$P(r',z') = 2\,N(z) d_q e^{-iq\left(tan^{-1}\left(\frac{2z}{b}\right) - \frac{2k_1 r^2 z}{b^2+4z^2}\right)} \tag{3.13}$$

where, the complex phase mismatch $\Delta\Phi_q$ can be derived from:

$$\Delta\Phi_q = \int_{-\infty}^{Z}(r,z'') \, dz'' - i\int_{z}^{+\infty} k_q\left(r,z''\right) dz'' \qquad (3.14)$$

With the imaginary part to represent the absorption coefficient at frequency $q\omega$, equal to $N(Z)\sigma_q/2$, where σ_q denotes the photoionization cross section.

Different terms contribute to the total harmonic field generated in the non-linear medium. The harmonic yield is severely limited by phase mismatch phenomena, such as the difference between the diffraction rates for the fundamental beam and the individual harmonic radiation due to geometrical propagation effects, the wavelength dependent index of refraction of the neutral atomic and ionized medium, and the dependence of the intrinsic phase of the harmonics on the laser intensity in both the longitudinal and radial directions. In general, the total phase mismatch is the sum of four terms and can be expressed as mismatch between the qth harmonic field and the induced polarization at frequency $q\omega$.

$$\Delta k \; = \; \Delta k_{dipole} \, + \; \Delta k_{neutral} \; + \; \Delta k_{plasma} + \Delta k_{gouy} \qquad (3.15)$$

The terms in eq. (3.15) refer to the dipole phase, neutral dispersion, plasma dispersion and geometric phase accumulated, respectively.

The atomic dipole phase

The atomic dipole phase contribution arises from the single atom response. In the perturbative regime, the bound electron in the non-linear medium follows the external driving laser field and induces a polarization with no phase delay. In HHG, the atomic dipole phase mismatch is an intensity dependent phase mismatch and has been extensively studied theoretically and experimentally. The origin of this is the phase acquired by the electron wave packet as it is accelerated by the laser field before recombination leading to the emission of the qth harmonic in the continuum state. To a first approximation, the phase of the atomic dipole varies linearly with the laser intensity. The laser intensity can vary spatially in both the longitudinal and radial directions. Therefore, the atomic phase also varies axially as well as radially. This leads to reduced harmonic emission as well as strong spatial distortion depending on the beam's characteristics. It may be possible to find conditions in which the intrinsic phase counteract the geometrical phase mismatch caused from other sources and improves the

overall phase matching. For example, in the simple case when we only consider the contribution of the Gouy phase shift and dipole phase, the phase mismatch will be minimal when the variation of the harmonic phase with propagation is minimal. Figure 3.2 (b) shows the harmonic phase as a function of propagation distance relative to the laser focus at the maximum intensity of the pulse temporal envelope. When the laser confocal parameter is equal to 5 mm and the focus position is located at z = 0, P. Salières et al. find that when the laser is focused approximately 3 mm before the generating medium, as shown in figure 3.2 (b), the harmonic phase variation is minimal, i.e., the phase mismatch is minimum.

For a Gaussian laser beam with intensity along the direction of propagation given by:

$$I(z) = \frac{I_0}{\left[1+\left(\frac{2\,z}{b}\right)^2\right]} \tag{3.16}$$

the contribution of the dipole phase to the phase mismatch on axis of the qth harmonic, is derived by:

$$\Delta k_d = \nabla \phi_q = a_q \frac{dI}{dz} = \frac{8\,z\,a_q\,I_0}{b^2\left[1+\left(\frac{2\,z}{b}\right)^2\right]^2} \tag{3.17}$$

Where a_q is a coefficient related to the nature of the electron trajectories. Typically, the values in case of short trajectories varies in the range of $a_q^S=(1\text{-}5)\text{x}10^{-14}$ cm^2/W while for long trajectories $a_q^L=(20\text{-}25)\text{x}10^{-14}$ cm^2/W . The dependence of the laser field amplitude and phase on the propagation clearly shows that the dipole phase cannot be established assuming an unperturbed laser beam. In a long interaction length geometry, the accumulated dipole phase cannot be neglected and the phase gradient of the dipole phase allows the phase mismatch on axis to be reduced in the region where the laser intensity is high. This leads to an enhancement of the HHG efficiency because the atomic response is high. The atomic dipole phase gradient acts as an additional time dependent wave vector which allows a high plasma dispersion to be compensated.
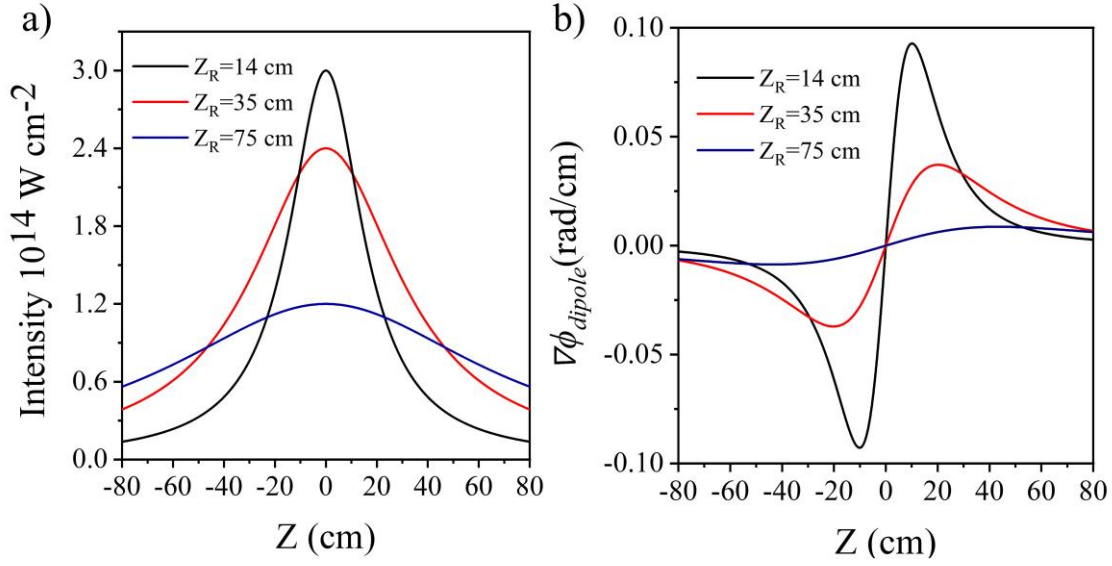
Figure 3.2 The atomic dipole phase. (a) Intensity variation of a Gaussian beam around the focus, along the propagation axis. (b) The derivative of the atomic phase of $q=15$ harmonic (assuming $a_q^S = 2 \times 10^{-14}$ cm^2/W) for short trajectories, as a function of the propagation distance across the focus for various Z_R.

Figure 3.2 (a) depicts the intensity variation assuming a Gaussian beam focused towards the non-linear medium implemented for the harmonic radiation. As can be observed by increasing the Raleigh length of the Gaussian distribution the variation of the atomic phase and thus the phase mismatch is rapidly decreasing. In Figure 3.2 (a) the peak intensity is calculated for a constant energy pulse and duration, with the parameter of the beam waist to vary according to experimental investigations for three different values of the initial beam radius. The focusing length is assumed to be 9m consistent with the experimental configuration employed in the beamline. The variation of the dipole phase and thus the resulted phase mismatch is respectively presented in figure 3.2 (b) for the three different focusing conditions of the driving electric field. It is worth noting that in case of Argon gas used as the nonlinear medium these levels of intensity lay bellow the saturation, a critical condition for making the value of a_q^S coefficient valid for the quantitative representation of the gradient of the phase variation.

Neutral gas dispersion phase mismatch

Most commonly high-order harmonics are produced in noble gases, which have ionization energies between 12.1 eV (Xenon) and 24.5 eV (Helium). The plateau of a high-order harmonic spectrum begins at harmonic orders with photon energies higher than I_p. Due to this, the refractive index is slightly smaller than 1. The wavenumber of the propagating, through the neutral gas, XUV field is:

$$k_{n,q} = \frac{\omega_{q\,(n-1)}}{c} \tag{3.18}$$

The phase mismatch due to the neutral-atom dispersion arises from the difference in linear index of refraction between the XUV and fundamental frequencies.

$$\Delta k_n = q\,\frac{\omega_1}{c}\,[\Delta n - n_2] \tag{3.19}$$

where $\Delta n = n(\omega_1) - n(\omega_q)$ is the difference in linear index of refraction between the XUV and fundamental frequencies, and n_2 is the intensity-dependent nonlinear Kerr index of refraction of the fundamental field. It is worth recalling that when a laser with high intensity propagates through a medium, this also causes a change in the refractive index in proportion to the laser intensity. Note that Δn and n_2 are both dependent on the neutral gas density. For above-threshold harmonics, Δn is negative while n_2 is typically small and positive (although higher order Kerr nonlinearities can be negative), making $\Delta k_{neutral}$ of negative sign. The determination of the refractive index in the XUV/X-ray region can be measured experimentally, or calculated from the Kramers-Kronig relation from experimentally measured absorption spectrum. Databases containing the values of atomic scattering factors for different gases are determining the refractive index related to these scattering factors according to the relation:

$$n(\omega) = 1 - \frac{2\,\pi\,N_\alpha\,r_e\,c^2}{\omega^2}\,[f_1(\omega) - i\,f_2(\omega)] \tag{3.20}$$

where N_a is the atomic density and $r_e = e^2/(4\pi\varepsilon_0 m_e c^2)$ is the classical electron radius.
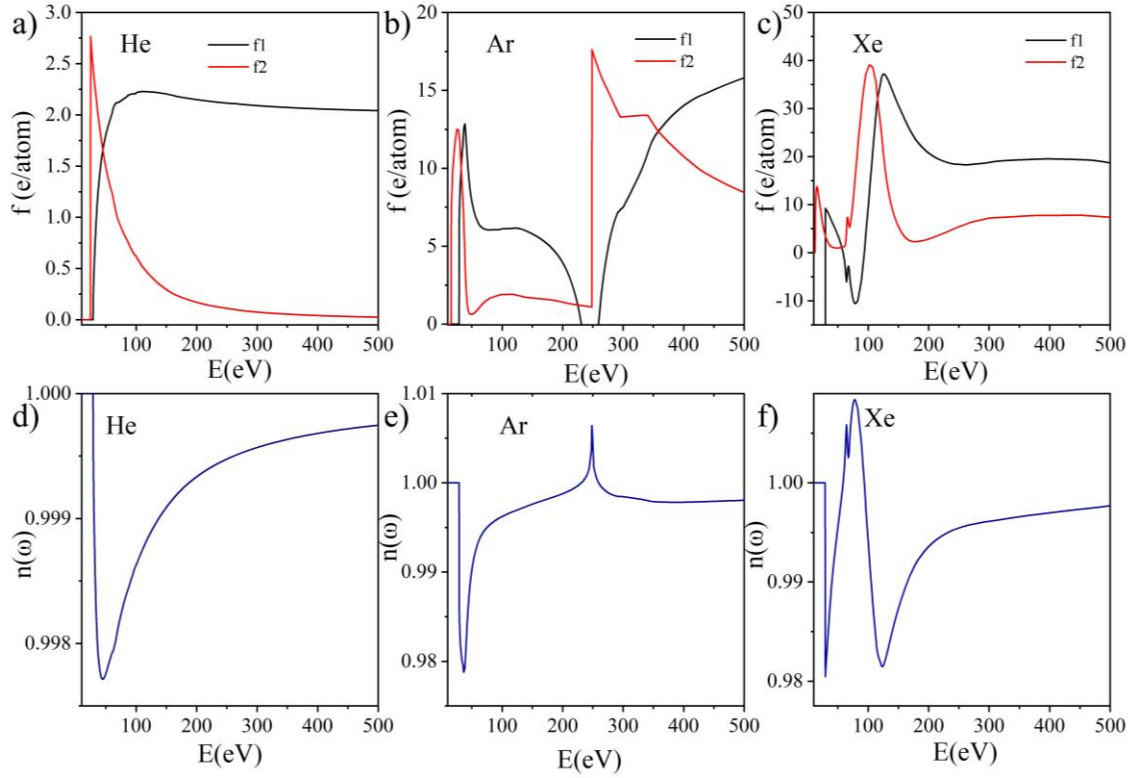
Figure 3.3 Refractive index of noble gases. (a), (b), (c) present the atomic scattering f_1, f_2 factors of He, Ar and Xe respectively, obtained from Henke database. The calculated refractive indexes of the noble gases determined for the above parameters of absorption and refractions are depicted in (d),(e) and (f) in case of He, Ar and Xe.

Critical parameter for having an accurate estimation of the dispersion induced is the fraction of ionization as described in a previous chapter determined from the ADK theory. Moreover, the pressure and thus the number of the atoms acting as the dispersion medium define the magnitude and significance of this term.

Critical parameter for having an accurate estimation of the dispersion induced is the fraction of ionization as described in a previous chapter determined from the ADK theory. Moreover, the pressure and thus the number of the atoms acting as the dispersion medium define the magnitude and significance of this term. Using the ionization rate W_{ADK} 1.14 the ionization fraction $n(t)$ defined as the free electron $n_e(t)$ and initial density of neutral atoms n_0 ratio can be estimated by:

$$n(t) = \frac{n_e(t)}{n_0} = 1 - e^{-\int_{-\infty}^{t} W(t\prime)dt\prime} \qquad (3.21)$$

Plasma dispersion phase mismatch

When an intense laser beam interacts with a gas medium, not only harmonics but also free electrons are emitted during the ionization process. The presence of free electrons induces additional dispersion through the well-studied plasma-induced index of refraction changes, reducing the coherence length, i.e., limit the harmonic yield. Similarly, to the dispersion originating from the propagation of the generated and driving field through the gas phase medium, plasma dispersion and its resulting phase mismatch can be determined from the refractive index. Free electrons contribute to the refractive index through their large negative polarizability resulting to a frequency-dependent susceptibility:

$$\chi_p = -\frac{N_e\ e^2}{m_e \varepsilon_0 \omega^2} \tag{3.22}$$

where N_e denotes the density of free electrons. The refractive index for a plasma is given by:

$$n_p(\omega) = \sqrt{1 - \frac{\omega_p{}^2}{\omega^2}} \approx 1 - \frac{\omega_p{}^2}{2\omega^2} \tag{3.23}$$

The plasma frequency corresponding to the rapid oscillations of the electron density can be derived from:

$$\omega_p = \sqrt{\frac{N_e\ e^2}{m_e \varepsilon_0}} \tag{3.24}$$

The wave vector mismatch due to dispersion originated from the plasma can be calculated similarly as the neutral dispersion term:

$$\Delta k_p = \frac{q\omega}{c}\ n_p(\omega_1) - n_p(\omega_q) \tag{3.25}$$

Geometric Phase Shift

The geometric phase originates from the focusing geometry of the driving field. The experimental configuration of focusing is causing curvature of the wave fronts and thus the so called Gouy phase shift. The phase mismatch due to the Gouy phase (geometric phase-slip across the focus) is an additional acquired phase shift of π, occurring in the propagation of focused Gaussian beams and directly affects the phase relation between driver field and harmonics and limits the phase matching ability. The resulting geometrical phase offset between the phase fronts of the focused beam and a plane wave due to an advanced propagation of the wavefront across the focus, increases linearly with wavelength.

$$E(z,t) = E_0 \frac{w_0}{w(z)} e^{i(kz + \varphi_G(z))} E(t) \tag{3.26}$$

Where φ_G is called the Gouy phase shift, and its variation around the focusing position of the electric field is described by:

$$\varphi_G(z) = -arctan\left(\frac{z}{z_r}\right) \tag{3.27}$$

In which the parameter $z_r = \pi w_0^2/\lambda$ is denoting the Rayleigh length of the focused beam. From the equation above, it becomes apparent that around the focus of a laser beam the phase experiences a shift of π, increasing the phase-velocity of the focused laser field on axis, as compared to a plane-wave. It is apparent that the Gouy phase shift is quicker for tightly focused beams (when z_R is small) depicted in figure 3.4 for three different Rayleigh lengths.

$$\Delta k_G = q \frac{\partial \varphi_G}{\partial z} = q \frac{\partial\left(-artan\left(\frac{z}{z_r}\right)\right)}{\partial z} \tag{3.28}$$
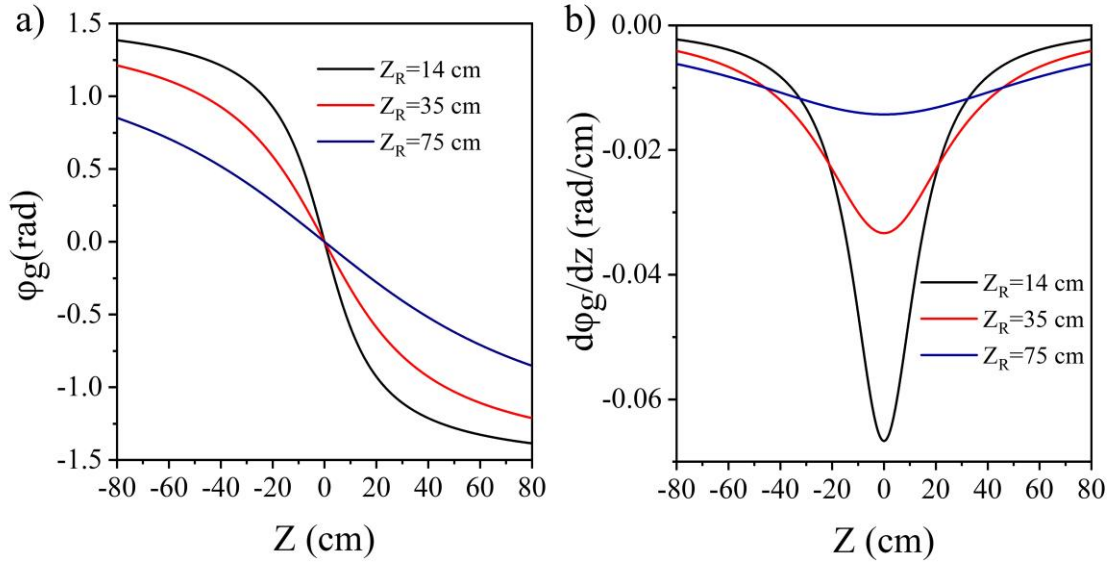
Figure 3.4 Geometric Phase shift. (a) Gouy phase variation along the focus for three different Rayleigh lengths. (b) the derivative of the geometric phase of the same focusing conditions used for the same confocal parameters.

Reabsorption

Once phase matching is achieved or more consistent speaking when the above parameters causing the mismatch are minimized, the generated harmonic yield is expected to grow proportional to the square of the medium length (L_{med}). However due to the photon energies that are generated in the nonlinear medium which are comparable and even higher to the ionization potential of the atomic target exploited for the frequency upconversion absorption effects are strongly influencing the flux of the radiation. Thus n realistic terms the effective length of the generating medium is simply limited by reabsorption effects. According to the investigation of Constant *et al*. the total harmonic yield generated in a homogeneous medium is expressed through the equation:

$$I_{HHG} \propto \frac{4\,L_{abs}^2}{1+4\pi^2\left[\frac{L_{abs}^2}{L_{coh}^2}\right]} \left[1 + e^{-\left(\frac{L_{med}}{L_{abs}}\right)} - 2\cos\left(\pi\,\frac{L_{med}}{L_{coh}}\right) e^{-\left(\frac{L_{med}}{2\,L_{abs}}\right)} \right] \quad (3.29)$$

Where $L_{abs} = 1/\rho\sigma(\omega)$ is defined as the length where the harmonic yield drops by a factor of $1/e$ of its initial value and $L_{coh}=\pi/\Delta k_q$ denoting the coherence length. "Absorption-limited HHG" corresponds to phase-matched generation limited by absorption. It can be defined by the relation:

$$L_{med} > 3\, L_{abs} \qquad\qquad L_{coh} > 5\, L_{abs} \qquad\qquad (3.30)$$

If the coherence length is comparable with the absorption length, the number of photons oscillates with the length of the medium, and a maximum is obtained over a length of medium approximately equal to L_{coh}. More than 95% of the maximum number of photons can be obtained when $L_{med}/L_{abs} > 10$ and $L_{coh}/L_{abs} > 100$ wich is presented in Figure 3. When the coherence length is finite, the harmonic yield will oscillate as a function of medium length, an interference effect known as Maker fringes. The shape of the spectrum will largely be determined by the counter-play between the phase mismatch and the absorption cross section [15, 318, 149]. The cross section actually enters into the macroscopic signal twice, and in opposite ways, since a larger cross section means that the single-atom EWP is more likely to recombine, but also means that previously generated XUV photons are more likely to be reabsorbed. In the limit of zero reabsorption, the shape of the spectral intensity will follow the cross section, as predicted by macroscopic response. In the opposite limit where the macroscopic signal is dominated by reabsorption, the spectral shape will follow the XUV transmission ratio given by the Beer-Lambert law

$$T(\omega) = \frac{S(\omega)}{S_0(\omega)} = e^{[-\rho L_{med} \sigma_{abs}(\omega)]} \qquad\qquad (3.31)$$

Thus even for perfect phase matching, the harmonic yield is exhibiting a plateau. This is due to absorption. The absorption rate of photons from the harmonic field by gas atoms scales as the number of photons in the field, whereas the harmonic emission rate does not. As the driving pulse propagates and the harmonic field grows, the harmonic absorption rate approaches the harmonic emission rate and the harmonic intensity approaches a maximum. The saturation of the harmonic yield with increasing medium length indicates that there is not much to be gained by making the noble gas medium much longer than a few absorption lengths.
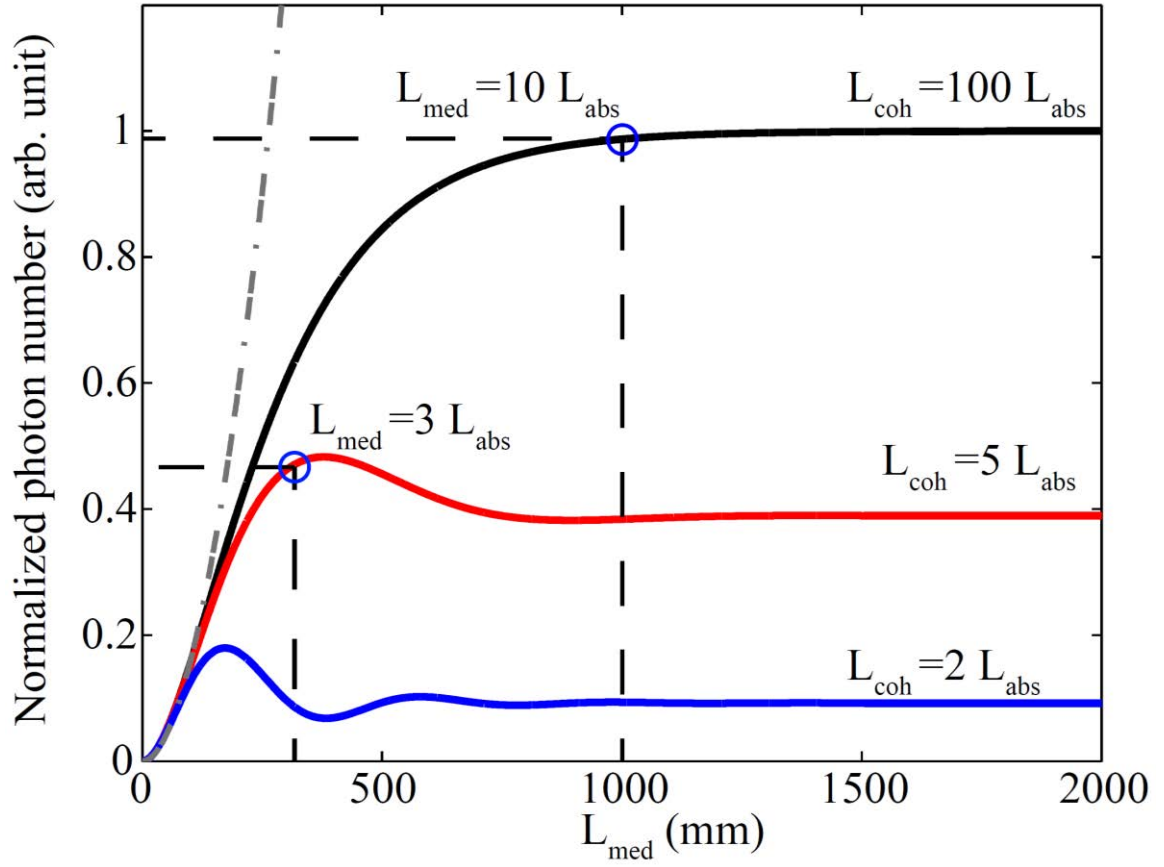
Figure 3.5 Absorption limited harmonic generation. Normalized harmonic yield as a function of the medium length depicting three different cases of L_{coh} with respect to the absorption length

3.2 Quasi Phase Matching Techniques

In case of phase-limited HHG (e.g. absorption plays a minor role), the phase shift within the interaction length exceeds π or even higher orders of the coherence length. This leads to oscillations of the harmonic yield with a period of $\Delta\Phi = 2\pi$ as shown. The brightness of the generated XUV pulses cannot exceed the value achieved at a density corresponding to one coherence length (N_{max}). The normalized density $N_n = N_a / N_{max}$ corresponds to the number of coherence lengths L_{coh} with the atomic density N_a. For efficient HHG it is desirable to enhance the brightness of such pulses resulting in a harmonic intensity higher than that at N_{max}. In this sense, achieving absolute and independent phase control between multiple harmonic generation zones represents a major advance for HHG sources. It will allow the coherent superposition of multiple sources created by the same laser - an approach commonly known as quasi-phase matching (QPM).

In cases where conventional phase matching is not possible, quasi-phase matching has proven an extremely useful technique, very often implemented in the case of second-harmonic generation in periodically poled nonlinear crystals. The nonlinear polarization causes the second-harmonic light field to grow. After the coherence length, however, the second-harmonic field that is just being generated is out of phase by π with respect to the second-harmonic field generated first due to the phase velocity walk-off in the non-phase matched case. The idea of quasi-phase matching is to interrupt frequency conversion in these regions or to correct the phase relation by replacing the crystal by its inversion image. In the so-called periodically poled crystals, the bulk medium orientation is switched just after one coherence length so that the nonlinear susceptibility $\chi^{(2)}$ and therefore the nonlinear polarization change signs as well. The linear optical properties remain the same, and the new second-harmonic signal can now interfere constructively with the already generated, thereby contributing to the build-up instead of canceling it off. A periodic repetition of this switching then leads to a steady build-up of the signal. In general, to obtain quasi-phase matching, we can introduce some modulation.

The exploitation of this "trick" can be extended in higher order frequencies upconversion also applicable in the case of High Order Harmonic generation, with a variety of configurations to lead in sufficient ways overcoming the physical limitations accompanying the process. Unlike the classical approach of phase matching, where the phase velocity of the driving field and the harmonic field must be equal, as described in the previous section, quasi-phase matching allows the coherent build-up of harmonic radiation, especially if phase matching cannot be achieved, like in the case of the absorption limited macroscopic response. This is particularly important for the optimization of other critical parameters of the harmonic fields, for example the cutoff photon energy, the spectral and temporal shape of the harmonic frequencies produced, and last but not least the flux of the generated radiation. For instance, shortest wavelengths in the cutoff require high intensities leading to a high ionization fraction. However, for high ionization fractions the dispersion is dominated by the free electron dispersion and phase matching can no longer be achieved over the complete interaction length.

Under such conditions Quasi-Phase-Matching is generally the only option for achieving coherent signal growth along the non-linear medium and hence to reach high brightness and high conversion efficiencies. In the case of High Harmonic Generation, Quasi-Phase-Matching is typically implemented by allowing the signal to build up over one coherence length $L_{coh} = \pi/|\Delta k|$ and subsequently suppressing the process for another coherence length (the matching half period), until the driving field and harmonic field are again in phase. Since the harmonic intensity of N atoms emitting radiation coherently increases as N^2, the superposition of N_{QPM} identical HHG sources will increase the intensity of the qth harmonic as $I_q \sim (N_{QPM})^2$ under ideal conditions. N_{QPM} is the number of QPM periods and consists the generating and a matching half period. QPM can be achieved by any means that allow modulation of the source term strength. The modulation of the source term can be achieved with different methods, modulating either the driving field or the generating medium. By modulating the driving field, the intensity should be below the threshold intensity for HHG process in the matching zones, whereas highest intensities should be reached in the generating zones.

3.3 Optimization of Quasi Phase Matched High Harmonic Generation

The 20-GW XUV source is based on the increase of the number of the gas phase emitters contributing in HHG process and thus to the generated energy. For this aspect the GWatt attosecond beamline is founded on the utilization of loose IR focusing geometry and the precise control of phase matching conditions achieved by means of thin single-gas targets in a dual-jet configuration with controllable distance between the jets. The formation and determination of these conditions resulting unpresented conversion efficiencies in XUV region, establish this work as the highest reported so far energy coherently emitted from High Harmonic Generation source. In this section the experimental realization of this achievement will be discussed.

As already described in the previous chapter an intense p-polarized IR pulse is focused by a spherical mirror into the HHG area in which the non-linear medium is hosted. After opting for the Gas Jet configuration as the preferable one for the beamline for this work (conclusion determined from a comparative study presented in section 2.3), experimental investigations focused on maximizing the photon flux of the emitted XUV radiation. Towards this goal studies referring to pressure as well as the position of the generated medium with respect to the driving laser focus, were performed. The generation chamber is capable of hosting up to four pulsed-jets configuration operated with a noble gas (Xe, Ar, He) as nonlinear medium for the interaction leading to HHG. In all gas-jets used, the medium length was the same ensured from the fact that they contain the same orifice diameter having the same chamber dimensions. The backing pressure of gas supply was found to be optimum at 3.5 bar in case of Argon while on the contrary a rather lower value of 1.5 bar was found to be optimum in the case of Xenon as the generation medium and in the case of Helium 5 bar were applied in the generation gas jet valve. By operating individually the pulsed gas get valves filed with Argon gas, figure 3.5 is constructed regarding the applied voltage on the piezo crystal with the backing pressure to be kept at 3.5 bar while the width of the opening time also be kept constant for all the measurements. Figure 3.5 (a) presents typical spectra of HHG originating from Argon gas for different voltages applied in the piezo based gas jet valve while Figure 3.5 (b) is depicting the total harmonic yield obtained from the total integration over the photoelectron signal, with Argon gas to be the target of the

detection gas jet. Note that since the one-photon induced, single ionization yield of Argon is directly proportional to the generated XUV flux, thus the photoelectrons produced from the linear interaction of the harmonic radiation with the atomic target can provide a quantitative parameter when comparing HHG efficiencies.
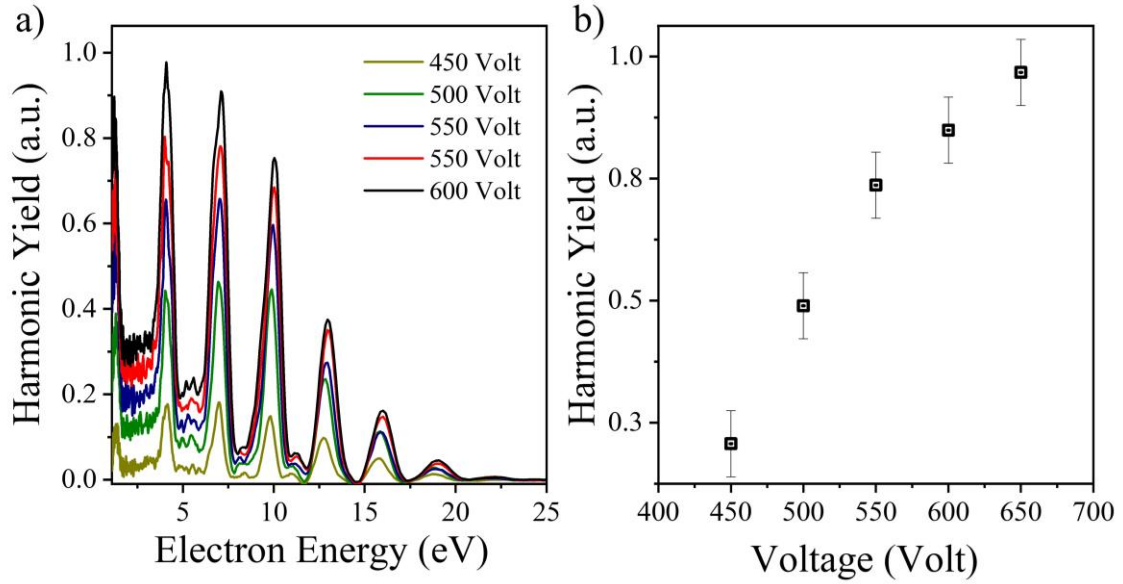
Figure 3.6 Pulsed gas jet voltage. (a) HHG spectra from Argon for different voltages applied in the gas jet valve (b) the integrated signal over the total spectrum as function of the voltages applied in the piezo based crystal.

The pulsed valves housed in the generation chamber can be manipulated by the voltage applied for the opening of the orifice (figure 3.5), the time delay between the opening time of the valve and the arriving IR pulse and finally the width of the time window of the opening time. These parameters directly affect the pressure of the atomic target interacting with the driving Laser and thus the macroscopic response. It is worth noting that one can assume a constant length of interaction since the orifice diameter and the distance between the focusing spot and the pulsed valve is not altered by the above manipulations. At this point it should be stressed that for the following discussion this distance is roughly kept the same for all of the experimental investigations. The distance of the orifice with respect to the laser beam is set at ~ 1 mm leading to a medium length L ~ 1.5 mm considering a Lorentzian distribution characterizing the gas expansion as a function of the distance from the nozzle.
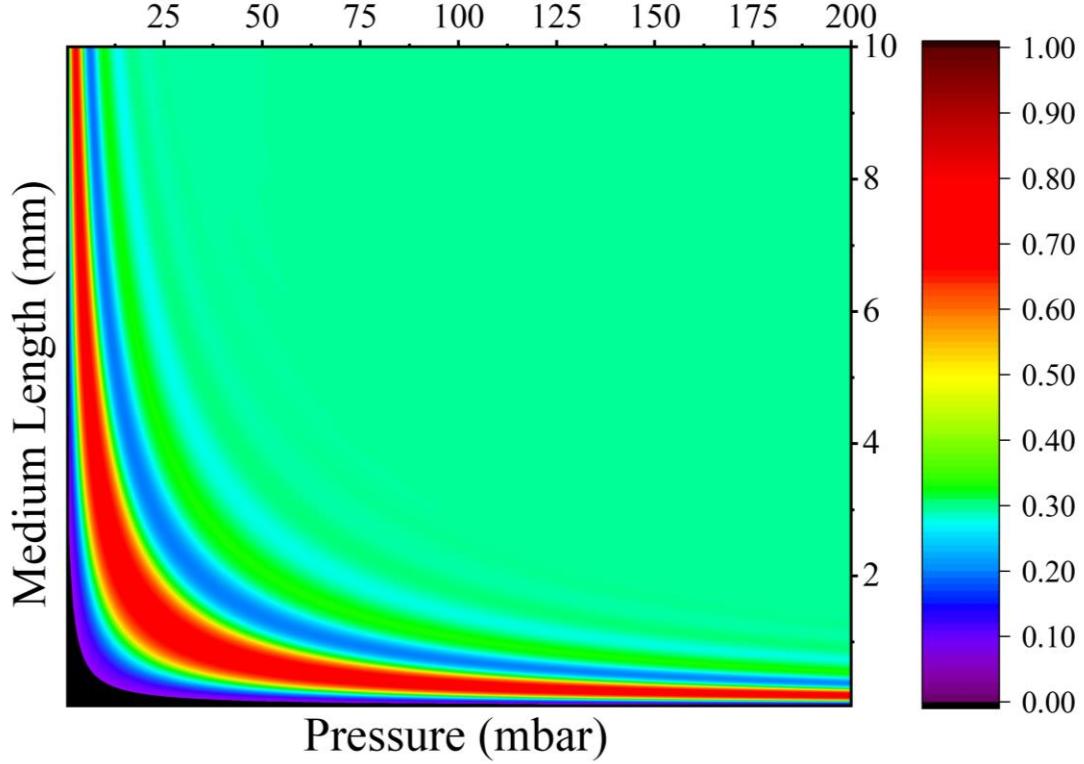
Figure 3.7 Calculated Macroscopic Response of Argon. The harmonic yield generated in Ar gas as a function of the gas pressure (P) and medium length (L) for I_L $\approx 1.5 \times 10^{14}$ Wcm^{-2}.

The above parameters regarding the dimensions and pressure in the interaction region are in fair agreement with previously reported values in the literature. In gas-phase harmonics, the amount of the XUV energy exiting the gas medium is an interplay between the microscopic (single atom) and macroscopic (atomic ensemble) response of the medium. On the microscopic level, for a specific driving laser field wavelength (λ_L), the probability of the emission of a single XUV photon depends non-linearly on the driving laser field intensity (I_L) and the atomic properties. Considering that the probability of the single XUV photon emission is maximized for a fixed I_L lying just below the ionization saturation threshold of the atom (which for Xenon and Argon atoms is $I_L < 3 \; 10^{14}$ W cm^{-2}), it is evident that for the enhancement of the energy of the XUV radiation one has to increase the number of the atomic XUV emitters and consider the macroscopic response of the medium. While keeping I_L, at the level of saturating single atom ionization the number of the emitters can be increased either by increasing the interaction volume (by increasing focal length together with laser pulse energy) or the atomic density of the medium. Incorporating the macroscopic response taking into

account the propagation effects in the gas medium, it has been shown that for $L_{coh} \gg L_{abs}$ and $L_{coh} \gg L_{med}$ the XUV yield is proportional to $(\rho \cdot L_{med})^2$. In the former expressions $L_{coh} = \pi/\Delta k$, $L_{abs} = 1/\rho \sigma^{(1)}$ and L_{med} are the coherence length, the absorption length of the XUV radiation and the gas medium length, respectively, with $\Delta k = kL - qkL$, q the harmonic order, kL the wave number of the driving field, ρ the atomic density of the medium and $\sigma^{(1)}$ the single-XUV-photon ionization cross section of the atoms in the medium, and A being the interaction area (or spot area of the driving field). This product constitutes the main scaling factor towards the enhancement of the produced energy. Using one gas jet, for fixed I_L the dependence of the harmonic yield on P and L_{med} is shown in the contour plot of Fig. 3.6. The red color area corresponds to the area of maximum XUV production and the black-circled area depicts the values of P and L_{med} used in the present work. The 50% reduction of the XUV emission for "large"-length and "high"-pressure media (green color area in Fig. 3.6) is associated with the XUV absorption effects and IR-XUV phase mismatch induced by the neutral atoms and plasma generation in the medium which confines the coherent harmonic build-up to a short propagation length.

In the experimental investigations aiming at the characterization /optimization of HHG from Gas jets, a driver can control the time delay of the time opening of the valve respectively to the arriving time of the IR pulse. Figure 3.7 presents the emitted flux as a function of this time delay providing the characterization curve of the valves with the rather lower yield of GJ1 and GJ4 to be attributed to rather farther position respectively to the focusing position of the IR beam (~15 cm). The XUV beam can then be steered towards the detection chamber after been filtered out by metallic foils with figure 3.7 (e) depicting the product of the linear interaction with the atomic target of Argon. In the excitation scheme the kinetic energies of the photoelectrons produced correspond to the difference between the excitation photon energy and the ionization potential of Argon. By introducing an XUV photodiode by means of motorized translation stage, placed in the "filter chamber", one can directly measure the total energy of the pulse. The procedure of the XUV energy measurements has been described extensively in the previous chapter of this thesis.
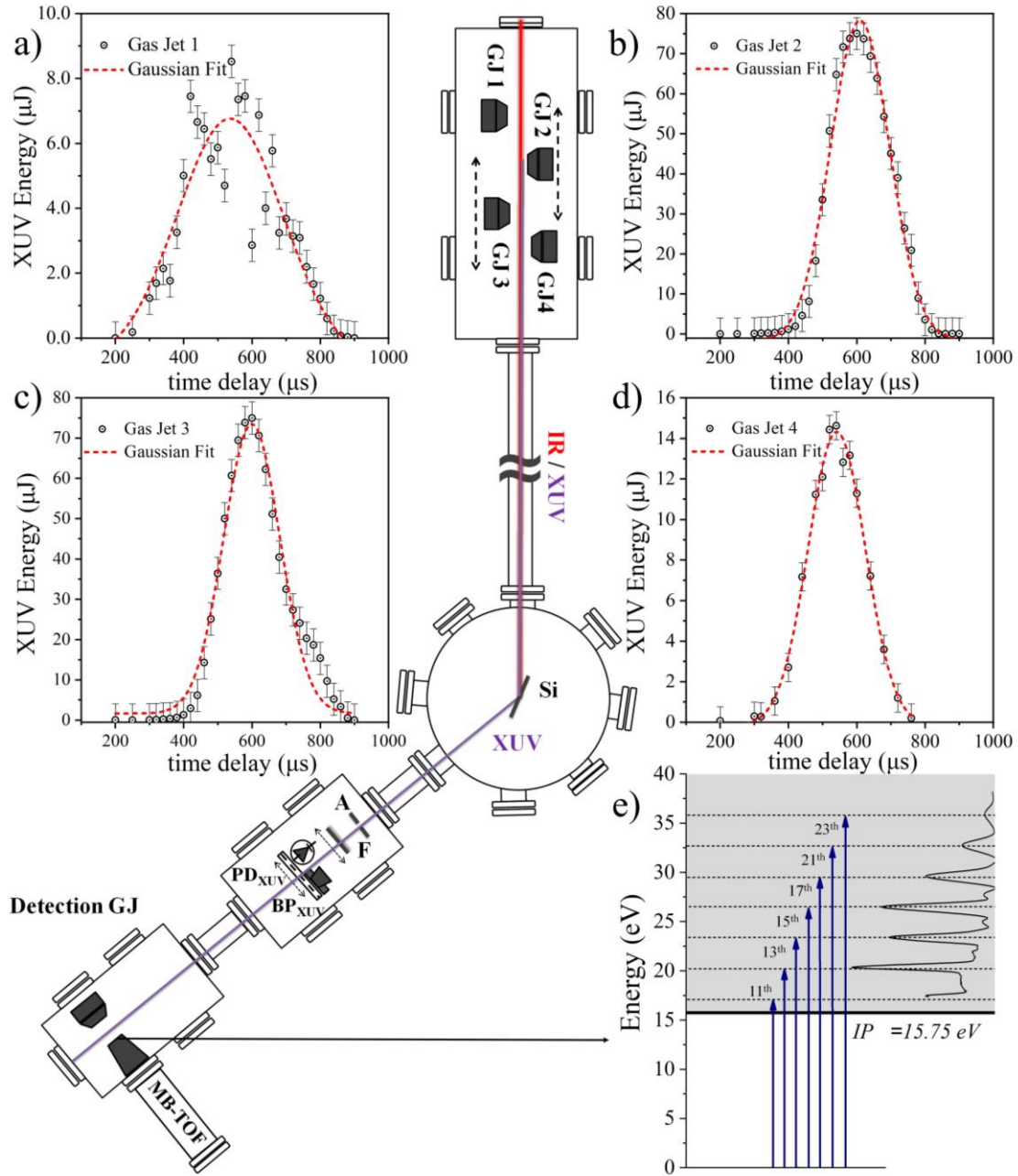
Figure 3.8 Experimental configuration of Quasi Phase Matching experiments. The HHG chamber hosts four Gas Jets mounted on translation stages. (a)-(d) depict the emitted XUV energy for each individually each one as a function of the time delay. (e) represents the excitation scheme of Argon gas used for the measurements of enhancement of the harmonic radiation. The blue arrows represent the Higher Order Harmonic spectrum generated in Argon gas while the black curve the photoelectron spectrum produced through single XUV photon absorption.

The vertical and horizontal manipulation of the Gas Jets are enabled via micrometric stages controlled through external mechanical feedthroughs allowing the alignment of the gas jets with respect to the IR beam. The translation stage of each Gas Jet can support 30 cm of total displacement with GJ2 and GJ3 ,as named in figure 3.7, having a 10 cm of overlapping distance. Thus GJ1 and GJ4 are placed at a rather longer positions with respect to the focal position resulting significantly lower harmonic emission. For the measurements of figure 3.7, GJ2 and GJ3 are placed at the same position which at the same time coincides with the focus of driving beam. Except for the harmonic yield generated, a subject of interest is also the shape of the harmonic spectrum emitted containing vital features and information about the nonlinear interaction and thus about HHG in spectral and also time domain. In order to shed more light into the mechanisms underlying the interaction in the case of Argon as the medium of HHG, photoelectron spectra were recorded as a function of the time delay. As can be observed in figure 3.8 a "splitting" in the photoelectron distribution is appeared in case of GJ 3 strong indication of higher intensity than optimum concerning the microscopic response of the medium. A quite interesting but different characteristic is also appearing to be featured in the case of GJ2 spectrum, where a clear broadening is revealing a macroscopic pressure induced effect. At the same time the higher energy peaks in the photoelectron spectra for all of the cases are becoming broader compared to the energetically lower electrons. This characteristic could be possibly attributed to the Magnetic Bottle Time of Flight electron spectrometer performance rather than an XUV generation effect. Figure 3.9 presents the single (individual) harmonic integration of the radiation produced. By integrating over each different photoelectron distribution and thus considering individually the generation spectrum components, the plots are (a)-(d) can be constructed referring to GJ1-GJ4 respectively. It is apparent that the maximum of the signal coincides for all the frequencies with negligible differences indicated by the center of the Gaussian fit of every individual gas jet pulsed valve. On the contrary deviation is appearing to the center of the maximum comparing the different Gas Jets. At this point it should be noted that due to small kinetic energy of the photoelectron ejected from Argon by the 11th harmonic (1.3 eV) cannot be clearly resolved in these measurements (roughly observed in the lower part of graph 3.8).
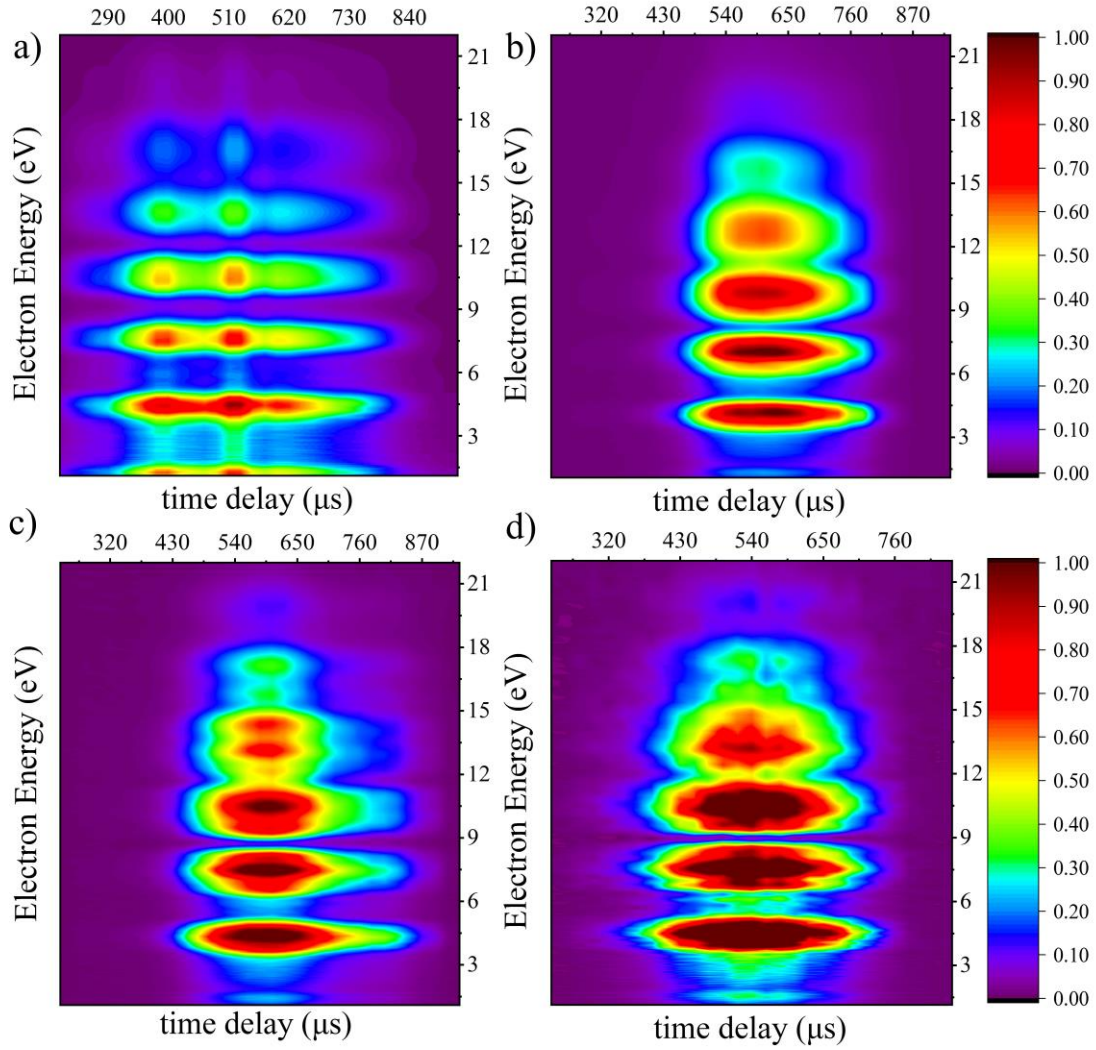
Figure 3.9 Contour plots of Photoelectron spectra of Ar Gas Jets. The figures (a)-(d) represents the spectrum generated from the interaction of Argon gas with the Laser pulses. The x axis corresponds to the value of time delay between the arrival of the Laser pulse and the opening time of the valve while the y axis to the photoelectron kinetic energy. The photoelectrons are produced through single photon ionization of Argon by 13th-23rd harmonic leading to energies 4.4 eV, 7.5 eV ,10.6eV, 13.7 eV ,16.8 eV and 19.9 eV respectively.
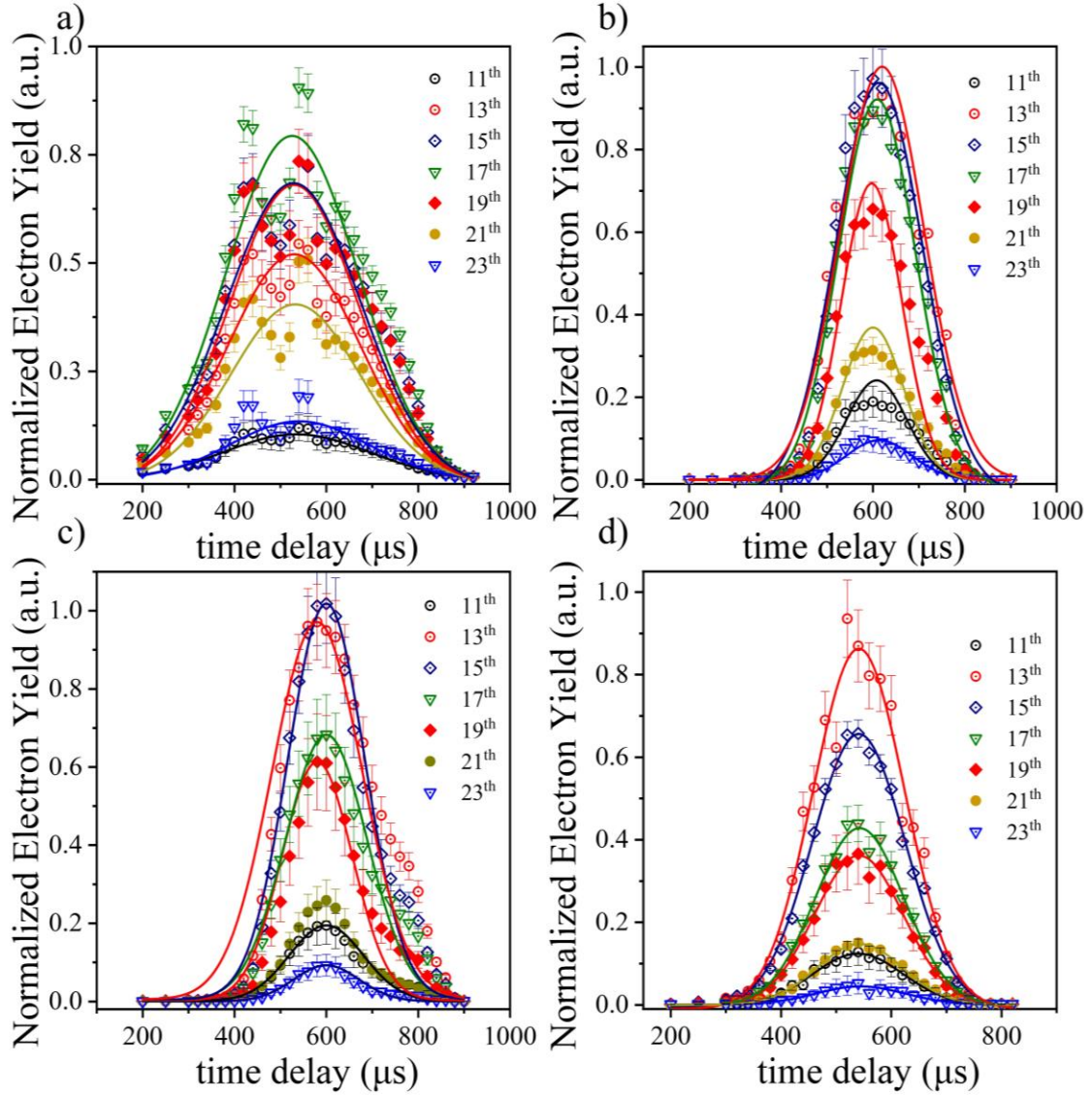
Figure 3.10 Normalized Harmonic yield of HHG. The normalized harmonic yield of the individual harmonics consisting the generated spectrum obtained from the photoelectrons recorded in case of (a) GJ1(b) GJ2 (c) GJ3 (d) GJ4.The data points are depicted with the error bars originated from the integrated area used for each case while the solid lines represent the Gaussian fits performed.

In order to improve the enhancement of the harmonic emission, it appeared very useful to obtain better knowledge of the intensity and ionization in the area of the focus. An examination of the broadening and splitting of the harmonic lines may – with further analysis – provide some information to this end. Scans of gas pressure provide insight into the mechanisms of line shifting and splitting, for ionization blue shifting is proportional to pressure while non-adiabatic blue shifting is independent of it. Pressure scans by varying the delay of the gas jet valve as described above also performed by implementing the flat field spectrometer providing the needed accuracy and also better resolution. The resolved spectra produced by Xenon reveal a blue shift in the frequency domain with the increase of the pressure in the non-linear medium.
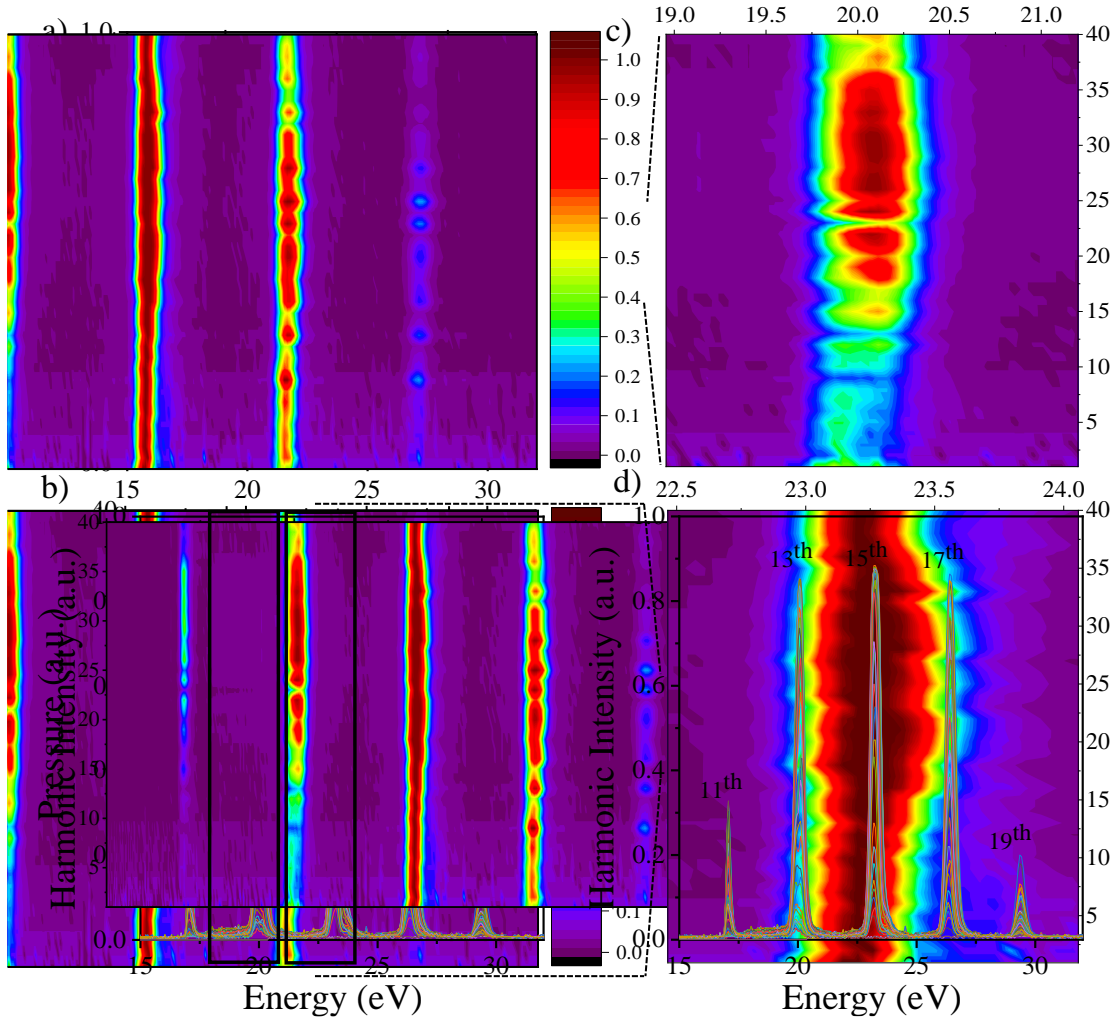
Figure 3.11 Pressure-dependent blue shift in HHG. (a) The normalized harmonic yield produced from Xenon gas for different time delays of the pulsed valve corresponding to different gas pressure (b) normalized contour plot of the total produced spectra. (c),(d) extended areas of 13th and 15th harmonic respectively.
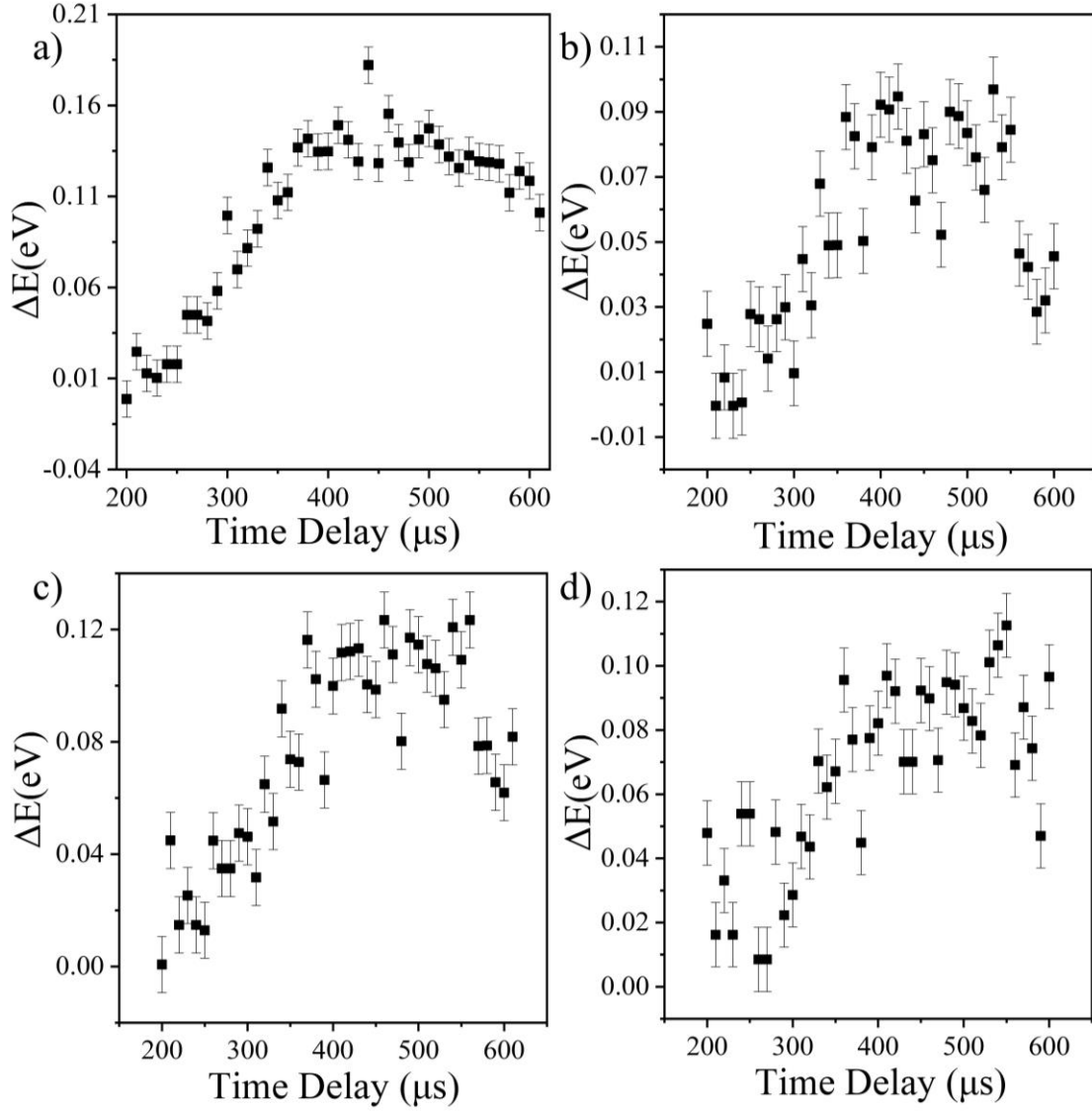
Figure 3.12 Pressure-dependent energy shift in HHG. The panels represent the harmonic energy shift appearing with the variation of the pressure of the gas controlled by the time delay between the opening time of the valve and the arrival of the pulse in case of (a)13th, (b)15th, (c)17th and (d)19th harmonic field.

Having optimized the harmonic generation process for each individual gas jet regarding the pressure and length of medium parameters, experimental investigations where then focused on enhancing the photon flux of the XUV radiation regarding the position of the medium with respect to the focus. For all of the upcoming investigations it should be noted that the beam diameter used for the HHG process is D=2.3 cm resulting to a confocal parameter measured to be $b \approx 70$ cm (1.22 larger than the value obtained according to the relation) as determined by performing beam profile described in chapter 2. Moreover, the energy of the IR pulses where found to be 25 and 45 mJ in case of Xenon and Argon respectively employed as the non-linear medium. The above parameters where carefully well-preserved constant and one should note that the deviation from those will dramatically affect the below findings.

A crucial factor for the harmonic emission is the position of the medium relatively to the focusing plane of the driving pulse. It is well known that the above condition dramatically affects not only the emitted yield but also the vital characteristics (spatial and also temporal) of the generated light. By measuring the total photoelectron yield, product of the single photon ionization of Argon by the XUV unfocused beam generated in Argon, figure 3.12 is revealing a quantitative picture regarding the efficiency of the generation. In figure 3.12 (a) the beam profile of the IR beam is presented in case of D=2.3 cm beam diameter while the lower panel represents the XUV normalized yield as a function of the medium position relatively to the focus of the Laser. The harmonic yield is the result of the integrated photoelectron signal originated from Argon gas as the product of the single photon ionization induced by the generated XUV beam. As can be observed GJ1 and GJ4 due to large distance from the IR focus are characterized by rather weak efficiency concerning the XUV radiation. One can improve the emission by increasing the driving pulse energy reducing at the same time the beam diameter. This would directly lead to the increase of the confocal parameter maintaining the peak intensity of the laser pulse below saturation avoiding the depletion of the medium around the focus. For the studies of this thesis only GJ2 and GJ3 were investigated regarding the optimization of the XUV generation regarding the position of the medium along the propagation axis and further investigations referring to the quasi phase matching conditions when double gas jet configuration where implemented.
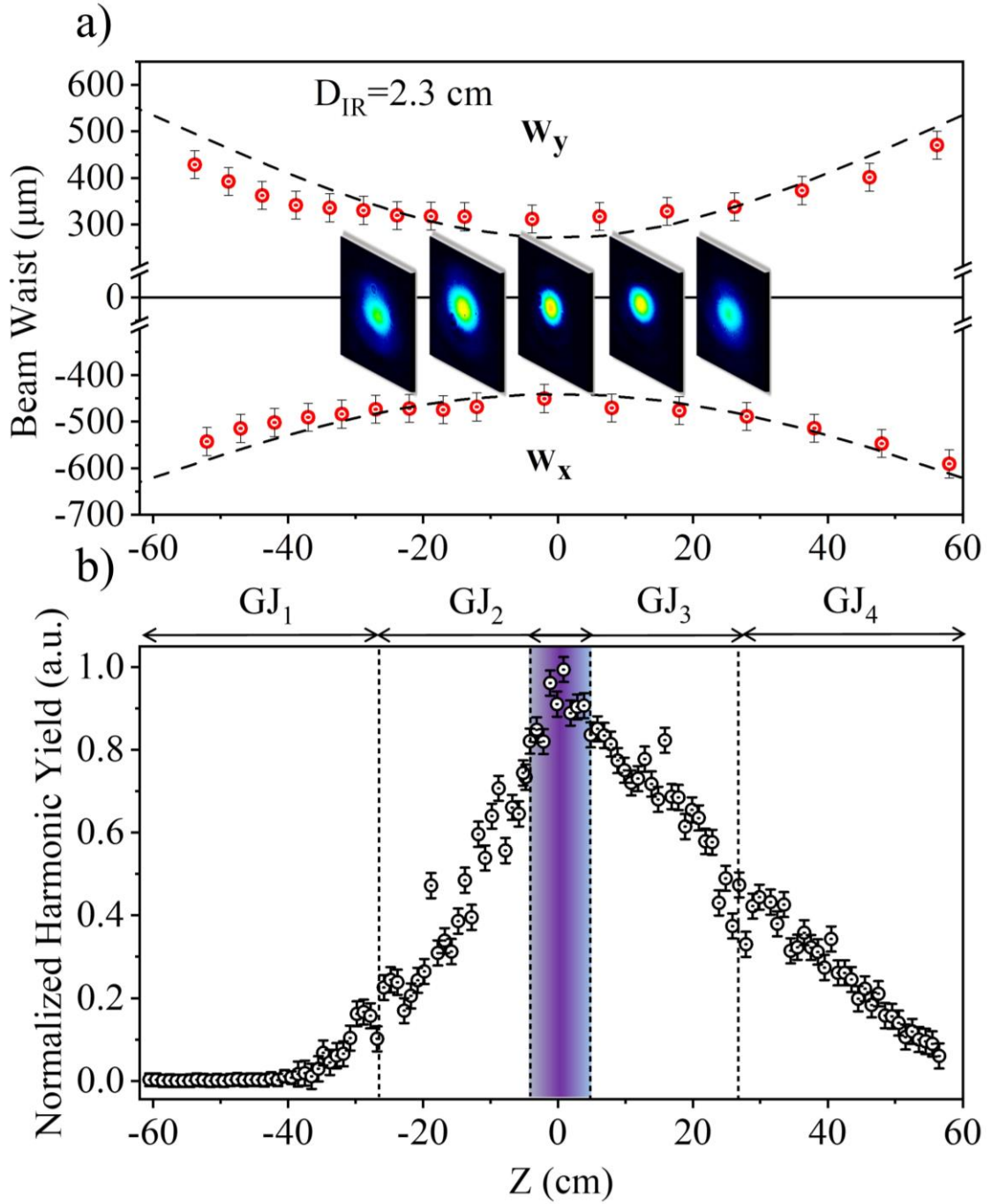
Figure 3.13 Measurements regarding the GJs position. (a) IR beam profile around the focus with D=2.3 cm initial beam diameter (b)The normalized harmonic yield of the XUV beam generated as a function of the Gas Jets position with Argon used as the non-linear medium. In the upper part of the graph the four different regions are labeled and marked with the arrows. The color field area corresponds to the overlapping region of the gas jets placed at the focusing area.

Measurements of the single Gas Jet emission by varying the medium position relatively to the driving pulse's focus are depicted in Figure 3.13 for Ar exploited as the non-linear medium. The upper panel presents the XUV energy produced in Argon as a function of the depth of the focus. The error bars represent the standard deviation of the measured data points. The measured trace resulting the contour plot in 3.13 (b) is constructed from the photoelectron spectrum produced by the unfocused XUV beam. The x-axis depicts the distance of gas jet from the position of the IR focus while the color map is presented in the right part of the lower panel revealing the yield produced from the process. The y-axis reveals the harmonic order as well as the kinetic energy of the corresponding electron extracted in the continuum.
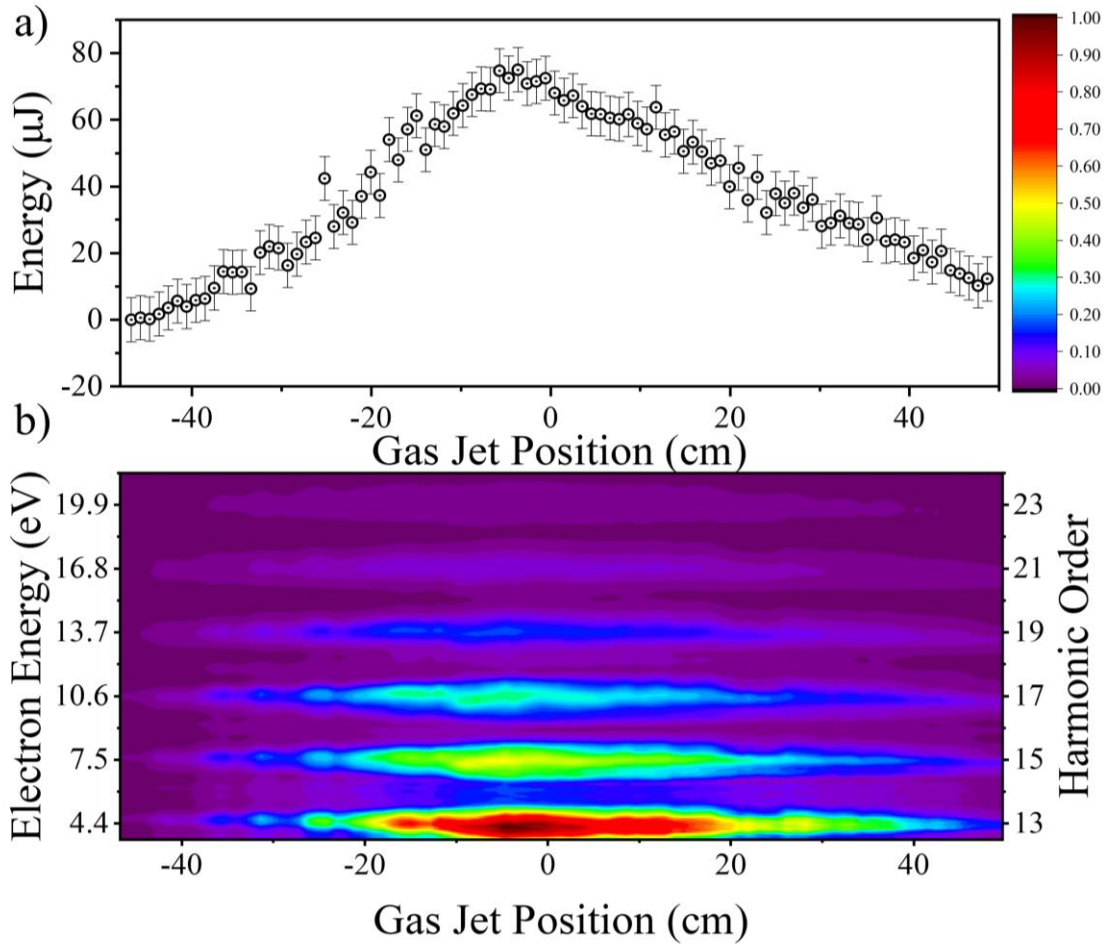
Figure 3.14 High Harmonic Generation in Argon with single gas jet configuration. (a) The dependence of XUV energy emitted from Argon on the relative position of Gas jet to the Laser focus (b) The corresponding high harmonic spectrum measured in the target area by recording the single-photon PE spectra produced by the interaction of Ar gas with the incoming XUV beam.

The energy emitted from Argon gas shows a maximum around the focus with the superior value to be E=75 µJ. The XUV energy curve shows the dependence on the position of the medium, observation in a relative contrast with previous studies regarding these investigations. In many cases due to the microscopic response but also the macroscopic effects in HHG process, a local maximum is present in the XUV yield curve when the non-linear medium is located before the driving pulse focus. This is attributed to the higher yield of the emission when long path trajectories of the electrons attributing to HHG are favorable. In this measurements a rather Gaussian-like distribution is characterizing the XUV flux as a function of the propagation axis.
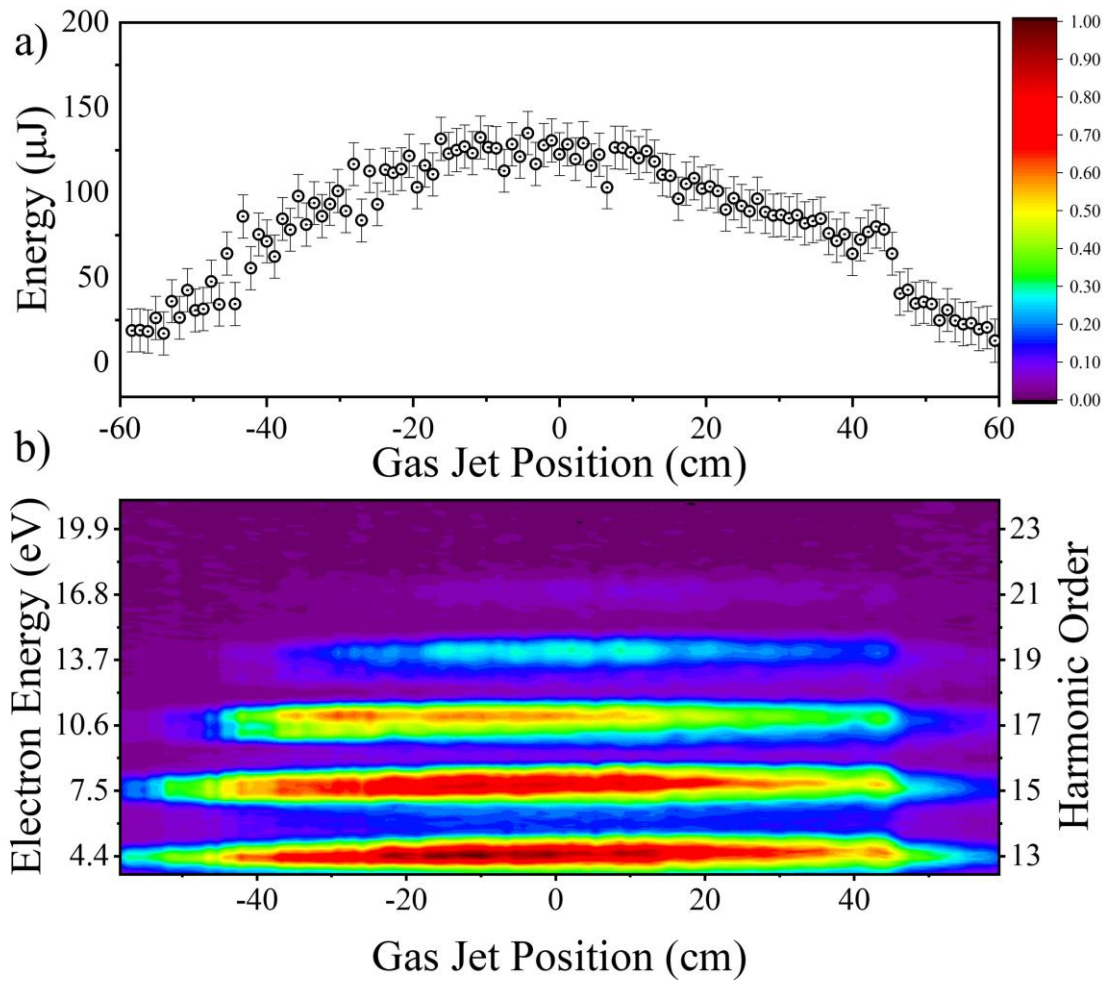
Figure 3.15 High Harmonic Generation in Xenon with single gas jet configuration. (a) The dependence of XUV energy emitted from Xenon on the relative position of Gas jet to the Laser focus (b) The corresponding high harmonic spectrum measured in the target area by recording the single-photon PE spectra produced by the interaction of Ar gas with the incoming XUV beam.

Experimental realization of the scan of single Gas Jet emission by varying the medium position relatively to the driving pulse's focus is depicted in Figure 3.14 for Xenon exploited as the non-linear medium. Measurements of the single Gas Jet filed with Xenon where carried out at the same experimental condition regarding the pulsed valve operation and also the focusing parameters as in case of Argon. On the contrary lower energy of the IR was used due to lower saturation intensity of Xenon comparing the Argon target with the value of the pulse to be 25 mJ. More over the backing pressure was also rather lower than the previous case with the optimum value to be 1.5 bar in comparison with Argon gas as the non-linear medium. It is worth noting that due to higher efficiency in case of Xenon regarding the HHG process (in comparison with Argon) a slightly larger is appearing to be the valuable area concerning the efficiency of XUV photons generated as a function of the position across the propagation axis of the driving beam. Due to the lower ionization potential owed by Xenon the generated energy is significantly higher compared to other noble gases, followed although by the compromise of lower cut-off law concerning the highest photon energy of the emission. These observations are illustrated by the energy curve as a function of the position and by the photoelectron spectrum produced by the unfocused XUV beam in the contour plot of figure 3.14. The maximum XUV energy measured in Xenon is E=135 μJ (a factor of ~2 higher than Argon).

After having determined the optimum conditions in case of the single gas jet configuration, further enhancement of the harmonic yield was achieved by applying quasi-phase-matching conditions using two gas jets, a way for partially overcoming the physical limitations regarding the macroscopic response of the medium. This is mainly referred to XUV absorption effects and IR-XUV phase mismatch induced by the neutral atoms and plasma generation in the medium which confines the coherent harmonic build-up to a short propagation length. The same gas is used in both jets. Results are shown in Fig. 3.15 and Fig. 3.16. for Argon and Xenon respectively. The dependence of the harmonic yield, generated by Argon and Xenon gas, on the distance between the two Gas Jets is shown in Fig. 3.15 (a) and Fig. 3.16 (a) respectively. The lower panels of the graphs are depicting the photoelectron spectra for each case as a function of the distance of the two different mediums of the same noble gas.
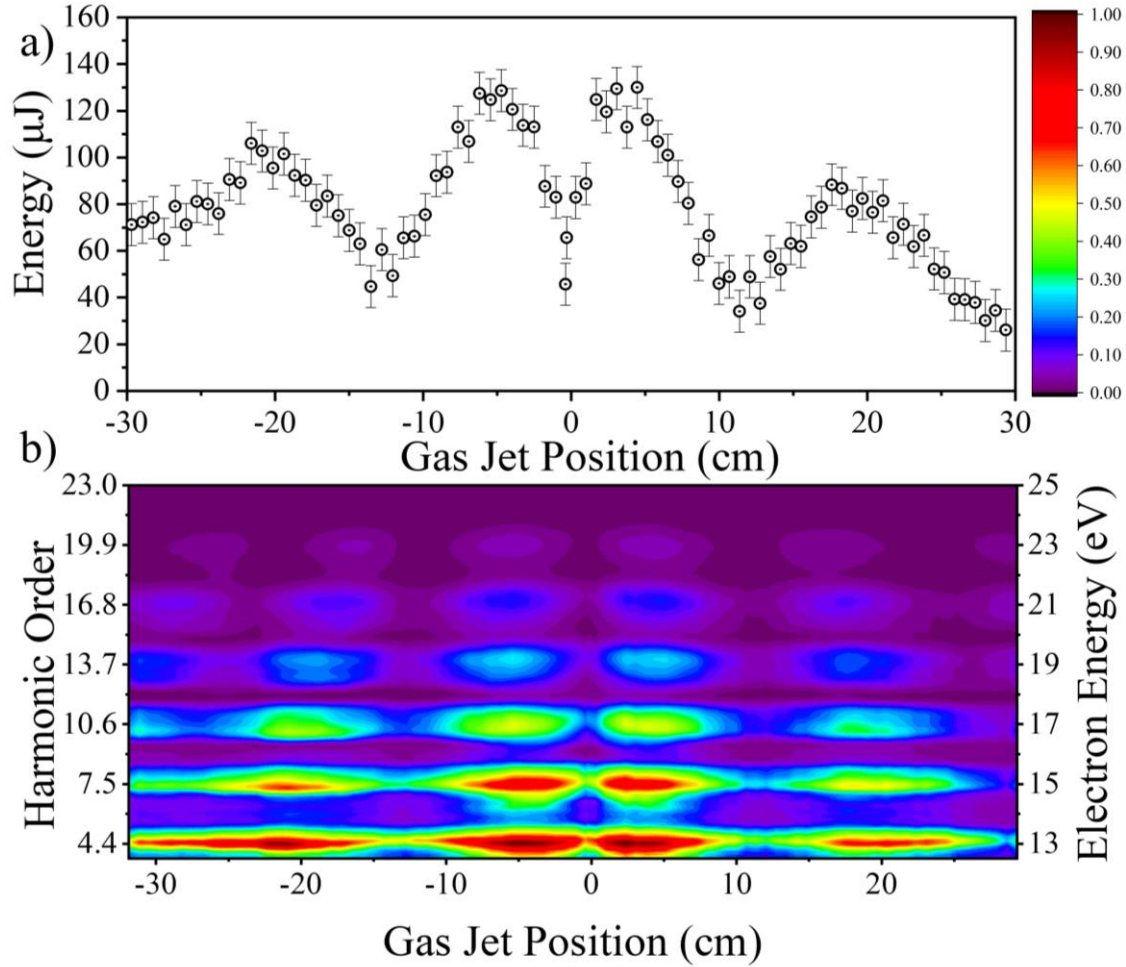
Figure 3.16 High Harmonic Generation in Argon with double jet configuration.
(a) The dependence of XUV energy emitted by Argon on the relative position between the two Gas jets and relatively to the Laser focus (b) The corresponding high harmonic spectrum measured in the target area by recording the single-photon PE spectra produced by the interaction of Ar gas with the incoming XUV beam.

Setting the first Gas Jet at the optimum position coinciding the focusing plane of the IR Laser pulse the scan of the second gas jet was then performed. For both of gas jets the parameters were kept the same regarding the applied voltage on the valve the, time delay between the opening time of the pulsed valve and the arrival of the exciting pulse, the width of the exposure time of the gas to the driving field and finally the backing pressure (3.5 bar for Argon and 1.5 bar for Xenon). Note that the experimental conditions were reserved the same as in each single Gas jet investigations presented above, with the IR Laser pulse to be set at 45 mJ and 25 mJ in case of Argon and Xenon respectively while the beam diameter is set at 2.3 cm.
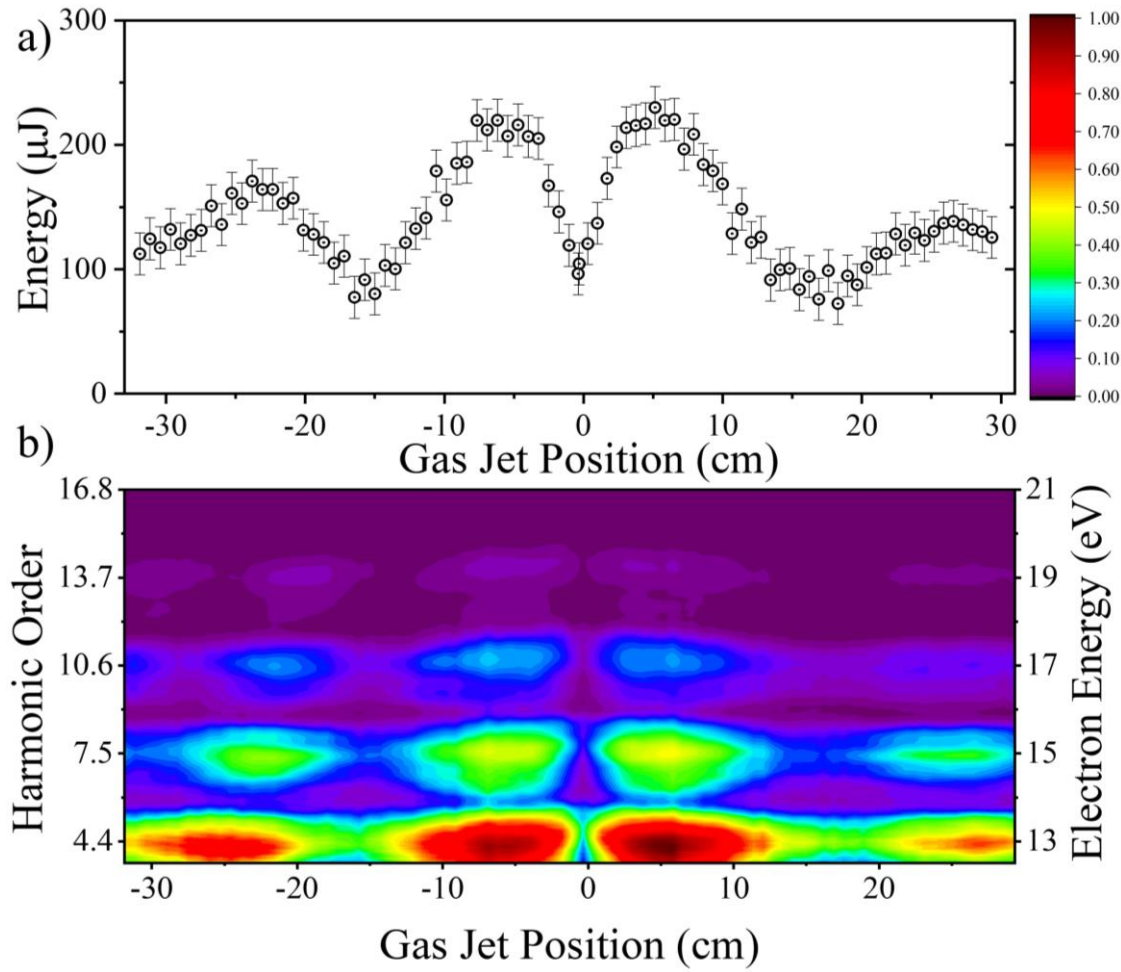
Figure 3.17 High Harmonic Generation in Xenon with double jet configuration.
(a) The dependence of XUV energy emitted by Xenon on the relative position between the two Gas jets and relatively to the Laser focus (b) The corresponding high harmonic spectrum measured in the target area by recording the single-photon PE spectra produced by the interaction of Ar gas with the incoming XUV beam.

The first Gas jet is located at fixed position $z \approx 0$ and the second one at variable positions (L and P are the same in both jets). In both cases, the energy increases by a factor of ≈ 1.7 when the GJ2 is placed at $z \approx \pm 5$ cm, verified by calculations taking into account the propagation effects in the dual-gas medium. At this position, the generated XUV energy was found to be E=130 μJ and E=230 μJ per pulse for Argon and Xenon respectively. The reduction of the energy around $z \approx 0$ is attributed to phase-mismatch effects induced due to the increase of the medium pressure and/or medium length, while the oscillations observed at $z > + 5$ cm and $z < - 5$ cm are attributed to the Gouy phase shift of the focused IR beam. In these positions the macroscopic geometric phase induced due to variation of the position of the gas jet as a respect of the focus can be

considered negligible regarding and thus the harmonics are in relative phase. This is verified by the appearance of maxima when the individual yield of each contributing is take into account.

For better visualization and also understanding the mechanism underlying the above investigations 2-D plots are revealing the picture of merit regarding the harmonic yield. In figure 3.17 the XUV yield is plotted as a function of distance in case of single gas jet configuration regarding (a) Argon and (b) Xenon gas as the source of HHG process respectively. Panels (c) and (d) are depicting the emitted harmonic intensity with respect to the distance of gas jets along the propagation axis of the driving laser beam. For all cases the accumulated data points are referring to the product of the integration over each individual photoelectron distribution, recorded by the time of flight electron spectrometer, corresponding directly to the harmonic photon energy responsible for its injection in the continuum. In the measured data points an error bar is denoting the standard deviation of the mean value extracted by the uncertainty of the Gaussian-like distribution of the photoelectron peaks integrated, the standard error accompanying the width of the distribution and also the integration area limits used for each case. In case of single gas jet scan measurements, a polynomial fit over each curve is also presented for visualization purposes revealing the trend of the signal over the z direction. It is clear that in case of double gas jet for both noble gases case a modulation for each harmonic is appearing and furthermore the maximums are located at different positions, attributed to the different gouy phase shift regarding different harmonic order. Considering the propagation of the generated XUV generated at a specific point along the propagation with the assumption of a plane wave on can expression the electric field as:

$$E_1(z) = E_1(z_1) \, e^{-iqk(z-z_1)} \tag{3.32}$$

While taking into account the geometric phase describing the propagation of the XUV light one can derive that the electric field amplitude is:

$$E_1(z) = E_1(z_1)e^{-i(qkz_1 + q\varphi_{Gouy}(z_1))} \tag{3.33}$$

Considering the above hypothesis for two different sources separated in space along the propagation axis, as the experimental investigations in this work, Z_1 and Z_2 for the total electric field the coherent sum must be deduced.

$$E_t \propto E_1 + E_2 \propto e^{-iqkz_2}\{1 + \exp(iq[\varphi_{Gouy}(z_2) - \varphi_{Gouy}(z_1)])\} \quad (3.34)$$

Then one can extract the harmonic yield produced which is proportional to the intensity of the total electric field of the two coherently attributing sources.

$$S(q, z_2) \propto |E_t|^2 \propto 2\{1 + \cos(q\Delta\varphi_{Gouy}(z_1, z_2))\} \quad (3.35)$$
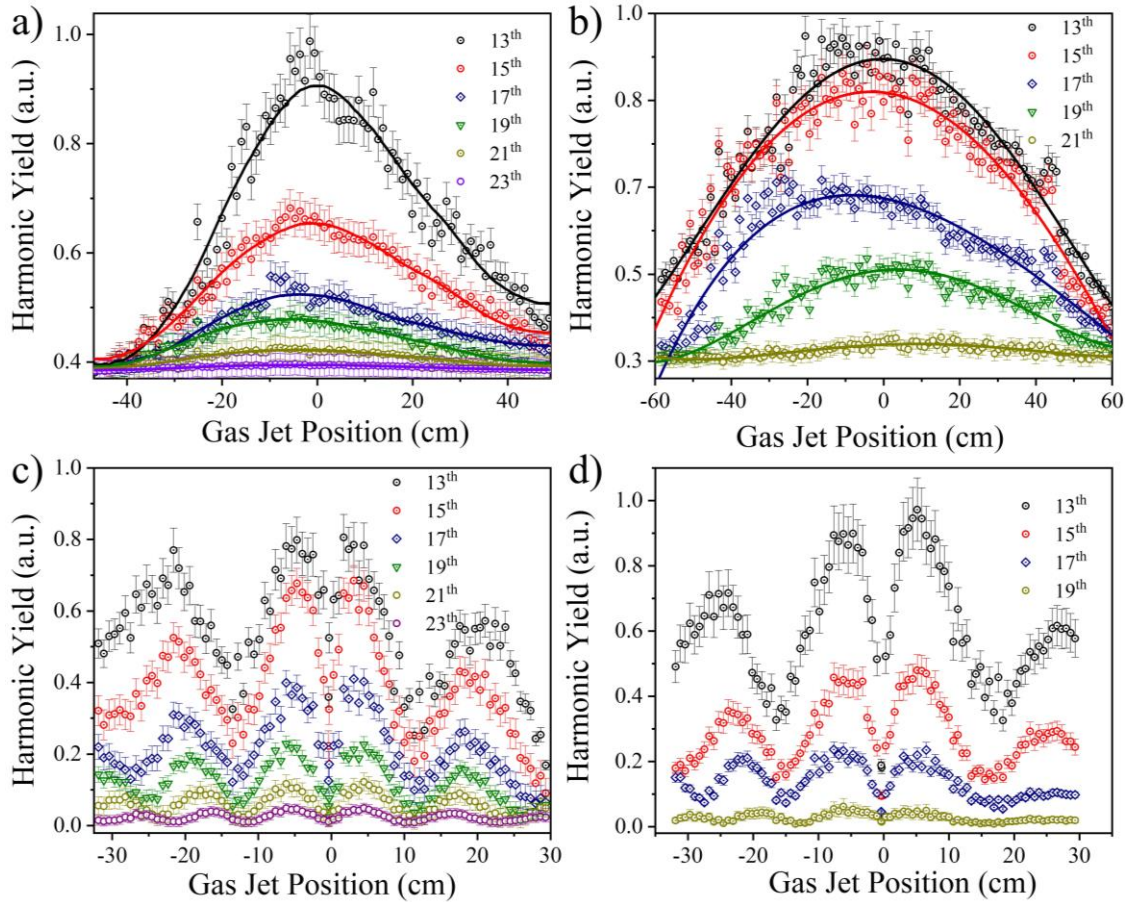
Figure 3.18 High Harmonic Generation in Argon and Xenon using single and double jet configuration. (a), (b)Show the harmonic signal originated for each harmonic as a function of the position of the Gas Jet for Argon and Xenon respectively. (c), (d) are representing the modulation due to two the sources contributing to the total yield for Argon and Xenon respectively with the variation of gas jet distance.

In the following conclusive table, the results of quasi phase matched high harmonic generation regarding the Argon and Xenon cases and also the single and

double gas jets configuration are assembled. The table contains the vital information concerning the XUV sources (i.e. maximum yield, cut-off, conversion efficiency.) obtained for the experimental condition described referring to the driving laser pulses and standard geometry was maintained for the series of the experimental investigations.

Non-Linear medium	Energy (μJ)	Conversion efficiency	Cut-off (eV)
Argon	75	2×10^{-4}	48
Argon Double Gas Jet	130	3×10^{-4}	48
Xenon	135	1×10^{-3}	32
Xenon Double Gas Jet	230	2×10^{-3}	32

Table: Summarized parameters for the non-linear upconversion in case of Argon and Xenon in single and double gas jet configurations.

Further investigations regarding Helium gas medium implemented for High Harmonic generation process revealed, as expected, higher cut-off frequencies compromising though the produced yield over the spectrum. On the contrary with the previously presented studies (Argon, Xenon) the trace obtained from dual gas jet configuration, appears a maximum in the focusing area showing the absence of saturation-like behavior. Figure 3.19 depicts the experimental studies of single gas jet filed with Helium. Regarding the single gas jet scan presented the "effective" area efficient for the generation of XUV radiation is significantly reduced compared to the other two noble gases cases implemented for the same measurements. An enhancement scaled by a factor of ~1.5 is observed when both gas jets are on while the oscillations attributed to geometric phase shift is also illustrated in the contour plot of figure 3.20. It is worth noting that due to lack of flux generated in the helium medium the upper panels in both 3.19 and 3.20 plots are presenting the normalized harmonic yield. The yield is the product of the integration over the total photoelectron spectrum originated from the interaction of the incoming beam with the Argon gas filed detection gas jet.
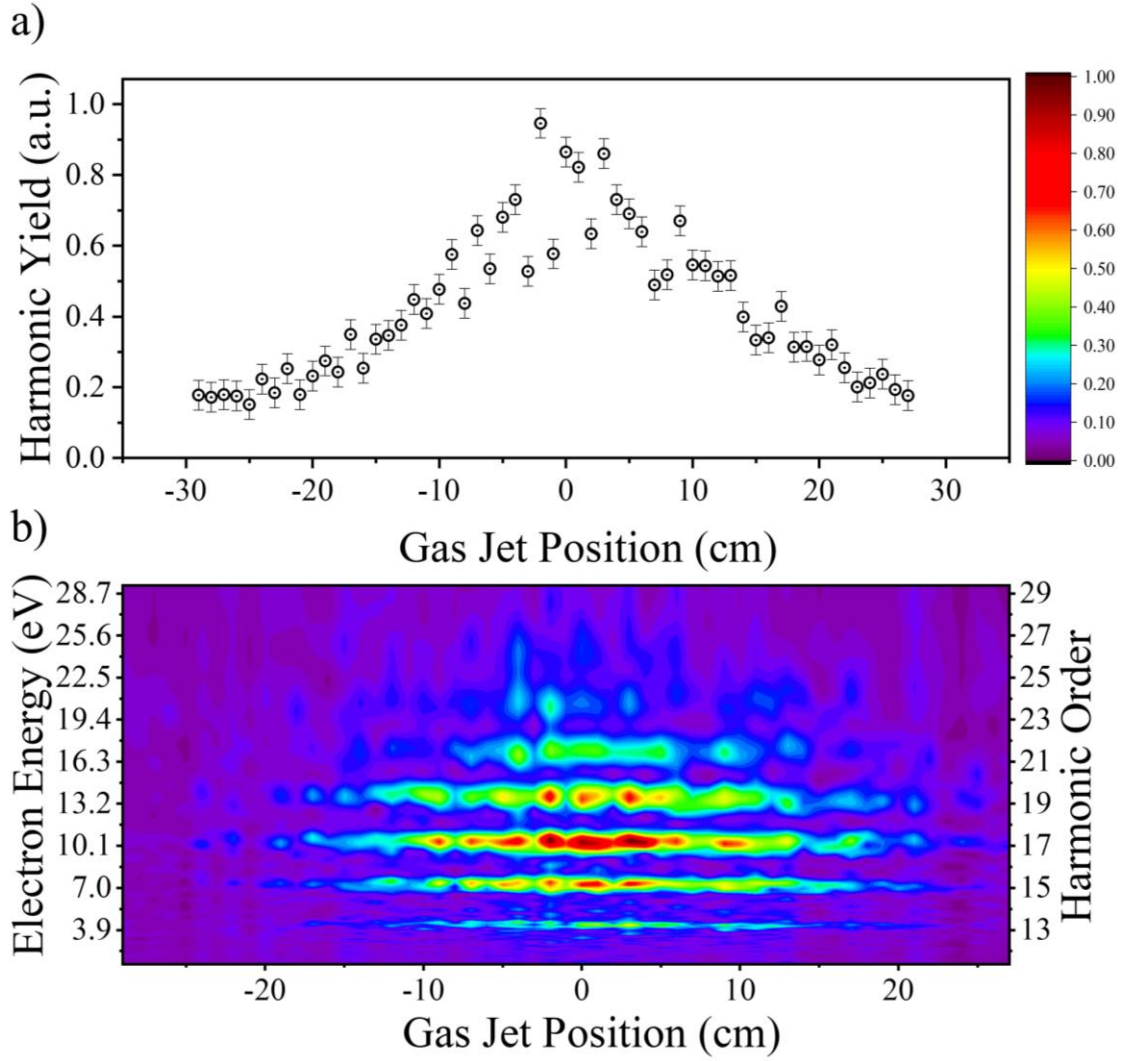
Figure 3.19 High Harmonic Generation in Helium with single gas jet configuration. (a) The dependence of XUV yield emitted by Helium on the relative position of Gas jet to the Laser focus (b) The corresponding high harmonic spectrum measured in the target area by recording the single-photon PE spectra produced by the interaction of Ar gas with the incoming XUV beam.

The lower efficiency of Helium gas is preventing the absolute measurement of the XUV generated energy and thus the harmonic yield is presented in the upper panel of the graph. Moreover, noisy appears the signal corresponding to the contour plot containing the time of flight spectra as a function of the gas jet position with high energy photons to suffer the most. Thus for improvement of the above comments a further increase of the energy of the driving Laser pulses in conjunction with the beam diameter decrease (leading to larger confocal parameter) would lead to higher XUV output.
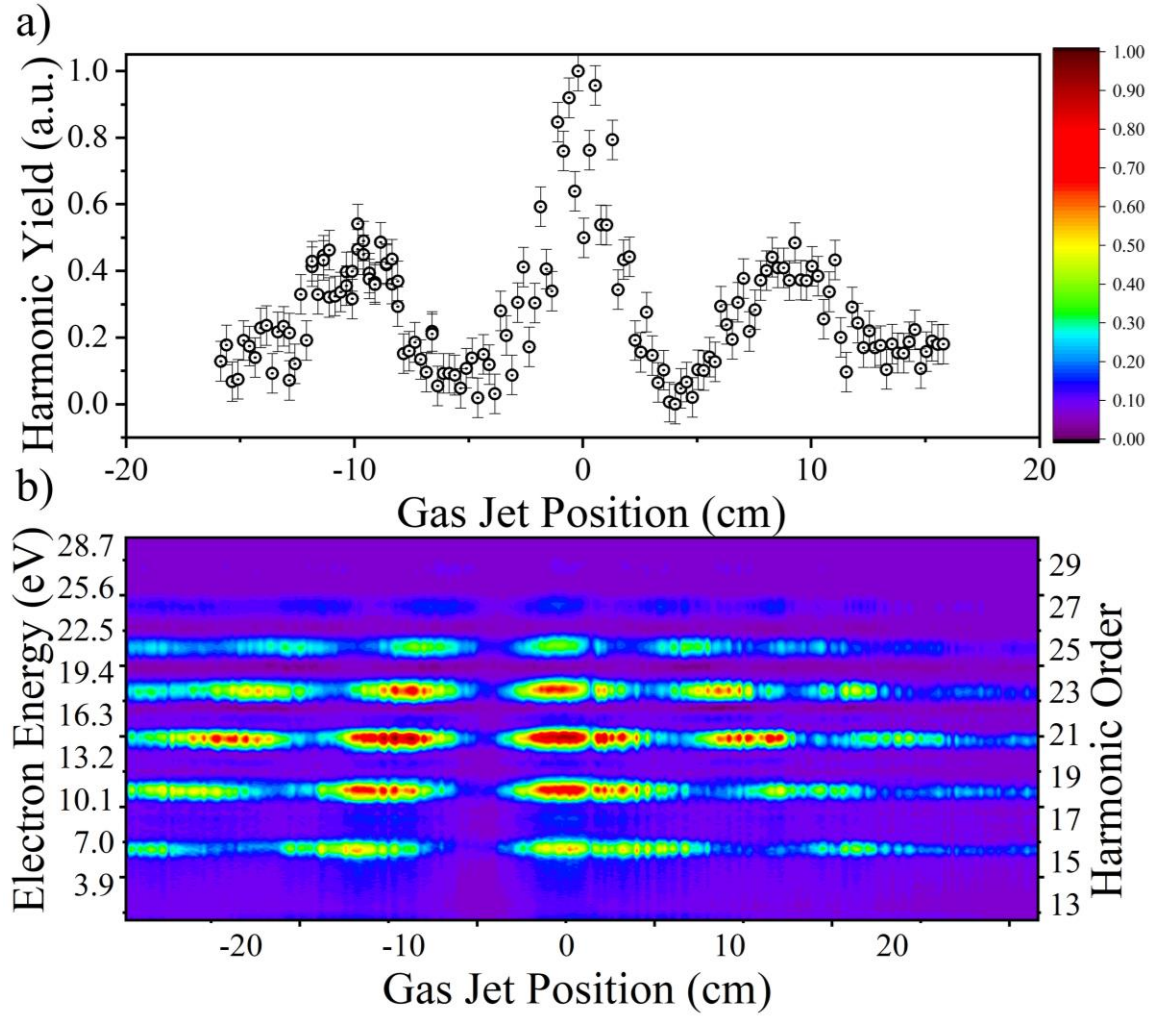
Figure 3.20 High Harmonic Generation in Helium with double jet configuration.
(a) The dependence of XUV energy emitted by Helium on the relative position between the two Gas jets and relatively to the Laser focus (b) The corresponding high harmonic spectrum measured in the target area by recording the single-photon PE spectra produced by the interaction of Ar gas with the incoming XUV beam.

Note that for the Helium gas as the nonlinear medium for the frequency upconversion the IR beam was set ~70 mJ with the beam diameter to be 3 cm. Furthermore, the backing pressure of the generation gas jets was 5 bar, value rather higher compared to previous investigations regarding Argon and Xenon. The higher energies presented in the photoelectron spectrum in both the single and double gas get configurations is accredited to higher photon energies generated in the case of a higher ionization potential has such as Helium.

Chapter 4: Metrology of Attosecond Pulses

Introduction

Real time observation of electron motion in all states of matter requires temporal resolution in the attosecond (1 attosecond (asec) = 10^{-18} sec) time scale. Tools for tracing such dynamics are flashes of light with asec duration. Nowadays, such pulses are routinely produced in laboratories by synthesizing broadband coherent radiation generated in the extreme ultraviolet (XUV) spectral range after the interaction of matter with intense fs pulses. Taking into account that conventional pulse characterization techniques, routinely employed in the visible and UV spectrum, cannot be applied in the XUV regime attosecond pulse metrology has proven to be one of the most innovative chapters in the field of ultra-short pulse metrology as notable methods have been implemented for attosecond pulse characterization. For more than two decades since the generation of coherent broadband XUV radiation, continues efforts in asec pulse metrology led to the development of impressive techniques for pulse duration measurements as well as also the complete reconstruction of those pulses. Among these methods, two main categories have prevailed: those based on cross correlation (CC) and the ones based on non-linear volume autocorrelation (AC). Both provide pulse characterization in the region where the asec pulses interact with matter. The CC approach rely on the reconstruction of the pulse which occurs after analyzing the data obtained by the interaction of atoms with the superposition of the XUV pulse with an IR field. Most commonly used schemes are the RABBITT and Attosecond Streak Camera techniques. The AC approach relies on the interaction of two parts of the pulse to be characterized that are considered to be identical and results in a direct measurement of the pulse duration. AC measurements can be accomplished by recording ions or photoelectrons (PEs) induced by two-photon ionization processes in an appropriate target medium.

In this chapter a brief introduction of the non-linear processes driving the second order volume autocorrelation (2-IVAC) approach is presented for the temporal characterization of attosecond pulse trains and isolated pulses. XUV-FROG applications are discussed as well as how the XUV-FROG technique is used to retrieve the spectral phase and amplitude distribution and fully (except for the right-left

asymmetry) reconstruct the APTs and IAPs, respectively. Finally, the detailed 2-IVAC method providing the experimental results regarding the temporal characterization of the of attosecond pulse trains produced in the 20GW XUV FORTH-IESL beamline will be presented.

4.1 Non-linear ionization processes

Before an AC measurement can be performed with confidence, it is of utmost importance to confirm that the ionization in the gas jet is indeed dominated by the two-photon process and is thus suitable for the second-order AC. In a first step, it is therefore necessary to verify that the focused intensity in the interaction region is high enough to generate enough ions/electrons through two-photon ionization (Fig. 4.1). In order to estimate the XUV intensity (I_{XUV}) required to induce and observe a nonlinear process in atoms, the two-XUV-photon non-resonant ionization yield (Y_2) (ions/electrons) has to be calculated under realistic experimental conditions. For an XUV pulse of duration τ_{XUV} and intensity I_{XUV}, the ionization probability rate (W_2) and the Y_2 per pulse for a two-photon absorption process are given by:

$$W_2 = \sigma^{(2)}\left(\frac{I_{XUV}}{\hbar\omega_{XUV}}\right)^2 \qquad\qquad (4.1)$$

$$Y_2 = \sigma^{(2)}\left(\frac{I_{XUV}}{\hbar\omega_{XUV}}\right)^2 \tau_{XUV}\, n_a\, V \qquad\qquad (4.2)$$

with n_a being the atomic density in the interaction volume V and $\sigma^{(2)}$ the generalized two-photon ionization cross-section with values ranging from 10^{-49} to 10^{-52} cm^{4}s. In the case of a Three Photon Sequential double ionization (ThPSDI) process, AC measurements can also be valid but with the requirement of the saturation of the first step of the excitation. In this case the ground state of the system is practically saturated and thus the produced yield is essentially the result of a direct two photon process.

$$I_{XUV} = \frac{E_{XUV}}{A\,\tau_{XUV}} > 10^{12}\;W/cm^2 \qquad N_{ion} = n_a V \sigma^{(2)} \int_{-\infty}^{+\infty} \left(\frac{I_{XUV}}{\hbar\omega}\right)^2 dt$$
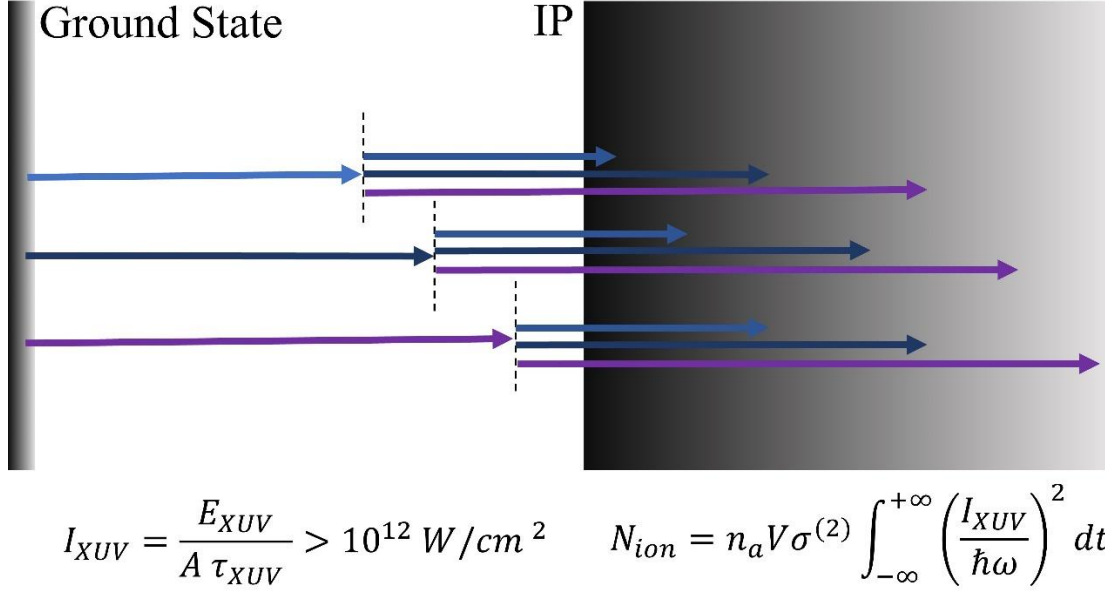
Figure 4.1 Two-XUV-photon ionization scheme of an atom A. IP is the ionization potential of A. For realistic experimental atomic densities (e.g. $n_a = 10^{15}$ atoms/cm^3) and interaction volume (e.g. $V = 10^{-9}$ cm^3) an observable two-photon ionization yield would require $I_{XUV} > 10^{10}$ W/cm^2. Ions and photoelectrons produced by a two-XUV-photon non-resonant ionization process have been observed using XUV pulses in the nJ energy range.

The spatial characteristics of the XUV beam at the interaction region can be obtained experimentally by means of an Ion Microscope (IM). Fig. 4.2 shows an example of the spatial distribution of the XUV radiation at the focus recorded in a single shot. Besides the measurement of the XUV beam spatial characteristics in the interaction region, the Ion Microscope can be also exploited for obtaining quantitative information about generalized cross sections in the linear and non-linear XUV region. Furthermore, a proposed method exploiting the IM as a tool for pulse duration characterization has been presented. The approach provides high temporal and spectral resolution in a single-shot measurement. This can be done by imaging the spatial ion distribution, created by a two-photon process, along the propagation axis of two focusing counter propagating asec pulses.
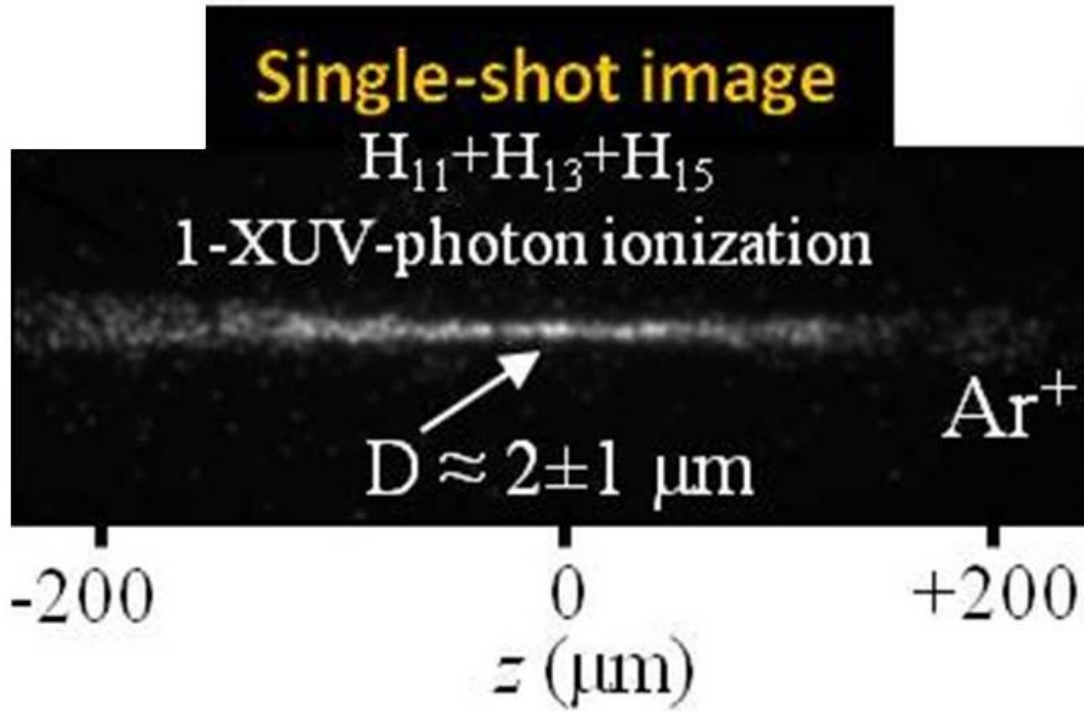
Figure 4.2 Single-shot image of the intensity distribution at the focus of the XUV radiation (induced by the 11th, 13th, 15th harmonics of the IR driving field). z is the propagation axis of the XUV. The image has been obtained by recording the ion distribution induced by single-photon ionization of Argon atoms at the focus of the XUV beam. Fig. from ref [80].

The ionization potential of the atom (A) sets an upper limit to the harmonic order q that is permitted to be included in the superposition and thus a lower limit to the duration of the characterized XUV pulse. In order to overcome this limitation, an alternative two-XUV-photon ionization scheme would have to be exploited. Possible schemes are the non-resonant direct double ionization (DDI), sequential double ionization (SDI) or ionic ionization (II) and above threshold ionization (ATI) (Fig.4.3).
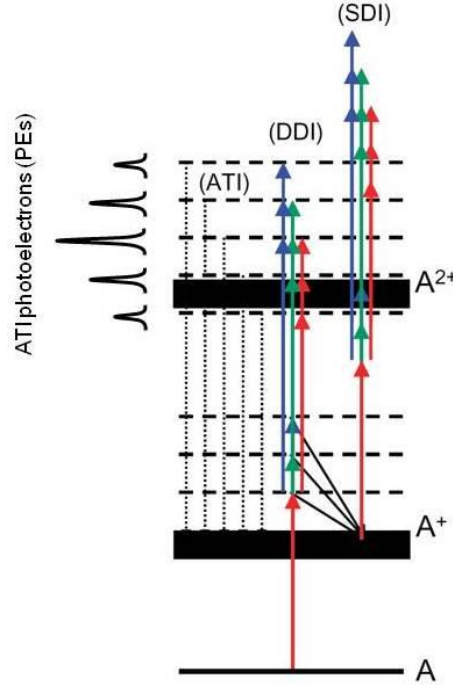
Figure 4.3 Above Threshold direct and sequential double ionization scheme.
Ionization scheme showing the ATI, DDI and SDI processes of an atom A. ATI leads
to the generation of a singly charged ion and photoelectrons (PEs) with energies
depending on the energies of the photons involved in the ionization process. DDI and
SDI generate doubly charged ions and PEs with energies depending on the energies of
the photons involved in the ionization process. These processes allow the extension of
the AC method to higher photon energies.

In these schemes, ionic products such as electrons or ions are to be detected by means
of energy resolved PE or TOF ion-mass spectroscopy, respectively.

The ATI scheme allows the continuous extension of the second-order AC
method to shorter wavelengths. Provided that the region of the continuum reached by
the ATI process is structureless (no autoionizing bound states are embedded in the
continuum), the only restriction of the method is the rapidly decreasing cross-section
with photon energy ($\propto(\hbar\omega)^{-6}$).

The two-photon-ATI scheme leads to the production of A^+ ions and electrons
with energies $PE_{ch}^{ATI} = \hbar\omega_{ch} - IP_1$, where $ch = q_{min} + q_{max} + n$ with $n = 1 - N \ldots N - 1$,
q_{min} and q_{max} the minimum and maximum harmonic orders, N the number of harmonics
in the superposition and IP_1 the first ionization potential of the atom. The method
requires energy-resolved PE spectroscopy. The DDI schemes allow the extension of the

second-order AC method to shorter wavelengths with photon energies in the region $IP_1 < \hbar\omega_q < IP_2 - IP_1$, where IP_2 in analogy to IP_1 is the second ionization potential of the atom. Here, ion mass spectrometry, selecting the doubly charged ions, or PE spectroscopy can be used. For this photon energy region, ionization processes such as single-photon, two-photon DDI (TPDDI) and three-photon SDI (ThPSDI) can contribute, with different rates, to the ionic products. The single-photon ionization mechanism can be ignored since it does not contain any information about the temporal pulse characteristics. The TPDDI and ThPSDI schemes lead to the production of doubly charged ions (A^{2+}) and electrons with energies $0 < PE_{ch}^{DDI} < \hbar\omega_{ch} - IP_2$ and $PE_{ch}^{ThPSDI} = \hbar\omega_{ch} - (IP_2 - IP_1)$, respectively. Since both schemes coexist in the ionization process, the temporal evolution of the system can be evaluated at different intensities using rate equations.

Nevertheless, according to previous studies in He, Ar and Kr, the intensity regions where DDI could be used for asec pulse train characterization by means of second-order AC can be roughly estimated. Based on previous studies in He, for $I_{XUV} < 10^{13}$ W/cm^2, far below the SDI saturation intensities, the TPDDI and ThPSDI rates can be expressed as:

$$W_2^{DDI} = \sigma_{DDI}^{(2)} I_{XUV}^{(q)} I_{XUV}^{(p)} / (\hbar^2 \omega_q \omega_p) \tag{4.3}$$

And

$$W_3^{ThPSDI} = \left[\sigma^{(1)} I_{XUV}^{(q)} / \hbar\omega_q \right] \left[\sigma_{TPII}^{(2)} I_{XUV}^{(q)} I_{XUV}^{(p)} / [\![(\hbar]\!]^2 \omega_q \omega_p) \right] \tag{4.4}$$

respectively. Here, σ_{TPII} denotes the two-photon ionization cross-section of the ion. DDI is then the dominant process that could be used for as-pulse characterization. For much higher intensities ($I_{XUV} > 3 \times 10^{15}$ W/cm^2), far above the SPI saturation intensities, the ThPSDI rate may by written as the product of the saturated ground state of the singly charged ion population times the ionic two-photon ionization rate, i.e.

$$W_3^{ThPSDI} = \left[Y_1^{(q)} / N \right] \left[\sigma_{TPII}^{(2)} I_{XUV}^{(q)} I_{XUV}^{(p)} / (\hbar^2 \omega_q \omega_p) \right], \tag{4.5}$$

which indicates a second-order process. In this case, the SDI process is the dominant one that could be used for a measurement of the asec pulse duration.

4.2 Operation principle of the 2-IVAC

The 2-IVAC approach was first demonstrated by Tzallas *et al.* [124] in 2003 using gas phase harmonics and in 2006 using harmonics emitted from laser-plasma interactions [70]. Autocorrelation measurements in the visible/infrared spectral region are based on the interference between two replica pulses created by a beam splitter and separated in time by adding optical path to one of the arms corresponding to various time delays in their propagation. However, since no conventional dispersionless beam splitter is available in the XUV wavelengths, the XUV pulse replicas are created using an XUV wave front splitting device. Such a device is a split spherical mirror where one of the two-halves is fixed and the other on a piezo translation stage as shown in Figure 4.4. This device provides also a feasible solution for the introduction of time delay between the two replicas not only for pulse duration measurements but also for XUV pump – XUV probe experiments in atoms and molecules. Using the non-linear ionization schemes described in Section 4.1 the measured autocorrelation signal is provided by the ionization products (electrons or ions) collected and recorded by a TOF spectrometer.

The operation principle of the 2-IVAC relies on the integration of 2-XUV-photon ionization yield produced in the interaction volume by the coherent superposition of the XUV pulse replicas created by the wavefront XUV beam splitter (additional information can be found in ref. 158). For asec pulses synthesized by the harmonics 7th, 9th, 11th and 13th, the field distribution is given by

$$E(D, x, y, z) \ = \sum_{n=7}^{n=13} E_n(D, x, y, z) \tag{4.6}$$

(D is the displacement introduced be the delay stage between the XUV replica) at the focal spot of the focusing element. The projection of the intensity distribution

$$I(D, x, y, z) \ = \ E(D, x, y, z) \, E^*(D, x, y, z) \tag{4.7}$$

on the z-y plane for the particular values of the displacement D = 0, $\lambda/4$, and $\lambda/2$ is shown in Figure 4.4 (c). The beam follows an Airy distribution in the focus and for a displacement of D = $\lambda/2$ it is divided into two parts of equal size. It is worth to note the

fact that the total energy in the interaction volume remains constant and as a result the splitting of the focal spot would not affect the measured signal (integrated over the whole interaction volume) in case of single photon ionization (linear detector), *i.e.*, the signal would be constant with respect to the time delay. In case of two-photon ionization (quadratic detector), the rearrangement of the local intensity inside the interaction volume would produce a modulation in the ionization signal

$$S(D) \propto \iiint_{\Delta V} I^2(D, x, y, z) \, dx \, dy \, dz \qquad (4.8)$$
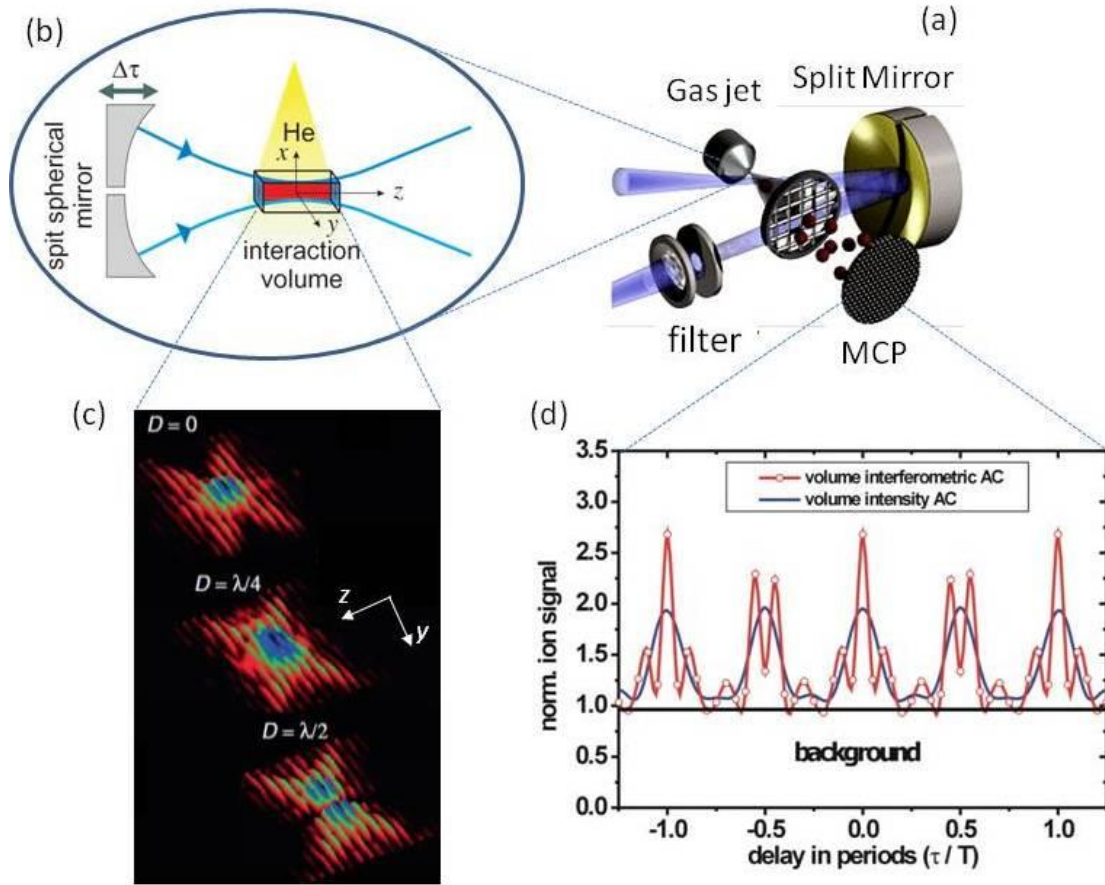
Figure 4.4 Second Order Volume Autocorrelation technique. (a) Schematic of the experimental set-up of the second-order XUV volume autocorrelator utilizing split mirror configuration. (b) Interaction volume in case of using atomic gas phase target as a two-photon detector. (c) Two-dimensional (z–y) contour plots showing the snapshots of the calculated intensity distribution of the harmonic superposition (7th+9th+11th+13th) in the interaction region of the volume autocorrelator for displacement $D = 0$, $D = \lambda/4$ and $D = \lambda/2$. (d) Calculated interferometric and intensity volume autocorrelation traces.

T is the period of the IR laser field. In these calculations the peak to background ratio, in 2nd-order interferometric volume autocorrelation is $\approx 2.75: 1$ and in case of in case of 2nd-order intensity volume autocorrelation (2-IVAC) is $\approx 2: 1$. However, detailed calculations performed in 2009 by O. Faucher *et al.*, for the 5th harmonic, which have been confirmed experimentally [50] have shown that the peak to background ratio, interferometric and intensity volume autocorrelation are $\approx 3.4: 1$ and $\approx 2.4 : 1$, respectively. The *asec* pulse duration τ_{XUV} can be determined from the measured autocorrelation trace (AC) using the well-known relation $\tau_{XUV} = \tau_{AC}/\sqrt{2}$ (where τ_{AC} is the full width at half maximum of the AC trace). It must be noted that in the case of pulse trains the resulted duration reflects the average duration of the individual asec pulses in the train.

4.2.1 2-IVAC in attosecond pulse trains and isolated asec pulses

The 2-IVAC approach (2nd-order intensity volume autocorrelation) is proven to be applicable in measurement of an APT but also for isolated XUV pulses. The APTs have been produced by focusing a high-power multi-cycle fs IR pulse into a Xenon gas jet. The laser focus was placed before the Xenon gas jet at a position which is favorable for temporal confinement in the asec scale. The harmonic beam was passing through 150 nm thick Indium filter which selects the 9th to 15th odd harmonics. This beam was then focused by a split spherical gold mirror of 5 cm in focal length into a Helium pulsed gas jet. The relative field amplitudes of the harmonics in the interaction region were 1, 0.4, 0.3, and 0.25 for the 9th, 11th, 13th, and 15th harmonics, respectively. The Helium ions produced by a 2-XUV photon ionization process were recorded by a μ-metal-shielded time-of-flight (TOF) spectrometer. The trace was obtained by recording the He$^+$ signal as a function of the delay between the XUV replicas. The average duration of the asec pulses in the train was found to be 660 ± 50 asec.

In the case of isolated attosecond pulse a few cycle driving field is required. Otherwise a necessity is gating technique limiting the harmonic generation over only one cycle. For the generation of IAPs a polarization gating (PG) arrangement is proven to be a powerful approach. In this case the generated XUV spectrum switches from a harmonic comb to a continuum. Measurements regarding the isolated pulses were first reported in 2011 by Tzallas *et al* [48]. The XUV beam was passed through 150 nm

thick Sn filter to select a bandwidth of ≈ 10 eV in the photon energy range of ≈ 19 eV. This beam was then focused by a split spherical gold mirror of 5 cm in focal length into a Xenon pulsed gas jet. The Xe^{2+} ions produced by a 2-XUV-photon direct double ionization process (TPDDI) were recorded by a time-of-flight (TOF) spectrometer. The trace was obtained by recording the Xe^{2+} signal as a function of the delay between the XUV replicas in an interval around zero delay values. At longer delay times the 2-IVAC trace provides information about the wave packet evolution induced by the atomic coherences associated with the coherent excitation of the AIS. The duration of the XUV pulse was found to be $\approx 1.5^{+0.2}_{-0.7}$ fs, which is an overestimation of the pulse duration. The measured "broad" pulse is a consequence of the appearance of non-resolved side peaks present due to the unstable CEP of the high power multi-cycle laser system and the measurement of averages for many laser shots at each delay. It should be mentioned that although the single photon ionization is leading to an excitation over a manifold of automating states the process does not affect the pulse duration measurement. The authors report that the influence of the AIS in the measured pulse duration is negligible as the width of the states is much smaller compared to the bandwidth of the XUV pulse or equivalently the measured beating periods are much larger than the pulse duration. Detail information on this matter can be found in Ref [138].

The first interferometric volume autocorrelation trace of an APT has been demonstrated in 2006 by Nebekawa et.al [45]. Using two-XUV-photon ionization process induced in N_2 upon interaction with an APT which was formed by synthesizing 9th-19th harmonics of a driving fs IR laser pulse. The AC trace was obtained by measuring N^+ (resulting from the Coulomb explosion of N_2 after absorbing two-XUV-photons as a function of the delay between the XUV pulse replicas. The same approach was used to measure the duration of the IAPs of ≈ 9eV bandwidth in the spectral range of ≈ 31 eV.

4.2.2 XUV FROG-type measurements

APTs have been also temporally characterized by means of mode-resolved autocorrelation techniques using 2-XUV-photon-above-threshold ionization (ATI). This technique is promising for extending the 2-IVAC method to high XUV photon energies and performing FROG-type measurements in the XUV domain. Attempts towards this direction have been reported for isolated XUV pulses by T. Sekikawa et al., in 2004 [154]and for APTs by Y. Nabekawa et al., in 2006 [155]. In these studies,

using the 2-IVAC approach, the amount of PEs signal generated by an ATI ionization process was recorded as a function of the delay between the XUV pulse replicas.

In the work of T. Sekikawa *et al*. [154], isolated XUV pulses with photon energy ≈28 eV (9th harmonic of a 400nm driving laser field) and bandwidth of ≈ 2 eV have been generated by the interaction of Argon gas phase atoms with ≈ 8.3 fs driving laser field of carrier photon energy at 3.1 eV. Two optically delayed replicas of the XUV pulse were focused into Helium gas inducing a 2-XUV-photon ATI process. The ejected photoelectrons were collected and energy-resolved by a magnetic bottle photoelectron spectrometer. An autocorrelation trace having an overall width of ≈ 4 fs was recorded by measuring the electron number at each optical delay between the XUV pulse replica resulting to a pulse of 950 asec duration.

The experimental technique used by Y. Nabekawa *et.al*. [155] for the characterization of APTs using two-photon ATI processes is called PANTHER (photoelectron analysis with non-resonant two-photon-ionization for harmonic electric-field reconstruction). In their experiment APTs synthesized by the superposition of 11th, 13th, 15th harmonics of the fundamental IR beam have been generated by the interaction of Xenon gas with multi cycle fs IR laser pulse. The generated radiation was focused into Argon gas inducing a 2-XUV-photon ATI process. By the nonlinear interaction photoelectrons were produced and recorded as a function of the delay between the two pulses. An autocorrelation trace of the individual 2-XUV-photon ATI peaks was recorded by varying the delay between the XUV pulse replicas. The ATI photoelectron peaks exhibited correlated AC signals. The period of this modulation was determined to be 1.33 fs (1/*f*), which corresponds to the half period of the optical field of the fundamental laser pulse. According to the analysis for frequency-resolved optical gating technique (FROG), the mode-resolved AC trace at the 24th (S_{24}), 26th (S_{26}) and 28th (S_{28}) orders, is given by:

$$S_{24}(\tau) \propto 2I_{11}I_{13}[1 + \cos(2\omega_f\tau)] \qquad (4.9)$$

$$S_{26}(\tau) \propto \left[I_{13} + 2\sqrt{I_{13}I_{15}}\cos(2\omega_f\tau)\right]^2 - 8I_{13}\sqrt{I_{11}I_{15}}\sin^2(\Delta\Phi)\cos(2\omega_f\tau) \qquad (4.10)$$

$$S_{28}(\tau) \propto 2I_{13}I_{15}[1 + \cos(2\omega_f\tau)] \qquad (4.11)$$

Using the above equations (for the detailed analysis see ref.153) the authors have managed to obtain the chirp among the three harmonic fields and reconstruct the APT.

Nowadays the only existing FROG measurement of an isolated sub-fs XUV pulse is the one that has been reported in 2006 by A. Kosuge et al. This has been achieved by recording with high energy resolution (~200meV) the two-XUV-photon ATI photoelectron peak resulting to the pulse duration measurement. The retrieved pulse was found to be 860 asec.

Despite the large applicability of the 2-VAC approach for the asec pulse characterization, as any experimental technique suffers from a series of limitations. The first one is associated with the fundamental principle of any AC approach. An AC approach measures the spatiotemporal averages of pulse durations (in case of APT provides the average duration of the asec pulses in the train) but does not contain any information about the phase thus not allowing the full pulse reconstruction. The other limitations can be divided in three categories. The first, concerns the non-linear detector used for the pulse characterization. As any conventional AC approach the non-linear detector should be spectrally flat with instantaneous response. Because the asec pulses are generated in different spectral regions with bandwidth > 2 eV to find the proper non-linear detector is an issue far from trivial. To ensure that the properties of the non-linear detector fulfill the requirements for *asec* pulse characterization the proper non-linear ionization processes (as those described in section 4.1) need to be chosen. In order to estimate the flatness and the temporal response of the detector, the TDSE needs to be solved.

The second, is associated with the stability of the XUV source and the 2-VAC technique. A 2-VAC measurement suffers from the intrinsic limitations that accompany any pump-probe approach that involves an interferometer (or an XUV-wave front beam splitter) as a delay line between the XUV pulses. In a 2-VAC experiment, the XUV pulse duration is obtained by multiple shot measurements at different time delays between the XUV pulse replica. During these measurements instabilities relevant with XUV-IR-laser parameters (XUV-pulse duration, XUV-intensity, carrier-envelope-phase (CEP) of the IR pulse, etc) together with the relatively "low" peak to background ratio provided in an ideal spatiotemporal overlap of the XUV pulse replica by a 2-IVAC trace are limiting the temporal resolution of the measurement which to our knowledge is in the range of 50-100 asec. This value can be significantly improved by means of high rep. rate asec beam lines or the development of single-shot XUV autocorrelator. The third, deals with the difficulties on performing XUV FROG measurements. Such

measurements, additionally with the limitations mentioned above, they suffer from limitations on the photoelectron energy resolution which are associated with resolution provided by the available electron spectrometers (which is in the range of $\Delta E / E=1\%$, where E is the electron kinetic energy), the low PE signal and the presence of space charge effects.

4.3 Temporal Characterization of the Attosecond Pulse Trains of the GWatt attosecond Beamline

In this section the experimental realization of the temporal characterization of the attosecond beamline will be discussed. In order to characterize the temporal properties of Attosecond pulse train resulted from the high harmonic generation, the 2nd order Intensity (or Interferometric) Volume Auto Correlation (2-IVAC) technique, is implemented. A dispersionless XUV autocorrelator required for the measurement consisted of a spherical gold split mirror mounted on a piezoelectric delay stage works both as wavefront divider and delay selector. Similarly, to a conventional 2nd order AC used in ultrafast pulse duration metrology, the interaction of the under investigation radiation with a non-linear medium is necessary. In the case of XUV, the single or multiple ionizations of some noble gases can be exploited as the mechanism revealing the pulse duration of the interactions. On the contrary the extension of the widely used metrology of second order autocorrelation the technique from the conventional Michelson interferometer based on a nonlinear crystal or a nonlinear photodiode, the signal produced emanates from the interaction of the XUV pulse with the non-linear medium within a volume defined by the focusing properties of the spherical mirror and not from a plane as in the case of a nonlinear crystal. Unlike the amplitude splitting arrangements, the split mirror technique is a wavefront splitting device and as such, a delay variation results not in a change of the energy reaching the detector, but simply in a spatial redistribution of the energy in the focal volume according to the direction principle. Because of these differences, the signal to background ratio is lower than in the conventional methods. It has been shown that the theoretical S/B ratio for 2-IVAC (interferometric AC) is in the range 2:8 S/B 3:4, (for conventional AC methods S/B = 8) depending upon the considered volume of interaction (in finite or small volume). In the corresponding Intensity 2- IVAC, which is obtained from the interferometric by cycle-averaging the fast oscillations, the values are 2:1 S/B 2:4, to be compared with S/B = 3 in the conventional cases. In experimental traces S/B values are usually lower,

mainly because of the difficulty in overlapping perfectly the two replicas of the pulse. The relation which connects the duration of the Intensity 2-IVAC trace to the duration of the pulse is $AC = 1:41$ pulse, like in conventional AC traces. In order for the detector to be non-linear, it is important to avoid any contributions from single photon ionization. Also, since the bandwidth of the asec pulses is much broader (several eV) compared to that of any of the IR pulses, it is not straightforward that the conditions of flatness and instantaneous response can be filled over the whole bandwidth. Finally, only direct processes are suitable for the temporal characterization of the XUV pulse. If also a sequential process is involved, the measured AC trace will be a convolution of a squared 1st order AC trace (resulting from the photons involved in the sequential process) and a 2nd order AC trace resulting from the photons involved in the direct 2nd order process).

After having set up, characterized and tested the piezoelectric split and delay unit described in section 2.6, measurements towards temporal characterization of the Attosecond Pulse Train (APT) synthesized by the harmonic spectrum have been performed. It is worth noting that in these measurements the diameter of the aperture in the "XUV filtering and diagnostics" chamber was reduced as to decrease the XUV signal to about half of its maximum value. Thus the outer part of the XUV beam cross-section was blocked by introducing a 3 mm pinhole. Consequently, i) aberrations in the XUV beam were limited and ii) the ratio of the short to long trajectory contribution in the transmitted XUV beam was increased. The method used is the 2nd IVAC utilizing the delay line and TOF spectrometer discussed in chapter 2. As second order non-linear process, the two-XUV-photon ionization of both Ar^+ and He^+ were used. This is in order to demonstrate different two-photon schemes that can be used in pulse duration measurements at higher photon energies. The excitation schemes accompanied with the power dependences ensuring the non-linearity of the processes are presented in figure for Helium and Argon respectively while characteristic recording of the time of flight are presented in the next pages.
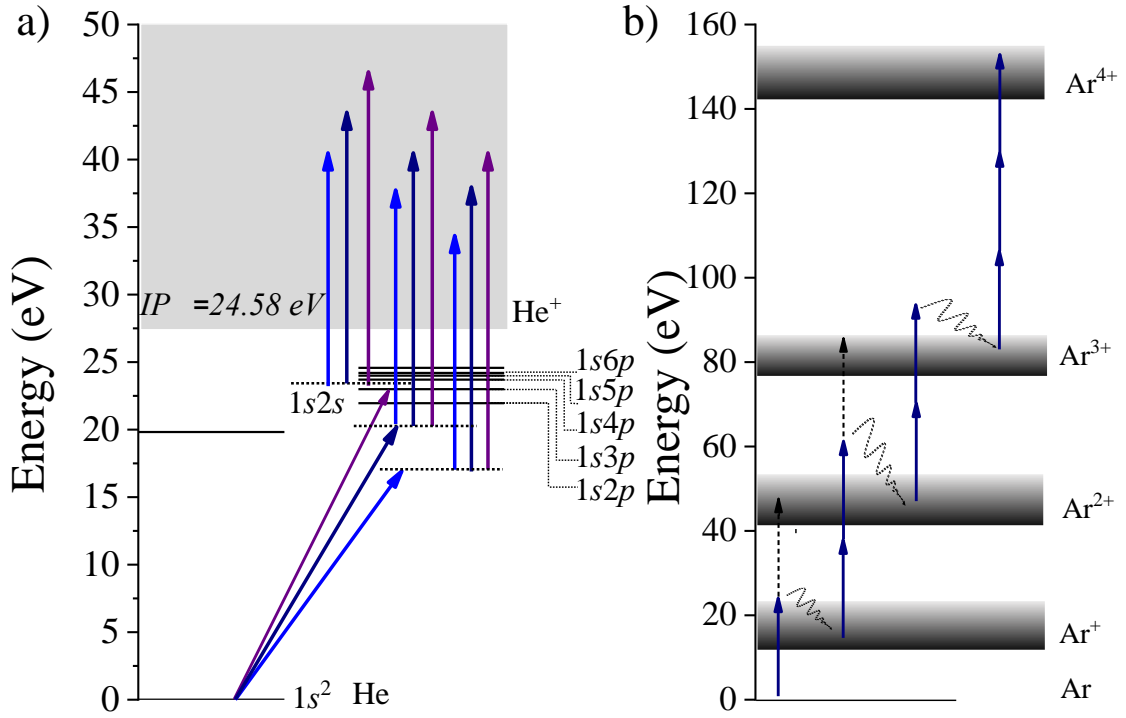
Figure 4.5 XUV Non-linear ionization schemes (a) 2-XUV-photon process of excitation scheme of helium involving 11th - 15th harmonic of the fundamental field (b) Multi-XUV-photon multiple ionization scheme of Argon. The ionization energy levels (excluding higher order processes (ATI) and decays to excited ionic states) is depicting the direct and sequential channels. In this case the arrows are representing the central frequency of the spectrum (11th - 15th harmonic) corresponding to 20.15 eV.

In performing the 2nd order IVAC measurements the gas pressure in the interaction area was kept below the threshold at which space charge effects become visible, broadening the TOF ion-mass peaks. In Ar the traces are obtained by the superposition of the harmonics transmitted through the Sn filter. Before saturation, the Ar^{2+} yield as a function of the I_{XUV} in log-log scale has a linear dependence with slope ~2 57. This slope is compatible with either two-XUV-photon direct double ionization of Ar or two-XUV-photon ionization of Ar^{+} after saturation of the single photon ionization of Ar. Numerical calculations have shown that the latter channel, i.e. saturated single photon ionization of Ar followed by two photon ionization of Ar^{+} is the dominant channel in the XUV range in which the present experiments have been performed. In the case of Helium used as the nonlinear detector things are easier and extensively described in the previous works.
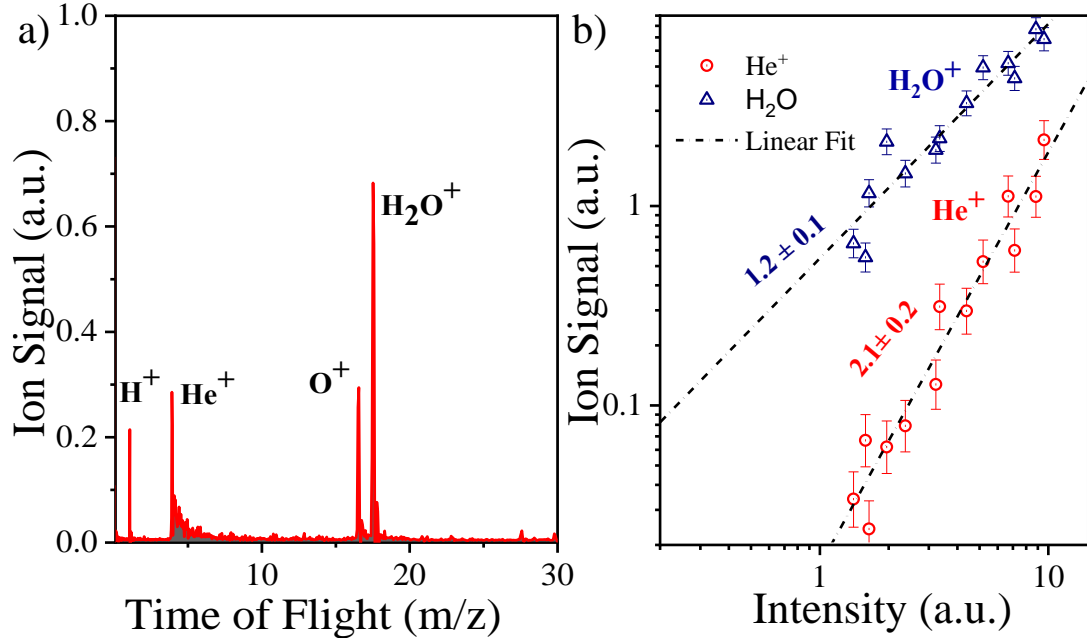
Figure 4.6 Non-Linear ionization of Helium. (a) Time of Flight mass spectrum produced by the interaction of the focused 11th-15th harmonics with Helium. In the time-of-flight spectrum, besides the two-photon ionization of the He atoms two of the mass peaks can be assigned to single photon ionization of H_2O hydrogen and oxygen. (b) XUV intensity dependence of singly charged state of He. The black dashed lines depict a linear fit on the raw data and the error bars represent one standard deviation of the mean. The slopes of the lines, are in agreement with lowest-order perturbation theory i.e. with the order of the underlying non-linear process resulting 2.1±0.2 in case of He^+ and 1.2±0.1 for H_2O. For the intensity dependent yields presented the single photon ionization process of O is exploited, with O^+ yield to be used for calibration of the x axis.
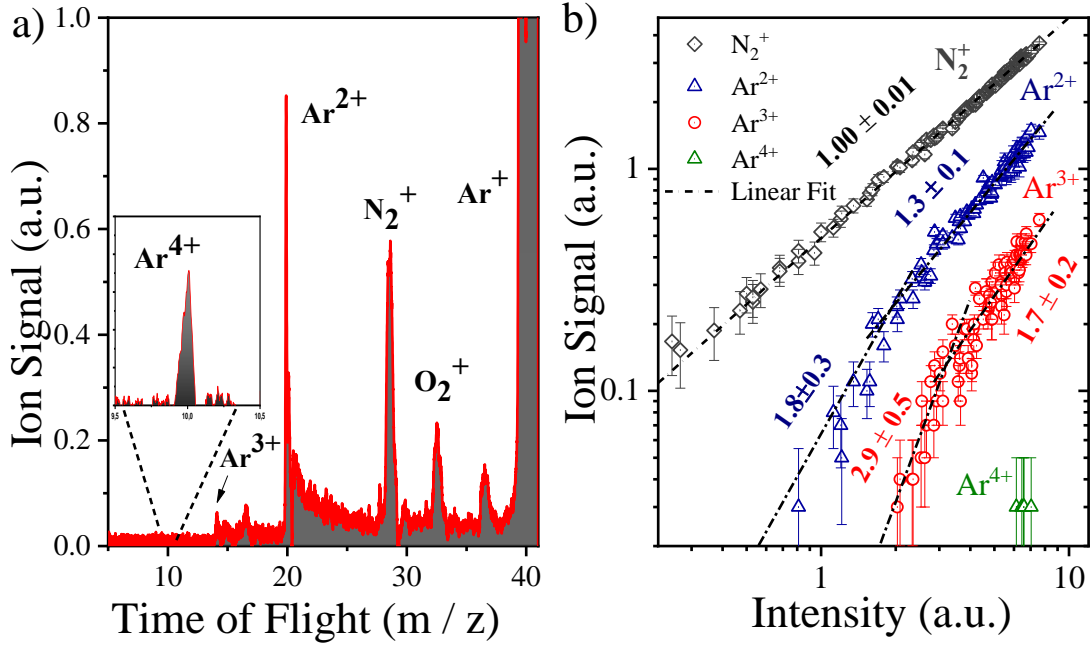
Figure 4.7 Multiple ionization of Argon atoms. (a) Time of Flight mass spectrum produced by the interaction of the focused 11th-15th harmonics with Argon. The spectrum shows multiple charged Ar ions (Ar^{n+}) with n up to 4. (b) Dependence of $Ar^{2,3+}$ yield on the I_{XUV}. For calibrating the XUV energy (x-axis) the O^{2+} signal was used. The black dashed lines show the linear fit on the raw data. The dependence of N^{2+} with slope $\approx$1 indicates a single-photon ionization process. The error bars represent one standard deviation of the mean.

Figure 4.6 (a) shows the measured ion mass spectrum of He, in which He^+ is clearly observable. It should be noted that for this measurement an Sn filter was used (*i.e.* 11th-15th harmonic). The XUV intensity dependence of the ion yield is depicted in Figure 4.6 (b). The slope of the fitted line in the He^+ data is 2.1± 0.2, as expected, underlying two photon ionization process, while the slope of the line fitted in the H_2O^+ date is 1.2±0.1, as water molecules are single photon ionized at the XUV photon energies used. The verified two-XUV-photon ionization of He is a very convenient process in performing 2nd order autocorrelation measurements of XUV radiation with wavelengths > 51nm.The same holds in the case of the Ar^{2+} which undergoes a second or third order process depending on the intensity with respect to the ionization saturation intensity. The Argon TOF mass spectra are shown in Figure 4.7 (a). The spectrum reveals the recorded charge states of Ar up to +4 (Ar^{4+}).

Measured 2nd order IVAC traces are shown in Figure 4.8 (a) and (b). The blue rhombus is the trace obtained from the single photon ionization of H_2O. As expected for a linear process the IVAC shows no modulation. The Ar^{2+} ion yield (produced by the XUV radiation generated using only one gas jet) is measured here as a function of the delay between the two XUV pulses introduced by the translation of one part of the bisected spherical mirror. The gas jet in the HHG chamber was set at 20 cm after the laser focus in order to minimize the contribution of the long electron trajectory. Low temporal resolution scans recorded with a step of 350 asec have been performed in determining the duration of the APT envelope (Fig. 4.8 (a)). The red points are the raw data, averages of 50 laser points and the error bar corresponds to the standard deviation of the mean value. The black curve is a Gaussian fit to the data. The fit results in an XUV pulse envelope having a duration of 9.8±0.9 fs, verifying the estimated duration used in ref. 57. A fine scan using a time delay step of 50 asec is shown in Fig. 14b. The Ar^{2+} ion yield, as expected, is modulated with the half period of the driving field. The gray circles are the recorded raw data (averages of 50 laser shots). The raw data in the fine scan of Figure 4.8 (b) are fluctuating around the mean value mainly due to interferometric instabilities (within the cycle of the XUV field) and XUV beam pointing instabilities, which are both enhanced by the non-linearity of the process. Long averaging and calculating moving averages substantially reduce the strong shot-to-shot fluctuation of the recoded data. The red circles are the moving averages of the raw data taken over 10 points. The black curve is fit of a series of Gaussian distributions to the averaged points. In this fit the free parameters are the common width, height of the Gaussians as well as the peak to peak distance. Furthermore the comb of Gaussians are multiplied by a fixed envelope distribution taken from the fit of Figure 4.8 (a). The pulse width resulting from the Gaussian distributions is found to be $\tau_{XUV} = 650 \pm 80$ asec. The error of 80 asec appearing in all measurements is the largest resulted standard deviation, among all the fits in the raw data of all measured traces. The above pulse duration of the attosecond pulses in the APT is synthesized essentially by the three harmonics 11th, 13th and 15th. Since here only one gas jet was utilized, the APT beam-line power to be rigorously reported is 11.0±3.5 GW, the error originating mainly from the uncertainty in the calibration of the XUV photodiode.
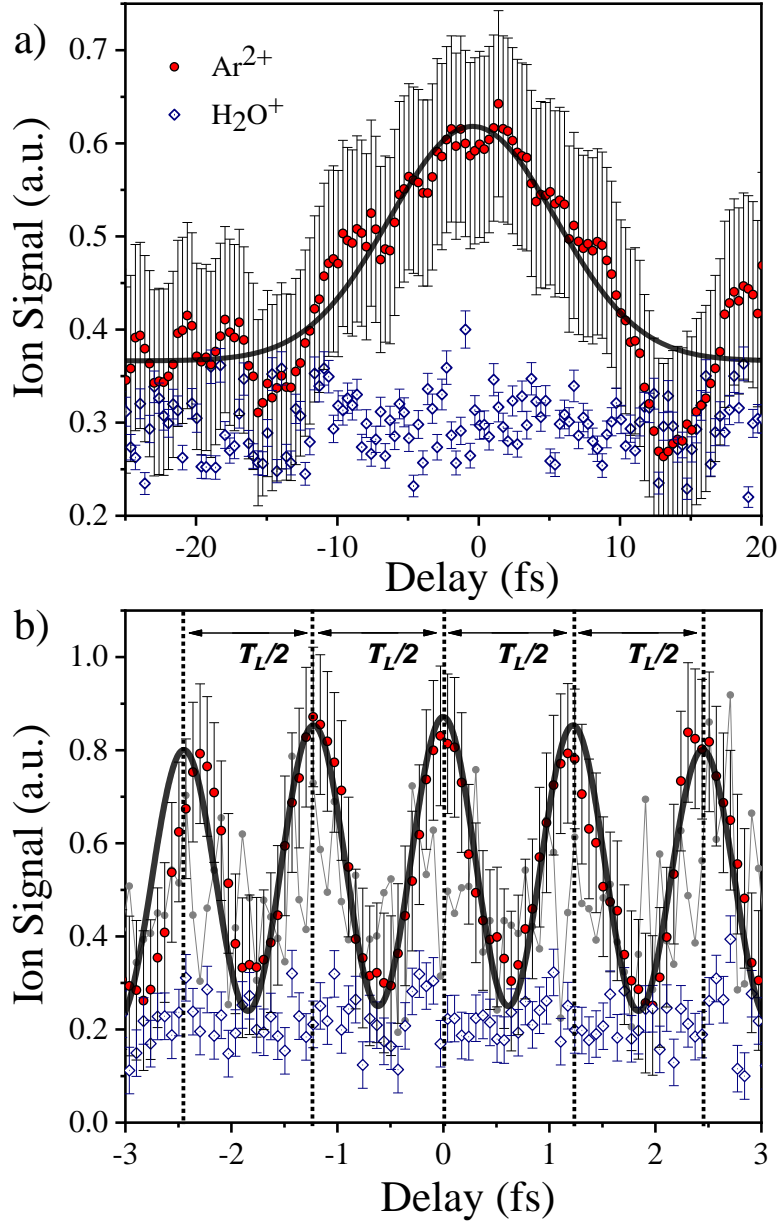
Figure 4.8 Measured 2nd IVAC trace of Argon. The XUV radiation is produced by a single gas Jet of xenon and is transmitted through a Sn filter. (a) A coarse time delay scan with 350 asec step is revealing a modulation in Ar^{2+} ion signal represented by the red circles, while the blue rhombus depicting the single photon ionization of H_2O shows no modulation. A Gaussian fit in the data points of Ar^{2+} yields a time duration of τ_{XUV} = 9.8±0.9 fs. (b) A fine scan with time delay step of 50 asec. The gray circles correspond to the raw data recorded for Ar^{2+}. The moving averages of the raw data taken over 10 points are represented by the red circles. The black curve is a fit of a sequence of Gaussian pulses in the averaged points.

The two-XUV-photon ionization of He^+ has also been used to measure the produced APTs through 2nd IVAC, shown in Figure 4.9 (a) and alongside with Fig. 15b showing a 2nd IVAC trace of Ar^{2+}. The trace of Figure 4.9 (b) is a different run than the one shown in Figure 4.9 (b) verifying reproducibility of the results. All points, error bars and curves are as those in Figure 4.9(b), with the only difference being that here we do not use any envelope distribution in the fit either for the He or the Ar trace. This is because in these runs the peak hight distribution within the error bars did not depict any envelope type modulation. The pulse duration measured using He as non-linear medium is 670±80 asec and the one of the superposition of harmonics 11th, 13th and 15th measured in Ar^{2+} is the same as the one of Fig. 4.9 (b). The two values are well within the error bar and thus essentially identical.
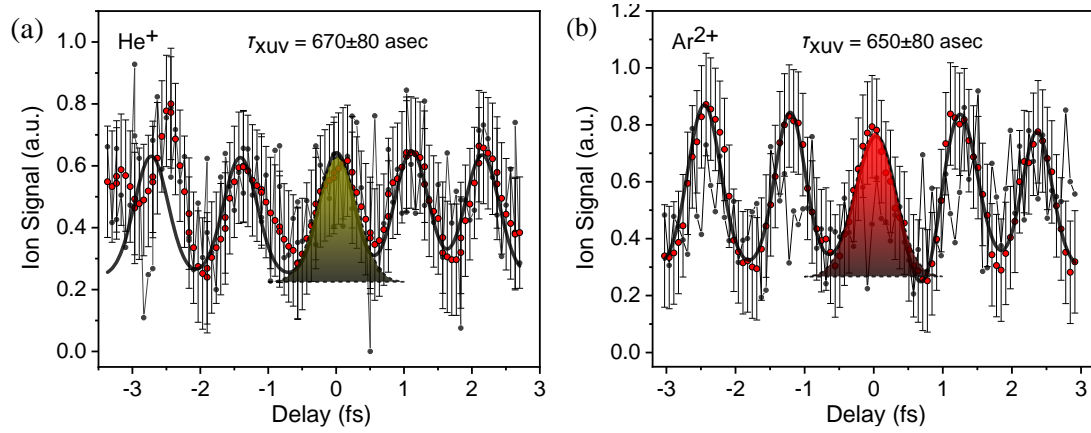
Figure 4.9 2nd IVAC in case of Helium and Argon as the no-linear medium (a) Measured 2nd IVAC trace of the He+ (b) 2nd IVAC trace of the Ar+2 ion signal as a function of the delay of the XUV-XUV delay line. The gray circles correspond to the raw data recorded, the moving averages of the raw data taken over 10 points are represented by the red circles. The black curves is a Gaussian fit over the averaged points. The temporal width of the Gaussian fit corresponds to a pulse duration of 670±80 as and 650±80, for He+ and Ar+2 respectively.

The measured durations here are similar to those retrieved in previous experiments implemented in a 3m focal length beam-line applying 2nd IVAC in two photon ionization of He but about 65 % longer than those measured through the RABBIT technique. The discrepancy between the 2nd IVAC and RABBIT originates from the fact that 2nd IVAC measures averages of spatiotemporally dependent pulse durations and the contribution of both long and short trajectories, while RABBIT measures average phases. An additional effect to be considered is pointed out recently. Different harmonics, due to their different divergence are focused at different positions, have different focal spots and therefore lead to only partial spatial overlap of the superimposed harmonics and to different Gouy phase contributions in the harmonic superposition. At specific conditions, e.g. spectrum with harmonics of very different order, the spatial overlap becomes notably small and the Gouy phase difference large, thus reducing a lot the temporal confinement. 2nd IVAC is sensitive to these effects and thus reveals fairly realistic pulse durations. However, for the three harmonics employed in this experiment substantial spatial overlap is present as indicated by the results of a recent work [157], were separation of the harmonic foci was not observed.

In order to verify the significant spatial overlap of the three harmonics used in the 2nd-IVAC measurements we have performed calculations of the focal areas of the three harmonics, for a bandwidth spanning from the 9th to the 17th harmonic and Xe gas as harmonic generating medium. We are using the expression

$$\theta_{S,L} = \frac{\lambda_q}{\pi w_q}\sqrt{1 + 4\alpha_{S,L}^2 I_L^2 \frac{w_q^4}{w_f^4}} \tag{4.12}$$

of the divergence of the harmonics originating from the electron short (S) and long (L) trajectories at the point of the interaction for the harmonic order q, as given in ref. [157]. λ_q, w_q, are the wavelength and the beam waist of the harmonic q, w_f is the waist size of the laser beam, $\alpha_{S,L}$ is the S and L trajectory coefficient and I_L is the IR driving laser peak intensity. The beam waist was measured at the emission plane and it was found to be $w_f \approx 350\mu$m. Using Gaussian optics the harmonic beam waist can be obtained by:

$$w_q = \frac{w_f}{\sqrt{q_{eff}}} \tag{4.13}$$

where q_{eff} is the effective nonlinearity coefficient with $q_{eff} \approx 5$ for all the harmonics laying in the plateau of the harmonic spectrum. For a peak intensity 10^{14} W/cm^2 all the studied harmonics are laying in the plateau and the trajectory coefficient $\alpha_{S,L}$ is extracted by solving the three-step semi-classical model. The results are summarized in table 1.

Harmonic order	*9*	*11*	*13*	*15*	*17*
λ_q(nm)	88.9	72.7	61.5	53.3	47.0
α_S	1	0.435	-0.4	-1.5	-2.96
α_L	-23.97	-23.56	-22.88	-21.96	-20.71
θ_S(mrad)	0.195	0.15	0.127	0.126	0.148
θ_L(mrad)	1.74	1.40	1.15	0.96	0.79

TABLE I. Parameters of the 9th to the 17th harmonics generated in Xe. The intensity of the laser field used is 10^{14} W/cm^2 and the unit for α is 10^{-14} W$^{-1} \cdot$cm^2.

After extracting the divergence of the different harmonics, the virtual source positions for each of the generated harmonics is calculated assuming only short trajectory contribution. The focus positions of the harmonics, after reflection on the spherical mirror of focal length $f = 5$ cm, are calculated using geometrical optics. Here the paraxial approximation is applied since the divergence of the harmonics is below the paraxial limit. The results of the calculations are shown in Figure 4.10
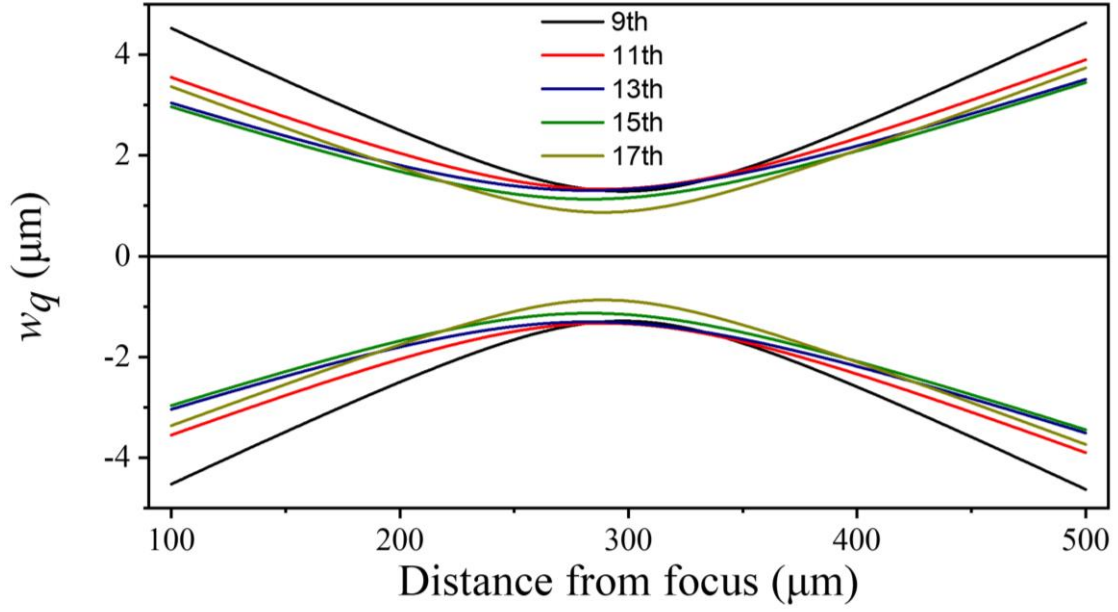
Figure 4.10. **Calculated focal areas of the five harmonics 9th, 11th, 13th, 15th and 17th**. The graph depicts the harmonic beam waist as a function of the distance from the focus of the spherical mirror. The x-axis shows the focus position of the harmonics on the propagation axis. The focus position of the harmonics is found to be ≈ 290 μm away from the focus of the 5 cm mirror. Their beam waist ratios are 0.99:1.01:1:0.87:0.67 for harmonic 9th, 11th, 13th, 15th and 17th respectively.

The distance of the positions of the five foci is 8.2 μm between the 9th and 11th, 6.3 μm between the 11th and 13th harmonic, ~0 μm between the 13th and 15th harmonic, 5.9 μm between the 15th and 17th harmonic and thus it is negligibly small with respect to their confocal parameter (≈ 170 μm for 13th harmonic). The size of the focal spots is slightly different. The ratios for the beam waists at the focus are 0.99:1.01:1:0.87:0.67 for the harmonics 9th, 11th, 13th, 15th and 17th respectively. Under these conditions, the spatial overlap of the five harmonics is substantial. The Gouy phase at the beam waist for each harmonic can be calculated and is shown in Figure 4.11. Its variation for the different harmonics (assuming as central frequency the 13th harmonic) $\varphi_9 = 0.24$ rad, $\varphi_{11} = 0.08$ rad, $\varphi_{13} = 0$ rad, $\varphi_{15} = 0$ rad, $\varphi_{17} = 0.13$ rad is also negligibly small . In this case, the duration of the APT pulses is not significantly affected. In fact, the different beam waists of the 11th, 13th, 15th harmonics lead to more similar amplitudes of the interfering harmonics than those generated.
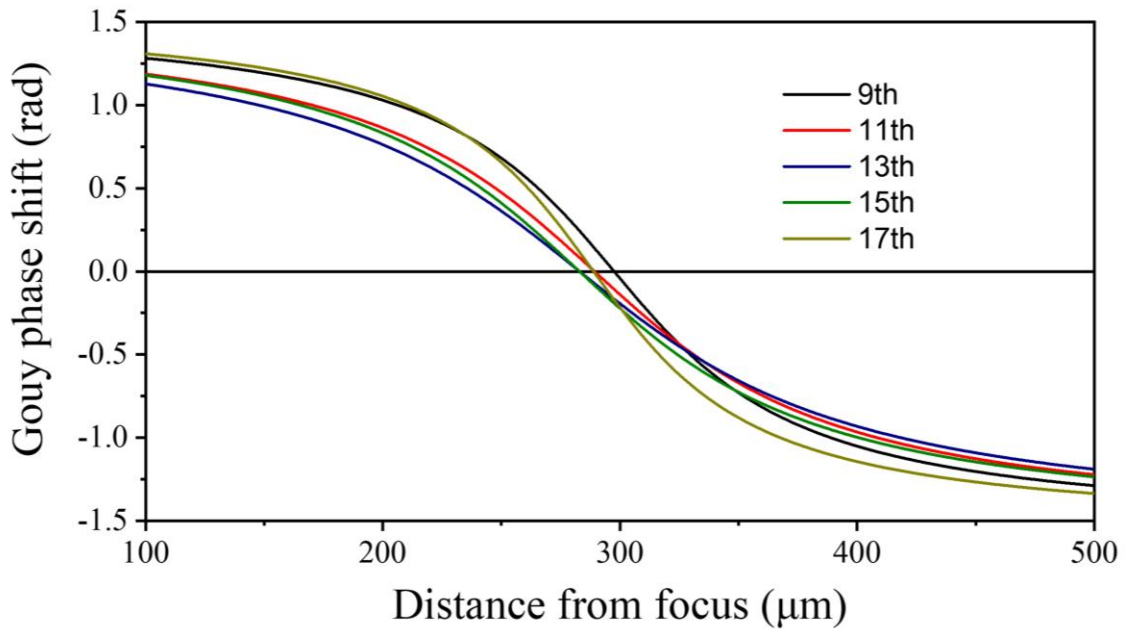
Figure 4.11 Calculated Gouy phase shift of the five harmonics 9th, 11th, 13th, 15th and 17th. The x-axis shows the focus position of the harmonics on the propagation axis. The focus position of the harmonics is found to be ≈ 290 μm away from the focus position of the 5 cm mirror.

Similar calculations have been further performed for the long electron trajectories, which present larger harmonic divergence. In this case, the virtual foci are placed closer to the focusing element. It is found that the difference of the foci positions between *L* and *S* trajectories is ≈30 μm which is consistent with previous experimental findings and also smaller than the confocal parameter, thus not substantially affecting the APT pulse duration in particular because the long trajectory contributions are reduced through the geometry used.

Chapter 5: Summary and outlook

In summary in this work is presenting the development and characterization of a powerful gas phase High Harmonic Generation based, attosecond beamline installed and operational in the Attosecond Science and Technology Laboratory FORTH IESL. A detailed description of an ultra-intense attosecond XUV beam line has been presented revealing the up to now highest reported energy of coherent radiation in the XUV spectral region 15–25 eV. The focused intense radiation is resulting a GW class average peak power attosecond source in the XUV spectral with those specifications characterizing the beamline as unique for an XUV source. While in the publication of Nayak *et al.* the high power of the source (20 GW) was reported attosecond confinement, although expected, could not be rigorously claimed as in this work did not include any pulse duration measurements. Attosecond Pulse Trains durations of the order of 650 asec have been measured at ten-GW a world record in attosecond sources in this spectral region. The source is based on harmonic generation in long (9 m) focusing geometry of the driving IR laser radiation. The pulse duration of both the APT pulses and the envelope have been measured though 2nd IVAC i) in He employing two-XUV-photon ionization as a second order process as well as ii) in Ar exploiting two-XUV-photon ionization of Ar^+ under saturation of neutral Ar ionization. Measurements with both gases resulted in the same pulse durations within the experimental error. High non-linear XUV-optics in terms of multiple multi-XUV-photon ionization of He, Ar and Ne atoms, have been further demonstrated using the above beam line. The combination of high pulse energy and short duration opens up excellent perspectives for sub-fs XUV-pump-XUV-probe experiments in all states of matter. At the same time the XUV intensity levels reached enable the study of strong field effects in the XUV spectral region. As a further perspective, scaling previous parameters of isolated attosecond pulses, our source holds promise of generating few μJ level isolated attosecond pulses through polarization gating approaches. Those are advanced perspectives for the Hellenic National Research Infrastructure HELLAS-CH, part of which is the present beam line. The results of the present work further hints towards an unprecedented performance of the two 1-kHz repetition rate attosecond beam lines of the Extreme Light Infrastructure – Attosecond Light Pulse Source (ELI-ALPS) facility currently being under implementation, driven by shorter laser pulses with similar pulse energies. The geometry of one of the two beam-lines of ELI-ALPS is very close to that

of the present source, while the second one is several times longer and offers advanced phase matching control capacities. Thus, it is expected to further scale up the source throughput. The 1 kHz repetition rate of these sources in combination with the CEP stabilized driving laser will provide the by far best ever conditions for attosecond XUV-pump-XUV-probe investigations using isolated attosecond pulses and cinematically nearly complete experiments through e-e, e-ion and ion-ion coincidence measurements.

Towards these directions as a feature work, isolated attosecond pulses will be investigated. Since the attosecond beamline is driven by a multicycle Laser field (~25fs) as described, High Harmonic Generation process is resulting a frequency comb consisting of odd harmonics of the fundamental field in the frequency domain. In time domain this corresponds to a pulse train and thus in order to produce an isolated pulse one has to implement a gating technique limiting the process of generation over a single optical cycle. A well-known and established method is the Polarization Gating (PG) and an extension of its principles named Double Optical Gating (OPG). In both cases taking advantage of the dependence of the recollision probability of the electron to the parent ion on the polarization of the driving field, the Laser pulse is shaped in such a way that only a small fraction of the pulse remains linear. In attosecond beamline a Polarization Gating device is already installed and partially tested accompanied with some preliminary results regarding the generated HHG spectrum recorded by the Time of Flight Spectrometer operating in electron mode. Since the Laser system is not CEP stabilized the relative variance between the carrier and the pulse envelope will result in a sequence of single and double attosecond pulse for different Laser shots accumulated. Thus the temporal characterization of the isolated pulses a CEP tagging measurement will be required. For the CEP tagging measurements the Flat Field Spectrometer (FFS) already installed and fully operational will be exploited revealing the vital information on the features of the HHG process.

By implementing the polarization gating and the 2nd –order volume autocorrelation technique already used for the attosecond pulse trains the temporal characterization of the isolated pulses will be done in conjunction with the tagging measurements distinguishing the single and double XUV pulse features. Moreover, a feature objective is the exploitation of the intense attosecond source in XUV-pump -XUV-probe experiments implementing CEP tagging in the framework of time resolved studies of ultra-fast dynamics in atoms in these high photon energies and short time

scales. Towards the generation of isolated attosecond pulses a compact collinear multi-cycle-polarization gating apparatus have been installed and implemented. High Harmonic generation from multi-cycle IR field is leading to a formation of series of pulses with attosecond duration consisting a pulse train within an envelope of overall duration ≈ 10 *fs*. The above is attributed to the mechanism of the high harmonic generation and is leading to high harmonic frequency combs of the fundamental field. Implementing the polarization gating technique quasi-continuum XUV radiation by a multi-cycle field can be achieved and thus resulting to isolated attosecond pulses generation. Since the generation of isolated asec pulses depends on the relative phase between the carrier frequency and the pulse envelope which is not stabilized a tagging measurement is required. For the above reason a flat field spectrometer is installed, for monitoring and recording the shot-to-shot spectrum of the emitted strongly dependent from the CEP variation.

Furthermore, for the XUV-pump-XUV probe studies prototype systems like noble gases will be used. The Helium atom will be used for the studies of the electron wave-packet dynamics when the system is coherently excited into its all optically allowed bound states. Argon, and Krypton atoms will be used for the studies of the electron wave-packet dynamics when they are coherently excited into a large number of autoionizing states. In case of Helium, identical broadband XUV pulses (with photon energy 15-24 eV) with duration ≈ 500 *asec* will be used for measuring the wave packet evolution of the $1snp$ states via a two-XUV-photon ionization process. The 1st pulse (pump pulse) will coherently excite the bound states and the electronic wave packet evolution will be probed by measuring the He$^+$ ion signal induced by the 2nd pulse (probe pulse). The dynamics of the system will be revealed by the quantum beats which are expected to be observed at time delays (between the XUV-pump and the XUV-probe beam) > 500asec. Regarding the studies of autoionization state dynamics, the noble gases of Krypton and Argon will be used. Identical broadband (15-35 eV) XUV pulses with duration ≈ 500 *asec* will be used for measuring the wave packet evolution via a two-XUV-photon direct double ionization process. The 1st pulse (pump pulse) will coherently excite the autoionizing manifold and the electronic wave packet evolution will be probed by measuring the Ar^{2+}, Kr^{2+} ion signal induced by the 2nd pulse (probe pulse). The quantum beats with frequencies from ≈ 0.5 PHz down to $\approx 1/\tau_d$ are (τ_d is the decay time of the autoionizing states) are going to be used for unraveling the dynamics

of the systems and the decay times of the autoionizing states. In the same experiment the measured temporal trace will provide information about the temporal characteristics of the sub-fs XUV pulsed. Here tagging of the measurement CEP will be an important advancement in these series of experiments.

Finally, since the expected intensities are $>10^{15}$ W/cm^2, strong field effects such as AC-Stark shifting of states will become observable. The observation of such effects in this spectral region will open up the era of strong field interactions in the XUV.

References

[1] M. Goeppert-Mayer, Ann. Phys. (Leipzig). 9, 273-294 (1931).

[2] Ahmed H. Zewail. Femtochemistry: Atomic-Scale Dynamics of the Chemical Bond Using Ultrafast Lasers (Nobel Lecture)

[3] A. B. Arons and M. B. Peppard. Einstein's Proposal of the Photon Concept|a Translation of the Annalen der Physik Paper of 1905. American Journal of Physics, 33(5):367{374 (1965).

[4] G. S. Voronov and N. B. Delone. "Ionization of the xenon atom by the electric field of ruby laser emission". Soviet Journal of Experimental and Theoretical Physics Letters, 1965.

[5] N.B. Delone Vladimir P. Krainov "Direct (Nonresonant) Multiphoton Ionization of Atoms" Multiphoton Processes in Atoms pp 81-117

[6] G. Mainfray and G. Manus. "Multiphoton ionization of atoms. Reports on Progress in Physics", 54(10):1333, October 1991.

[7] L. A. Lompre, G. Mainfray, C. Manus, and J. Thebault. "Multiphoton ionization of rare gases by a tunable-wavelength 30-psec laser pulse at 1.06 m." Physical Review A, 15(4) 1977.

[8] M. Protopapas, C. H. Keitel, and P. L. Knight. "Atomic physics with super-high intensity lasers". Reports on Progress in Physics, 60(4):389 1997.

[9] P. Agostini, F. Fabre, G. Mainfray, G. Petite, and N. K. Rahman "Free-Free Transitions Following Six-Photon Ionization of Xenon Atoms"Phys. Rev. Lett. 42, 1127 1979.

[10] Y. Gontier, M. Poirier and M. Trahin "Multiphoton absorptions above the ionisation threshold" Journal of Physics B: Atomic and Molecular Physics Journal of Physics B: Atomic and Molecular Physics, Volume 13, Number 7 1980.

[11] H. G. Muller, A. Tip, and M. J. van der Wiel. "Ponderomotive force and AC Stark shift in multiphoton ionization". Journal of Physics B: Atomic and Molecular Physics, 16(22):L679, 1983.

[12] A.M. Bonch-Bruevich, N.N. Kostin, V.A. Khodocoi, and V.V. Khromov. "Changes in the Atomic Absorption Spectrum in the Field of a Light Wave" Soviet Physics JETP, 29(1):82, 1969.

References

[13] P. H. Bucksbaum, R. R. Freeman, M. Bashkansky, and T. J. McIlrath. "Role of the ponderomotive potential in above-threshold ionization". JOSA B, 4(5):760 764, 1987.

[14] P. Kruit, J. Kimman, H. G. Muller, and M. J. van der Wiel. Electron spectra from multiphoton ionization of xenon at 1064, 532, and 355 nm. Physical Review A, 28(1):248 255 1983.

[15] G. S. Voronov, and H. B. Delone, "Ionization of the xenon atom by the electric field of ruby laser emission" Soviet Physics Letters JETP. 1, 66-68 (1965).

[16] M. V. Ammosov, N. B. Delone, and V. P. Krainov. "Tunnel ionization of complex atoms and of atomic ions in an alternating electromagnetic field". Soviet Physics - JETP, 64(6):1191, 1986.

[17] S. Augst, D. D. Meyerhofer, D. Strickland, and S. L. Chin. "Laser ionization of noble gases by Coulomb-barrier suppression". Journal of the Optical Society of America B Optical Physics, 8:858 867, April 1991.

[18] L.V. Keldysh. "Ionization in the Field of a Strong Electromagnetic Wave". Soviet Physics JETP, 20(5):1307{1314, May 1965.

[19] Vladimir S. Popov. "Tunnel and multiphoton ionization of atoms and ions in a strong laser field (Keldysh theory)". Physics-Uspekhi, 47(9):855, 2004.

[20] N. H. Burnett, H. A. Baldis, M. C. Richardson, and G. D. Enright. "Harmonic generation in CO2 laser target interaction".Applied Physics Letters, 31(3):172174, 1977.

[21] A. McPherson, G. Gibson, H. Jara, U. Johann, T. S. Luk, I. A. McIntyre, K. Boyer, and C. K. Rhodes, "Studies of multiphoton production of vacuum-ultraviolet radiation in the rare gases," Journal of the Optical Society of America B Optical Physics, 4, 595, (1987).

[22] M. Ferray, A. L'Huillier, X. F. Li, L A Lomprk, G. Mainfray and C Manus, "Multiple-harmonic conversion of 1064 nm radiation in rare gases" J. Phys. B: At., Mol. Opt. Phys 21, L31, (1988).

[23] X. F. Li, A. L'Huillier, M. Ferray, L. A. Lompre, and G. Mainfray, "Multiple-harmonic generation in rare gases at high laser intensity," Phys. Rev. A, 39, 5751, (1989).

[24] Ph. Balcou and Anne L'Huillier. "Phase-matching effects in strong-field harmonic generation". Physical Review A, 47(2):1447{1459, 1993.

[25] J. Tate, T. Auguste, H. G. Muller, P. Sali_eres, P. Agostini, and L. F. DiMauro. "Scaling of Wave-Packet Dynamics in an Intense Midinfrared Field". Physical Review Letters, 98(1):013901, 2007.

[26] A. D. Shiner, C. Trallero-Herrero, N. Kajumba, H.-C. Bandulet, D. Comtois, F. Legare, M. Giguere, J-C. Kiefer, P. B. Corkum, and D. M. Villeneuve. "Wavelength Scaling of High Harmonic Generation Efficiency". Physical Review Letters, 103(7):073902, August 2009

[27] P. Salieres, A. L'Huillier, and M. Lewenstein. "Coherence Control of High-Order Harmonics". Physical Review Letters, 74(19):37763779 1995.

[28] P. Balcou, P. Salieres, A. L'Huillier, and M. Lewenstein. "Generalized phase matching conditions for high harmonics: The role of field-gradient forces". Physical Review A, 55(4):32043210,1997.

[29] T. F. Gallagher, Phys. Rev. Lett. **61**, 2304 (1988).

[30] J. L.Krause, , K. J Schafer,. & K. C Kulander,. (1992). "High-order harmonic generation from atoms and ions in the high intensity regime". Phys. Rev. Lett. 68(24): 3535–3538. (1992).

[31] J. L. Krause, K. J. Schafer, and K. C. Kulander, Phys. Rev. A **45**, 4998 (1992).

[32] P.B. Corkum, "Plasma perspective on strong-field multiphoton ionization," Phys. Rev. Lett. 71, 13 1994 (1993).

[33] A. L'Huilliert, K. J. Schafert and K. C Kulandert "Theoretical aspects of intense field harmonic generation" J. Phys. E: At. Mol. Opt. Phys. 24 3315-3341 (1991)

[34] K. L. Ishikawa, "High-Harmonic Generation," in Advances in Solid-State Lasers: Development and Applications, edited by M. Grishin (InTech, 2011) Chap. 19, pp. 439–464.

[35] L. F. DiMauro and P. Agostini, "Ionization Dynamics in Strong Laser Fields," in Advances In Atomic, Molecular, and Optical Physics, Vol. 35, edited by B. Bederson and H. Walther (Academic Press, 1995) pp. 79–120.

[36] P. Agostini and L. F. DiMauro, "The physics of attosecond light pulses"Rep. Prog. Phys. **67**, 813 (2004).

[37] P. Agostini and G. Petite, "Photoelectric effect under strong irradiation" Contemp. Phys. **29**, 57 (1988).

[38] J. H. Eberly and J. Javanainen "Above-threshold ionisation", Eur. J. Phys. **9**, 265 (1988).

[39] N. Delone and M. Fedorov, "Above threshold ionization" Prog. Quant. Electron. **13**, 267 (1989).

[40] M. Lewenstein, P. Balcou, M. Y. Ivanov, A. L'Huillier, and P. B. Corkum, "Theory of high harmonic generation by low-frequency laser fields," Phys. Rev. A 49, 3, 2117 (1994).

[41] Y. Kobayashi, T. Sekikawa, Y. Nabekawa, and S. Watanabe, "27-fs extreme ultraviolet pulse generation by high-order harmonics," Opt. Lett. 23, 64 (1998).

[42] P. Tzallas, E. Skantzakis, L. A. A. Nikolopoulos, G. D. Tsakiris, and D. Charalambidis, "Extreme-ultraviolet pump–probe studies of one-femtosecond-scale electron dynamics," Nat. Phys. 7, 781 (2011).

[43] P. A. Carpeggiani, P. Tzallas, A. Palacios, D. Gray, F. Martín, and D. Charalambidis, "Disclosing intrinsic molecular dynamics on the 1-fs scale through extreme-ultraviolet pump-probe measurements," Phys. Rev. A 89 (2014)

[44] Y.Nabekawa, Y. Furukawa, T. Okino, A A. Eilanlou, E. J. Takahashi, K.Yamanouchi and K. Midorikawa. "Sub-10-fs control of dissociation pathways in the hydrogen molecular ion with a few-pulse attosecond pulse train". Nature communications 7, 12835 (2016).

[45] A.Palacios, , A.González-Castrillo and F.Martín, "Molecular interferometer to decode attosecond electron-nuclear dynamics". Proceedings of the National Academy of Sciences of the United States of America 111,.1316762111 (2014).

[46] E. J. Takahashi, P. Lan, O. D. Mucke, Y. Nabekawa, and K. Midorikawa, "Attosecond nonlinear optics using gigawatt-scale isolated attosecond pulses," Nature Communications. 4, 2691 (2013).

[47] P.Tzallas, D. Charalambidis, N. A.Papadogiannis, , K.Witte, G. D.Tsakiris "Direct observation of attosecond light bunching". *Nature* **426,** 267–271 (2003).

[48] L.A. A. Nikolopoulos, E. P. Benis, P. Tzallas, D. Charalambidis, K. Witte, and G. D. Tsakiris. "Second order autocorrelation of an XUV attosecond pulse train. *Physical review letters* **94,** 113905; 10.1103/PhysRevLett.94.113905 (2005).

[49] Nabekawa, Y. *et al.* Interferometric autocorrelation of an attosecond pulse train in the single-cycle regime. *Physical review letters* **97,** 153904; 10.1103/PhysRevLett.97.153904 (2006).

[50]   Nabekawa, Y. *et al.* Conclusive evidence of an attosecond pulse train observed with the mode-resolved autocorrelation technique. *Physical review letters* **96,** 83901; 10.1103/PhysRevLett.96.083901 (2006).

[51]   Faucher, O. *et al.* Four-dimensional investigation of the 2nd order volume autocorrelation technique. *Appl. Phys. B* **97,** 505–510; 10.1007/s00340-009-3559-z (2009).

[52]   P. Heissler, R. Hörlein, J.M. Mikhailova, L. Waldecker, P. Tzallas, A. Buck, K. Schmid, C.M.S. Sears, F. Krausz, L. Veisz, M. Zepf, G.D. Tsakiris "Two-photon above-threshold ionization using extreme-ultraviolet harmonic emission from relativistic laser–plasma interaction". *New J. Phys.* **14,** 43025; (2012).

[53]   G. Kolliopoulos, B. Bergues, H. Schröder, P. A. Carpeggiani, L. Veisz, G. D. Tsakiris, D. Charalambidis, P. Tzallas. "Single-shot autocorrelator for extreme-ultraviolet radiation". *J. Opt. Soc. Am. B* **31,** 926; 10.1364/JOSAB.31.000926 (2014).

[54]   J. E. Kruse, P. Tzallas, E. Skantzakis, C. Kalpouzos, G. D. Tsakiris and D. Charalambidis, "Inconsistencies between two attosecond pulse metrology methods: A comparative study," Physical. Review. A 82, 021402 (2010).

[55]   Y.Kobayashi, , T. Sekikawa, , Y.Nabekawa, and S.Watanabe, "27-fs extreme ultraviolet pulse generation by high-order harmonics". *Opt. Lett.* **23,** 64; 10.1364/OL.23.000064 (1998).

[56]   D.Descamps, L. Roos, C.Delfin, , L'Huillier, A. & Wahlström, C.-G. Two- and three-photon ionization of rare gases using femtosecond harmonic pulses generated in a gas medium. *Phys. Rev. A* **64,** 273; 10.1103/PhysRevA.64.031404 (2001).

[57]   Sekikawa, T., Ohno, T., Yamazaki, T., Nabekawa, Y. & Watanabe, S. Pulse Compression of a High-Order Harmonic by Compensating the Atomic Dipole Phase. *Phys. Rev. Lett.* **83,** 2564–2567; 10.1103/PhysRevLett.83.2564 (1999).

[58]   Nabekawa, Y., Hasegawa, H., Takahashi, E. J. & Midorikawa, K. Production of doubly charged helium ions by two-photon absorption of an intense sub-10-fs soft x-ray pulse at 42 eV photon energy. *Physical review letters* **94,** 43001; 10.1103/PhysRevLett.94.043001 (2005).

[59]   Manschwetus, B. *et al.* Two-photon double ionization of neon using an intense attosecond pulse train. *Phys. Rev. A* **93**; 10.1103/PhysRevA.93.061402 (2016).

[60] Miyamoto, N. *et al.* Observation of two-photon above-threshold ionization of rare gases by xuv harmonic photons. *Physical review letters* **93,** 83903; 10.1103/PhysRevLett.93.083903 (2004).

[61] Sekikawa, T., Katsura, T., Miura, S. & Watanabe, S. Measurement of the intensity-dependent atomic dipole phase of a high harmonic by frequency-resolved optical gating. *Physical review letters* **88,** 193902; 10.1103/PhysRevLett.88.193902 (2002).

[62] S. Chatziathanasiou, S. Kahaly, E. Skantzakis, G. Sansone, R. Lopez-Martens, S. Haessler, K. Varju, G. Tsakiris, D. Charalambidis and P. Tzallas , "Generation of Attosecond Light Pulses from Gas and Solid State Media," Photonics 4, 26 (2017).

[63] Chen, S., Rever, M., Zhang, P., Theobald, W. & Umstadter, D. Observation of relativistic cross-phase modulation in high-intensity laser-plasma interactions. *Physical review. E, Statistical, nonlinear, and soft matter physics* **74,** 46406; 10.1103/PhysRevE.74.046406 (2006).

[64] Gordienko, S., Pukhov, A., Shorokhov, O. & Baeva, T. Relativistic Doppler effect: universal spectra and zeptosecond pulses. *Phys. Rev. Lett.* **93,** 115002; 10.1103/PhysRevLett.93.115002 (2004).

[65] Bulanov, S. V., Naumova, N. M. & Pegoraro, F. Interaction of an ultrashort, relativistically strong laser pulse with an overdense plasma. *Physics of Plasmas* **1,** 745–757; 10.1063/1.870766 (1994).

[66] Tarasevitch, A., Lobov, K., Wünsche, C. & Linde, D. von der. Transition to the relativistic regime in high order harmonic generation. *Phys. Rev. Lett.* **98,** 103902; 10.1103/PhysRevLett.98.103902 (2007).

[67] Jafari, B. & Soofi, H. High bandwidth and responsivity mid-infrared graphene photodetector based on a modified metal-dielectric-graphene architecture. *Applied optics* **58,** 6280–6287; 10.1364/AO.58.006280 (2019).

[68] Kahaly, S. *et al.* Direct observation of density-gradient effects in harmonic generation from plasma mirrors. *Physical review letters* **110,** 175001; 10.1103/PhysRevLett.110.175001 (2013).

[69] Thaury, C. *et al.* Plasma mirrors for ultrahigh-intensity optics. *Nat Phys* **3,** 424–429; 10.1038/nphys595 (2007).

References

[70]   Tsakiris, G. D., Eidmann, K., Meyer-ter-Vehn, J. & Krausz, F. Route to intense single attosecond pulses. *J. Opt. Soc. Am. B* **8,** 19; 10.1088/1367-2630/8/1/019 (2006)

[71]   Nomura, Y. et al. Attosecond phase locking of harmonics emitted from laser-produced plasmas. Nat Phys 5, 124–128; 10.1038/nphys1155 (2008).

[72]   Heyl, C. M., Arnold, C. L., Couairon, A. & L'Huillier, A. Introduction to macroscopic power scaling principles for high-order harmonic generation. J. Phys. B: At. Mol. Opt. Phys. 50, 13001; 10.1088/1361-6455/50/1/013001 (2017).

[73]   A. Nayak, I. Orfanos, I. Makos, M. Dumergue, S. Kühn, E. Skantzakis, B. Bodi, K. Varju, C. Kalpouzos, H. I. B. Banks, A. Emmanouilidou, D. Charalambidis and P. Tzallas "Multiple ionization of argon via multi-XUV-photon absorption induced by 20-GW high-order harmonic laser pulses," Phys. Rev. A 98, 023426 (2018).

[74]   Duris, J. et al. "Tunable isolated attosecond X-ray pulses with gigawatt peak power from a free-electron laser". Nature Photonics 14, 30–36, (2020).

[75]   Y. Kobayashi, T. Ohno, T. Sekikawa, Y. Nabekawa, S. Watanabe, "Pulse width measurement of high-order harmonics by autocorrelation" *Appl. Phys. B* **70**, 389 (2000).

[76]   N.A. Papadogiannis, L.A.A. Nikolopoulos, D. Charalambidis, G.D. Tsakiris, P. Tzallas, K. Witte, " Two-Photon Ionization of He through a Superposition of Higher Harmonics" *Phys. Rev. Lett.* **90**, 133902 (2003).

[77]   E.P. Benis, P. Tzallas, L.A.A. Nikolopoulos, M. Kovacev, C. Kalpouzos, D. Charalambidis , G.D. Tsakiris, "Two-photon double ionization of rare gases by a superposition of harmonics" *New J. Phys.* **8**, 92 (2006).

[78]   K. Midorikawa, Y. Nabekawa,A. Suda "XUV multiphoton processes with intense high-order harmonics" , *Prog. Quant. Elect.* **32**, 43 (2008).

[79]   B. Manschwetus, L. Rading, F. Campi, S. Maclot, H. Coudert-Alteirac, J. Lahl, H. Wikmark, P. Rudawski, C. M. Heyl, B. Farkas, T. Mohamed, A. L'Huillier, P. Johnsson. "Two-photon double ionization of neon using an intense attosecond pulse train" *Phys. Rev. A* **93**, 061402(R) (2016).

[80]   N. Tsatrafyllis, B. Bergues, H. Schröder, L. Veisz, E. Skantzakis, D. Gray, B. Bodi, S. Kuhn, G. D. Tsakiris, D. Charalambidis ,P. Tzallas, *Sci. Rep.* **6**, 21556 (2016).

[81]   G. Kolliopoulos, B. Bergues, H. Schröder, P. A. Carpeggiani, L. Veisz, G. D. Tsakiris, D. Charalambidis, P. Tzallas, *Phys. Rev. A* **90**, 013822 (2014).

References

[82] B. Bergues, D.E. Rivas, M. Weidman, A.A. Muschet, W. Helml, A. Guggenmos, V. Pervak, U. Kleineberg, G. Marcus, R. Kienberger, D. Charalambidis, P. Tzallas, H. Schröder, F. Krausz, L. Veisz, *Optica* **5**, 237 (2018).

[83] P. Tzallas, B. Bergues, D. Rompotis, N. Tsatrafyllis, S. Chatziathanassiou, A. Muschet, L. Veisz, H. Schröder, D. Charalambidis, *J. Opt.* **20**, 024018 (2018).

[84] Constant, E. et al. "Optimizing High Harmonic Generation in Absorbing Gases: Model and Experiment". Phys. Rev. Lett. 82, 1668–1671, (1999).

[85] Hergott, J.-F. et al. "Extreme-ultraviolet high-order harmonic pulses in the microjoule range". Phys. Rev. A 66 (2002).

[86] Y. Tao, S. J. Goh, H. M. J. Bastiaens, P. J. M. van der Slot, S. G. Biedron, S. V. Milton, and K.-J. Boller, Opt. Express 25, 3621 (2017).

[87] A. Paul, R. A. Bartels, R. Tobey, H. Green, S. Weiman, I. P. Christov, M. M.Murnane, H. C. Kapteyn and S. Backus. Quasi-phase-matched generation of coherent extreme-ultraviolet light. Nature 421, 51 (2003).

[88] S. Kazamias, D. Douillet, F.Weihe, C. Valentin, A. Rousse, S. Sebban, G. Grillon, F. Auge´, D. Hulin, and Ph. Balcou "Global Optimization of High Harmonic Generation" Phys Rev A 2003.

[89] E. A. Gibson, A. Paul, N. Wagner, R. I. Tobey, D. Gaudiosi, S. Backus, I. P.Christov, A. Aquila, E. M. Gullikson, D. T. Attwood, M. M. Murnane, and H. C.Kapteyn, "Coherent soft x-ray generation in the water window with quasi-phase matching," Science 302, 95 (2003)

[90] A. Rundquist, C. G. Durfee, Z. Chang, C. Herne, S. Backus, M. M. Murnane, and H. C. Kapteyn, "Phase-matched generation of coherent soft x-rays," Science 280, 1412 (1998).

[91] A. L'Huillier and P. Balcou, "High-order harmonic generation in rare gases with 1-ps 1053-nm laser," Physical Review Letters 70, 774 (1993).

[92] C. Winterfeldt, C. Spielmann, and G. Gerber, "Colloquium: Optimal control of high-harmonic generation," Reviews of Modern Physics 80, 117 (2008).

[93] P. Balcou, and A. L'Huillier, "Phase-matching effects in strong-field harmonic generation," Physical Review A 47, 1447 (1993).

[94] A. L'Huillier, X. F. Li, and L. A. Lompré, "Propagation effects in high-order harmonic generation in rare gases," Journal of the Optical Society of America B 7, 527 (1990).

[95] A. L'Huillier, K. J. Schafer and K. C. Kulander, "Theoretical aspects of intense

References

field harmonic generation," Journal of Physics B: Atomic, Molecular, and Optical Physics 24, 3315 (1991).

[96]   A. L. Lytle, "Phase Matching and Coherence of High Order Harmonic Generation in Hollow Waveguides" PhD thesis, University of Colorado (2008)

[97]   A. Averchi, D. Faccio, R. Berlasso, M. Kolesik, J. V. Moloney, A. Couairon, and Di Trapani, "Phase matching with pulsed Bessel beams for high-order harmonic generation," Physical Review A 77, 021802 (2008).

[98]   T. Popmintcheva, M. C. Chena, A. Bahabada, M. Gerritya, P. Sidorenkob, O. Cohenb, I. P. Christovc, M. M. Murnanea, and H. C. Kapteyna, "Phase matching of high harmonic generation in the soft and hard X-ray regions of the spectrum," Proceedings of the National Academy of Sciences of the United States of America 106, 10516 (2009).

[99]   J. Peatross, M. V. Fedorov, and K. C. Kulander, "Intensity-dependent phase-matching effects in harmonic generation," Journal of the Optical Society of America B 12, 863 (1995).

[100]   V. Tosa, E. Balogh, and K. Kovacs. Phase-matched generation of water-window x-rays. Phys. Rev. A, 80(4):045801, Oct 2009.

[101]   R Lopez-Martens, K Varju, P Johnsson, J Mauritsson, Y Mairesse, P Salieres, MB Gaarde, KJ Schafer, A Persson, S Svanberg, CG Wahlstrom, and A L'Huillier. Amplitude and phase control of attosecond light pulses. Phys. Rev. Lett., 94(3):033001, JAN 28 2005.

[102]   C. Dolle, C. Reinhardt, P. Simon, and B.Wellegehausen. Spectral phase matching for highly efficient frequency tripling of short-pulse krf laser radiation in argon. Applied Physics B, 76 (8)2003.

[103]   H. Merdji, M. Kovacev, W. Boutu, P. Salieeres, F. Vernay, and B. Carree. Macroscopic control of high-order harmonics quantum-path components for the generation of attosecond pulses. Phys. Rev. A, 74:043804, Oct 2006.

[104]   Shkolnikov, P. L. et al. Optimal quasi-phase matching for high-order harmonic generation in gases and plasmas. Phys. Rev. A, 50, R4461 (1994).

[105]   Peatross, J. et al. Phase matching of high-order harmonic generation in helium- and neon-filled gas cells. J. Mod. Opt., 51, 2675 (2004).

[106]   A. Willner, A. Hage, R. Riedel, I. Grguraš, A. Simoncig, M. Schulz, T. Dzelzainis, H. Höppner, S. Huber, M. J. Prandolini, B. Dromey, M. Zepf, A. L. Cavalieri, and F. Tavella, "Coherent spectral enhancement of carrier-envelopephase

stable continua with dual-gas high harmonic generation," Opt. Lett., OL 37, 3672–3674 (2012).

[107] Sutherland, J. R. et al. High harmonic generation in a semi-infinite gas cell. Opt. Expr. 12, 4430 (2004).

[108] A. Willner, F. Tavella, M. Yeung, T. Dzelzainis, C. Kamperidis, M. Bakarezos, D. Adams, R. Riedel, M. Schulz, M. C. Hoffmann, W. Hu, J. Rossbach, M. Drescher, V. S. Yakovlev, N. A. Papadogiannis, M. Tatarakis, B. Dromey, and M. Zepf, "Efficient control of quantum paths via dual-gas high harmonic generation," New Journal of Physics 13, 113001 (2011).

[109] A. H. Sheinfux, Z. Henis, M. Levin, and A. Zigler, "Plasma structures for quasi phase matched high harmonic generation," Applied Physics Letters 98, 141110–141110–3 (2011).

[110] I. Christov, H. Kapteyn, and M. Murnane, "Quasi-phase matching of high-harmonics and attosecond pulses in modulated waveguides," Opt. Express 7, 362–367 (2000).

[111] B. Dromey, M. Zepf, M. Landreman, and S. M. Hooker, "Quasiphasematching of harmonic generation via multimode beating in waveguides," Opt. Express 15, 7894–7900 (2007).

[112] X. Zhang, A. L. Lytle, T. Popmintchev, X. Zhou, H. C. Kapteyn, M. M.Murnane, and O. Cohen, "Quasi-phase-matching and quantum-path control of high-harmonic generation using counterpropagating light," Nature Physics 3, 270–275 (2007).

[113] A. Pirri, C. Corsi, and M. Bellini, "Enhancing the yield of high-order harmonics with an array of gas jets," Phys. Rev. A 78, 011801 (2008).

[114] A. Willner, "A High Repitition Rate XUV Seeding Source for FLASH2," Dissertation, Universität Hamburg (2011).

[115] E. M. Bothschafter, A. Schiffrin, V. S. Yakovlev, A. M. Azzeer, F. Krausz, R. Ernstorfer, and R. Kienberger, "Collinear generation of ultrashort UV and XUV pulses," Optics Express 18, 9173 (2010).

[116] T. Ruchon, C. P. Hauri, K. Varju, E. Mansten, M. Swoboda, R. Lopez-Martens, and A. L'Huillier. Macroscopic effects in attosecond pulse generation. New Journal of Physics, 10:025027, FEB 29 2008.

[117] Peatross, J. et al. Selective zoning of high-harmonic generation using counter-propagating light. Opt. Expr., 1, 114 (1997).

[118]   Voronov, S. L. et al. Control of laser high-harmonic generation with counter-propagating light. Phys. Rev. Lett., 87, 133902 (2001).

[119]   Lange, H. R. et al. High-order harmonic generation and quasi-phase matching in xenon using sefl-guided femtosecond pulses. Phys. Rev. Lett., 81, 1611 (1998).

[120]   R. W. Boyd, "Nonlinear Optics", 3rd revised edition. (Academic Press, 2008).

[121]   Armstrong, J. A. et al. "Interactions between light waves in a nonlinear dialectric". Phys. Rev., 127, 1918 (1962).

[122]   Franken, P. A. et al. "Generation of optical harmonics". Phys. Rev. Lett., 7, 118 (1961).

[123]   P. Tzallas, D. Charalambidis, N.A. Papadogiannis, K. Witte, G.D. Tsakiris, Nature (2003) doi:10.1038/nature02091

[124]   O. Faucher, P. Tzallas, E.P. Benis, J. Kruse, A. Peralta Conde, C. Kalpouzos, D. Charalambidis, Appl. Phys. B (2009)

[125]   E. Constant, E. Mével, A. Zaïr, V. Bagnoud, F. Salin, J. Phys. IV France (2001) doi:10.1051/jp4:20012105

[126]   C.G. Durfee, S. Backus, H.C. Kapteyn, M.M. Murnane, Opt. Lett. (1999) doi:10.1364/OL.24.000697

[127]   H. Mashiko, A. Suda, K. Midorikawa, Appl Phys B (2003) doi:10.1007/s00340-003-1148-0

[128]   K. Midorikawa, Y. Nabekawa, A. Suda, Progress in Quantum Electronics (2008) doi:10.1016/j.pquantelec.2008.04.001

[129]   P. Tzallas, D. Charalambidis, N.A. Papadogiannis, K. Witte, G.D. Tsakiris, Journal of Modern Optics (2005)

[130]   L.A.A. Nikolopoulos, E.P. Benis, P. Tzallas, D. Charalambidis, K. Witte, G.D. Tsakiris, Physical review letters (2005) doi:10.1103/PhysRevLett.94.113905

[131]   M. Schultze, B. Bergues, H. Schröder, F. Krausz, K.L. Kompa, New J. Phys. (2011) doi:10.1088/1367-2630/13/3/033001

[132]   P. Tzallas, E. Skantzakis, D. Charalambidis, J. Phys. B: At. Mol. Opt. Phys. (2012) doi:10.1088/0953-4075/45/7/074007

[133]   F. Campi, H. Coudert-Alteirac, M. Miranda, L. Rading, B. Manschwetus, P. Rudawski, A. L'huillier, P. Johnsson, A. L'huillier, The Review of scientific instruments (2016) doi:10.1063/1.4941722

[134] Y. Nabekawa, T. Shimizu, T. Okino, K. Furusawa, H. Hasegawa, K. Yamanouchi, K. Midorikawa, Physical review letters (2006) doi:10.1103/PhysRevLett.97.153904

[135] M. Reduzzi, P. Carpeggiani, S. Kühn, F. Calegari, M. Nisoli, S. Stagira, C. Vozzi, P. Dombi, S. Kahaly, P. Tzallas, D. Charalambidis, K. Varju, K. Osvay, G. Sansone, Journal of Electron Spectroscopy and Related Phenomena (2015) doi:10.1016/j.elspec.2015.09.002

[136] I.J. Sola, E. Mével, L. Elouga, E. Constant, V. Strelkov, L. Poletto, P. Villoresi, E. Benedetti, J.-P. Caumes, S. Stagira, C. Vozzi, G. Sansone, M. Nisoli, Nat Phys (2006) doi:10.1038/nphys281

[137] G. Sansone, E. Benedetti, F. Calegari, C. Vozzi, L. Avaldi, R. Flammini, L. Poletto, P. Villoresi, C. Altucci, R. Velotta, S. Stagira, S. de Silvestri, M. Nisoli, Science (New York, N.Y.) (2006) doi:10.1126/science.1132838

[138] P. Tzallas, E. Skantzakis, C. Kalpouzos, E.P. Benis, G.D. Tsakiris, D. Charalambidis, Nat Phys (2007) doi:10.1038/nphys747

[139] P. Tzallas, E. Skantzakis, L.A.A. Nikolopoulos, G.D. Tsakiris, D. Charalambidis, Nat Phys (2011) doi:10.1038/nphys2033

[140] E.J. Takahashi, P. Lan, O.D. Mucke, Y. Nabekawa, K. Midorikawa, IEEE J. Select. Topics Quantum Electron. (2015) doi:10.1109/JSTQE.2015.2405899

[141] E.J. Takahashi, P. Lan, O.D. Mucke, Y. Nabekawa, K. Midorikawa, Nature communications (2013) doi:10.1038/ncomms3691

[142] Gibbon, Physical review letters (1996) doi:10.1103/PhysRevLett.76.50

[143] P. Heissler, R. Hörlein, M. Stafe, J.M. Mikhailova, Y. Nomura, D. Herrmann, R. Tautz, S.G. Rykovanov, I.B. Földes, K. Varjú, F. Tavella, A. Marcinkevicius, F. Krausz, L. Veisz, G.D. Tsakiris, Appl. Phys. B (2010) doi:10.1007/s00340-010-4281-6

[144] F. Quéré, C. Thaury, P. Monot, S. Dobosz, P. Martin, J.-P. Geindre, P. Audebert, Physical review letters (2006) doi:10.1103/PhysRevLett.96.125004

[145] B. Dromey, D. Adams, R. Hörlein, Y. Nomura, S.G. Rykovanov, D.C. Carroll, P.S. Foster, S. Kar, K. Markey, P. McKenna, D. Neely, M. Geissler, G.D. Tsakiris, M. Zepf, Nature Phys (2009) doi:10.1038/NPHYS1158

[146] T. Baeva, S. Gordienko, A. Pukhov, Physical review. E, Statistical, nonlinear, and soft matter physics (2006) doi:10.1103/PhysRevE.74.046404

References

[147] R. Lichters, J. Meyer-ter-Vehn, A. Pukhov, Physics of Plasmas (1996) doi:10.1063/1.871619

[148] N. Miyamoto, M. Kamei, D. Yoshitomi, T. Kanai, T. Sekikawa, T. Nakajima, S. Watanabe, Physical review letters (2004) doi:10.1103/PhysRevLett.93.083903

[149] Y. Nabekawa, H. Hasegawa, E.J. Takahashi, K. Midorikawa, Physical review letters "Production of doubly charged helium ions by two-photon absorption of an intense sub-10-fs soft x-ray pulse at 42 eV photon energy" PhysRevLett 2005.

[150] P. Heissler, R. Hörlein, J.M. Mikhailova, L. Waldecker, P. Tzallas, A. Buck, K. Schmid, C.M.S. Sears, F. Krausz, L. Veisz, M. Zepf, G.D. Tsakiris, "Generation of attosecond light pulses from gas and solid state media" Physical review letters (2012)

[151] Y. Mairesse, A. de Bohan, L.J. Frasinski, H. Merdji, L.C. Dinu, P. Monchicourt, P. Breger, M. Kovacev, R. Taïeb, B. Carré, H.G. Muller, P. Agostini, P. Salières, "Attosecond synchronization of high-harmonic soft x-rays" Science (2003)

[152] T. Sekikawa, T. Kanai, S. Watanabe, "Frequency-resolved optical gating of femtosecond pulses in the extreme ultraviolet" Physical review letters (2003)

[153] T. Sekikawa, A. Kosuge, T. Kanai, S. Watanabe, "Nonlinear optics in the extreme ultraviolet" Nature (2004)

[154] Y. Nabekawa, T. Shimizu, T. Okino, K. Furusawa, H. Hasegawa, K. Yamanouchi, K. Midorikawa, "Interferometric autocorrelation of an attosecond pulse train in the single-cycle regime" Physical review letters (2006)

[155] S. Kühn, M. Dumergue, S. Kahaly, S. Mondal, M. Füle, T. Csizmadia, B. Farkas, B. Major, Z. Várallyay, E. Cormier, M. Kalashnikov, F. Calegari, M. Devetta, F. Frassetto, E. Månsson, L. Poletto, S. Stagira, C. Vozzi, M. Nisoli, P. Rudawski, S. Maclot, F. Campi, H. Wikmark, C.L. Arnold, C.M. Heyl, P. Johnsson, A. L'Huillier, R. Lopez-Martens, S. Haessler, M. Bocoum, F. Boehle, A. Vernier, G. Iaquaniello, E. Skantzakis, N. Papadakis, C. Kalpouzos, P. Tzallas, F. Lépine, D. Charalambidis, K. Varjú, K. Osvay, G. Sansone, "The ELI-ALPS facility: the next generation of attosecond sources" J. Phys. B: At. Mol. Opt. Phys. (2017)

[156] M. Dumergue, S. Kuhn, A. Nayak, E. Skantzakis, I. Makos, I. Orfanos, D. Charalambidis, P. Tzallas (eds.), "Towards Generation of Ultrahigh Energy XUV Pulses" Optical Society of America Conference Papers EUVXRAY EW2B 2018.

[157] I Orfanos, I Makos, I Liontos, E Skantzakis, Benjamin Förg, D Charalambidis, P Tzallaset al APL Applied Physics Letters Photonics 4, 080901 (2019)

[158] He, X. et al. "Spatial and spectral properties of the high-order harmonic emission in argon for seeding applications". Phys. Rev. A 79,888, (2009).

Publications

1. "Non-linear processes in the extreme ultraviolet" **I. Orfanos***, I. Makos*, I. Liontos, E. Skantzakis, B. Major, A. Nayak, M. Dumergue, S. Kühn, S. Kahaly, K. Varju, G. Sansone, B. Witzel, C. Kalpouzos, P. Tzallas and D. Charalambidis. Journal of Physics B: Atomic, Molecular and Optical Physics 2020.

2. "A 10-gigawatt attosecond source for non-linear XUV optics and XUV-pump-XUV-probe studies" I. Makos*****, **I. Orfanos***, A. Nayak, J. Peschel, B. Major, I. Liontos, E. Skantzakis, N. Papadakis1, C. Kalpouzos, M. Dumergue, S. Kühn, K. Varju, P. Johnsson, A. L'Huillier, P. Tzallas and D. Charalambidis. Sci Rep,Nature 2020.

3. "Attosecond pulse metrology" **I. Orfanos***, I. Makos*, I. Liontos, E. Skantzakis, B. Förg, D. Charalambidis and P. Tzallas, APL Photonics 2019.

4. "Towards Single-Shot XUV-Pump-XUV-Probe Studies" **I. Orfanos**, I. Makos, N. Tsatrafyllis, S. Chatziathanasiou, E. Skantzakis, D. Charalambidis and P. Tzallas, Book Chapter in Springer Series in Chemical Physics: Progress in Ultrafast Intense Laser Science Volume 118 chapter 11 ISBN: 978-3-030-03786-4, 2019.

5. "Multiple ionization of argon via multi-xuv-photon absorption induced by 20-gigawatt high-harmonic pulses" A. Nayak, **I. Orfanos**, I. Makos, M. Dumergue, S. Kühn, E. Skantzakis, B. Bodi, K. Varju, C. Kalpouzos, H. I. B. Banks, A. Emmanouilidou, D. Charalambidis and P. Tzallas, Phys. Rev. A, 2018.

6. "Towards generation of ultrahigh energy XUV pulses" M. Dumergue, S. Köhn, A. Nayak, E. Skantzakis, I. Makos, **I. Orfanos**, D. Charalambidis, and P. Tzallas, Conference Paper Compact EUV & X-ray Light Sources 2018 Strasbourg France 26–28 March 2018.

Non-linear processes in the extreme ultraviolet

View the article online for updates and enhancements.

Journal of Physics: Photonics

Non-linear processes in the extreme ultraviolet

I Orfanos[1,2,9], I Makos[1,2,9], I Liontos[1] (iD), E Skantzakis[1] (iD), B Major[3] (iD), A Nayak[3,4], M Dumergue[3], S Kühn[3], S Kahaly[3] (iD), K Varju[3,5] (iD), G Sansone[6], B Witzel[7], C Kalpouzos[1], L A A Nikolopoulos[8] (iD), P Tzallas[1,3] and D Charalambidis[1,2,3] (iD)

1 Foundation for Research and Technology - Hellas, Institute of Electronic Structure & Laser, PO Box 1527, GR 71110, Heraklion (Crete), Greece
2 Department of Physics, University of Crete, PO Box 2208, GR 71003, Heraklion (Crete), Greece
3 ELI-ALPS, ELI-HU Non-Profit Ltd., Wolfgang Sandner utca 3., Szeged 6728, Hungary
4 Institute of Physics, University of Szeged, Dom tér 9, 6720, Szeged, Hungary
5 Department of Optics and Quantum Electronics, University of Szeged, Dom tér 9, 6720, Szeged, Hungary
6 Physikalisches Institut, Albert-Ludwigs-Universität Freiburg, Stefan-Meier-Str. 19, D-79104, Freiburg, Germany
7 Université Laval, Centre d'Optique, Photonique et Laser (COPL), Quebéc G1V 0A6, Canada
8 School of Physical Sciences, Dublin City University, Glasnevin, Dublin 9, Ireland

E-mail: chara@iesl.forth.gr

Abstract

Recent developments in extreme ultraviolet (XUV) and x-ray radiation sources have pushed pulse energies and durations to unprecedented levels that opened up the era of non-linear XUV and x-ray optics. In this quest, laser driven high order harmonic generation sources providing attosecond resolution in the XUV spectral region enabled XUV-pump-XUV-probe experiments, while Free Electron Laser research infrastructures offer unique x-ray brilliances for highly non-linear interactions and since recently, they too entered the sub-fs temporal regime. This topical review discusses the conceptual intricacies of non-linear XUV and x-ray processes, addresses experimental particularities and highlights recent applications of such processes with emphasis to laser driven XUV-attosecond source related research.

1. Introduction to non-linear extreme ultraviolet processes

Substantial advances in short wavelength pulsed radiation sources, in the last two decades, have allowed pulse energies and durations to reach such levels that non-linear optics experiments in the extreme ultraviolet (XUV) and x-ray spectral domains have become a reality. This has revealed a direction to exciting physics and offers an optimal tool for time domain studies of ultrafast dynamics. While Free Electron Lasers (FELs) are by far the highest peak brightness sources in the soft and hard x-ray regions [1], coherent, laser driven, table top XUV sources have reached comparable peak brightness at shorter pulse durations [2]. Consequently, non-linear XUV optics became an active research field both in the FEL and the laser driven coherent XUV radiation communities, including attosecond scientists. While energetic attosecond pulses have been recently reported by FEL laboratories [3, 4], attosecond applications have been so far demonstrated only in the laser driven High-order Harmonic Generation (HHG) sources in the XUV spectral region. In the present manuscript, we review the topic of non-linear XUV processes focusing mainly on recent developments of the laser driven XUV and attosecond source user community. In the introductory section, multi-photon (MP) processes are reviewed with emphasis on the intricacies of the XUV spectral region. In the second section experimental developments towards energetic XUV sources and attosecond applications exploiting solely XUV radiation are presented. In the third section we review recent XUV non-linear applications in the femtosecond (fs) and attosecond temporal regimes.

Figure 1. The laser-atom interaction regimes. For adiabaticity parameters larger than unity the photon aspect of the interaction prevails leading to a multi-photon process. For adiabaticity parameters smaller than unity the field aspect dominates, the field modifies the atomic potential forming time dependent (oscillating) barriers and the process is initiated through tunneling or over the barrier ionization.
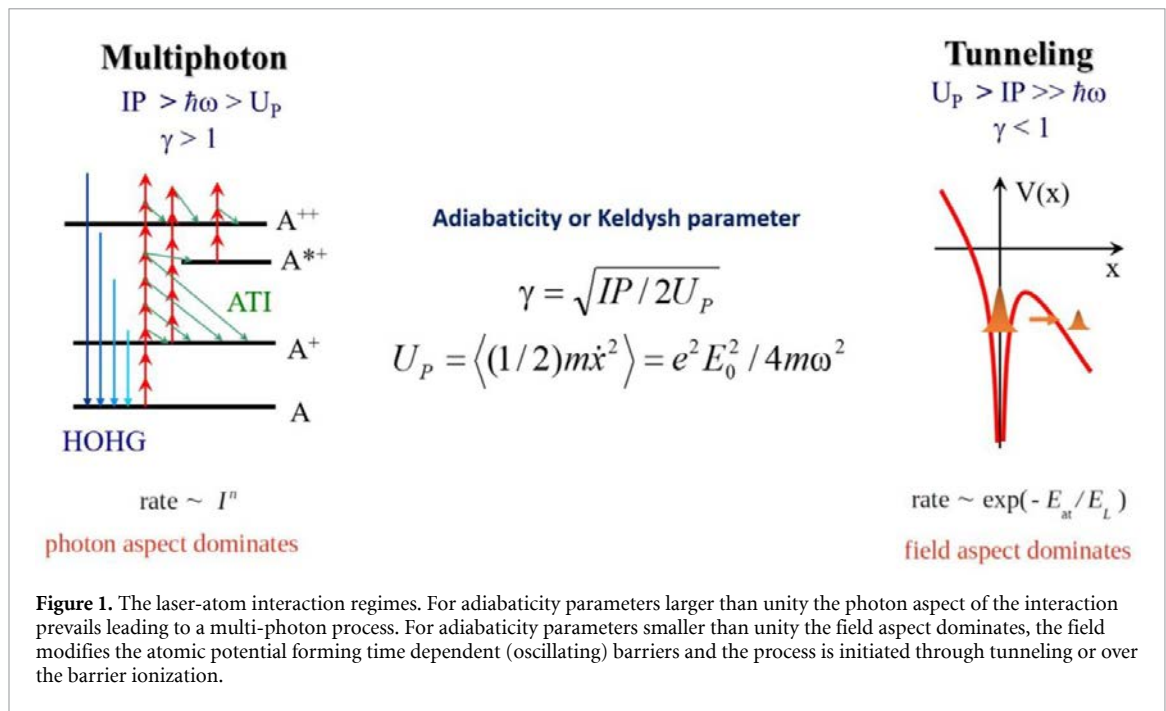
1.1. Tunneling vs multi-photon

An adequate description of the interaction of intense radiation with matter depends on the interplay between the radiation's field-strength, carrier frequency and pulse duration, as well as the ionization energy of the matter species. At low frequencies (infrared and lower) and high radiation field-strengths the atomic/molecular Coulombic potential is severely distorted by the potential of the interaction, and the combined Coulombic and radiation field potentials form a barrier that oscillates with the frequency of the radiation. If the degree of distortion is comparable or larger than the ionization potential, an electron can tunnel through the barrier or escape above it respectively. Since the frequency is low, the potential distortion process is quasi-static and thus the tunneling probability is not negligible. The tunneling rate can be treated, in the appropriate limit, as the DC tunneling ionization rate [5] averaged over a single period of the field. Here the field aspects dominate the interaction process (figure 1 right panel). In the opposite side, at not too high field-strengths and high frequencies (ultra-violet, vacuum ultra-violet, x-rays) the degree of the potential distortion is much lower than the ionization potential, the oscillations are much faster and thus the tunneling probability (or over-the-barrier ionization) is strongly reduced. The interaction is now dominated by the photon aspects of the radiation, namely the interaction leads to MP absorption and eventually to ionization (figure 1 left panel). The ionization rate in that case can be treated through lowest order perturbation theory (LOPT).

The above discussion can be quantified by a parameter known as adiabaticity or Keldysh parameter [6], given by

$$\gamma = \sqrt{IP/2U_p} \tag{1.1.1}$$

IP being the ionization energy and U_p the so called ponderomotive potential, which is the mean kinetic energy of the oscillation of a free electron interacting with the radiation field

$$U_p = \langle \frac{1}{2}m\dot{x}^2 \rangle = e^2 E_0^2 / 4m\omega^2 \tag{1.1.2}$$

with *m, x* and *e* being the mass, position and charge of the electron respectively and E_0 $\hbar$ and ω the field amplitude and radial frequency respectively.

A practical numerical evaluation formula for U_p is:

$$U_p\,(eV) = 9.3 \cdot 10^{-14} \cdot I\left(\frac{W}{cm^2}\right) \cdot \lambda^2\,(\mu m). \tag{1.1.3}$$

When $U_p > IP \gg \hbar\omega$ then $\gamma < 1$ and the strong field interaction leads to tunnel ionization, while when $IP > \hbar\omega > U_p$ then $\gamma > 1$ and the interaction and ionization has a MP character. It should be noted that we can safely talk about tunneling or MP only if $\gamma \ll 1$ or $\gamma \gg 1$, respectively.

Table 1. Scaling of U$_P$ with the photon energy.

$\hbar\omega$ (eV)	λ (μm)	U_p (eV) (@10^{14} W cm^{-2})	I (W cm^{-2}) (when $U_p = \hbar\omega$)	I (W cm^{-2}) (when $IP = 13.6$ eV $= 2\,U_p$)
1	1.242	14.4	$6.97 \cdot 10^{12}$	$4.74 \cdot 10^{13}$
5	0.248	$5.7 \cdot 10^{-1}$	$8.7 \cdot 10^{14}$	$1.18 \cdot 10^{15}$
10	0.124	$1.44 \cdot 10^{-1}$	$6.97 \cdot 10^{15}$	$4.74 \cdot 10^{15}$
50	0.0248	$5.7 \cdot 10^{-3}$	$8.7 \cdot 10^{17}$	$1.18 \cdot 10^{17}$
100	0.0124	$1.44 \cdot 10^{-3}$	$6.97 \cdot 10^{18}$	$4.74 \cdot 10^{17}$
500	0.00248	$5.7 \cdot 10^{-5}$	$8.7 \cdot 10^{20}$	$1.18 \cdot 10^{19}$
1000	0.001242	$1.44 \cdot 10^{-5}$	$6.97 \cdot 10^{21}$	$4.74 \cdot 10^{19}$

Apparently, because γ is inversely proportional to the wavelength the MP character will be more pronounced at short wavelengths. Moreover, increasing the ponderomotive potential, via the field's intensity, has an upper limit set by the depletion of the medium. Indeed, the radiation pulse has a temporal distribution. Even if intensities could be increased limitlessly, ionization would be saturated at the leading edge of the pulse due to the finite rise time of the radiation pulse. Hence, the medium would never 'see' the peak intensity [7] as it would be depleted before the top of the pulse is reached; an effect sometimes referred to as 'The Lambropoulos curse' [8, 9], because it invalidated as non-realistic several fascinating effects predicted in high intensity laser-matter interactions in the 80 s. The large frequency and limited intensity 'seen' by the matter ensure that interactions in the XUV and much more pronounced in the x-ray spectral region, are of MP character.

Table 1 gives some numerical examples of the scaling of the ponderomotive energy with photon energy. The third column gives the ponderomotive energy at 10^{14} W cm^{-2} intensity. The fourth column gives the intensity at which the ponderomotive shift becomes equal to the photon energy and the last column the intensity at which it becomes equal to half the ionization energy. From table 1 one can extract that for photon energies ≥ 10 eV, γ becomes < 1 at intensities that the atom/molecule will not be subjected to, unless the interaction is with pulses of very short duration. The role of the pulse duration will be discussed in the next section. In figure 2 the blue curved surface shows the dependence of the Keldysh parameter, γ, on the wavelength and intensity of the radiation, for the case, where the photon energy is about half the ionization energy. The horizontal flat yellow surface consists of all wavelength-intensity value pairs for which $\gamma = 1$. As can be seen in this graph the tunneling regime is safely reached at intensities $> 10^{16}$ W cm^{-2} for 20 eV photons and at higher intensities for larger photon energies. For pulses with durations > 0.1 fs, these intensities are above the atomic/molecular ionization saturation intensity, meaning that the atom/molecule will be essentially fully ionized before the peak intensity is reached. Therefore, one can safely conclude that for photon energies ≥ 20 eV and pulse durations ≥ 0.1fs the interaction is of MP character. However, strong field effects become observable in specific cases at the today's available FEL intensities [10].
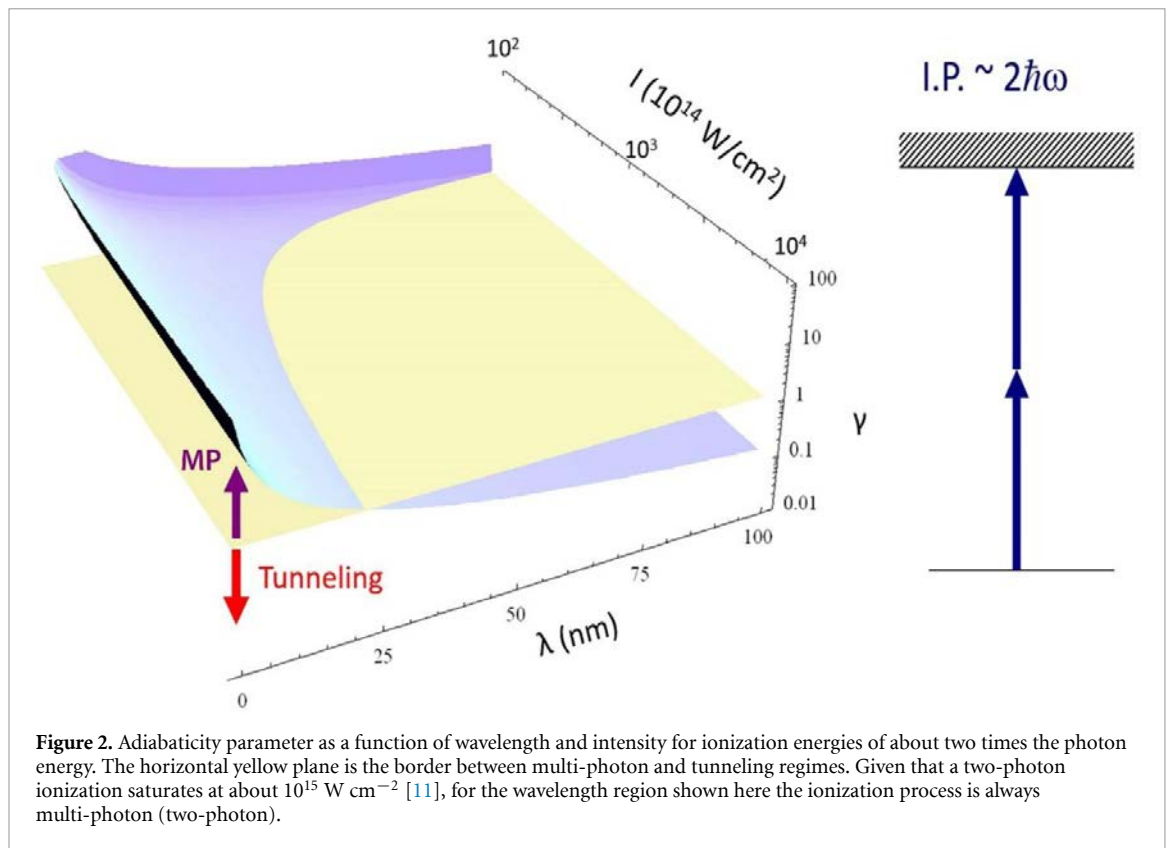
It is worth adding here that the effect of ionization saturation during the raising edge of the radiation pulse is not always a disabling effect. Indeed this effect underlies the temporal gating technique known as 'ionization gating' that enables the generation of isolated attosecond pulses [12, 13].

1.2. The ionization of an atom/molecule. 'Coring' vs 'Peeling'

The intricacies of ionization upon interaction of short wavelength radiation with matter are governed by the ratio of the *photon energy* over *ionization energy* of the first inner shell of the matter.

If this ratio is > 1 an inner shell electron is ejected with notably higher probability than an outer one (a process frequently referred to as 'coring') leaving an inner shell hole behind. The hole is eventually filled, in the vast majority of the cases, through an Auger or Coster–Kronig process [14], producing a doubly ionized atom/molecule. Absorption of subsequent photons leads to repetition of the process described, as long as the above mentioned ratio is larger than unity. High charge state ions are thus produced through a sequence of single photon absorption processes (and eventually subsequent relaxation processes), each of which leads to the next charge state of the ion.

The photo-ejection of an inner-shell electron discussed here theoretically can also proceed via MP absorption. However, in order for this process to compete with the ejection of an outer electron, a challenging combination of pulse duration and energy, not available in any laboratory or research infrastructure so far, is required. Thus 'coring' processes are so far sequences of single photon absorption events (sequential coring). In contrast, for a ratio < 1 an outer shell electron is ejected leaving a singly ionized ion behind and absorption of further photons leads to the ejection of additional outer electrons provided that the ejection is energetically allowed (a process frequently referred to as sequential peeling). Under specific conditions, ejection of two electrons leads to a doubly ionized ion without intermediate production

Figure 2. Adiabaticity parameter as a function of wavelength and intensity for ionization energies of about two times the photon energy. The horizontal yellow plane is the border between multi-photon and tunneling regimes. Given that a two-photon ionization saturates at about 10^{15} W cm^{-2} [11], for the wavelength region shown here the ionization process is always multi-photon (two-photon).

of a singly ionized ion, a process known as direct double (or multiple) ionization. An inner shell non-linear process, i.e. absorption of more than one photons by one or more inner shell electrons leading to some stage of ionization, without formation of intermediate charge states, is currently not possible, since it requires very short pulse durations at high pulse energies, a matter that will be discussed in the next section. Such a process can currently be considered only as a future perspective. On the contrary multi-XUV-photon absorption by outer electrons is feasible at the currently available XUV intensities in FEL infrastructures as well as in laser driven HHG [15, 16] sources. This has led to the revitalization of MP processes, a forefront research topic at optical frequencies in the 70 s, 80 s and 90 s, now in the XUV/x-ray regimes.

1.3. The era of non-linear XUV processes, their contribution in attosecond metrology and science

Historically, MP processes trace back to the 30 s. It was Maria Göppert Mayer who first predicted two-photon processes, talking about 'two quanta jumps' (Über Elementarakten mit zwei Quantensprünge") [17]. About 30 years later, in the 60 s, the invention of the laser led to the first experimental observation of MP processes [18, 19]. Another 30 years later, in the 90 s, the development of intense laser HHG sources [20, 21] led to the first experimental observation of multi-XUV-photon processes [22]. The importance of observable multi-XUV-photon processes relates to a number of advanced applications.

Concerning applications in temporal pulse characterization, non-linear XUV processes hold promise for rigorous attosecond pulse reconstruction. The most frequently used methods for the temporal characterization of fs pulses are based on non-linear processes both in the time domain, like second- and higher-order autocorrelation, frequency resolved optical gating (FROG) [23], attosecond spatial interferometry [24] or in the frequency domain like Spectral Phase Interferometry for the Direct Electric Field Reconstruction (SPIDER) [25] to mention some. In attosecond pulse metrology, due to the lack of sufficient pulse energy, a number of cross-correlation (infrared (IR)/XUV) techniques have been developed such as Reconstruction of Attosecond Beating By Interference of two-photon Transitions (RABBIT) [26], Frequency Resolved Optical Gating for Complete Reconstruction of Attosecond Bursts (FROG-CRAB) [27], Phase Retrieval by Omega Oscillation Filtering [28], *in-situ* [29], atto-clock [30], double-blind holography [31] and the attosecond streaking [32] methods. A summary of these approaches can be found in the perspective article on the attosecond pulse metrology [33]. Non-linear XUV processes allowing the performance of second-order autocorrelation based techniques relying solely on the XUV radiation provide an alternative attosecond pulse characterization approach bypassing possible inconsistencies inherent in the other methods [34]. Still, robust utilization of non-linear XUV processes in attosecond pulse

characterization is subject to the availability of sufficient stability of the XUV radiation parameters and high repetition rate sources.

Applications in the investigation of ultra-fast dynamics using attosecond pulses follow similar pathways. Cross-correlation (IR/XUV) approaches like RABBIT, RAINBOW RABBIT [35] and attosecond streaking have been successfully used in numerous fascinating applications; atomic inner-shell spectroscopy [36], real-time observation of ionization [37], light wave electronics [38] and molecular optical tomography [39, 40] are some examples of such experiments. Other more recent applications of attosecond pulses include ionization delay in solids [41] and atoms [36, 37] and molecules [42, 43], electron dynamics [44], charge migration [45, 46], build-up of a Fano-Beutler resonance [35], ionization dynamics in chiral molecules [47], to mention some from the very many. Alternatively, non-linear XUV processes allow conducting XUV-pump-XUV-probe experiments with sub-fs temporal resolution overcoming complications, that may arise in some cases in conventional IR/XUV pump-probe experiments, related to distortions suffered by the system under investigation due to the IR laser/matter interaction that may obscure the intrinsic dynamics of it [48]. XUV-pump-XUV-probe schemes involve at least two-XUV-photon processes and thus non-linear XUV processes offer an advantageous tool in attosecond metrology.

An additional advanced application of non-linear XUV processes arises from the spatial selectivity they provide. Since the non-linear process becomes observable at high intensities and thus in focused beams, the focal area provides spatial selectivity allowing 3D mapping of a sample. Spatio-temporal resolution (4D) may reach the sub-μm and attosecond regimes.

Attosecond pulses as coherent pulses allow frequency domain Ramsey spectroscopy type of measurements [49–51] as well. The superposition of two mutually delayed attosecond pulses result in a modulated broad frequency spectrum. Variation of the delay between the two pulses translates to a variation of the position of the frequency peaks. The distance of two consecutive frequency peaks is inversely proportional to the delay of the two pulses. This allows frequency domain measurements the frequency resolution of which is increased when two-XUV-photon transitions are involved coupling narrow spectral width metastable states.
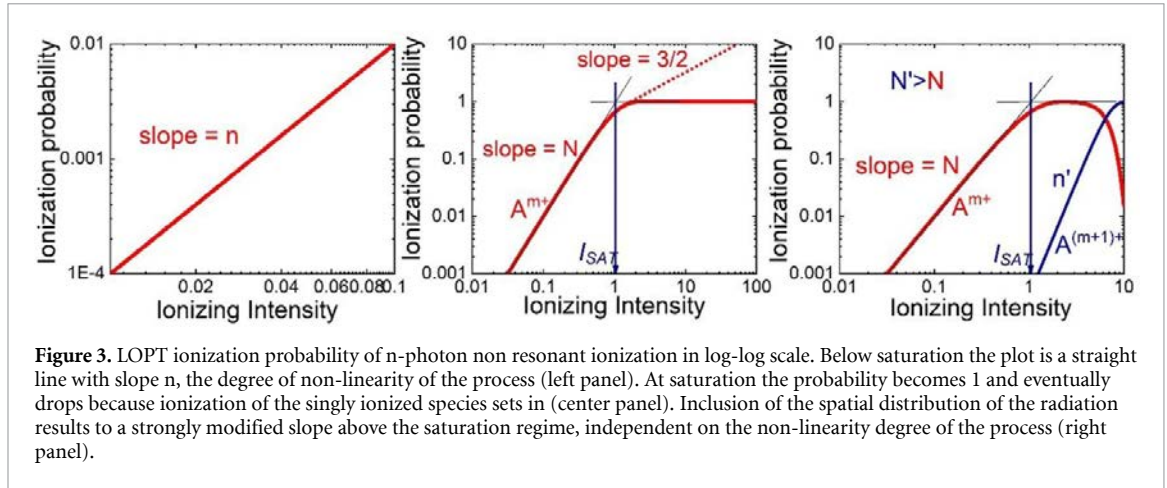
Nonlinear XUV spectroscopy could also be considered an important tool for the validation of numerical models for the description of electronic correlation in atoms and small molecules. In this research direction, the process of two-photon double ionization represents an ideal benchmark. When confined to the attosecond timescale, the correlated electronic dynamics should be manifested in the relative angular distribution of the photoionized electrons [52]. Such an experiment still represents a formidable technological challenge for nonlinear XUV spectroscopy as it would require the combination of high-intensity XUV pulses, attosecond pulse durations (and control of relative delay between two pulses on a similar timescale) and high-repetition rate sources (for the coincidence characterization of the two-photoelectrons). Even though preliminary, partial experimental data on double ionization of helium and neon were obtained at FLASH [53, 54], there are several characteristics of the process that still need to be investigated.

Non-linear XUV processes made their debut some 20 years ago. Limitations preventing their earlier observation relate to the high intensity they require, while their utilization in applications was hampered since they are inherently absorbed by any material. The latter restriction further prohibits the use of refractive optical elements in the experimental set-ups.

High intensity limitations relate to the low throughput of gas target HHG sources and XUV optical elements, while an additional restriction arises from possible reabsorption of the XUV radiation at the source itself. Limitations on the throughput of gas target HHG sources originate from the depletion of the generation medium, which at a given intensity is fully ionized and no medium emitters remains to generate harmonics. Since HHG relies on the interaction of matter with an IR pulse, even if very high laser pulse energies are available ionization will saturate at the leading edge of the laser pulse once the ionization saturation limit is reached. The emitter will be fully ionized and thus the higher intensities will not be 'seen' by the depleted generating medium. Moreover, in the created plasma the index of refraction at a given angular frequency ω, $n_\omega \approx 1 - \frac{\omega_p^2}{2\omega^2}$ is determined by the plasma frequency $\omega_p = e\sqrt{\frac{N_e}{m\varepsilon_0}}$, with N_e the electron's density and ε_0 the vacuum permittivity. Saturation of ionization will result to a large electron density N_e leading to negative dispersion that may destroy phase-matching.

Reabsorption of the XUV radiation at the source sets additional limitations in the generation medium length and atomic density. The absorption length in the generation medium is given by $L_{abs} \approx (\sigma N_a)^{-1}$, where σ is the absorption cross section and N_a the atomic density. Therefore, increasing the medium length or the gas pressure such that $L_{abs}N_a > \sigma$ would be meaningless as reabsorption would prevent an increased throughput. Mitigation strategies of medium depletion and reabsorption are described in section 2.

Figure 3. LOPT ionization probability of n-photon non resonant ionization in log-log scale. Below saturation the plot is a straight line with slope n, the degree of non-linearity of the process (left panel). At saturation the probability becomes 1 and eventually drops because ionization of the singly ionized species sets in (center panel). Inclusion of the spatial distribution of the radiation results to a strongly modified slope above the saturation regime, independent on the non-linearity degree of the process (right panel).

Other source throughput limitations are raised by the necessity to use only reflection optics in steering, focusing or splitting the XUV beam, because XUV radiation is highly absorbed when it propagates in matter. This point will also be discussed in section 2.

1.4. MP ionization yields and the required XUV intensity and pulse duration parameters

In a *n*-photon non-resonant ionization process the time evolution of the ionization probability $P(t)$ can be described by the rate equation:

$$\frac{dP(t)}{dt} = (1 - P(t))\,\sigma^{(n)}F^n(t) \tag{1.4.1}$$

where

$$F^n(t) = \frac{I(t)}{\hbar\omega} = F_0 f(t) \tag{1.4.2}$$

is the photon flux, $I(t)$ the intensity envelope, F_0 the instantaneous peak photon flux, ω the angular frequency, $f(t)$ the temporal pulse profile with $f(t = 0) = 1$ and $\sigma^{(n)}$ the generalized *n*-photon ionization cross section usually given in $cm^{2n}s^{n-1}$ so that the rate dP/dt is given in s^{-1} when the intensity is given in W/cm^2 .

Defining an effective time $t_{eff} = \int_{-\infty}^{\infty} f^n(t')\,dt'$ integration of (equation 1.4.1) yields an ionization probability at the end of the ionizing pulse:

$$P(t \to \infty) = 1 - \exp\left(-\sigma^{(n)}F_0^n t_{eff}\right). \tag{1.4.3}$$

Below saturation of ionization, i.e. when $\sigma^{(n)}F_0^n t_{eff} \ll 1$

$$\ln P(t \to \infty) = n\ln F_0 + \ln\sigma^{(n)} + \ln t_{eff}. \tag{1.4.4}$$

Thus, the ionization probability depends linearly on the photon flux (or intensity) in log-log scale below saturation, with a slope equal to the degree of the non-linearity *n* as shown in figure 3 (left panel). Including saturation and defining the ionization saturation intensity as $I_{SAT} = \frac{\hbar\omega}{\sqrt[n]{\sigma^{(n)}t_{eff}}}$, the ionization probability at the end of the pulse becomes

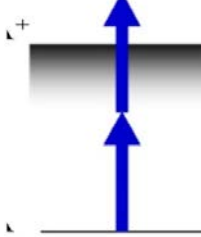$$P(t \to \infty) = 1 - e^{-\left(\frac{I}{I_{SAT}}\right)^n} \tag{1.4.5}$$

and for $I \ll I_{SAT}$ reduces to $P(t \to \infty) = \left(\frac{I}{I_{SAT}}\right)^n = \sigma^{(n)}F_0^n t_{eff}$. A plot of (equation 1.4.5) in log-log scale is shown in figure 3 (right panel). As I approaches I_{SAT} the increase of the probability slows down and at saturation becomes 1. Above saturation ($I > I_{SAT}$) the probability drops because the ionization of the singly ionized species sets in.

It should be noted that because the ionization radiation at the focus has a 3D intensity distribution $I = I(x,y,z)$ the ionization probability will also have a spatial distribution $P = P(x,y,z)$ and even if the central part of the interaction volume is saturated the surrounding will not be. When the ionization probability

Table 2. Typical two-XUV-photon ionization parameters. τ_ω denotes the duration of the XUV pulse.

$\sigma^{(2)}$	10^{-50} cm^4 s
$\hbar\omega$	20 eV
τ_ω	2 fs
V_{int}	10^{-7} cm^3
n_{atom}	2.6×10^{15} cm^{-3}
I_ω	10^{11} W cm^{-2}
η	0.5

measurement is not spatially confined, but it is integrated for the entire interaction volume the probability $P(t \to \infty) \int \int \int p(x,y,z) dx dy dz = \int \int \int \frac{I(x,y,z)}{I_{SAT}} dx dy dz$ will neither stabilize at unity nor drop at and above the saturation intensity respectively. It will continue increasing due to the volume integration.

For a Gaussian distribution in cylindrical coordinates the spatiotemporal intensity distribution is

$$I(r,z;t) = I(t) \frac{w_0^2}{w(z)^2} exp\left[-\frac{2r^2}{w(z)^2} \right] \tag{1.4.6}$$

where r is the radius, z is the beam propagation axis and $w(z)$ is the beam radius, defined in terms of the beam waist w_0 as $w(z) = w_0\sqrt{1 + (z/z_R)^2}$. The ion yields can then be integrated using the expression

$$P(t \to \infty) = \int\limits_{0}^{r_{max}} \int\limits_{z_{min}}^{z_{max}} 2\pi r P(r,z) \, dz dr \tag{1.4.7}$$

where $P(t \to \infty)$ is the integrated over the volume ionization probability at the end of the pulse and $P(r,z)$ the ionization probability at each point (r,z). Above saturation, (equation 1.4.7) results to a line with a slope of 3/2 as shown in figure 3 (middle panel). This effect known as the 'volume effect' can be eliminated by a spatially confined measurement of the ions as will be discussed in section 2.

The generalized n-photon ionization cross section in the electric dipole approximation within the LOPT reads:

$$\sigma^{(n)} \propto \left| \frac{\sum_{i_1} \dots \sum_{i_1} \langle g | \vec{r}\hat{e} | i_1 \rangle \dots \langle i_{n-1} | \vec{r}\hat{e} | f \rangle + \int d\varepsilon \langle g | \vec{r}\hat{e} | \varepsilon \rangle \langle \varepsilon | \vec{r}\hat{e} | f \rangle}{\left[E_{i_{n-1}} - E_g - (n-1)\hbar\omega \right] \dots \left[E_{i_{n-1}} - E_g - \hbar\omega \right]} \right|^2 \tag{1.4.8}$$

where $|g\rangle$, $|f\rangle$, $|i_k\rangle$ (k = 1,…n-1) and $|\varepsilon >$ are the ground, final, all electric dipole allowed intermediate bound states involved and all electric dipole allowed continuum states involved respectively. E_g, E_f, E_{ik} and E are the corresponding eigenenergies, $\vec{r}$ is the electron position operator and $\hat{e}$ the electric field polarization unity vector. *Ab initio* calculations of $\sigma^{(n)}$ are feasible for some atoms for which the eigenstate wave functions can be deduced from the Schrödinger equation when exact or accurate atomic potentials are available, as for instance for H and He atoms [55]. In general, generalized ionization cross section can be calculated to some degree of approximation. However, good estimates of $\sigma^{(n)}$, sufficient to describe the essential features of the process, can be obtained from the corresponding cross section of Hydrogen atom using scaling laws [56, 57].

Based on the above discussion one can estimate the required XUV intensities in order to achieve observable two-XUV-photon ionization, i.e. the lowest possible non-linear ionization process. The measured number of ions N_{Ion} per pulse will be given by

$$N_{Ion} = P \times V_{int} \times n_{atom} \times \eta \tag{1.4.9}$$

where P is the ionization probability, V_{int} the interaction volume, n_{atom} the target atomic (/molecular) density and η the detection efficiency of the measuring device. Typical values of the above quantities are summarized in table 2. These parameters result $N_{Ion} = 2$–3 ions/pulse. Thus, intensities of 10^{11} W cm^{-2} are at the limits of observable two-XUV-photon ionization. Intensities $\geq 10^{12}$ W cm^{-2} are required for reliable two-XUV-photon ionization intensity dependence experiments.

In large pulse duration interactions ionization yields are enhanced if the process is resonant with one (or more) of the eigenstates. Large pulse duration here means that the duration is comparable or larger than the lifetime of the state, when decaying through spontaneous emission. For a two-photon resonantly enhanced ionization by a bichromatic field the ionization rate becomes

$$P = \int\limits_{-\infty}^{\infty} \sigma_1 \times F_1 dt \times \int\limits_{-\infty}^{\infty} \sigma_2 \times F_2 dt = \sigma_1 \times \sigma_2 \int\limits_{-\infty}^{\infty} \frac{I_1}{\hbar\omega_1} dt \times \int\limits_{-\infty}^{\infty} \frac{I_2}{\hbar\omega_2} dt \tag{1.4.10}$$

Table 3. Typical two-XUV-photon resonantly enhanced ionization parameters. Two XUV frequencies are assumed. The first being resonant with the transition frequency from the ground to the excited state and the second one is in general different than the first one. τ_i ($i = 1,2$) are the pulse durations of the two XUV frequencies, which are assumed to be equal.

$\sigma_1 \times \sigma_2$	10^{-34} cm^4
$\hbar\omega_{1,2}$	10 eV
$\tau_{1,2}$	2 fs
V_{int}	10^{-7} cm^3
n_{atom}	2.6×10^{15} cm^{-3}
$I_{1,2}$	10^{11} W cm^{-2}
η	0.5
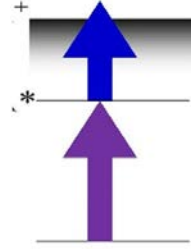
with σ_i ($i = 1,2$) being the single photon absorption cross sections of the two steps and F_i, I_i, ω_i the photon fluxes, intensities and angular frequencies of the two fields, respectively. Using typical values for all the quantities (e.g. those of table 3) one can evaluate the number of generated ions per pulse from (equation 1.4.9) to be $N_{Ion} \approx 2500$ ions/pulse, which is three orders of magnitude larger than in the non-resonant.

In obtaining the above number of ions we used as the effective duration of a Gaussian pulse $\tau_{eff} = \int_{-\infty}^{\infty} e^{-\left(\frac{t}{2\tau_{1,2}}\right)^2} dt = 3.5\tau_{1,2}$. However, for the evaluation of the ion yield here, no account is taken that from the broad spectrum of the radiation pulse only the part that corresponds to the state width is resonant and thus only this fraction should be used from the initial intensity (10^{11} W cm^{-2}).

Ionization by the two parts of the spectrum lying above and below the resonance will cancel due to the opposite detuning and thus to the opposite phases of the corresponding ionization pathways. Taking this into account for bound states with lifetimes of the order of 1 ns, the resonant channel of the ionization becomes negligibly small compared to the non-resonant channel. For this reason, for very short pulses in the attosecond and few fs temporal regime the resonant character of the process is lost unless the lifetime of the state is comparable to the pulse duration as is the case for fast decaying autoionizing states (AIS). In this case the resonant character will be present and may enhance the yield. The situation may become more complex if the experimental parameters become such that the population of the resonant state becomes comparable to the remaining population in the ground state. In such cases the ionization yield may be enhanced. Under such conditions the problem is treated more accurately as described in the following paragraphs and even better if it is solved numerically, since then parameters, such as the width and position of the resonant state, are becoming time dependent.

Rigorously, the problem should be treated through the time dependent Schrödinger equation (TDSE) and not through rate equations. In solving the TDSE for the case of a two-photon ionization it is assumed that the system is initially in the ground state, $|g\rangle$ (energy Eg), subject to a radiation field E(t) with a central-carrier frequency, ω, which is near resonant with an excited state $|a\rangle$ (energy E_a).

The atom can be ionized through two different ionization channels; (a) by absorbing two photons non-resonantly (direct channels) and (b) via the excited state, following the absorption of one-photon and ionization from further photon absorption (sequential channel). However, the atom, once found in the excited state can also be de-excited back to its ground state by photon emission. The photoionization scheme is depicted in figure 4.

The TDSE is solved by first transforming to a slowly-varying-amplitude (SVA) [58] system and then applying the rotating wave approximation (RWA) [58, 59] on the amplitude equations for the ground and the excited state, i.e. eliminating the resulting high frequency terms $[(E_a\text{-}E_g)/\hbar + \omega]$ keeping terms oscillating at $[(E_a\text{-}E_g)/\hbar-\omega]$. It is worth emphasizing that the change to a system of SVA variables does not involve any approximation and as such the transformed TDSE is still exact in the context of a two-level system interacting with a laser field. The applied transformation effectively extracts the fast-oscillating part of the amplitude coefficients due to the energy difference of the two states $\sim(E_a\text{-}E_g)$ (also known as the interaction picture). The SVA transformation combined with the RWA results in expressing the TDSE in terms exclusively of slowly-varying variables, namely, the field's envelope and the periodic $\sim \exp(i(E_a\text{-}E_g)/\hbar-\omega)/t]$ factor. The corresponding (strongly-oscillating) term $\sim[(E_a\text{-}E_g)/\hbar + \omega]$ is discarded. This method is effective if i) it can be modeled in factors of an envelope-like amplitude $E_0(t)$ and a periodic term oscillating with a central carrier frequency e.g. $\sim E_0(t)\times\cos(\omega_{XUV}\times t)$; for the latter assumption a quantitative condition is $dE_0(t)/dt \ll \omega_{XUV} E_0(t)$, which generally holds for a few fs pulse with central frequency in the XUV regime and ii) as long as the field is not extremely intense so that $\Omega_0 \ll \omega_{XUV}$, Ω_0 being the Rabi frequency. The transformed amplitude equations for the ground and the excited state now obey the following coupled-system of differential equations,
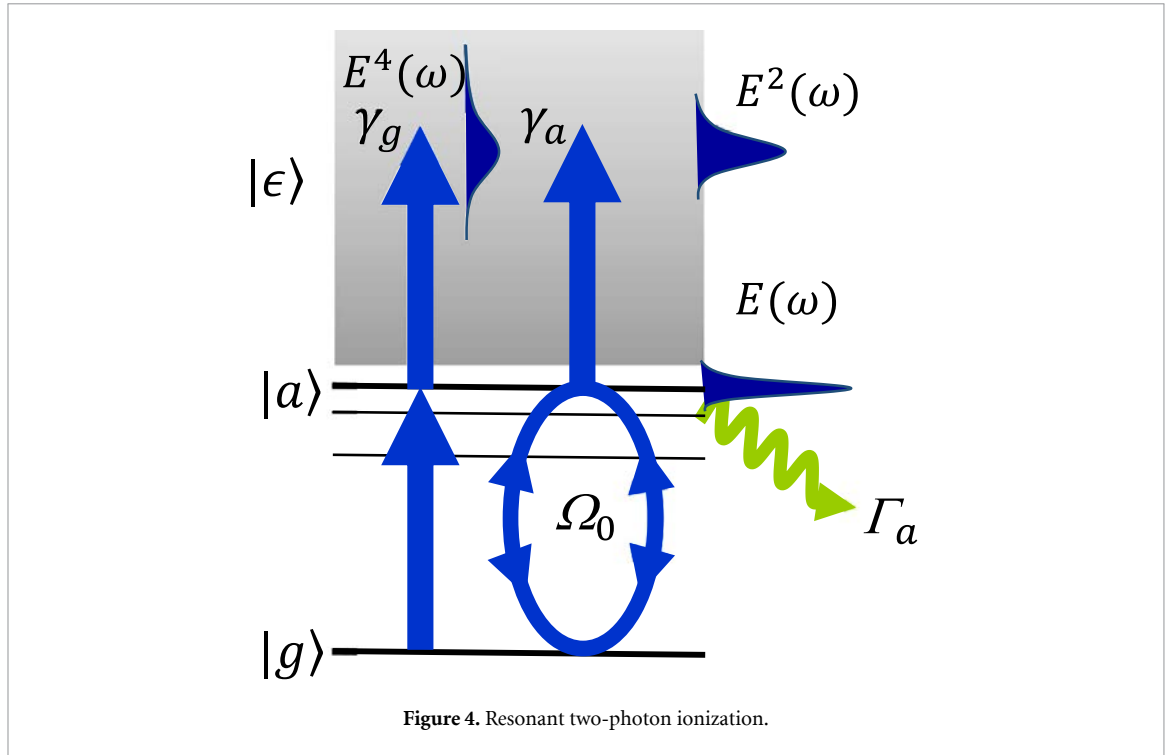
Figure 4. Resonant two-photon ionization.

$$i \begin{bmatrix} \dot{c}_g & (t) \\ \dot{c}_a & (t) \end{bmatrix} = \begin{bmatrix} \varepsilon_g(t) - \frac{\gamma_g(t)}{2} & \Omega_0 - \frac{i}{2} \\ \Omega_0 - \frac{i}{2} & \varepsilon_a(t) - \frac{\Gamma_a + \gamma_a(t)}{2} \end{bmatrix} \begin{bmatrix} c_g(t) \\ c_a(t) \end{bmatrix} \tag{1.4.11}$$

where $q = \frac{2\Omega_0}{\sqrt{\gamma_g \gamma_a}}$, $\varepsilon_i(t) = E_i + s_i(t)$, $i = g$, a and $c_g(t)$, $c_a(t)$ the time dependent state amplitudes, i.e. the square root of the probability to find the system in the corresponding state at time t. In these relations s_g, s_a and γ_g, γ_a are the light shifts, i.e. the shift of the energy of the atom/molecule states induced by the radiation and the widths of the states. Γ_a is the ionization width of the excited state due to other decay channels (e.g. autoionization). Therefore, the dynamic energies $\varepsilon_g, \varepsilon_a$ have incorporated the ac-Stark shifts; also the q-parameter describes the interference between the resonant (sequential) and the non-resonant (direct) ionization channels (similar to the traditional q- Fano parameter). In the above form of the TDSE, all quantities, but Γ_a, are (non-oscillating) time-dependent quantities varying with the field's envelope,

$$s_g(t) = s_g I_0^2 f^4(t) \ , \ \gamma_g(t) = \gamma_i I_0^2 f^4(t) \tag{1.4.12}$$

$$s_a(t) = s_a I_0^2 f^4(t) \ , \ \gamma_a(t) = \gamma_a I_0^2 f^4(t) \tag{1.4.13}$$

$$\Omega_0(t) = \Omega_0 f(t) \ , \ \Omega_0(t) = \frac{1}{2} d_{ga} E_0 f(t) \tag{1.4.14}$$

where $f(t)$ is the field's normalized envelope and $I_0 = |E_0|^2/4$. The above system of equations results in a time-dependent ionization probability:

$$\dot{P}(t) = \left| \sqrt{\gamma_g} C_g + \sqrt{\gamma_a} C_a \right|^2 \tag{1.4.15}$$

(in density matrix notation $\gamma_g \rho_{gg} + \gamma_a \rho_{aa} + 2\sqrt{\gamma_g \gamma_a} Re(\rho_{ga})$, the diagonal matrix elements of ρ_{gg}, ρ_{aa} being the state amplitudes, i.e. the square root of the population of the states g and a respectively, and the non-diagonal matrix element ρ_{ga} being the so called coherence that relates to the induced dipole moment).

Note that for the ac-Stark shifts, in the range of intensities where the RWA is applicable, the following inequalities apply: $s_g \ll \varepsilon_g$ and $s_a \ll \varepsilon_a$. The reason for this resides in the structure of s_g and s_a quantities; the numerator is positive while the denominator is positive up to a certain value and then becomes negative, thus amounting to a reduced value due to mutual cancellations.

Solutions for the amplitudes.
In the general case the TDSE system should be solved numerically, especially in the case where all involved parameters are of comparable magnitude i.e. detuning, decay widths, Rabi frequency. Nevertheless, an

approximate analytical expression for the state amplitudes and the ionization is possible for a many cycle field; the general solution for the amplitudes takes a very simple form, as a linear combination of exponentials:

$$c_g(t) = \frac{e^{i\hat{\delta}t/2}}{\hat{\Omega}}\left[\hat{\Omega}\hat{s}_+(t) - \hat{\Delta}\,\hat{s}_-(t)\right] \tag{1.4.16}$$

$$c_a(t) = \frac{\widehat{\Omega}_0}{\hat{\Omega}}e^{i\hat{\delta}t/2}\hat{s}_-(t) \tag{1.4.17}$$

where all the quantities with hats are complex numbers and determined by the generalized Rabi-frequency, the effective ionization widths and the dynamic detunings,

$$\hat{s}_{\pm} = \frac{1}{2}\left(e^{i\hat{\Omega}t/2} \pm e^{-i\hat{\Omega}t/2}\right), \quad \hat{\Omega} = \sqrt{\hat{\delta}^2 + 4\hat{\Omega}_0^2} \tag{1.4.18}$$

$$\Gamma = \gamma_a + \Gamma_a + \gamma_g, \quad \gamma = \gamma_a + \Gamma_a - \gamma_g \tag{1.4.19}$$

$$\hat{\Delta} = \delta + i\frac{\Gamma}{2}, \quad \hat{\delta} = \delta + i\frac{\gamma}{2} \tag{1.4.20}$$

$$\widehat{\Omega}_0 = \Omega_0\left(1 - \frac{i}{q}\right) \tag{1.4.21}$$

$$\delta = \varepsilon_g + \omega - \varepsilon_a. \tag{1.4.22}$$

In the general case where Γ_a is present, ionization may be calculated by,

$$P(t) = 1 - \left|C_g(T)\right|^2 - \left|C_a(T)\right|^2 e^{-\Gamma_a(t-T)} \tag{1.4.23}$$

where T is the interaction time (e.g. the pulse duration). The expression when only photoionization is present is calculated to be,

$$P(t) = 1 - e^{-\Gamma t/2}\left[\left|\hat{s}_+\right|^2 + \frac{\hat{\Delta}^2 + \left|\widehat{\Omega}_0\right|^2}{\left|\hat{\Omega}\right|^2}\left|\hat{s}_-\right|^2 + 2Re\left\{\frac{\hat{\delta}^*\widehat{\Omega}}{\left|\hat{\Omega}\right|^2}\hat{s}_+\hat{s}_-\right\}\right]. \tag{1.4.24}$$

In all the cases below one can check the role of the interaction time (pulse duration), T, in the observed yields in addition to the role of the ionization width γ, Rabi-frequency, Ω_0, and the detuning δ.

1.5. Resonant case $\delta \simeq 0$ and no direct-channel ($\gamma_g = 0$) (strong-field)
In this case all quantities become real and the expression for the amplitudes take a very simple oscillatory form. Since,

$$\Gamma = \gamma_a = \gamma, \quad 1/q = 0, \quad \Omega = \sqrt{4\Omega_0^2 - (\gamma/2)^2} \tag{1.4.25}$$

assuming the strong-field case where $4\Omega_0^2 > (\gamma/2)^2$ one easily can arrive to the expressions,

$$c_g(t) = \frac{2\Omega_0}{\Omega}e^{-\Gamma t/4}sin\left(\frac{\Omega t}{2} + \varphi\right) \tag{1.4.26}$$

$$c_a(t) = i\frac{2\Omega_0}{\Omega}e^{-\Gamma t/4}sin\left(\frac{\Omega t}{2}\right) \tag{1.4.27}$$

with the phase-lag φ defined as, $tan\varphi = \frac{2\Omega}{\gamma}$ ($cos\varphi = \frac{\gamma}{4\Omega_0}$ and $sin\varphi = \frac{\Omega}{2\Omega_0}$) .Note that the phase-lag between the ground and the excited state is determined by the ratio $\frac{\gamma}{\Omega_0}$. In this case the ionization probability is given by,

$$P(t) = 1 - \frac{4\Omega_0^2}{\Omega^2} e^{-\gamma t/2} \left[1 - \frac{\gamma}{4\Omega_0} \cos\left(\Omega t - \varphi\right) \right]. \tag{1.4.28}$$

Therefore, the ionization probability is purely oscillatory with a period determined by the generalized Rabi frequency. In the 'weak'-field case ($4\Omega_0^2 < (\gamma/2)^2$) the results are obtained if one sets $\Omega \rightarrow i\Omega$, and the oscillatory functions become purely exponential.

1.6. Strong and short pulse ($\gamma, \Gamma \ll \Omega_0$ and $\gamma T, \Gamma T \ll 1$)
In this case where both the direct- and the sequential channels are present the following expression for the ionization rate can be derived,
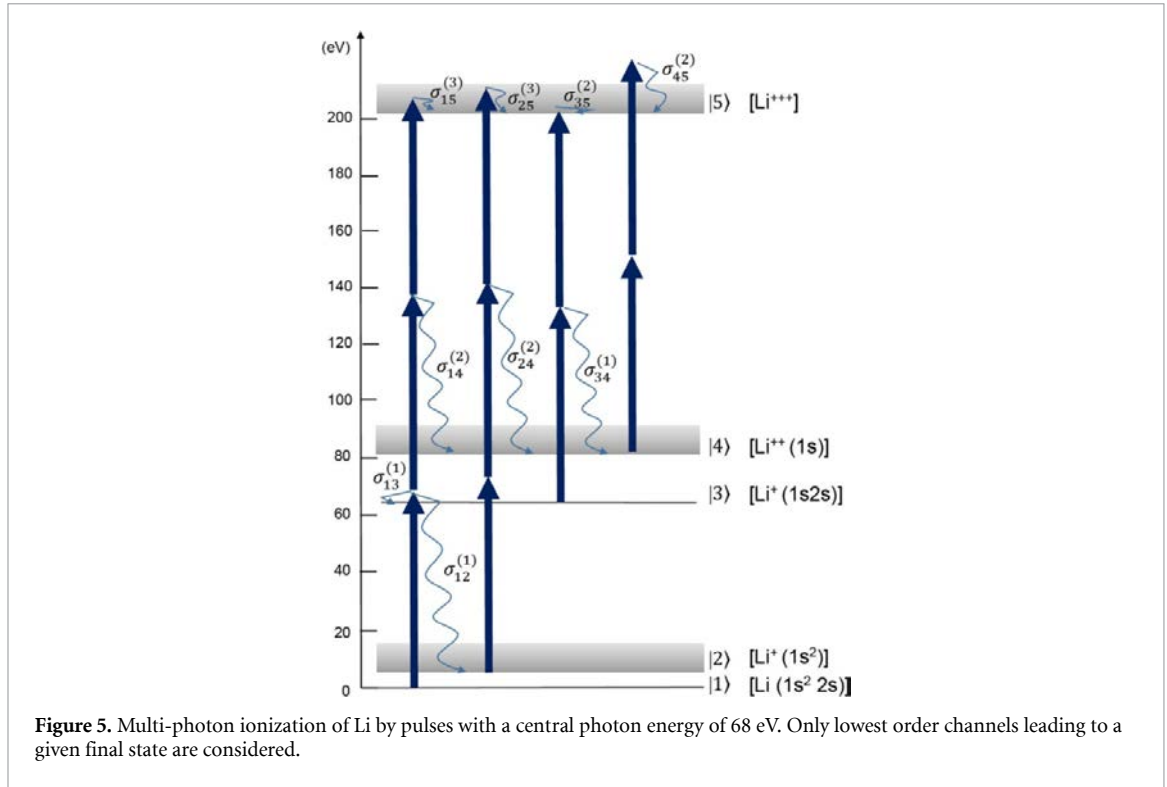
$$\dot{P}(t) \cong \gamma_a \frac{4\Omega_0^2}{\delta^2 + 4\Omega_0^2} sin^2 \Omega\, t + \gamma_g + 2q\gamma_a\gamma_g \frac{\delta}{\delta^2 + \Omega_0^2} sin^2 \,\Omega t. \tag{1.4.29}$$

If the interaction time is much larger than the Rabi's period ($|\Omega|t \gg 1$) then integration of the above time-dependent ionization probability provides an 'average' ionization rate, which resembles a Fano-profile placed on a constant background (of the direct ionization channel).

1.7. MP multiple ionization
When the intensity is sufficiently high multiple ionization may occur involving i) sequential processes where all intermediate charge states get populated and the next charge state is reached through photon absorption by the previous populated charge states, ii) direct processes in which two or more electrons are ejected without formation of the lower charge states and iii) processes populating excited bound or AIS of the ionic stages. Thus, different channels can contribute to the formation of a certain charge state. The temporal evolution of the processes involved can be described through rate equations from which the ionization probability can be evaluated.

At this point, it should be made clear that the most general treatment of the ionization processes should involve the density matrix formulation for all possible states of the combined atom and laser system with both the coherent (relative atomic amplitude's phases are important) and incoherent processes incorporated on an equal footing. Additionally, the density matrix is a statistical approach appropriate not only for pure states but also for mixed states, i.e. ensembles of which we only know their statistical distribution. In this sense the TDSE and the rate equations have a different validity range of parameters, in fact they are placed on opposite sides. When the relative atomic phases are unimportant then one can obtain a simplified model of the ionization process, that of rate equations. In the opposite case, i.e. the case when the relative atomic phases cannot be ignored, the TDSE formulation can be used in order to describe an ionization process; thus it represents the other 'simplified' extreme (treating only pure states and only partially decoherence phenomena) where the relative phases are crucial for the system's dynamics. However, for the latter case TDSE is only nominally a simplified system of 'equations-of-motion' since all the excited (bound and continuum) atomic states in principle should be included. Nevertheless, a simpler form can be obtained under certain conditions involving amplitude equations, of the same type as discussed in the two-level system model earlier. In all of its full generality, the TDSE system can be solved very accurately only for the lighter atomic systems, such as the hydrogen and helium. For all other atomic systems more drastic approximation models are used, especially when multiphoton processes contribute to the excitation and ionization. One may loosely say that the rate equations treat the ionization process in an 'averaged' fashion thus ignoring any phase relationship between the atomic states (bound or excited). The state's population are the main actors in this model. The SVA and the RWA are applied into the TDSE with the additional assumption that the relative phases follow adiabatically the populations of the atomic states. Eventually, the ionization process is described by a single absorption rate, via the (multiphoton) ionization cross section. Therefore, any resonance features are only implicitly incorporated in the values of the cross section for the given field's frequency. This particular approximation gradually loses its meaning as the spectrum of the field broadens (or equivalently the pulse shortens) since the cross sections are, in principle, meaningful quantities only for monochromatic pulses. Hence, one may not hope to fully replicate the results either of a model based on a full density-matrix or TDSE formulation but only to estimate ionization rates for experimental schemes which meet the physical conditions set above. The resulting rate equations have the structure of a system of ordinary differential equations which normally may be calculated without complications. This is the task of the rate equations model as it, very nicely, factorizes the ionization process into its main

Figure 5. Multi-photon ionization of Li by pulses with a central photon energy of 68 eV. Only lowest order channels leading to a given final state are considered.

constituents: the states' population, N_i, the field part via its flux $F(t)$ and their interaction strength through the various cross-sections σ_{ab}. The formidable task is the calculation of the cross sections rather than solving the rate equations. The structure of the rate equations is such that the total rate of the system sums to zero as one should expect from a population-transfer modeling, a model which in other fields is not the exception but the rule e.g. in biology, chemistry, statistics etc. Computationally, the rate equations' approach is by far the less demanding one, followed by the TDSE. The reader interested in a more extensive account of the rate equations ionization model could find it in the classic text by Shore [60].

To give an example of a simple system, assume ionization of Li atoms by a pulse of 1fs duration with central photon energy 68 eV and a peak intensity of 10^{15} W cm^{-2}. The equations of motion for the Li charge states following ionization from the ground state by a pulse with central frequency at 68 eV are given below:

$$Li\left(1s^2 2s\right)\frac{dN_1}{dt} = -\left[\left(\sigma_{12}^{(1)}+\sigma_{13}^{(1)}\right)F(t)+\sigma_{14}^{(2)}F^2(t)+\sigma_{15}^{(3)}F^3(t)\right]N_1 \tag{1.4.30}$$

$$Li^+\left(1s^2\right)\frac{dN_2}{dt} = \sigma_{12}^{(1)}F(t)N_1-\left[\sigma_{24}^{(2)}F^2(t)+\sigma_{25}^{(3)}F^3(t)\right]N_2 \tag{1.4.31}$$

$$Li^+\left(1s2s\right)\frac{dN_3}{dt} = \sigma_{13}^{(1)}F(t)N_1-\sigma_{34}^{(1)}F(t)N_3 \tag{1.4.32}$$

$$Li^{2+}\left(1s\right)\frac{dN_4}{dt} = \sigma_{14}^{(2)}F^2(t)N_1-\sigma_{45}^{(2)}F^2(t)N_4+\sigma_{24}^{((2))}F^2(t)N_2 \tag{1.4.33}$$

$$Li^{3+}\frac{dN_5}{dt} = \sigma_{25}^{(3)}F^3(t)N_2+\sigma_{45}^{(2)}F^2(t)N_4+\sigma_{15}^{((3))}F^2(t)N_1 \tag{1.4.34}$$

where $F(t) = I(t)/\hbar\omega$ is the field's flux and $\sigma_{ij}^{(n)}$ the generalized cross sections for the respective ionization processes. The order of the cross sections is denoted in parenthesis and is equal to the flux's appearance power. The various pathways are depicted in figure 5 while the ionization yields for the given pulse are plotted in figure 6.

It should be noted that, although the channel to the Li$^+$(1s2p) continuum is energetically open through electron-electron correlation, it is much weaker (~15 times weaker than the channel to Li$^+$(1s2 s)) and thus has been neglected. Also, the two-photon ejection of two electrons from the Li$^+$ 1s2 s state (transition $|3\rangle \rightarrow |5\rangle$) has been neglected because this channel is open to only a small part of the bandwidth of the radiation.
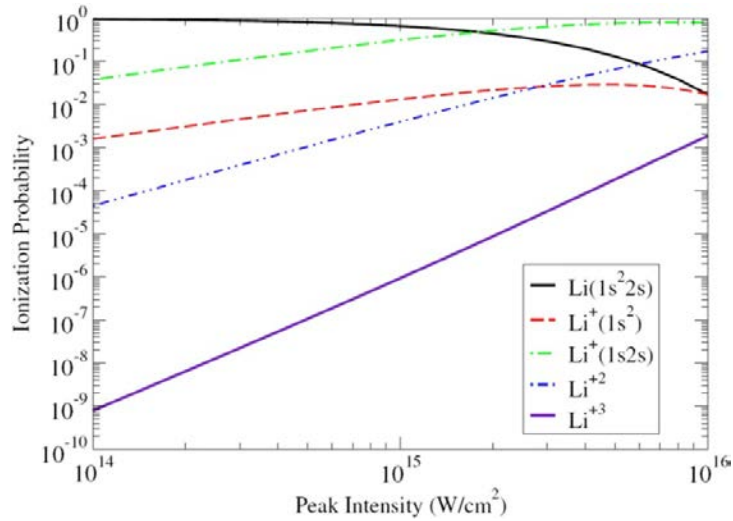
Figure 6. Ionization yields of all Li charge states as a function of the ionizing intensity.

The field's intensity is modelled by $I(t) = I_0 e^{-\left(t/\tau\right)^2}$, where τ is related to the effective pulse duration. The main difficulty in solving the above system of rate equations resides in the calculation of the atomic parameters σ_{ij} since generally several of them have not been yet calculated with a rigorous calculation method. These are then estimated based on scaling properties of atomic systems as well as properties related to the nature of the electromagnetic field interaction. In the present case the following values have been chosen for the calculation of the ionization yields: $\sigma_{12}^{(1)} = 10^{-19} \text{cm}^2$; $\sigma_{13}^{(1)} = 2 \cdot 10^{-18} \text{cm}^2$, $\sigma_{14}^{(2)} = 10^{-53} \text{cm}^4 \text{ s}$; $\sigma_{24}^{(2)} = 10^{-51} \text{cm}^4 \text{ s}$; $\sigma_{35}^{(2)} = 10^{-53} \text{cm}^4 \text{ s}$; $\sigma_{34}^{(1)} = 10^{-19} \text{cm}^2$; $\sigma_{45}^{(2)} = 10^{-53} \text{cm}^4 \text{ s}$; $\sigma_{25}^{(3)} = 10^{-87} \text{cm}^6 \text{s}^2$ and $\sigma_{15}^{(3)} = 10^{-87} \text{cm}^6 \text{s}^2$.

As it is beyond the scope of the present work to describe the calculation details we delegate the interested reader to other more elaborate works for this task [61, 62] (and references therein). A package for the *ab-initio* calculation of one-and two-photon cross sections of two-electron atoms, using a configuration interaction (CI) B-splines method can be found in [63]. There is a large number of publications involving rate equations of two- (or few-) photon ionization. The 'simplest' case is He for which a study in the photon energy range 45–54 eV can be found in e.g. [64]. In case of more complex systems and more photon ionization cases the number of rate equations increases significantly [65].

There are many publicly available packages for numerical calculations in atomic and molecular systems such as, the COWAN package [66], BSR [67], BSPCI2E [63], QPROP [68], RMT [67], and the quantum chemistry packages UKRmol [69] and MOLPRO, to mention a few; but, due to the highly specialized numerical approaches, the codes are mostly developed and used in-house.

The above discussion and parameters concern multi-XUV-photon absorption by an outer shell electron, which are processes that have been realized utilizing initially individual harmonics of laser radiation and later on radiation of FEL sources, as well as laser based attosecond-pulse sources. Apart from sequences of single photon inner-shell absorption processes leading to multiple ionization, two- or more XUV photon absorption by an inner-shell electron has not been demonstrated yet. This is attributed mainly to the lack of the required experimental parameters that would allow such a process to compete with lower linear processes of the outer shell electrons. In order to estimate such experimental parameters, cross sections of two- (or multi-) photon inner-shell ionization are required. Good estimates of two-photon K-shell cross-sections can be calculated for hydrogen-like ions using scaling. For a two-photon ionization (equation 1.4.8) reads

$$\sigma^{(2)} \propto \omega^2 \left| \frac{\sum_{\iota_1} \langle g|\vec{r}\hat{e}|\iota\rangle \langle \iota|\vec{r}\hat{e}|f\rangle + \int d\epsilon \langle g|\vec{r}\hat{e}|\epsilon\rangle \langle \epsilon|\vec{r}\hat{e}|f\rangle}{E_\iota - E_g - \hbar\omega} \right|^2 . \tag{1.4.36}$$

Continuum renormalization $\langle \varepsilon|\varepsilon'\rangle = \delta(E - E')$ results in $|f\rangle$, $|\varepsilon\rangle \propto Z^{-1}$, Z being the charge of the nucleus of the hydrogen-like ion. Thus, the matrix elements and $d\varepsilon$ in (1.4.36) scale with Z like:

$$\langle g|r|i\rangle \propto Z^{-1}, \ \langle i|r|f\rangle \propto Z^{-2}, \ \langle g|r|\epsilon\rangle \propto Z^{-2}, \ \langle \epsilon|r|f\rangle \propto Z^{-3} \tag{1.4.37}$$
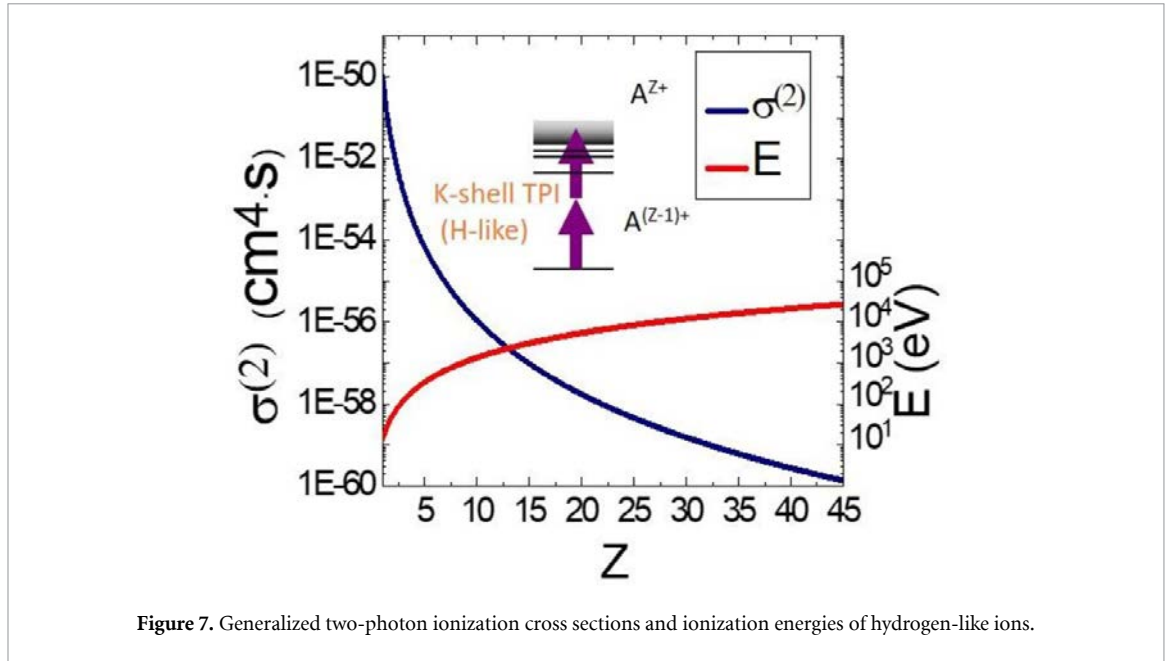
Figure 7. Generalized two-photon ionization cross sections and ionization energies of hydrogen-like ions.

and

$$d\epsilon \propto Z^2. \tag{1.4.38}$$

Hence, the cross section

$$\sigma^{(2)}(Z,\omega) = \frac{1}{Z^6}\sigma^{(2)}\left(Z=1, \frac{\omega}{Z^2}\right) \tag{1.4.39}$$

drops dramatically for heavier ions.

Figure 7 shows the Z dependence of a two-photon K-shell ionization generalized cross section of hydrogen-like ions and the corresponding photon energy threshold at which the two-photon ionization channel opens. Due to the Z^{-6} dependence of the cross section, in order for the two-photon ionization process of the inner shell to compete with the single photon ionization of the outer sell at intensities lower than the ionization saturation intensity, the pulse duration has to be extremely short. To give an example, for Z = 4 (beryllium atom) and photon energy 110 eV, approximating the two-photon K-shell ionization of the atom with that of the hydrogen-like ion of the same Z, the two photon generalized cross section becomes $\sigma^{(2)}{}_K = 5 \cdot 10^{-54}$ cm$^4 \cdot$ s. The L-shell single photon ionization cross section is $\sigma^{(1)}{}_L \sim 10^{-20}$ cm^2. For a pulse duration of 40 asec the two-photon K-shell ionization will become the dominant process at intensities larger than $5 \cdot 10^{16}$ W cm^{-2}, while ionization saturation occurs at $\sim 10^{18}$ W cm^{-2}. Therefore, for a large interval of intensities, ionization will essentially occur via two-photon K-shell absorption.

For a pulse duration of 1 fs, two-photon K-shell ionization becomes comparable to the L-shell single photon ionization just before saturation sets in. It becomes obvious that energetic attosecond pulses are required in order for the process to become observable. For the time being, even for the relative low Z of our example, the parameters discussed are not available in any currently operational XUV source. Nevertheless, they are close to become available in the near future. However, when going to higher Z the parameters become extreme. To give an example, for neon intensities of the order of 10^{20} W cm^{-2} and pulse durations of the order of 10 asec, are necessary.

It is worth noting that (equation 1.4.1) is rigorously valid only if the field is fully coherent i.e. if its quantum state is the coherent sate of light. For any quantum state of light, the ionization probability rate is

$$\frac{dP(t)}{dt} \propto \sigma^{(n)}G^{(n)} \tag{1.4.40}$$

where $G^{(n)}$ is the n-th order intensity correlation function of the field. For the coherent state of light $G^{(n)} \cong \langle N \rangle^n$, N being the photon number and thus (1.4.40) reduces to 1.4. For the chaotic state of light (thermal light) $G^{(n)} \cong n!\langle N \rangle^n$, and for a photon number squeezed state of light $G^{(n)} \cong (2n-1)!!\langle N \rangle^n$ [70–72]. Thus, at first glance and kind of counterintuitively MP ionization by chaotic light is more efficient than by coherent light. However, if one realizes that in chaotic light, the photons are statistically more
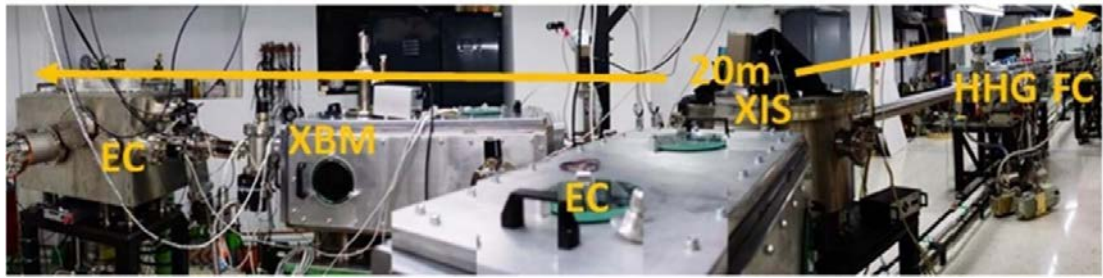
Figure 8. The 20GW HHG beamline of the attosecond science and technology lab of FORTH. EC: Experimental chamber; XBM: XUV Beam Manipulation chamber; XIS: XUV-IR separation chamber; HHG: High Harmonic Generation chamber; FC: Focusing Optics chamber.

'bunched' than those of a coherent light, this observation is of no surprise. This is experimentally verified already in the 70's [73] and recently in a more controllable way [74]. This dependence of the efficiency of MP processes on the quantum state of the light may lead to differences in experiments conducted at FELs and XUV sources based on the process of HHG by lasers [11].

2. Experimental methods for non-linear XUV optics

As stated in the introductory section we address mainly laser-driven tabletop XUV sources. In this section we focus on methods and instrumentation dedicated to the investigation of non-linear XUV processes exploiting such sources. Several of the methods and instrumentation coincides with those used in FEL infrastructures. Methods and instrumentation that are exclusively used in FEL facilities are beyond the scope of this manuscript and thus will not be addressed here.

2.1. High photon-flux laser driven, tabletop XUV sources based on harmonic generation in gas targets
Laser-driven attosecond sources are based on HHG ([20, 21] and references therein). Harmonic generation is a highly non-linear process and consequently its throughput is drastically increased with the driving intensity and more precisely with the order of non-linearity, which is between 4 and 5 [75–77]. As mentioned in section 1.3, the main obstacles in reaching the high XUV photon fluxes, required for inducing non-linear XUV processes in laser based attosecond sources using gas targets as non-linear media are the depletion of the generating medium, the phase mismatch due to plasma formation and the XUV radiation reabsorption by the generating medium itself. Partial mitigation of these limitations, leading to a higher source throughput, is to drive the harmonic generation process using long focal length optical elements to focus the laser in the medium. In this way the cross section of the laser beam in the interaction region increases and thus a higher number of emitters and photons contribute to the generation while ionization remains below saturation.

When a small length medium in comparison to the confocal parameter is used, as is the case when pulsed nozzles are employed, the interaction length remains effectively unchanged when the focal length is increased. When a large length medium, as compared to the confocal parameter is used, as is the case when long cells are used, increasing the focal length will increase the interaction length and the product $L_{abs}N_a$ will became larger than σ. Reabsorption will then prevail. In this case the gas pressure must be decreased such that the product will remain smaller than σ. A detailed investigation of the scaling of the source parameters focal length, laser field and atomic density can be found in [78].

An implementation of large focal length (9 m) gas jet source is the 20 GW XUV beamline of the Attosecond Science and Technology lab of the Foundation for Research and Technology, Hellas (FORTH) (figure 8). Using Xe as harmonic generating medium a maximum XUV pulse energy of the order of 200 μJ in the spectral region 15–30 eV has been demonstrated [11]; more recently a train of pulses with sub-fs pulse durations have been measured [79]. The longest focal length used so far is 17 m at the Max Planck Institute for Quantum Optics. In this beamline using Ne as harmonic generating medium, despite its three orders of magnitude lower conversion efficiency than Xe [80], 40 nJ pulse energies have been achieved in the spectral region 60–130 eV [81].

A similar to FORTH's but more advanced beamline is currently under commissioning at the Extreme Light Infrastructure-Attosecond Light Pulse Source (ELI-ALPS) research infrastructure currently operating at 10 Hz and soon to be operational at 1 kHz repetition rate. Due to the shorter pulse duration of the laser systems at ELI-ALPS a slightly higher pulse energy due to the slightly higher ionization saturation intensity and a significantly higher power is expected. In the same infrastructure a much longer beamline (50 m focal
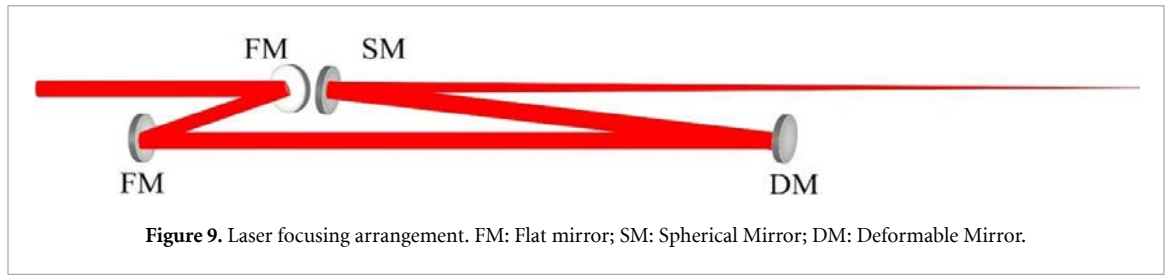
Figure 9. Laser focusing arrangement. FM: Flat mirror; SM: Spherical Mirror; DM: Deformable Mirror.

length) with a series of 15 long gas cells of individually controllable low gas pressure is also under implementation [82].

Due to the relative high IR peak power and short pulse duration used, the focusing of the laser beam occurs through reflective optics. Spherical mirrors of large focal length are a common focusing element. In order to avoid astigmatism introduced by the spherical surface, as small as possible incidence angle has to be used. The phase front of the IR beam in the HHG region can be further improved using of a Deformable Mirror (DM). While a DM is not available in the FORTH beamline, it is used in the ELI-ALPS beamlines. Correcting astigmatism and spatial phase modulations of the IR carrier frequency is important because it improves: i) the focusability of the IR beam and ii) the spatiotemporal properties of the XUV pulses that in turn affect the focusability and pulse duration of the XUV radiation and consequently its intensity. Here spatiotemporal properties refer to spatial wave-front distortions and thus to the overall (non-local) duration of the XUV pulses. A commonly used optical set-up is shown in figure 9. Two parallel flat mirrors introduce a parallel shift of the laser beam such that it bypasses the focusing element steering the beam towards a third flat mirror positioned at furthest long distance possible that reflects the beam towards a focusing spherical mirror at an appropriately small angle of incidence. The long distance between the third flat mirror and the rest of the mirrors is important in order to maintain astigmatism as low as possible. In this arrangement the outgoing beam is propagating in the same direction as the incoming one. In order to achieve best focusability of the laser, its wave-front is often corrected using DMs [83], either in order to directly focus the laser or in combination with another focusing arrangement. DMs allow also varying the position of the focus.

A related approach in improving focusability is to use Bessel-Gauss laser beams that are essentially diffractionless, as demonstrated by Altucci *et al* [84]. Nevertheless, in that work pulses with durations of the order of 100 fs and energies of the order of 100 μJ were used that allowed the use of diffractive optics in forming the Bessel-Gauss beams. For the parameters of the ELI-ALPS (<7 fs, > 100 mJ) relevant laser system lots of development is required toward the formation of such beams with uncertain outcome.

2.2. High photon-flux laser driven, tabletop XUV sources based on harmonic generation in laser-surface plasma

An alternate mitigation measure against the limiting factors in reaching high photon fluxes is the exploitation of non-depleting non-linear media. Such a medium is the laser induced surface plasma and the XUV generating process is high harmonic generation emission by this plasma. Due to the non-depleting non-linear medium, laser fields well in the relativistic regime can be used. During laser-matter interaction the electrons of charge q are driven by the Lorentz force applied by the electric *E* and magnetic *B* field of the radiation according to

$$\vec{F} = q\left(\vec{E} + \left(\frac{\vec{V}}{c} \wedge \vec{B}\right)\right). \tag{2.1}$$

If the velocity of the electrons *v* remains much smaller than the velocity of light *c* ($v \ll c$), the magnetic term can be neglected and the electron motion in a linearly polarized field reduces to a harmonic oscillation. For velocities comparable with the light velocity, the action of the magnetic term sets in, introducing a force component along the light propagation direction within the plasma, resulting into a negative-positive charge separation underlying laser particle acceleration and harmonic generation processes. A quantity defined by the wavelength λ and the field amplitude E_0 or the vector potential A_0 that distinguishes between relativistic and non-relativistic interactions is the so-called normalized vector potential

$$\alpha_L = \frac{eA_0}{mc^2} = \frac{eE_0\lambda}{mc^2}. \tag{2.2}$$

For $\alpha_L < 1$ the interaction is non-relativistic, while for $\alpha_L > 1$ is essentially relativistic. For a driving laser with central wavelength $\lambda = 800$ nm α_L becomes unity for an intensity of the order of 10^{18} W cm^{-2}. Thus, at this
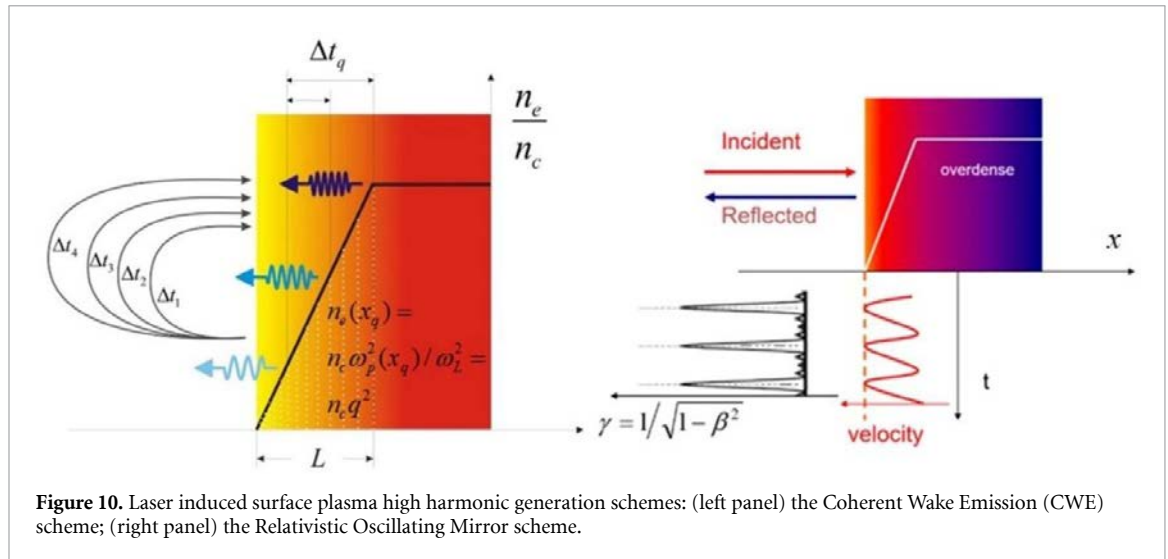
Figure 10. Laser induced surface plasma high harmonic generation schemes: (left panel) the Coherent Wake Emission (CWE) scheme; (right panel) the Relativistic Oscillating Mirror scheme.

wavelength, the relativistic regime is reached for intensities higher than 10^{18} W cm^{-2}. However, for longer wavelengths, i.e. wavelength in the mid-IR or far-IR spectral region, the relativistic regime is reached as much lower intensities. E.g. at $\lambda = 12$ μm α_L becomes unity already at intensities $\sim 5 \cdot 10^{15}$ W cm^{-2}, which introduces a new area of applications of new intense mid-IR and far-IR laser sources.

In the sub-relativistic regime the harmonics are produced through the so called Coherent Wake Emission process [85, 86] (figure 10, left panel). Electrons emerging from the plasma gradient are accelerated in the vacuum driven by the field, and upon sign reversal of the field are returned to the plasma exciting a plasma wave that due to the multi-cycle driving field emits harmonics. The emitted frequency is the plasma frequency $\omega_p(x_q)$, x being the axis perpendicular to the surface, and the index q denotes the corresponding harmonic. $\omega_p(x_q)$ relates to the plasma electron density and the harmonic order as $n_e\left(x_q\right) = n_c \frac{\omega_p^2(x_q)}{\omega_L^2} = n_c q^2$, n_c being the critical plasma density. Hence the emitted radiation has a spectral chirp and the shorter the emitted wavelength the deeper point in the plasma it is emitted from [87]. When the solid density is reached no shorter wavelengths can be emitted and thus the harmonic spectrum depicts a cut-off. Due to the different time the electrons spend in the vacuum when emitting different wavelengths, the emitted XUV radiation has a temporal chirp.

As α_L increases beyond 1 the relativistic interaction effects start to play a more dominant role [88]. The laser drives an overdense plasma such that there is charge separation. The electrons are moving under the interaction with the E and B fields of the laser as well as under the restoring force. Ions are considered to remain essentially at rest due to their much larger than the electron mass. The resulting motion is a non-harmonic periodic motion of the electron-vacuum interface that reaches in short time intervals velocities close to the velocity of light. This motion generates the so called γ spikes, γ being the Lorenz factor $\gamma = \sqrt{\frac{1}{1-\frac{v^2}{c^2}}} = \sqrt{\frac{1}{1-\beta^2}}$ (figure 10, right panel). The incoming laser radiation is reflected by the fast moving plasma surface and thus its wavelength is Doppler shifted by the generating γ spikes towards very short wavelengths. The processes often referred to as Relativistic Oscillating Mirror have been extensively studied both theoretically and experimentally [2, 86, 89–93]. Through laser surface plasma harmonic generation emission of keV photons [94], XUV pulse energies at the source of 40μJ [95], and sub-fs duration XUV pulse trains have been reported [96]. The collective nature of the plasma medium, the diversity of the laser-plasma parameter space, and a variety of potential geometrical irradiation configurations give rise to a large degree of freedom in tuning the generation process from high harmonic XUV [97, 98] down to the THz [99] domain. This also necessitates appropriate control of the interaction in order to achieve optimal HHG conditions, setting state of the art technological demands [100]. The main of those are high laser peak power, high laser peak to background contrast, elimination of unwanted laser pre-pulses, demanding 'cleaning' procedures of the laser pulse through additional plasma mirrors, control of the plasma density gradient [101], micrometer accurate positioning of the tight focus on the target, sensitive alignment of the tightly focusing element commonly an off axis parabola and debris management. An optimal implementation rests on developing a robust method that efficiently balances all these sensitive parameters. Laser surface plasma harmonic generation holds the promise of delivering unprecedented pulse energies of short wavelength radiation with ultra-short pulse duration [102] and has also been proposed as a potential candidate in achieving super high intensities [103, 104] for probing vacuum quantum electrodynamic effects with

Figure 11. Reflectivity of five metal coatings for an angle of incidence of 88 deg.
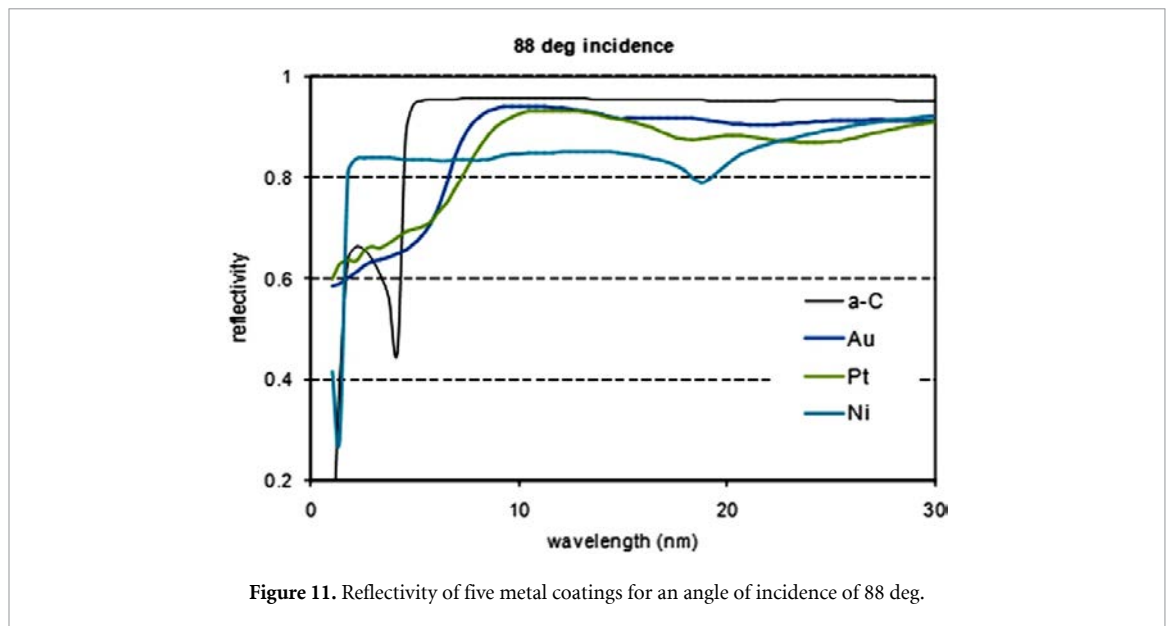
currently available lasers. Nonetheless, gas target HHG sources, based on well-established and less challenging technologies, have for the time being more advanced operational parameters such as pulse energies and pulse durations compared to current laser surface plasma harmonic generation sources.

2.3. XUV optical elements for high photon-flux laser driven, XUV/attosecond sources

The photon flux and power that reaches the area where the XUV radiation interacts with the system under investigation in an experimental attosecond beamline is notably reduced due to reflections from the steering optics in the beamline.

Obviously only reflective optical elements can be used as refractive materials absorb the XUV radiation. For low XUV photon energies 10–30 eV close to normal incidence metal (commonly Au) coated optics can be used supporting the large bandwidth of the XUV radiation. Normal incidence, which in many cases is more convenient to use, is also possible exploiting multilayer mirrors. The drawback in this case is that the more broadband a multilayer mirror is, the higher the losses it introduces. For the spectral regions not covered by multilayer mirrors and/or ultra-broadband optics, grazing incidence geometries and metal coated reflectors are used. Figure 11 shows the wavelength reflectivity dependence of several metal coatings for an 88° angle of incidence. Reflectivity of the order of 90% is feasible using grazing incidence geometries. Nevertheless, positioning and alignment of optical elements at grazing incidence is a highly sensitive and tedious procedure.

From the optics' field point of view, a further challenge when HHG sources are used to induce non-linear XUV processes is the separation of the unwanted IR laser beam from the XUV radiation. Thin filters transmitting the XUV and absorbing the IR cannot be directly used because they would be destroyed by the strong IR radiation. They can only be used for selection of the desired spectral region and for blocking any residual IR radiation, after the IR photon flux has been substantially reduced. The reduction of the flux can be achieved by the use of Si plates.

A Si surface placed at the Brewster angle of the p-polarized IR beam (75° for radiation of 800 nm) strongly absorbs the IR field and efficiently reflects the XUV radiation. Figure 12 depicts the reflectivity of 800 nm and 50 nm radiation as a function of incidence angle for s and p polarizations. At 75° there is a strong suppression of the IR while the reflectivity of the XUV exceeds 90%.

For high average power IR laser sources [82] absorption of the IR may modify the surface due to thermal effects. In this case IR transmitting materials, like grazing incidence multilayer based antireflections coatings can be used. Such elements can also provide XUV reflectivity > 70% at photon energies > 40 eV.

Another IR suppression approach is the use of annular driving laser beams. Due to the non-linearity of the HHG process, at specific phase-matching conditions, the XUV propagates with smaller divergence than the IR radiation. Driving the non-linear medium with an annular beam formed using a circular beam stop at the center of the IR beam, one can achieve that, after the generation of the harmonics, the XUV beam propagates in a small angle cone, while the IR propagation is essentially outside this cone and thus can be blocked using an aperture. The XUV propagates through the aperture, while the IR is stopped by it. Any residual IR radiation inside the XUV beam can now be absorbed by thin metal filters that also select the XUV
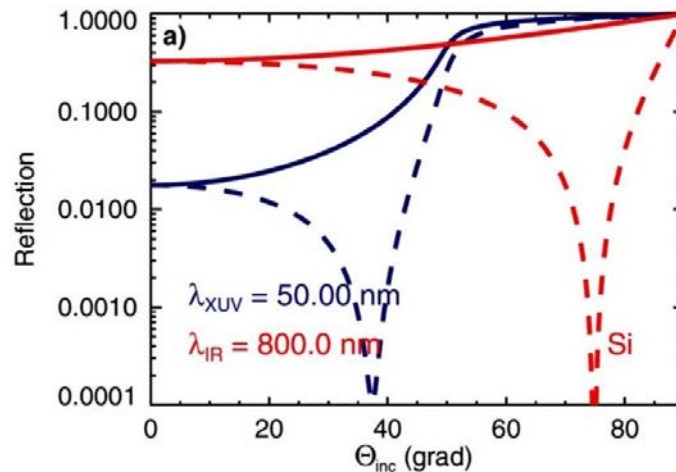
Figure 12. Reflectivity of Si as a function of angle of incidence for radiation of 800 and 50 nm. The dash line is the reflectivity of the p-polarization and the solid line that of the s-polarization.

spectral region of interest. Annular beams are also very useful when the IR radiation is not exclusively p-polarized, as is the case when polarization gating is used [105, 106].

In reaching high XUV intensities tight focusing of the XUV radiation is required. Close to normal incidence spherical mirrors, metal coated or multilayer whenever satisfying the requirements of the experiment is the most convenient approach. When spherical reflecting surfaces cannot be used because of large losses in photon number or low quality focal areas, reflection at grazing incidence on focusing surfaces other than spherical is the alternative that is commonly used. Ellipsoidal surfaces [107] are able to focus to the smallest focal spots positioning the XUV source in the one of the ellipse focus and obtaining the XUV focus at the second focus of the ellipse. Since in this case grazing incidence is needed, large ellipsoidal surfaces have to be used with high surface flatness which is a technological challenge. Moreover, aligning the ellipsoidal such that minimal focal spots are reached is a tedious procedure. An approximation of the ellipsoidal surface is a toroidal one which is a very common focusing surface employed in the XUV spectral region [108]. Today set-ups consisting of two toroidal mirrors are commercially available. The first mirror focuses and the second one corrects focusing errors [109]. Another optical arrangement that is used in XUV and x-ray radiation laboratories is the so called Kirkpatrick-Baez (KB) [110] mirror arrangement that uses two focusing surfaces (often spherical ones) where one is focusing horizontally and the other vertically. KB systems are of variable focal length by varying the distance between the two focusing elements [111].

2.4. Attosecond delay lines and non-linear autocorrelators

The absence of refractive optics suitable for the XUV spectral region (due to the immediate absorption of XUV radiation upon propagation in any material), introduces a challenge in time domain applications of non-linear XUV processes like in non-linear autocorrelation (AC) measurements and studies of ultra-fast dynamics. XUV delay-lines cannot use Michelson interferometers, as commonly used in the IR, visible, and x-ray spectral regions, owing to the lack of appropriate transmission-reflection beam-splitters. An XUV Michelson interferometer proposed and demonstrated in the UV uses a diffraction grating as the beam splitter. The principle of the interferometer/delay-line is shown in figure 13. The XUV beam is split in two different diffraction orders (0,1), the diffracted beams are reflected by XUV mirrors and are recombined at the grating through diffraction in the appropriate orders (1,0). Modeling of such a spectrometer has demonstrated dispersionless operation in the attosecond regime [112]. Using such an interferometer a second order AC measurement of UV pulses was performed [113] demonstrating the applicability of the device. In these works, the grating considered or used was a transmission grating. Transmission gratings offer the advantage of having a flat spectral response up to the wavelengths where their material becomes transparent. However, they have the drawback of low diffraction power, which, in the case of double diffraction, as in figure 11, results in a 1% throughput. At the photon fluxes of attosecond XUV beam-lines available today, such a throughput hardly allows the observation of non-linear XUV processes. Furthermore, XUV transmission gratings have to be free standing gratings and they cannot be easily fabricated; moreover, they are sensitive to high average power.
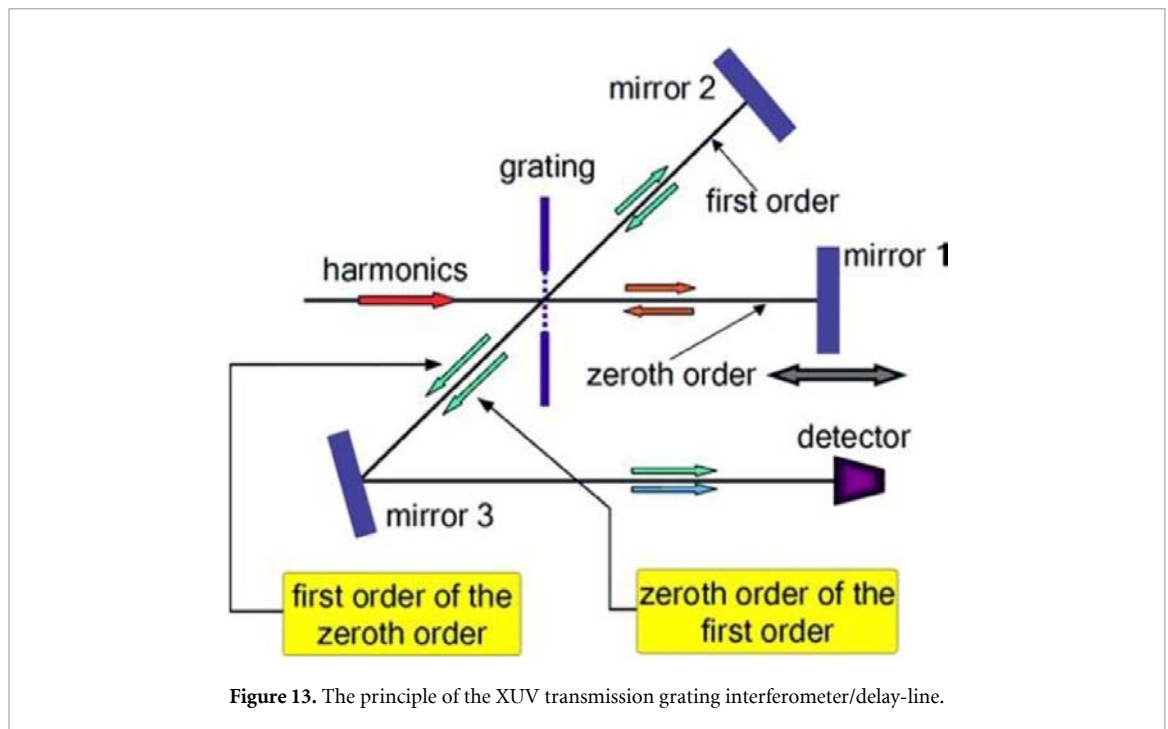
Figure 13. The principle of the XUV transmission grating interferometer/delay-line.

Using XUV reflection gratings substantially higher throughputs may be achieved [114], but the diffraction power becomes wavelength dependent affecting the bandwidth and thus the duration of the XUV pulses. Nevertheless XUV reflection gratings are successfully used in time compensation XUV monochromators [115–119].
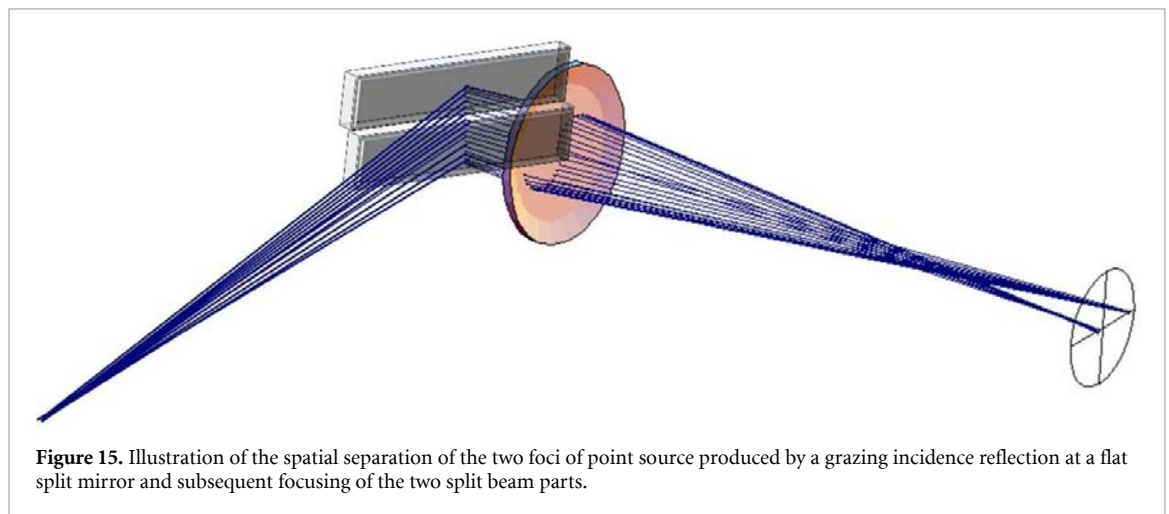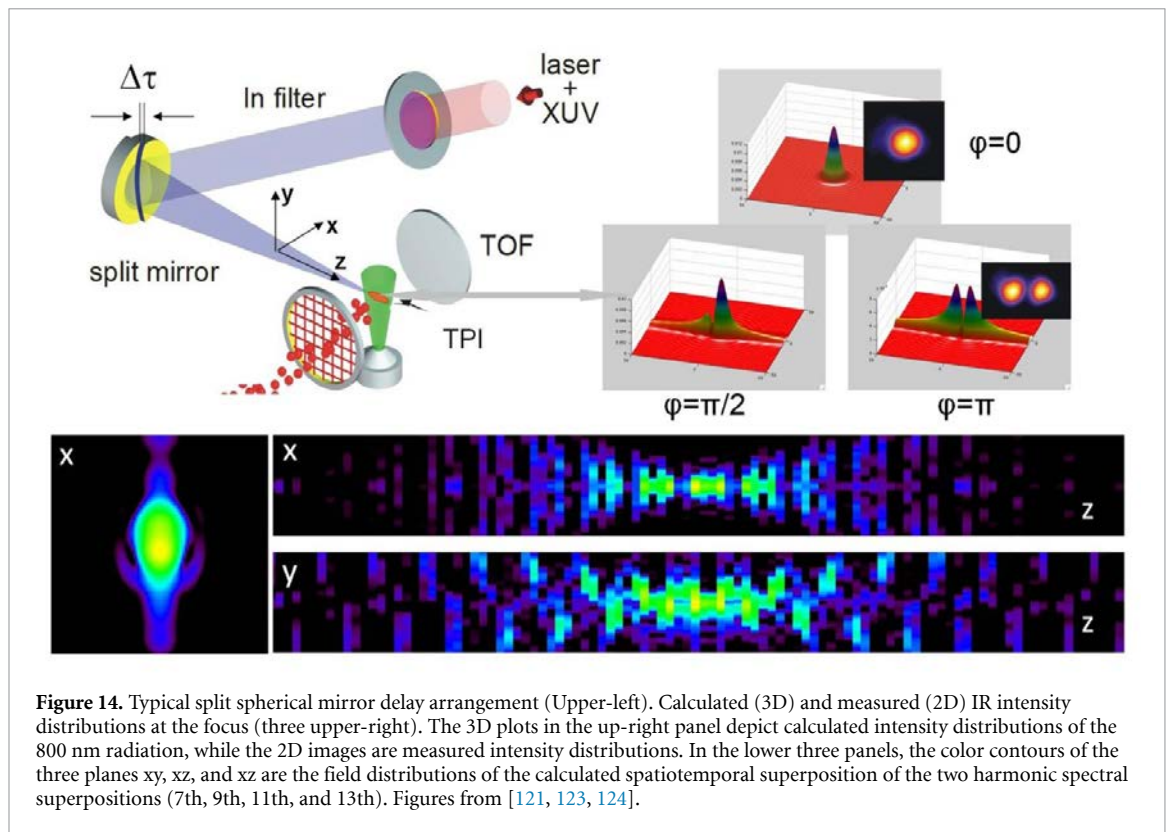
The most frequently used set-ups in introducing XUV/attosecond pulse delays are split reflective optical elements [120], one part of which is translated with nm accuracy through piezoelectric translation stages. The split and delay device is not an interferometer as it does not have two arms between which the energy is oscillating with the delay. It is a wave front divider, splitting the beam in two halves, with the one half being delayed in time with respect to the other with attosecond accuracy through the piezoelectric translation. Assuming cylindrical symmetry of the impinging XUV beam the reflected parts are considered to be close to identical. Unless there is spatial selection of part of the out-coming beam, this device cannot produce a first order interferogram by varying the delay. This is because, and in order for energy to be conserved, the spatially integrated out-going beam remains constant due to the lack of second arm. Nevertheless if the two overlapping parts of the beam are inducing a second or higher order process, the yield of this process is delay dependent and thus can be used for the temporal characterization of the XUV pulses [121] as well as in XUV-pump-XUV-probe experiments [106, 122]. Different types of split-delay set ups are used today. In some of them the split optical element is a spherical mirror that produces the two mutually delayed pulses and at the same time focuses the XUV radiation in the interaction area of the study.

Incidence to split spherical mirrors has to be close to normal for keeping astigmatism as low as possible. Metal coated split spherical mirrors can be used for photon energies < 30 eV. Multilayer spherical mirrors are also available for specific spectral regions with the limitations of reflecting power for broadband XUV radiation discussed in section 2.2. A representative set-up of such a spherical mirror split and delay unit is shown in figure 14 (upper left panel). A thin metal filter selects the XUV spectral region, the XUV radiation is then impinging on the split spherical mirrors at effectively normal incidence and is subsequently focused in a gas jet that is ionized and the ionization products are measured with a Time of Flight (TOF) spectrometer. The intensity distribution at the focus of the fundamental wavelength (800 nm) for different delays, corresponding to a phase difference between the two pulses of 0, $\pi/2$ and π, is shown in figure 14 (upper right panels).

The field distribution of a superposition of harmonics, produced by the spatiotemporal overlap of the two XUV parts at the focus for a delay of $T_L/4$ (bottom panel of figure 14), is shown in the lower color contour panels, with T_L being the period of the IR laser. Alternatively, split flat reflectors are used at grazing incidence and an additional optical element or optical system is used also at grazing incidence for focusing.

A limiting factor, when split optical elements are used, is the spatial separation (introduced by the translation of one of the two mirror parts) of the two foci in the overlapping region. This separation may lead to a non-negligible departure from the spatial overlap of the two beams that would distort the results of

Figure 14. Typical split spherical mirror delay arrangement (Upper-left). Calculated (3D) and measured (2D) IR intensity distributions at the focus (three upper-right). The 3D plots in the up-right panel depict calculated intensity distributions of the 800 nm radiation, while the 2D images are measured intensity distributions. In the lower three panels, the color contours of the three planes xy, xz, and xz are the field distributions of the calculated spatiotemporal superposition of the two harmonic spectral superpositions (7th, 9th, 11th, and 13th). Figures from [121, 123, 124].

Figure 15. Illustration of the spatial separation of the two foci of point source produced by a grazing incidence reflection at a flat split mirror and subsequent focusing of the two split beam parts.

the measurement. For close to normal incidence on split spherical mirrors, the delay induced displacement of the two parts of the mirror, does not affect the results for delays up to 200 fs [123]. Thus, such geometries can be safely used, without corrections, in measuring from attosecond to few hundreds of fs dynamics and/or pulse durations. The situation changes drastically when using grazing incidence geometries. Even small delays may introduce a spatial separation of the two foci.

The effect is illustrated in figure 15 for a flat split mirror in a grazing incidence geometry. It has been shown [108] that for a specific focusing arrangement, delays of tens of fs may introduce a spatial separation of the two foci larger than the focal spot itself and thus corrective actions are required. Such a problem can be solved by means of an optical feedback system [109].

The above described split and delay devices cover the entire VUV-XUV spectral regions. Apart from the above discussed set-ups a Mach-Zender type of split and delay device has been developed and used at FLASH [125]. Proposals for single shot non-linear split and delay devices can be found in the literature [126]

2.5. Diagnostics and detection systems

Prerequisites in achieving sufficiently high XUV intensities for non-linear XUV applications that have been addressed in the previous sections are high pulse energy, short pulse duration and XUV radiation with minimum wave-front distortions. The pulse duration in the above described high XUV power beamlines is measured through the 2nd order intensity volume autocorrelation technique (2nd IVAC) [121] utilizing the split spherical mirror delay line described in the previous section and two-XUV-photon ionization as non-linear process detecting the resulting ions as a function of the delay. Due to the high XUV intensities available in these beamlines the 2nd IVAC technique could be used instead of RABBITT based temporal characterization approaches used in low intensity sources. The pulse energy in [11] was measured using calibrated XUV photodiodes that are commonly used in XUV pulse energy determination.

Alternatively, a method to measure on-line the intensity of the XUV pulse uses a gas ionization detector [127, 128], i.e. an absolutely calibrated detector based on photoionization of noble gases at a low target density and detecting photoions and photoelectrons. The number of electrons/ions generated is proportional to the number of photons, to the target density, to the photoionization cross-section and to the length of the interaction volume. Some advantages of this method are: 1) it is almost transparent to the beam and does not alter the beam properties and thus ideal for on-line measurements; 2) it has a wide dynamic range; 3) it is independent from the beam position; and 4) it can be absolutely calibrated with $\approx 10\%$ accuracy.

In determining the XUV intensity at its focus, where the non-linear XUV processes are studied, the XUV beam waist dimensions are needed. Realistic dimensions can be estimated assuming Gaussian distributions. An advanced direct method for measuring the XUV intensity distribution at its focal area is based on an ion imaging device, known as ion microscope, which measures spatially resolved ion distributions with a spatial resolution of 1 μm. If the ions are produced through single-photon ionization, the measured spatial ion distribution is identical to the XUV spatial distribution due to the linearity of the ionization process. This device that essentially measures 2D spatial distributions of different ionic charge states with variable magnification is extensively presented in [129–131]. XUV intensity beam profiles are measured either by an XUV beam profiler [11] or through the knife edge technique. The focusability of the XUV beam however depends on the wavefront of the XUV beam. Recently a single shot XUV Hartmann sensor has been developed and used in wavefront measurements of high-order harmonics [132].

In addition to the diagnostics of the XUV beam that are addressed in the previous paragraph, alternative methods in detecting the products of the non-linear XUV processes will be summarized in this section. The so far deducted products are ions in different charge stages [11, 111, 133]. The non-linearity of the process is usually deduced from the slope of the dependence of the ion yield on the XUV intensity (in log-log scale) or by measuring photoelectron spectra [134]. The former is achieved by varying the energy of the XUV radiation in the HHG area. When measuring the ion yield dependence as a function of the XUV intensity, the generalized MP ionization cross sections can be extracted from the ionization saturation intensities (see section 1.4) without knowledge of the atomic density in the interaction area. However, due to the volume effect (section 1.4) the determination of the saturation intensity becomes ambiguous, particularly in two-photon ionization processes where the expected slope of 2 is not easily distinguishable from the slope of 3/2 appearing due to the volume effect after saturation. This obstacle can be overcome by measuring spatially resolved ion yields from confined areas in which the radiation intensity is effectively constant.

In the 90's 3D confinement of the area from which ions where detected was achieved through a "four grid reflectron Time of Flight ion mass spectrometer (TOF) [135–137]. The principle of such a measurement is illustrated in figure 16. The blue cube depicts the confined volume for which ions are measured. 2D confinement is realized through an aperture of the second electrode in the ion extraction area of the TOF. Confinement in the third dimension (along the acceleration axis of the ions) is through the four-grid-reflectron. Ions that are exiting the extraction area, are passing through the central hole of the MCP detector (MCPs detector with a central hole) and enter the four-grid-reflectron configuration. The voltage between the second and the third grid in the four-grid-reflectron arrangement gives an additional acceleration to the ions entering the area between these two electrodes. Ions generated on the right of the blue cube area see lower voltage and are less accelerated, thus are reflected between the 1st and 2nd grid of the reflectron (red-trajectory). Ions generated on the left of the blue cube are experiencing the highest acceleration and thus penetrate through all four grids (blue trajectory).

Ions produced within the confined area (blue cube) are passing through the first, second and third grid and are reflected between the third and the fourth ones getting an additional acceleration between grid 2 and 3, i.e. are reaching the MCP detector at earlier times than those produced on the right of the blue cube (green trajectory). The mass peak is split into two corresponding to the two groups of ions. If the volume of the cube is sufficiently small, ionization in it can be fully saturated free of volume effects. This is illustrated in the mass spectra shown in the lower panel of figure 16 and measured at two different intensities. The 'fast' peak
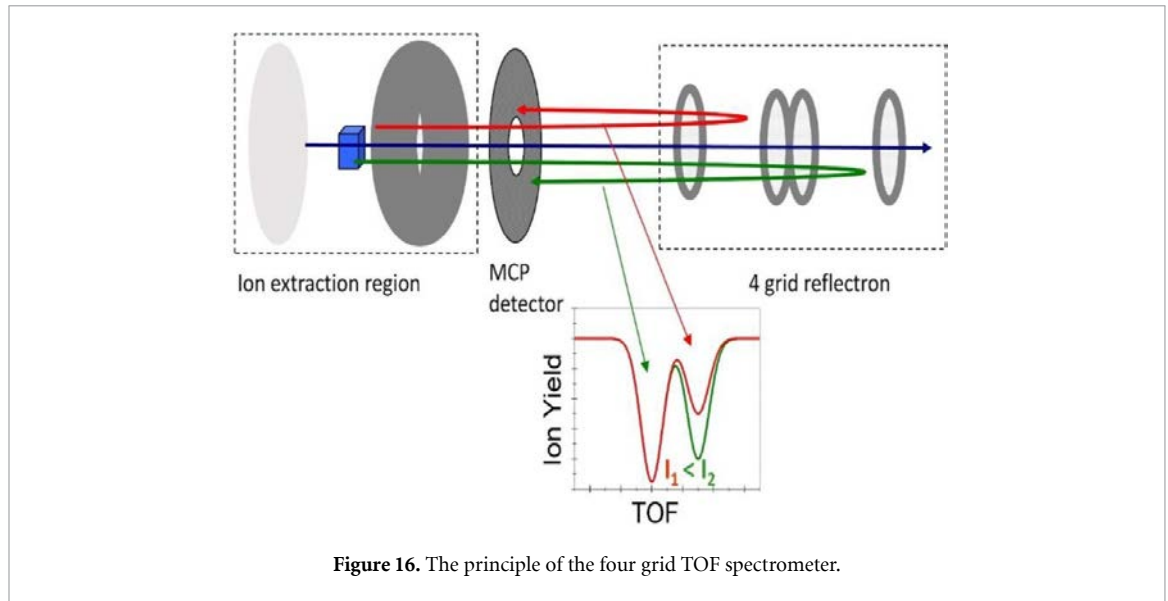
Figure 16. The principle of the four grid TOF spectrometer.
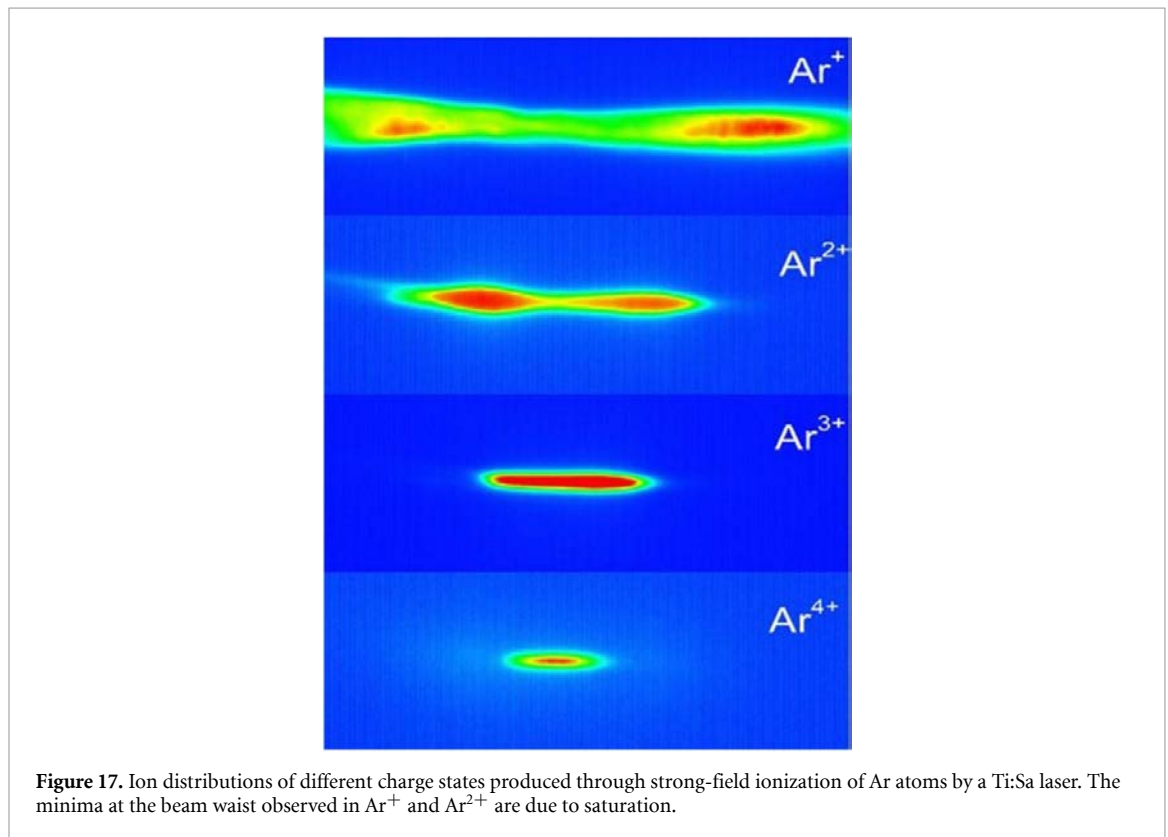
Figure 17. Ion distributions of different charge states produced through strong-field ionization of Ar atoms by a Ti:Sa laser. The minima at the beam waist observed in Ar^+ and Ar^{2+} are due to saturation.

has the same height at both intensities because of saturation, while the 'slow' one increases at the higher intensity (I_2) due to volume effects.

An advanced version of measuring volume-effect-free MP ionization is using the previously mentioned ion microscope [129–131]. Here the spatial imaging provides the confinement. Figure 17 shows images of distributions of different ionic charge states produced at the focus of a Ti:Sa laser beam. Saturation of ionization is clearly seen in the distributions of Ar^+ and Ar^{2+} for which around the beam waist, where the intensity is higher, the number of ions drops due to saturation and formation of higher charge states through ionization of Ar^+ and Ar^{2+}. Details can be found in [131].

An alternative method for the extraction of saturation intensities and hence generalized MP cross-sections is based on the measurement of ponderomotive shifts as a function of the ionizing intensity observed in photoelectron spectra. The saturation intensity is essentially the intensity at which the shift is

saturating. This method has been applied in multi-UV-photon ionization of atoms [138, 139] and it can be extended to the XUV spectral region at high intensity XUV sources [11].

Studies of multi-XUV-photon processes measuring absorption of XUV photons have not been performed so far because absorption in MP processes is a very weak effect. However, recent works [140, 141] indicate that such measurements (e.g. transient absorption measurements) might be feasible. Also, ion and electron spectra so far deal with measurements of total yields. However, ion signals are meanwhile high enough to allow electron/ion imaging methods i.e. measuring angular distributions of products.

Finally, coincidence measurements of products of multi-XUV-photon ionization have not yet been performed because high peak power XUV/attosecond sources so far were low repetition rate (10 Hz) sources, leading to data statistics that are prohibitive for coincidence measurements free of false coincidences. However, new developments of high repetition rate XUV sources (laser based like ELI-ALPS and FELs like Linac Coherent Light Source-LCLS) hold the promise of studies of non-linear XUV processes through coincidence techniques. For such measurements the simplest device, allowing measurement of total yields of products in coincidence, is a time-of-flight spectrometer with time gated repelling voltage. In this way electrons move and reach the detector in a field free environment, while ions remain in the interaction area essentially not moving, and after electrons are detected the ion acceleration voltage is switched on producing the ion mass TOF spectrum. Thus, is the same measured trace, the first part is the electron spectrum and the second one the ion mass spectrum. Keeping the counting rate in single event detection mode, low enough true coincidences may become dominant. This technique has been applied in the first coincidence measurements of strong-field ionization [140, 143]. The most advanced device for electron-ion coincidence measurements is the Reaction Microscope (ReMi) or Cold Target Recoil Ion Momentum Spectroscopy that uses two spectrometers equipped with position sensitive detectors commonly delay detection line detectors [144, 145] detecting electrons and ions respectively. The device, in combination with data analysis packages, allows the measurement of the three-dimensional momentum vector of a recoiling target ion with high resolution and 4π solid angle of detection for kinematically complete or close to complete studies. Such devices are foreseen as end-stations in the ELI-ALPS research infrastructure for XUV-pump-XUV-probe coincidence experiments at 1 kHz repetition rate.

## 3. Applications of non-linear XUV processes

The first applications of non-linear XUV processes trace back around year 2000. Those include pioneering work completed with individual harmonics in the few tens of fs temporal regime, including atomic two- [22], three- [146] and four- [147] XUV-photon ionization, two-XUV-photon double ionization [148, 149] as well as the corresponding 2nd [22] and 4th order AC measurements [147], two-XUV-photon Above Threshold Ionization (ATI) [150] (i.e. the processes in which one photon absorption ionizes the atom and the ejected electron absorbs an additional photon undergoing a continuum-continuum transition) and a FROG based-XUV pulse reconstruction [151] .

Non-linear XUV applications with a superposition of harmonics, eventually forming attosecond pulse trains, made their debut with the observation of two-photon ionization of He atoms by a superposition of the 7th to the 13th harmonic of a Ti:sapphire laser [111]. The non-linearity of the process was evidenced by the measured slope of the dependence of the ion yield on the ionization XUV radiation intensity in log-log scale. This result was later verified measuring the frequency resolved photoelectron spectra resulting from the same process and comparing it with *ab initio* calculations solving the TDSE of He interacting with the superposition of the four harmonics [134].

Two-XUV-photon double ionization of rare gases by an attosecond pulse train was demonstrated in ionization schemes where the sequential double ionization processes is a three-photon processes (one photon absorption ionizes the atom and absorption of two further photons ionizes the ion) leading to double ionization while the direct one is a two-photon process (absorption of two photons ejects two electrons without intermediate formation of a singly ionized atom) and thus prevails [133]. These works have established the feasibility of non-linear XUV processes induced by laser driven HHG sources. Using advanced detection approaches spatially resolved two-XUV-photon ionization of He by the superposition of harmonics 11–15 was measured exploiting the capabilities of the ion-microscope device [130]. In the work of ref. 129 the generalized two-photon ionization cross section was extracted from one solely measured spatial ion distribution. The main results of this experiment are summarized in figure 18.

More recently multiple multi-XUV-photon processes have been demonstrated in the ionization of Ar [11] and Ne [79] by intense XUV pulses of the 10 GW class harmonic source of FORTH.

Higher non-linearity processes in the XUV and x-ray spectral regions have been observed in FEL infrastructures. Highlighting selected examples: i) formation of very high charge stages of Xe (up to Xe^{21+}) has been demonstrated at the 93 eV photon energy at FLASH and the dependence of the charge state yield on
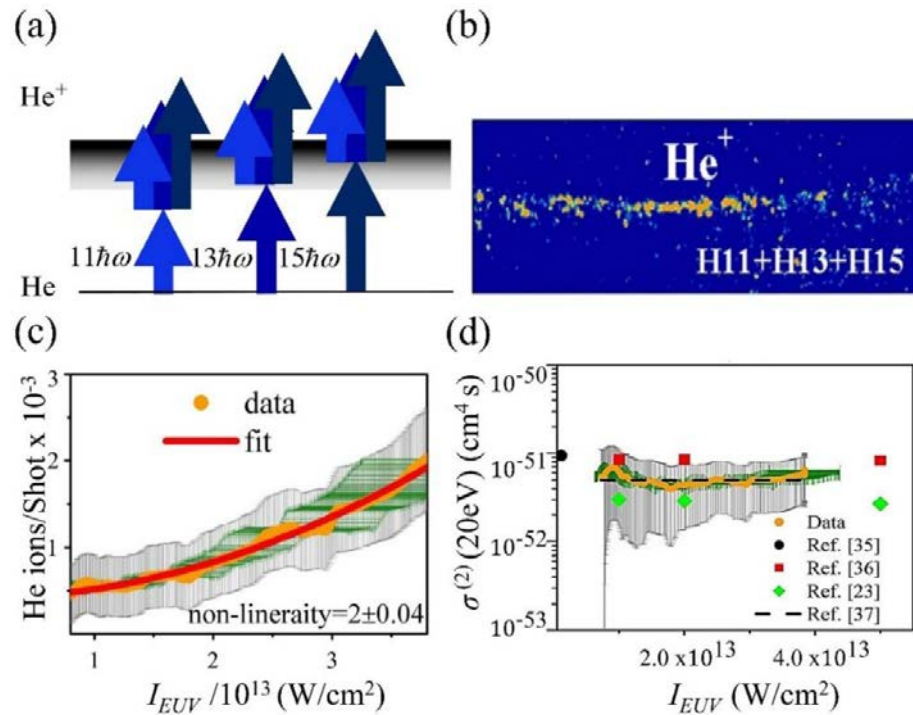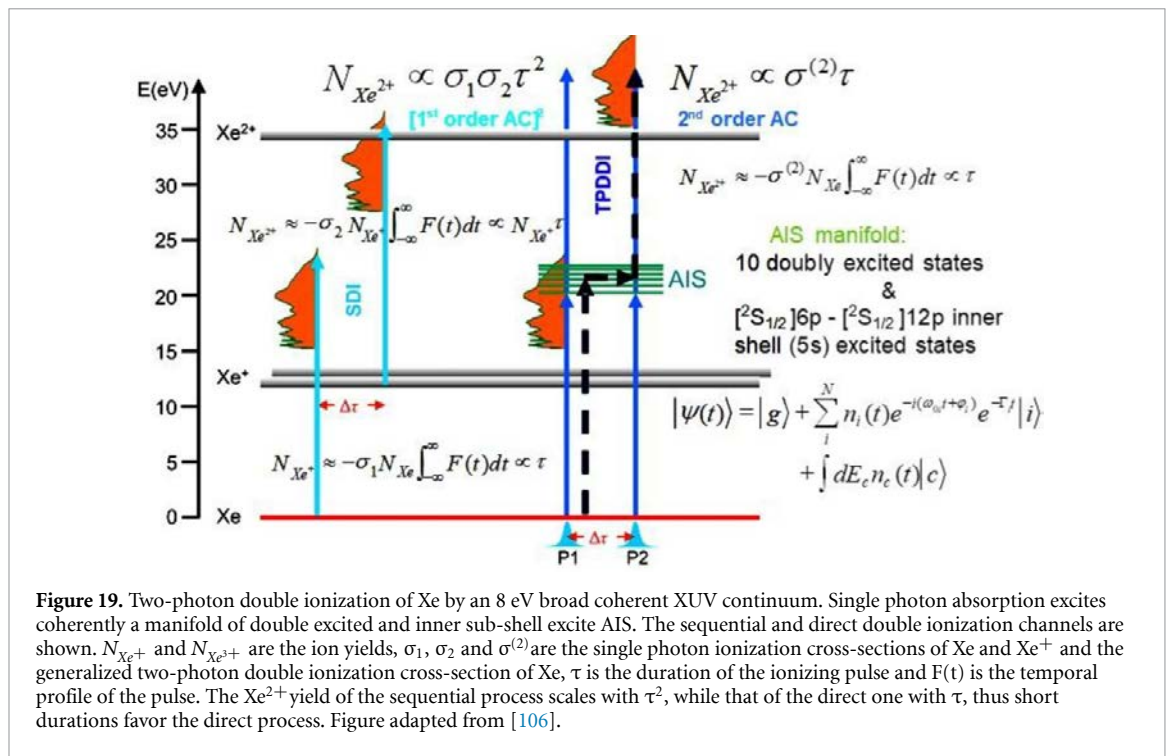
Figure 18. (a) Spatially resolved two-photon ionization of He by a superposition of harmonics 11–15 using an ion microscope. (b) Ionization scheme. Measured spatial He ion distribution at the focus of the XUV beam. (c) Ion yield as a function of the intensity of the harmonic radiation. Measured data are in orange, the red line is a polynomial fit, while the green and gray shadowed areas are the experimental error bars for the number of He$^+$ per shot and the XUV intensity, respectively. (d) Measured generalized two-photon ionization cross-section as a function of intensity (yellow line) compared to measured (green rhombus), calculated values (red squares, black points) and estimated values (dash line). The green and gray shadowed area are the experimental error bars for the cross section and the XUV intensity, respectively. Figure taken from [130].

the XUV intensity (up to ~8 · 10^{15} W cm^{-2}) has been measured [152] and interpreted through numerical calculations [65]. The formation of the high charge states is through sequential ionization processes, each of which involves absorption of a large number of photons; ii) 'coring' and 'pealing' ionization of Ne atoms with photon energies 0.8–2 KeV was demonstrated at LCLS [153]; iii) Formation of Ne^{9+} through two-x-ray-photon ionization of Ne^{8+} ground state and a high-order sequential process involving single-photon production and ionization of transient excited states on a time scale faster than the Auger decay was studied at LCLS [154]; iv) multiple sequential multi-x-ray-ionization of Xe (up to Xe^{36+}) with 80 fs pulses with 2.4–2.6 mJ pulse energy and 1.5 and 2 keV photon energies was demonstrated and x-ray peak fluence dependencies of the ion yields where measured and calculated at LCLS [155]; while v) similar studies have been performed in Xe sequential multiple ionization by 5.5 keV photons and 47 μJ/μm^2 peak fluence at the Spring-8 Angstrom Compact Free-Electron Laser (SACLA) [156]; vi) two color phase control of ionization was demonstrated at the FERMI FEL, using its fundamental (19.7 eV) and second harmonic (39.4 eV) and varying their relative phase. Quantum interference of single-photon (second harmonic) and two-photon (fundamental) ionization pathways results in phase dependent and thus phase controlled angularly resolved photoelectron yields [157], and vii) two x-ray photon non-sequential absorption of solid targets detecting K-shell fluorescence was reported from SACLA [158, 159].

Investigation of dynamics using pump-probe schemes can optimally be performed exploiting non-linear XUV/x-ray processes. The vast majority of dynamics measured using HHG sources have been performed using hybrid XUV/IR schemes that are beyond the scope of this work as they do not involve any non-linear XUV processes. Hybrid x-ray/optical (see for example [160, 161]) and UV/x-ray (see, for example [162, 163]) pump-probe schemes have been also used in FEL infrastructures and will not be addressed here. x-ray pump-probe studies of picosecond scale dynamics in biological samples have been recently studied in FEL infrastructures (see for example [164]), while the fastest dynamics measured in FEL sources are from the AMO community and are in the 10 fs temporal scale. Those include ultrafast isomerization studies [165] or hetero-site-specific intramolecular dynamics [166].

Experimental investigation of shorter time scales has been conducted exploiting XUV non-linear processes induced by laser driven XUV radiation sources. Thus, two-photon ionization has been used in

Figure 19. Two-photon double ionization of Xe by an 8 eV broad coherent XUV continuum. Single photon absorption excites coherently a manifold of double excited and inner sub-shell excite AIS. The sequential and direct double ionization channels are shown. N_{Xe+} and $N_{Xe^{3+}}$ are the ion yields, σ_1, σ_2 and $\sigma^{(2)}$ are the single photon ionization cross-sections of Xe and Xe$^+$ and the generalized two-photon double ionization cross-section of Xe, τ is the duration of the ionizing pulse and F(t) is the temporal profile of the pulse. The Xe^{2+} yield of the sequential process scales with τ^2, while that of the direct one with τ, thus short durations favor the direct process. Figure adapted from [106].

performing attosecond pulse train duration measurements via the 2nd IVAC technique discussed in section 2.4. The technique has been applied for the temporal characterization of attosecond trains emitted by the interaction of fs laser pulses with gas targets [121] but also in demonstrating phase locking in CWE surface plasma harmonics forming a *sub-fs* XUV pulse train [95]. In the domain of pulse metrology energy resolved second order AC measurements have also been achieved [167] constituting a step towards pure XUV FROG measurements, while interferometric second order AC traces have been measured in the same year by the same team [168] showing an alternating double to triple peak structure in the trace corresponding to a harmonic field phase change of π between successive peaks that originates from the electron trajectories that are ejected in opposite directions every half laser cycle.

Apart from pulse metrology there have been two works of pure XUV-pump-XUV-probe studies of atomic and molecular dynamics in the 1 fs temporal scale. In both experiments a gold coated split spherical mirror was used as an XUV delay line. In the first one a coherent superposition of AIS of Xe is excited by an 8 eV broad coherent XUV continuum generated through polarization gating of many cycle laser pulses [106, 169], while a second delayed XUV pulse is doubly ionizing the Xe atoms. The ionization scheme, including the sequential and the direct double ionization channel is shown in figure 19 together with the expressions giving the ion yields of the step involved in the two channels. In the work of [106] it was shown that the dominant double ionization process is the direct one. This is because i) the ionizing pulses have ultra-short pulse duration that favours the direct process due to its linear dependence on the pulse duration, in contrast to the quadratic one of the sequential process and ii) the sequential ionization process is mainly a three-photon process and only the tail of the spectrum ionizes sequentially through two-photon absorption.

The dominance of the direct process was verified by the fact that the sequential process would result (in the temporal trace produced by the two mutually delayed XUV pulses) to the square of a first order AC function because each of the steps results a first order AC function, while the direct process results a second order AC function. The width of the square of a first order AC trace is the coherence time of the radiation that can be found through a Fourier transform of the spectrum. The width of a second order AC trace of a Gaussian profile is the pulse duration times the square root of 2. Since the measured temporal width of the trace around zero delay was found much larger than the coherence time of the radiation it was concluded that the direct process is the dominant one.

The measured trace is shown in figure 20. The fast oscillations at longer delays originate from the oscillatory dynamics of the electron wave packet of the coherent superposition of the AIS. The peak around zero delay relates to the pulse duration which though could not be extracted, because the laser carrier-envelope phase (CEP) was not stabilized and thus averaging over several laser pulses creates an overlap of traces produced by single and double pulses, depending on the CEP.
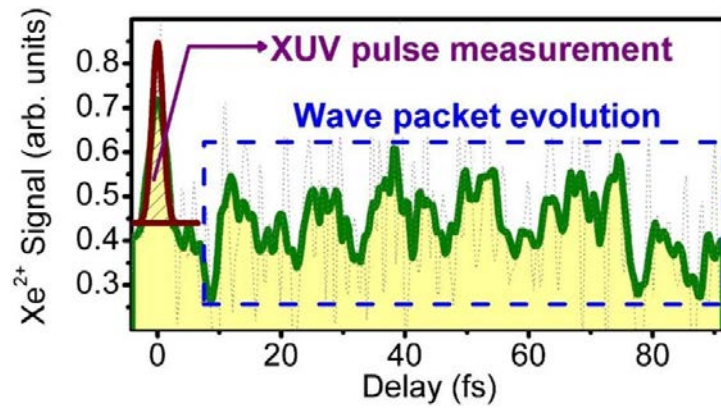
Figure 20. Measured temporal trace. The maximum around zero delay relates to the ionizing pulse duration while the oscillatory part of the trace relates to the temporal evolution of the coherently excited AIS manifold. Figure taken from [106].
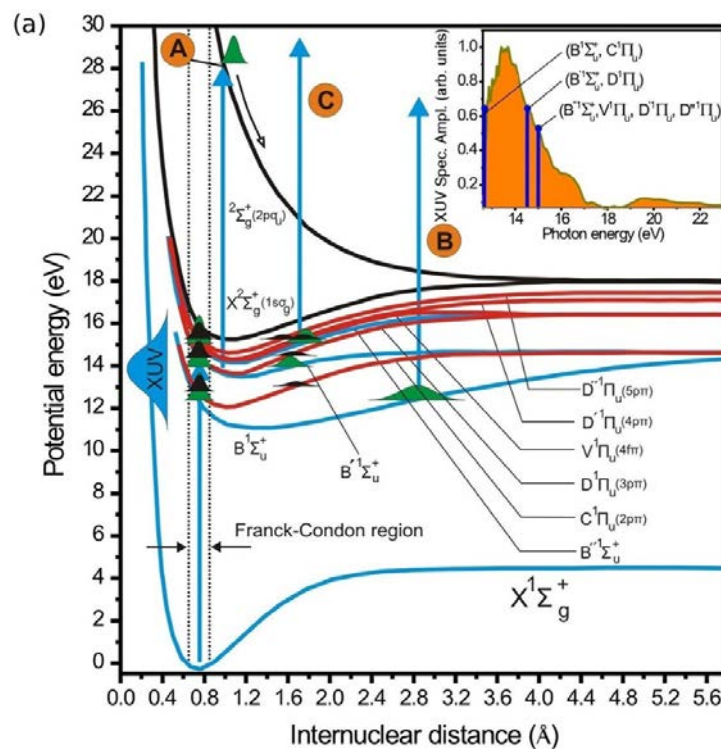
Figure 21. Two-photon dissociative ionization scheme of H_2 by broad coherent XUV continuum radiation. The XUV-pump-XUV-probe measurement reveals dissociative ionization, electron and vibrational wavepacket dynamics. The inset shows the bandwidth of the XUV radiation used and the excited intermediate electronic states of the neutral molecule. Figure taken from [122].

A second XUV-pump-XUV-probe experiment at 1 fs time scale was performed in molecular hydrogen [122]. The ionization scheme is shown in figure 21. One photon absorption from a broad coherent XUV continuum excites coherently all the electric dipole allowed electronic bound states of H_2 that are within the Franck-Condon region creating a superposition of electronic and vibrational wave packets (rotational wave packets are not considered here because of their much slower dynamics). A second delayed pulse is ionizing the molecule in the electronic ground state of the ion. After ~1fs the molecule is stretched such that the channel to the dissociative ionization continuum $^2\Sigma_g^+(2p\sigma_u)$(repulsive potential) is opened (Process A in figures 21). B and C in figure 22 refer to the vibrational dynamics in the $B'^1\Sigma_u^+$ (B) and $C^1\Pi_u/B'^1\Sigma_u^+/D^1\Pi_u$ (C) intermediate electronic states of the neutral molecule. The opening of the dissociative ionization channel after ~1 fs was revealed in the measured trace as at zero delay a minimum was observed in the proton yield and this yield is maximized after approximately 1 fs. Vibrational wavepacket dynamics where observed at longer delays. One measured pump-probe trace and its Fourier around 1fs reveals the opening of the channel. The high peak in the Fourier transform (blue curve) corresponds to the vibrational wavepacket
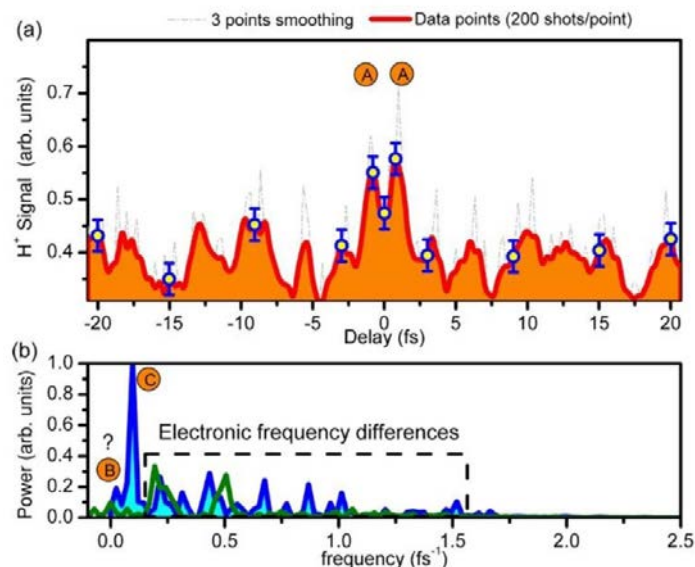
Figure 22. (a) Measured XUV-pump-XUV-probe trace and (b) its Fourier transform. Figure taken from [122].

dynamics in the state, while the high frequency peaks are potentially electronic coherences but their low intensity did not allow a firm assignment.

The experimental conditions under which the XUV-pump-XUV-probe experiments reported so far have the following two disadvantages. First, the many cycle high peak power driving laser pulses were not CEP stabilized. This prohibits the evaluation of the pulse duration of the XUV pulses and reduces the contrast of the oscillatory features of the measured coherences in the temporal trace. CEP tagging is one approach that overcomes this disadvantage; however, no such experiments have been reported so far. The second disadvantage is the low repetition rate (10 Hz) of the laser used, as few tens of mJ pulse energies at higher repetition rates have been only very recently developed. The low repetition rate in turn prohibits coincidence measurements between interaction products (electron–electron, electron-ion, ion-ion) keeping important details of the investigation hidden.

Very recent developments in laser technologies effectively eliminate both shortcomings. Indeed, CEP stabilized multi-10mJ laser systems are becoming available commercially. One such system, the so called SYLOS 2 A system, is already installed at the ELI-ALPS Research Infrastructure. This system is planned to drive two gas targets and one solid target HOHG generation beamlines. The CEP stabilization together with the expected high XUV photon flux of these attosecond beamlines and the availability of advanced experimental end-stations for coincidence measurements enable rigorous attosecond pulse metrology approaches and kinematically complete experiments utilizing non-linear XUV optics at attosecond temporal resolution.

4. Conclusions

Non-linear XUV/x-ray optics made their debut in the beginning of the century. Such processes are central in the investigation of ultrafast dynamics through pump-probe approaches as well as in ultrashort pulse metrology. Since the XUV/x-ray spectral region supports ultrashort pulse synthesis down to the attosecond regime, multi-XUV/x-ray photon processes offer a highly valuable tool in the study of sub-fs dynamics, such as electron dynamics in all states of matter. Moreover, these spectral regions give access to inner-shell dynamics and, eventually, side selective investigation, providing high spatial resolution. Since their debut continuous efforts in source and related instrumentation development have generated notable scientific results and have stimulated new theoretical challenges. While the first non-linear processes have been demonstrated in the XUV spectral region by individual harmonics of fs laser radiation, soon it became feasible to induce them by a superposition of harmonics as well as by coherent continua, thus enabling studies with sub-fs temporal resolution. Few years later FEL sources emitting x-ray pulses with unprecedented photon fluxes gave access to inner-shell investigations and induced highly non-linear processes. In the first 20 years of non-linear processes, laser based harmonic sources and FEL sources played a complementary role, harmonic sources serving the XUV spectral region at the highest temporal resolution

and FEL sources offering unique brilliance in the x-ray and hard x-ray spectral region. Today the sub-fs regime is becoming available at FEL sources and harmonic sources enter the x-ray regime, still the highest temporal resolution of the order of 100 asec is being a feature of harmonic sources, while highest peak power of the order of 100 GW in the x-ray region remains a unique feature of FEL sources. Open technology challenges, where substantial progress was made lately, are the reduction of jitter in pump—probe set-ups, beam pointing stability, CEP stabilization and high repetition rate in high peak-power laser systems. These developments together with innovative imaging and coincidence diagnostic tools boost the capabilities of non-linear XUV/x-ray optics, foreshadowing optimal perspectives for advanced studies of structural dynamics in gas, liquid and condensed phase with highest ever spatio-temporal resolution. In this work we have reviewed non-linear XUV/x-ray processes with emphasis to those induced by laser driven sources, those being our main expertise component in this topic.

Acknowledgments

ORCID iDs

I Liontos ⓘ https://orcid.org/0000-0003-0195-0123
E Skantzakis ⓘ https://orcid.org/0000-0003-3896-9856
B Major ⓘ https://orcid.org/0000-0001-5981-340X
S Kahaly ⓘ https://orcid.org/0000-0001-7600-3310
K Varju ⓘ https://orcid.org/0000-0001-6577-7417
L A A Nikolopoulos ⓘ https://orcid.org/0000-0002-5996-5400
D Charalambidis ⓘ https://orcid.org/0000-0002-6468-5868

References

[1] Seddon E A *et al* 2017 *Rep. Prog. Phys.* **80** 115901
[2] Jahn O *et al* 2019 *Optica* **6** 280
[3] Duris J *et al* 2020 *Nat. Photon.* **14** 30–36
[4] Maroju P *et al* 2020 Nature **578** 386–91
[5] Landau L D, Lifšic E M, Landau L D, Lifshits E M, Sykes J B and Bell J S 1977 *Quantum Mechanics: Non-relativistic Theory//Non-relativistic Theory* ed L D Landau and E M Lifshitz 3rd edn (Oxford: Butterworth-Heinemann) vol 3
[6] Keldysh L V 1965 *Sov. Phys. JETP* **20** 1307–14
[7] Lambropoulos P 1985 *Phys. Rev. Lett.* **55** 2141–4
[8] Müller H-G and Fedorov M V 1996 *Super-intense Laser-atom Physics IV (NATO ASI Series. 3, High Technology)* vol 3 (Dordrecht: Kluwer Academic)
[9] Agostini P and Dimauro L F 2012 Atomic and molecular ionization dynamics in strong laser fields: from optical to x-rays *Advances in Atomic, Molecular, and Optical Physics* ed P R Berman *et al* (New York: Academic) vol 61 pp 117–58
[10] Ott C *et al* 2019 *Phys. Rev. Lett.* **123** 163201
[11] Nayak A *et al* 2018 *Phys. Rev. A* **98** 66
[12] Abel M J, Pfeifer T, Nagel P M, Boutu W, Bell M J, Steiner C P, Neumark D M and Leone S R 2009 *Chem. Phys.* **366** 9–14
[13] Altucci C *et al* 2010 *Opt. Lett.* **35** 2798–800
[14] Coster D and Kronig R D L 1935 *Physica* **2** 13–24
[15] McPherson A, Gibson G, Jara H, Johann U, Luk T S, McIntyre I A, Boyer K and Rhodes C K 1987 *J. Opt. Soc. Am.* B **4** 595
[16] Ferray M, L'huillier A, Li X F, Lompre L A, Mainfray G and Manus C 1988 *J. Phys. B: At. Mol. Opt. Phys.* **21** L31-35
[17] Göppert-Mayer M 1931 *Ann. Phys.* **401** 273–94
[18] Voronov G S and Delone N B 1965 *JETP Lett.* **1** 66–8
[19] Voronov G S, Delone G A and Delone N B 1966 *JETP Lett.* **3** 313
[20] Chatziathanasiou S, Kahaly S, Skantzakis E, Sansone G, Lopez-Martens R, Haessler S, Varju K, Tsakiris G, Charalambidis D and Tzallas P 2017 *Photonics* **4** 26
[21] Nayak A *et al* 2019 *Phys. Rep.* **833** 1–52

[22] Kobayashi Y, Sekikawa T, Nabekawa Y and Watanabe S 1998 *Opt. Lett.* **23** 64
[23] Trebino R 2000 *Frequency-Resolved Optical Gating: The Measurement of Ultrashort Laser Pulses* (New York: Springer)
[24] Carpeggiani P *et al* 2017 *Nat. Photon.* **11** 383–9
[25] Iaconis C and Walmsley I A 1998 *Opt. Lett.* **23** 792–4
[26] Paul P M, Toma E S, Breger P, Mullot G, Auge F, Balcou P, Muller H G and Agostini P 2001 *Science* **292** 1689–92
[27] Mairesse Y and Quéré F 2005 *Phys. Rev. A* **71** 803
[28] Chini M, Gilbertson S, Khan S D and Chang Z 2010 *Opt. Express* **18** 13006–16
[29] Spanner M, Bertrand J B and Villeneuve D M 2016 *Phys. Rev. A* **94** 023825
[30] Eckle P, Smolarski M, Schlup P, Biegert J, Staudte A, Schöffler M, Muller H G, Dörner R and Keller U 2008 *Nat. Phys.* **4** 565–70
[31] Pedatzur O *et al* 2019 *Nat. Photon.* **13** 91–95
[32] Constant E, Taranukhin V D, Stolow A and Corkum P B 1997 *Phys. Rev. A* **56** 3870–8
[33] Orfanos I, Makos I, Liontos I, Skantzakis E, Förg B, Charalambidis D and Tzallas P 2019 *APL Photon.* **4** 80901
[34] Kruse J E, Tzallas P, Skantzakis E, Kalpouzos C, Tsakiris G D and Charalambidis D 2010 *Phys. Rev. A* **82** 021402(R)
[35] Gruson V *et al* 2016 *Science* **354** 734–8
[36] Drescher M, Hentschel M, Kienberger R, Uiberacker M, Yakovlev V, Scrinzi A, Westerwalbesloh T, Kleineberg U, Heinzmann U and Krausz F 2002 *Nature* **419** 803–7
[37] Uiberacker M *et al* 2007 *Nature* **446** 627–32
[38] Goulielmakis E *et al* 2004 *Science* **305** 1267–9
[39] Itatani J, Levesque J, Zeidler D, Niikura H, Pépin H, Kieffer J C, Corkum P B and Villeneuve D M 2004 *Nature* **432** 867–71
[40] Haessler S *et al* 2010 *Nat. Phys.* **6** 200–6
[41] Cavalieri A L *et al* 2007 *Nature* **449** 1029–32
[42] Huppert M, Jordan I, Baykusheva D, von Conta A and Wörner H J 2016 *Phys. Rev. Lett.* **117** 93001
[43] Biswas S *et al* 2020 *Nat. Phys.* **16** 778–83
[44] Goulielmakis E *et al* 2010 *Nature* **466** 739–43
[45] Calegari F *et al* 2014 *Science* **346** 336–9
[46] Kraus P M *et al* 2015 *Science* **350** 790–5
[47] Beaulieu S *et al* 2017 *Science* **358** 1288–94
[48] Palacios A, González-Castrillo A and Martín F 2014 *Proc. Natl Acad. Sci. USA* **111** 3973–8
[49] Skantzakis E, Tzallas P, Kruse J E, Kalpouzos C, Faucher O, Tsakiris G D and Charalambidis D 2010 *Phys. Rev. Lett.* **105** 43902
[50] Eramo R, Cavalieri S, Corsi C, Liontos I and Bellini M 2011 *Phys. Rev. Lett.* **106** 213003
[51] Dreissen L S, Roth C, Gründeman E L, Krauth J J, Favier M and Eikema K S E 2019 *Phys. Rev. Lett.* **123** 143001
[52] Palacios A, Horner D A, Rescigno T N and McCurdy C W 2010 *J. Phys. B: At. Mol. Opt. Phys.* **43** 194003
[53] Kurka M *et al* 2009 *J. Phys. B: At. Mol. Opt. Phys.* **42** 141002
[54] Kurka M *et al* 2010 *New J. Phys.* **12** 73035
[55] Karule E 1971 *J. Phys. B: At. Mol. Phys.* **4** L67-L70
[56] Lambropoulos P and Tang X 1987 *J. Opt. Soc. Am. B* **4** 821
[57] Madsen L B and Lambropoulos P 1999 *Phys. Rev. A* **59** 4574–9
[58] Allen L and Eberly J H 1975 *Monographs and Texts in Physics and Astronomy* (New York: Wiley)
[59] Beers B L and Armstrong L 1975 *Phys. Rev. A* **12** 2447–54
[60] Shore B W 1990 *The Theory of Coherent Atomic Excitation* (New York: Wiley)
[61] Hanks W, Costello J and Nikolopoulos L 2017 *Appl. Sci.* **7** 294
[62] Emmanouilidou A, Hakobyan V and Lambropoulos P 2013 *J. Phys. B: At. Mol. Opt. Phys.* **46** 111001
[63] Nikolopoulos L A A 2003 *Comput. Phys. Commun.* **150** 140–65
[64] Nakajima T and Nikolopoulos L A A 2002 *Phys. Rev. A* **66** 64
[65] Makris M G, Lambropoulos P and Mihelic A 2009 *Phys. Rev. Lett.* **102** 33002
[66] Cowan R D 1981 *The Theory of Atomic Structure and Spectra (Los Alamos Series in Basic and Applied Sciences)* (Berkeley, CA: University of California Press)
[67] Brown A C, Armstrong G S J, Benda J, Clarke D D A, Wragg J, Hamilton K R, Mašín Z, Gorfinkiel J D and van der Hart H W 2020 *Comput. Phys. Commun.* **250** 107062
[68] Tulsky V and Bauer D 2020 *Comput. Phys. Commun.* **251** 107098
[69] Mašín Z, Benda J, Gorfinkiel J D, Harvey A G and Tennyson J 2020 *Comput. Phys. Commun.* **249** 107092
[70] Lambropoulos P 1976 Topics on multiphoton processes in atoms *Advances in Atomic and Molecular Physics*, ed D R Bates and B Bederson (New York: Academic) pp 87–164
[71] Georges A T and Lambropoulos P 1979 *Phys. Rev. A* **20** 991–1004
[72] Nikolopoulos G M and Lambropoulos P 2012 *Phys. Rev. A* **86** 033420
[73] Lecompte C, Mainfray G, Manus C and Sanchez F 1974 *Phys. Rev. Lett.* **32** 265–8
[74] Spasibko K Y, Kopylov D A, Krutyanskiy V L, Murzina T V, Leuchs G and Chekhova M V 2017 *Phys. Rev. Lett.* **119** 223603
[75] Wahlstroem C-G, Larsson J, Persson A, Starczewski T, Svanberg S, Salières P, Balcou P and L'Huillier A 1993 *Phys. Rev. A* **48** 4709–20
[76] Quintard L *et al* 2019 *Sci. Adv.* **5** eaau7175
[77] Chatziathanasiou S, Kahaly S, Charalambidis D, Tzallas P and Skantzakis E 2019 *Opt. Express* **27** 9733
[78] Heyl C M *et al* 2016 *Optica* **3** 75
[79] Makos I *et al* 2020 *Sci. Rep.* **10** 3759
[80] Hergott J-F, Kovacev M, Merdji H, Hubert C, Mairesse Y, Jean E, Breger P, Agostini P, Carré B and Salières P 2002 *Phys. Rev. A* **66** 021801(R)
[81] Rivas D E *et al* 2018 *Optica* **5** 1283
[82] Kühn S *et al* 2017 *J. Phys. B: At. Mol. Opt. Phys.* **50** 132002
[83] Villoresi P, Bonora S, Pascolini M, Poletto L, Tondello G, Vozzi C, Nisoli M, Sansone G, Stagira S and de Silvestri S 2004 *Opt. Lett.* **29** 207–9
[84] Altucci C, Bruzzese R, D'Antuoni D, de Lisio C and Solimeno S 2000 *J. Opt. Soc. Am. B* **17** 34
[85] Quéré F, Thaury C, Monot P, Dobosz S, Martin P, Geindre J-P and Audebert P 2006 *Phys. Rev. Lett.* **96** 125004
[86] Thaury C *et al* 2007 *Nat. Phys.* **3** 424–9
[87] Malvache A, Borot A, Quéré F and Lopez-Martens R 2013 *Phys. Rev. E* **87** 035101

[88] Vincenti H, Monchocé S, Kahaly S, Bonnaud G, Martin P and Quéré F 2014 *Nat. Commun.* **5** 3403
[89] Dromey B *et al* 2007 *Phys. Rev. Lett.* **99** 85001
[90] Baeva T, Gordienko S and Pukhov A 2006 *Phys. Rev. E* **74** 46404
[91] Gordienko S, Pukhov A, Shorokhov O and Baeva T 2004 *Phys. Rev. Lett.* **93** 115002
[92] Bulanov S V, Naumova N M and Pegoraro F 1994 *Phys. Plasmas* **1** 745–57
[93] Tarasevitch A, Lobov K, Wünsche C and von der Linde D 2007 *Phys. Rev. Lett.* **98** 103902
[94] Dromey B *et al* 2006 *Nat. Phys.* **2** 456–9
[95] Nomura Y *et al* 2008 *Nat. Phys.* **5** 124–8
[96] Hörlein R *et al* 2010 *New J. Phys.* **12** 43020
[97] Gonoskov A A, Korzhimanov A V, Kim A V, Marklund M and Sergeev A M 2011 *Phys. Rev. E* **84** 46403
[98] Edwards M R and Mikhailova J M 2020 *Sci. Rep.* **10** 5154
[99] Mondal S, Wei Q, Fareed M A, Hafez H A, Ropagnol X, Sun S, Kahaly S and Ozaki T 2020 *Phys. Rev. Appl.* **13** 034044
[100] Mondal S *et al* 2018 *J. Opt. Soc. Am. B* **35** A93
[101] Kahaly S, Monchocé S, Vincenti H, Dzelzainis T, Dromey B, Zepf M, Martin P and Quéré F 2013 *Phys. Rev. Lett.* **110** 175001
[102] Tsakiris G D, Eidmann K, Meyer-ter-vehn J and Krausz F 2006 *J. Opt. Soc. Am. B* **8** 19
[103] Vincenti H 2019 *Phys. Rev. Lett.* **123** 105001
[104] Karbstein F, Blinne A, Gies H and Zepf M 2019 *Phys. Rev. Lett.* **123** 91802
[105] Tzallas P, Skantzakis E, Kalpouzos C, Benis E P, Tsakiris G D and Charalambidis D 2007 *Nat. Phys.* **3** 846–50
[106] Tzallas P, Skantzakis E, Nikolopoulos L A A, Tsakiris G D and Charalambidis D 2011 *Nat. Phys.* **7** 781–4
[107] Motoyama H, Sato T, Iwasaki A, Takei Y, Kume T, Egawa S, Hiraguri K, Hashizume H, Yamanouchi K and Mimura H 2016 *Rev. Sci. Instrum.* **87** 51803
[108] Poletto L, Frassetto F, Calegari F, Anumula S, Trabattoni A and Nisoli M 2013 *Opt. Express* **21** 13040–51
[109] Campi F, Coudert-Alteirac H, Miranda M, Rading L, Manschwetus B, Rudawski P, L'huillier A and Johnsson P 2016 *Rev. Sci. Instrum.* **87** 23106
[110] Kirkpatrick P and Baez A V 1948 *J. Opt. Soc. Am.* **38** 766–74
[111] Papadogiannis N A, Nikolopoulos L A A, Charalambidis D, Tsakiris G D, Tzallas P and Witte K 2003 *Phys. Rev. Lett.* **90** 133902
[112] Goulielmakis E, Nersisyan G, Papadogiannis N A, Charalambidis D, Tsakiris G D and Witte K 2002 *Appl. Phys. B* **74** 197–206
[113] Papadogiannis N A, Nersisyan G, Goulielmakis E, Rakitzis T P, Hertz E, Charalambidis D, Tsakiris G D and Witte K 2002 *Opt. Lett.* **27** 1561–3
[114] Pascolini M, Bonora S, Giglia A, Mahne N, Nannarone S and Poletto L 2006 *Appl. Opt.* **45** 3253–62
[115] Poletto L 2004 *Appl. Phys. B* **78** 1013–6
[116] Poletto L and Villoresi P 2006 *Appl. Opt.* **45** 8577–85
[117] Poletto L, Villoresi P, Benedetti E, Ferrari F, Stagira S, Sansone G and Nisoli M 2007 *Opt. Lett.* **32** 2897–9
[118] Poletto L 2009 *Appl. Opt.* **48** 4526–35
[119] Poletto L, Villoresi P, Frassetto F, Calegari F, Ferrari F, Lucchini M, Sansone G and Nisoli M 2009 *Rev. Sci. Instrum.* **80** 123109
[120] Constant E, Mével E, Zaïr A, Bagnoud V and Salin F 2001 *J. Phys.* **11** Pr2-537–540
[121] Tzallas P, Charalambidis D, Papadogiannis N A, Witte K and Tsakiris G D 2003 *Nature* **426** 267–71
[122] Carpeggiani P A, Tzallas P, Palacios A, Gray D, Martín F and Charalambidis D 2014 *Phys. Rev. A* **89** 023420
[123] Faucher O, Tzallas P, Benis E P, Kruse J, Peralta Conde A, Kalpouzos C and Charalambidis D 2009 *Appl. Phys. B* **97** 505–10
[124] Tzallas P, Charalambidis D, Papadogiannis N A, Witte K and Tsakiris G D 2005 *J. Mod. Opt.* **52** 321–38
[125] Wöstmann M, Mitzner R, Noll T, Roling S, Siemer B, Siewert F, Eppenhoff S, Wahlert F and Zacharias H 2013 *J. Phys. B: At. Mol. Opt. Phys.* **46** 164005
[126] Kolliopoulos G, Tzallas P, Bergues B, Carpeggiani P A, Heissler P, Schröder H, Veisz L, Charalambidis D and Tsakiris G D 2014 *J. Opt. Soc. Am. B* **31** 926
[126] Treusch R 2005 *HASYLAB Annual Report 2005 DESY (2005)*
[127] Tiedke K 2003 *HASYLAB Annual Report 2003 DESY (2003)*
[129] Kolliopoulos G, Bergues B, Schröder H, Carpeggiani P A, Veisz L, Tsakiris G D, Charalambidis D and Tzallas P 2014 *Phys. Rev. A* **90** 013822
[130] Tsatrafyllis N *et al* 2016 *Sci. Rep.* **6** 21556
[131] Tzallas P, Bergues B, Rompotis D, Tsatrafyllis N, Chatziathanassiou S, Muschet A, Veisz L, Schröder H and Charalambidis D 2018 *J. Opt.* **20** 024018
[132] Dacasa H *et al* 2019 *Opt. Express* **27** 2656–70
[133] Benis E P, Charalambidis D, Kitsopoulos T N, Tsakiris G D and Tzallas P 2006 *Phys. Rev. A* **74** 051402(R)
[134] E P B, Tzallas P, Nikolopoulos L A A, Kovačev M, Kalpouzos C, Charalambidis D and Tsakiris G D 2006 *New J. Phys.* **8** 92
[135] Wagner M and Schröder H 1993 *Int. J. Mass Spectrom. Ion Process.* **128** 31–45
[136] Schröder H, Wagner M, Kaesdorf S and Kompa K L 1993 *Ber. Bunsen Ges. Phys. Chem.* **97** 1688–91
[137] Laude L D 1994 *Excimer Lasers* (Dordrecht: Springer)
[138] Charalambidis D, Xenakis D, Uiterwaal C J G J, Maragakis P, Zhang J, Schröder H, Faucher O and Lambropoulos P 1997 *J. Phys. B: At. Mol. Opt. Phys.* **30** 1467–79
[139] Uiterwaal C J G J, Xenakis D, Charalambidis D, Maragakis P, Schröder H and Lambropoulos P 1998 *Phys. Rev. A* **57** 392–400
[140] Tsatrafyllis N, Kominis I K, Gonoskov I A and Tzallas P 2017 *Nat. Commun.* **8** 15170
[141] Tsatrafyllis N *et al* 2019 *Phys. Rev. Lett.* **122** 193602
[142] Witzel B, Papadogiannis N A and Charalambidis D 2000 *Eur. Phys. J. D* **12** 21–25
[143] Witzel B, Papadogiannis N A and Charalambidis D 2000 *Phys. Rev. Lett.* **85** 2268–71
[144] Dörner R, Mergel V, Jagutzki O, Spielberger L, Ullrich J, Moshammer R and Schmidt-Böcking H 2000 *Phys. Rep.* **330** 95–192
[145] Ullrich J, Moshammer R, Dorn A, Dorner R, Schmidt L P H and Schmidt-Bocking H 2003 *J. Phys. B: At. Mol. Opt. Phys.* **66** 1463–545
[146] Descamps D, Roos L, Delfin C, L'Huillier A and Wahlström C-G 2001 *Phys. Rev. A* **64** 273
[147] Sekikawa T, Ohno T, Yamazaki T, Nabekawa Y and Watanabe S 1999 *Phys. Rev. Lett.* **83** 2564–7
[148] Nabekawa Y, Hasegawa H, Takahashi E J and Midorikawa K 2005 *Phys. Rev. Lett.* **94** 43001
[149] Manschwetus B *et al* 2016 *Phys. Rev. A* **93** 061402(R)
[150] Miyamoto N, Kamei M, Yoshitomi D, Kanai T, Sekikawa T, Nakajima T and Watanabe S 2004 *Phys. Rev. Lett.* **93** 83903
[151] Sekikawa T, Katsura T, Miura S and Watanabe S 2002 *Phys. Rev. Lett.* **88** 193902

[152] Sorokin A A, Bobashev S V, Feigl T, Tiedtke K, Wabnitz H and Richter M 2007 *Phys. Rev. Lett.* **99** 213002

[153] Young L *et al* 2010 *Nature* **466** 56–61

[154] Doumy G *et al* 2011 *Phys. Rev. Lett.* **106** 83002

[155] Rudek B *et al* 2012 *Nat. Photon.* **6** 858–65

[156] Fukuzawa H *et al* 2013 *Phys. Rev. Lett.* **110** 173005

[157] Prince K C *et al* 2016 *Nat. Photon.* **10** 176–9

[158] Tamasaku K *et al* 2014 *Nat. Photon.* **8** 313–6

[159] Ghimire S, Fuchs M, Hastings J, Herrmann S C, Inubushi Y, Pines J, Shwartz S, Yabashi M and Reis D A 2016 *Phys. Rev. A* **94** 043418

[160] Glownia J M *et al* 2010 *Opt. Express* **18** 17620–30

[161] Canton S E *et al* 2015 *Nat. Commun.* **6** 6359

[162] Wolf T J A *et al* 2017 *Nat. Commun.* **8** 29

[163] Squibb R J *et al* 2018 *Nat. Commun.* **9** 63

[164] Levantino M, Schirò G, Lemke H T, Cottone G, Glownia J M, Zhu D, Chollet M, Ihee H, Cupane A and Cammarata M 2015 *Nat. Commun.* **6** 6772

[165] Liekhus-Schmaltz C E *et al* 2015 *Nat. Commun.* **6** 8199

[166] Picón A *et al* 2016 *Nat. Commun.* **7** 11652

[167] Nabekawa Y, Shimizu T, Okino T, Furusawa K, Hasegawa H, Yamanouchi K and Midorikawa K 2006 *Phys. Rev. Lett.* **96** 83901

[168] Nabekawa Y, Shimizu T, Okino T, Furusawa K, Hasegawa H, Yamanouchi K and Midorikawa K 2006 *Phys. Rev. Lett.* **97** 153904

[169] Skantzakis E, Tzallas P, Kruse J, Kalpouzos C and Charalambidis D 2009 *Opt. Lett.* **34** 1732–4

SCIENTIFIC REPORTS
natureresearch

A 10-gigawatt attosecond source for non-linear XUV optics and XUV-pump-XUV-probe studies

I. Makos[1,2,7], I. Orfanos[1,2,7], A. Nayak[1,3,6], J. Peschel[5], B. Major[3], I. Liontos[1], E. Skantzakis[1], N. Papadakis[1], C. Kalpouzos[1], M. Dumergue[3], S. Kühn[3], K. Varju[3,4], P. Johnsson[5], A. L'Huillier[5], P. Tzallas[1,3] & D. Charalambidis[1,2,3*]

The quantum mechanical motion of electrons and nuclei in systems spatially confined to the molecular dimensions occurs on the sub-femtosecond to the femtosecond timescales respectively. Consequently, the study of ultrafast electronic and, in specific cases, nuclear dynamics requires the availability of light pulses with attosecond (asec) duration and of sufficient intensity to induce two-photon processes, essential for probing the intrinsic system dynamics. The majority of atoms, molecules and solids absorb in the extreme-ultraviolet (XUV) spectral region, in which the synthesis of the required attosecond pulses is feasible. Therefore, the XUV spectral region optimally serves the study of such ultrafast phenomena. Here, we present a detailed review of the first 10-GW class XUV attosecond source based on laser driven high harmonic generation in rare gases. The pulse energy of this source largely exceeds other laser driven attosecond sources and is comparable to the pulse energy of femtosecond Free-Electron-Laser (FEL) XUV sources. The measured pulse duration in the attosecond pulse train is 650 ± 80 asec. The uniqueness of the combined high intensity and short pulse duration of the source is evidenced in non-linear XUV-optics experiments. It further advances the implementation of XUV-pump-XUV-probe experiments and enables the investigation of strong field effects in the XUV spectral region.

In the 20 years of attosecond science[1,2], numerous exciting ideas have been conceived and sound applications have been demonstrated, the majority of which is based on pump-probe studies, exploiting combinations of infrared (IR) and XUV pulses.

Already the domain of attosecond pulse characterization gave access to fascinating physics, novel methodologies and innovative technologies. Those are to be found in the Reconstruction of Attosecond Beating By Interference of two-photon Transitions (RABBIT)[3], Frequency Resolved Optical Gating for Complete Reconstruction of Attosecond Bursts (FROG-CRAB)[4], Phase Retrieval by Omega Oscillation Filtering (PROOF)[5,6], Rainbow RABBIT[7], In-situ[8], Spectral Phase Interferometry for the Direct Electric Field Reconstruction (SPIDER)[9,10], atto-clock[11], double-blind holography[12], attosecond spatial interferometry[13], and the attosecond streaking[14] methods and in the devices developed towards their implementation. A summary of these approaches is presented in the perspective article on attosecond pulse metrology[15].

In parallel, abundant, significant proof of principle experiments enriched the pallet of attosecond applications. Atomic inner-shell spectroscopy[16], real-time observation of ionization[17], light wave electronics[18], and molecular optical tomography[19] are some examples of such experiments. Other more recent applications of attosecond pulses include ionization delays in solids[20] and atoms[21,22], electron dynamics[23], charge migration[24,25], build-up of a Fano-Beutler resonance[7], and ionization dynamics in chiral molecules[26]. It should be noted that the above examples are only a representative fraction of many studies performed in attosecond laboratories.

Following a somewhat different path, a group of attosecond laboratories focused for several years their efforts towards the development of high photon flux attosecond beam lines. The aim of these efforts was to reach sufficiently high attosecond pulse intensities as to induce observable two- (or more) XUV-photon transitions, a

[1]Foundation for Research and Technology - Hellas, Institute of Electronic Structure & Laser, GR71110, Heraklion, Crete, Greece. [2]Department of Physics, University of Crete, GR71003, Heraklion, Crete, Greece. [3]ELI-ALPS, ELI-Hu Non-Profit Ltd., Dugonics tér 13, H-6720, Szeged, Hungary. [4]Department of Optics and Quantum Electronics, University of Szeged, Dom tér 9, 6720, Szeged, Hungary. [5]Department of Physics, Lund University, SE-221 00, Lund, Sweden. [6]Institute of Physics, University of Szeged, Dom tér 9, 6720, Szeged, Hungary. [7]These authors contributed equally: I. Makos and I. Orfanos. *email: chara@iesl.forth.gr

central prerequisite for XUV-pump-XUV-probe experiments in the one femtosecond (fs) and sub-fs temporal regime[27–29]. The importance of XUV-pump-XUV-probe schemes relies on the fact that when temporally over-lapping IR and XUV pulses are used for pump-probe studies, the high IR intensities that have to be employed may cause distortions to the system under investigation obscuring its intrinsic dynamics[30]. XUV-pump-XUV-probe experiments benefit substantially from the existence of intense isolated[27,28] or essentially isolated[31] XUV pulses. At the same time, observable two-(or more) XUV-photon transitions allow temporal characterization of attosecond pulses based on non-linear XUV autocorrelation (AC) measurements[32–38], bypassing complications that may arise from IR-XUV cross-correlation based pulse characterization techniques[39]. It should be noted that these develop-ments were a follow up of pioneering non-linear XUV experiments completed with individual harmonics in the few tens of fs temporal regime, including two-[40], three-[41] and four-XUV-photon[42] ionization, two-XUV-photon double ionization[43,44] as well as the corresponding 2nd [40,43] and 4th order AC measurements[42], two-XUV-photon above threshold ionization (ATI)[45] and even a FROG based XUV pulse reconstruction[46].

Towards reaching high XUV photon fluxes there are certain hurdles including depletion of the generating medium above a certain threshold of the driving laser intensity, XUV radiation reabsorption by the generating medium, as well as phase mismatch due to high generating gas pressures and high degree of ionization of the gen-erating medium (see the review article of ref. [47]). A way to overcome these obstacles is to use non depleting media as non-linear harmonic generation targets. This is the case in the generation of harmonics from laser induced surface plasma[48–53], often referred to as plasma mirrors[54]. Indeed, for surface plasma harmonics, very high photon fluxes have been predicted in particle in cell (PIC) simulations[55] and sub-fs temporal confinement has been exper-imentally demonstrated[56]. Laser surface plasma harmonic generation requires however, increased technological demands such as high laser peak to background contrast, including elimination of unwanted laser pre-pulses, demanding "cleaning" procedures of the laser pulse through additional plasma mirrors, tedious control of the plasma density gradient[53], μm positioning of the focus on the target and debris to mention a few. Although laser surface plasma harmonic generation holds promise of high photon flux attosecond pulses, the so far achieved maximum XUV pulse energy is 40 μJ[56].

The alternative to laser surface plasma harmonic generation in avoiding the above mentioned obstacles is to use gas targets combined with loose focusing of the driving laser beam. The scalability of gas phase harmonic generation sources has been recently studied in ref. [57]. The work by Heyl et al. demonstrates that long focal lengths combined with low pressure gas cells, allowing control of phase matching, can lead to high throughputs and thus to high XUV photon fluxes. At the same time it has been recently shown that multi-cycle high peak power laser beams, focused in the generation medium using long focal lengths of several meters, in combina-tion with quasi-phase matching[58] arrangements, achieved through a chain of small length gas media i.e. pulsed gas jets, can reach emission of 20-GW XUV harmonic power at the source in the spectral region of 15–30 eV[59]. In the work of Nayak et al. apart from the measurement of the harmonic source power the high focused XUV intensities achieved were evidenced through the observation of multi-XUV-photon multiple ionization of argon atoms. While FEL sources have much higher peak brightness at shorter wavelengths and in particular in the x-ray regime, in the spectral region of 15–30 eV the measured peak brightness of the harmonic spectra is competing with that of FELs[52].

In the present work we provide an in-detail presentation of the 20-GW XUV source developed at the Instutute of Electronic Structure and Laser of the Foundation for Research and Technology-Hellas (FORTH-IESL) together with multi-XUV-photon multiple atomic ionization measurements in helium, argon and neon, while 10 GW attosecond pulse trains have been demonstrated at this source. Two-photon ionization of helium atoms and argon ions is used in second order intensity volume autocorrelation (2nd IVAC) measurements of the pulse dura-tion of the attosecond pulse train (APT). Since the measured duration of the pulses in the train is found to be $\tau_{XUV} = 670 \pm 80$ asec and $\tau_{XUV} = 650 \pm 80$ asec in He and Ar respectively, the present work introduces the most powerful table top XUV attosecond source.

The structure of the manuscript is as follows. In section 2 we give a detailed illustration of the XUV beam-line. In section 3 we report a quantitative characterization of the different parameters of the beam-line. In section 4 we present results of non-linear XUV-optics experiments. In section 5 results of the attosecond pulse trains tem-poral characterization are shown, followed by the concluding section of the work. It should be noted that after submission of the present work tunable attosecond x-ray pulses with 100 GW peak power were demonstrated in the SLAC FEL large scale infrastructure[60].

The High XUV Photon Flux Source

The high XUV-photon flux beam-line mentioned in the previous section has been recently developed and tested in the Attosecond Science & Technology laboratory of FORTH-IESL[59]. In this section, a detailed description of the beam line and its characterization is presented.

The 20-GW XUV beam-line. The high photon throughput of the XUV beam-line relies on the exploitation of: I) 9 m focal length optics focusing the laser beam into the non-linear medium, as to increase the number of harmonic emitters in the interaction cross section, keeping the driving intensity below the ionization saturation thresholds of the generating medium, II) a dual gas jet as target with variable jet distance as to achieve optimal phase matching, III) optimized gas pressure in both jets, and IV) Xe gas as non-linear medium, the conversion efficiency of which is the highest of all rare gasses[61,62] with the trade-off of the low cut-off photon energy. However, in test measurements Ar gas was also used as generating medium.

The beam-line, as shown in Fig. 1, consists of the following units: (a) laser beam steering/shaping, placed in the "compressor chamber" and "IR steering optics and Polarization Gating" chambers, (b) laser beam focusing, placed in the "IR focusing optics" chamber, (c) XUV generation, placed in the "HHG" chamber, (d) XUV separa-tion/steering, placed in the "XUV separation/steering" chamber, (e) XUV manipulation and diagnostics, placed
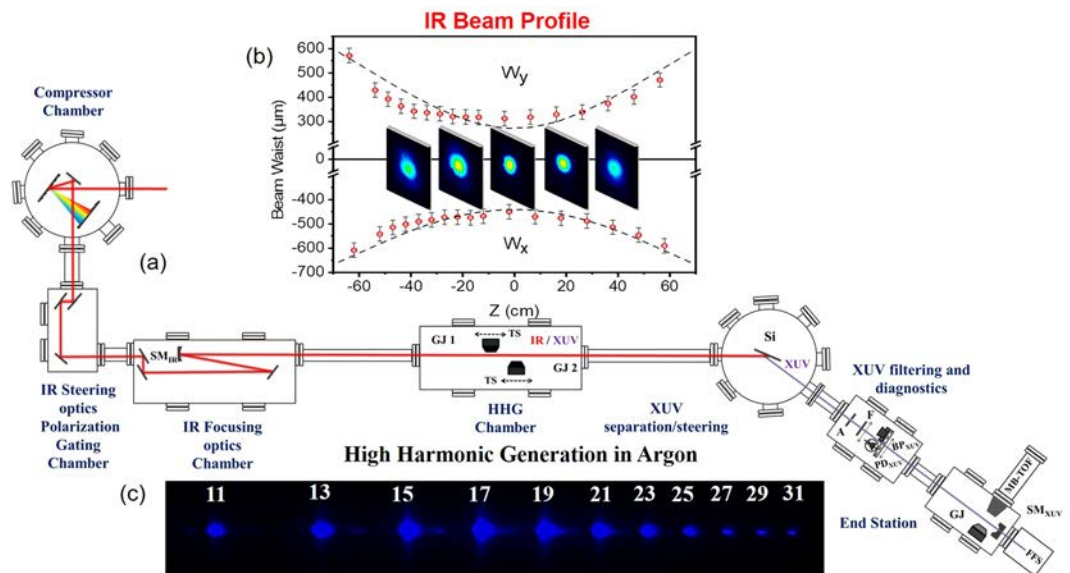
Figure 1. The 20-GW XUV beam line. (**a**) Optical layout of the 20-GW XUV beam-line. SM_{IR}: spherical mirror of 9-m focal length. $GJ_{1,2}$: dual-pulsed-jet configuration placed on translation stages (TS). Si: silicon plate. F: Al or Sn filter. A: aperture. BP_{XUV}: XUV beam profiler. SM_{XUV}: gold coated spherical mirror of 5-cm focal length. Ar-GJ: Ar gas jet. MB-TOF: magnetic bottle time-of-flight spectrometer. PD_{XUV}: calibrated XUV photodiode. FFS: flat-field spectrometer. (**b**) IR beam profile around the focus measured with a CCD camera. (**c**) measured HHG spectrum produced in Argon gas phase medium spreading up to 48 eV corresponding to the 31st harmonic of the fundamental frequency of the driving field. Part of the figure is copied from reference[59].

in the "XUV filtering and diagnostics" chamber and (e) XUV pulse temporal characterization and XUV radiation use unit placed in the "end station".

The laser steering and shaping takes place in two different vacuum chambers. In the first one a two grating arrangement compresses the amplified laser beam (Amplitude Technologies Ti:Sapphire chain) and delivers pulses of 800 nm central wavelength, ≈400 mJ maximum energy and ≈24 fs duration at 10 Hz repetition rate. Since 400 mJ pulse energy would deplete the harmonic generation medium at the used geometry the energy is reduced to 25–45 mJ after compression depending on the gas used for the generation.

The beam is then steered into the focusing unit through three plane mirrors placed in the second chamber. The same mirror set up is used for the alignment of the laser through the entire beam-line. This second chamber hosts also a Polarization Gating (PG) optical arrangement for the generation of isolated attosecond pulses. Since no isolated pulses are used in the present work the PG arrangement is not described here but can be found in previous works[63–65]. The polarization of the laser beam entering the focusing unit is *parallel* to the optical table. The beam diameter is $D \approx 2.3$ cm. The focusing unit uses three silver protected low dispersion plane mirrors and a spherical mirror (SM) of 9 m focal length. The optical layout shown in Fig. 1a aims to reduce astigmatism introduced by the spherical mirror due to the deviation from the normal incidence. The angle of incidence at the spherical mirror is as close as possible to normal (~3°). In this way the astigmatism is kept low but is not negligible. Figure 1b shows the beam profile at the focus of the IR beam (measured with a CCD camera) which reveals a small degree of elongation along the x-axis. The confocal parameter is measured to be $b \approx 70$ cm which is a factor of ≈ 1.22 larger than the value obtained according to the relation $b = 2\pi R^2/\lambda_L$ (where R and λ_L is the radius and the wavelength of the IR beam) given by Gaussian optics. Although these imperfections of the IR beam do not affect the XUV beam profile (measured with an XUV beam profiler placed after the metal filter in the "XUV diagnostics" chamber) as can be seen in Fig. 1 of ref.[59] and further down in this work, according to ref.[66], they may introduce distortions in XUV wavefront and hence influence the duration of the emitted attosecond pulses at the "end station" where the XUV beam is refocused. This matter will be further discussed in Section 4 of the manuscript. Further measurements of the IR profile have been performed at several positions around the focus as shown in Fig. 1b.

The XUV generation unit can host up to four gas-jets placed on *x, y, z* translation stages. All gas-jets of the beamline are home made piezoelectric crystal based gas-jets. These translations are used for optimization of the laser-gas interaction. In addition, the translation in the *z* direction (beam propagation direction) permits the variation of the inter-jet distance, optimizing phase matching. Due to the large focal length, the distance between the jets is several cm and thus phase matching can be accurately controlled through translation in the *z* direction. The minimum step of the stage was 5 μm, much smaller than the needed accuracy in the range of cm. In the present study only two gas jets (GJ_1, GJ_2) have been used with the scanning step of the translation stages set at 0.75 cm. The gas jets are operated by piezoelectrically driven pulsed nozzles. For comparison reasons a 10 cm long gas cell bounded by two pinholes (entrance-exit pinholes) of 2 mm diameter has also been used in one of the experiments. The generated XUV co-propagates with the IR towards the "XUV separation/steering" chamber. The two beams (IR, XUV) first impinge a silicon plate (Si) placed at the Brewster angle (~75°) of the IR radiation. This plate significantly attenuates the IR and reflects ~60% of the XUV radiation deflecting the XUV beam
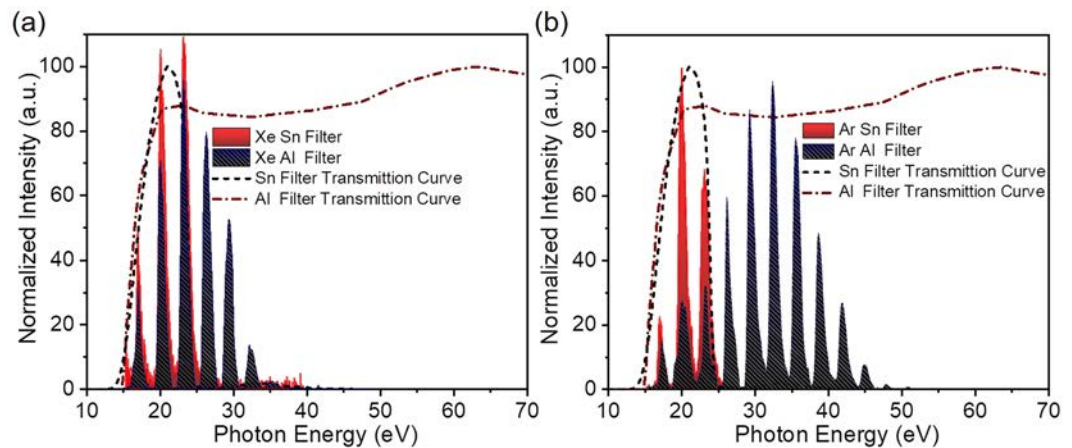
Figure 2. Harmonic spectra recorded by FFS after spectral selection by metallic foils. The generation medium was (**a**) Xe and (**b**) Ar gas. In both panels, the blue and red peaks correspond to harmonics after transmission through 150 nm thick Al and Sn respectively, while the red dash-dotted (Al) and black dashed (Sn) are transmission curves for 150 nm thickness.

towards the "XUV filtering and diagnostics" and "end station" chambers. In the "XUV filtering and diagnostics" chamber, the beam after passing through a 7 mm diameter aperture, is spectrally selected by 150 nm thick metal foils (Al or Sn) mounted on an x, y translation stage. The foils are acting as band pass filters in the XUV spectral range and eliminate any residual IR radiation. The transmission curve of these filters is shown in Fig. 2 together with harmonic spectra obtained using xenon (Fig. 2a) and argon (Fig. 2b) as generating gas, recorded by the XUV flat-field-spectrometer (FFS).

In the "XUV filtering and diagnostics" chamber the pulse energy of the XUV radiation was also measured introducing a calibrated XUV photodiode (PD_{XUV}) into the XUV beam and its beam profile was recorded introducing an XUV beam profiler (BP_{XUV}) (consisting of a pair of multichannel plates (MCPs) and a phosphor screen followed by a CCD camera). Figure 3 shows the XUV beam profiles recorded after the filtering through Al foil with the GJ_1 to be placed at the focusing position of the driving field. For further investigation, recordings have been carried out for several positions of the GJ_1 producing the XUV radiation. No significant change was observed when GJ_1 was placed before ($z_{GJ1} = -b$, $-b/2$), on ($z_{GJ1} = 0$) or after ($z_{GJ1} = b$, b/2) the driving laser focus. For an IR focus displacement of $\approx \pm 30$ cm relative to the gas jet position, a significant change in the beam XUV profile is expected when both the short and long trajectory harmonics are recorded by the beam profiler. This is because, as it is well known, the divergence of the short trajectory harmonics is smaller than the long trajectory harmonics which have an annular-like beam profile. Focusing the IR beam before (after) the gas jet, the contribution of the short (long) trajectory harmonics is dominating. In the present measurements, the diameter of the aperture that has been placed before the beam profiler was reduced to ≈ 5 mm, thus selecting mainly the short trajectory harmonics (without excluding the presence of the long trajectories for harmonics lying close to the cut-off spectral region), and thus it does not "significantly" change when moving the jet before and after the focus. To double check the spatial intensity distribution of the XUV beam recorded by the BP_{XUV}, the knife edge technique was also used for $z_{GJ1} = 0$. The XUV radiation photoionizes argon gas and the photoelectron yield is measured as a function of the knife edge position. The measured curve shown in Fig. 3c (black dots) is then differentiated resulting in the intensity distribution (red dots). The colored area is defined by a Gaussian fit to the measured data. The results of the knife edge measurements were in agreement with the values of the XUV beam radius obtained by the BP_{XUV}.

The last chamber (end station) of the beam-line is the temporal characterization and pump-probe unit. It hosts an attosecond delay line based on a split spherical gold coated mirror of 5 cm focal length, fixed on a multiple-translation-rotation stage. This stage enables control in 3 degrees of freedom for the one D-shaped half of the mirror i.e. the displacement along the z axis (i.e. the beam propagation axis) with a maximum value of 80 μm and rotation in the x-z and y-z plane. The other part of the mirror position is altered only along the propagation direction with a maximum translation of 400 μm. All movements of the split-mirror are controlled by piezo crystals operated in closed loop mode. A 1.5 nm minimum step of the translation of the first, as described above, of the two parts of the bisected mirror introduces a temporal delay between the two parts of the beam. It is worth noting that for such time delays (80 μm total translation), effects of spatial displacements of the two parts of the focused beam are negligibly small[36]. The XUV beam is focused in front of a pulsed gas jet whose forefront serves also as a repeller of a magnetic bottle time of flight (MB-TOF) spectrometer. The TOF can be operated either in an ion mass spectrometer or electron energy analyzer mode measuring the products of the interaction of the XUV pulses with the gas target. This arrangement is used either for performing 2nd IVAC measurements of the XUV pulse duration or in XUV-pump-XUV-probe experiments. Finally, the FFS is placed at the end of the beam line monitoring and recording the XUV radiation spectrum that is "leaking" through the slit of the bisected mirror.
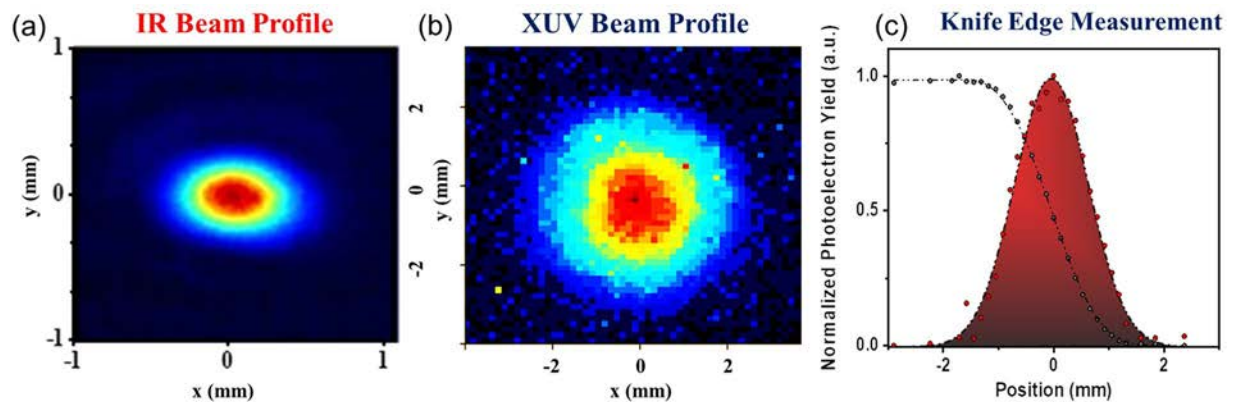
Figure 3. IR and XUV beam profiles. (**a**) IR beam profile at the focal plane measured by a commercial CCD profile camera. (**b**) XUV beam profile recorded using the BP_{XUV}. For this measurement Xe gas was used as harmonic generation medium. (**c**) Knife edge measurement of the XUV beam profile presented with black dots while the red dots show the obtained intensity distribution. The colored area is defined by a Gaussian fit to the measured data. In both (**b,c**) measurements, harmonics are generated using xenon with the GJ placed at the IR focus.

Characterization of the XUV Beam-line

In this section, vacuum, XUV pulse energy, attosecond delay line stability and temporal resolution measurements are discussed.

Vacuum conditions. The rest vacuum, i.e. the vacuum when all gas jets are off, in all chambers of the beam-line is: ~10^{-6} mbar except for the "end station" chamber in which it is ~10^{-7} mbar. The generating nozzles are operating with a backing pressure in the range of 2 bar. The estimated gas pressure of the jets in the interaction area is ~25 mbar as reported in a previous work[59]. When the two generation jets are on, the pressure in the HHG chamber increases to ~10^{-4} mbar. The jet pressure conditions in the detection chamber depend on the type of experiment that is performed. A 1000 l/min turbo-molecular pump in the "end station" chamber secures an adequate vacuum pressure during operation of the gas target jet. An additional turbo pump differentially pumping the FFS spectrometer ensures that the pressure where the multichannel plate detector is located, is lower than 10^{-6} mbar.

Measurement and optimization of the XUV pulse energy. Typical harmonic spectra generated in Ar and Xe, recorded by the FFS after the XUV radiation has passed through 150 nm thick Al or Sn filters are shown in Fig. 2. The harmonic cut-off region when Xe gas and Al filter are used is around 30 eV (and the highest harmonic observed is the 23rd), while harmonics higher than the 15th are not transmitted through the Sn filter. In Ar the cut-off region extends to about 48 eV (the highest harmonic observed is the 31st).

Figure 4 shows the dependence of the energy of the XUV radiation (integrated over the Al-filter-selected harmonics spectrum and measured with the PD_{XUV}) on the argon gas pressure (changed by varying the delay of the gas nozzles, both positioned at z = 0, with respect to the arrival time of the laser pulse) as well as the comparison between one gas jet and one gas cell with respect to the XUV energy emission. In particular, Fig. 4a shows the emitted XUV pulse energy as a function of the time delay between the trigger pulse of the GJ_1 nozzle opening and the laser pulse, for an arbitrary IR intensity well below the saturation threshold. The emission maximizes for a time delay of 600 μs. At this value the harmonic signal was then further optimized by setting the IR intensity just below the ionization saturation intensity. Figure 4b shows essentially the same behavior for GJ_1 and GJ_2. Figure 4c is devoted to the comparison between the XUV pulse energy obtained when using a single gas jet and a cell in the present beam line. It presents the XUV pulse energy emitted by (i) GJ_1 as a function of the pulsed nozzle time delay and (ii) by the gas cell as a function of the cell gas pressure. For the given cell length of 10 cm, the emission maximizes for a pressure value between 8 and 9 mbar. The maximum harmonic yield in the cell is found to be slightly lower (~25%) than the one of the gas jet. In these measurements Ar is used as generating medium and thus the pulse energy throughput is not the highest possible. Apart from the gas-jet/cell comparison measurement, the beam-line is operated exclusively with gas-jets, mainly because at 10 Hz repetition rate they consume less gas, and because of their demonstrated slightly higher measured XUV energy throughput. After opting for the GJ configuration as the preferable one for the beamline of this work, experimental investigations focused on maximizing the photon flux of the emitted XUV radiation. Measurements of the single GJ emission by varying the medium position relatively to the driving pulse's focus are depicted in Fig. 5a,b for Ar and Xe respectively. The x-axis reveals the harmonic order, measured in the photoelectron spectrum produced by the unfocused XUV beam, the y-axis depicts the distance of gas jet from the position of the IR focus and the z-axis the XUV pulse energy. Having optimized the emission resulting from the single GJ configuration further enhancement of the harmonic yield was achieved by applying quasi- phase-matching conditions using two gas jets. The same gas is used in both jets. Results are shown in Fig. 5c,d. The dependence of the harmonic yield, generated by Ar and Xe gas, on the distance between GJ_2 and GJ_1 is shown in Fig. 5c,d, respectively. The x-axis denotes the distance
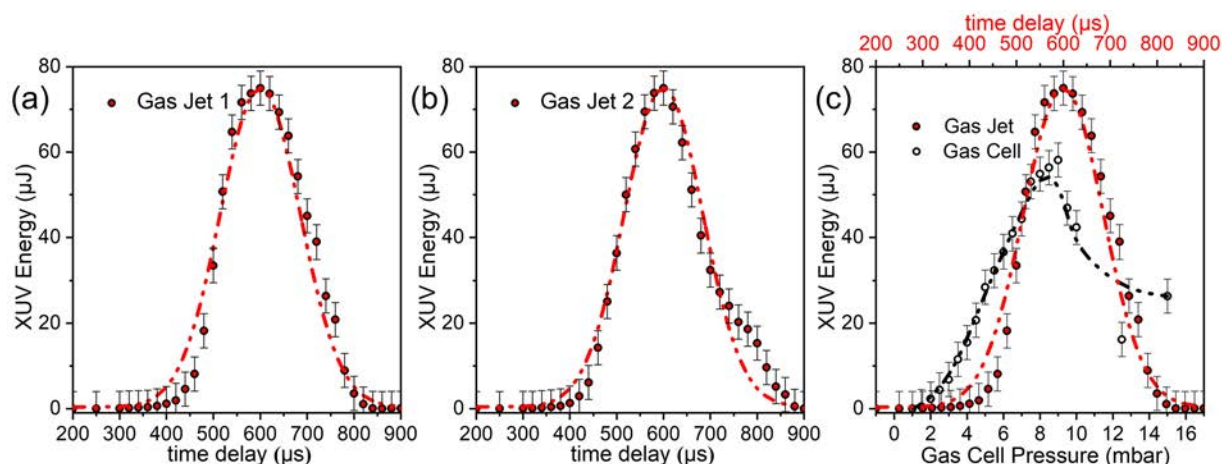
Figure 4. Harmonic emission using a single pulsed gas-jet and the comparison with a single gas-cell. (**a,b**) Pulse energy of the XUV radiation emitted by GJ_1 and GJ_2, respectively, as a function of the delay between the laser pulse arrival at the focus and the opening of the nozzle. Both jets are positioned at $z = 0$. The time delay of $\approx 600\,\mu s$ corresponds to the value where the laser pulse meets the maximum atomic density. The dots are the measured data and the red line is a Gaussian fit. (**c**) Comparison of a single gas jet vs 10 cm long gas cell yield for optimized conditions. The upper part axis represents the time delay of the pulsed nozzle while the lower one the measured pressure of the Gas cell. In all panels the generated medium was Ar, while the XUV energy was determined by PD_{XUV} placed after an Al filter.
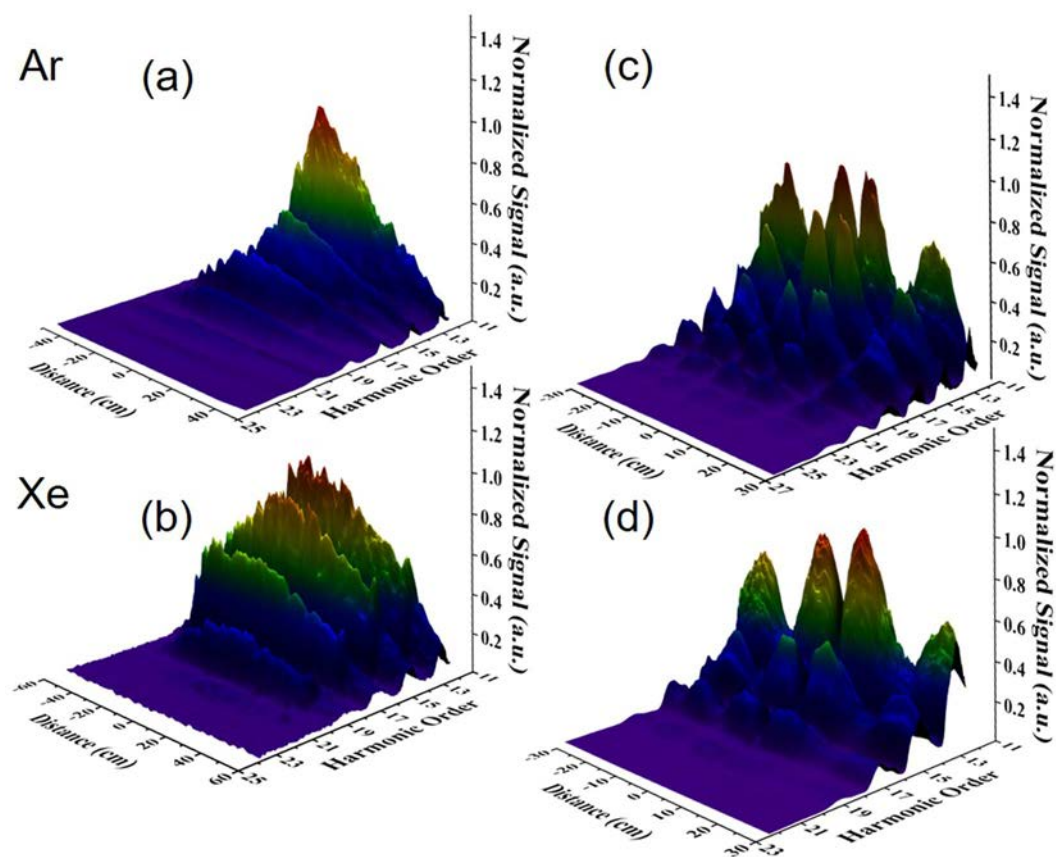
Figure 5. Harmonic generation in single and dual gas-jet configuration. Generation of GW high-harmonics using single (**a,b**) and dual gas-jet (**c,d**) configuration for Xe and Ar. In all panels the corresponding harmonic signal was determined by recording the single-photon photoelectron spectra produced by the interaction of Ar gas with the incoming XUV beam after passing trough the Al filter.
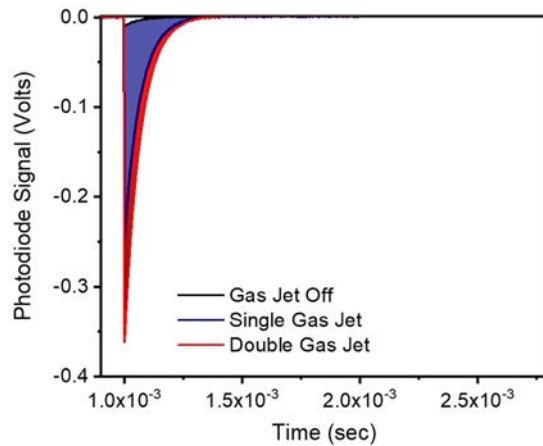
Figure 6. Measurement of the XUV energy. XUV photodiode signal obtained with one GJ (blue shaded area), two GJs (red shaded) and with the harmonic generation switched off (black line). For the extraction of the pulse energy the XUV photodiode quantum efficiency as a function of photon energy provided by the manufacturing company Opto Diode Corp was used.

between the two jets, the y-axis the harmonic order and the z-axis the XUV pulse enegy. GJ_1 is positioned at fixed $z \approx 0$ while GJ_2 moves at variable positions.

All spectra emitted by Ar extend to higher cut-off energies than those emitted by Xe due to the higher ionization energy of Ar, while the pulse energy is lower than the one in Xe due to the lower conversion efficiency of Ar[61,62]. When two jets (filled with the same gas) are used a clear modulation of the signal is observed as a function of the jet distance. This is attributed to the quasi-phase matching resulting from the jet distance dependent Gouy phase and it is verified by numerical calculations[59]. The maximum measured pulse energy at the source is: I) 75 µJ (one jet) and 130 µJ (two jets), for Ar driven by 45 mJ IR pulse energy; and II) 135 µJ (one jet) and 230 µJ (two jets), for Xe driven by 25 mJ IR pulse energy. This last value corresponds to ~$5 \cdot 10^{13}$ photons/pulse, a photon flux that competes with photon fluxes of FELs in this spectral region. More details on the above quasi-phase-matching generation scheme and XUV throughputs can be found in ref. [59].

The pulse energy measurement procedure followed is described below. Once optimization of harmonic emission is achieved, the XUV Photodiode (Opto Diode AXUV100G) is placed after the Sn filter (F). Figure 6 shows the photodiode signal of the radiation transmitted through the Sn filter produced with the single (blue shaded area) and the dual (red shaded area) GJ configuration. The black line is IR light detected by the PD_{XUV}, when the gas jet of the HH generation was off. Although significantly small, this signal was subtracted from the measured total one, when harmonic generation was on.

The signal was measured with an oscilloscope (50 Ω input impedance) and the measured trace was integrated. The pulse energy E_{PD} measured at the position where the photodiode was placed is calculated by

$$E_{PD} = \sum_q \frac{n_e \cdot w \cdot h\nu_q}{\eta_q} \cdot e$$

where q is the harmonic order, n_e is the number of produced photoelectrons, w is the statistical weight of the qth harmonic, $h\nu_q$ is the harmonic photon energy, η_q is the photodiode quantum efficiency of the photodiode and e is the electron charge. The photoelectron number is given by

$$n_e = \frac{S_T - S_{IR}}{e \cdot R}$$

where S_T is the total time integrated photodiode signal, S_{IR} is the time integrated photodiode signal when the harmonic generation is off, e is the electron charge and R is the oscilloscope impedance. The quantum efficiency of the photodiode as a function of the photon energy is provided by the manufacturing company (See legend of Fig. 6). The pulse energy E at the harmonic generation source is given by:

$$E = \sum_q \frac{n_e \cdot w \cdot h\nu_q}{\eta_q \cdot R_q^{Si} \cdot T_q^{Sn}} \cdot e$$

where T_q^{Sn} is the 4% transmission of the Sn filter in this spectral region measured by recording the harmonic spectrum with and without filter, and R_q^{Si} is the ~50–60% reflectivity of the Si plate. It is worth noting that after having published in ref. [59] the above given XUV pulse energies, a second slightly different calibration curve was published in the documents of the manufacturing company of the photodiode. Using this second calibration curve the above given and in ref. [59] published XUV pulse energy values reduce by 35% i.e. for Ar 48 µJ (one jet) and 85 µJ (two jets) and for Xe 88 µJ (one jet) and 150 µJ (two jets) for Xe.
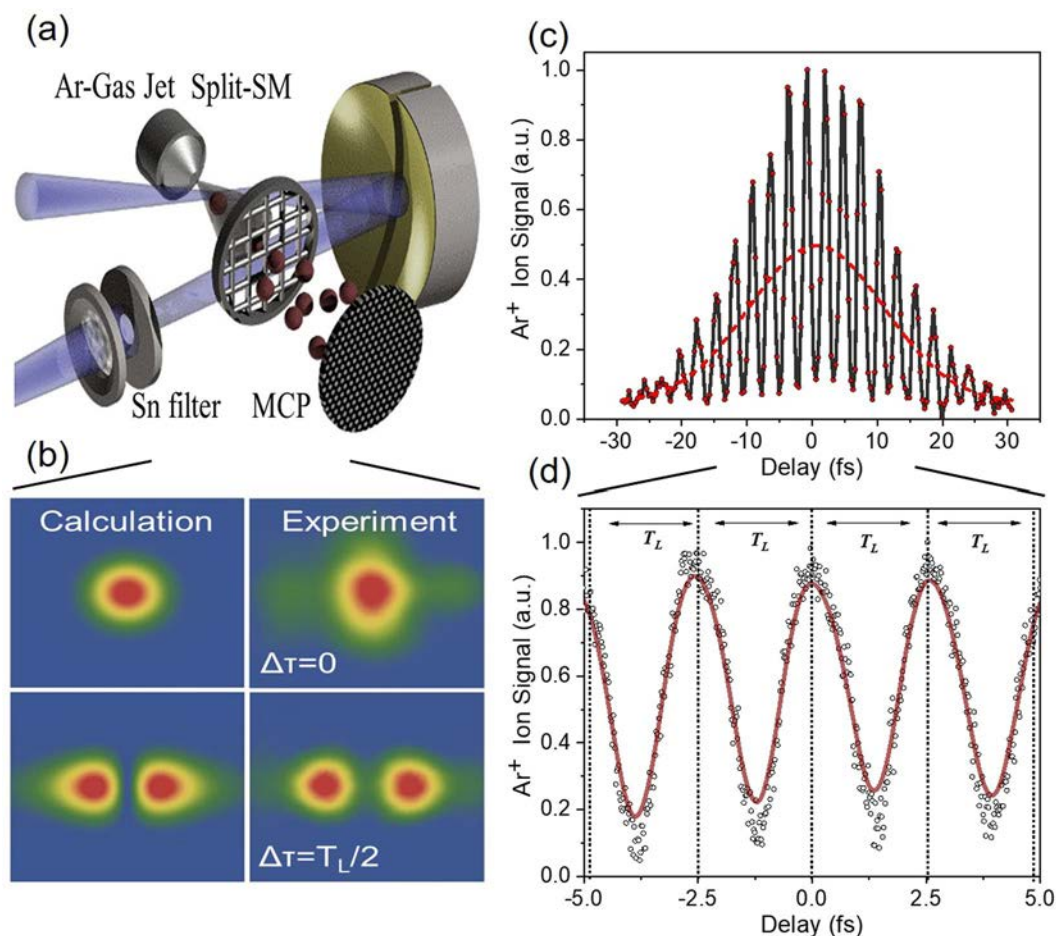
Figure 7. Split mirror arrangement. (**a**) A schematic of the experimental set-up of the autocorrelator consisting of a split spherical mirror and a TOF spectrometer. (**b**) Calculated (left panels) and measured (right panels) transverse intensity distribution of a CW 532 nm laser at the focus of the spherical mirror for $\Delta\tau = 0$ and $\Delta\tau = T_L/2$ (double maximum distribution) delay. (**c**) High-order autocorrelation trace of the fundamental laser field (IR) obtained measuring the Ar^+ yield as a function of the time delay between the two pulses produced by the split mirror. For this acquisition, the harmonic generation was turned off and the Sn filter was removed. (**d**) Expanded area of the AC trace. The signal is oscillating at the laser period of 2.67 fs.

Temporal resolution. The temporal resolution of the beam line has been tested by measuring the beam pointing stability at the end station, the performance of the split mirror device and its interferometric stability. This has been done using the IR laser beam and a CW diode laser at 532 nm wavelength.

Figure 7a shows a schematic of the split mirror assembly. The focal area of the gold coated spherical mirror was magnified by a lens and imaged by a CCD camera. Figure 7b shows the calculated (left panels) and measured (right panels) images of the focal spot area for two different delays, i.e. for two different displacements of the one-half of the mirror. The upper pannels show the intensity distribution at the focus formed when the phase difference between the two parts of the laser wave-front reflected by the two mirror halves is equal or close to $2n\pi$, $n = 0, 1, 2, 3...$, i.e. when the delay between the two wave-fronts is $\sim nT_L$, with T_L being the period of the laser field.

The phase difference is controlled by finely adjusting the position of the piezoelectric translator connected with the one part of the split mirror. The position of the piezo translation stage was measured by a capacitive sensor feedback system of the piezo system. When the phase difference of the two wave-fronts becomes equal or close to $(2n + 1)\pi$, $n = 0, 1, 2, 3...$, i.e. when the delay between the two wave-fronts is $(n + 1/2)T_L$, the intensity distribution at the focus splits into two bright spots shown at the lower part of Fig. 7b. The two bright spots ideally have the same intensity. Additionally, a higher-order autocorrelation trace of the fundamental laser field (IR) was recorded. For this acquisition, the harmonic generation was turned off and all filters were removed, thus ionization of Ar occurs only through the fundamental laser frequency by multi-IR-photon absorption.

The measured trace is shown in Fig. 7c where the interferometric interference fringes are clearly visible. The red dashed line is the cycle average of the data. The interference fringes are used for the calibration of the delay scale of the measured autocorrelation traces. The period of the observed oscillation, depicted in the expanded AC area trace in Fig. 7d is equal to the laser period that is 2.67 fs, where the red line is a cosine fit in the measured data.
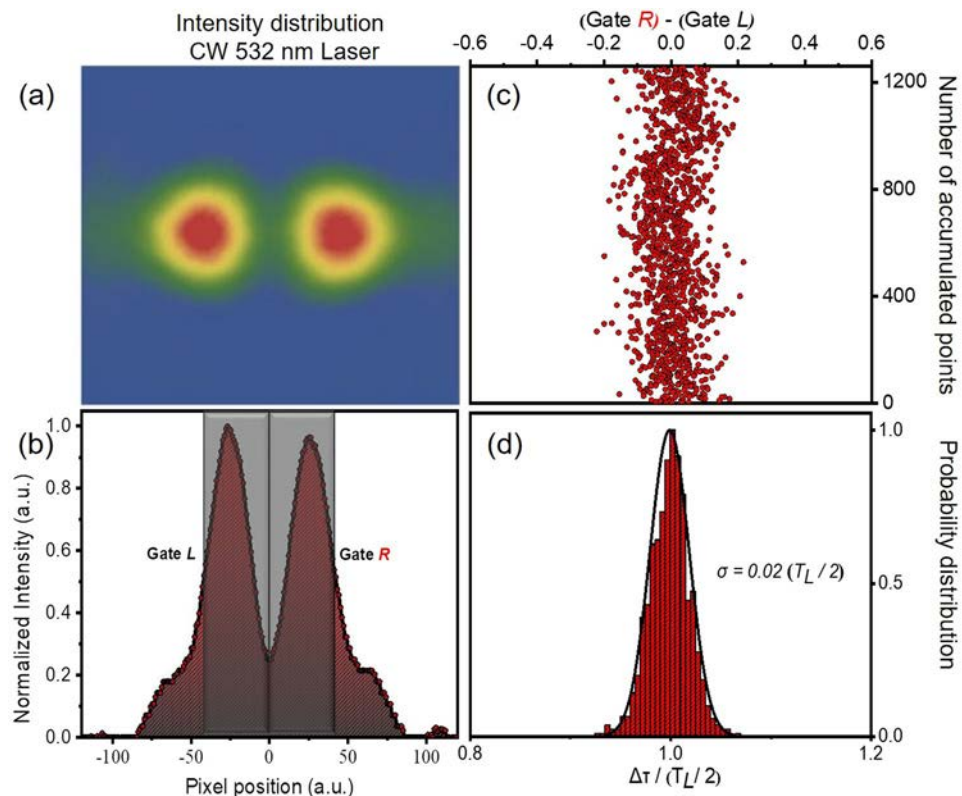
Figure 8. Stability measurements of the split-mirror autocorrelator. (**a,b**) Measured transverse intensity distribution of a CW 532 nm laser at the focus of the spherical mirror for $\Delta\tau = T_L/2$ (double maximum distribution) delay. It is noted that in this graph T_L corresponds to the period of the 532 nm CW laser. (**c**) The difference of the integrated signals of the Gate L and R. (**d**) Probability distribution of the above difference (1260 points were accumulated). The standard deviation of the mean yields a temporal resolution of $\sim$17 asec.

Shot-to-shot fluctuations of the XUV intensity distribution may be introduced because of: i) the non-perfect pointing stability of the laser and consequently of the XUV beam and ii) mechanical instabilities of the split mirror arrangement. The above factors affect the interferometric stability of the delay line. The interferometric stability of the split mirror was measured using a CW laser of $\lambda = 532$ nm by the following procedure. The displacement of the two halves of the spherical mirror was fixed such as introducing a delay of $T_L/2$ (Fig. 8a). Consequently in the line-out of the focal spot area, the integrated areas of the two gates L and R, introduced in Fig. 8b, are essentially equal. Any deviation from this picture can be correlated to the instability of the split spherical mirror, since it originates from the optical path difference between the two interfering wave fronts. The interferometric stability of the split mirror device is extracted from the standard deviation of the mean value of the probability distribution for 1260 points as a function of time and is found to be $\approx$17 asec (Fig. 8c,d).

The interferometric stability of the device may be different when the IR laser is used as its pointing stability is not the same with that of the CW one. The pointing stability of the IR was measured with an IR beam profiler placed just in front of the split mirror. The shot to shot position of the maximum of the intensity distribution is plotted in Fig. 9 for 150 laser shots. The mean FWHM of the contour is about 75 μm and thus substantially smaller than the 3 mm FWHM of the XUV intensity distribution at the split mirror, not affecting the measured interferometric stability and time resolution.

Non-Linear XUV Optics Using the 20-GW XUV Beam-Line

The highest focused XUV intensity achieved was $\sim7\cdot10^{15}$ W/cm^2 assuming a 10 fs long pulse train envelope[59], an XUV focal spot size of 2 μm measured with an ion-microscope[67], the gold reflectivity ($\sim$12%) of the spherical mirror, the $\sim$60% reflectivity of the Si plate, the $\sim$20% transmission of the Sn filter for the given wavelengths and the 230 μJ generated pulse energy at the harmonic source. Such intensity allows the investigation of multi-XUV-photon multiple ionization. Here, we summarize the results obtained in He, Ar and Ne atoms. Some of the multi-XUV-photon schemes of this chapter have been used for the measurement of the attosecond pulse duration through 2nd IVAC measurements (schemes in He and Ar), which will be described in the next section.

Figure 10a shows the measured ion mass spectrum of He, in which He$^+$ is clearly observable. It should be noted that for this measurement an Sn filter was used. The XUV intensity dependence of the ion yield is depicted in Fig. 10b. The slope of the fitted line in the He$^+$ data is 2.1 $\pm$ 0.2, as expected for the underlying two photon ionization process, while the slope of the line fitted in the H$_2$O$^+$ date is 1.2 $\pm$ 0.1, as water molecules are single photon ionized at the XUV photon energies used. The verified two-XUV-photon ionization of He is a very convenient process in performing 2nd order autocorrelation measurements of XUV radiation with wavelengths $\geq$51 nm. The
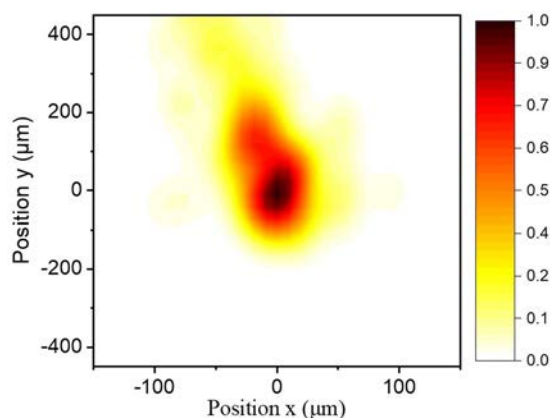
Figure 9. Measurement of the IR laser pointing instability. The contour illustrates the shot to shot distribution of the maximum of the IR laser intensity distribution measured just before the split mirror. The colorbar shows the normalized probability distribution of laser shots.
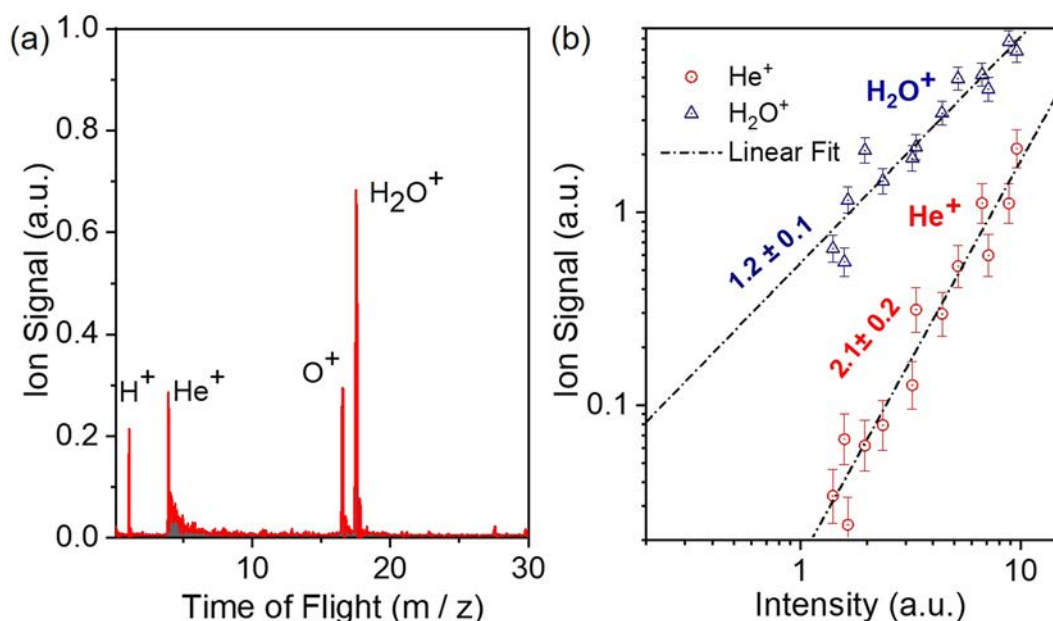

Figure 10. 2-XUV-photon ionization process of He. (**a**) TOF mass spectrum produced by the interaction of the XUV comb ($11^{th}-15^{th}$) with He gas.(**b**) XUV intensity dependence of the He^+. The slope of 2.1 ± 0.2 ascertains the second-order nonlinearity of the ionization process. The intensity axis in (b) has been calibrated using the O^+ ion signal, which is linear with the XUV intensity.

Ar and Ne ion TOF mass spectra are shown in Fig. 11a,b respectively. The latter reveals the formation of singly and doubly charged Ne, while the former shows recorded charge states of Ar up to +4 (Ar^{4+}). Figure 12 depicts the ionization schemes of Ne and Ar, while Fig. 13a shows the dependence of the Ar^{2+}, Ar^{3+} and N_2^+ yield and Fig. 13b the dependence of the Ne^+, Ne^{2+} and N_2^+ yield on the XUV pulse intensity I_{XUV}.

The Ar^+ ion mass peak of Fig. 11b was used for the calibration of the XUV energy scale (x-axis) of the Ne ion yield power dependence graph (Fig. 13b). The black dashed-dot lines in Fig. 13 are linear fits to the raw data. The error bars represent one standard deviation of the mean.

The results for Ar gas have been extensively discussed in ref. [59]. In brief, intensity dependence measurements performed for Ar^+, Ar^{2+} and Ar^{3+} were supported by numerical calculations revealing the dominant channels of these multi-XUV-photon multiple ionization studies. Comparison with the data obtained using FEL source indicates that there are differences in multiphoton ionization induced by the two different sources, which can be attributed to the different photon statistics of the two sources[59].

As expected for a single-photon ionization process, the dependence of the Ne^+ and N_2^+ yields on I_{XUV} is linear (Fig. 13b). The slope of the Ne^{2+} yield is found to be 3.1 ± 0.4 compatible with a three-photon ionization process. For the photon energies employed in this experiment both the sequential and the direct double ionization of Neon are three photon processes. Above the ionization saturation intensity the slope becomes 1.5 ± 0.1. For the
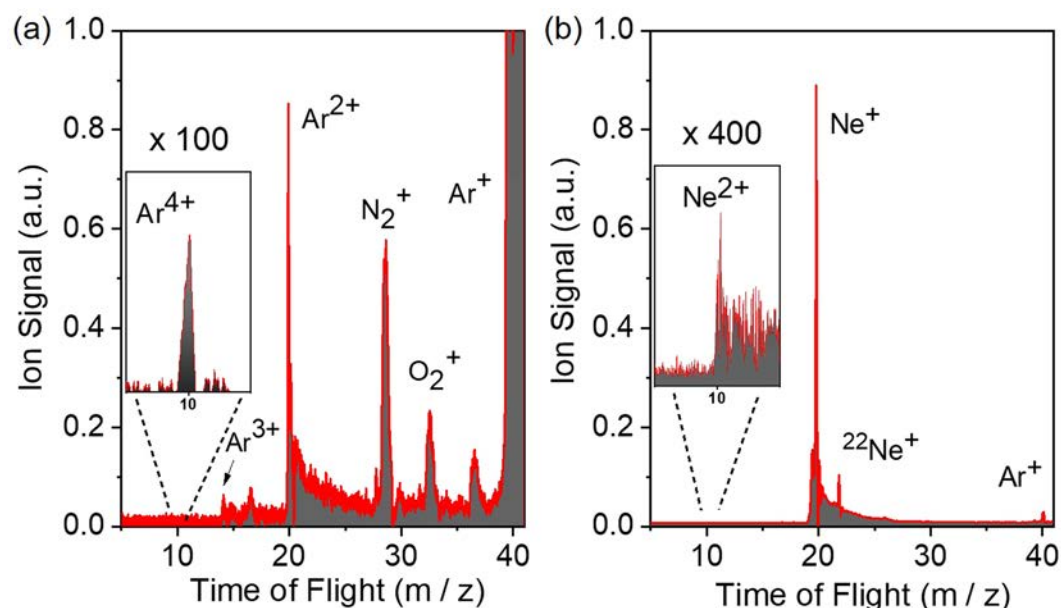
Figure 11. Time of Flight mass spectrum of Ar and Ne. (**a**) TOF mass spectrum produced by the interaction of the focused $11^{th}-15^{th}$ harmonics with Ar. The spectrum shows multiple charged Ar ions (Ar^{n+}) with n up to $+4$. (**b**) Measured Ne ion mass spectrum produced by the XUV radiation. In the spectrum two Ne^{+} ion mass peaks are to be seen corresponding to the two most abundant isotopes, ^{20}Ne and ^{22}Ne. A small Ne^{2+} peak and an Ar^{+} peak are also observed. The Ar^{+} peak originating from residual Ar gas is used for calibration of the mass ion spectrometer.
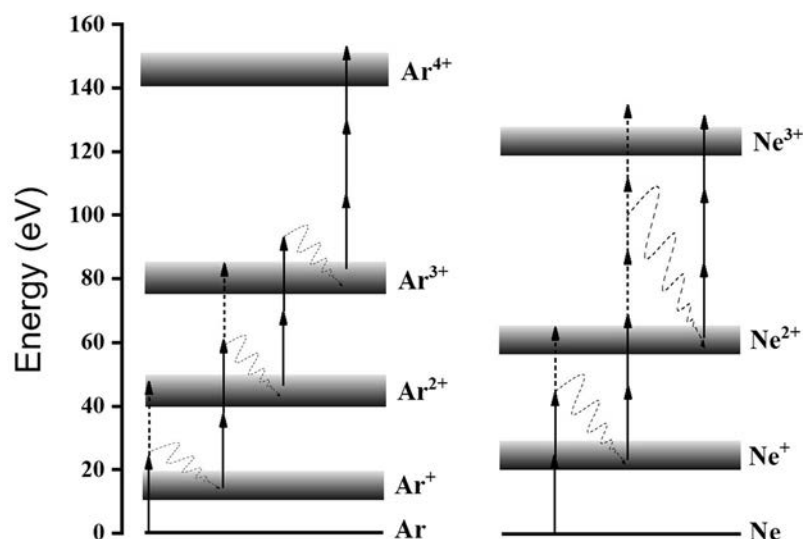
Figure 12. Multi-XUV-photon multiple ionization scheme. The ionization energy level schemes for Ar and Ne (excluding higher order processes (ATI) and decays to excited ionic states) depicting the direct and sequential channels.

next charge state, i.e. Ne^{3+}, six or more photon absorption is required. This charge state is not observable in the measured ion mass spectra.

Temporal Characterization of the Attosecond Pulse Trains

After having set up, characterized and tested the high photon flux beam-line, measurements towards temporal characterization of the APTs synthesized by the harmonic spectrum have been performed. It is worth noting that in these measurements the diameter of the aperture (A) in the "XUV filtering and diagnostics" chamber (Fig. 1) was reduced as to decrease the XUV signal to about half of its maximum value. Thus the outer part of the XUV beam cross-section was blocked. Consequently i) aberrations in the XUV beam were reduced and ii) the ratio of the short to long trajectory contribution in the transmitted XUV beam was increased. The method used is the 2nd
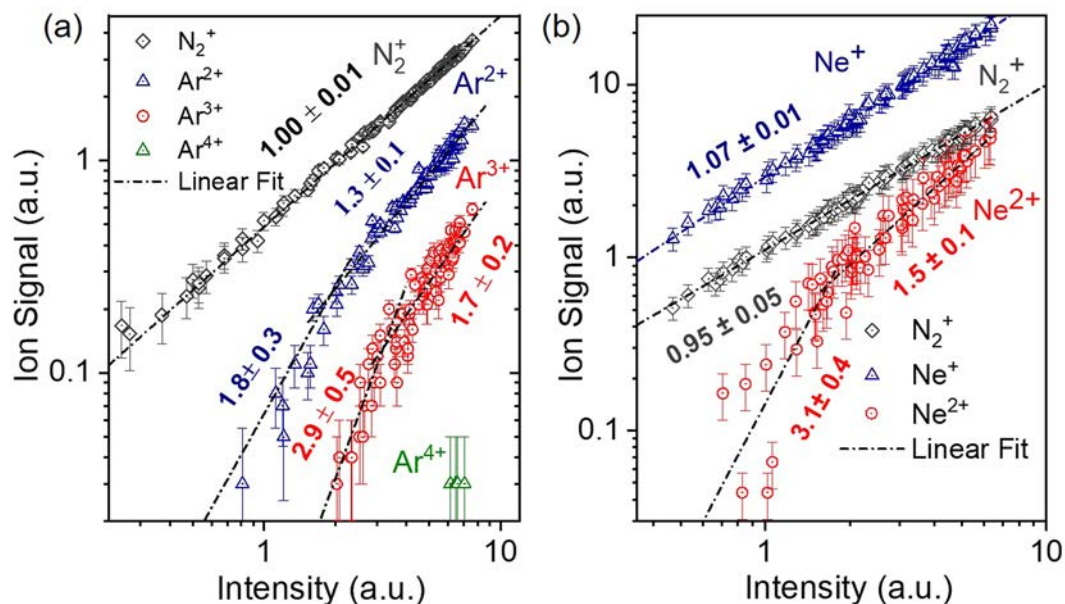
Figure 13. Ion yield dependence on the XUV radiation. XUV intensity dependence of different charge states of Ar (**a**) and Ne (**b**). In both panels the black dashed lines depict a linear fit on the raw data and the error bars represent one standard deviation of the mean. The slopes of the lines in both measurements, are in agreement with lowest-order perturbation theory i.e. with the order of the underlying non-linear process.

IVAC utilizing the delay line and TOF spectrometer discussed in section 3 and shown in Fig. 7a. As second order non-linear process, the two-XUV-photon ionization of both Ar^+ and He were used. This is in order to demonstrate different two-photon schemes that can be used in pulse duration measurements at higher photon energies. In performing the 2nd IVAC measurements the gas pressure in the interaction area was kept as low as possible in order to minimize the space charge effects which become visible by broadening the TOF ion-mass peaks. In Ar the traces are obtained by the superposition of the harmonics transmitted through the Sn filter. Before saturation, the Ar^{2+} yield as a function of the I_{XUV} in log-log scale has a linear dependence with slope ~2[59]. This slope is compatible with either two-XUV-photon direct double ionization of Ar or two-XUV-photon ionization of Ar^+ after saturation of the single photon ionization of Ar (see Fig. 12). Numerical calculations in[59] have shown that the latter channel, i.e. saturated single photon ionization of Ar followed by two photon ionization of Ar^+ is the dominant channel in the I_{XUV} range in which the present experiments have been performed.

Measured 2nd IVAC traces are shown in Fig. 14a,b. The blue rhombus is the trace obtained from the single photon ionization of H_2O. As expected for a linear process the IVAC shows no modulation. The Ar^{2+} ion yield (produced by the XUV radiation generated using only one gas jet) is measured here as a function of the delay between the two XUV pulses introduced by the translation of one part of the bisected spherical mirror. The gas jet in the HHG chamber was set at 20 cm after the laser focus in order to minimize the contribution of the long electron trajectory. Low temporal resolution scans recorded with a step of 350 asec have been performed in determining the duration of the APT envelope (Fig. 14a). The red points are the raw data, averages of 50 laser points and the error bar corresponds to the standard deviation of the mean value. The black curve is a Gaussian fit to the data. The fit results in an XUV pulse envelope having a duration of 9.8 ± 0.9 fs, verifying the estimated duration used in ref. [59]. A fine scan using a time delay step of 50 asec is shown in Fig. 14b. The Ar^{2+} ion yield, as expected, is modulated with the half period of the driving field. The gray circles are the recorded raw data (averages of 50 laser shots). The raw data in the fine scan of Fig. 14b are fluctuating around the mean value mainly due to interferometric instabilities (within the cycle of the XUV field) and XUV beam pointing instabilities, which are both enhanced by the non-linearity of the process. Long averaging and calculating moving averages substantially reduce the strong shot-to-shot fluctuation of the recoded data. The red circles are the moving averages of the raw data taken over 10 points. The black curve is fit of a series of Gaussian distributions to the averaged points. In this fit the free parameters are the common width, height of the Gaussians as well as the peak to peak distance. Furthermore the comb of Gaussians are multiplied by a fixed envelope distribution taken from the fit of Fig. 14a. The pulse width resulting from the Gaussian distributions is found to be $\tau_{XUV} = 650 \pm 80$ asec. The error of 80 asec appearing in all measurements is the largest resulted standard deviation, among all the fits in the raw data of all measured traces. The above pulse duration of the attosecond pulses in the APT is synthesized essentially by the three harmonics 11th, 13th and 15th. Since here only one gas jet was utilized, the APT beam-line power to be rigorously reported is 11.0 ± 3.5 GW, the error originating mainly from the uncertainty in the calibration of the XUV photodiode.

The two-XUV-photon ionization of He^+ has also been used to measure the produced APTs through 2nd IVAC, shown in Fig. 15a and alongside with Fig. 15b showing a 2nd IVAC trace of Ar^{2+}. The trace of Fig. 15b is a different run than the one shown in Fig. 14b verifying reproducibility of the results. All points, error bars and curves are as those in Fig. 14b. with the only difference being that here we do not use any envelope distribution in the fit either
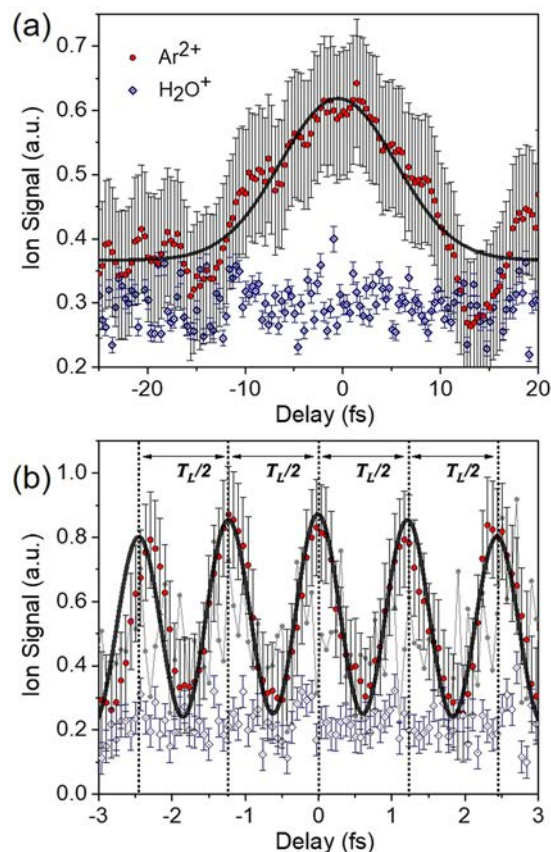
Figure 14. Measured 2nd IVAC trace i.e. Ar^{2+} ion signal as a function of the XUV-XUV delay line. The XUV radiation is produced by a single gas jet of xenon and is transmitted through a Sn filter. (**a**) A coarse time delay scan with 350 asec step is revealing a modulation in Ar^{2+} ion signal represented by the red circles, while the blue rhombus depicting the single photon ionization of H_2O shows no modulation. A Gaussian fit in the data points of Ar^{2+} yields a time duration of $\tau_{XUV} = 9.8 \pm 0.9$ fs. (**b**) A fine scan with time delay step of 50 asec. The gray circles correspond to the raw data recorded for Ar^{2+}. The moving averages of the raw data taken over 10 points are represented by the red circles. The black curve is a fit of a sequence of gaussian pulses in the averaged points.
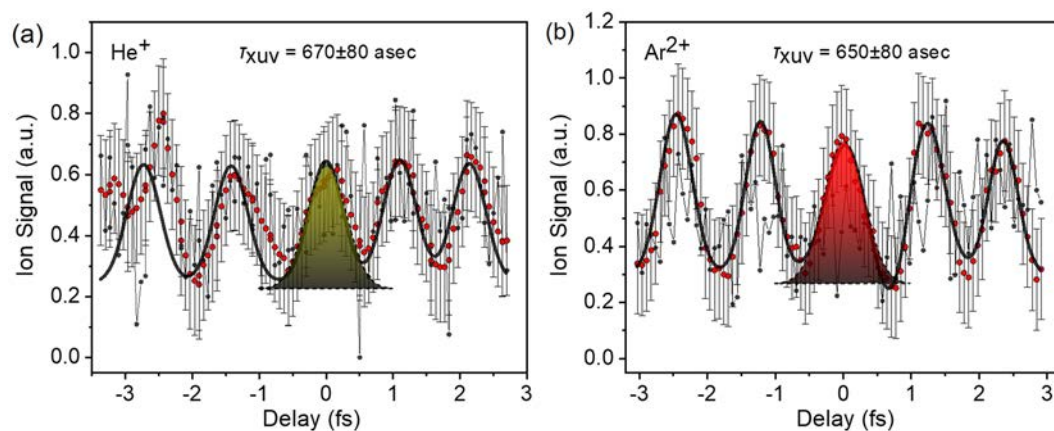
Figure 15. (**a**) Measured 2nd IVAC trace of the He^+ (**b**) 2nd IVAC trace of the Ar^{2+} ion signal as a fuction of the delay of the XUV-XUV delay line. The gray circles correspond to the raw data recorded, the moving averages of the raw data taken over 10 points are represented by the red circles. The black curves is a Gaussian fit over the averaged points. The temporal width of the Gaussian fit corresponds to a pulse duration of 670 ± 80 as and 650 ± 80, for He^+ and Ar^{2+} respectively.

Harmonic order	9	11	13	15	17
λ_q(nm)	88.9	72.7	61.5	53.3	47.0
α_S	1	0.435	−0.4	−1.5	−2.96
α_L	−23.97	−23.56	−22.88	−21.96	−20.71
θ_S(mrad)	0.195	0.15	0.127	0.126	0.148
θ_L(mrad)	1.74	1.40	1.15	0.96	0.79

Table 1. Parameters of the 9th to the 17th harmonics generated in Xe. The intensity of the laser field used is 10^{14} W/cm² and the unit for α is 10^{-14} W⁻¹·cm².
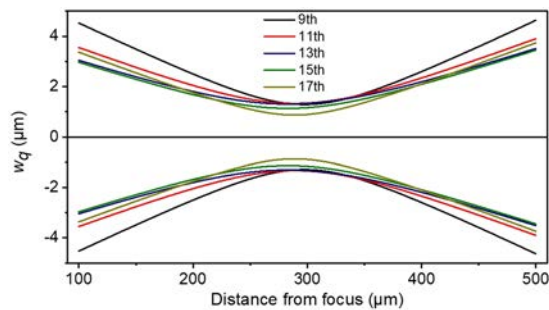
Figure 16. Calculated focal areas of the five harmonics 9th, 11th, 13th, 15th and 17th. The graph depicts the harmonic beam waist as a function of the distance from the focus of the spherical mirror. The x-axis shows the focus position of the harmonics on the propagation axis. The focus position of the harmonics is found to be $\approx$ 290 μm away from the focus of the 5 cm mirror. Their beam waist ratios are 0.99:1.01:1:0.87:0.67 for harmonic 9th, 11th, 13th, 15th and 17th respectively.

for the He or the Ar trace. This is because in these runs the peak height distribution within the error bars did not depict any envelope type modulation. The pulse duration measured using He as non-linear medium is 670 ± 80 asec and the one of the superposition of harmonics 11th, 13th and 15th measured in Ar²⁺ is the same as the one of Fig. 14b. The two values are well within the error bar and thus essentially identical.

The measured durations here are similar to those retrieved in previous experiments implemented in a a 3 m focal length beam-line applying 2nd IVAC in two photon ionization of He but about 65% longer than those measured through the RABBIT technique[39]. The discrepancy between the 2nd IVAC and RABBIT originates from the fact that 2nd IVAC measures averages of spatiotemporally dependent pulse durations and the contribution of both long and short trajectories, while RABBIT measures average phases[39]. An additional effect to be considered is pointed out recently in refs. [66,68]. Different harmonics, due to their different divergence are focused at different positions, have different focal spots and therefore lead to only partial spatial overlap of the superimposed harmonics and to different Gouy phase contributions in the harmonic superposition. At specific conditions, e.g. spectrum with harmonics of very different order, the spatial overlap becomes notably small and the Gouy phase difference large, thus reducing a lot the temporal confinement. 2nd IVAC is sensitive to these effects and thus reveals fairly realistic pulse durations. However, for the three harmonics employed in this experiment substantial spatial overlap is present as indicated by the results of a recent work[69], were separation of the harmonic foci was not observed.

In order to verify the significant spatial overlap of the three harmonics used in the 2nd IVAC measurements we have performed calculations of the focal areas of the three harmonics, for a bandwidth spanning from the 9th to the 17th harmonic and Xe gas as harmonic generating medium. We are using the expression $\theta_{S,L} = \frac{\lambda_q}{\pi w_q}\sqrt{1 + 4\alpha_{S,L}^2 I_L^2 \frac{w_q^4}{w_f^4}}$ of the divergence of the harmonics originating from the electron short (S) and long (L) trajectories at the point of the interaction for the harmonic order q, as given in ref. [70]. λ_q, w_q, are the wavelength and the beam waist of the harmonic q, w_f is the waist size of the laser beam, $\alpha_{S,L}$ is the S and L trajectory coefficient and I_L is the IR driving laser peak intensity. The beam waist was measured at the emission plane and it was found to be $w_f \approx 350$ μm. Using Gaussian optics the harmonic beam waist can be obtained by $w_q = \frac{w_f}{\sqrt{q_{eff}}}$ where q_{eff} is the effective nonlinearity coefficient with $q_{eff} \approx 5$ for all the harmonics laying in the plateau of the harmonic spectrum[69,71,72]. For a peak intensity 10^{14} W/cm² all the studied harmonics are laying in the plateau and the trajectory coefficient $\alpha_{S,L}$ is extracted by solving the three-step semi-classical model[73]. The results are summarized in Table 1.

After extracting the divergence of the different harmonics, the virtual source positions for each of the generated harmonics is calculated assuming only short trajectory contribution. The focus positions of the harmonics, after reflection on the spherical mirror of focal length $f = 5$ cm, are calculated using geometrical optics. Here the paraxial approximation is applied since the divergence of the harmonics is below the paraxial limit. The results of the calculations are shown in Fig. 16.
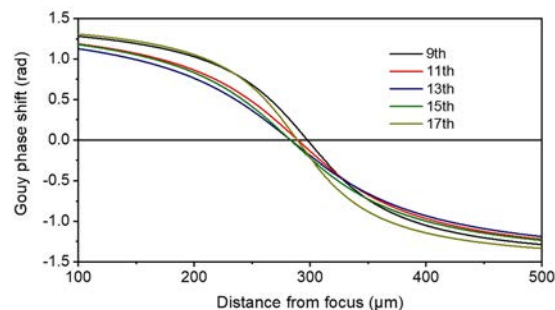
Figure 17. Calculated Gouy phase shift of the five harmonics 9th, 11th, 13th, 15th and 17th. The x-axis shows the focus position of the harmonics on the propagation axis. The focus position of the harmonics is found to be ≈ 290 μm away from the focus position of the 5 cm mirror.

The distance of the positions of the five foci is 8.2 μm between the 9th and 11th, 6.3 μm between the 11th and 13th harmonic, ~0 μm between the 13th and 15th harmonic, 5.9 μm between the 15th and 17th harmonic and thus it is negligibly small with respect to their confocal parameter (≈170 μm for 13th harmonic). The size of the focal spots is slightly different. The ratios for the beam waists at the focus are 0.99:1.01:1:0.87:0.67 for the harmonics 9th, 11th, 13th, 15th and 17th respectively. Under these conditions, the spatial overlap of the five harmonics is substantial. The Gouy phase at the beam waist for each harmonic can be calculated and is shown in Fig. 17. Its variation for the different harmonics (assuming as central frequency the 13th harmonic) $\varphi_9 = 0.24$ rad, $\varphi_{11} = 0.08$ rad, $\varphi_{13} = 0$ rad, $\varphi_{15} = 0$ rad, $\varphi_{17} = 0.13$ rad is also negligibly small. In this case, the duration of the APT pulses is not significantly affected. In fact, the different beam waists of the 11th, 13th, 15th harmonics lead to more similar amplitudes of the interfering harmonics than those generated.

Similar calculations have been further performed for the long electron trajectories, which present larger harmonic divergence. In this case, the virtual foci are placed closer to the focusing element. It is found that the difference of the foci positions between L and S trajectories is ≈30 μm which is consistent with previous experimental findings[69,72,74] and also smaller than the confocal parameter, thus not substantially affecting the APT pulse duration in particular because the long trajectory contributions are reduced through the geometry used.

Conclusions

In summary, a detailed description of an ultra-intense attosecond XUV beam line has been presented. A ten GW class average peak power attosecond source in the XUV spectral region 15–25 eV is demonstrated. These specifications are to our knowledge unique for an XUV source. While in a previous publication the high power of the source (20 GW) was reported[59] attosecond confinement, although expected, could not be rigorously claimed as the previous work did not include any pulse duration measurements. In the present work, APT durations of the order of 650 asec have been measured opening the way to ten-GW class attosecond XUV sources. The source is based on harmonic generation in long (9 m) focusing geometry of the driving IR laser radiation. The pulse duration of both the APT pulses and the envelope have been measured though 2nd IVAC i) in He employing two-XUV-photon ionization as a second order process as well as ii) in Ar exploiting two-XUV-photon ionization of Ar+ under saturation of neutral Ar ionization. Measurements with both gases resulted in the same pulse durations within the experimental error. High non-linear XUV-optics in terms of multiple multi-XUV-photon ionization of He, Ar and Ne atoms, have been further demonstrated using the above beam line. The combination of high pulse energy and short duration opens up excellent perspectives for sub-fs XUV-pump-XUV-probe experiments in all states of matter. At the same time the XUV intensity levels reached enable the study of strong field effects in the XUV spectral region. As a further perspective, scaling previous parameters of isolated attosecond pulses[64], our source holds promise of generating few μJ level isolated attosecond pulses through polarization gating approaches. Those are advanced perspectives for the Hellenic National Research Infrastructure HELLAS-CH, part of which is the present beam line.

The results of the present work further hints towards an unprecedented performance of the two 1-kHz repetition rate attosecond beam lines of the Extreme Light Infrastructure – Attosecond Light Pulse Source (ELI-ALPS) facility currently being under implementation[75], driven by shorter laser pulses with similar pulse energies. The geometry of one of the two beam-lines of ELI-ALPS is very close to that of the present source, while the second one is several times longer and offers phase matching control capacities. Thus, it is expected to further scale up the source throughput. The 1 kHz repetition rate of these sources in combination with the CEP stabilized driving laser will provide the by far best ever conditions for attosecond XUV-pump-XUV-probe investigations using isolated attosecond pulses and kinematically nearly complete experiments through e-e, e-ion and ion-ion coincidence measurements.

References

1. Träger, F. ed. *Springer handbook of lasers and optics* (Springer, Dordrecht, New York, 2012).
2. Krausz, F. & Ivanov, M. Attosecond physics. *Rev. Mod. Phys.* **81**, 163–234, https://doi.org/10.1103/RevModPhys.81.163 (2009).
3. Paul, P. M. *et al.* Observation of a train of attosecond pulses from high harmonic generation. *Science (New York, N.Y.)* **292**, 1689–1692, https://doi.org/10.1126/science.1059413 (2001).

4. Mairesse, Y. & Quéré, F. Frequency-resolved optical gating for complete reconstruction of attosecond bursts. *Phys. Rev. A* **71**, 803, https://doi.org/10.1103/PhysRevA.71.011401 (2005).
5. Chini, M., Gilbertson, S., Khan, S. D. & Chang, Z. Characterizing ultrabroadband attosecond lasers. *OPTICS EXPRESS* **18**, 13006–13016, https://doi.org/10.1364/OE.18.013006 (2010).
6. Conference on Lasers and Electro-Optics (CLEO), 2013. 9–14 June 2013, San Jose, CA, USA (IEEE, Piscataway, NJ, 2013).
7. Gruson, V. *et al.* Attosecond dynamics through a Fano resonance: Monitoring the birth of a photoelectron. *Science (New York, N.Y.)* **354**, 734–738, https://doi.org/10.1126/science.aah5188 (2016).
8. Spanner, M., Bertrand, J. B. & Villeneuve, D. M. *In situ* attosecond pulse characterization techniques to measure the electromagnetic phase. Phys. Rev. A 94; https://doi.org/10.1103/PhysRevA.94.023825 (2016).
9. Mairesse, Y. *et al.* High harmonic XUV spectral phase interferometry for direct electric-field reconstruction. *Phys. Rev. Lett.* **94**, 173903, https://doi.org/10.1103/PhysRevLett.94.173903 (2005).
10. Iaconis, C. & Walmsley, I. A. Self-Referencing Spectral Interferometry For Measuring Ultrashort Optical Pulses - Quantum Electronics, IEEE Journal of // Self-referencing spectral interferometry for measuring ultrashort optical pulses. *IEEE J. Quantum Electron.* **35**, 501–509, https://doi.org/10.1109/3.753654 (1999).
11. Eckle, P. *et al.* Attosecond angular streaking. *Nat Phys* **4**, 565–570, https://doi.org/10.1038/nphys982 (2008).
12. Pedatzur, O. *et al.* Double-blind holography of attosecond pulses. *Nature Photonics* **13**, 91–95, https://doi.org/10.1038/s41566-018-0308-z (2019).
13. Carpeggiani, P. *et al.* Vectorial optical field reconstruction by attosecond spatial interferometry. *Nature Photon* **11**, 383–389, https://doi.org/10.1038/nphoton.2017.73 (2017).
14. Constant, E., Taranukhin, V. D., Stolow, A. & Corkum, P. B. Methods for the measurement of the duration of high-harmonic pulses. *Phys. Rev. A* **56**, 3870–3878, https://doi.org/10.1103/PhysRevA.56.3870 (1997).
15. Orfanos, I. *et al.* Attosecond pulse metrology. *APL Photonics* **4**, 80901, https://doi.org/10.1063/1.5086773 (2019).
16. Drescher, M. *et al.* Time-resolved atomic inner-shell spectroscopy. *Nature* **419**, 803–807, https://doi.org/10.1038/nature01143 (2002).
17. Uiberacker, M. *et al.* Attosecond real-time observation of electron tunnelling in atoms. *Nature* **446**, 627–632, https://doi.org/10.1038/nature05648 (2007).
18. Goulielmakis, E. *et al.* Direct measurement of light waves. *Science (New York, N.Y.)* **305**, 1267–1269, https://doi.org/10.1126/science.1100866 (2004).
19. Itatani, J. *et al.* Tomographic imaging of molecular orbitals. *Nature* **432**, 867–871, https://doi.org/10.1038/nature03183 (2004).
20. Cavalieri, A. L. *et al.* Attosecond spectroscopy in condensed matter. *Nature* **449**, 1029–1032, https://doi.org/10.1038/nature06229 (2007).
21. Schultze, M. *et al.* Delay in photoemission. *Science (New York, N.Y.)* **328**, 1658–1662, https://doi.org/10.1126/science.1189401 (2010).
22. Isinger, M. *et al.* Photoionization in the time and frequency domain. *Science (New York, N.Y.)* **358**, 893–896, https://doi.org/10.1126/science.aao7043 (2017).
23. Goulielmakis, E. *et al.* Real-time observation of valence electron motion. *Nature* **466**, 739–743, https://doi.org/10.1038/nature09212 (2010).
24. Calegari, F. *et al.* Ultrafast electron dynamics in phenylalanine initiated by attosecond pulses. *Science (New York, N.Y.)* **346**, 336–339, https://doi.org/10.1126/science.1254061 (2014).
25. Kraus, P. M. *et al.* Measurement and laser control of attosecond charge migration in ionized iodoacetylene. *Science (New York, N.Y.)* **350**, 790–795, https://doi.org/10.1126/science.aab2160 (2015).
26. Beaulieu, S. *et al.* Attosecond-resolved photoionization of chiral molecules. *Science (New York, N.Y.)* **358**, 1288–1294, https://doi.org/10.1126/science.aao5624 (2017).
27. Tzallas, P., Skantzakis, E., Nikolopoulos, L. A. A., Tsakiris, G. D. & Charalambidis, D. Extreme-ultraviolet pump–probe studies of one-femtosecond-scale electron dynamics. *Nat Phys* **7**, 781–784, https://doi.org/10.1038/nphys2033 (2011).
28. Carpeggiani, P. A. *et al.* Disclosing intrinsic molecular dynamics on the 1-fs scale through extreme-ultraviolet pump-probe measurements. Phys. Rev. A 89; https://doi.org/10.1103/PhysRevA.89.023420 (2014).
29. Nabekawa, Y. *et al.* Sub-10-fs control of dissociation pathways in the hydrogen molecular ion with a few-pulse attosecond pulse train. *Nature communications* **7**, 12835, https://doi.org/10.1038/ncomms12835 (2016).
30. Palacios, A., González-Castrillo, A. & Martín, F. Molecular interferometer to decode attosecond electron-nuclear dynamics. *Proceedings of the National Academy of Sciences of the United States of America* **111**, 3973–3978, https://doi.org/10.1073/pnas.1316762111 (2014).
31. Takahashi, E. J., Lan, P., Mucke, O. D., Nabekawa, Y. & Midorikawa, K. Attosecond nonlinear optics using gigawatt-scale isolated attosecond pulses. *Nature communications* **4**, 2691, https://doi.org/10.1038/ncomms3691 (2013).
32. Tzallas, P., Charalambidis, D., Papadogiannis, N. A., Witte, K. & Tsakiris, G. D. Direct observation of attosecond light bunching. *Nature* **426**, 267–271, https://doi.org/10.1038/nature02091 (2003).
33. Nikolopoulos, L. A. A. *et al.* Second order autocorrelation of an XUV attosecond pulse train. *Physical review letters* **94**, 113905, https://doi.org/10.1103/PhysRevLett.94.113905 (2005).
34. Nabekawa, Y. *et al.* Interferometric autocorrelation of an attosecond pulse train in the single-cycle regime. *Physical review letters* **97**, 153904, https://doi.org/10.1103/PhysRevLett.97.153904 (2006).
35. Nabekawa, Y. *et al.* Conclusive evidence of an attosecond pulse train observed with the mode-resolved autocorrelation technique. *Physical review letters* **96**, 83901, https://doi.org/10.1103/PhysRevLett.96.083901 (2006).
36. Faucher, O. *et al.* Four-dimensional investigation of the 2nd order volume autocorrelation technique. *Appl. Phys. B* **97**, 505–510, https://doi.org/10.1007/s00340-009-3559-z (2009).
37. Heissler, P. *et al.* Two-photon above-threshold ionization using extreme-ultraviolet harmonic emission from relativistic laser–plasma interaction. *New J. Phys.* **14**, 43025, https://doi.org/10.1088/1367-2630/14/4/043025 (2012).
38. Kolliopoulos, G. *et al.* Single-shot autocorrelator for extreme-ultraviolet radiation. *J. Opt. Soc. Am. B* **31**, 926, https://doi.org/10.1364/JOSAB.31.000926 (2014).
39. Kruse, J. E. *et al.* Inconsistencies between two attosecond pulse metrology methods. A comparative study. Phys. Rev. A 82; https://doi.org/10.1103/PhysRevA.82.021402 (2010).
40. Kobayashi, Y., Sekikawa, T., Nabekawa, Y. & Watanabe, S. 27-fs extreme ultraviolet pulse generation by high-order harmonics. *Opt. Lett.* **23**, 64, https://doi.org/10.1364/OL.23.000064 (1998).
41. Descamps, D., Roos, L., Delfin, C., L'Huillier, A. & Wahlström, C.-G. Two- and three-photon ionization of rare gases using femtosecond harmonic pulses generated in a gas medium. *Phys. Rev. A* **64**, 273, https://doi.org/10.1103/PhysRevA.64.031404 (2001).
42. Sekikawa, T., Ohno, T., Yamazaki, T., Nabekawa, Y. & Watanabe, S. Pulse Compression of a High-Order Harmonic by Compensating the Atomic Dipole Phase. *Phys. Rev. Lett.* **83**, 2564–2567, https://doi.org/10.1103/PhysRevLett.83.2564 (1999).
43. Nabekawa, Y., Hasegawa, H., Takahashi, E. J. & Midorikawa, K. Production of doubly charged helium ions by two-photon absorption of an intense sub-10-fs soft x-ray pulse at 42 eV photon energy. *Physical review letters* **94**, 43001, https://doi.org/10.1103/PhysRevLett.94.043001 (2005).
44. Manschwetus, B. *et al.* Two-photon double ionization of neon using an intense attosecond pulse train. *Phys. Rev. A* **93**; https://doi.org/10.1103/PhysRevA.93.061402 (2016).

45. Miyamoto, N. *et al*. Observation of two-photon above-threshold ionization of rare gases by xuv harmonic photons. *Physical review letters* **93**, 83903, https://doi.org/10.1103/PhysRevLett.93.083903 (2004).

46. Sekikawa, T., Katsura, T., Miura, S. & Watanabe, S. Measurement of the intensity-dependent atomic dipole phase of a high harmonic by frequency-resolved optical gating. *Physical review letters* **88**, 193902, https://doi.org/10.1103/PhysRevLett.88.193902 (2002).

47. Chatziathanasiou, S. *et al*. Generation of Attosecond Light Pulses from Gas and Solid State Media. *Photonics* **4**, 26, https://doi.org/10.3390/photonics4020026 (2017).

48. Chen, S., Rever, M., Zhang, P., Theobald, W. & Umstadter, D. Observation of relativistic cross-phase modulation in high-intensity laser-plasma interactions. *Physical review. E, Statistical, nonlinear, and soft matter physics* **74**, 46406, https://doi.org/10.1103/PhysRevE.74.046406 (2006).

49. Gordienko, S., Pukhov, A., Shorokhov, O. & Baeva, T. Relativistic Doppler effect: universal spectra and zeptosecond pulses. *Phys. Rev. Lett.* **93**, 115002, https://doi.org/10.1103/PhysRevLett.93.115002 (2004).

50. Bulanov, S. V., Naumova, N. M. & Pegoraro, F. Interaction of an ultrashort, relativistically strong laser pulse with an overdense plasma. *Physics of Plasmas* **1**, 745–757, https://doi.org/10.1063/1.870766 (1994).

51. Tarasevitch, A., Lobov, K., Wünsche, C. & Linde, Dvonder Transition to the relativistic regime in high order harmonic generation. *Phys. Rev. Lett.* **98**, 103902, https://doi.org/10.1103/PhysRevLett.98.103902 (2007).

52. Jafari, B. & Soofi, H. High bandwidth and responsivity mid-infrared graphene photodetector based on a modified metal-dielectric-graphene architecture. *Applied optics* **58**, 6280–6287, https://doi.org/10.1364/AO.58.006280 (2019).

53. Kahaly, S. *et al*. Direct observation of density-gradient effects in harmonic generation from plasma mirrors. *Physical review letters* **110**, 175001, https://doi.org/10.1103/PhysRevLett.110.175001 (2013).

54. Thaury, C. *et al*. Plasma mirrors for ultrahigh-intensity optics. *Nat Phys* **3**, 424–429, https://doi.org/10.1038/nphys595 (2007).

55. Tsakiris, G. D., Eidmann, K., Meyer-ter-Vehn, J. & Krausz, F. Route to intense single attosecond pulses. *J. Opt. Soc. Am. B* **8**, 19, https://doi.org/10.1088/1367-2630/8/1/019 (2006).

56. Nomura, Y. *et al*. Attosecond phase locking of harmonics emitted from laser-produced plasmas. *Nat Phys* **5**, 124–128, https://doi.org/10.1038/nphys1155 (2008).

57. Heyl, C. M., Arnold, C. L., Couairon, A. & L'Huillier, A. Introduction to macroscopic power scaling principles for high-order harmonic generation. *J. Phys. B: At. Mol. Opt. Phys.* **50**, 13001, https://doi.org/10.1088/1361-6455/50/1/013001 (2017).

58. Seres, J. *et al*. Coherent superposition of laser-driven soft-X-ray harmonics from successive sources. *Nat Phys* **3**, 878–883, https://doi.org/10.1038/nphys775 (2007).

59. Nayak, A. *et al*. Multiple ionization of argon via multi-XUV-photon absorption induced by 20-GW high-order harmonic laser pulses. *Phys. Rev. A* **98**, 66, https://doi.org/10.1103/PhysRevA.98.023426 (2018).

60. Duris, J. *et al*. Tunable isolated attosecond X-ray pulses with gigawatt peak power from a free-electron laser. *Nature Photonics* **14**, 30–36, https://doi.org/10.1038/s41566-019-0549-5 (2020).

61. Constant, E. *et al*. Optimizing High Harmonic Generation in Absorbing Gases: Model and Experiment. *Phys. Rev. Lett.* **82**, 1668–1671, https://doi.org/10.1103/PhysRevLett.82.1668 (1999).

62. Hergott, J.-F. *et al*. Extreme-ultraviolet high-order harmonic pulses in the microjoule range. Phys. Rev. A 66; https://doi.org/10.1103/PhysRevA.66.021801 (2002).

63. Tzallas, P. *et al*. Generation of intense continuum extreme-ultraviolet radiation by many-cycle laser fields. *Nat Phys* **3**, 846–850, https://doi.org/10.1038/nphys747 (2007).

64. Skantzakis, E., Tzallas, P., Kruse, J., Kalpouzos, C. & Charalambidis, D. Coherent continuum extreme ultraviolet radiation in the sub-100-nJ range generated by a high-power many-cycle laser field. *Opt. Lett.* **34**, 1732–1734, https://doi.org/10.1364/OL.34.001732 (2009).

65. Kolliopoulos, G., Carpeggiani, P. A., Rompotis, D., Charalambidis, D. & Tzallas, P. A compact collinear polarization gating scheme for many cycle laser pulses. *The Review of scientific instruments* **83**, 63102, https://doi.org/10.1063/1.4725590 (2012).

66. Dacasa, H. *et al*. Single-shot extreme-ultraviolet wavefront measurements of high-order harmonics. *Opt. Express* **27**, 2656–2670, https://doi.org/10.1364/OE.27.002656 (2019).

67. Tzallas, P. *et al*. Time gated ion microscopy of light-atom interactions. *J. Opt.* **20**, 24018, https://doi.org/10.1088/2040-8986/aaa326 (2018).

68. Isinger, M. *et al*. Accuracy and precision of the RABBIT technique. *Philosophical transactions. Series A, Mathematical, physical, and engineering sciences* **377**, 20170475, https://doi.org/10.1098/rsta.2017.0475 (2019).

69. Chatziathanasiou, S., Kahaly, S., Charalambidis, D., Tzallas, P. & Skantzakis, E. Imaging the source of high-harmonics generated in atomic gas media. *Opt. Express* **27**, 9733, https://doi.org/10.1364/OE.27.009733 (2019).

70. He, X. *et al*. Spatial and spectral properties of the high-order harmonic emission in argon for seeding applications. *Phys. Rev. A* **79**, 888, https://doi.org/10.1103/PhysRevA.79.063829 (2009).

71. Wahlstroem, C.-G. *et al*. High-order harmonic generation in rare gases with an intense short-pulse laser. *Phys. Rev. A* **48**, 4709–4720, https://doi.org/10.1103/PhysRevA.48.4709 (1993).

72. Quintard, L. *et al*. Optics-less focusing of XUV high-order harmonics. *Science advances* **5**, eaau7175, https://doi.org/10.1126/sciadv.aau7175 (2019).

73. Lewenstein, M., Balcou, P., Ivanov, M. Y., L'Huillier, A. & Corkum, P. B. Theory of high-harmonic generation by low-frequency laser fields. *Phys. Rev. A* **49**, 2117–2132, https://doi.org/10.1103/PhysRevA.49.2117 (1994).

74. Wikmark, H. *et al*. Spatiotemporal coupling of attosecond pulses. Proceedings of the National Academy of Sciences of the United States of America; https://doi.org/10.1073/pnas.1817626116 (2019).

75. Kühn, S. *et al*. The ELI-ALPS facility. The next generation of attosecond sources. *J. Phys. B: At. Mol. Opt. Phys.* **50**, 132002, https://doi.org/10.1088/1361-6455/aa6ee8 (2017).

Acknowledgements

Author contributions

I.M., I.O., E.S., I.L. have participated in all experimental runs, in the data analysis and in the preparation of the manuscript, and P.T. has designed the beamline and participated in all parts of the work, A.N. participated in the Ar measurements and did numerical calculation, J.P. and B.M. participated in the Ne and He measurements, C.K. did laser work and participated in the preparation of the manuscript, N.P. has performed all I.T. and automation work, M.D. and S.K. took part in initial experimental runs and in the data analysis, K.V., P.J. and A.Ľ.H. contributed to the evaluation of the beam-line, to the preparation of the non-linear studies and to the preparation of the manuscript and DC has coordinated the work and contributed to the majority of its different parts.

Competing interests

The authors declare no competing interests.

Additional information

Correspondence and requests for materials should be addressed to D.C.

Reprints and permissions information is available at www.nature.com/reprints.

Publisher's note Springer Nature remains neutral with regard to jurisdictional claims in published maps and institutional affiliations.

Attosecond pulse metrology ⒻF

I. Orfanos, I. Makos, I. Liontos ⒾD, E. Skantzakis ⒾD, B. Förg, D. Charalambidis, and P. Tzallas

COLLECTIONS

Ⓕ   This paper was selected as Featured

View Online   **Export Citation**   **CrossMark**

ARTICLES YOU MAY BE INTERESTED IN

Interaction of semiconductor metasurfaces with short laser pulses: From nonlinear-optical response toward spatiotemporal shaping
Journal of Applied Physics **126**, 085705 (2019); https://doi.org/10.1063/1.5108630

Photovoltaic field effect transistor (PVFET)-based Ge/Si photodetector for low-power silicon photonics
AIP Advances **9**, 085226 (2019); https://doi.org/10.1063/1.5100039

GaSb photovoltaic cells for laser power conversion
AIP Conference Proceedings **2149**, 050007 (2019); https://doi.org/10.1063/1.5124192

Attosecond pulse metrology Ⓕ

I. Orfanos,[1,2] I. Makos,[1,2] I. Liontos,[1] ⓘD E. Skantzakis,[1] ⓘD B. Förg,[3,4] D. Charalambidis,[1,2] and P. Tzallas[1,a]

AFFILIATIONS

[1] Foundation for Research and Technology - Hellas, Institute of Electronic Structure & Laser, P.O. Box 1527, GR71110 Heraklion (Crete), Greece
[2] Department of Physics, University of Crete, P.O. Box 2208, GR71003 Heraklion (Crete), Greece
[3] Max Planck Institute of Quantum Optics, Garching, Germany
[4] Department of Physics, Ludwig-Maximilians-Universität München, München, Germany

[a] Author to whom correspondence should be addressed: ptzallas@iesl.forth.gr

ABSTRACT

The long-standing scientific quest of real-time tracing electronic motion and dynamics in all states of matter has been remarkably benefited by the development of intense laser-based pulsed sources with a temporal resolution in the attosecond [1 attosecond = 10^{-18} s] time scale. Nowadays, attosecond pulses are routinely produced in laboratories by the synthesis of the frequency components of broadband coherent extreme ultraviolet (XUV) radiation generated by the interaction of matter with intense femtosecond (fs) pulses. Attosecond pulse metrology aims at the accurate and complete determination of the temporal and phase characteristics of attosecond pulses and is one of the most innovative challenges in the broad field of ultrashort pulse metrology. For more than two decades since coherent high-brilliance broadband XUV sources have become available, fascinating advances in attosecond pulse metrology have led to the development of remarkable techniques for pulse duration measurements as well as the complete reconstruction of those pulses. Nonetheless, new challenges born from diverse fields call upon for additional efforts and continuously innovative ideas in the field. In this perspective article, we follow the history of ultrashort pulse technology tracing attosecond pulse production and characterization approaches, focus on the operation principles of the most commonly used techniques in the region where they interact with matter, address their limitations, and discuss future prospects as well as endeavors of the field to encounter contemporary scientific progress.

I. HISTORICAL OVERVIEW

A. Chronoscopy of ultrashort pulse technology advances

The complete description of light-matter interaction was always considered to be one of the most challenging tasks for the scientific community as it involves the understanding of the coupled dynamics of the building blocks of matter such as nuclei, electrons, and photons. The measurement of short time intervals and the perception of the dynamics of the microcosm are largely dependent on tools used for tracing these dynamics. Such tools are the light pulses used to trigger and detect, via nonlinear processes, the evolution of the systems in the microcosm. The need for finer time resolution and the quest for higher peak power underlie the continuous efforts toward shorter laser pulses almost since the inception of the laser.

The historical progress of ultrashort pulse technology is summarized in Fig. 1.

In the 1960s, the breakthrough of the invention of Continuum Wave (CW) lasers[1] meant to change the course of history on light technology and light–matter interactions. Countless fascinating discoveries and applications are based on the coherent properties of these light sources and their linear interaction with matter. Almost a decade after the discovery of CW lasers, the development of nanosecond (ns) pulsed laser sources[2] allowed the scientific community to enter the nonlinear light-matter interaction regime. Due to the low (relative to the Coulomb field of the atomic potential) electric field of these laser pulses, the interaction can be treated by the lowest-order perturbation theory. Only with the development of shorter pulses, picosecond (ps)[3] and especially the femtosecond[4,5] laser systems [combined with the chirped-pulse amplification
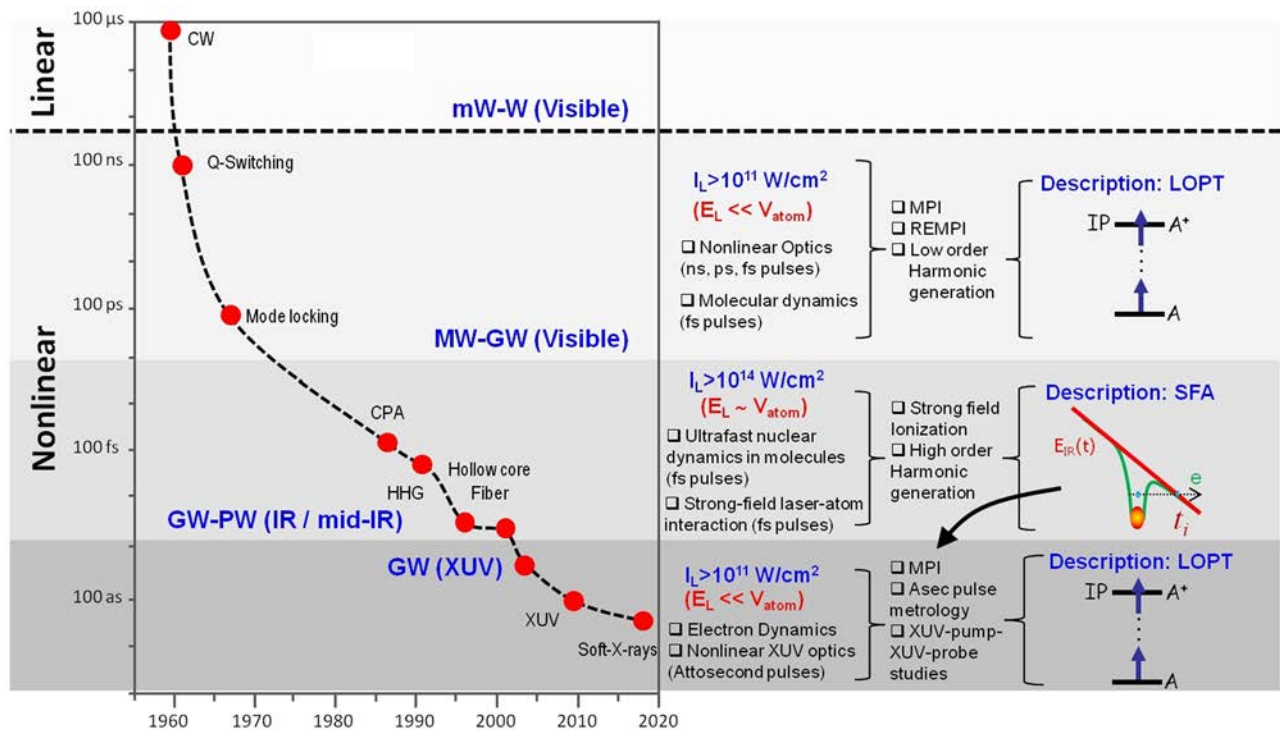
FIG. 1. Historical progress of the ultrashort pulse technology. E_L: laser electric field; V_{atom}: atomic potential; MPI: multiphoton ionization; REMPI: resonance enhanced multiphoton ionization; LOPT: lowest-order perturbation theory; SFA: strong field approximation; and E_{IR}: electric field of the infrared (IR) laser at the moment of ionization t_i.

(CPA) technology[6,7]] at the end of the 1980s, it became possible for the scientific community to access ultrafast molecular dynamics in the time domain[8] and perform studies beyond the perturbative regime. In this strong-field regime, the system is exposed to laser electric fields comparable to or stronger than the field of the atomic potential. The latter had a tremendous impact on atomic and molecular physics and eventually led to the development of the semiclassical "three-step" model[9–11] underlying the generation of high harmonics (HH)[12–14] and attosecond science,[15–19] which have been recently linked with quantum optical technology[20] through the quantum optical description of strongly laser driven interactions.[21–23]

B. Attosecond pulse production

Nowadays, subfemtosecond subcycle electric fields can be synthesized using broadband radiation in the visible spectral range[24] and attosecond pulses are generated in the XUV spectral range.[25,26] Additionally, the recent development of mid-IR few cycle-laser systems led to the generation of coherent soft x-ray radiation[27–29] with the shorter ever measured duration to be ≈43 as.[30] Presently, gases are considered among the most favorable nonlinear media in use for the production of attosecond pulses in the 20–100 eV XUV photon energy regime, yielding photon fluxes ranging from 10^7 to 10^{11} photons/pulse.[31–40] The most recent development with respect to XUV pulse energies is the ≈20 GW XUV beam line constructed at the Attosecond Science and Technology Laboratory of the

Foundation of Research and Technology (FORTH)[39] which delivers XUV pulses with ≈6×10^{13} photons/pulse in the spectral region of 20–30 eV.

By focusing intense linearly polarized multicycle femtosecond driving laser pulses [Fig. 2(a)] on gases, an XUV frequency comb, consisting of the HH of the driving laser frequency ω_L [Fig. 2(b)], is emitted in the direction of the laser propagation. Under proper phase matching conditions, the phase locking between the harmonics forms an attosecond pulse train (APT) [Fig. 2(c)]. The overall duration of the train is limited by the average bandwidth of the individual harmonics, while the duration of the attosecond pulses in the train is limited by the full bandwidth of the XUV harmonics spectrum. Confining the High-Harmonic Generation (HHG) process to occur within a fraction of the cycle of the driving laser field [Fig. 2(d)] may lead to the production of an Isolated Attosecond Pulse (IAP) and with a continuum spectral power distribution [Fig. 2(e)]. The shortest duration of an IAP is limited by the bandwidth of the continuum XUV spectrum [Fig. 2(f)]. Examples of attosecond beam line arrangements can be found in Refs. 25 and 40–48.

C. Repertoire of attosecond pulse characterization approaches

Despite the tremendous progress in attosecond pulse engineering over the last 20 years, attosecond pulse metrology is still one of the most challenging research directions. Independent of the high
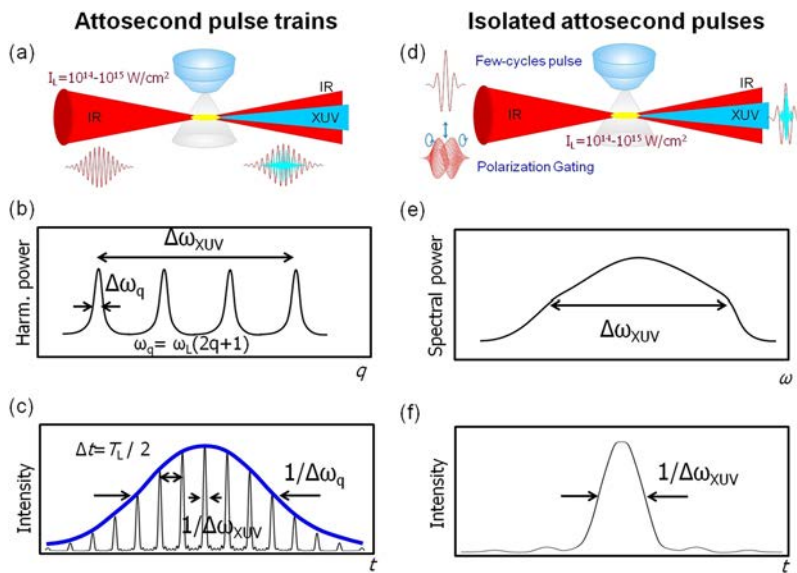
FIG. 2. Schematic representation of the attosecond pulse generation in gas phase media. q is the harmonic order, ω_q is the harmonic frequency, ω_L is the laser frequency, T_L is the period of the laser cycle, ω_{XUV} is the carrier frequency of the XUV pulse, $\Delta\omega_q$ is the harmonic bandwidth, and $\Delta\omega_{XUV}$ is the bandwidth of the XUV pulse.

harmonic source used for synthesizing the attosecond pulses, the difficulty in conducting pulse characterization experiments arises from the inherently low reflectivity, the high absorption/dispersion of the XUV optics, and the lack of spectrally flat with instantaneous temporal response materials. These factors make the use of nonlinear crystals and conventional beam splitters not feasible for experimental implementation, hence preventing the direct translation in the XUV spectral domain of conventional techniques employed for temporal characterization of ultrashort pulses in the visible and near-infrared (IR) spectral regions. However, notable methods for attosecond pulse characterization have been implemented owing to the continuous scientific advances in both ultrafast light-matter interaction and engineering in the XUV spectral range. These methods can be divided into two main categories: those that are based on cross correlation (CC) and the ones based on nonlinear volume autocorrelation (AC) approaches; both characterize the attosecond pulses in the region where they interact with matter. *In situ*[49,50] and Spectral Phase Interferometry for the Direct Electric Field Reconstruction (SPIDER)[51,52] methods have also been developed. The former provides information about the attosecond pulses at the point of their generation, while the latter utilizes generation of harmonics from two different sources with slightly shifted central frequency, assuming identical harmonic generation in these two sources. In addition, a conceptually new all-optical approach has been recently demonstrated experimentally.[53] The method is stimulated by double-blind holography and is based on the spectral measurement of two unknown XUV-attosecond pulses and their interference.

The AC approach[40,54–56] (which requires high XUV intensities $>10^{11}$ W/cm^2) relies on the interaction of two parts of the pulse to be characterized that are considered to be identical and results in a direct measurement of the pulse duration. The approach was used for the temporal characterization of attosecond pulses generated in gases[34,54,57,58] and solid-surfaces.[59] The same experimental setup has been employed for XUV-pump-XUV-probe studies of the 1-fs

electron dynamics of atoms/molecules[34,35,60–62] and time delay spectroscopic studies in atoms.[63] As has been stated before, the implementation of AC experiments and measurements in the XUV by means of nonlinear crystals is hindered by the absence of suitable optics in this spectral region and so far, remains an open challenge. On the contrary, AC measurements can be accomplished by recording ions or photoelectrons (PEs) induced by two-photon ionization processes in an appropriate target medium. In this context, several materials and ionization schemes have been proposed and explored, such as two-photon ionization of helium,[54,64] two-photon above-threshold ionization (ATI) of helium,[55,59,65] two-photon double ionization of helium, and two-photon ATI of argon.[65,66] In all cases, ions or PEs are collected using appropriate ion or electron time-of-flight (TOF) spectrometers, respectively. A dispersionless Michelson-type interferometer for AC measurements using two identical replicas of the XUV pulses has been developed and modeled.[67] Due to the high losses that it introduces to the XUV radiation, it has been used so far only in the UV spectral region.[68–70]

In contrast to AC, the CC approaches relax the requirement of high XUV intensities but they do not provide direct information (in the sense that a second field is needed for the characterization) on the pulse duration. They rely on the reconstruction of the pulse which occurs after analyzing the data obtained by the interaction of atoms with the superposition of the XUV pulse with an IR field. These principles have been incorporated in the following schemes. The Reconstruction of Attosecond Beating By Interference of two-photon Transitions (RABBIT) technique[71] (applicable for APTs) uses the fundamental laser field to create sidebands in the photoelectron (PE) spectra generated by the XUV harmonics. The average duration of the pulses within the attosecond pulse train can be deduced by recording the products of the quantum interference of different two-photon (XUV and IR) ionization channels. Another technique known as attosecond streak camera [applicable for isolated attosecond pulses (IAPs) and free-electron laser (FEL) light sources][72–74] uses the fundamental electric field to

modulate the energy distribution of the PEs generated by the XUV photons. This modulation was used to determine the duration of the IAP[72,75,76] and has subsequently also been applied to study the attosecond dynamics in gases[77,78] as well as solids.[79] The tool box of CC approaches also contains a technique named Frequency Resolved Optical Gating for Complete Reconstruction of Attosecond Bursts (FROG-CRAB) which is applicable for arbitrary attosecond fields[80] and a technique named Phase Retrieval by Omega Oscillation Filtering (PROOF) which is applicable for arbitrary attosecond fields with bandwidth >70 eV.[81] An advanced version of the RABBIT technique is the so-called RAINBOW RABBIT,[82,83] which detects frequency resolved CC interaction products, thus allowing the study of subtle phenomena not attainable by RABBIT. In Secs. II–VI, we will review these approaches restricting ourselves to methods capable of characterizing attosecond pulses generated by a single source and detected in the region of their interaction with matter.

II. AUTOCORRELATION APPROACHES

After a brief introduction in the nonlinear processes employed in the autocorrelation approaches, we describe the second-order intensity volume autocorrelation (2-IVAC) approach used for the temporal characterization of attosecond pulse trains and isolated pulses. Then, the XUV-FROG applications are discussed as well as how the XUV-FROG technique is used to retrieve the phase and fully reconstruct APTs and IAPs, respectively.

A. Nonlinear ionization processes

In order to conduct a 2nd order AC measurement in a gas medium with confidence, it is of paramount importance to verify that the two-photon process dominates the gas ionization and hence, is suitable for second-order AC. First, it should be confirmed that the focused intensity at the point of interaction with the gas target is adequately high and capable of producing a recordable number of ions or electrons induced by two-photon ionization (Fig. 3).
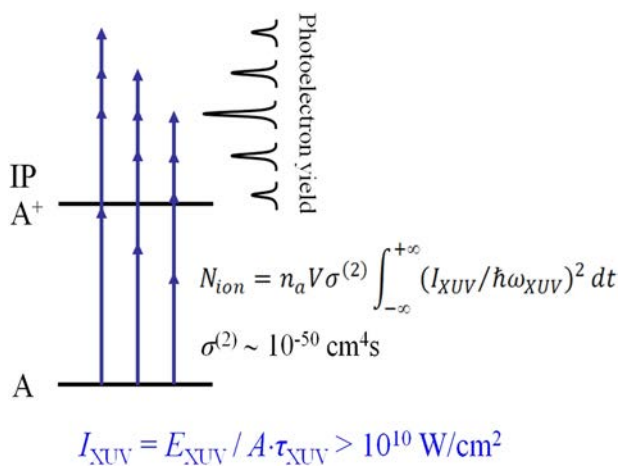
FIG. 3. Two-XUV-photon ionization scheme of an atom A. IP is the ionization potential of A.
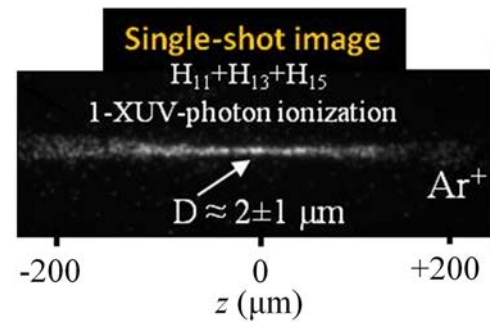
FIG. 4. Single-shot image of the intensity distribution at the focus of the XUV radiation (which consists of the 11th, 13th, and 15th harmonics of the IR driving field). z is the propagation axis of the XUV. The image has been obtained by recording the ion distribution induced by single-photon ionization of argon atoms at the focus of the XUV beam. Reproduced with permission from Tzallas *et al.*, J. Opt. **20**, 24018 (2018). Copyright 2018 IOP Publishing. All rights reserved.

Therefore, one must make a calculated estimation, under realistic experimental conditions, of the two-XUV-photon nonresonant ionization yield (Y_2) (ions/electrons), and hence the XUV intensity (I_{XUV}) that would be sufficient to induce such a nonlinear atomic process. The transition probability rate W_2 and the Y_2 per pulse for a two-photon absorption process are given by $W_2 = \sigma^{(2)}(I_{XUV}/\hbar\omega_{XUV})^2$ and $Y_2 = W_2\tau_{XUV}n_aV$, respectively; n_a is the atomic density at the volume V of interaction and $\sigma^{(2)}$ is the generalized two-photon ionization cross section with values ranging from 10^{-49} to 10^{-52} cm^4 s. Taking into account typically reached experimental atomic densities of ~10^{15} atoms/cm^3 and an interaction volume of ~$V = 10^{-9}$ cm^3, then a recordable two-photon ionization yield would require $I_{XUV} > 10^{10}$ W/cm^2.

Ions and photoelectrons produced by a two-XUV-photon nonresonant[84] ionization process have been observed using XUV pulses in the nano-Joule energy range.[54,56,63,85–88] The spatial characteristics of the XUV beam at the interaction region can be obtained experimentally by means of an Ion Microscope (IM).[89–91] Figure 4 shows an example of the spatial distribution of the XUV radiation at the focus recorded in a single shot.

Apart from the measurement of the XUV beam spatial characteristics in the interaction region, the IM can also be used in obtaining quantitative information about generalized cross sections in the linear and nonlinear XUV spectral regions.[89,90,92]

B. Operation principle of the 2-IVAC

The 2-IVAC approach was first demonstrated in 2003[54] using gas phase harmonics and in 2009 using harmonics emitted from laser-plasma interactions.[59,93] Autocorrelation measurements in the visible/infrared spectral region are based on the interference between two cotraveling replicas of the pulse created by a beam splitter and separated in time by adding the optical path to one of the arms corresponding to various time delays in their propagation. However, since no conventional dispersionless beam splitter is available for XUV wavelengths, the two XUV pulses are created using an XUV wave front splitting device. Such a device is a split spherical mirror where one of the two-halves is fixed and the other is
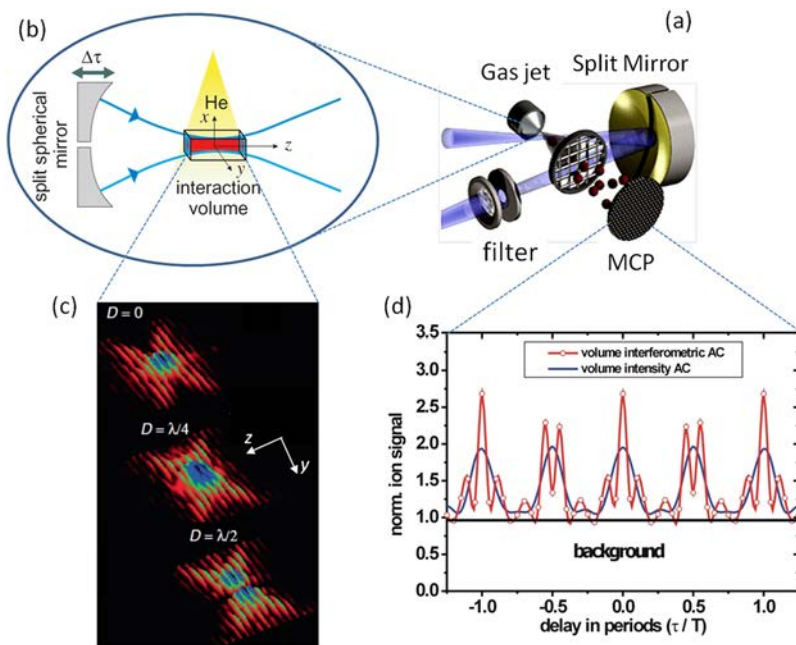
FIG. 5. (a) Schematic of the experimental setup of the second-order XUV volume autocorrelator utilizing the split mirror configuration. (b) Interaction volume in the case of using He gas as a two-photon detector. (c) Two-dimensional (z–y) contour plots showing the snapshots of the calculated intensity distribution of the harmonic superposition (7th + 9th + 11th + 13th) in the interaction region of the volume autocorrelator for displacement D = 0, D = $\lambda/4$, and D = $\lambda/2$ between the two pulses. (d) Calculated interferometric and intensity volume autocorrelation traces. T is the period of the IR laser field. In these calculations, the peak to background ratio of the interferometric trace is $\approx$2.75:1 with the cycle average resulting in a ratio of $\approx$2:1.[56] However, detailed calculations performed in 2009[94] for the 5th harmonic, which have been confirmed experimentally,[94,96] have shown that the peak to background ratio and the interferometric and intensity volume autocorrelation ratio are $\approx$3.4:1 and $\approx$2.4:1, respectively. (b)–(d) Reprinted with permission from Charalambidis *et al.*, *Progress in Ultrafast Intense Laser Science*. Copyright 2009 Springer Nature. Reprinted with permission Springer Nature.[97]

on a piezotranslation stage [Fig. 5(a)]. This device provides a solution to the introduction of a variable time delay between the two pulses not only for pulse duration measurements but also for XUV-pump–XUV-probe experiments in atoms and molecules. Using the nonlinear ionization schemes described in Sec. II A, the autocorrelation trace results in measuring the ionization products (electrons or ions) recorded by a TOF spectrometer as a function of the delay.

The operation principle of the 2-IVAC relies on the spatial integration of 2-XUV-photon ionization yield produced in the interaction volume [Fig. 5(b)] by the coherent superposition of the two XUV pulses created by the XUV wave front divider[54,56] (additional information can be found in Refs. 94 and 95).

For attosecond pulses synthesized from the harmonics 7th, 9th, 11th, and 13th, the field distribution is given by $E(D, x, y, z) = \sum_{n=7}^{n=13} E_n(D, x, y, z)$ (D is the displacement introduced by the delay stage between the two XUV pulses) at the focal spot of the focusing element. The projection of the intensity distribution $I(D, x, y, z) = E(D, x, y, z)E^*(D, x, y, z)$ on the z-y plane for the particular values of the displacement D = 0, $\lambda/4$, and $\lambda/2$ is shown in Fig. 5(c). The beam profile is an airy distribution in the focus, and for a displacement of D = $\lambda/2$, it is divided into two parts of equal size. It is worth noting that the total energy in the interaction volume remains constant, and as a result, the splitting of the focal spot would not affect the measured signal (integrated over the whole interaction volume) in the case of single photon ionization (linear detector), i.e., the signal would remain constant at all time delays. In the case of two-photon ionization (quadratic detector), a modulation in the ionization signal $S(D) \propto \iiint_{\Delta V} I^2(D, x, y, z)dxdydz$ would occur due to the rearrangement of the local intensity inside the interaction volume. The blue and red curves in Fig. 5(d) correspond to the calculated two-photon intensity and interferometric volume autocorrelation, respectively.

The peak-to-background ratio in the 2nd-order interferometric volume autocorrelation is $\approx$3.4:1 and in the 2nd-order intensity volume autocorrelation is $\approx$2.4:1.[94] The attosecond pulse duration τ_{XUV} can be determined from the measured autocorrelation trace (AC) using the well-known relation valid for Gaussian pulses $\tau_{XUV} = \tau_{AC}/\sqrt{2}$ (where τ_{AC} is the full width at half maximum of the AC trace). At this point, it should be noted that the measured pulse duration, in the case of pulse trains, reflects the average duration of the individual attosecond pulses composing the train.

C. 2-IVAC in attosecond pulse trains and isolated attosecond pulses

2-IVAC pulse duration measurements of an APT as well as of an isolated ~1 fs XUV pulse are shown in Figs. 6(b) and 6(c) and [Figs. 6(d) and 6(e)], respectively. A common experimental apparatus has been used for both cases, which is drawn in Fig. 6(a). For the production of the APT, a high-power multicycle femtosecond IR pulse is focused on a xenon gas jet target. The focusing position of the driving field was set before the xenon gas jet, a position which experimentally is considered to be favorable for temporal confinement in the attosecond scale. The latter is attributed to the phase accumulated by the ejected electrons following a short trajectory before recombining with the parent ion. A 150 nm-thick indium foil filter selects the 9th to 15th odd harmonics with the relative field amplitudes in the interaction region to be 1, 0.4, 0.3, and 0.25 for the 9th, 11th, 13th, and 15th harmonics, respectively. By focusing the radiation on a helium pulsed gas jet using a split spherical gold mirror of 5 cm focal length, the 2-XUV-photon ionization process was observed and single-charge helium ions [Fig. 6(b)] were collected utilizing a μ-metal-shielded time-of-flight (TOF) spectrometer. The experimental 2-IVAC trace obtained by recording the He$^+$ signal as
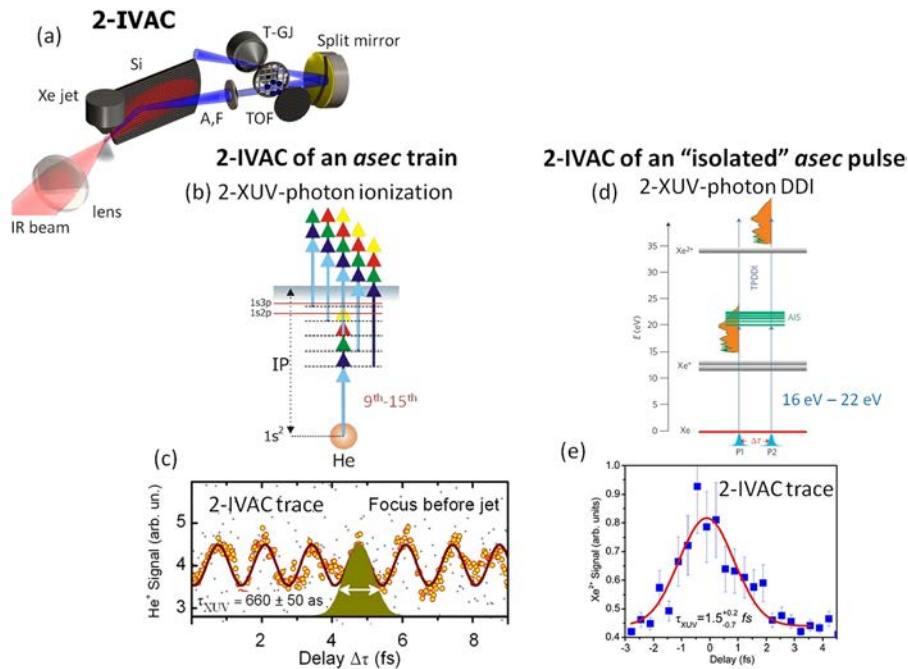
FIG. 6. (a) Experimental setup. (b) 2-XUV-photon ionization scheme of helium using the 9th–15th harmonics passing through indium filter. (c) 2-IVAC trace of an APT synthesized by the 9th–15th harmonics. Gray dots are the raw data, and the yellow correspond to a 10-point running average. The purple line is a 12-peak sum of Gaussians fit to the raw data. (d) 2-XUV-photon direct double ionization (TPDDI) scheme of xenon using the broadband coherent continuum XUV radiation (orange filled areas) generated in a xenon gas jet by means of PG arrangement. In this process, the single XUV photon absorption is passing through an ensemble of autoionizing states (AIS). (e) 2-IVAC trace. The blue squares are the raw data, and the red line is a Gaussian fit to the raw data. The pulse broadening is a consequence of the appearance of side pulses due to the unstable carrier-envelope-phase (CEP) of the high-power multicycle laser system. (c) Reprinted with permission from Kruse et al., Phys. Rev. A **82**, 021402(R) (2010). Copyright 2010 American Physical Society. (d) Reprinted with permission from Tzallas et al., Nat. Phys. **7**, 781 (2011). Copyright 2009 Springer Nature. (e) Reproduced with permission from P. Tzallas, E. Skantzakis, and D. Charalambidis, J. Phys. B: At. Mol. Opt. Phys. **45**, 074007 (2012). Copyright 2012 IOP Publishing. All rights reserved.

a function of the time delay between the XUV replicas is shown in Fig. 6(c). The average duration of attosecond pulses within the pulse train was found to be 660 ± 50 as.[98]

Volume autocorrelation measurements can be carried out not only for the characterization of APTs but also for IAPs, which are more suitable for pump-probe experimental schemes in attosecond time scale. For the setup sketched in Fig. 6(a), IAPs are produced, using a many-cycle laser field, with the Polarization Gating method (PG), presented in more detail in Refs. 100 and 101. In this case, the generated XUV spectrum is not a comb, like in APTs, but rather a continuum or quasi continuum depending on the CEP variation. Experimental manifestation of the IAP characterization has been presented in Ref. 34 implementing similar configuration as described above for the APT. The XUV radiation was spectrally selected by a 150 nm-thick Sn filter allowing transmission of photon energies centered at ≈19 eV with a bandwidth of ≈10 eV [orange filled area in Fig. 6(d)]. The generated IAPs are focused by an f/5 cm split spherical gold mirror on xenon pulsed gas target up, where up to Xe^{2+} ions were observed by means of a TOF ion mass spectrometer. Doubly charged ions are produced by a 2-XUV-photon direct double ionization process (TPDDI) [Fig. 6(d)]. In this excitation pathway, single-XUV-photon absorption occurs in a continuum that is rich in structure by the presence of an ensemble of autoionizing states (AIS), which are eventually coherently excited.

The 2-IVAC trace obtained by recording the Xe^{2+} signal as a function of the delay between the XUV replicas is shown in Fig. 6(e). For longer delay times, and acting like an XUV-pump-XUV-probe scheme, information about the wave packet evolution induced by the atomic coherences can be extracted. The obtained temporal duration of the XUV pulse was ≈ $1.5^{+0.2}_{-0.7}$ fs. This result is an overestimation of the actual pulse duration, mainly due to the unstable CEP of the high-power multicycle driving laser pulses which leads to a double pulse structure of the generated XUV. The latter effect is exhibited by the presence of side peaks in the 2nd order AC trace, which due to the lack of resolution cannot be resolved and thus determined.[99] It should be noted that the effect the AIS have in the measured pulse duration can be safely neglected since the width of the states is much smaller than the bandwidth of the XUV pulse or equivalently the measured beating periods are significantly larger than the pulse duration. A more detailed discussion on this topic can be found in Refs. 34 and 84.

The first interferometric volume autocorrelation trace of an APT has been demonstrated in 2006.[102] Using a two-XUV-photon ionization process induced in N_2 upon interaction with an APT which was formed by the 9th–19th harmonics of a driving 40 fs IR laser pulse. The AC trace was obtained by measuring N^+ {resulting from the Coulomb explosion of N_2 after absorbing two-XUV-photons [Fig. 7(a)]}, as a function of the delay between the two XUV
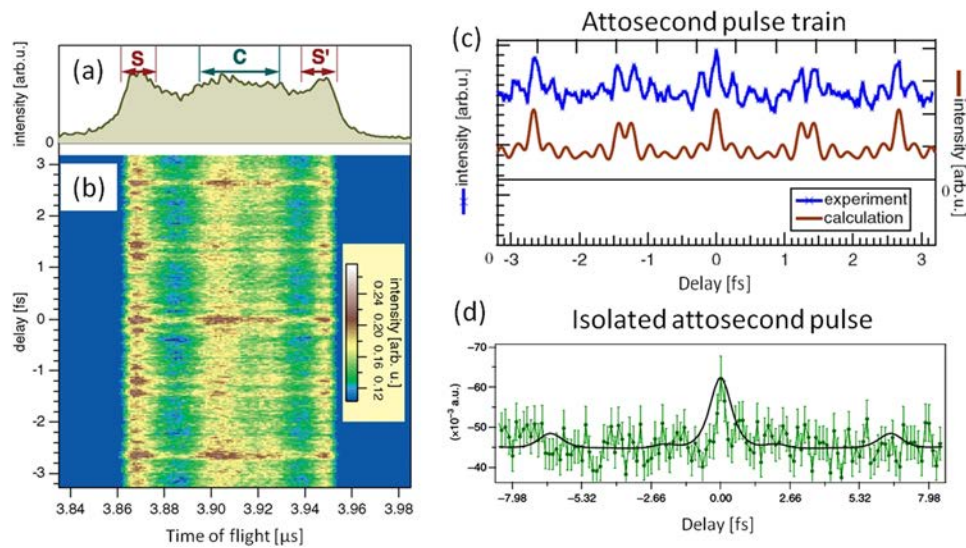
FIG. 7. Left panel: time-of-flight mass spectrum at $m/e = 14$. (a) Typical spectrum of ions originating from a N_2 molecule with two-photon absorption of high-order harmonic fields. (b) Variation of the spectrum by translating the delay between the two pulses of the harmonic fields. Bunches with a period of 1.33 fs and fringes with a much shorter period reveal the interferometric autocorrelation of the harmonic fields. The color scale of the intensity is shown in the inset. (c) Interferometric autocorrelation trace of the APT resulted from the data analysis of (b) (blue line). The calculated correlation trace is shown as the lower curve (orange line). (d) Autocorrelation trace of an IAP obtained following the approach used to obtain the trace the APTs. (a)–(c) Reprinted with permission from Nabekawa et al., Phys. Rev. Lett. **97**, 153904 (2006). Copyright 2006 American Physical Society. (d) reprinted with permission from Takahashi et al., Nat. Commun. **4**, 2691 (2013). Copyright 2013 Springer Nature.

pulses [Fig. 7(b)]. The same approach was used to measure the duration of an IAP in the spectral range around ≈31 eV and a bandwidth of ≈9 eV.[36]

D. XUV FROG-type measurements

The work in Ref. 57 presents a mode-resolved autocorrelation technique applied for the determination of the temporal duration of attosecond pulses. It introduced the use of the 2-IVAC approach through 2-XUV-photon above-threshold-ionization (ATI) schemes,

opening up the possibility of extending the applicability of 2-IVAC to high XUV photon energies and enabling FROG-type[103] measurement. It is considered to be the proof-of-principle experiment of the XUV FROG-type technique. In Ref. 57 isolated XUV pulses with photon energy ≈28 eV (9th harmonic of a 400 nm driving laser field) and bandwidth of ≈2 eV have been generated by the interaction of argon gas phase atoms with ≈8.3 fs driving laser field of carrier photon energy at 3.1 eV. Two optically delayed replicas of the XUV pulse were focused on helium gas inducing a 2-XUV-photon ATI ionization [Fig. 8(a)].
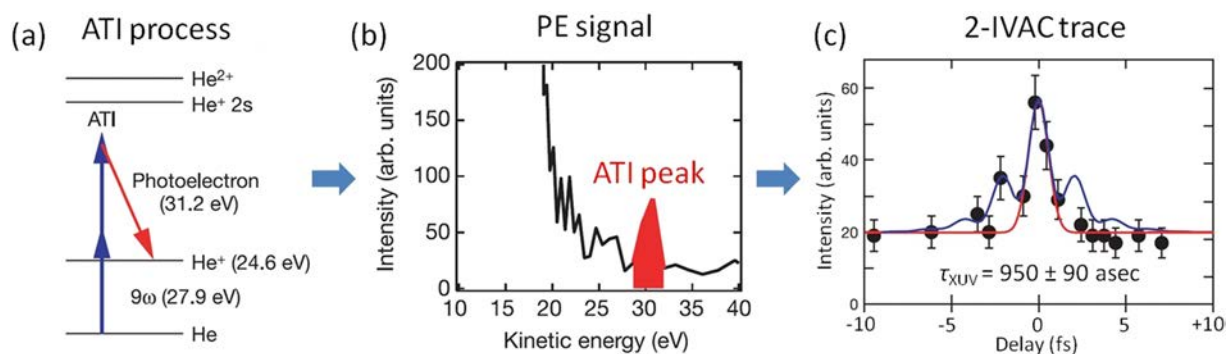
FIG. 8. (a) 2-XUV-photon ATI process of He using isolated XUV pulses with central photon energy ≈28 eV and bandwidth of ≈2 eV. The XUV pulses were generated by the interaction of argon gas with a ≈8.3 fs long driving laser field of carrier photon energy at 3.1 eV. (b) Produced photoelectron spectrum. The ATI peak is shown in red. (c) Recorded AC trace (black points). The red line shows the Gaussian fit on the raw data. Reprinted with permission from Sekikawa et al., Nature **432**, 605 (2004). Copyright 2004 Springer Nature.
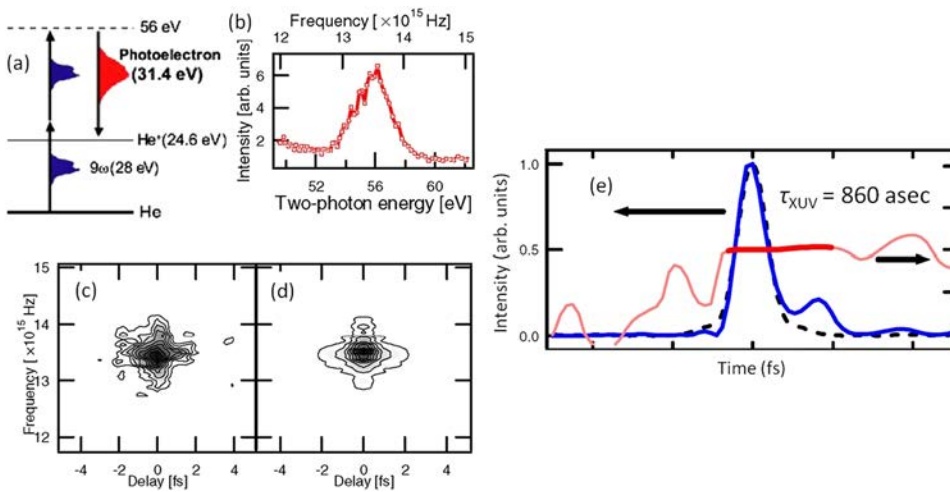
FIG. 9. (a) 2-XUV-photon ATI process of He using isolated XUV pulses with central photon energy ≈28 eV and bandwidth ≈2 eV. (b) Recorded 2-XUV-photon ATI photoelectron spectrum. (c) Measured time-frequency map of the spectrum vs time delay between two replica of the ninth harmonic pulses. (d) Time-frequency map retrieved from (c) by the iterative Fourier-transform algorithm with generalized projection. (e) Retrieved pulse shape and spectral phase distribution. Reprinted with permission from Kosuge *et al.*, Phys. Rev. Lett. **97**, 263901 (2006). Copyright 2006 American Physical Society.

The ejected photoelectrons were collected and energy-resolved by a magnetic bottle photoelectron spectrometer. Figure 8(b) shows the photoelectron spectrum of two-photon ATI. An autocorrelation trace having an overall width of ≈4 fs was recorded by measuring the electron number at each optical delay between the two XUV pulses [Fig. 8(c)]. A Gaussian fit on the central part of the trace resulted in an XUV pulse duration of 950 as. A relatively low experimental spectral resolution prevented a FROG-type analysis, but it sparked additional experimental efforts which proved to be fruitful soon after.

To our knowledge, the only existing XUV FROG-type measurement of an isolated subfemtosecond XUV pulse is the one reported in 2006.[58] This has been achieved by recording with high energy resolution (~200 meV) autocorrelation traces of a two-XUV-photon ATI photoelectron peak. The relevant two-XUV-photon ATI process is drawn in Fig. 9(a), while [Fig. 9(b)] shows the recorded PE ATI peak. The FROG traces are presented in Figs. 9(c) and 9(d) and the retrieved XUV pulse in Fig. 9(e). The duration of the retrieved isolated pulse was found to be 860 as.

In Ref. 57, an experimental technique is introduced for XUV FROG-type attosecond pulse train characterization, termed PANTHER (Photoelectron Analysis with Nonresonant Two-photon-ionization for Harmonic Electric-field Reconstruction). It is a two-photon volume autocorrelation approach mediating through a two-XUV-photon ATI scheme (a process treated according to the lowest-order perturbation theory) in argon gas. By recording autocorrelation traces of energy-resolved ATI photoelectrons, and in combination with FROG-based considerations analysis, the authors managed to retrieve the chirp, among the involved harmonic fields forming the APT, and obtain an upper bound of 450 as for the temporal duration of the APT.

III. CROSS CORRELATION APPROACHES

The following techniques were proposed and implemented for the complete, *phase and amplitude*, characterization of attosecond pulses, as knowledge of both parameters allows obtaining the full picture for the temporal intensity distribution of the pulses. They are based on the measurement of the photoelectron spectrum produced in gaseous media by their interaction with an XUV attosecond field in the presence of a copropagating femtosecond IR field, as a function of the time delay between the XUV and IR pulses.
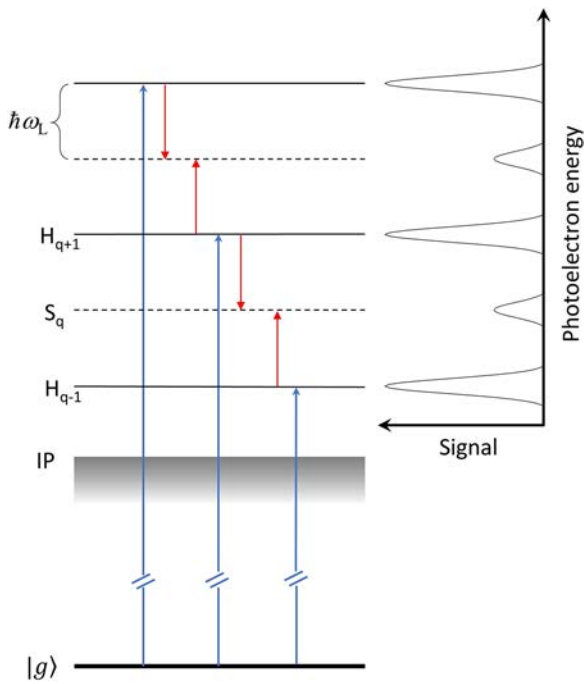
A. RABBIT

The RABBIT method aims at characterizing an APT in phase and amplitude. The birth of RABBIT (Reconstruction of Attosecond Beating By Interference of Two-photon Transitions) is traced back in 2001 when Paul *et al.*[71] through their groundbreaking experiment introduced the technique, following the pivotal theoretical work by Véniard *et al.* in 1996.[104] Since then, the approach has been routinely employed in the spectral phase characterization of harmonics and the resulting attosecond pulses (Refs. 105–111).

1. Operation principle of RABBIT

The operation principle of RABBIT is based on the recording of the photoelectron spectrum induced by two-photon two-color ionization (e.g., one-XUV + one-IR photon) of the target medium, e.g., a gas phase noble atom, as a function of the time delay between the XUV attosecond pulse train and the IR fs pulses. A general RABBIT scheme is shown in Fig. 10. If the XUV harmonic comb photon energy exceeds the atomic ionization potential of the experimental target, interaction of atoms with the XUV leads to a photoelectron energy spectrum comprising peaks assigned to single-photon ionization induced by the different harmonic orders of the comb. The attosecond pulse characteristics will be imprinted onto the produced electron wave packet modified by the ionization cross section and the atomic phase. This property is of particular importance when photoemission dynamics, i.e., atomic delays, are to be extracted.[112–114]

Since harmonics are produced at every half optical cycle, the peaks are evenly spaced at $2\hbar\omega_L$ distance, with $\hbar\omega_L$ being the photon energy of the driver laser field. When the second color, usually a weaker (but sufficiently intense) portion of the IR driver pulse, is temporally overlapped with the XUV comb then sideband peaks appear in the photoelectron energy spectrum between the photoelectron peaks solely by the harmonic photons at $\pm\hbar\omega_L$ distances

FIG. 10. Ionization scheme of RABBIT. Two-color two-photon ionization of an atom with a ground state $|g\rangle$, by an XUV frequency-comb with a harmonic spacing of $2\hbar\omega_L$ and a synchronized probe field of angular frequency ω_L. In the presence of the probe field, two pathways lead to the formation of sidebands (here, q denotes the sideband order) as depicted in the photoelectron energy spectrum.

from the peaks. Sidebands stem from two-photon two-color ionization, namely, one-XUV photon and absorption or emission of an additional IR photon (Fig. 10).

These continuum states are not excited in the absence of the IR field, a beneficial condition as the measurement can be performed essentially background free. Provided that the IR intensity is weak enough so no multiphoton ionization of the target due to IR occurs, and only one IR photon may be absorbed or emitted,[71] then there are two possible pathways, i.e., two consecutive harmonics, contributing to each sideband. As the temporal delay between the XUV and IR pulses is varied, the amplitude S of these sidebands exhibits a periodical modulation due to the phase difference between adjacent harmonics,[71]

$$S_q(\tau) \propto \cos(2\omega_L\tau + \Delta\varphi_{q+1,q-1} + \Delta\varphi_q^{at}), \quad (1)$$

where q is the order of the sideband, ω_L is the carrier wave frequency, τ is the XUV-IR time delay, $\Delta\varphi_{q+1,q-1} = \varphi_{q+1} - \varphi_{q-1}$ is the phase difference between $q + 1$ and $q - 1$ harmonics, and $\Delta\varphi_q^{at}$ is the intrinsic phase difference due to the ionization process itself for the qth sideband.[104] $\Delta\varphi_q^{at}$ is usually negligible compared to $\Delta\varphi_{q+1,q-1}$ but can either be calculated or measured.[115–119] The phase between harmonics $\Delta\varphi_{q+1,q-1}$ can be determined by the Fourier transform of the periodical modulation of S_q as a function of τ. The XUV spectrum is measured by blocking the IR beam, taking into account the ionization cross section σ_n of the gas target, where n is the harmonic order (i.e., related to the sideband order q by $q = n + 1$).

The average attosecond pulse in the APT can then be reconstructed by the relative harmonic spectral amplitudes, A_n, obtained by the XUV spectrum, and the interharmonic phases retrieved by the time delay graph. Finally, the average intensity profile I_{avg} of the attosecond pulse in the APT is calculated by the sum of the individual harmonic fields,

$$I_{avg}(t) = \left| \sum_n A_n e^{-in\omega_L t - i\varphi_n} \right|^2, \quad (2)$$

where $\varphi_n = \sum \Delta\varphi_{q+1,q-1}$ is the obtained spectral phase distribution for harmonic order n, with n spanning the XUV comb forming the APT. The FWHM of the intensity profile $I_{avg}(t)$ gives the temporal duration of the attosecond pulse.

In the advanced version of RAINBOW RABBIT,[82,83] the measured signal of the sidebands is not energy integrated, thus allowing us to follow signal modulations for different spectral components within the spectral bandwidth of the harmonics. This is not crucial when RABBIT is used for the retrieval of the phase difference of subsequent harmonics for which the "classical" RABBIT is sufficient. However, it may become important when RABBIT is used for the measurement of phases related to the structure and dynamics of the atom, in particular when these phases vary fast within the bandwidth of one harmonic, where the energy integration inherent in the "classical" RABBIT may lead to a smearing of the phase information. Nevertheless, such measurements go beyond the scope of this review.

For the sake of comprehensiveness, it should be mentioned that the RABBIT scheme shown in Fig. 10 is incomplete. Apart from the channels involving absorption of an XUV photon with subsequent absorption/emission of an IR photon, there are channels involving first absorption/emission of an IR photon followed by absorption of an XUV photon leading to the same final continuum state. Thus, there are four interfering channels contributing to each sideband $[(\omega_q + \omega_L), (\omega_{q+1} - \omega_L), (\omega_L + \omega_q), (-\omega_L + \omega_{q+1})]$. Usually the last two $[(\omega_L + \omega_q), (-\omega_L + \omega_{q+1})]$ are being considered negligible[120] as they are far detuned from the eigenstates of the system. However, for the first two channels one-photon absorption, and thus the virtual state of the two-photon ionization process, is in the continuum and thus with many continuum states above and many continuum and bound states below the intermediate virtual state. The opposite sign detuning of these two groups results in two-photon ionization amplitudes with opposite sign and thus in partial cancelation. In the two last channels, all allowed excited states (bound and continuum) are above the intermediate virtual state. Despite far detuned from the eigenstates of the atom, all detunings have the same sign and thus no cancelation is occurring. For the two first channels, the Cauchy principal value in the two-photon ionization transition amplitude together with the contribution of the bound states can be comparable if not smaller than the two-photon transition amplitude in the two last channels. Nevertheless, the presence of two or four interfering two-photon ionization channels does not affect the retrieval of the spectral phase distribution as described above.

2. RABBIT in attosecond pulse trains

For the experimental realization of the technique, a multicycle femtosecond intense laser field is used to produce an XUV APT via high-harmonic generation in a gas medium. A typical setup is illustrated in Fig. 11.
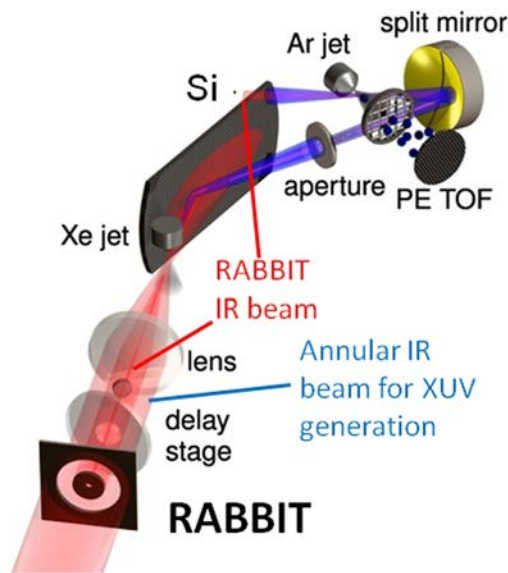
FIG. 11. Typical RABBIT experimental arrangement. Reproduced with permission from Kruse et al., Phys. Rev. A **82**, 021402(R) (2010). Copyright 2010 American Physical Society.

In this arrangement, multicycle IR laser pulses, focused on a Xe gas jet, are used for the XUV harmonic generation. After the Xe jet, a silicon wafer is placed at Brewster angle reflecting the XUV radiation while attenuating the IR field. The XUV radiation is appropriately filtered to select plateau harmonics and both XUV and IR are focused by means of a gold spherical mirror on the target gas jet. The time delay between the XUV and IR is varied by rotating a plate placed in the common beam line path. The two-color (XUV+IR) photoelectron spectra are recorded, for all three different focus positions in the HHG Xe gas jet (focus before jet, on jet, and after jet), by means of a μ-metal shielded time of a flight electron spectrometer [Fig. 12(a)]. It shows peaks corresponding to single-XUV (harmonic)-photon ionization and in between them sidebands corresponding to two-color (XUV+IR) photoionization. Variation of the XUV-IR time delay results in periodical modulation of the sideband peaks. The total electron signal modulation is also exhibiting an oscillation period corresponding to one of the fundamentals, i.e., ~2.7 fs, as expected. From the RABBIT traces, the relative harmonic phases are retrieved [Fig. 12(b)] and the attosecond pulse trains are reconstructed [Fig. 12(c)] for all three focus positions.

B. Attosecond streak camera

RABBIT is a powerful tool of attosecond metrology when dealing with attosecond pulse trains. A different approach has to be
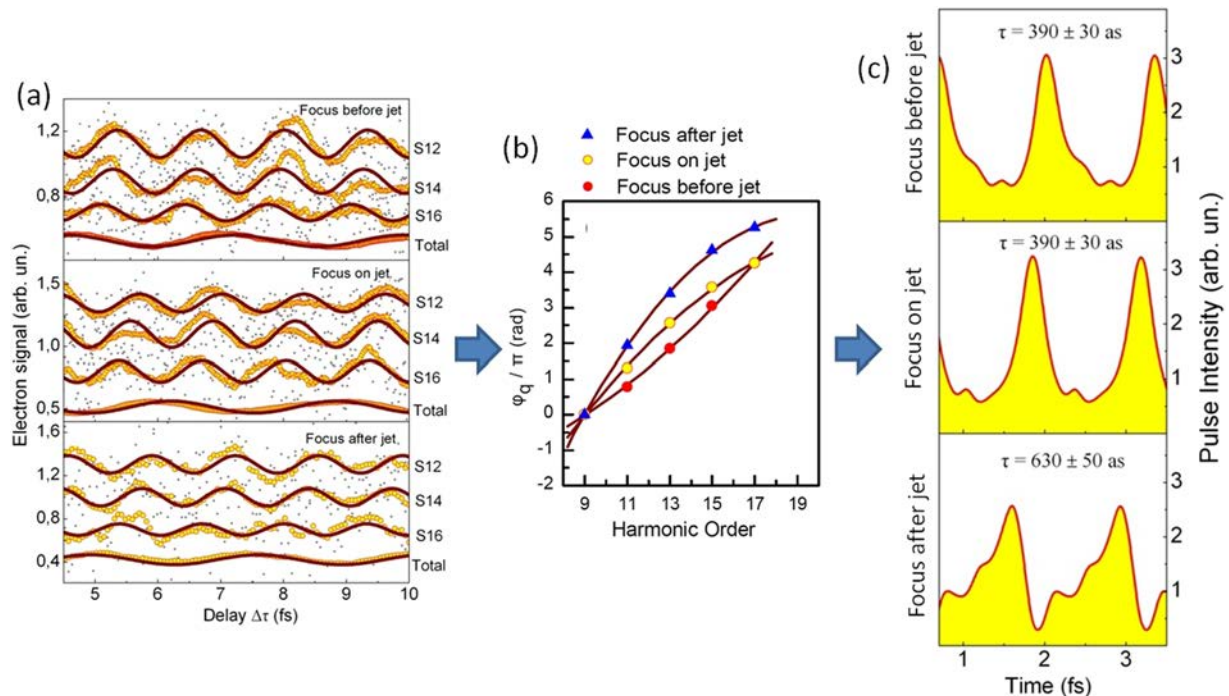
FIG. 12. (a) RABBIT traces at three different positions of the laser focus with respect to the xenon gas jet (focus before jet, focus on jet, and focus after jet) normalized to the corresponding total signal. The gray dots are the measured data, and the yellow circles correspond to a running average of 15 points and 40 points for the total signal. The solid purple lines are sinusoidal fits to the raw data over 13 oscillations on the sideband traces and over 6 oscillations on the total signal. (b) Phases of the consecutive harmonics obtained by the RABBIT traces. (c) Reconstructed APTs. Reprinted with permission from Kruse et al., Phys. Rev. A **82**, 021402(R) (2010). Copyright 2010 American Physical Society.

followed when an isolated attosecond pulse (IAP) comes into play mainly because a harmonic continuum is required for the IAP production. Several different methods for creating IAPs have been realized up to date including amplitude gating,[72,121] ionization gating,[57,122] polarization gating,[123,124] interferometric polarization gating,[100] double optical gating,[125] two-color gating,[126,127] lighthouse,[128] and spatiotemporal gating[129] methods. In all cases, full access to the electric field amplitude and phase of the IAPs is offered by utilizing an experimental technique termed the *attosecond streak camera* formulated around the late 1990s[130,73,74] and demonstrated experimentally for the first time in 2004.[75] Since then, it has been widely applied for the complete characterization of the isolated attosecond pulses.

1. Operation principle of the attosecond streak camera

In a conventional streak camera, the time-varying signal is transformed into a spatial profile on a detector mapping its spatial change when a time-varied deflection is applied on the signal. This concept has been extrapolated in the attosecond streak camera where the role of the time-varied deflection is now being served by a fast-changing, typically few-cycle, IR field which dresses the electron pulse production.

The attosecond streak camera, as a cross correlation technique, relies on the photoionization of a target medium by the XUV IAP in the presence of a synchronized strong IR pulse. Although the initial idea of this method is to measure the photoelectron spectra at specific delays (in principle, one delay is enough), where the laser field streaks the photoelectron energy, and to compare these spectra to the laser-free photoelectron spectrum, traditionally the IAP duration is retrieved by recording a streaking trace obtained by varying the XUV-IR time delay. Both XUV and IR pulses are considered to possess the same linear polarization. The measured electron kinetic energy spectrum can be recorded in various streaking detection angles with the most favorable being the one parallel to the laser polarization axis. Several assumptions are in order,[130] (i) the product of the XUV single photon ionization in the form of an electron pulse is an exact replica of the IAP, i.e., unstructured continuum over the IAP bandwidth, (ii) in the spirit of strong-field approximation, no strong field modification due to XUV occurs, i.e., ground state atoms are promoted directly to the continuum with no intermediate resonances with excited states, and (iii) the IR streaking intensity, typically realized at around 10^{11}–10^{13} W/cm^2, is kept low to not ionize the atom.

The initial momentum P_i of the released electron with charge e and mass m_e when appearing in the continuum, determined by Einstein's photoemission law, is $P_i = \sqrt{2m_e K_i}$, with $K_i = \hbar\omega_{XUV} - IP$ being the initial kinetic energy of the launched electron, where $\hbar\omega_{XUV}$ is the XUV central photon energy of the attosecond isolated pulse and IP is the atomic ionization threshold. The electron's motion upon release can be calculated from Newton's equations of motion in the presence of the linearly polarized along the propagating z-axis oscillating electric IR field $\boldsymbol{E}_{IR}(t)$. After the end of the laser pulse, a final modification will be imparted in the electron's momentum component parallel to the laser polarization, $\Delta p_z(\tau)$,[73,74]

$$\Delta P_z(\tau) = -eA_{IR}(\tau) = -e \int_\tau^\infty E_0(t)\cos(\omega_{IR}t + \varphi_{CE})dt, \quad (3)$$

where τ is the photoelectron's initial time of release, $A_{IR}(t)$ designates the vector potential related to the electric field $\boldsymbol{E}_{IR}(t) = E_0(t)\cos(\omega_{IR}t+\varphi_{CE})$ by $\boldsymbol{E}_{IR}(t) = -\frac{\partial A_{IR}(t)}{\partial t}$, and $E_0(t)$ is the IR's amplitude envelope of finite temporal duration meaning that only electrons being set free during the time duration of the IR pulse are streaked. Assuming the IR field vanishes for $t \to \infty$ and in the adiabatic limit $E_0\omega_{IR} \gg dE_0/dt$, Eq. (3) is written as[74]

$$\Delta P_z(\tau) = \frac{eE_0(\tau)}{\omega_{IR}} \sin(\omega_{IR}\tau + \varphi_{CE}) = \sqrt{4U_p(\tau)m_e} \sin(\omega_{IR}\tau + \varphi_{CE}),$$
$$(4)$$

where $U_p(\tau) = e^2 E_0^2(\tau)/4m_e\omega_{IR}^2$ is the ponderomotive energy of the laser field at the time of ionization τ. Given that the initial kinetic energy is substantially greater than the ponderomotive energy in order to satisfy $K_i > 2U_p$, the released photoelectrons will experience a drift in their final kinetic energy, K_f, as a function of τ,[73]

$$K_f(\tau) = K_i + 2U_p(\tau)\cos 2\theta \sin^2(\omega_{IR}\tau + \varphi_{CE})$$
$$+ a\sqrt{8U_p(\tau)K_i}\cos\theta\sin(\omega_{IR}\tau + \varphi_{CE}), \quad (5)$$

where θ is the angle of observation measured from the z-axis and $a = \{1 - 2(U_p/K_i)\sin^2\vartheta\sin^2(\omega_{IR} + \varphi_{CE})\}^{1/2}$. Equation (5) shows that the final kinetic energy drift depends not only on the electron release time τ but also on the detection angle. For a detection angle perpendicular to the laser polarization, the kinetic energy drift will shift below K_i twice per laser period. When the detection angle is parallel to the laser polarization then the kinetic energy drift will wiggle up and down K_i as the phase of birth varies from 0 to 2π.[73] Assuming an experimental arrangement such that only photoelectrons emitted parallel to the laser polarization axis are collected ($\theta = 0°$) and that $\hbar\omega_{XUV} - I_p \gg U_p(\tau)$ (a requirement that can be relaxed since for typical working streaking IR intensities of ~10^{13} W/cm^2 the ponderomotive energy is of the order of a few tens of millielectron volt when initial kinetic energies of the released electron are in the range of several tens of electron volt), then Eq. (5) turns to

$$\Delta K(\tau) \approx \sqrt{8U_p(\tau)K_i} \sin(\omega_{IR}\tau + \varphi_{CE}) = -A_{IR}(\tau)\sqrt{\frac{2e^2}{m_e}K_i}. \quad (6)$$

Equation (6) implies that the vector potential A_{IR} of the linearly polarized streaking IR pulse is imprinted in the kinetic energy of the released electron and it can be mapped, upon varying the release time τ, into the streaking field. Hence, a streaking measurement (or spectrogram), which is composed of a series of photoelectron spectra obtained by temporally scanning the isolated attosecond pulse through the much longer femtosecond pulse, may further be used for the full characterization of the streaking laser field in the time domain.[44]

The temporal characteristics of the attosecond ionizing pulse can be derived from the photoelectron energy spectrum exploiting the effect that electron pulses released at different streaking probe times will exhibit different final spectral widths.[75,131] The ionizing pulse will reflect its temporal and time-frequency dependence (chirp) characteristics on the released electron wave packet. Since the streaking field varies over the time that photoionization takes place, the launched photoelectrons, depending on their release time t, experience different final momenta after the end of the ionizing pulse has passed. A direct consequence of this streaking effect is that the photoelectron spectrum will be generally quite different from
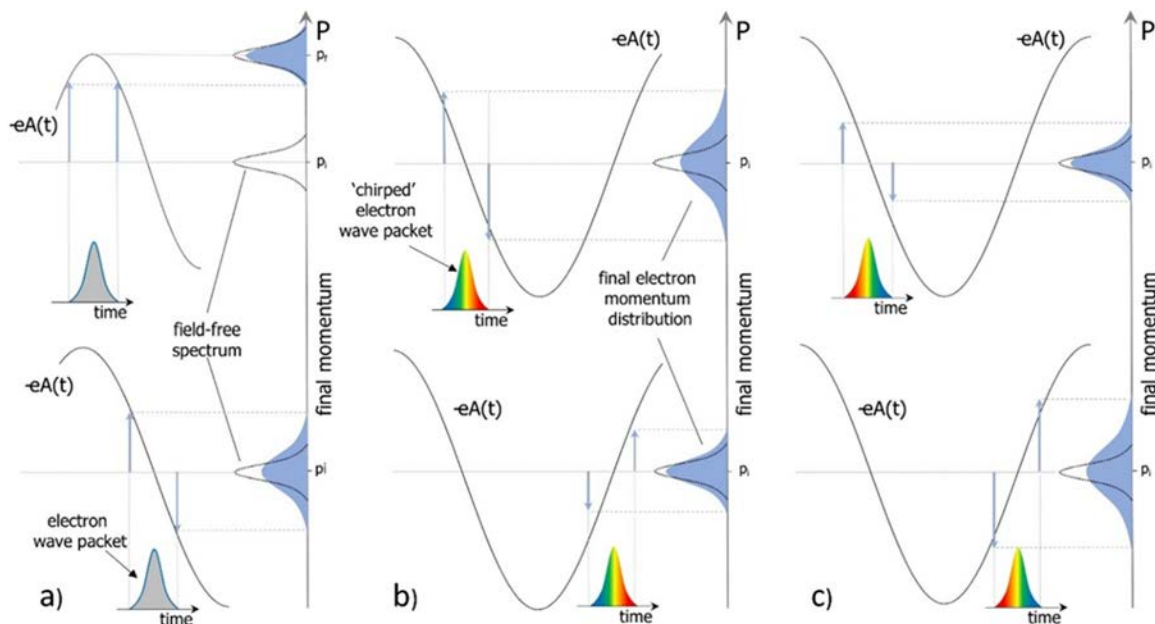
FIG. 13. (a) For unchirped (constant time-frequency evolution) electron pulses ejected at different times, a broadening of the photoelectron momentum distribution, as compared to the field-free spectrum, is exhibited whenever the release times coincide with a zero-crossing of the vector potential $A(t)$ of the streaking laser field. (b) and (c) For a positively (negatively) chirped electron pulse, the final momentum distribution is broadened (narrowed) when the electron is probed at a zero-crossing of a negative (positive) vector potential slope. Figure adapted from Ref. 132.

the streak-field-free one, i.e., when the streaking field is switched off. At a first approximation, assuming a constant vector potential within the ionizing pulse duration and an unchirped electron wave packet, an overall energy shift would be observed in the photoelectron spectrum. This is why the streaking spectrogram reflects the driver laser pulse shape. However, the vector potential does change within the ionizing pulse duration. This subtle change is being manifested as a further broadening on the photoelectron energy distribution. A broadening that is more evident when the electron release time coincides with a zero-crossing of the streaking vector potential, i.e., local electric field maximum, because in this case photoelectrons acquire opposite direction momentum shifts [Fig. 13(a)]. For a chirped attosecond pulse, the streaking effect causes a broadening or narrowing of the launched electron's final energy distribution for adjacent zero-crossings, depending on the slope sign of the streaking vector potential $-e \cdot A(t)$ probing the released photoelectron [Figs. 13(b) and 13(c)]. Assuming a positive (negative) chirp, when the electron wave packet is probed at a zero-crossing of a negative (positive) vector potential slope then the streaked photoelectron distribution will result in a broader (narrower) final electron energy distribution.

Based on the above arguments, a retrieval algorithm can be employed to fully extract the temporal characteristics of the isolated attosecond pulses. This will be discussed in more detail in Sec. III C.

2. Experimental implementation of attosecond streak camera

A typical attosecond streak camera experimental arrangement is sketched in Fig. 14. The XUV generation process is driven by a linearly polarized few-cycle IR pulse. Neon gas serves as a suitable gas target for generating the isolated attosecond XUV pulses with photon energies in the range of ~40 eV–150 eV. Both XUV and IR beams are temporally and spatially overlapped and focused on a second gas jet placed in the target area. XUV single photon ionization of ground state atoms creates a free electron wave packet with a kinetic energy K_i that is modulated by the presence of the synchronized IR few-cycle field. The final momentum of the released photoelectron depends strongly on the phase of the streaking IR electric field oscillation, i.e., the delay between the IR and XUV pulse. A positive streaking field amplitude accelerates the free electron, whereas negative amplitude leads to deceleration. Both XUV and IR pulses are considered to possess the same linear polarization, whereas the measured electron kinetic energy spectrum can be measured in various streaking detection angles with the most favorable being in parallel to the laser polarization axis. The progressive modification of the kinetic energy of the electron pulse is finally detected as a function of the time delay between the XUV and IR pulses.

C. FROG-CRAB

It was demonstrated by Refs. 80 and 133 that the attosecond streaking spectrogram allowed complete reconstruction of attosecond pulses. The technique termed FROG-CRAB is a descendent of the known FROG method[134] which is widely applied in the spectral and temporal characterization of ultrashort fs pulses. FROG-type retrieval algorithms, analyzing the measurement characteristics, can then be employed to achieve complete temporal characterization
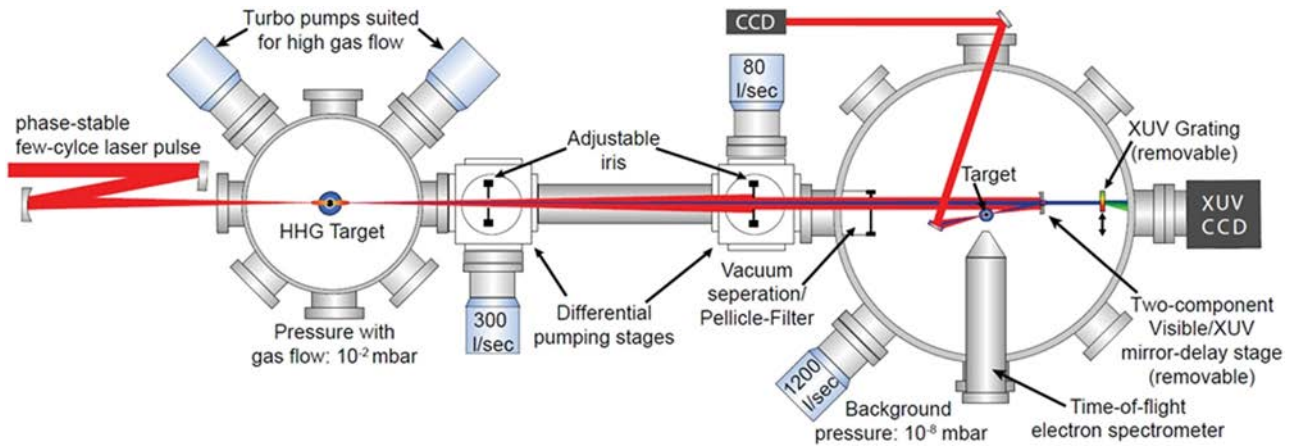
FIG. 14. Experimental setup arrangement for the attosecond streak camera technique. Figure taken from Ref. 132.

of the isolated attosecond pulses[80,121,133,135–138] and attosecond pulse trains.[139,140]

A FROG spectrogram, i.e., a 2D data spectrum set acquired as a function of time delay, is generally expressed as

$$S(\omega, \tau) = \left| \int_{-\infty}^{\infty} dt\, G(t) E(t - \tau) e^{i\omega t} \right|^2, \quad (7)$$

where $E(t - \tau)$ is the unknown field to be measured and $G(t)$ is the gating field. For an attosecond laser field, it was derived[80] that a similar formula with Eq. (7) can be obtained. The transition amplitude of exciting a final continuum state $|v\rangle$ of electron momentum v when only the XUV field is present, in the single active electron approximation, is expressed as[133]

$$a(v) = -i \int_{-\infty}^{\infty} dt\, E_{XUV}(t) \boldsymbol{\mu}_{vg} e^{i(W+I_p)t}, \quad (8)$$

where $\boldsymbol{E}_{XUV}(t) = E_{XUV}(t) \cdot e^{-i\omega_{XUV}t}$ is the description of the ionizing isolated attosecond XUV pulse, with $E_{XUV}(t)$ being the pulse envelope, $\boldsymbol{\mu}_{vg} = \langle g|r|v\rangle$ is the dipole matrix element connecting the ground state wave function $|g\rangle$ with the continuum state wave function $|v\rangle$, $W = \frac{v^2}{2}$ is the final kinetic energy (in atomic units), and I_p is the ionization potential. If a photoelectron experiment could measure directly $\alpha(v)$ [it measures $|\alpha(v)|^2$], then $E_{XUV}(t)$ could be recovered by a Fourier transform of $\alpha(v)$. Introducing in the picture the streaking IR laser field with vector potential $\boldsymbol{A}(t)$, the free electron's instantaneous momentum in the field $\boldsymbol{p}(t) = v + \boldsymbol{A}(t)$, including the time delay τ between the XUV-IR, in the framework of the strong field approximation and assuming that the streaking field effect on the dipole matrix is weak enough to be neglected, Eq. (8) is rewritten as[73,80,133,141]

$$a(\boldsymbol{p}, \tau) = -i \int_{-\infty}^{\infty} dt\, E_{XUV}(t - \tau) \boldsymbol{\mu}_{pg} e^{i\Theta(t-\tau)} e^{i(W+I_p)t},$$
$$\Theta(\tau) = -\int_{t}^{\infty} dt' \left[\left(\boldsymbol{p}\boldsymbol{A}(t') + \frac{1}{2} A^2(t') \right) \right]. \quad (9)$$

The resemblance of Eq. (9) with Eq. (7) becomes obvious by setting $G(t - \tau) = e^{i\Theta(t-\tau)}$, signifying that the streaking's field vector

potential modulates the emitted photoelectron wave packet as a gate function of the varying delay τ. With the use of appropriately built algorithms, complete retrieval of the attosecond pulse envelope E_{XUV} and the phase $\Theta(\tau)$ can be achieved.[80,135]

While FROG-CRAB is now a well-established method to fully characterize attosecond pulses, its application to few-femtosecond XUV pulses is not considered trivial. In particular, the associated narrower bandwidth and the subsequent loss of subcycle resolution reduce the otherwise rich level of information provided by a FROG-CRAB trace. Evolution of the ptychographic technique[137] proved its capacity to also reconstruct XUV few-femtosecond pulses down to 5 fs.[142]

1. IAP characterization with FROG-CRAB attosecond streak camera technique

The XUV broadband continuum generated with the amplitude gating method capable of supporting the isolated attosecond pulses is presented in Fig. 15(a). It was created by focusing CEP-stabilized ~5 fs NIR pulses centered at 730 nm, on a Ne gas jet. Figure 15(b) shows an experimental streaking spectrogram acquired with an XUV pulse energy centered at ~93 eV ionizing Ne gas phase atoms.[132] Both NIR and XUV copropagate to the experimental chamber of Fig. 14. Spatial separation is achieved by means of a concentric Zr foil-filter, blocking the IR beam in the center, and the inner concentric part of a focusing two-component mirror. The reflectivity of the inner mirror is centered at 93 eV with a 6.5 eV bandwidth. As shown in Fig. 15(b), the dominant contribution comes from photoelectrons stemming from the Ne 2p-cell single-photon XUV ionization centered around 71 eV, as pointed by the black solid line, while the black dashed line indicates photoelectrons coming from Ne 2s-cell ionization. In this case, the collection efficiency of the e-TOF was optimized for final energies around 70 eV. The streaking trace exhibits a low broadening, while photoelectrons are up- and down-streaked demonstrating a good interferometric stability. Employing the least squared generalized projection algorithm retrieval algorithm (LSGPA),[135] the amplitude and spectral phase of the XUV pulse can be extracted with
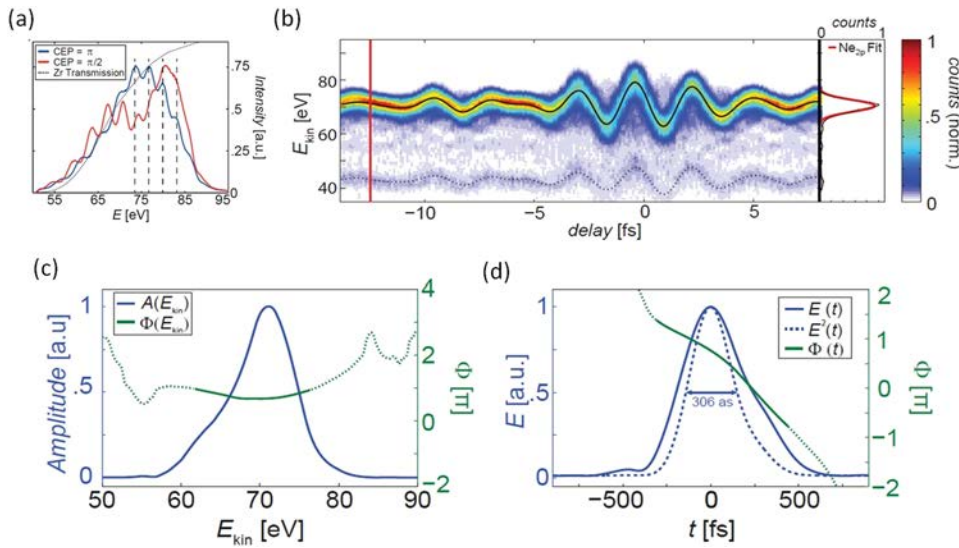
FIG. 15. (a) CEP dependence of the XUV spectra. From the superimposed dashed lines with an energy spacing of 2×1.6 eV, the central wavelength of the driving pulse can be estimated to be 729 nm. (b) Experimental streaking trace for Ne 2p-cell (solid black line) and 2s-cell (black dashed line) ionization. The right panel shows the photoelectron spectrum for the delay pointed in (b) with the red solid line. (c)–(d) LSPGA reconstructed amplitude and spectral phase. Figures taken from Ref. 132.

the results shown in Figs. 15(c) and 15(d). The inherent positive attochirp of short trajectories is partially compensated by the Zr foil filter and the XUV focusing mirror. The retrieved pulse duration is 306 as which is fairly close to the anticipated Fourier-limit of 280 as.[132]

D. Phase retrieval by omega oscillation filtering (PROOF)

An alternative to the FROG-CRAB method based on the measurement of photoelectrons spectra generated by the attosecond pulse to be characterized under the perturbation of an IR electric field is the Phase Retrieval by Omega Oscillation Filtering (PROOF) method, which is mainly appropriate for the characterization of

ultrabroadband attosecond pulses in the region of few attosecond.[81] Like the RABBIT technique, the IR perturbating dressing field is expected to be rather weak, so its action on the photoelectron spectra can be treated by means of the lowest-order perturbation theory. Both RABBIT and PROOF techniques are based on the hypothesis that only single IR photon paths are involved and contribute to the signal. It is demonstrated that the photoelectron spectrum, $I(v, \tau)$, can be expressed as the sum of three terms: $I(v, \tau) = I_o(v) + I_{\omega_L}(v, \tau) + I_{2\omega_L}(v, \tau)$ (Fig. 16), where τ is the optical delay introduced between the XUV and IR fields.

The component $I_o(v)$ signifies a term which does not depend on the delay, whereas the other two terms $I_{\omega_L}(v, \tau)$ and $I_{2\omega_L}(v, \tau)$ oscillating with frequency ω_L and $2\omega_L$, respectively, where ω_L is the IR perturbing dressing field's angular frequency. In particular, the
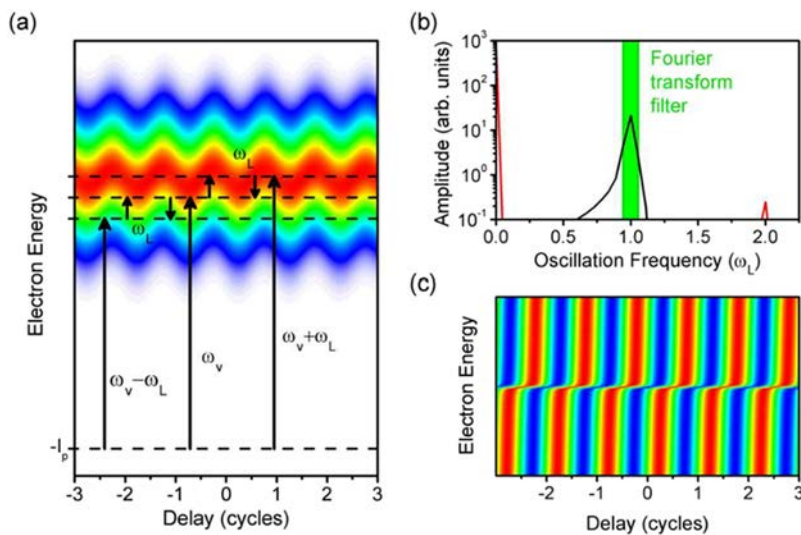
FIG. 16. Operation principle of PROOF. (a) Photoionization of electrons from an attosecond pulse to continuum states. Those continuum states separated by the laser central frequency ω_L are coupled by the perturbating IR laser, leading to the characteristic oscillation of the photoelectron signal with delay. (b) The amplitude after Fourier transforming the signal in (a). The amplitude peaks are originating from the oscillation frequencies of zero (red line), ω_L (black line), and $2\omega_L$ (red line). The ω_L component is selected by using a band-pass filter. (c) Inverse Fourier transform of the filtered ω_L component of the oscillation gives the spectrogram presented, from which the spectral phase of the attosecond pulse can be extracted. Reprinted with permission from Chini et al., Opt. Express 18, 13006 (2010). Copyright 2010 The Optical Society.

term $I_o(v)$ represents the shared probability of one (XUV) photon and two (XUV+IR) photon absorption which does not have any dependence on the delay while the terms $I_{\omega_L}(v, \tau)$ and $I_{2\omega_L}(v, \tau)$ outcome from the interferences among the different one- and two-photon channels to a given final state which are oscillated with the delay τ at the IR perturbing dressing field with laser frequency ω_L and at $2\omega_L$, respectively [Fig. 16(a)]. Since the spectral phase of the attosecond pulse is imprinted on the photoelectron wavepacket, the spectral phase of the attosecond field alterations between the interfering channels is established in the dependence of $I_{\omega_L}(v, \tau)$ on the time delay and can be extracted using a suitable mathematical method where details can be found in Ref. 81. In particular, the operation principle of the PROOF approach is summarized as follows. The atom is excited by the attosecond pulse to the continuum states in the presence of the IR dressing field. The energy of the emitted photoelectrons depicts a periodic modulation with delay as is shown in Fig. 16(a). The Fourier transform of the spectrogram in Fig. 16(a) results in the appearance of peaks at ω_L and $2\omega_L$ frequencies [Fig. 16(b)]. By applying a narrow spectrum filter, the ω_L component is filtered out from the spectrogram of Fig. 16(b) and the trace $I_{\omega_L}(v, \tau)$ is revealed [Fig. 16(c)] and used to measure the spectral phase distribution of the attosecond pulse.

PROOF was implemented in 2012 for the measurement of the isolated pulses of duration down to 67 as[143] (Fig. 17). The broadband XUV continuum radiation was generated by the Double Optical Gating (DOG) technique. The laser system used was delivering at 1 kHz rep. rate, few-cycle CEP stable IR pulses of ≈ 7 fs duration and energy 1.4 mJ/pulse. The laser pulses provided by this laser system were sent through the DOG optics and focused on a Ne-filled gas cell to produce the isolated attosecond pulses. Figure 17(a) shows a streaking trace obtained experimentally by ionizing Ne gas with XUV pulses of photon energy in the range of ~62 eV. Figures 17(b) and 17(c) show the $I_{\omega_L}(v, \tau)$ and the spectral phase of the attosecond pulse, respectively.

IV. LIMITATIONS, BOTTLENECKS, AND POTENTIAL PATHWAYS

A. 2-IVAC

Despite the large applicability of the 2-IVAC approach for the attosecond pulse characterization, as any experimental technique suffers from a series of limitations. The first one is associated with the fundamental principle of any energy not-resolved AC approach. An AC approach measures the spatiotemporal averages of pulse durations (in the case of APT provides the average duration of the
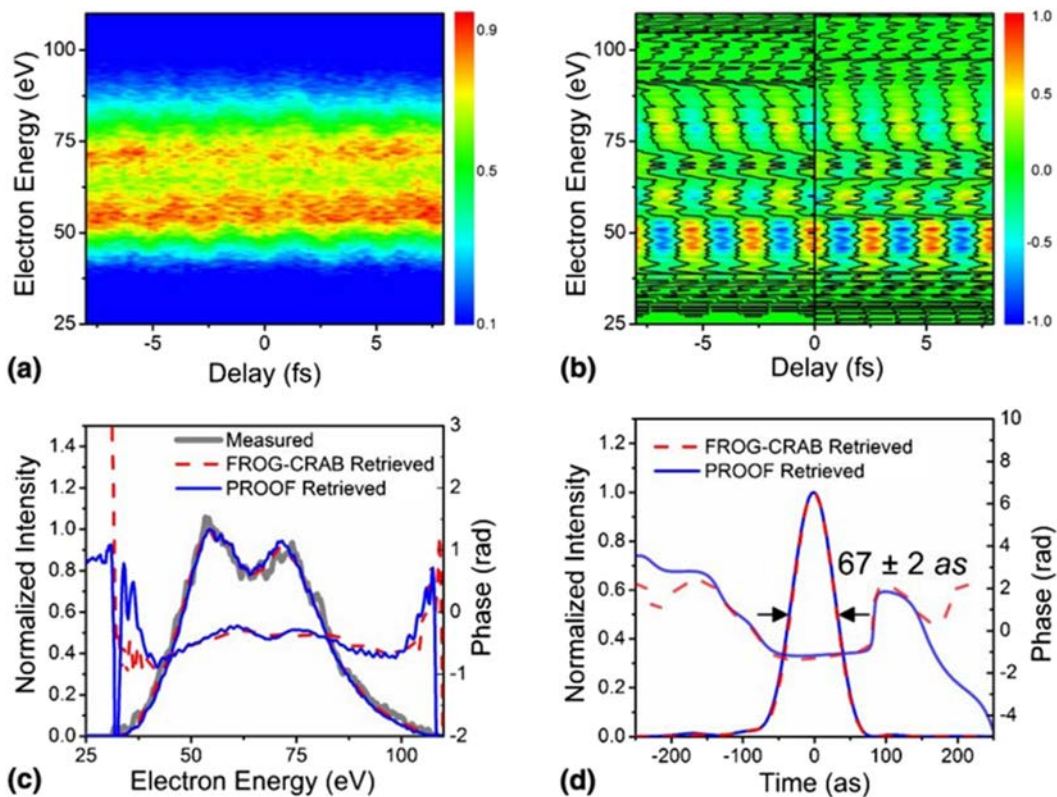
FIG. 17. XUV pulse characterization by implementing the PROOF technique. (a) Photoelectron spectrogram obtained experimentally. (b) Filtered $I_{\omega_L}(v, \tau)$ from the spectrogram in (a). (c) Photoelectron spectrum obtained experimentally (thick solid line) and retrieved spectra and spectral phases from PROOF (solid line) and FROG-CRAB (dashed line). (d) Recovered temporal profiles and spectral phases from PROOF (solid line) and FROG-CRAB (dashed line). Reprinted with permission from Zhao *et al.*, Opt. Lett. **37**, 3891 (2012). Copyright 2012 The Optical Society.

attosecond pulses in the train) and does not allow the full pulse reconstruction. We note that the attosecond pulse duration retrieved by an AC trace recorded by measuring ions, is obtained assuming Gaussian pulses (using the relation $\tau_{XUV} = \tau_{AC}/\sqrt{2}$), an assumption which is not required in the case of XUV FROG-type measurements. Other limitations are

(a) The response of the nonlinear detector used for the pulse characterization: As any conventional AC approach, the nonlinear detector should be spectrally flat and with instantaneous response. Because the attosecond pulses are generated in different spectral regions with a bandwidth of >2 eV, to find the proper nonlinear detector is an issue far from trivial. To ensure that the properties of the nonlinear detector fulfill the requirements for attosecond pulse characterization, the proper nonlinear ionization processes need to be chosen. In order to estimate the flatness and the temporal response of the detector, the time-dependent Schrodinger equation (TDSE) needs to be solved.[84]

(b) The stability of the XUV source and both the 2-IVAC and XUV FROG techniques: A 2-IVAC measurement suffers from the intrinsic limitations that accompany any pump-probe approach that involves an interferometer (or an XUV-wave front beam splitter) as a delay line between the XUV pulses. In a 2-IVAC experiment, the XUV pulse duration is obtained by multiple shot measurements at different time delays. During these measurements, instabilities relevant to XUV-IR-laser parameters [XUV-pulse duration, XUV-intensity, carrier-envelope-phase (CEP) of the IR pulse, etc.] together with the relatively "low" peak to the background ratio provided in an ideal spatiotemporal overlap of the two XUV pulses by a 2-IVAC trace are limiting the temporal resolution of the measurement which to the best of our knowledge is in the range of 50–100 as. This value can be significantly improved by means of high rep. rate attosecond beam lines[98] or the development of single-shot XUV autocorrelator.[90,144] In addition, a robust retrieval of the phase-amplitude distributions requires high shot to shot data stability, which is rather challenging for the by nature noisy harmonic fields.

(c) The surface quality of the XUV optics: The temporal resolution of all approaches is limited by the wave front distortion upon reflection of the radiation on XUV optical elements. Achieving a surface flatness equal to a small fraction of the wavelength, assuring negligible wave front distortion is a technological challenge of, with photon energy, increasing degree of complexity and cost.

(d) The finite energy resolution of the spectrometer in XUV FROG measurements: Such measurements, in addition to the limitations mentioned above, suffer from the limited photoelectron energy resolution which is associated with resolution provided by the available electron spectrometers (which is in the range of $\Delta E/E = 1\%$, where E is the electron kinetic energy), the low PE signal, and the presence of space charge effects.

B. RABBIT

Although RABBIT has proven itself as a multipurpose method with a broad range of applications, there are several limits to its applicability in attosecond metrology. One is its capacity to only yield the average pulse shape in a given attosecond pulse train. In effect, the harmonic amplitude becomes a function of time as each harmonic field has a lower pulse duration than the fundamental pulse, with the lower orders in the XUV comb having the longest duration while the shortest belongs to the harmonics in the other end. Hence, I_{avg} in Eq. (2) becomes the average of all pulses in the attosecond pulse train. Varjú et al.[116] proposed a method to reconstruct pulse-to-pulse variations by performing the RABBIT measurement at different generation intensities. The method from Ref. 116 was employed in Ref. 145 to access the pulse-to-pulse variations where it was retrieved as a pulse duration which varied from 120 as in the center of the train to 140 as in the FWHM, while a pulse duration of 190 as was found at the FWTM (full-width at tenth maximum).

Measurement of average phases results in another limitation of the RABBIT approach as it was pointed out in Ref. 98 through a comparative study between 2-IVAC and RABBIT. There it was revealed as an underestimation of the APT duration when measured with the RABBIT method which was attributed to contribution effects of short and long electron trajectories in the HHG process. Overall, the findings of that first comparative study between 2-IVAC and RABBIT[98] revealed that the latter will retrieve the temporal profile of the attosecond pulse train reliably only when only one electron trajectory contributes to the wave form, particularly the short one. Elimination of the long trajectory may prove a challenging experimental requirement to relax, particularly when plateau harmonics are involved like in the case of RABBIT and APTs. Toward this direction, the use of relatively short focal length and filtering stages may be adapted to prevent the long trajectories enter the interaction region.

Another challenge in the RABBIT technique arises from the experimental necessity to keep the intensity of the dressing IR probe pulse sufficiently low in order to only act on the process as a perturbation. The validity of RABBIT will begin to break down when higher IR field intensities are involved and multiple IR photon absorption may occur, resulting in terms oscillating at higher odd and even multiples of the fundamental frequency, leading to different additional phases for a given single final state component and eventually prevent a reliable extraction of the harmonic spectral phase differences. However, such higher modulation frequencies may become useful so as to attain an unperturbed measurement for the harmonic chirp rate.[146] Furthermore, a newly developed data analysis approach termed mixed-FROG[147] is able to retrieve with greater precision the profile and pulse characteristics in a RABBIT measurement by disentangling coherent and incoherent contributions. A more recent discussion on the accuracy and precision of RABBIT measurements can be found in Ref. 148.

C. Attosecond streak camera and FROG-CRAB

Attempts on reaching shorter isolated attosecond pulse durations necessitate a broader XUV spectrum. Thus, the attosecond streak camera measurement is limited by definition of a reduced spectral resolution since the bandwidth of an IAP would be directly translated to the photoelectron energy bandwidth. The precise value of the temporal resolution of the streak camera shall be depended

on the experimental parameters such as spectrometer resolution and signal-to-noise ratio. A reasonable, though, order of magnitude estimation for the time resolution limit of a streaking measurement, indicating also the shortest pulse duration that can be measured, can be deduced by quantum mechanical time-energy uncertainty relation considerations, assuming streaking detection parallel to the laser polarization axis and electron release time near the maximum electric field strength where the vector potential is approximately linear over time. In order to resolve streaks by two distinct Δt-distanced events, the induced energy shift by the streaking field should be greater than the initial energy spread of each event,[73,131,149] which results in a fundamental quantum limitation, $\Delta t > (\hbar/E_0 p_i)^{1/2}$. It is instructive to express Δt in relation to the maximum streaked energy shift imparted on an electron with initial momentum p_i at release time T_0, $\Delta K_{max} = \frac{E_0 p_i}{\omega_{IR}}$, $\Delta t \sim (T_0/2\pi)\sqrt{\hbar\omega_{IR}/\Delta K_{max}}$. For a streaking carrier wavelength of 800 nm, a release time of ~2 fs, and typical maximum streaking shifts of 20 eV, the time dynamics of ~100 as can be potentially resolved.

Achieving better time resolution would require use of higher streaking intensities and increased ΔK_{max}, thus greater initial electron energy. An intense streaking field capable of imparting significant momentum shifts to the electron released by the IAP is required for the streaking measurement, but a more intense streaking field could ignite ATI effects to the point that may become significant generating a large amount of background electrons overlapping the useful signal. Suppression of ATI could be achieved by changing the angle (i.e., experimental geometry) of streaking detection or in the parallel detection geometry a slight ellipticity may be introduced. On the other hand, photoionization cross sections decrease with photon energy which may pose a stringent constrain to future applications of streaking-based techniques to higher photon energies and shorter pulses. To this end, observation of streaked electrons at different direction angles with respect to the laser polarization offers various advantages, for example for the perpendicular streaking detection ($\theta = 90°$), the third term of Eq. (5) is zeroed and so is the dependence of streaking shift with initial electron energy. A dependence that may become a weakness in the parallel streaking detection arrangement [$\theta = 0°$ in Eq. (5)] when electron mean release energy becomes comparable to its wave packet bandwidth. In contrast, parallel geometry offers the largest streaking effect, owing to the exact same third term of Eq. (5) which vanishes for $\theta = 90°$, along with a more direct one-to-one resemblance of the streaking spectrogram to the laser pulse shape, especially when near Fourier-transform limited pulses are in play. The parallel geometry also offers an improved streaking collection efficiency since an active detection cone as large as ±30° is reached, and it is the geometry that is mostly favored for attosecond streaking measurement setups.

It is well understood that for the streaking spectrogram, active stabilization of the carrier envelope phase φ_{CE} of the IR field is a prerequisite. The momentum shift of the released electron depends on that parameter as well. In combination with the necessity of small delay steps (in the order of few tens of attosecond) between the IAP and the streaking field so as to be able to resolve subtle changes in the attosecond time scale streaking experiments, these factors place a substantial challenge for the long-term stability of the system, in particular, because streaking measurements are performed in an electron counting regime and are intrinsically very slow (e.g., target gas

pressure, that could lead to higher count rates, is compromised by the microchannel plate detector).

A common characteristic in HHG setups is the creation of one or at cases even two, presumably weaker, satellite pulses at a distance of half-streaking laser-cycle following or preceding the main attosecond pulse. Such pulses may result in electrons being accelerated and decelerated at the same time by the streaking field which will be exhibited in more periodical oscillations in the streaking spectrogram creating spectral interference fringes in the energy domain between the different contributions. Ideally, the contribution of satellite pulses can be easily noted in the streaking spectrogram and by careful adjustment of the CEP, these may be eliminated by concentrating power to the main pulse. Else, these satellite pulses should be accounted for and through a proper fringe-resolved analysis can be integrated in the algorithm reconstruction model.[135,150]

Streaking spectrograms are formed over many laser shots, when the electron wave packet may present shot to shot uncertainties due to fluctuations of experimental parameters. To some extent, measured electron streaking spectra are an averaged result over an ensemble of wave packets. In addition, an attosecond pulse is coupled in both space and time. Under the assumption that the driving attosource is being replicated into the target medium through the produced electron pulse, then the streaking IR pulse dressing the full replica may be argued that measures the spatially averaged pulse.

Investigating the robustness of the streak camera technique and the pulse reconstruction algorithms, it relies on the identification of the effect that several key parameters (including central photon energy, bandwidth and group-delay-dispersion, and timing of the IAP and XUV-NIR delay) pose on the electron wave packet and thus in the streaking measurement itself.[151] Uncertainties in these parameters tent to be imaged as a smearing and distortions in the streaking spectrogram along the energy axis. At times, they may even result in a loss of the relative narrowing and broadening effect of the streaked wave packet when released at consecutive zero-crossings of the vector potential, affecting the recovery of the attosecond chirp. Overall, the effect of these uncertainties to some extent is reflected in overestimating the bandwidth; hence an underestimation of the pulse duration. Although each of the experimental parameters cannot be decoupled from the rest so as to determine its solely effect on the streaking and retrieval algorithms (for example, a relative time jitter will most certainly alter the relative phase), uncertainties in central photon energy, bandwidth, and group-delay dispersion at cases have been found to lead to an underestimation in the order of ~10%–15% of the original pulse, while the XUV-IR delay seems to have an even minor effect in the correct pulse reconstruction.[150]

Atomic delays, which depend on the target system, state, and photon energy, have been found to vary by several attoseconds/eV[152] and may have an impact of even 10% on the measurement accuracy of a ~100 as IAP. Disentangling the atomic response from the properties of the attosecond pulses is highly desirable, especially for sub-100 as pulses. An interesting method proposed recently reports the beneficial properties of using Rydberg wave packets to characterize attosecond UV pulses, while the technique could be readily extended to the study of shorter wavelength x-ray attosecond pulses.[153,154]

D. PROOF

The PROOF method is an extension of the RABBIT to the isolated attosecond pulses. It relies on the use of a weak dressing IR field with intensity lower that 10^{12} W/cm^2 and is based on the assumption that only paths involving a single-IR-photon absorption contribute to the signal. If the IR dressing perturbating field intensity is increased, this hypothesis becomes invalid and a systematic error can be presented in the reconstruction of the attosecond pulse. For this reason, the PROOF method suffers from the limitations described for the RABBIT approach. In addition, since PROOF relies on second order perturbation theory and deals with the metrology of pulse in the few-attosecond time scale, any participation streaking in the photoelectron signal, may introduce substantial errors on the retrieval of the spectral phase distribution of the IAP. A promising alternative to PROOF as well as to FROG-CRAB methods on retrieving spectral phases with neural networks has been recently developed, with potential application to the characterization of x-ray FEL pulses.[155]

V. CHALLENGES AND FUTURE DIRECTIONS

### A. High photon flux attosecond pulses in the XUV range

Noble gas atoms driven by high power infrared (IR) laser pulses have been routinely employed over the years for the production of subfemtosecond pulses in the 20–100 eV XUV photon energy regime, yielding photon fluxes ranging from 10^7 to 10^{11} photons/pulse.[31–40] The latest technological advance toward an XUV high photon flux attosecond pulsed source is the newly constructed $\approx$18 m long (HHG) beam line based on loose focusing geometry (driving laser focused using 9 m focal length) and a double gas jet target arrangement of the Attosecond Science and Technology Laboratory of the Foundation of Research and Technology (FORTH).[39] By operating the beam line at optimal driving intensities and xenon gas pressure/two-jet-distance, enabling optimal phase matching, an XUV energy per pulse of 230 μJ has been demonstrated in the spectral region 20–30 eV. The corresponding photon flux of 0.6×10^{14} photons/pulse is competitive with FEL photon fluxes in this spectral region. Although not measured yet, it is expected from previous measurements that the harmonics form an APT. An estimated envelope width of 10 fs duration and a measured XUV focal spot size of 2 μm[89,90] result in an achieved focused intensity of ~7 $\times$ 10^{15} W/cm^2, a value that by using high reflectivity XUV optics can be increased to 10^{17} W/cm^2. These high XUV intensities are evidenced by witnessing multiply charged argon atoms (observed charge states up to Ar^{4+}) produced by multi-XUV-photon ionization processes. Combining polarization gating approaches[100,101] with CEP tagging schemes[156] it is estimated that such a beam line can deliver the isolated attosecond pulses with power in the experimental target area in the range of ~few GW/pulse. Such unprecedented high power, for the current table-top HHG arrangements, will open up unique and exciting pathways toward XUV-pump-XUV-probe electronic studies in atoms, molecules, and solids while it will pave the way for exploiting new nonlinear schemes for attosecond pulse characterization.

The measurement of the temporal duration of an XUV pulse under investigation may be down limited by the ionization potential of the target atom (A) which inherently sets an upper limit to the harmonic order q that would be permitted to be included in the superposition. This limitation can be surpassed by exploiting alternative two-XUV-photon ionization schemes, such as the nonresonant direct double ionization (DDI), sequential double ionization (SDI), and above threshold ionization (ATI) (Fig. 18),[34,39,40,47,58,157–159] where the corresponding products of ionization, ions or electrons are collected by means of ion-TOF mass or time-resolved photoelectron, spectroscopy.

The ATI scheme offers the advantage of continuously extending the 2nd order AC technique to shorter wavelengths, thus higher photon energies. Given that the ATI photons reach a structureless continuum (i.e., there are no autoionizing bound atomic states present), then this advantage becomes the only constraint of the method, as the cross section decreases rapidly with photon energy [$\propto(\hbar\omega)^{-6}$[160]].

The two-photon-ATI scheme produces singly charged ions and electrons with discrete energies $PE_m^{ATI} = \hbar\omega_m - IP_1$, where $m = q_{min} + q_{max} + n$ with $n = 1 - N, \ldots, N - 1$; q_{min} and q_{max} are the minimum and maximum harmonic orders spanning the XUV comb, N is the number of harmonics in the superposition and IP_1 is the first atomic ionization threshold. Photoelectron spectroscopy is required to energy-resolve the different groups of electron energies.
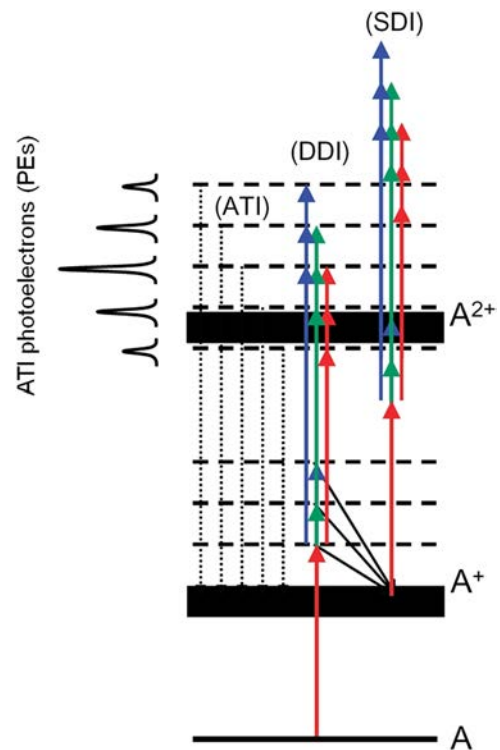
FIG. 18. Ionization scheme showing the ATI, DDI, and SDI processes of an atom A. ATI leads to the generation of a singly charged ion and photoelectrons (PEs) with energies depending on the energies of the photons involved in the ionization process. DDI and SDI generate doubly charged ions and PEs with energies depending on the energies of the photons involved in the ionization process. These processes allow the extension of the AC method to higher photon energies.

The DDI and SDI schemes also allow an extension of the second-order AC method to shorter wavelengths, but with the additional constraint that photon energies lie in the region $IP_1 < \hbar\omega_q < IP_2 - IP_1$, with IP_2 being the second atomic ionization potential. Here, both ion mass spectrometry collecting doubly charged ions and PE spectroscopy can be employed. In this photon energy region, there are several ionization pathways that can contribute to the products of ionization, such as single-photon, two-photon DDI (TPDDI), and three-photon SDI (ThPSDI), each with its own ionization rate. The single-photon ionization process is not taken into consideration because it does not contain any temporal pulse characteristic information. The TPDDI and ThPSDI mechanisms lead to the formation of doubly charged ions (A^{2+}) and electrons with energies $0 < PE_{ch}^{DDI} < \hbar\omega_{ch} - IP_2$ and $PE_{ch}^{ThPSDI} = \hbar\omega_{ch} - (IP_2 - IP_1)$, respectively. Since there is no direct way of discriminating the coexisting contribution of both schemes in the recorded signal in the ionization process, the temporal evolution of the system can be evaluated at different intensities using rate equations.[161,162] Nonetheless, results of previous studies in He, Ar, and Kr[40,57,58,66,157,158,161,162] render possible a rough estimation of the intensity regions where the second-order AC method can be applied for attosecond pulse train characterization through DDI or SDI excitation schemes. According to previous studies in the He atom,[162] for XUV intensities well below the SDI saturation intensity of the atom ($I_{XUV} < 10^{13}$ W/cm^2), the TPDDI and ThPSDI rates are expressed as $W_2^{DDI} = \sigma_{DDI}^{(2)} I_{XUV}^{(q)} I_{XUV}^{(p)} / (\hbar^2 \omega_q \omega_p)$ and $W_3^{ThPSDI} = \left[\sigma^{(1)} I_{XUV}^{(q)} / \hbar\omega_q\right]\left[\sigma_{TPII}^{(2)} I_{XUV}^{(q)} I_{XUV}^{(p)} / (\hbar^2 \omega_q \omega_p)\right]$, respectively; σ_{TPII} denotes the two-photon ionization cross section of the ion. In that case, DDI becomes the dominant process that could be used for attosecond pulse characterization. When employed intensities are far above the SDI saturation intensity of the atom ($I_{XUV} > 3 \times 10^{15}$ W/cm^2), the ThPSDI rate is expressed as the product of the ionic saturated ground state population times the ionic two-photon ionization rate, i.e., $W_3^{ThPSDI} = \left[Y_1^{(q)} / N\right]\left[\sigma_{TPII}^{(2)} I_{XUV}^{(q)} I_{XUV}^{(p)} / (\hbar^2 \omega_q \omega_p)\right]$, which effectively is a second-order process. Then, the SDI process dominates and is favored to be used for attosecond pulse duration measurements, namely, through its second step, i.e., the two-photon ionization of the ion, with the atomic population being depleted.

Besides the usefulness of the above schemes on characterizing intense attosecond pulses in different XUV spectral regions, the relatively low peak to background ratio provided by the 2-IVAC technique is limiting the temporal resolution of the measurement. Hence, high dynamic range correlation approaches which are commonly used in the Ti:sa laser fs metrology are missing from the toolbox of the attosecond pulse metrology. Such approaches are now feasible to be implemented in the XUV spectral range using high nonlinear processes induced by XUV pulses with power in the GWatt range.

B. Attosecond pulses in the water-window regime

Hitherto, most attosecond science studies have been confined at <125 eV photon energies where predominantly valence electron related dynamics can be investigated. Scaling attosecond pulses, and their characterization, to the soft x-ray regime would allow ionization of core level electrons and give access to a number of fundamental processes and triggering events, including key elements of biological systems. Longer driver wavelengths, i.e., mid-IR, have proved to be beneficial for HHG overcoming plasma-induced dispersion related constraints and could lead to the production of attosecond pulses with photon energies up to the kilo-electron-volt range.[163,164] Recently, an elaborate water-window beam line at the Institute of Photonic Sciences (ICFO)[165,166] has provided exciting new results. They report on a cross correlation streaking measurement, evidencing an ultrabroadband soft x-ray isolated attosecond pulse, produced by means of HHG in neon gas, using a 2-cycle (~12 fs) Ti:sa seeded CEP-stabilized laser source of carrier wavelength at 1.85 μm, 0.4 mJ/pulse at the 1 kHz repetition rate. Even if a direct application of streaking retrieval algorithms was not possible, simulations based on FROG-CRAB or LSGPA algorithms yield an upper time limit for its temporal duration of ~320 as.[166] Further efforts are required, and several are currently under way to overcome experimental difficulties and circumvent retrieval algorithm related constraints, so as to produce and fully characterize high brilliance coherent ultrabroad band water-window attosecond pulses.[167]

C. Novel attosecond pulse sources at ELI-ALPS

Of particular importance here are the perspectives opened these days by the development of high average-, high peak-power, CEP stabilized few cycle laser systems acting as driving laser sources of attosecond beam-lines similar to the one of FORTH-IESL.[39] One such example is the so called SYLOS laser system recently installed at the Extreme Light Infrastructure Attosecond Light Source (ELI-ALPS).[168] With such driving sources, 10 GW (or higher) class, attosecond sources can be operated at 1 kHz repetition rates which in combination with advance devices, such as Reaction Microscopes, allow for electron-electron, electron-ion, and ion-ion coincidence experiments. XUV-pump-XUV-prove coincidence measurements with attosecond temporal resolution will allow kinematically complete or close to complete experiments in a very broad spectrum of forefront topics in ultrafast Atomic, Molecular and Optical (AMO) physics, chemistry, and biology. It is expected that in the next decade such experimental opportunities will be available at several laboratories worldwide, starting from large Research Infrastructures and going over to Research Institutions and Universities, beneficial for research and education.

VI. CONCLUSIONS

The harvest of a two decades long trip through the intricacies of attosecond pulse metrology is abundant in groundbreaking science that has created a rich arsenal of novel methods and technologies. Together with the advancement in laser technology and laser based coherent XUV beam-lines, attosecond pulse metrology enjoys a continuous improvement, circumventing all the bottlenecks arising when entering the XUV spectral range. This progress has enabled increased accuracy, reliability, robustness, and more complete information on the parameters underlying the deduction of the temporal shape of attosecond pulses. Temporal resolution reaches the order of 1 as and allows the metrology of ten attosecond scale pulses and characteristic times of ultrafast phenomena. Novel methods, increased stability, and resolution permit the extraction of detailed parameters necessary for the reconstruction of attosecond pulse profiles. Despite the massive advancement, there is still a number of limitations in all the developed methods and the lack

of rigorous comparative studies between the different methods toward the establishment of norms. Thus, attosecond pulse metrology remains an open research field with notable potential for innovative initiatives, upgrades, and vanguard science. In this article, the most frequently used attosecond pulse metrology methods and technologies have been reviewed highlighting their capacity and limitations that signalize future progressions.[169] Advancement in laser technology, in particular toward high average-, high peak-power driving laser systems, will play pivotal role in attosecond science in the coming years.

ACKNOWLEDGMENTS

REFERENCES

[1] T. Maiman, "Stimulated optical radiation in Ruby," Nature 187, 493 (1960).

[2] F. J. McClung and R. W. Hellwarth, "Giant optical pulsations from Ruby," J. Appl. Phys. 33, 828 (1962).

[3] A. J. DeMaria, D. A. Stetser, and H. Heynau, "Self mode-locking of lasers with saturable absorbers," Appl. Phys. Lett. 8, 174 (1966).

[4] P. F. Moulton, "Spectroscopic and laser characteristics of Ti:Al₂O₃," J. Opt. Soc. Am. B 3, 125 (1986).

[5] R. L. Fork, C. H. Brito Cruz, P. C. Becker, and C. V. Shank, "Compression of optical pulses to six femtoseconds by using cubic phase compensation," Opt. Lett. 12, 483 (1987).

[6] D. Strickland and G. Mourou, "Compression of amplified chirped optical pulses," Opt. Commun. 56, 219 (1985).

[7] D. Strickland, "Nobel Lecture: Generating high-intensity ultrashort optical pulses," Rev. Mod. Phys. 91, 030502 (2019).

[8] A. H. Zewail, "Femtochemistry: Atomic-scale dynamics of the chemical bond," J. Phys. Chem. A 104, 5660–5694 (2000).

[9] K. J. Schafer, B. Yang, L. I. DiMauro, and K. C. Kulander, "Above threshold ionization beyond the high harmonic cutoff," Phys. Rev. Lett. 70, 1599 (1993).

[10] P. B. Corkum, "Plasma perspective on strong-field multiphoton ionization," Phys. Rev. Lett. 71, 1994 (1993).

[11] M. Lewenstein, Ph. Balcou, M. Yu. Ivanov, A. L'Huillier, and P. B. Corkum, "Theory of high harmonic generation by low-frequency laser fields," Phys. Rev. A 49, 2117 (1994).

[12] A. McPherson, G. Gibson, H. Jara, U. Johann, T. S. Luk, I. A. McIntyre, K. Boyer, and C. K. Rhodes, "Studies of multiphoton production of vacuum-ultraviolet radiation in the rare gases," J. Opt. Soc. Am. B 4, 595 (1987).

[13] M. Ferray, A. L'Huillier, X. F. Li, L. A. Lomprk, G. Mainfray, and C. Manus, "Multiple-harmonic conversion of 1064 nm radiation in rare gases," J. Phys. B: At., Mol. Opt. Phys. 21, L31 (1988).

[14] X. F. Li, A. L'Huillier, M. Ferray, L. A. Lompre, and G. Mainfray, "Multiple-harmonic generation in rare gases at high laser intensity," Phys. Rev. A 39, 5751 (1989).

[15] T. W. Hänsch, "A proposed sub-femtosecond pulse synthesizer using separate phase-locked laser oscillators," Opt. Commun. 80, 71 (1990).

[16] Gy. Farkas and Cs. Tóth, "Proposal for attosecond light pulse generation using laser induced multiple-harmonic conversion processes in rare gases," Phys. Lett. A 168, 447 (1992).

[17] S. E. Harris, J. J. Macklin, and T. W. Hänsch, "Atomic scale temporal structure inherent to high-order harmonic generation," Opt. Commun. 100, 487 (1993).

[18] P. B. Corkum and F. Krausz, "Attosecond science," Nat. Phys. 3, 381 (2007).

[19] F. Krausz and M. Ivanov, "Attosecond physics," Rev. Mod. Phys. 81, 163 (2009).

[20] A. Acín, I. Bloch, H. Buhrman, T. Calarco, C. Eichler, J. Eisert, D. Esteve, N. Gisin, S. J. Glaser, F. Jelezko, S. Kuhr, M. Lewenstein, M. F. Riedel, P. O. Schmidt, R. Thew, A. Wallraff, I. Walmsley, and F. K. Wilhelm, "The quantum technologies roadmap: A European community view," New J. Phys. 20, 080201 (2018).

[21] I. A. Gonoskov, N. Tsatrafyllis, I. K. Kominis, and P. Tzallas, "Quantum optical signatures in strong-field laser physics: Infrared photon counting in high-order-harmonic generation," Sci. Rep. 6, 32821 (2016).

[22] N. Tsatrafyllis, I. K. Kominis, I. A. Gonoskov, and P. Tzallas, "High-order harmonics measured by the photon statistics of the infrared driving-field exiting the atomic medium," Nat. Commun. 8, 15170 (2017).

[23] N. Tsatrafyllis, S. Kuhn, M. Dumergue, P. Foldi, S. Kahaly, E. Cormier, I. A. Gonoskov, B. Kiss, K. Varju, S. Varro, and P. Tzallas, "Quantum optical signatures in a strong laser pulse after interaction with semiconductors," Phys. Rev. Lett. 122, 193602 (2019).

[24] A. Wirth, M. T. Hassan, I. Grguras, J. Gagnon, A. Moulet, T. T. Luu, S. Pabst, R. Santra, Z. A. Alahmed, A. M. Azzeer, V. S. Yakovlev, V. Pervak, F. Krausz, and E. Goulielmakis, "Synthesized light transients," Science 334, 195 (2011).

[25] S. Chatziathanasiou, S. Kahaly, E. Skantzakis, G. Sansone, R. Lopez-Martens, S. Haessler, K. Varju, G. Tsakiris, D. Charalambidis, and P. Tzallas, "Generation of attosecond light pulses from gas and solid state media," Photonics 4, 26 (2017).

[26] C. M. Heyl, H. Coudert-Alteirac, M. Miranda, M. Louisy, K. Kovacs, V. Tosa, E. Balogh, K. Varjú, A. L'Huillier, A. Couairon, and C. L. Arnold, "Scale-invariant nonlinear optics in gases," Optica 3, 75 (2016).

[27] F. Silva, D. R. Austin, A. Thai, M. Baudisch, M. Hemmer, D. Faccio, A. Couairon, and J. Biegert, "Multi-octave supercontinuum generation from mid-infrared filamentation in a bulk crystal," Nat. Commun. 3, 807 (2012).

[28] F. Silva, S. M. Teichmann, S. L. Cousin, M. Hemmer, and J. Biegert, "Spatiotemporal isolation of attosecond soft X-ray pulses in the water window," Nat. Commun. 6, 6611 (2015).

[29] T. Popmintchev, M. C. Chen, D. Popmintchev, P. Arpin, S. Brown, S. Ališauskas, G. Andriukaitis, T. Balčiunas, O. D. Mücke, A. Pugzlys, A. Baltuška, B. Shim, S. E. Schrauth, A. Gaeta, C. Hernández-García, L. Plaja, A. Becker, A. Jaron-Becker, M. M. Murnane, and H. C. Kapteyn, "Bright coherent ultrahigh harmonics in the keV x-ray regime from mid-infrared femtosecond lasers," Science 336, 1287 (2012).

[30] T. Gaumnitz, A. Jain, Y. Pertot, M. Huppert, I. Jordan, F. Ardana-Lamas, and H. J. Wörner, "Streaking of 43-attosecond soft-X-ray pulses generated by a passively CEP-stable mid-infrared driver," Opt. Express 25, 27506 (2017).

[31] E. Constant, D. Garzella, P. Breger, E. Mével, C. Dorrer, C. Le Blanc, F. Salin, and P. Agostini, "Optimizing high harmonic generation in absorbing gases: Model and experiment," Phys. Rev. Lett. 82, 1668 (1999).

[32] J.-F. Hergott, M. Kovacev, H. Merdji, C. Hubert, Y. Mairesse, E. Jean, P. Breger, P. Agostini, B. Carré, and P. Salières, "Extreme-ultraviolet high-order harmonic pulses in the microjoule range," Phys. Rev. A 66, 021801 (2002).

[33] E. Skantzakis, P. Tzallas, J. Kruse, C. Kalpouzos, and D. Charalambidis, "Coherent continuum extreme ultraviolet radiation in the sub-100-nJ range generated by a high-power many-cycle laser field," Opt. Lett. 34, 1732 (2009).

[34] P. Tzallas, E. Skantzakis, L. A. A. Nikolopoulos, G. D. Tsakiris, and D. Charalambidis, "Extreme-ultraviolet pump–probe studies of one-femtosecond-scale electron dynamics," Nat. Phys. 7, 781 (2011).

[35] G. Sansone, L. Poletto, and M. Nisoli, "High-energy attosecond light sources," Nat. Photonics 5, 655 (2011).

[36] E. J. Takahashi, P. Lan, O. D. Mucke, Y. Nabekawa, and K. Midorikawa, "Attosecond nonlinear optics using gigawatt-scale isolated attosecond pulses," Nat. Commun. 4, 2691 (2013).

[37]Y. Wu, E. Cunningham, H. Zang, J. Li, M. Chini, X. Wang, Y. Wang, K. Zhao, and Z. Chang, "Generation of high-flux attosecond extreme ultraviolet continuum with a 10 TW laser," Appl. Phys. Lett. **102**, 201104 (2013).

[38]E. J. Takahashi, P. Lan, O. D. Mucke, Y. Nabekawa, and K. Midorikawa, "Infrared two-color multicycle laser field synthesis for generating an intense attosecond pulse," Phys. Rev. Lett. **104**, 233901 (2010).

[39]A. Nayak, I. Orfanos, I. Makos, M. Dumergue, S. Kühn, E. Skantzakis, B. Bodi, K. Varju, C. Kalpouzos, H. I. B. Banks, A. Emmanouilidou, D. Charalambidis, and P. Tzallas, "Multiple ionization of argon via multi-XUV-photon absorption induced by 20-GW high-order harmonic laser pulses," Phys. Rev. A **98**, 023426 (2018).

[40]K. Midorikawa, Y. Nabekawa, and A. Suda, "XUV multiphoton processes with intense high-order harmonics," Prog. Quantum Electron. **32**, 43 (2008).

[41]S. M. Teichmann, F. Silva, S. L. Cousin, M. Hemmer, and J. Biegert, "0.5-keV soft X-ray attosecond continua," Nat. Commun. **7**, 11493 (2016).

[42]B. Schütte, P. Weber, K. Kovács, E. Balogh, B. Major, V. Tosa, S. Han, M. Vrakking, K. Varjú, and A. Rouzée, "Bright attosecond pulse generation under transient phase-matching in two-colour high-order harmonic generation," Opt. Express **23**, 33947 (2015).

[43]G. G. Paulus, F. Grasbon, H. Walther, P. Villoresi, M. Nisoli, S. Stagira, E. Priori, and S. de Silvestri, "Absolute-phase phenomena in photoionization with few-cycle laser pulses," Nature **414**, 182 (2001).

[44]E. Goulielmakis, V. S. Yakovlev, A. L. Cavalieri, M. Uiberacker, V. Pervak, A. Apolonski, R. Kienberger, U. Kleineberg, and F. Krausz, "Attosecond control and measurement: Lightwave electronics," Science **317**, 769 (2007).

[45]F. Frank, C. Arrell, T. Witting, W. A. Okell, J. McKenna, J. S. Robinson, C. A. Haworth, D. Austin, H. Teng, I. A. Walmsley, J. P. Marangos, and J. W. G. Tisch, "Technology for attosecond science," Rev. Sci. Instrum. **83**, 071101 (2012).

[46]F. Frassetto, A. Trabattoni, S. Anumula, G. Sansone, F. Calegari, M. Nisoli, and L. Poletto, "High-throughput beamline for attosecond pulses based on toroidal mirrors with microfocusing capabilities," Rev. Sci. Instrum. **85**, 103115 (2014).

[47]B. Manschwetus, L. Rading, F. Campi, S. Maclot, H. Coudert-Alteirac, J. Lahl, H. Wikmark, P. Rudawski, C. M. Heyl, B. Farkas, T. Mohamed, A. L'huillier, and P. Johnsson, "Two-photon double ionization of neon using an intense attosecond pulse train," Phys. Rev. A **93**, 061402 (2016).

[48]S. Kühn, M. Dumergue, S. Kahaly, S. Mondal, M. Füle, T. Csizmadia, B. Farkas, B. Major, Z. Várallyay, E. Cormier, M. Kalashnikov, F. Calegari, M. Devetta, F. Frassetto, E. Månsson, L. Poletto, S. Stagira, C. Vozzi, M. Nisoli, P. Rudawski, S. Maclot, F. Campi, H. Wikmark, C. L. Arnold, C. M. Heyl, P. Johnsson, A. L'Huillier, R. Lopez-Martens, S. Haessler, M. Bocoum, F. Boehle, A. Vernier, G. Iaquaniello, E. Skantzakis, N. Papadakis, C. Kalpouzos, P. Tzallas, F. Lépine, D. Charalambidis, K. Varjú, K. Osvay, and G. Sansone, "The ELI-ALPS facility," J. Phys. B: At., Mol. Opt. Phys. **50**, 132002 (2017).

[49]N. Dudovich, O. Smirnova, J. Levesque, Y. Mairesse, M. Yu. Ivanov, D. M. Villeneuve, and P. B. Corkum, "Measuring and controlling the birth of attosecond XUV pulses," Nat. Phys. **2**, 781 (2006).

[50]K. T. Kim, C. Zhang, A. D. Shiner, B. E. Schmidt, F. Légaré, D. M. Villeneuve, and P. B. Corkum, "Petahertz optical oscilloscope," Nat. Photonics **7**, 958 (2013).

[51]Y. Mairesse, O. Gobert, P. Breger, H. Merdji, P. Meynadier, P. Monchicourt, M. Perdrix, P. Salières, and B. Carré, "High harmonic XUV spectral phase interferometry for direct electric-field reconstruction," Phys. Rev. Lett. **94**, 173903 (2005).

[52]E. Cormier, I. A. Walmsley, E. M. Kosik, A. S. Wyatt, L. Corner, and L. F. DiMauro, "Self-referencing, spectrally, or spatially encoded spectral interferometry for the complete characterization of attosecond electromagnetic pulses," Phys. Rev. Lett. **94**, 033905 (2005).

[53]O. Pedatzur, A. Trabattoni, B. Leshem, H. Shalmoni, M. C. Castrovilli, M. Galli, M. Lucchini, E. Månsson, F. Frassetto, L. Poletto, B. Nadler, O. Raz, M. Nisoli, F. Calegari, D. Oron, and N. Dudovich, "Double-blind holography of attosecond pulses," Nat. Photonics **13**, 91 (2019).

[54]P. Tzallas, D. Charalambidis, N. A. Papadogiannis, K. Witte, and G. D. Tsakiris, "Direct observation of attosecond light bunching," Nature **426**, 267 (2003).

[55]Y. Nabekawa, T. Shimizu, T. Okino, K. Furusawa, H. Hasegawa, K. Yamanouchi, and K. Midorikawa, "Conclusive evidence of an attosecond pulse train observed with the mode-resolved autocorrelation technique," Phys. Rev. Lett. **96**, 083901 (2006).

[56]P. Tzallas, D. Charalambidis, N. A. Papadogiannis, K. Witte, and G. D. Tsakiris, "Second-order autocorrelation measurements of attosecond XUV pulse trains," J. Mod. Opt. **52**, 321 (2005).

[57]T. Sekikawa, A. Kosuge, T. Kanai, and S. Watanabe, "Nonlinear optics in the extreme ultraviolet," Nature **432**, 605 (2004).

[58]A. Kosuge, T. Sekikawa, X. Zhou, T. Kanai, S. Adachi, and S. Watanabe, "Frequency-resolved optical gating of isolated attosecond pulses in the extreme ultraviolet," Phys. Rev. Lett. **97**, 263901 (2006).

[59]Y. Nomura, R. Hörlein, P. Tzallas, B. Dromey, S. Rykovanov, Z. Major, J. Osterhoff, S. Karsch, L. Veisz, M. Zepf, D. Charalambidis, F. Krausz, and G. D. Tsakiris, "Attosecond phase locking of harmonics emitted from laser-produced plasmas," Nat. Phys. **5**, 124 (2009).

[60]P. A. Carpeggiani, P. Tzallas, A. Palacios, D. Gray, F. Martín, and D. Charalambidis, "Disclosing intrinsic molecular dynamics on the 1-fs scale through extreme-ultraviolet pump-probe measurements," Phys. Rev. A **89**, 023420 (2014).

[61]T. Okino, Y. Furukawa, Y. Nabekawa, S. Miyabe, A. Amani Eilanlou, E. J. Takahashi, K. Yamanouchi, and K. Midorikawa, "Direct observation of an attosecond electron wave packet in a nitrogen molecule," Sci. Adv. **1**, e1500356 (2015).

[62]Y. Nabekawa, Y. Furukawa, T. Okino, A. A. Eilanlou, E. J. Takahashi, K. Yamanouchi, and K. Midorikawa, "Settling time of a vibrational wavepacket in ionization," Nat. Commun. **6**, 8197 (2015).

[63]E. Skantzakis, P. Tzallas, J. E. Kruse, C. Kalpouzos, O. Faucher, G. D. Tsakiris, and D. Charalambidis, "Tracking autoionizing-wave-packet dynamics at the 1-fs temporal scale," Phys. Rev. Lett. **105**, 043902 (2010).

[64]Y. Kobayashi, T. Sekikawa, Y. Nabekawa, and S. Watanabe, "27-fs extreme ultraviolet pulse generation by high-order harmonics," Opt. Lett. **23**, 64 (1998).

[65]K. Furusawa, T. Okino, T. Shimizu, H. Hasegawa, Y. Nabekawa, K. Yamanouchi, and K. Midorikawa, "Photoelectron spectroscopy of two-photon ionisation of rare-gas atoms by multiple high order harmonics," Appl. Phys. B **83**, 203 (2006).

[66]E. P. Benis, D. Charalambidis, T. N. Kitsopoulos, G. D. Tsakiris, and P. Tzallas, "Two-photon double ionization of rare gases by a superposition of harmonics," Phys. Rev. A **74**, 051402(R) (2006).

[67]E. Goulielmakis, G. Nersisyan, N. A. Papadogiannis, D. Charalambidis, G. D. Tsakiris, and K. Witte, "A dispersionless Michelson interferometer for the characterization of attosecond pulses," Appl. Phys. B **74**, 197 (2002).

[68]N. A. Papadogiannis, G. Nersisyan, E. Goulielmakis, T. P. Rakitzis, E. Hertz, D. Charalambidis, G. D. Tsakiris, and K. Witte, "Temporal characterization of short-pulse third-harmonic generation in an atomic gas by a transmission-grating Michelson interferometer," Opt. Lett. **27**, 1561 (2002).

[69]E. Papalazarou, M. Kovačev, P. Tzallas, E. P. Benis, C. Kalpouzos, G. D. Tsakiris, and D. Charalambidis, "Spectral phase distribution retrieval through coherent control of harmonic generation," Phys. Rev. Lett. **96**, 163901 (2006).

[70]P. Tzallas, E. Skantzakis, E. P. Benis, C. Kalpouzos, G. D. Tsakiris, and D. Charalambidis, "Full temporal reconstruction of a lower order harmonic superposition," New J. Phys. **9**, 232 (2007).

[71]P. M. Paul, E. S. Toma, P. Breger, G. Mullot, F. Auge, P. Balcou, H. G. Muller, and P. Agostini, "Observation of a train of attosecond pulses from high harmonic generation," Science **292**, 1689 (2001).

[72]M. Hentschel, R. Kienberger, C. Spielmann, G. A. Reider, N. Milosevic, T. Brabec, P. B. Corkum, U. Heinzmann, M. Drescher, and F. Krausz, "Attosecond metrology," Nature **414**, 509 (2001).

[73]J. Itatani, F. Quéré, G. L. Yudin, M. Y. Ivanov, F. Krausz, and P. B. Corkum, "Attosecond streak camera," Phys. Rev. Lett. **88**, 173903 (2002).

[74]M. Drescher, M. Hentschel, R. Kienberger, G. Tempea, C. Spielmann, G. A. Reider, P. B. Corkum, and F. Krausz, "X-ray pulses approaching the attosecond frontier," Science **291**, 1923 (2001).

[75]E. Goulielmakis, M. Uiberacker, R. Kienberger, A. Baltuska, V. Yakovlev, A. Scrinzi, T. Westerwalbesloh, U. Kleineberg, U. Heinzmann, M. Drescher, and F. Krausz, "Direct measurement of light waves," Science **305**, 1267 (2004).

[76]R. Kienberger, M. Hentschel, M. Uiberacker, Ch. Spielmann, M. Kitzler, A. Scrinzi, M. Wieland, T. Westerwalbesloh, U. Kleineberg, U. Heinzmann, M. Drescher, and F. Krausz, "Steering attosecond electron wave packets with light," Science **297**, 1144 (2002).

[77]M. Uiberacker, T. Uphues, M. Schultze, A. J. Verhoef, V. Yakovlev, M. F. Kling, J. Rauschenberger, N. M. Kabachnik, H. Schröder, M. Lezius, K. L. Kompa, H.-G. Muller, M. J. J. Vrakking, S. Hendel, U. Kleineberg, U. Heinzmann, M. Drescher, and F. Krausz, "Attosecond real-time observation of electron tunnelling in atoms," Nature **446**, 627 (2007).

[78]M. Reduzzi, P. Carpeggiani, S. Kühn, F. Calegari, M. Nisoli, S. Stagira, C. Vozzi, P. Dombi, S. Kahaly, P. Tzallas, D. Charalambidis, K. Varju, K. Osvay, and G. Sansone, "Advances in high-order harmonic generation sources for time-resolved investigations," J. Electron Spectrosc. Relat. Phenom. **204**, 257 (2015).

[79]A. L. Cavalieri, N. Müller, T. Uphues, V. S. Yakovlev, A. Baltuška, B. Horvath, B. Schmidt, L. Blümel, R. Holzwarth, S. Hendel, M. Drescher, U. Kleineberg, P. M. Echenique, R. Kienberger, F. Krausz, and U. Heinzmann, "Attosecond spectroscopy in condensed matter," Nature **449**, 1029 (2007).

[80]Y. Mairesse and F. Quéré, "Frequency-resolved optical gating for complete reconstruction of attosecond bursts," Phys. Rev. A **71**, 011401 (2005).

[81]M. Chini, S. Gilbertson, S. D. Khan, and Z. Chang, "Characterizing ultrabroadband attosecond lasers," Opt. Express **18**, 13006 (2010).

[82]V. Gruson, L. Barreau, Á. Jiménez-Galan, F. Risoud, J. Caillat, A. Maquet, B. Carré, F. Lepetit, J.-F. Hergott, T. Ruchon, L. Argenti, R. Taïeb, F. Martín, and P. Salières, "Attosecond dynamics through a Fano resonance: Monitoring the birth of a photoelectron," Science **354**, 734 (2016).

[83]D. Busto, L. Barreau, M. Isinger, M. Turconi, C. Alexandridi, A. Harth, S. Zhong, R. J. Squibb, D. Kroon, S. Plogmaker, M. Miranda, Á. Jiménez-Galán, L. Argenti, C. L. Arnold, R. Feifel, F. Martín, M. Gisselbrecht, A. L'Huillier, and P. Salières, "Time–frequency representation of autoionization dynamics in helium," J. Phys. B: At., Mol. Opt. Phys. **51**, 044002 (2018).

[84]L. A. A. Nikolopoulos, E. P. Benis, P. Tzallas, D. Charalambidis, K. Witte, and G. D. Tsakiris, "Second order autocorrelation of an XUV attosecond pulse train," Phys. Rev. Lett. **94**, 113905 (2005).

[85]Y. Kobayashi, T. Ohno, T. Sekikawa, Y. Nabekawa, and S. Watanabe, "Pulse width measurement of high-order harmonics by autocorrelation," Appl. Phys. B **70**, 389 (2000).

[86]N. A. Papadogiannis, L. A. A. Nikolopoulos, D. Charalambidis, G. D. Tsakiris, P. Tzallas, and K. Witte, "Two-photon ionization of He through a superposition of higher harmonics," Phys. Rev. Lett. **90**, 133902 (2003).

[87]E. P. Benis, P. Tzallas, L. A. A. Nikolopoulos, M. Kovačev, C. Kalpouzos, D. Charalambidis, and G. D. Tsakiris, "Frequency-resolved photoelectron spectra of two-photon ionization of He by an attosecond pulse train," New J. Phys. **8**, 92 (2006).

[88]D. Descamps, L. Roos, C. Delfin, A. L'Huillier, and C.-G. Wahlström, "Two- and three-photon ionization of rare gases using femtosecond harmonic pulses generated in a gas medium," Phys. Rev. A **64**, 031404(R) (2001).

[89]N. Tsatrafyllis, B. Bergues, H. Schroder, L. Veisz, E. Skantzakis, D. Gray, B. Bodi, S. Kuhn, G. D. Tsakiris, D. Charalambidis, and P. Tzallas, "The ion microscope as a tool for quantitative measurements in the extreme ultraviolet," Sci. Rep. **6**, 21556 (2016).

[90]P. Tzallas, B. Bergues, D. Rompotis, N. Tsatrafyllis, S. Chatziathanassiou, A. Muschet, L. Veisz, H. Schröder, and D. Charalambidis, "Time gated ion microscopy of light-atom interactions," J. Opt. **20**, 24018 (2018).

[91]G. Kolliopoulos, B. Bergues, H. Schröder, P. A. Carpeggiani, L. Veisz, G. D. Tsakiris, D. Charalambidis, and P. Tzallas, "Revealing quantum path details in high-field physics," Phys. Rev. A **90**, 013822 (2015).

[92]B. Bergues, D. E. Rivas, M. Weidman, A. A. Muschet, W. Helml, A. Guggenmos, V. Pervak, U. Kleineberg, G. Marcus, R. Kienberger, D. Charalambidis, P. Tzallas, H. Schröder, F. Krausz, and L. Veisz, "Tabletop nonlinear optics in the 100-eV spectral region," Optica **5**, 237 (2018).

[93]R. Hörlein, Y. Nomura, P. Tzallas, S. G. Rykovanov, B. Dromey, J. Osterhoff, Z. Major, S. Karsch, L. Veisz, M. Zepf, D. Charalambidis, F. Krausz, and G. D. Tsakiris, "Temporal characterization of attosecond pulses emitted from solid-density plasmas," New J. Phys. **12**, 043020 (2010).

[94]O. Faucher, P. Tzallas, E. P. Benis, J. Kruse, A. Peralta Conde, C. Kalpouzos, and D. Charalambidis, "Four-dimensional investigation of the 2nd order volume autocorrelation technique," Appl. Phys. B **97**, 505 (2009).

[95]H. Mashiko, A. Suda, and K. Midorikawa, "All-reflective interferometric autocorrelator for the measurement of ultra-short optical pulses," Appl. Phys. B **76**, 525 (2003).

[96]A. Peralta Conde, J. Kruse, O. Faucher, P. Tzallas, E. P. Benis, and D. Charalambidis, "Realization of time-resolved two-vacuum-ultraviolet-photon ionization," Phys. Rev. A **79**, 061405 (2009).

[97]D. Charalambidis, P. Tzallas, E. P. Benis, and G. D. Tsakiris, "Attosecond scale multi-XUV-photon processes," in *Progress in Ultrafast Intense Laser Science*, Springer Series in Chemical Physics Vol. 91, edited by K. Yamanouchi, A. Becker, R. Li, and S. L. Chin (Springer, Berlin, Heidelberg, 2009).

[98]J. E. Kruse, P. Tzallas, E. Skantzakis, C. Kalpouzos, G. D. Tsakiris, and D. Charalambidis, "Inconsistencies between two attosecond pulse metrology methods: A comparative study," Phys. Rev. A **82**, 021402(R) (2010).

[99]P. Tzallas, E. Skantzakis, and D. Charalambidis, "Direct two-XUV-photon double ionization in xenon," J. Phys. B: At., Mol. Opt. Phys. **45**, 074007 (2012).

[100]P. Tzallas, E. Skantzakis, C. Kalpouzos, E. P. Benis, G. D. Tsakiris, and D. Charalambidis, "Generation of intense continuum extreme-ultraviolet radiation by many-cycle laser fields," Nat. Phys. **3**, 846 (2007).

[101]G. Kolliopoulos, P. A. Carpeggiani, D. Rompotis, D. Charalambidis, and P. Tzallas, "A compact collinear polarization gating scheme for many cycle laser pulses," Rev. Sci. Instrum. **83**, 063102 (2012).

[102]Y. Nabekawa, T. Shimizu, T. Okino, K. Furusawa, H. Hasegawa, K. Yamanouchi, and K. Midorikawa, "Interferometric autocorrelation of an attosecond pulse train in the single-cycle regime," Phys. Rev. Lett. **97**, 153904 (2006).

[103]R. Trebino, *Frequency-Resolved Optical Gating: The Measurement of Ultrashort Laser Pulses* (Springer Science & Business Media, 2000).

[104]V. Véniard, R. Taïeb, and A. Maquet, "Phase dependence of (N+1)-color (N>1) IR-UV photoionization of atoms with higher harmonics," Phys. Rev. A **54**, 721 (1996).

[105]R. López-Martens, K. Varjú, P. Johnsson, J. Mauritsson, Y. Mairesse, P. Salières, M. B. Gaarde, K. J. Schafer, A. Persson, S. Svanberg, C.-G. Wahlström, and A. L'Huillier, "Amplitude and phase control of attosecond light pulses," Phys. Rev. Lett. **94**, 033001 (2005).

[106]H. G. Muller, "Reconstruction of attosecond harmonic beating by interference of two-photon transitions," Appl. Phys. B **74**, s17 (2002).

[107]Y. Mairesse, A. de Bohan, L. J. Frasinski, H. Merdji, L. C. Dinu, P. Monchicourt, P. Breger, M. Kovačev, R. Taïeb, B. Carré, H. G. Muller, P. Agostini, and P. Salières, "Attosecond synchronization of high-harmonic soft x-rays," Science **302**, 1540 (2003).

[108]K. Varjú, P. Johnsson, R. López-Martens, T. Remetter, E. Gustafsson, J. Mauritsson, M. B. Gaarde, K. J. Schafer, Ch. Erny, I. Sola, A. Zaïr, E. Constant, E. Cormier, E. Mével, and A. L'Huillier, "Experimental studies of attosecond pulse trains," Laser Phys. **15**, 888 (2005).

[109]S. Haessler, B. Fabre, J. Higuet, J. Caillat, T. Ruchon, P. Breger, B. Carré, E. Constant, A. Maquet, E. Mével, P. Salières, R. Taïeb, and Y. Mairesse, "Phase-resolved attosecond near-threshold photoionization of molecular nitrogen," Phys. Rev. A **80**, 011404 (2009).

[110]R. Locher, L. Castiglioni, M. Lucchini, M. Greif, L. Gallmann, J. Osterwalder, M. Hengsberger, and U. Keller, "Energy-dependent photoemission delays from noble metal surfaces by attosecond interferometry," Optica **2**, 405 (2015).

[111]S. Heuser, A. Jiménez Galán, C. Cirelli, C. Marante, M. Sabbar, R. Boge, M. Lucchini, L. Gallmann, I. Ivanov, A. S. Kheifets, J. M. Dahlström, E. Lindroth, L. Argenti, F. Martín, and U. Keller, "Angular dependence of photoemission time delay in helium," Phys. Rev. A **94**, 063409 (2016).

[112]M. Schultze, M. Fieß, N. Karpowicz, J. Gagnon, M. Korbman, M. Hofstetter, S. Neppl, A. L. Cavalieri, Y. Komninos, Th. Mercouris, C. A. Nicolaides, R. Pazourek, S. Nagele, J. Feist, J. Burgdörfer, A. M. Azzeer, R. Ernstorfer, R. Kienberger, U. Kleineberg, E. Goulielmakis, F. Krausz, and V. S. Yakovlev, "Delay in photoemission," Science **328**, 1658 (2010).

[113]M. Isinger, R. J. Squibb, D. Busto, S. Zhong, A. Harth, D. Kroon, S. Nandi, C. L. Arnold, M. Miranda, J. M. Dahlström, E. Lindroth, R. Feifel, M. Gisselbrecht,

and A. L'Huillier, "Photoionization in the time and frequency domain," Science **358**, 893 (2017).

[114]J. M. Dahlström, A. L'Huillier, and A. Maquet, "Introduction to attosecond delays in photoionization," J. Phys. B: At., Mol. Opt. Phys. **45**, 183001 (2012).

[115]E. S. Toma and H. G. Muller, "Calculation of matrix elements for mixed extreme ultraviolet-infrared two-photon above-threshold ionization of argon," J. Phys. B: At., Mol. Opt. Phys. **35**, 3435 (2002).

[116]K. Varjú, Y. Mairesse, P. Agostini, P. Breger, B. Carré, L. J. Frasinski, E. Gustafsson, P. Johnsson, J. Mauritsson, H. Merdji, P. Monchicourt, A. L'Huillier, and P. Salières, "Reconstruction of attosecond pulse trains using an adiabatic phase expansion," Phys. Rev. Lett. **95**, 243901 (2005).

[117]J. Mauritsson, M. B. Gaarde, and K. J. Schafer, "Accessing properties of electron wave packets generated by attosecond pulse trains through time-dependent calculations," Phys. Rev. A **72**, 013401 (2005).

[118]K. Klünder, J. M. Dahlström, M. Gisselbrecht, T. Fordell, M. Swoboda, D. Guénot, P. Johnsson, J. Caillat, J. Mauritsson, A. Maquet, R. Taïeb, and A. L'Huillier, "Probing single-photon ionization on the attosecond time scale," Phys. Rev. Lett. **106**, 143002 (2011).

[119]C. Palatchi, J. M. Dahlström, A. S. Kheifets, I. A. Ivanov, D. M. Canaday, P. Agostini, and L. F. DiMauro, "Atomic delay in helium, neon, argon and krypton," J. Phys. B: At., Mol. Opt. Phys. **47**, 245003 (2014).

[120]E. Lindroth and J. M. Dahlström, "Attosecond delays in laser-assisted photodetachment from closed-shell negative ions," Phys. Rev. A **96**, 013420 (2017).

[121]E. Goulielmakis, M. Schultze, M. Hofstetter, V. S. Yakovlev, J. Gagnon, M. Uiberacker, A. L. Aquila, E. M. Gullikson, D. T. Attwood, R. Kienberger, F. Krausz, and U. Kleineberg, "Single-cycle nonlinear optics," Science **320**, 1614 (2008).

[122]F. Ferrari, F. Calegari, M. Lucchini, C. Vozzi, S. Stagira, G. Sansone, and M. Nisoli, "High-energy isolated attosecond pulses generated by above-saturation few-cycle fields," Nat. Photonics **4**, 875 (2010).

[123]O. Tcherbakoff, E. Mevel, D. Descamps, J. Plumridge, and E. Constant, "Time-gated high-order harmonic generation," Phys. Rev. A **68**, 043804 (2003).

[124]G. Sansone, E. Benedetti, F. Calegari, C. Vozzi, L. Avaldi, R. Flammini, L. Poletto, P. Villoresi, C. Altucci, R. Velotta, S. Stagira, S. De Silvestri, and M. Nisoli, "Isolated single-cycle attosecond pulses," Science **314**, 443 (2006).

[125]H. Mashiko, S. Gilbertson, C. Li, S. D. Khan, M. M. Shakya, E. Moon, and Z. Chang, "Double optical gating of high-order harmonic generation with carrier-envelope phase stabilized lasers," Phys. Rev. Lett. **100**, 103906 (2008).

[126]Y. Oishi, M. Kaku, A. Suda, F. Kannari, and K. Midorikawa, "Generation of extreme ultraviolet continuum radiation driven by a sub-10-fs two-color field," Opt. Express **14**, 7230 (2006).

[127]H. C. Bandulet, D. Comtois, E. Bisson, A. Fleischer, H. Pépin, J.-C. Kieffer, P. B. Corkum, and D. M. Villeneuve, "Gating attosecond pulse train generation using multicolor laser fields," Phys. Rev. A **81**, 013803 (2010).

[128]K. T. Kim, C. Zhang, T. Ruchon, J.-F. Hergott, T. Auguste, D. Villeneuve, P. Corkum, and F. Quéré, "Photonic streaking of attosecond pulse trains," Nat. Photonics **7**, 651 (2013).

[129]M. B. Gaarde and K. J. Schafer, "Generating single attosecond pulses via spatial filtering," Opt. Lett. **31**, 3188 (2006).

[130]E. Constant, V. D. Taranukhin, A. Stolow, and P. B. Corkum, "Methods for the measurement of the duration of high-harmonic pulses," Phys. Rev. A **56**, 3870 (1997).

[131]R. Kienberger, E. Goulielmakis, M. Uiberacker, A. Baltuska, V. Yakovlev, F. Bammer, A. Scrinzi, T. Westerwalbesloh, U. Kleineberg, U. Heinzmann, M. Drescher, and F. Krausz, "Atomic transient recorder," Nature **427**, 817 (2004).

[132]B. Förg, "Attosecond dynamics of collective electron effects in nanostructures and molecules," Ph.D. thesis, Ludwig-Maximilians-Universität, 2017.

[133]F. Quéré, Y. Mairesse, and J. Itatani, "Temporal characterization of attosecond XUV fields," J. Mod. Opt. **52**, 339 (2005).

[134]R. Trebino, K. W. DeLong, D. N. Fittinghoff, J. N. Sweetser, M. A. Krumbügel, B. A. Richman, and D. J. Kane, "Measuring ultrashort laser pulses in the time-frequency domain using frequency-resolved optical gating," Rev. Sci. Instrum. **68**, 3277 (1997).

[135]J. Gagnon, E. Goulielmakis, and V. S. Yakovlev, "The accurate FROG characterization of attosecond pulses from streaking measurements," Appl. Phys. B **92**, 25 (2008).

[136]I. Thomann, A. Bahabad, X. Liu, R. Trebino, M. M. Murnane, and H. C. Kapteyn, "Characterizing isolated attosecond pulses from hollow-core waveguides using multi-cycle driving pulses," Opt. Express **17**, 4611 (2009).

[137]M. Lucchini, M. H. Brügmann, A. Ludwig, L. Gallmann, U. Keller, and T. Feurer, "Ptychographic reconstruction of attosecond pulses," Opt. Express **23**, 29502 (2015).

[138]P. D. Keathley, S. Bhardwaj, J. Moses, G. Laurent, and F. X. Kärtner, "Volkov transform generalized projection algorithm for attosecond pulse characterization," New J. Phys. **18**, 073009 (2016).

[139]I. Thomann, E. Gregonis, X. Liu, R. Trebino, A. S. Sandhu, M. M. Murnane, and H. C. Kapteyn, "Temporal characterization of attosecond wave forms in the sub-optical-cycle regime," Phys. Rev. A **78**, 011806(R) (2008).

[140]K. T. Kim, D. H. Ko, J. Park, V. Tosa, and C. H. Nam, "Complete temporal reconstruction of attosecond high-harmonic pulse trains," New J. Phys. **12**, 083019 (2010).

[141]M. Kitzler, N. Milosevic, A. Scrinzi, F. Krausz, and T. Brabec, "Quantum theory of attosecond XUV pulse measurement by laser dressed photoionization," Phys. Rev. Lett. **88**, 173904 (2002).

[142]M. Lucchini, G. D. Lucarelli, M. Murari, A. Trabattoni, N. Fabris, F. Frassetto, S. De Silvestri, L. Poletto, and M. Nisoli, "Few-femtosecond extreme-ultraviolet pulses fully reconstructed by a ptychographic technique," Opt. Express **26**, 6771 (2018).

[143]K. Zhao, Q. Zhang, M. Chini, Y. Wu, X. Wang, and Z. Chang, "Tailoring a 67 attosecond pulse through advantageous phase-mismatch," Opt. Lett. **37**, 3891 (2012).

[144]G. Kolliopoulos, P. Tzallas, B. Bergues, P. A. Carpeggiani, P. Heissler, H. Schröder, L. Veisz, D. Charalambidis, and G. D. Tsakiris, "Single-shot auto-correlator for extreme-ultraviolet radiation," J. Opt. Soc. Am. B **31**, 926 (2014).

[145]E. Gustafsson, T. Ruchon, M. Swoboda, T. Remetter, E. Pourtal, R. López-Martens, Ph. Balcou, and A. L'Huillier, "Broadband attosecond pulse shaping," Opt. Lett. **32**, 1353 (2007).

[146]M. Swoboda, J. M. Dahlström, T. Ruchon, P. Johnsson, J. Mauritsson, A. L'Huillier, and K. J. Schafer, "Intensity dependence of laser-assisted attosecond photoionization spectra," Laser Phys. **19**, 1591 (2009).

[147]C. Bourassin-Bouchet and M.-E. Couprie, "Partially coherent ultrafast spectrography," Nat. Commun. **6**, 6465 (2015).

[148]M. Isinger, D. Busto, S. Mikaelsson, S. Zhong, C. Guo, P. Salières, C. L. Arnold, A. L'Huillier, and M. Gisselbrecht, "Accuracy and precision of the RABBIT technique," Philos. Trans. R. Soc., A **377**, 20170475 (2019).

[149]V. S. Yakovlev, F. Bammer, and A. Scrinzi, "Attosecond streaking measurements," J. Mod. Opt. **52**, 395 (2005).

[150]J. Gagnon and V. S. Yakovlev, "The robustness of attosecond streaking measurements," Opt. Express **17**, 17678 (2009).

[151]H. Wang, M. Chini, S. D. Khan, S. Chen, S. Gilbertson, X. Feng, H. Mashiko, and Z. Chang, "Practical issues of retrieving isolated attosecond pulses," J. Phys. B: At., Mol. Opt. Phys. **42**, 134007 (2009).

[152]A. S. Kheifets, "Time delay in valence-shell photoionization of noble-gas atoms," Phys. Rev. A **87**, 063404 (2013).

[153]S. Pabst and J. M. Dahlström, "Eliminating the dipole phase in attosecond pulse characterization using Rydberg wave packets," Phys. Rev. A **94**, 013411 (2016).

[154]J. M. Dahlström, S. Pabst, and E. Lindroth, "Pulse analysis by delayed absorption from a coherently excited atom," APL Photonics **4**, 011101 (2019).

[155]J. White and Z. Chang, "Attosecond streaking phase retrieval with neural network," Opt. Express **27**, 4799 (2019).

[156]P. Tzallas, E. Skantzakis, and D. Charalambidis, "Measuring the absolute carrier-envelope phase of many-cycle laser fields," Phys. Rev. A **82**, 061401(R) (2010).

[157]Y. Nabekawa, H. Hasegawa, E. J. Takahashi, and K. Midorikawa, "Production of doubly charged helium ions by two-photon absorption of an intense sub-10-fs soft x-ray pulse at 42 eV photon energy," Phys. Rev. Lett. **94**, 043001 (2005).

[158]N. Miyamoto, M. Kamei, D. Yoshitomi, T. Kanai, T. Sekikawa, T. Nakajima, and S. Watanabe, "Observation of two-photon above-threshold ionization of rare gases by xuv harmonic photons," Phys. Rev. Lett. **93**, 083903 (2004).

[159]P. Heissler, R. Hörlein, J. M. Mikhailova, L. Waldecker, P. Tzallas, A. Buck, K. Schmid, C. M. S. Sears, F. Krausz, L. Veisz, M. Zepf, and G. D. Tsakiris, "Few-cycle driven relativistically oscillating plasma mirrors: A source of intense isolated attosecond pulses," Phys. Rev. Lett. **108**, 235003 (2012).

[160]F. H. M. Faisal, *Theory of Multiphoton Processes* (Plenum, New York, 1987).

[161]M. A. Kornberg and P. Lambropoulos, "Photoelectron energy spectrum indirect two-photon double ionization of helium," J. Phys. B: At., Mol. Opt. Phys. **32**, L603 (1999).

[162]P. Lambropoulos, L. A. A. Nikolopoulos, and M. G. Makris, "Signatures of direct double ionization under XUV radiation," Phys. Rev. A **72**, 727 (2005).

[163]K. D. Schultz, C. I. Blaga, R. Chirla, P. Colosimo, J. Cryan, A. M. March, C. Roedig, E. Sistrunk, J. Tate, J. Wheeler, P. Agostini, and L. F. DiMauro, "Strong field physics with long wavelength lasers," J. Mod. Opt. **54**, 1075 (2007).

[164]V. S. Yakovlev, M. Ivanov, and F. Krausz, "Enhanced phase-matching for generation of soft x-ray harmonics and attosecond pulses in atomic gases," Opt. Express **15**, 15351 (2007).

[165]S. L. Cousin, F. Silva, S. Teichmann, M. Hemmer, B. Buades, and J. Biegert, "High-flux table-top soft x-ray source driven by sub-2-cycle, CEP stable, 1.85-μm 1-kHz pulses for carbon K-edge spectroscopy," Opt. Lett. **39**, 5383 (2014).

[166]S. L. Cousin, N. Di Palo, B. Buades, S. M. Teichmann, M. Reduzzi, M. Devetta, A. Kheifets, G. Sansone, and J. Biegert, "Attosecond streaking in the water window: A new regime of attosecond pulse characterization," Phys. Rev. X **7**, 041030 (2017).

[167]X. Ren, J. Li, Y. Yin, K. Zhao, A. Chew, Y. Wang, S. Hu, Y. Cheng, E. Cunningham, Y. Wu, M. Chini, and Z. Chang, "Attosecond light sources in the water window," J. Opt. **20**, 023001 (2018).

[168]R. Budriūnas, T. Stanislauskas, J. Adamonis, A. Aleknavičius, G. Veitas, D. Gadonas, S. Balickas, A. Michailovas, and A. Varanavičius, "53 W average power CEP-stabilized OPCPA system delivering 5.5 TW few cycle pulses at 1 kHz repetition rate," Opt. Express **25**, 5797 (2017), https://www.eli-alps.hu/en/Research-Technology/Lasers.

[169]In the present article, we have tried to include all representative papers in the field of attosecond pulse metrology. Given the existence of a vast number of relevant literature in the field, we apologize for any unintentional omission of original research papers having significant contribution on the development of the field.

Multiple ionization of argon via multi-XUV-photon absorption induced by 20-GW high-order harmonic laser pulses

A. Nayak,[1] I. Orfanos,[1,2] I. Makos,[1,2] M. Dumergue,[3] S. Kühn,[3] E. Skantzakis,[1] B. Bodi,[4] K. Varju,[3,5] C. Kalpouzos,[1] H. I. B. Banks,[6] A. Emmanouilidou,[6] D. Charalambidis,[1,2,3,*] and P. Tzallas[1,*]

[1]*Foundation for Research and Technology–Hellas, Institute of Electronic Structure and Laser, P.O. Box 1527, GR71110 Crete, Greece*
[2]*Department of Physics, University of Crete, P.O. Box 2208, GR71003 Crete, Greece*
[3]*ELI-ALPS, ELI-Hu Kft., Dugonics ter 13, H-6720 Szeged, Hungary*
[4]*MTA "Lendület" Ultrafast Nanooptics Group, Wigner Research Center for Physics, 1121 Budapest, Hungary*
[5]*Department of Optics and Quantum Electronics, University of Szeged, Szeged, Hungary*
[6]*Department of Physics and Astronomy, University College London, Gower Street, London WC1E 6BT, England, United Kingdom*

We report the observation of multiple ionization of argon through multi-XUV-photon absorption induced by an unprecedentedly powerful laser driven high-order harmonic generation source. Comparing the measured intensity dependence of the yield of the different argon charge states with numerical calculations we can infer the different channels—direct and sequential—underlying the interaction. While such studies were feasible so far only with free electron laser (FEL) sources, this paper connects highly nonlinear XUV processes with the ultrashort time scales inherent to the harmonic pulses and highlights the advanced perspectives of emerging large scale laser research infrastructures.

I. INTRODUCTION

Multiphoton processes trace back to 1931 [1]. One third of a century later, the invention of lasers has allowed their observation [2], followed by several decades of flourishing multiphoton and strong-field science. Another third of a century later two-photon processes made their debut in the XUV spectral region [3], paving the way to XUV-pump and XUV-probe studies in the 1-fs scale [4] and below. Instrumental to these studies is high-order harmonic generation (HHG), which apart from its importance in understanding strong-field laser-atom interactions [5–7] led to the development of coherent XUV sources with pulse durations in the attosecond regime [8–14]. While HHG and attosecond sources induced so far few-photon (mainly two-photon) processes, FEL sources have achieved the production of high charge states through absorption of many XUV [15] or x-ray [16–18] photons. Attaining insight into such processes is considered of central importance [15–18], as they govern a wide-ranging spectrum of applications of energetic XUV and x-ray sources. Multiple multi-XUV-photon ionization by harmonic and attosecond sources provides an advanced tool for the study of ultrafast dynamics in correlated systems and/or of coupled motions due to the unprecedentedly short duration of their pulses. Towards this goal a substantial increase of their pulse energy is required. Despite FELs' markedly higher pulse energy (hundreds of μJ at ~ 60 nm) [19], their capacity in ultrafast XUV science is determined by their so far longer pulse durations [20] and shot-to-shot instabilities. Consequently, the enhancement of the HHG pulse energy in parallel with the reduction of the

FEL pulse duration remain challenging tasks serving the same goal.

Here, using the high-order harmonics generated by the interaction of high-power IR femtosecond laser pulses with xenon (Xe) and argon (Ar), we demonstrate a 20-GW XUV source which delivers pulses with carrier wavelength $\lambda_{XUV} \approx 50$ nm and pulse energy $E_{XUV} \approx 230$ and $130\ \mu$J, respectively. Using this source, highly charged Ar ions (up to Ar^{+4}) have been observed (an accomplishment that was up to now feasible only with FEL sources [21]) and the process of multiple ionization of Ar has been investigated by measuring the dependence of the multiply charged ions on the intensity of the XUV pulses.

II. EXPERIMENTAL PROCEDURE

The 20-GW XUV source is based on the increase in the number of the XUV emitters using loose IR focusing geometry and the precise control of phase-matching conditions achieved by means of thin single-gas targets in a dual-jet configuration with controllable distance between the jets. The ≈ 18-m-long beam line [Fig. 1(a)] was recently developed in the Attosecond Science and Technology laboratory of the Foundation of Research and Technology (FORTH). It is driven by a 10-Hz repetition rate Ti:sapphire laser system, which delivers $\tau_L \approx 20$-fs pulses at 800-nm carrier wavelength (IR) and energy up to ≈ 400 mJ/pulse. A p-polarized IR pulse of 25–45-mJ energy is focused by a spherical mirror of 9-m-long focal length into the HHG area which hosts a dual-pulsed-jet (GJ1,2) configuration operated with the same noble gas (either Ar or Xe) as nonlinear medium. In the dual gas-jet configuration, the gas pressure and the medium length were the same for both gas jets. This was confirmed by measuring the same harmonic yield generated by the individual jets when they were

---
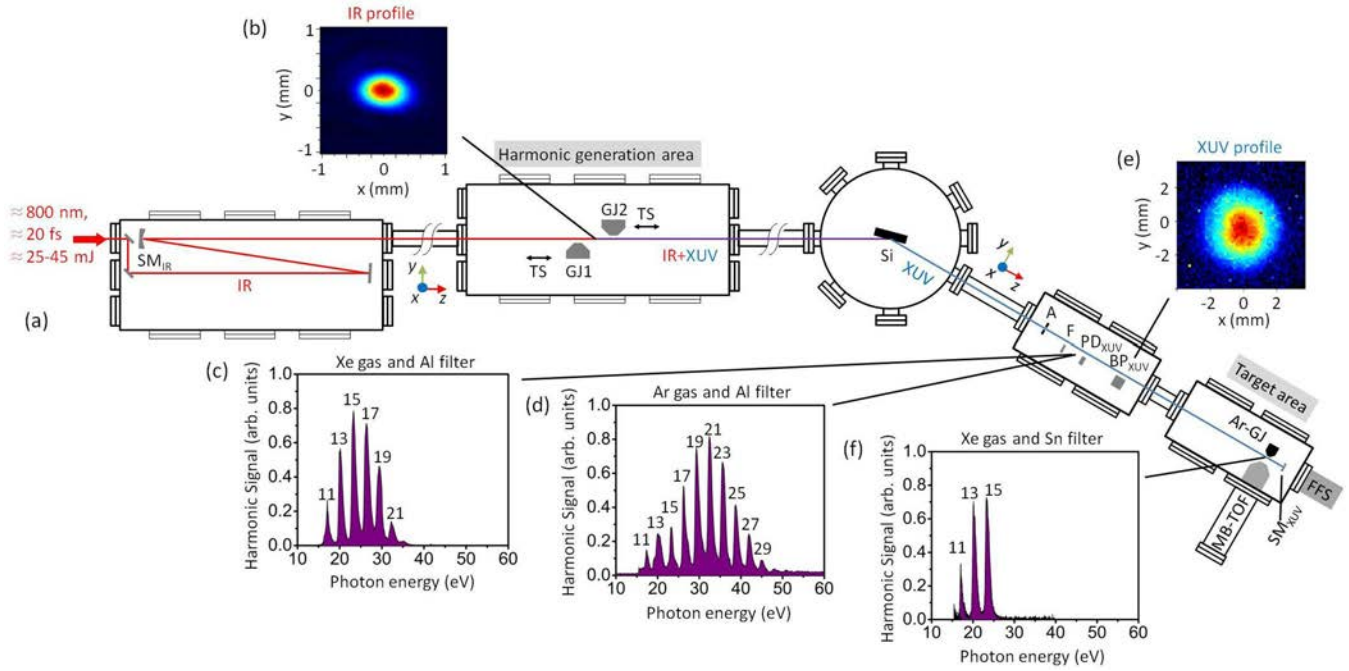*Corresponding authors: chara@iesl.forth.gr; ptzallas@iesl.forth.gr

FIG. 1. (a) A drawing of the 20-GW XUV beam line. SM_{IR}: Spherical mirror of 9-m focal length. GJ1,2: Dual-pulsed-jet configuration placed on translation stages (TS). Si: Silicon plate. F: Al or Sn filter. BP_{XUV}: XUV beam profiler. SM_{XUV}: Gold coated spherical mirror of 5-cm focal length. Ar-GJ: Ar gas jet. MB-TOF: Magnetic bottle time-of-flight spectrometer. PD_{XUV}: Calibrated XUV photodiode. FFS: Flat-field spectrometer. (b) IR beam profile at the focus. (c), (d) Harmonic spectra generated in Xe and Ar gases and transmitted by the Al filter. (e) XUV beam profile. (f) Harmonic spectrum generated in Xe gas transmitted by the Sn filter.

placed at the same position relative to focus of the IR beam. The slit shaped orifice of the piezo-based pulse nozzle has dimensions 0.3×2 mm. The pressure and the medium length were estimated taking into account the backing pressure of the nozzle, the conductance of the orifice, and the distance between the orifice and the laser focus, which was ~ 1 mm. The values are in agreement with those reported in Ref. [22] where piezo-based pulsed nozzles have been used. The gas jets were placed on x, y, and z translation stages with the movement on the x and y axes being manually controlled, while the displacement along the propagation z axis was done by a motorized translation stage using ≈ 0.75-cm steps (the minimum step of the stage was 5 μm). The IR beam profile in the HHG area is shown in Fig. 1(b). A silicon (Si) plate, placed after the harmonic generation at the Brewster angle for the fundamental (i.e., 75 deg), reflects the harmonics towards the detection area, while substantially attenuating the IR field. The reflectivity of the Si plate is $\approx 60\%$ in the spectral range of 15 to 45 eV [23]. After reflection from the Si plate, the XUV radiation passes through a 5-mm-diameter aperture (A) which blocks the residual outer part of the IR beam. The harmonics used in the experiments were selected by means of thin metal filters. A tin (Sn) filter with $\approx 20\%$ transmission in the spectral range 17–23 eV was used for studying the multiple ionization of Ar, while for the measurement of the XUV energy and XUV beam profile a low transmission ($\approx 5\%$ in the spectral range 17–60 eV) aluminum (Al) filter was used in order to avoid damaging and/or saturating the detectors. The transmission of the filters was measured by recording the harmonic spectra with and without the filters. Also, the transmission of the IR

beam after the metal filters was negligible. This was confirmed by the zero response of the BP_{XUV} (consisting of a pair of multichannel plates (MCPs) and a phosphor screen) and PD_{XUV} (XUV calibrated photodiode) detectors (both sensitive to the IR radiation) after blocking the XUV beam by a 2-mm-thick BK7 window. The harmonic spectra were measured by a flat-field spectrometer (FFS) attached to the back side of the target area chamber. The profile of the XUV beam was recorded by the BP_{XUV} placed after the Al filter. The harmonic spectra generated in Xe and Ar gases and the XUV beam profile after the Al filter are shown in Figs. 1(c)–1(e), respectively. For the studies of the multiple ionization of Ar, the beam transmitted through the Sn filter was then focused by a gold coated spherical mirror (SM_{XUV} positioned at $\sim 2°$ angle of incidence) of 5-cm focal length into an Ar gas jet (Ar-GJ) placed in the target area. The harmonic spectrum at the position of the Ar-GJ is shown in Fig. 1(f). The ionization products were measured by a magnetic bottle time-of-flight (MB-TOF) spectrometer that can be set to record either the photoelectron energy (PE) distribution or the ion-mass spectrum. In some cases the harmonics passing through the filters have been, for convenience, also measured by recording the single-photon Ar ionization PE spectra produced by the incoming (unfocused) harmonic beam. The intensity of the XUV radiation is changed by changing the atomic density of the harmonic generation target through variation of the delay between the laser and the gas nozzle trigger pulse. The reflectivity of the gold mirror ($\approx 12\%$) is constant in the spectral region of 17–23 eV [24]. We note that in the spectral range from 15 to 30 eV, the measured photoelectron distribution does not differ significantly from

the spectrum measured by the FFS as in this photon energy range the single-photon-ionization cross section of argon is almost constant at ≈ 30 Mb [25]. The deviation (compared to the spectra recorded by the flat-field spectrometer) appearing at photon energies >30 eV is attributed to the reduction of the single-photon ionization cross section. The energy of the XUV radiation in the generation region and the target area was determined by means of PD_{XUV}, taking into account the transmission of the filters and the reflectivity of the XUV optics.

III. PULSE ENERGY AND CONVERSION EFFICIENCY OF THE XUV SOURCE

In gas-phase harmonics, the amount of the XUV energy exiting the gas medium is an interplay between the microscopic (single atom) and macroscopic (atomic ensemble) response of the medium. On the microscopic level, for a specific driving laser field wavelength (λ_L), the probability of the emission of a single XUV photon depends nonlinearly on the driving laser field intensity (I_L) and the atomic properties. Considering that the probability of the single-XUV-photon emission is maximized for a fixed I_L lying just below the ionization saturation threshold of the atom (which for xenon and argon atoms is $I_L < 3 \times 10^{14}$ W cm^{-2}), it is evident that for the enhancement of the energy of the XUV radiation one has to increase the number of the atomic XUV emitters and consider the macroscopic response of the medium. While keeping I_L, at the level of saturating single atom ionization the number of the emitters can be increased by increasing either the interaction volume (by increasing focal length together with laser pulse energy) or the atomic density of the medium. Incorporating the macroscopic response taking into account the propagation effects in the gas medium, it has been shown (see Refs. [26–28] and references therein) that for $L_{coh} \gg L_{abs}$ and $L_{coh} \gg L_{med}$ the XUV yield is proportional to $\propto (\rho L_{med})^2$. In the former expressions $L_{coh} = \pi/\Delta k$, $L_{abs} = 1/\rho\sigma^{(1)}$, and L_{med} are the coherence length, the absorption length of the XUV radiation, and the gas medium length, respectively, with $\Delta k = k_L - qk_L$, q the harmonic order, k_L the wave number of the driving field, ρ the atomic density of the medium, and $\sigma^{(1)}$ the single-XUV-photon ionization cross section of the atoms in the medium. This product constitutes the main scaling factor towards the enhancement of the produced energy. Using one gas jet, for fixed I_L the dependence of the harmonic yield on gas pressure (P) and L_{med} is shown in the contour plot of Fig. 2. The red color area corresponds to the area of maximum XUV production and the black-circled area depicts the values of P and L_{med} used in the present paper. The $\sim 50\%$ reduction of the XUV emission for "large"-length and "high"-pressure media (green color area in Fig. 2) is associated with the XUV absorption effects and IR-XUV phase mismatch induced by the neutral atoms and plasma generation in the medium which confines the coherent harmonic buildup to a short propagation length. This limitation can be overcome applying quasi-phase-matching conditions discussed below.

The optimization of the generated energy in the dual-jet configuration was performed after maximizing the harmonic yield of the single-gas jet (GJ1). This was achieved by measuring the XUV energy as a function of the driving IR field
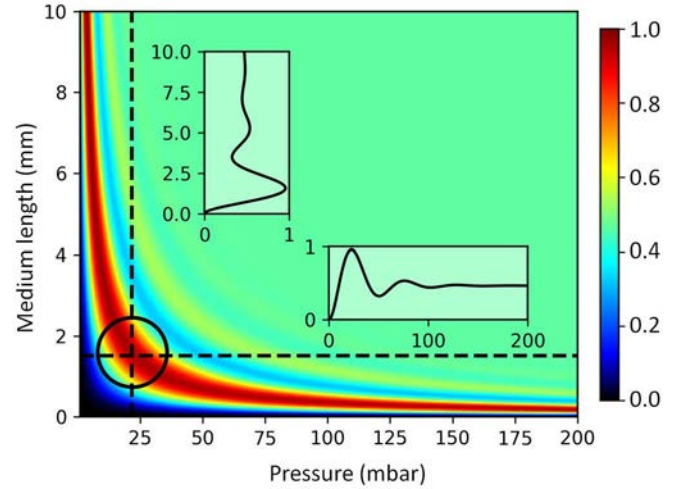

FIG. 2. Calculated harmonic yield generated in Ar gas as a function of the gas pressure (P) and medium length (L) for $I_L \approx 1.5 \times 10^{14}$ W cm^{-2}. The values of P and L used in the experiment fall within the area defined by the black circle. The insets show a line out of the harmonic yield along the dashed lines at $L \approx 1.5$ mm, $P \approx 25$ mbars.

intensity (I_L), the medium length (L), the gas pressure (P), and the position of the GJ1 relative to the focus position of the IR beam. The optimum conditions were found when GJ1 was set to be at the focus of the IR beam ($z = 0$) where the IR was just below the ionization saturation intensity of Xe and Ar atoms, for $P \sim 25$ mbars and $L \sim 1.5$ mm [Figs. 3(a) and 3(b)]. These optimal conditions are in fair agreement with the results obtained by calculations [26–28] (Fig. 2). Further enhancement of the harmonic yield was achieved by applying quasi-phase-matching conditions [26,29] using two gas jets. GJ1 is positioned at fixed $z \approx 0$ and GJ2 at variable positions (L and P are the same in both jets). The dependence of the XUV energy generated by Xe and Ar gas on the distance between GJ2 and GJ1 is shown in Figs. 4(a) and 4(b), respectively. In both cases, the energy increases by a factor of ≈ 1.7 when GJ2 is placed at $z \approx \pm 5$ cm, verified by calculations taking into account the propagation effects in the dual-gas medium [26] [Fig. 4(c)]. At this position, the generated XUV energy for Xe and Ar gas was ≈ 230 and 130 μJ per pulse, respectively. The reduction of the energy around $z \approx 0$ is attributed to phase-mismatch effects induced due to the increase of the medium pressure and/or medium length, while the oscillations observed at $z > +5$ cm and $z < -5$ cm are due to the Gouy phase shift of the focused IR beam [30].

In order to estimate the conversion efficiency ($C_{(q)} = E_{XUV}^{(q)}/E_{IR}$) of the harmonic generation process the energy per harmonic (q) per pulse ($E_{XUV}^{(q)}$) was calculated taking into account the transmission of the filter, the reflectivity of the Si plate, and the quantum efficiency of PD_{XUV}. For the single-jet configuration, and for the optimum generating conditions, it has been found that the maximum generated XUV energy (integrated over the spectrum) was ≈ 135 and 75 μJ per pulse for Xe and Ar, respectively. This corresponds to $E_{XUV}^{(q)}$ ($q = 11$, 13, 15) ≈ 30 and 10 μJ for Xe and Ar gas, respectively, considering that the total energy is shared equally between
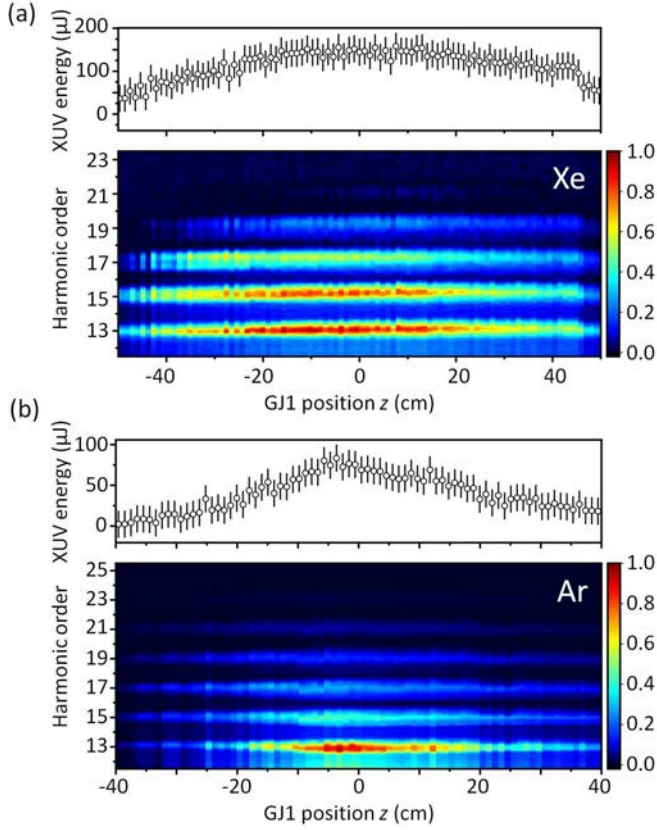
FIG. 3. (a), (b) The upper panels show the dependence of the XUV energy (integrated over the spectrum passing through the Al filter) generated in Xe and Ar gas on the position of the GJ1 relative to the laser focus, respectively. For obtaining the energy values just after the harmonic generation area, the measured by the PD_{XUV} energy values were divided by the reflectivity of the Si plate and the transmission of the Al filter. The error bars represent one standard deviation from the mean. The lower panels show the corresponding harmonic spectrum measured in the target area by recording the single-photon PE spectra produced by the interaction of Ar gas with the incoming XUV beam.

the plateau harmonics. This results in $C_{(11)} \approx C_{(13)} \approx C_{(15)} \approx 1 \times 10^{-3}$ and $\approx 2 \times 10^{-4}$, respectively. The enhancement by a factor of >2 as compared to previously reported values [31] (where $C_{(11)} \approx 5 \times 10^{-4}$) is associated with the increased interaction volume and is in agreement with the energy scaling law reported in Refs. [28,32]. The dual-jet configuration provides a factor of ≈ 1.7 further enhancement, resulting in a conversion efficiency $\approx 2 \times 10^{-3}$ and $\approx 3 \times 10^{-4}$, for Xe and Ar, respectively.

IV. MUTIPLE IONIZATION OF ARGON

Taking into account the measured XUV pulse energy and a focal spot size of $\approx 2\,\mu m$ [33], when low ($\approx 90\%$) energy loss XUV optics are used, this radiation can support trains of attosecond pulses with overall duration $\tau_{XUV} = \tau_L/\sqrt{n} \approx 10\,fs$ (where $n = 3-5$ is the order of nonlinearity of the generation of plateau harmonics [34]) and I_{XUV} up to $\sim 10^{17}\,W\,cm^{-2}$. However, in the present paper, for the investigation of multiple ionization process of Ar atoms the spectral region from 17.05 to 23.25 eV was selected [Fig. 1(f)] using XUV optical elements
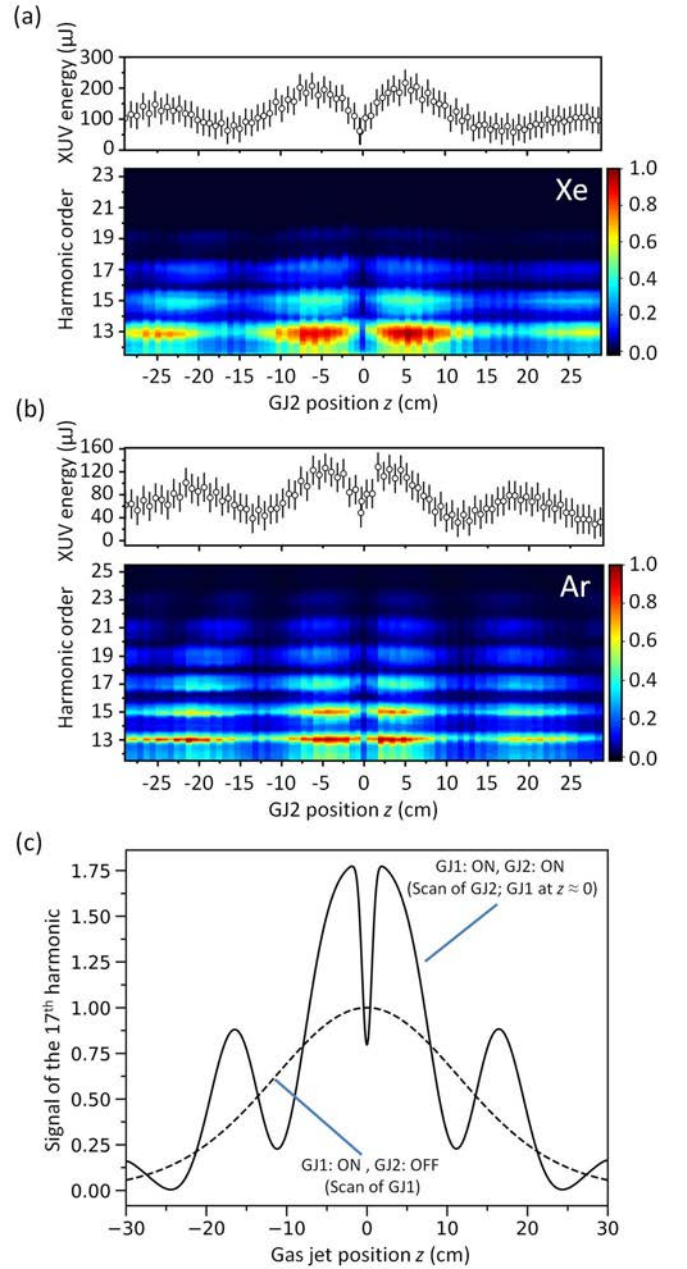
FIG. 4. Generation of 20-GW high-order harmonics using a dual gas jet. (a), (b) The upper panels shows the energy dependence of the XUV generated in Xe and Ar gas on the distance between GJ2 and GJ1 (placed at $z = 0$). The error bars represent one standard deviation. The lower panels show the harmonic spectrum measured in the target area by recording the PE produced by the single photon of Ar gas. (c) Calculated yield of the 17th harmonic generated in Ar as a function of the distance between the gas jets (black solid line). The yield was calculated for $I_L \approx 1.5 \times 10^{14}\,W\,cm^{-2}$ and $L \approx 1.5\,mm$, $P \approx 25\,mbars$ for both jets. For comparison, the dependence of the XUV energy generated in a single Ar gas jet on the position of the GJ1 relative to the laser focus is shown (black dashed line).

introducing $\approx 98\%$ losses. With the above given parameters, XUV intensities I_{XUV} up to $\approx 7 \times 10^{15}\,W\,cm^{-2}$ have been reached and multiply charged ions (Ar^{n+}) with $n = 1,2,3$ and 4 have been observed [Fig. 5(a)]. The signal of the single-charged

ions (Ar^+, O_2^+, N_2^+, etc.) is proportional to the XUV pulse energy as it is generated by a single-photon ionization process. These ions are mainly produced away from the focus in the target area. The singly charged ion signal produced at the focus of the beam is considered negligible compared to the signal of the singly charged ions produced outside of the focus due to volume and single-photon ionization saturation effects which according to the lowest-order-perturbation theory are taking place for $I_{XUV} > I_{XUV}^{(sat)} \approx 7 \times 10^{12}$ W cm^{-2} [24]. The dependence of the Ar^{n+} (for $n \geqslant 2$) yield on I_{XUV} is shown in Fig. 5(b). In order to gain insight into the measured XUV intensity dependence of the Ar^{2+} and Ar^{3+} ion yields, we set up rate equations (described in the next section) accounting for all energetically allowed processes for ions up to Ar^{4+} [solid lines in Fig. 5(b)]. For the two-photon ionization of Ar we take the cross section equal to 10^{-51} cm^4 s^{-1} (indicative two-photon ionization of a neutral atom [25]), while for all other two-photon-ionization processes we use a cross section of 10^{-52} cm^4 s^{-1}. However, we find that our results are robust for two-photon cross sections in the range from 10^{-51} to 10^{-53} cm^4 s^{-1}. For the three-photon processes we use a cross section of 10^{-85} cm^6 s^{-2}. The cross sections used in the numerical calculations are justified by the values deduced from the relevant saturation intensities (I_{SAT}) of the present paper (typical cross sections can be found in Refs. [35,36]). The measured Ar^{2+} signal after an increase with slope $s \approx 1.8 \pm 0.3$ saturates at $I_{SAT} \approx 2.2 \times 10^{15}$ W cm^{-2} where s drops to $\approx 1.3 \pm 0.1$. The Ar^{3+} signal has a slope $s \approx 2.9 \pm 0.5$ and saturates at $I_{SAT} \approx 3.2 \times 10^{15}$ W cm^{-2} with s dropping to $\approx 1.7 \pm 0.2$. From the measured I_{SAT} we deduce Ar^+ two-photon and Ar^{2+} three-photon ionization cross sections to be 2×10^{-52} cm^4 s^{-1} and 1×10^{-85} cm^6 s^{-2}, respectively, in good agreement with the values used in the calculations. Given the uncertainty factor of 2 in the intensity, the uncertainty factors of the measured cross sections are 4 and 9, respectively. The Ar^{4+} signal appeared at intensities above I_{SAT} of Ar^{3+} and was at the detection limit not allowing any intensity dependence measurement. The corresponding values from the calculations are $s = 1.8$ and $I_{SAT} \approx 2.4 \times 10^{15}$ W cm^{-2} for Ar^{2+} and $s = 3.1$ and $I_{SAT} \approx 3.7 \times 10^{15}$ W cm^{-2} for Ar^{3+}. Considering an uncertainty factor of ≈ 2 (mainly associated with the measurement of the XUV focal spot size) in the estimation of I_{XUV}, the results are in fair agreement. Figure 5(c) shows an excitation scheme that includes only the dominant processes. It is worth noting that comparing the results of our paper and those obtained using FEL sources [21] in the same spectral range one finds a striking difference in the intensity range of the two experiments. While in Ref. [21] Ar^{6+} is observed at intensities $1-2 \times 10^{14}$ W cm^{-2}, in our paper charged states higher than Ar^{4+} are not observable at intensities $\sim 7 \times 10^{15}$ W cm^{-2}. This difference can be attributed to interesting source dependent physics. The ionization yield for sequential processes depends linearly on the interaction volume and nonlinearly on the pulse duration depending on the number of sequential steps involved. The interaction volume in Ref. [21] (within the reported uncertainty) is the same or up to one order of magnitude larger than in this paper and the pulse duration is 100 fs, i.e., one order of magnitude larger. For the generation of Ar^{4+} a sequential process of three steps is necessary (and for the generation of Ar^{6+} another two).
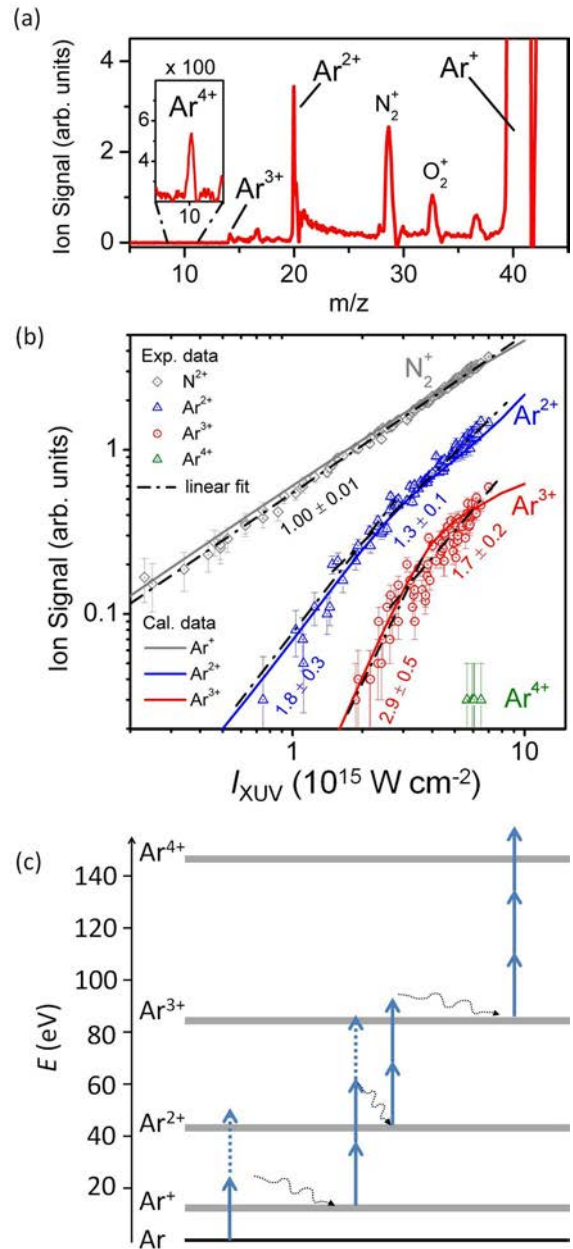

FIG. 5. Multiple ionization of argon atoms using the 20-GW high-order harmonic source. (a) TOF mass spectrum produced by the interaction of the focused 11th–15th harmonics with argon. The spectrum shows multiple charged Ar ions (Ar^{n+}) with n up to 4. (b) Dependence of the $Ar^{2,3+}$ yield on the I_{XUV}. For calibrating the XUV energy (x axis) the O_2^+ signal was used. The black dashed lines show a linear fit on the raw data. The error bars represent one standard deviation of the mean. The solid lines show the results of the numerical calculations, including volume integration. As is expected from a single-photon ionization process, the dependence of the calculated Ar^+ yield on I_{XUV} is linear and matches well with the experimental data of N_2^+. As the calculated Ar^+ yield (gray solid line) is orders of magnitude higher than the Ar^{2+} yield, for visualization reasons, the calculated Ar^+ signal was divided by a factor of 8×10^3, and the measured Ar^+ signal was normalized to it. In arbitrary units measured, Ar^{2+}, Ar^{3+}, and Ar^{4+} yield points are normalized to one and the same calculated single ion yield point. (c) Multi-XUV-photon multiple ionization scheme [excluding higher-order processes (ATI)] of Ar which supports the obtained results.

These parameters of Ref. [21] would produce three to four orders-of-magnitude higher Ar^{4+} yield for the same intensity as in our experiment. This is not enough to explain the intensity difference in the two experiments for the processes involved. However, it is well established that the yield of multiphoton processes depends on the coherence properties of the radiation used. Thus, for an N photon process, the yield is proportional to $N!$ for thermal (chaotic) radiation, proportional to $(2N-1)!!$ for squeezed vacuum states of light or proportional to unity for coherent radiation. The multiphoton yield dependence on the coherence properties of the light was theoretically shown already in the 1970s [37–39] and experimentally verified in 1974 [40] and more recently in Ref. [41]. It is also well established that FEL radiation is incoherent, unless seeded by laser harmonics, while harmonic radiation is coherent. Thus, for the many photon processes involved in this paper and in Ref. [21] even partial validity of the $N!$ dependence (due to not completely incoherent FEL radiation and not 100% coherent harmonic radiation) results in a much higher yield in Ref. [21] due to the incoherence of the source used. Hence the comparison of Ref. [21] with the present paper is compatible with the coherence properties of the different sources used. It also highlights the importance of the present achievement exactly because harmonic sources do not favor multiphoton processes in terms of yield.

V. NUMERICAL CALCULATIONS

The numerical calculations provide significant information about the individual contributing ionization channels by computing the ion yields of each allowed pathway contributing to the formation of Ar^{2+} and Ar^{3+}. In the calculations we use a Gaussian laser pulse of FWHM equal to $\tau_{XUV} = 10$ fs. Moreover, we perform a volume average for our results for the ion yields. We do so as follows. First, for a certain peak intensity we used the following equation [36] to determine the intensity, I_{XUV}, at each point (r, z) in cylindrical coordinates:

$$I_{XUV}(r, z; t) = I_{XUV}(t) \frac{w_0^2}{w(z)^2} \exp\left[-\frac{2r^2}{w(z)^2} \right] \quad (1)$$

where r is the radius and z is the beam propagation axis. $w(z)$ is the beam radius, defined in terms of the beam waist, $w_0 = 1\,\mu$m, and the Rayleigh length, $z_R = 51.5\,\mu$m, as

$$w(z) = w_0\sqrt{1 + (z/z_R)^2}. \quad (2)$$

We calculated the ion yield in a volume with limits $r_{max} = 3$ mm in the radial direction and $z_{min} = -3$ mm to $z_{max} = 3$ mm in the z direction. These ion yields were then integrated using the following expression [42]:

$$P_i = \int_0^{r_{max}} \int_{z_{min}}^{z_{max}} 2\pi r N_i(r, z)\, dz\, dr \quad (3)$$

where P_i is the yield of the ion i integrated over the volume and N_i is the yield of ion i. We have checked that our results for P_i converge. The yields for the main pathways leading to the formation of Ar^{2+} and Ar^{3+} are not volume integrated. In our computations the three-photon transition is energetically allowed when the photon energy is equal to or above 22 eV.
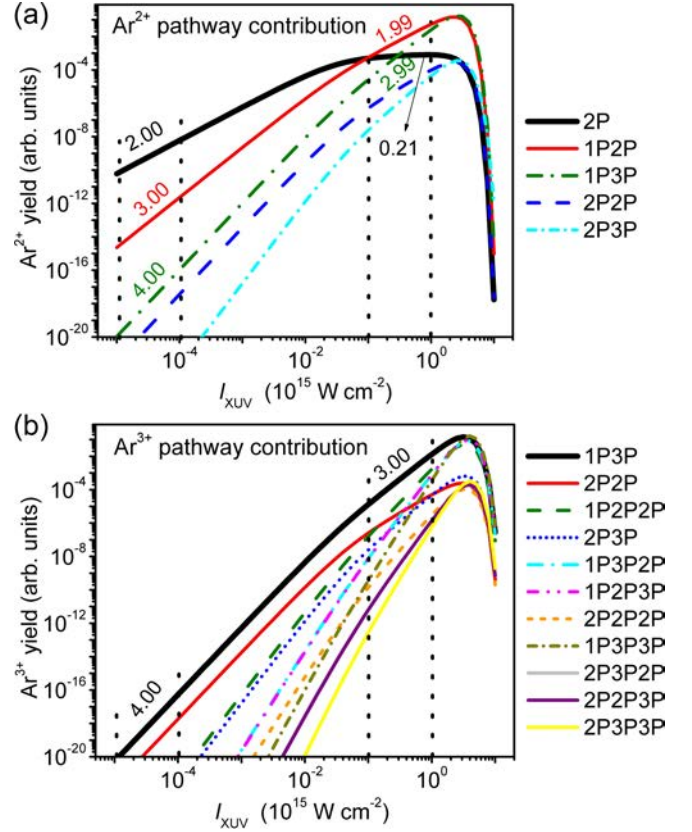

FIG. 6. Calculated ionization yields of different ionization pathways. These calculations are performed for a central photon energy of 22 eV and a pulse duration of 10 fs, and no volume integration has been included. (a) shows the yield of Ar^{2+} as a function of the XUV intensity. The black thick line is the yield of the two-photon DDI of the Ar pathway. All other curves denoted $nPmP$ ($m = 1, 2$; $n = 2, 3$) refer to the sequential pathways of n-photon ionization of Ar followed by m-photon ionization of Ar$^+$. From this graph we deduce that below saturation the two-photon DDI is the dominant pathway, while after saturation the lowest-order sequential process prevails. (b) shows the XUV intensity dependence of the Ar^{3+} yield. The black thick line is the single-photon ionization of Ar followed by three-photon direct ejection of two electrons from Ar$^+$, which is the dominant pathway at all intensities, while all other curves denoted $hPiPjP$ refer to the sequential processes of h-photon ($h = 1, 2$) ionization of Ar followed by i-photon ionization ($i = 2, 3$) of Ar$^+$ and eventually by j-photon ionization ($j = 2, 3$) of Ar^{2+}.

We find that our results do not change when the photon energy changes from 22 to 23.3 eV, which is the maximum energy considered in the experiment. However, if we reduce the photon energy below 22 eV then the sequential process of one-photon ionization of Ar followed by three-photon ionization of Ar$^+$ (1P3P) is not energetically allowed and the slope we obtain for the Ar^{3+} ion yield is closer to 4. We note that in our computations all energies are obtained with MOLPRO (a quantum chemistry package) using Hartree-Fock with a 6–311-G basis. We have used the same basis for previous FEL processes in Ar [43]. Figure 6(a) shows these yields for Ar^{2+} formation as a function of the XUV intensity. The black line is the yield of the two-photon direct-double-ionization (DDI)

channel. All other curves denoted $nPmP$ ($m = 1, 2$ and $n = 2, 3$) refer to the sequential pathways of n-photon ionization of Ar followed by m-photon ionization of Ar^+. Before saturation of the Ar^+ signal the dominant process for the Ar^{2+} production is the two-photon DDI, while upon saturation the sequential processes set in and eventually prevail. In Fig. 6(b) several different channels producing Ar^{3+} are compared. The notation $hPiPjP$ ($h = 1,2$; $i = 2, 3$; and $j = 2, 3$) stands for h-photon ionization of Ar, followed by i-photon DDI of Ar^+ or i-photon ionization of Ar^+ followed by j-photon ionization of Ar^{2+}. The dominating mechanism for the production of Ar^{3+} is the single-photon ionization of Ar followed by a three-photon DDI of Ar^+. The slope of 4 of this four-photon process reduces to 3 in the intensity region of the experiment as in this region the Ar single-photon ionization is saturated.

VI. CONCLUSIONS

This paper demonstrates the most powerful gas target HHG source ever, emitting XUV pulses with a pulse energy as high as published XUV pulse energies of FEL sources in the spectral region 17–30 eV. The unprecedented XUV intensities achieved with this source are evidenced by the observation of multi-XUV-photon multiple ionization of argon through a series of sequential and direct ionization processes as proven by numerical calculations. A comparison between HHG and FEL induced multiple ionization reveals differences that can be attributed to the different temporal and coherence characteristics of the two source types. The paper establishes that table-top HHG sources reached intensities allowing the study and exploitation of highly nonlinear XUV processes [44,45], advancing the capacities of ultrafast XUV science [10,33,46]. Besides the prospects opened in small and intermediate size laboratories the present results are highly relevant to the mission of the under-implementation Extreme Light Infrastructure - Attosecond Light Pulse Source

(ELI-ALPS) facility. Its GHHG SYLOS compact beam line [47] uses a similar arrangement operating at 1-kHz repetition rate operation. The XUV pulse energy levels of the present paper at 1-kHz repetition rate and isolated pulse operation open up unique prospects for few-body coincidence experiments in nonlinear XUV laser-matter interactions exploited in detailed studies of ultrafast dynamics.

[1] M. Goeppert-Mayer, Ann. Phys. (Leipzig). **9**, 273 (1931).

[2] G. S. Voronov and N. B. Delone, JETP Lett. **1**, 66 (1965).

[3] Y. Kobayashi, T. Sekikawa, Y. Nabekawa, and S. Watanabe, Opt. Lett. **23**, 64 (1998).

[4] P. Tzallas, E. Skantzakis, L. A. A. Nikolopoulos, G. D. Tsakiris, and D. Charalambidis, Nat. Phys. **7**, 781 (2011).

[5] M. Lewenstein, P. Balcou, M. Y. Ivanov, A. L'Huillier, and P. B. Corkum, Phys. Rev. A **49**, 2117 (1994).

[6] C. I. Blaga, F. Catoire, P. Colosimo, G. G. Paulus, H. G. Muller, P. Agostini and L. F. DiMauro, Nat. Phys. **5**, 335 (2009).

[7] N. Tsatrafyllis, I. K. Kominis, I. A. Gonoskov, and P. Tzallas, Nat. Commun. **8**, 15170 (2017).

[8] S. Chatziathanasiou, S. Kahaly, E. Skantzakis, G. Sansone, R. Lopez-Martens, S. Haessler, K. Varju, G. Tsakiris, D. Charalambidis, and P. Tzallas, Photonics **4**, 26 (2017).

[9] C. M. Heyl, C. L. Arnold, A. Couairon, and A. L'Huillier, J. Phys. B **50**, 013001 (2017).

[10] M. Reduzzi, P. Carpeggiani, S. Kühn, F. Calegari, M. Nisoli, S. Stagira, C. Vozzi, P. Dombi, S. Kahaly, P. Tzallas, D. Charalambidis, K. Varju, K. Osvay, and G. Sansone, J. Electron Spectros. Relat. Phenomena **204**, 257 (2015).

[11] F. Krausz and M. Ivanov, Rev. Mod. Phys. **81**, 163 (2009).

[12] P. B. Corkum and F. Krausz, Nat. Phys. **3**, 381 (2007).

[13] T. Gaumnitz, A. Jain, Y. Pertot, M. Huppert, I. Jordan, F. Ardana-Lamas, and H. J. Wörner, Opt. Express **25**, 27506 (2017).

[14] K. Zhao, Q. Zhang, M. Chini, Y. Wu, X. Wang, and Z. Chang, Opt. Lett. **37**, 3891 (2012).

[15] A. A. Sorokin, S. V. Bobashev, T. Feigl, K. Tiedtke, H. Wabnitz, and M. Richter, Phys. Rev. Lett. **99**, 213002 (2007).

[16] L. Young, E. P. Kanter, B. Krässig, Y. Li, A. M. March, S. T. Pratt, R. Santra, S. H. Southworth, N. Rohringer, L. F. DiMauro, G. Doumy, C. A. Roedig, N. Berrah, L. Fang, M. Hoener, P. H. Bucksbaum, J. P. Cryan, S. Ghimire, J. M. Glownia, D. A. Reis, J. D. Bozek, C. Bostedt, and M. Messerschmidt, Nature (London) **466**, 56 (2010).

[17] B. Rudek, S.-K. Son, L. Foucar, S. W. Epp, B. Erk, R. Hartmann, M. Adolph, R. Andritschke, A. Aquila, N. Berrah, C. Bostedt, J. Bozek, N. Coppola, F. Filsinger, H. Gorke, T. Gorkhover, H. Graafsma, L. Gumprecht, A. Hartmann, G. Hauser, S. Herrmann, H. Hirsemann, P. Holl, A. Hömke, L. Journel, C. Kaiser, N. Kimmel, F. Krasniqi, K.-U. Kühnel, M. Matysek, M. Messerschmidt, D. Miesner, T. Möller, R. Moshammer, K. Nagaya, B. Nilsson, G. Potdevin, D. Pietschner, C. Reich, D. Rupp, G. Schaller, I. Schlichting, C. Schmidt, F. Schopper,

S. Schorb, C.-D. Schröter, J. Schulz, M. Simon, H. Soltau, L. Strüder, K. Ueda, G. Weidenspointner, R. Santra, J. Ullrich, A. Rudenko, and D. Rolles, Nat. Photon. **6**, 858 (2012).

[18] H. Fukuzawa, S.-K. Son, K. Motomura, S. Mondal, K. Nagaya, S. Wada, X.-J. Liu, R. Feifel, T. Tachibana, Y. Ito, M. Kimura, T. Sakai, K. Matsunami, H. Hayashita, J. Kajikawa, P. Johnsson, M. Siano, E. Kukk, B. Rudek, B. Erk, L. Foucar, E. Robert, C. Miron, K. Tono, Y. Inubushi, T. Hatsui, M. Yabashi, M. Yao, R. Santra, and K. Ueda, Phys. Rev. Lett. **110**, 173005 (2013).

[19] W. Ackermann, G. Asova, V. Ayvazyan, A. Azima, N. Baboi, J. Bähr, V. Balandin, B. Beutner, A. Brandt, A. Bolzmann, R. Brinkmann, O. I. Brovko, M. Castellano, P. Castro, L. Catani, E. Chiadroni, S. Choroba, A. Cianchi, J. T. Costello, D. Cubaynes, J. Dardis, W. Decking, H. Delsim-Hashemi, A. Delserieys, G. Di Pirro, M. Dohlus, S. Düsterer, A. Eckhardt, H. T. Edwards, B. Faatz, J. Feldhaus, K. Flöttmann, J. Frisch, L. Fröhlich, T. Garvey, U. Gensch, C. Gerth, M. Görler, N. Golubeva, H.-J. Grabosch, M. Grecki, O. Grimm, K. Hacker, U. Hahn, J. H. Han, K. Honkavaara, T. Hott, M. Hüning, Y. Ivanisenko, E. Jaeschke, W. Jalmuzna, T. Jezynski, R. Kammering, V. Katalev, K. Kavanagh, E. T. Kennedy, S. Khodyachykh, K. Klose, V. Kocharyan, M. Körfer, M. Kollewe, W. Koprek, S. Korepanov, D. Kostin, M. Krassilnikov, G. Kube, M. Kuhlmann, C. L. S. Lewis, L. Lilje, T. Limberg, D. Lipka, F. Löhl, H. Luna, M. Luong, M. Martins, M. Meyer, P. Michelato, V. Miltchev, W. D. Möller, L. Monaco, W. F. O. Müller, O. Napieralski, O. Napoly, P. Nicolosi, D. Nölle, T. Nuñez, A. Oppelt, C. Pagani, R. Paparella, N. Pchalek, J. Pedregosa-Gutierrez, B. Petersen, B. Petrosyan, G. Petrosyan, L. Petrosyan, J. Pflüger, E. Plönjes, L. Poletto, K. Pozniak, E. Prat, D. Proch, P. Pucyk, P. Radcliffe, H. Redlin, K. Rehlich, M. Richter, M. Roehrs, J. Roensch, R. Romaniuk, M. Ross, J. Rossbach, V. Rybnikov, M. Sachwitz, E. L. Saldin, W. Sandner, H. Schlarb, B. Schmidt, M. Schmitz, P. Schmüser, J. R. Schneider, E. A. Schneidmiller, S. Schnepp, S. Schreiber, M. Seidel, D. Sertore, A. V. Shabunov, C. Simon, S. Simrock, E. Sombrowski, A. A. Sorokin, P. Spanknebel, R. Spesyvtsev, L. Staykov, B. Steffen, F. Stephan, F. Stulle, H. Thom, K. Tiedtke, M. Tischer, S. Toleikis, R. Treusch, D. Trines, I. Tsakov, E. Vogel, T. Weiland, H. Weise, M. Wellhöfer, M. Wendt, I. Will, A. Winter, K. Wittenburg, W. Wurth, P. Yeates, M. V. Yurkov, I. Zagorodnov, and K. Zapfe, Nat. Photon. **1**, 336 (2007).

[20] S. Serkez, G. Geloni, S. Tomin, G. Feng, E. V. Gryzlova, A. N. Grum-Grzhimailo, and M. Meyer, J. Opt. **20**, 24005 (2018).

[21] K. Motomura, H. Fukuzawa, L. Foucar, X.-J. Liu, G. Prümper, K. Ueda, N. Saito, H. Iwayama, K. Nagaya, H. Murakami, M. Yao, A. Belkacem, M. Nagasono, A. Higashiya, M. Yabashi, T. Ishikawa, H. Ohashi, and H. Kimura, J. Phys. B **42**, 221003 (2009).

[22] C. Altucci, C. Beneduce, R. Bruzzese, C. de Lisio, G. S. Sorrentino, T. Starczewski, and F. Vigilante, J. Phys. D: Appl. Phys. **29**, 68 (1996).

[23] E. J. Takahashi, H. Hasegawa, Y. Nabekawa, and K. Midorikawa, Opt. Lett. **29**, 507 (2004).

[24] N. Tsatrafyllis, B. Bergues, H. Schroder, L. Veisz, E. Skantzakis, D. Gray, B. Bodi, S. Kuhn, G. D. Tsakiris, D. Charalambidis, and P. Tzallas, Sci. Rep. **6**, 21556 (2016).

[25] J. A. R. Samson and W. C. Stolte, J. Electron Spectros. Relat. Phenomena **123**, 265 (2002).

[26] Y. Tao, S. J. Goh, H. M. J. Bastiaens, P. J. M. van der Slot, S. G. Biedron, S. V. Milton, and K.-J. Boller, Opt. Express **25**, 3621 (2017).

[27] E. Constant, D. Garzella, P. Breger, E. Mével, C. Dorrer, C. Le Blanc, F. Salin, and P. Agostini, Phys. Rev. Lett. **82**, 1668 (1999).

[28] K. Midorikawa, Y. Nabekawa, and A. Suda, Prog. Quantum Electron. **32**, 43 (2008).

[29] J. Seres, V. S. Yakovlev, E. Seres, C. Streli, P. Wobrauschek, C. Spielmann, and F. Krausz, Nat. Phys. **3**, 878 (2007).

[30] D. E. Laban, A. J. Palmer, W. C. Wallace, N. S. Gaffney, R. P. M. J. W. Notermans, T. T. J. Clevis, M. G. Pullen, D. Jiang, H. M. Quiney, I. V. Litvinyuk, D. Kielpinski, and R. T. Sang, Phys. Rev. Lett. **109**, 263902 (2012).

[31] E. J. Takahashi, Y. Nabekawa, and K. Midorikawa, Opt. Lett. **27**, 1920 (2002).

[32] E. J. Takahashi, Y. Nabekawa, T. Otsuka, M. Obara, and K. Midorikawa, Phys. Rev. A **66**, 021802(R) (2002).

[33] P. Tzallas, B. Bergues, D. Rompotis, N. Tsatrafyllis, S. Chatziathanassiou, A. Muschet, L. Veisz, H. Schröder, and D. Charalambidis, J. Opt. **20**, 24018 (2018).

[34] C.-G. Wahlstrom, J. Larsson, A. Persson, T. Starczewski, S. Svanberg, P. Saliéres, P. Balcou, and A. L'Huillier, Phys. Rev. A **48**, 4709 (1993).

[35] P. Lambropoulos, Comments At. Mol. Phys. **20**, 199 (1987).

[36] G. M. Nikolopoulos and P. Lambropoulos, J. Phys. B **47**, 115001 (2014).

[37] P. Lambropoulos, *Advances in Atomic and Molecular Physics* (Academic, New York, 1976), Vol. 12, p. 87.

[38] A. T. Georges and P. Lambropoulos, Phys. Rev. A **20**, 991 (1979).

[39] G. M. Nikolopoulos and P. Lambropoulos, Phys. Rev. A **86**, 033420 (2012).

[40] C. Lecompte, G. Mainfray, C. Manus, and F. Sanchez, Phys. Rev. Lett. **32**, 265 (1974).

[41] Kirill Yu. Spasibko, Denis A. Kopylov, Victor L. Krutyanskiy, Tatiana V. Murzina, Gerd Leuchs, and Maria V. Chekhova, Phys. Rev. Lett. **119**, 223603 (2017).

[42] E. T. Karamatskos, D. Markellos, and P. Lambropoulos, J. Phys. B **46**, 164011 (2014).

[43] A. O. G. Wallis, L. Lodi, and A. Emmanouilidou, Phys. Rev. A **89**, 063417 (2014).

[44] P. Lambropoulos, K. G. Papamihail, and P. Decleva, J. Phys. B **44**, 175402 (2011).

[45] M. G. Makris, P. Lambropoulos, and A. Mihelič, Phys. Rev. Lett. **102**, 033002 (2009).

[46] E. Foumouo, S. Laulan, B. Piraux, and H. Bachau, J. Phys. B **39**, S427 (2006).

[47] S. Kühn, M. Dumergue, S. Kahaly, S. Mondal, M. Füle, T. Csizmadia, B. Farkas, B. Major, Z. Várallyay, E. Cormier, M. Kalashnikov, F. Calegari, M. Devetta, F. Frassetto, E. Månsson, L. Poletto, S. Stagira, C. Vozzi, M. Nisoli, P. Rudawski, S. Maclot, F. Campi, H. Wikmark, C. L. Arnold, C. M. Heyl, P. Johnsson, A. L'Huillier, R. Lopez-Martens, S. Haessler, M. Bocoum, F. Boehle, A. Vernier, G. Iaquaniello, E. Skantzakis, N. Papadakis, C. Kalpouzos, P. Tzallas, F. Lépine, D. Charalambidis, K. Varjú, K. Osvay, and G. Sansone, J. Phys. B **50**, 132002 (2017).

Chapter 11
Towards Single-Shot
XUV-Pump-XUV-Probe Studies

Check for updates

I. Orfanos, I. Makos, N. Tsatrafyllis, S. Chatziathanasiou, E. Skantzakis, D. Charalambidis and P. Tzallas

Abstract During the last decades, systematic efforts in ultra-short pulse generation led to the development of table-top sources with the capability of producing such pulses in the extreme-ultraviolet spectral range (XUV). Such pulses have been extensively exploited in the investigation of ultrafast dynamics in all states of matter. Intense XUV radiation, that can induce non-linear processes in the XUV spectral range, advance such studies through time resolved measurements performed by means of XUV-pump-XUV-probe schemes. Although these schemes, as fully perturbative, are highly beneficial for such studies, they are inherited with spectroscopic limitations held by the stability of the experimental conditions and the delay lines of the pump-probe arrangement. Here, we describe an approach which provides high temporal and spectral resolution realized in a single-shot measurement. The approach is based on a recently developed method for measuring the spatially resolved photoionization yield resulting from the interaction of XUV pulses with gas phase media.

11.1 Introduction

Gas phase high-order-harmonic (HOH) sources have been extensively used for the generation of sub-fs intense XUV pulse trains as well as isolated pulses which upon focus can reach intensities sufficient to induce observable non-linear XUV processes [1–11]. Such sources have been exploited: for quantitative studies both in the linear as

I. Orfanos · I. Makos · N. Tsatrafyllis · S. Chatziathanasiou · E. Skantzakis · D. Charalambidis
P. Tzallas (✉)
Foundation for Research and Technology—Hellas, Institute of Electronic Structure and Laser,
PO Box 1527, Heraklion (Crete) 71110, Greece
e-mail: ptzallas@iesl.forth.gr

I. Orfanos · I. Makos · N. Tsatrafyllis · S. Chatziathanasiou · D. Charalambidis
Department of Physics, University of Crete, Heraklion 71103, Greece

D. Charalambidis · P. Tzallas
ELI-ALPS, ELI-Hu Kft, Dugonics Ter 13, Szeged 6720, Hungary

well as in the non-linear XUV spectral range employing an ion-microscope device [12–15]; for pulse metrology by means of 2nd-order volume autocorrelation (2-IVAC) measurements [1, 8, 9, 16–19]; for time-resolved spectroscopy studies [20]; and for XUV-pump-XUV-probe measurements of ~1 fs scale dynamics in atomic [9] and molecular systems [21].

XUV-pump-XUV-probe schemes, as fully perturbative, have notable advantages in studies of ultrafast dynamics compared to the IR-XUV pump-probe schemes. The latter occurs as a result that XUV pulse does not effectively distort the system under investigation, since much less number of photons lead to an XUV-pump-XUV-probe process comparing to that of an IR-XUV pump-probe scheme. However, an XUV-pump-XUV-probe measurement suffers from the intrinsic restrictions that accompany any pump-probe approach which involves an interferometer. In every pump-probe experiment, the evolution of the system is determined by multi-shot measurements at different time delays between the interacting pulses. Therefore, during the data acquisition all characteristics of the pulses and the experimental conditions must remain stable. Additionally, a pump-probe scheme with few-*fs/asec* temporal resolution is limited by the spectroscopic resolution originating from the difficulty to maintain the temporal resolution for long data acquisition times and long delay values between the pump-probe pulses.

One way to overcome these obstacles is the utilization of an approach which provides high temporal and spectral resolution revealed from a single-shot measurement. This is feasible by imaging the ion distribution, produced by a two-photon process, along the propagation axis of two focused counter propagating intense XUV pulses. The principle of the approach was reported 20 years ago [22, 23] in studies investigating the dynamics of 'slow' wave packets of coherently excited high lying Rydberg states. The extension to time scales of few-fs or less was not an attainable goal due to the lack of (I) intense ultrashort XUV pulses and (II) high spatial resolution ion imaging detectors.

Here, after a brief overview on the generation and the applications of intense ultrashort XUV pulses, utilized to trace the ultrafast dynamics of atoms and molecules (Sect. 11.2); we will describe the essentials of the "Time gated ion microcopy" (Sect. 11.3) focusing particularly on aspects related to its applicability on single-shot XUV-pump-XUV-probe measurements using counter propagated XUV pulses (Sect. 11.4).

11.2 Generation of Intense XUV Pulses and Applications in Ultrafast Non-linear XUV Optics

High power XUV pulses with duration ≤ 1.5 fs, capable of inducing two-photon processes, have been already produced [9, 11, 19] and implemented in XUV-pump-XUV-probe studies of atomic [9, 11] and molecular [21] dynamics on 1 fs timescale. Figure 11.1a illustrates an experimental set-up used for the generation, character-

ization, and applications of intense ultra-short XUV pulses produced in gas phase media. The enhancement of the pulse energy is achieved by utilizing, high power fs IR pulses, loose focusing geometries, and the proper phase-matching conditions in a single gas jet configuration. Briefly, the high-harmonics are generated by focusing (with an $f = 3$ m focal length lens) a ~30 fs p-polarized IR (centered at 800 nm) laser beam acquiring energy of tens-mJ/pulse into the generation area filled with Xe by a pulsed gas jet (P-GJ). A Silicon (Si) plate, placed after the jet at the Brewster angle for the fundamental (~75°), reflects the harmonics towards the detection area, while substantially attenuating the IR field. After reflection from the Si plate, the XUV radiation passes through an aperture (A) which blocks the residual outer part of the IR beam. Subsequently, the insertion of a ~150 nm thick band pass metal filter (F) allows the spectral selection of the XUV radiation. Finally, the XUV beam is focused into the target gas jet (T-GJ) (filled with gas under investigation) by of a spherical gold mirror (SM) with 5 cm focal length. With this configuration XUV peak intensities up to 10^{14} W/cm^2 have been achieved at the focus of the XUV beam [12]. The energy of the latter in the interaction region was determined by using an XUV calibrated photodiode (PD$_{XUV}$) considering also the reflectivity of the gold spherical mirror. The harmonic spectrum was obtained by recording energy resolved photoelectron spectra (PE) resulting from the single-photon ionization of Ar after the interaction with the harmonic frequency comb. Figure 11.1b shows the harmonic spectrum filtered by a band pass Sn foil (~150 nm thick). The electron spectra have been recorded by means of a μ-metal shielded time-of-flight (TOF) ion/electron spectrometer, attached to the upper branch of the XUV beam line shown in Fig. 11.1a. The TOF can be operated recording either the photoelectron energy distribution or ion-mass spectrum. The measured PE distribution does not differ significantly from the XUV spectral distribution since in the photon energy range spanning from 15 eV to 30 eV, the single-photon-ionization cross section of Argon does not varies substantially. When a polarization gating (PG) optical arrangement [24] is introduced in the beam line, the spectrum shown in Fig. 11.1b switches form a harmonic frequency comb to continuum (Fig. 11.1c) corresponding to the generation of isolated *asec* pulses.

Using a split spherical mirror (SM) of 5 cm focal length the duration of each *asec* pulse in the pulse train (Fig. 11.1d) as well as the duration of ~1-fs isolated XUV pulses (Fig. 11.1e) were obtained after performing 2-IVAC measurements. Intense XUV continua, generated after implementing the PG approach, have been exploited for tracing the 1-fs ultrafast dynamics in Xe atoms and H$_2$ molecules (Fig. 11.2). This was achieved by recording the XUV-pump-XUV-probe trace of Xe^{2+} generated by a two-XUV-photon double ionization process and H$^+$ generated by a two-photon XUV resonant ionization-fragmentation process of H$_2$ respectively.

Although the split-mirror XUV-pump-XUV-probe arrangement has been successfully implemented for the investigation of the ultrafast dynamics of these systems, intrinsic limitations associated with the stability of the interferometer for long data acquisition as well as delay times between the pump and the probe beams hinder further studies.
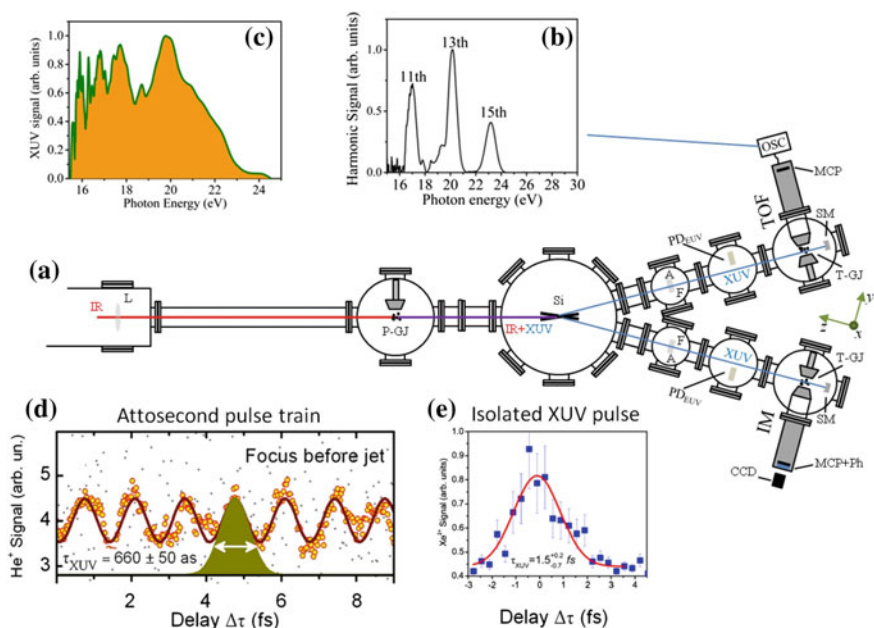
Fig. 11.1 **a** Beam line for the generation of intense XUV pulses in gas phase media. L: Lens; P-GJ: Pulsed gas jet used for the HHG; Si: Silicon plate; A: Aperture; F: Filter; PDEUV: Calibrated XUV photodiode; T-GJ: Target gas jet; TOF: Time of flight ion/electron spectrometer; IM: Ion Microscope; -SM: Split Spherical mirror; MCP: Microchannel plate detector. The y-axis is parallel to the TOF axis and the x-axis is parallel to the plane of the detector (MCP); **b** Harmonic spectrum recorded in case of using Sn filter. **c** Continuum XUV spectrum in the interaction area (Sn filter was used) when the PG optical arrangement [24] is introduced in the beam line. **d** 2nd order AC trace of an *asec* pulse train. **e** 2nd order AC trace of a ~1-fs isolated XUV pulse. Figure **a**, **b** from [12], Figure **c** from [9], Figure **d** from [17] and Figure **e** from [25]

A way to overcome the above obstacles is to utilize a XUV-pump-XUV-probe correlator which provides high temporal and spectral resolution in a single-shot measurement. The correlator relies on an approach named "Time gated ion microscopy" that provides an image of the ion distribution, produced by a two-photon process, along the propagation axis of two focused counter propagating intense XUV pulses. In the following section we present the conditions required for the successful implementation of the approach.

11.3 Time Gated Ion Microscopy

Time gated ion microscopy is a recently developed approach providing the imaging of the photoionization yield resulting from the interaction of IR/XUV ultra-short light pulses in gas phase media [15]. The aforementioned approach has been successfully
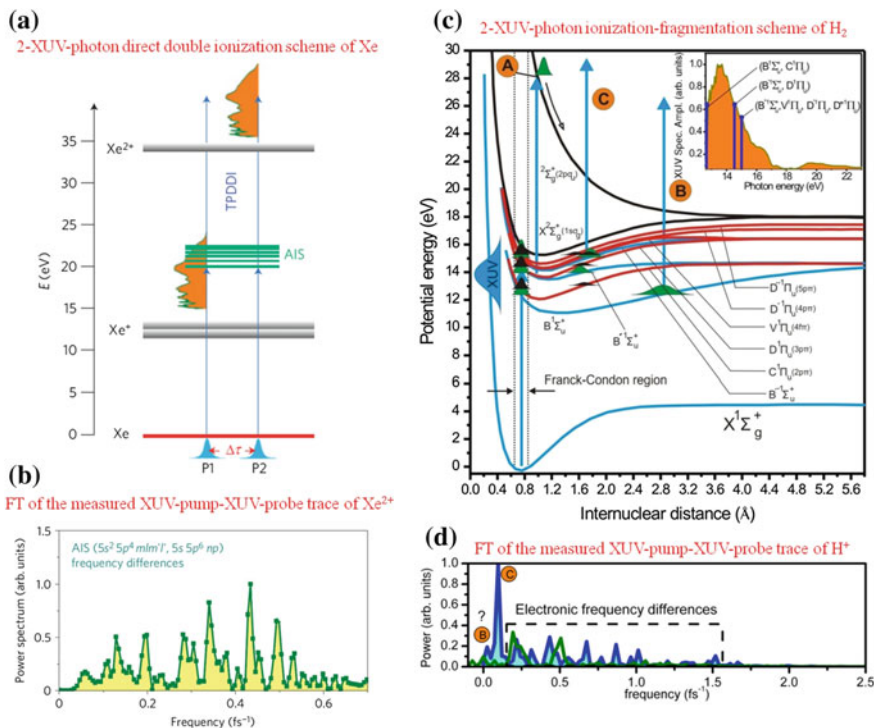
Fig. 11.2 a Two-XUV-photon direct double ionization scheme (in part through the autoionizing (AIS) manifold, induced in Xe by the interaction with the sequence of two mutually delayed intense broadband XUV pulses. The green line orange-filled area shows the spectrum used in the experiment. **b** Fourier Transform (FT) spectrum of the XUV-pump-XUV-probe trace of Xe^{2+} which reveals the frequency differences of the excited states. **c** The two-photon XUV resonant ionization-fragmentation scheme of H_2. The inset shows the XUV spectrum (green line (orange-filled area)) used in the experiment. XUV-pump-XUV-probe traces have been measured by recording the total proton yield and the non-zero kinetic energy protons. The XUV-pump-XUV-probe trace of total proton yield depicts minimum at zero delay times which is followed by a maximum at delay times of ~1 fs. The latter is attributed to the dynamics of the of the opening of the dissociation channel through $^2\Sigma_g^+$ ($2p\sigma_u$) repulsive potential (noted with "A"). **d** FT spectra of the XUV-pump-XUV-probe trace of the total (blue-filled line) and the non-zero kinetic energy (green-line) proton yield. "B" and "C" as in (**c**). The pronounced peak (noted with "C") at 0.09 fs^{-1} corresponds to half of the vibrational period of the $C^1\Pi_u$, $B'\Sigma_u^+$, $D^1\Pi_u$ (unresolved) excited states ($C^1\Pi_u$ being the main contributor). The small peak (noted with "B") at 0.04 fs^{-1} is compatible with half the vibrational period of the $B^1\Sigma_u^+$ state, but due to the limited frequency resolution such a measurement is marginal. The spectroscopic resolution of the FT spectra shown in **b** and **d** was in the range of ~0.1 eV. Figures **a**, **b** from [9] and figures **c**, **d** from [21]

implemented in quantitative studies in the linear and non-linear regime in the XUV spectral range [12–15]. These investigations are based on the "Ion Microscope" (IM), which is an ion imaging device facilitating the observation of the spatial distribution

of the ionization products produced in a focused beam as a function of their mass over charge ratio m/q, i.e. it is an ion mass spectrometer with spatial imaging capability.

A schematic representation of the IM is illustrated in Fig. 11.3a. A spherical mirror focuses the back reflected XUV radiation towards the interaction region filled with the under investigation gas. The ion distribution produced at the focus of the beam (located in the object plane) is mapped onto a position sensitive detector located at the image plane. The ionic species generated in the focusing region of the laser beam are first accelerated by an electric field applied between the repeller (being floated at a voltage of V_{rep}) and extractor electrodes (being floated at a voltage of V_{ext}). The first electrostatic lens (EL1) images the ion distribution on an intermediate ion image plane with a small magnification factor M1. This intermediate image is located at the focal plane of a second electrostatic lens (EL2) that projects a further magnified (a magnification factor of M2) image onto the detector consisting of a pair of MCPs and a phosphor screen. The image of the ion distribution which appears on the phosphor screen is magnified by a factor of $M = M1 \times M2$ and is recorded by a CCD camera. The particular IM configuration, leads to a total magnification in the range of $M \approx 150$ with a field of view $\approx 500\,\mu m$ and providing spatial resolution in the range of ≈ 270 nm. Thus the IM reveals their spatial distribution in a magnified high-resolution manner.

At this point it should be noted that an Abel transformation is required and so applied to obtain the actual size of the produced ion distribution, since the recording images are the projections of the three-dimensional ion cloud, characterized by cylindrical symmetry in the observation plane. Fragments with different times of flight (atomic ions A^+, A^{2+} or molecular ions AB^+ and fragments A^+, B^+), can be selected by gating (G) the detector (Fig. 11.3b and c). Spatially resolved ion distributions produced by one-XUV-photon and two-XUV-photon ionization process of Ar and He are shown in Fig. 11.3d and e, respectively. The ion distributions were recorded at the focus of an XUV radiation consisted from the up-converted harmonic frequencies (11–15th) of a ≈ 30 fs long IR laser pulse. The XUV beam was focused into the interaction region by a spherical gold mirror of 5 cm focal length.

Although the observation of the two-XUV-photon image in a multi-shot measurement is an important step towards the development of a single-shot XUV-pump-XUV-probe correlator, the single-shot measurement requires further enhancement of the XUV energy. A substantial increase of the XUV energy can be achieved by further improving the design of the table-top laser driven sources, implementing loose focusing geometries and quasi-phase matching conditions. Towards this direction "low" (10 Hz) and "high" (1 kHz) repetition rate XUV sources have been designed at FORTH, Lund, RIKEN, MPQ and ELI-ALPS [14, 26–29].

11.4 Single-Shot XUV-Pump-XUV-Probe Correlator

A schematic illustration of a high spatial resolution single-shot two-photon correlator is shown in Fig. 11.4a. A p-polarized high power XUV beam propagates towards the
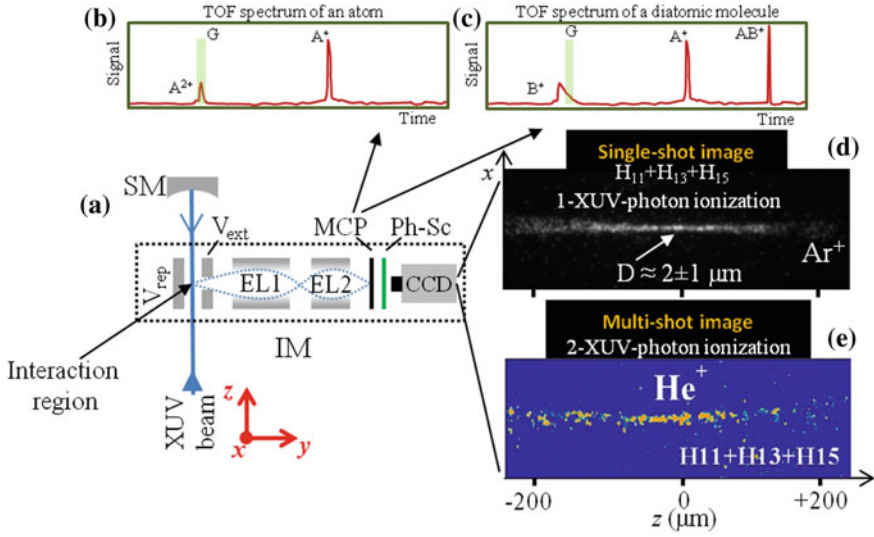
Fig. 11.3 **a** A schematic of the operation principle of the IM. The IM consists of the interaction region where an XUV laser pulse is focused and the electrostatic lenses, EL1, EL2, are used for magnifying and imaging the ion distribution produced in the interaction region on the MCP detector coupled with a phosphor screen (Ph-Sc). The image is recorded by a CCD camera. **b**, **c** A sketch of TOF mass spectra produced by the interaction of the focused beam with atoms (A) and diatomic molecules (AB), respectively. The shaded green area (G) in the mass spectra shows a temporally controlled gate which is applied on the MCP for imaging the ion distribution of a specific mass peak (m/q). **d** Single-shot ion distribution recorded at the focus of an XUV beam which contains the harmonics from 11 to 15th. The ion distribution was produced through 1-XUV-photon ionization of argon. The XUV energy at the focus was in the range of tens-nJ per pulse. In this measurement, the XUV focal spot diameter is found to be $\approx 2\,\mu$m, the spatial resolution of the device being $\approx 1\,\mu$m. **e** He + spatial ion distribution produced by a two-XUV-photon ionization process at the focus of the XUV beam. The XUV energy at the focus was in the range of hundred-nJ per pulse and the image was recorded accumulating 15,000 shots. Figures **a**–**d** from [15] and Figure **e** from [12]

single-shot two-XUV-photon correlator. A Si wedge manufactured with its surfaces at grazing angle incidence is located at the entrance of the correlator in order to split equally the XUV beam and substantially attenuating the IR pulse. The beams reflected by the Si plate XUV are transmitted through thin metal filters (F1, 2), which are implemented for XUV spectral selectivity. The two separated beams propagate towards the arms of the correlator using broadband high reflectivity XUV mirrors (*M*) and focused in the interaction region of the IM by a pair of gold SM. The sketch of the ion distribution produced by a two-XUV-photon non-linear ionization process in the region where the counter propagating XUV pulses interact with the gas medium is shown in Fig. 11.4b. It is assumed that the optical interference is taking place at $z \approx 0$ and the wave packet evolution is revealed at $z < 0$ and $z > 0$. The applicability of this approach has been explored and so tested out by the investigation of Xe$^+$ ion distribution resulting from the multi-photon ionization of Xenon atoms under the
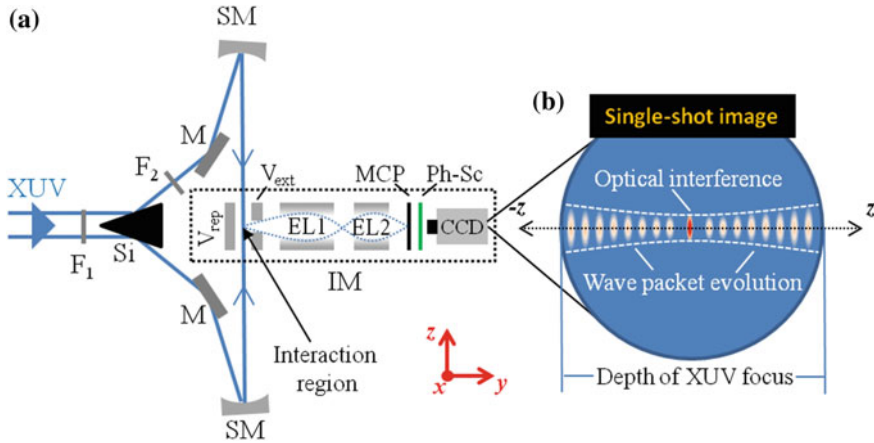
Fig. 11.4 a A schematic of the high spatial resolution single-shot two-XUV-photon correlator, showing its XUV optical set-up and the IM. Si, F1,2, M and SM are a silicon wedge, thin metal filters, mirrors and spherical mirrors, respectively. **b** A sketch of the imaged ion distribution along the propagation axis of the counter propagating pulses showing the areas where the optical interference ($z \approx 0$) and the wave packet evolution ($z < 0$ and $z > 0$) is taking place. Figure from [15]

influence of two counter propagating few-cycle mid-IR laser pulses with a central wavelength of 2.1 μm [15] and in UV spectral region by recording O_2^+ using UV pulses in the 20 fs range etc. [30–32].

Using the specifications of the IM as described in Sect. 11.3., a $\approx$500 μm long ion distribution can be resolved with $\approx$270 nm resolution i.e. the wave packet evolution can be traced with 2 fs resolution over a few-*psec* delay range resulting in a spectral resolution of $\approx$1 meV. The feasibility of recording a single-shot image induced by a two-XUV-photon process (hereafter called a 'non-linear single-shot image'), using few-fs XUV pulses with power of about 1 GWatt/pulse ($\tau_{XUV} = 1$ fs and $E_{XUV} = 1$ μJ/pulse), can be evaluated taking into account the conditions at which the image of Fig. 11.3e was recorded. The image of Fig. 11.3e was recorded by accumulating $\approx$15 000 shots, when an XUV beam with power $\sim$0.01 GWatt/pulse was focused (with $f = 5$ cm spherical mirror) into a He gas. The peak intensity of this XUV radiation at the focusing region was $\sim$10^{14} W/cm². In case of implementing an $\approx$1 GWatt/pulse XUV pulse and the correlator shown in Fig. 11.4 with focusing mirrors of $f = 40$ cm, intensities up to $I_{XUV} \approx 10^{15}$ W/cm² can be reached in the interaction region. These levels of intensity can lead to a 'non-linear single-shot image' with a signal much stronger compared to the 'non-linear image' of Fig. 11.3e and sufficient for performing single-shot XUV-pump-XUV-probe studies [for details see 15].

The temporal evolution of the wave packet can be directly obtained from the measured single-shot image induced by the counter propagating XUV beams. This relies on the fact that each position of the image along the propagation axis (z) corresponds to a specific delay value between the pump and the probe pulses according to the relation $\Delta T = 2z/c$ (where ΔT is the difference in the pulse delay for particles

which are separated by a distance z). The ion distribution (Fig. 11.4b) at $z = 0$ (zero delay between the pump and the probe pulses) contains information about the optical interference (i.e. duration of the XUV pulses when the pump and the probe pulses are identical) between the pump-probe pulses. For example, for an IM with spatial resolution of ≈ 270 nm, XUV pulses with a duration down to ≈ 2 fs can be measured. The modulation of the ion distribution (Fig. 11.4b) at $z < 0$ and $z > 0$ reflects the wave packet evolution. For identical XUV pulses the image will be symmetric with respect to $z = 0$ position. Considering that a sufficient amount of ions can be produced along a field of view ≈ 500 μm, it can be estimated that the evolution of the wave packet can be recorded with spectral resolution of ≈ 1 meV in the range of ≈ 3 psec. We note that the choice of the SM focal length f is of crucial importance since it is associated with (I) the aberrations of the XUV at the focus, (II) the XUV intensity in the interaction region and (III) the spectral resolution of the measurement which is inversely proportional to the maximum delay values at which the wave-packet evolution can be studied.

11.5 Conclusions

Summarizing, the operation principle and the requirements for the development of a single-shot XUV-pump-XUV-probe correlator which can be used for ultrafast time resolved studies with high spectral resolution is presented. The correlator relies on the imaging of the ion distribution, produced by a two-XUV-photon ionization non-linear process along the propagation axis of two focused counter propagating intense XUV pulses. This is based on the recently developed approach of the "Time gated ion microscopy" that has been successfully implemented for the spatially resolved photoionization yield investigations resulting from the linear and non-linear interaction of gas phase media with XUV harmonic pulses. We estimate, that for ~1 GWatt XUV pulses of ≈ 1 fs duration, the wave packet evolution can be recorded with temporal and spectral resolution of ≈ 2 fs and ≈ 1 meV, respectively, in a single-shot measurement.

References

1. Y. Kobayashi, T. Ohno, T. Sekikawa, Y. Nabekawa, S. Watanabe, Appl. Phys. B **70**, 389 (2000)
2. N.A. Papadogiannis, L.A.A. Nikolopoulos, D. Charalambidis, G.D. Tsakiris, P. Tzallas, K. Witte, Phys. Rev. Lett. **90**, 133902 (2003)
3. N.A. Papadogiannis, L.A.A. Nikolopoulos, D. Charalambidis, G.D. Tsakiris, P. Tzallas, K. Witte, Appl. Phys. B **76**, 721 (2003)
4. N. Miyamoto, M. Kamei, D. Yoshitomi, T. Kanai, T. Sekikawa, T. Nakajima, S. Watanabe, Phys. Rev. Lett. **93**, 083903 (2004)
5. Y. Nabekawa, H. Hasegawa, E.J. Takahashi, K. Midorikawa, Phys. Rev. Lett. **94**, 043001 (2005)
6. E.P. Benis, D. Charalambidis, T.N. Kitsopoulos, G.D. Tsakiris, P. Tzallas, Phys. Rev. A **74**, 051402(R) (2006)

7. E.P. Benis, P. Tzallas, L.A.A. Nikolopoulos, M. Kovacev, C. Kalpouzos, D. Charalambidis, G.D. Tsakiris, New J. Phys. **8**, 92 (2006)
8. K. Midorikawa, Y. Nabekawa, A. Suda, Prog. Quant. Elect. **32**, 43 (2008)
9. P. Tzallas, E. Skantzakis, L.A.A. Nikolopoulos, G.D. Tsakiris, D. Charalambidis, Nat. Phys. **7**, 781 (2011)
10. B. Manschwetus, L. Rading, F. Campi, S. Maclot, H. Coudert-Alteirac, J. Lahl, H. Wikmark, P. Rudawski, C.M. Heyl, B. Farkas, T. Mohamed, A. L'Huillier, P. Johnsson, Phys. Rev. A **93**, 061402(R) (2016)
11. S. Chatziathanasiou, S. Kahaly, E. Skantzakis, G. Sansone, R. Lopez-Martens, S. Haessler, K. Varju, G.D. Tsakiris, D. Charalambidis, P. Tzallas, Photonics **10**, 3390 (2017)
12. N. Tsatrafyllis, B. Bergues, H. Schröder, L. Veisz, E. Skantzakis, D. Gray, B. Bodi, S. Kuhn, G.D. Tsakiris, D. Charalambidis, P. Tzallas, Sci. Rep. **6**, 21556 (2016)
13. G. Kolliopoulos, B. Bergues, H. Schröder, P.A. Carpeggiani, L. Veisz, G.D. Tsakiris, D. Charalambidis, P. Tzallas, Phys. Rev. A **90**, 013822 (2014)
14. B. Bergues, D.E. Rivas, M. Weidman, A.A. Muschet, W. Helml, A. Guggenmos, V. Pervak, U. Kleineberg, G. Marcus, R. Kienberger, D. Charalambidis, P. Tzallas, H. Schröder, F. Krausz, L. Veisz, Optica **5**, 237 (2018)
15. P. Tzallas, B. Bergues, D. Rompotis, N. Tsatrafyllis, S. Chatziathanassiou, A. Muschet, L. Veisz, H. Schröder, D. Charalambidis, J. Opt. **20**, 024018 (2018)
16. P. Tzallas, D. Charalambidis, N.A. Papadogiannis, K. Witte, G.D. Tsakiris, Nature **426**, 267 (2003)
17. J.E. Kruse, P. Tzallas, E. Skantzakis, C. Kalpouzos, G.D. Tsakiris, D. Charalambidis, Phys. Rev. A **82**, 021402(R) (2010)
18. P. Tzallas, E. Skantzakis, D. Charalambidis, J. Phys. B **45**, 7 (2012)
19. E.J. Takahashi, P.F. Lan, O.D. Mucke, Y. Nabekawa, K. Midorikawa, Nat. Comm. **4**, 2691 (2013)
20. E. Skantzakis, P. Tzallas, J.E. Kruse, C. Kalpouzos, O. Faucher, G.D. Tsakiris, D. Charalambidis, Phys. Rev. Lett. **105**, 043902 (2010)
21. P.A. Carpeggiani, P. Tzallas, A. Palacios, D. Gray, F. Martín, D. Charalambidis, Phys. Rev. A **89**, 023420 (2014)
22. M.B. Campbell, T.J. Bensky, R.R. Jones, Opt. Exp. **1**, 197 (1997)
23. M.B. Campbell, T.J. Bensky, R.R. Jones, Phys. Rev. A **59**, 4117(R) (1999)
24. P. Tzallas, E. Skantzakis, C. Kalpouzos, E.P. Benis, G.D. Tsakiris, D. Charalambidis, Nat. Phys. **3**, 846 (2007)
25. P. Tzallas, E. Skantzakis, D. Charalambidis, J. Phys. B **45**, 074007 (2012)
26. A. Nayak, I. Orfanos, I. Makos, M. Dumergue, S. Kühn, E. Skantzakis, B. Bodi, K. Varju, C. Kalpouzos, H.I.B. Banks, A. Emmanouilidou, D. Charalambidis, P. Tzallas, Phys. Rev. A **98**, 023426 (2018)
27. F. Brizuela, C.M. Heyl, P. Rudawski, D. Kroon, L. Rading, J.M. Dahlström, J. Mauritsson, P. Johnsson, C.L. Arnold, A. L'Huillier, Sci. Rep. **3**, 1410 (2013)
28. K. Midorikawa, Y. Nabekawa, A. Suda, Prog. Quant. Electr. **32**, 43 (2008)
29. S. Kühn, M. Dumergue, S. Kahaly, S. Mondal, M. Füle, T. Csizmadia, B. Farkas1, B. Major, Z. Várallyay, E. Cormier, M. Kalashnikov, F. Calegari, M. Devetta, F. Frassetto, E. Månsson, L. Poletto, S. Stagira, C. Vozzi, M. Nisoli, P. Rudawski, S. Maclot, F. Campi, H. Wikmark, C. L Arnold, C. M Heyl, P. Johnsson, A. L'Huillier, R. Lopez-Martens, S. Haessler, M. Bocoum, F. Boehle, A. Vernier, G. Iaquaniello, E. Skantzakis, N. Papadakis, C. Kalpouzos, P. Tzallas, F. Lépine, D. Charalambidis, K. Varjú1, K. Osvay, G. Sansone, J. Phys. B **50**, 132002 (2017)
30. D. Rompotis, A. Baumann, O. Schepp, T. Maltezopoulos, M. Wieland, M. Drescher, Optica **4**, 871 (2017)
31. A. Baumann, S. Bazzi, D. Rompotis, O. Schepp, A. Azima, M. Wieland, D. Popova-Gorelova, O. Vendrell, R. Santra, M. Drescher, Phys. Rev. A **96**, 013428 (2017)
32. D. Rompotis, T. Gebert, M. Wieland, F. Karimi, M. Drescher, Opt. Lett. **40**, 1675 (2015)